TECHNISCHE UNIVERSITÄT MÜNCHEN

Lehrstuhl für Anorganische Chemie mit Schwerpunkt Neue Materialien

Substitution Effects in Alkali Metal Silicides and Germanides

Synthesis and Characterization of New Ternary and Quaternary Phases as Precursors for Semiconducting Materials

Lavinia Maria Scherf

Vollständiger Abdruck der von der Fakultät für Chemie der Technischen Universität München zur Erlangung des akademischen Grades eines

Doktors der Naturwissenschaften (Dr. rer. nat.)

genehmigten Dissertation.

Vorsitzender: Univ.-Prof. Dr. Michael Groll

Prüfer der Dissertation:

1. Univ.-Prof. Dr. Thomas F. Fässler
2. Univ.-Prof. Dr. Tom Nilges
3. Univ.-Prof. Dr. Leo van Wüllen

Die Dissertation wurde am 23.02.2017 bei der Technischen Universität München eingereicht und durch die Fakultät für Chemie am 15.03.2017 angenommen.

“Human beings are now carrying out a large scale geophysical experiment of a kind that could not have happened in the past nor be reproduced in the future. “

ROGER REVELLE (1909–1991), UNIVERSITY OF CALIFORNIA, SAN DIEGO

Danksagung

Zuallererst möchte ich mich bei meinem Doktorvater **Prof. Thomas Fässler** für die Aufnahme in die Arbeitsgruppe, das spannende Forschungsthema sowie die immer konstruktive Zusammenarbeit in angenehmer Arbeitsatmosphäre ganz herzlich bedanken.

Diese Arbeit wäre ohne die organisatorische, fachliche und persönliche Unterstützung vieler Kollegen nicht möglich gewesen. Mein Dank gilt daher:

Manuela Donaubauer, der Seele des Lehrstuhls, für die immer freundliche und verlässliche Hilfe und Unterstützung bei allen organisatorischen Fragen.

Michael Zeilinger, durch den ich an den Lehrstuhl gekommen bin, für die gute Zusammenarbeit und Betreuung insbesondere während meiner Masterarbeit und des Beginns meiner Promotion.

meinen Masteranden **Matthew Sammon**, **Nathalie Riphaus** und **Tassilo Restle** sowie meinen Forschungspraktikanten **Marius Bilke**, **Tassilo Restle**, **Max Schütz** und **Sebastian Hölzl** für die engagierte Mitarbeit und Unterstützung bei meinen Forschungsprojekten.

Annette Schier und **Prof. Florian Kraus** für die jederzeit gute Zusammenarbeit, insbesondere auch bei der Betreuung des AC1 Praktikums.

Maria Müller für die gute Zusammenarbeit bei der Betreuung des DSC-Messgeräts.

Felix Geitner, **Alexander Henze**, **Laura Jantke**, **Viktor Hlukkhy** und **Wilhelm Klein** für hilfreiche Diskussionen.

meinen Bürokollegen **Michael Zeilinger**, **Andrea Hoffmann**, **Patrick Woidy**, **Maria Müller**, **Felix Geitner**, **Christina Fischer** und **Sabine Frischhut** für die angenehme und konstruktive Arbeitsatmosphäre sowie den Niederbayrisch-Grundkurs.

allen Mitgliedern der **Arbeitsgruppen Fässler und Nilges** für die schöne Zeit in der Uni aber vor allem auch bei Konferenzreisen, Wanderungen, Radtouren und Skiwochenenden.

Oliver Pecher von der University of Cambridge und **Holger Kirchhain** von der Universität Augsburg für die immer angenehme, hervorragend funktionierende und letztlich sehr erfolgreiche Kooperation bei NMR-Experimenten für verschiedene Forschungsprojekte.

Kent Griffith, **Pieter Magusin**, **Prof. Clare Grey** von der University of Cambridge, **Prof. Leo van Wüllen** von der Universität Augsburg sowie **Gabriele Raudaschl-Sieber** für die Unterstützung bei NMR-Experimenten, quantenchemischen Berechnungen sowie beim Verfassen von Publikationen.

Prof. Antti Karttunen von der Aalto University für die sehr angenehme und erfolgreiche Zusammenarbeit im Bereich der quantenchemischen Rechnungen als Unterstützung meiner experimentellen Ergebnisse.

Prof. Ulrich Häussermann von der Universität Stockholm für die immer konstruktive Zusammenarbeit, für hilfreiche Diskussionen und die Unterstützung meines Forschungsaufenthaltes an der Arizona State University.

Kurt Leinenweber und **Craig Naseyowma** von der Arizona State University für die Unterstützung bei Hochdruck-Hochtemperatursynthesen.

Gero Neubüser und **Prof. Lorenz Kienle** von der Christian-Albrechts-Universität zu Kiel für die zuverlässige Kooperation und die Durchführung von TEM-Analytik.

Tobias Helbich und **Prof. Bernhard Rieger** sowie **Haoyang Yu** und **Prof. Jonathan Veinot** von der University of Alberta für die sehr fruchtbare Zusammenarbeit im Bereich der Silicium-und Germanium-Schichten.

Johannes Hattendorff, **Irmgard Buchberger**, **Sebastian Geier** und **Prof. Hubert Gasteiger** für die fortwährende Kooperation und Unterstützung bei elektrochemischen Untersuchungen.

Maria Müller und **Katia Rodewald** für die Durchführung von EDX-Messungen.

Herta Slavik und **Sebastian Geier** für die Durchführung von Raman-Messungen.

Andrea Hoffmann, **Gergana Nenova** und **Marina Boyko** für die Durchführung von magnetischen Messungen.

dem **Fonds der chemischen Industrie**, der **Studienstiftung des deutschen Volkes**, der **TUM Graduate School** sowie der TU München (**Laura-Bassi Preis**) für die finanzielle und ideelle Förderung meiner Promotion.

allen **Mitarbeitern der TU München**, die zum Gelingen dieser Arbeit beigetragen haben.

Ohne meine Freunde und Freizeitaktivitäten wäre meine Promotionszeit mit Sicherheit nicht halb so schön gewesen. Deshalb möchte ich mich auch besonders bedanken bei:

den Mitgliedern des **Abaco-Orchesters** für die intensive gemeinsam erlebte Zeit bei vielen tollen Projekten und den perfekten Ausgleich zum Alltag.

meinen Unifreunden (**Mahlzeit!**) für gemeinsames Lernen schon im Studium, intensive Diskussionen, Gespräche beim Mittagessen, gemeinsame Sport-, Ess- und Spieleabende, viele schöne Feiern sowie unvergessliche Ausflüge und Urlaube.

meiner besten Freundin **Julia** für ihre Unterstützung in allen Lebenslagen.

Ein besonderer Dank gilt auch meiner ganzen Familie, die mich schon mein ganzes Leben lang immer vorbehaltslos unterstützt. Insbesondere danke ich:

Mama und **Papa**, die mir so vieles ermöglicht haben.

Korbinian und **Benedikt**, die mich immer wieder auf den Boden der Tatsachen zurückholen.

Oma Josi und **Caspar-Heinrich** für viele schöne Pausenstopps auf meinen Fahrten zwischen München und Uedem sowie die große Hilfe bei Hochzeitsvorbereitungen und Jobsuche.

Zum Abschluss gebührt mein allergrößter Dank meinem Ehemann **Jens**, der mich liebt, der mich unterstützt und stärkt, der mich immer wieder daran erinnert, dass Arbeit nicht das Wichtigste im Leben ist und mit dem ich nun schon elf wunderbare gemeinsame Jahre verbracht habe. Ich freue mich sehr auf unsere gemeinsame Zukunft im nächsten Lebensabschnitt!

Zusammenfassung

Der derzeitige Klimawandel mit seinen potenziell dramatischen Folgen ist heute eine der größten globalen Bedrohungen. Um das Ziel, die globale Erwärmung im Vergleich zu vorindustriellen Zeiten unterhalb von 2 °C zu halten, muss die Atmosphärenkonzentration des Treibhausgases CO_2 reduziert werden. Dafür ist es notwendig, fossile durch erneuerbare Energiequellen zu ersetzen.

Dabei kann das ungefährliche, billige und reichlich vorkommende Element Silicium eine entscheidende Rolle spielen. Elementares Silicium ist heute schon das wichtigste Material für die Gewinnung von Solarenergie und verspricht hohe Energiedichten als Anodenmaterial in Lithiumionenbatterien. Das schwerere Homologe Germanium ist seltener und teurer, bietet aber mindestens ebenso gute Eigenschaften für Halbleiter- und Batterieanwendungen. Um die wirtschaftliche Umsetzbarkeit dieser Technologien zu verbessern, werden neue Materialien benötigt, die die noch bestehenden Probleme lösen können.

Zintl-Phasen sind bewiesenermaßen geeignete Vorläufer für neue Modifikationen und Morphologien von Silicium und Germanium. Um die Auswahl an geeigneten Ausgangsmaterialien zu vergrößern, wurden die Effekte von partiellen Substitutionen in Alkalimetallsiliciden und –germaniden erforscht. Die homologe Substitution der Alkalimetalle, also der kationischen Komponente, soll neue anionische Teilstrukturen stabilisieren, die sich als Vorläufer für neue Elementmodifikationen und –morphologien eignen. Durch die Substitution der Tetrelelemente, also der anionischen Komponente, sollen geeignete Vorläuferphasen für gemischte Tetrelmaterialien erhalten werden. Die (opto-)elektronischen Eigenschaften solcher Materialien könnten durch das Elementverhältnis optimal für Anwendungen etwa in der Halbleitertechnik angepasst werden. So verringert etwa die zunehmende Beimischung von Germanium zu $Si_{1-x}Ge_x$ mit Diamantstruktur die Bandlücke der festen Lösung.

Durch Substitutionen der kationischen Komponenten wurden einige neue Zintl-Phasen entdeckt. Sie beinhalten anionische Teilstrukturen, die in binären Systemen so nicht bekannt sind. Im System Li-Na-Ge wurden mit $Li_{18}Na_2Ge_{17}$, Li_3NaGe_2 und Na_7LiGe_8 die bisher ersten Verbindungen überhaupt gefunden. In $Li_{18}Na_2Ge_{17}$ liegen drei verschiedene Zintl-Anionen (Friauf-Polyeder $[Li@Li_4Ge_{12}]^{7-}$, Tetraeder $[Ge_4]^{4-}$ und isolierte Anionen Ge^{4-}) nebeneinander vor. Die Zintl-Phase Li_3NaGe_2 enthält anionische $[Ge_2]^{4-}$-Dimere mit außergewöhnlich kurzen Ge-Ge-Bindungen. Quantenmechanische Berechnungen und Festkörper-NMR-Experimente legen eine Ge=Ge-Doppelbindung nahe. Damit ist Li_3NaGe_2 ein Festkörperäquivalent von molekularem Sauerstoff O_2. Na_7LiGe_8 enthält $[Ge_4]^{4-}$-Tetraeder, die über η^3-koordinierende Li-Atome zu Dimeren verbrückt sind. Der Strukturtyp ist bereits von einigen ternären und quaternären Alkalimetallsiliciden und –germaniden bekannt.

Im System K-Na-Si wurden die Zintl-Phasen $K_{4-x}Na_xSi_4$ ($1 \le x \le 2.2$) und K_7NaSi_8 gefunden. Sie enthalten beide $[Si_4]^{4-}$Tetraeder und K_7NaSi_8 ist isostrukturell zu Na_7LiGe_8. Während K_7NaSi_8 eine stöchiometrisch exakte Verbindung ist, in der K und Na vollständig geordnet vorliegen, bildet $K_{4-x}Na_xSi_4$ eine feste Lösung mit variierenden Alkalimetallverhältnissen aus. Die ternäre Phase $Li_{12-y}Na_ySi_7$ ($0 \le y \le 0.5$) weist ebenfalls statistisch gemischte Alkalimetallpositionen auf.

Durch Mischung von Si und Ge in der anionischen Komponente wurden feste Lösungen $Li_{12}Si_{7-x}Ge_x$ ($0 \le x \le 7$), $Na_7LiSi_{8-z}Ge_z$ ($1.3 \le z \le 8$), und $Li_3NaSi_{6-v}Ge_v$ ($0 \le v \le 0.5$) erhalten. In $Li_{12}Si_{7-x}Ge_x$ und $Na_7LiSi_{8-z}Ge_z$ sind die Tetrelelemente über einen weiten Zusammensetzungsbereich mischbar, während nur geringe Mengen an Ge in $Li_3NaSi_{6-v}Ge_v$ eingebaut werden können. In allen drei Phasen teilen sich Silicium- und Germaniumatome die kristallografischen Positionen und Ge besetzt bevorzugt

die formal negativer geladenen Stellen. Versuche, Silicium mit Bor in ternären Li-B-Si Verbindungen zu mischen, ergaben ausschließlich bereits bekannte Phasen.

Darüber hinaus wurden weitere Lithiumverbindungen mit den leichten Elementen Bor und Kohlenstoff untersucht. In Anwesenheit der Templatverbindung Li_3N wurde der Lithiumionenleiter $Li_6B_{18}(Li_3N)_x$ mit offener Gerüststruktur erhalten. Dieser zeichnet sich durch eine extrem hohe Lithiumionenmobilität aus. Die Templatspezies lässt sich unter Erhalt der Gerüststruktur durch Extraktion mit Ethanol teilweise entfernen. Berechnung der elektronischen Struktur von $Li_6B_{18}(Li_3N)$ ergibt einen Halbleiter mit kleiner, indirekter Bandlücke. Die chemisch inspirierte Konstruktion von strukturanalogem $B_{12}C_6$ hingegen lässt einen Halbleiter mit deutlich größerer Bandlücke erwarten. Im System Li-C wurde ein neues binäres Lithiumcarbid entdeckt, dessen Struktur noch aufzuklären ist. Die bisherigen Analyseergebnisse weisen auf die Anwesenheit von mindestens mittelgroßen Kohlenstoff-Polyanionen mit konjugierten Doppelbindungen oder anellierten Aromaten hin.

Weiterhin wurden verschiedene (Erd-)Alkalimetalle als Ausgangsmaterialien für neue Materialien verwendet. Li_3NaSi_6 und $Li_3NaSi_{6-v}Ge_v$ ($v \approx 0.5$) wurden zu amorphen Materialien umgesetzt, die im Vergleich mit aus $Li_{15}Si_4$ hergestelltem amorphen Silicium sorgfältig untersucht wurden. Das amorphe $Si_{1-x}Ge_x$ enthält Si–Si, Si–Ge und Ge–Ge-Bindungen, wie durch Raman-Spektroskopie gezeigt wurde. Damit liegen die Tetrelelemente tatsächlich auf atomarer Ebene gemischt vor. Heterogene Reaktionen von Alkalimetallsiliciden und –germaniden mit Borhalogenidlösungen ergaben amorphe Produkte. Dabei fungiert das Borhalogenid lediglich als Oxidationsmittel. Ein Einbau von Bor in die Tetrelstrukturen wurde nicht beobachtet.

In elektrochemischen Studien an Lithiumhalbzellen wurde gezeigt, dass Li_7Ge_{12} nicht nur chemisch, sondern auch elektrochemisch in *allo*-Ge umgewandelt werden kann. Diese ungewöhnliche Germaniummodifikation durchläuft als Anodenmaterial die gleichen Phasenumwandlungen wie α-Ge. Allerdings weist sie eine deutlich geringe Zyklenstabilität auf, was möglicherweise auf die unterschiedlichen Morphologien der beiden Allotrope zurückgeführt werden kann. Darüber hinaus wurde die Synthese von $CaSi_2$ optimiert, sodass sehr reine zweidimensionale Polysilanschichten hergestellt werden konnten. Funktionalisierung der Silicium-Nanoschichten mittels radikalischer Hydrosilylierung mit Alkenen führt zur Stabilisierung und Delaminierung der Schichtstrukturen.

Abstract

The ongoing climate change with its potentially dramatic impacts represents one of today's biggest global threats. In order to meet the goal of keeping global warming below 2 °C with respect to pre-industrial times, the atmospheric content of the greenhouse gas CO_2 must be lowered. Thus, a shift from fossil to renewable energy sources is necessary.

Silicon as a non-hazardous, cheap and highly abundant element can play a decisive role in this shift. Elemental silicon is already the most important material for solar energy generation and promises high energy densities as an anode material in lithium ion batteries. Its heavier homologue germanium is scarcer and more expensive, but also offers great properties for semiconductor and battery applications. To improve the economic feasibility of these technologies, new materials are needed, which can mitigate the remaining problems.

Zintl phases have already proven to be suitable precursors for new modifications and morphologies of silicon and germanium. In order to broaden the selection of possible precursors, the effects of partial substitutions in alkali metal silicides and germanides were studied. Homologous substitutions of the alkali metals, representing the cationic component, can stabilize novel anionic substructures, which could function as precursors for new element modifications and morphologies. Substitution of the tetrel element, which represents the anionic component, aims for suitable precursors for mixed tetrel materials. The (opto-)electronic properties of such materials could be optimized for applications, e.g. in semiconductor technologies by changing the ratio of the elements. Thus, an increasing germanium content in $Si_{1-x}Ge_x$ with diamond structure lowers the bandgap of the solid solution.

By substitutions of the cationic component, several new Zintl phases were found. They comprise anionic substructures, which are not known from binary systems. In the Li-Na-Ge system, $Li_{18}Na_2Ge_{17}$, Li_3NaGe_2, and Na_7LiGe_8 are the first compounds to be reported. In $Li_{18}Na_2Ge_{17}$, three different Zintl anions (Friauf polyhedra $[Li@Li_4Ge_{12}]^{7-}$, tetrahedra $[Ge_4]^{4-}$ and isolated anions Ge^{4-}) exist next to each other. The Zintl phase Li_3NaGe_2 contains anionic $[Ge_2]^{4-}$ dimers with extraordinarily short Ge-Ge bonds. Quantum mechanical calculations and solid-state NMR experiments suggest a Ge=Ge double bond. Thus, Li_3NaGe_2 represents a solid-state equivalent of molecular oxygen O_2. Na_7LiGe_8 comprises $[Ge_4]^{4-}$ tetrahedra, which are bridged to dimers by η^3-coordinating lithium atoms. This structure type is well known from several ternary and quaternary alkali metal silicides and germanides.

In the K-Na-Si system the Zintl phases $K_{4-x}Na_xSi_4$ ($1 \le x \le 2.2$) and K_7NaSi_8 were found. They both contain $[Si_4]^{4-}$ tetrahedra and K_7NaSi_8 is isostructural with Na_7LiGe_8. While K_7NaSi_8 is a stoichiometrically exact compound in which K and Na are fully ordered, $K_{4-x}Na_xSi_4$ forms a solid solution with varying alkali metal contents. Similarly, the ternary phase $Li_{12-y}Na_ySi_7$ ($0 \le y \le 0.5$) also contains statistically mixed alkali metal positions.

Using mixtures of Si and Ge for the anionic components, the solid solutions $Li_{12}Si_{7-x}Ge_x$ ($0 \le x \le 7$), $Na_7LiSi_{8-z}Ge_z$ ($1.3 \le z \le 8$), and $Li_3NaSi_{6-v}Ge_v$ ($0 \le v \le 0.5$) were obtained. In $Li_{12}Si_{7-x}Ge_x$ and $Na_7LiSi_{8-z}Ge_z$, the tetrel elements are miscible over a broad compositional range, whereas only limited amounts of Ge can be incorporated into $Li_3NaSi_{6-v}Ge_v$. In all three phases, silicon and germanium atoms share crystallographic positions and Ge preferentially occupies formally more negative sites. Attempts to mix Si with B in ternary Li-B-Si compounds yielded only phases that were previously known.

Additionally, Li compounds with the light elements boron and carbon were investigated. In the presence of the template compound Li_3N, the lithium ion conductor $Li_6B_{18}(Li_3N)_x$ was obtained, featuring an open framework structure. It is characterized by an extremely high Li ion mobility. When partially removing the template species by extraction with ethanol, the framework structure is retained. Electronic structure calculations of $Li_6B_{18}(Li_3N)$ suggest a semiconductor with a small, indirect band gap. In contrast, chemically inspired construction of $B_{12}C_6$ with analogous structure anticipates a semiconductor with a much larger, direct band gap. In the Li-C system, a novel binary lithium carbide was discovered. Its structure is yet to be determined. Various characterization methods indicate the presence of at least medium-sized carbon polyanions with conjugated double bonds or fused aromatic rings.

Furthermore, different alkali and earth alkaline metal tetrelides were used as precursors for novel materials. Li_3NaSi_6 and $Li_3NaSi_{6-v}Ge_v$ ($v \approx 0.5$) were converted to amorphous materials, which were carefully characterized in comparison with amorphous Si prepared from $Li_{15}Si_4$. Amorphous $Si_{1-x}Ge_x$ contains Si–Si, Si–Ge, and Ge–Ge bonds as shown by Raman spectroscopy. Thus, the elements are indeed mixed on an atomic level. Heterogeneous reactions of alkali metal silicides and germanides with boron halide solutions yielded amorphous materials. The boron halide functions only as an oxidizing agent. An incorporation of boron into the tetrel structures was not observed.

Electrochemical studies in lithium half-cells demonstrated that Li_7Ge_{12} can be converted to *allo*-Ge not only chemically but also electrochemically. The unusual Ge modification undergoes the same phase transformations as conventional α-Ge when used as an anode material. However, it exhibits significantly poorer cycling stability, which could be attributed to the different morphologies of the two allotropes. In addition, the synthesis of $CaSi_2$ was optimized so that very pure two-dimensional polysilane sheets could be prepared. Functionalization of the silicon nanosheets with alkenes using radical hydrosilylation led to stabilization and exfoliation of the sheet-like structures.

List of Abbreviations

4-DDB	4-decylbenzene diazonium tetrafluoroborate
A	alkali metal
AFM	atomic force microscopy
AIBN	azobisisobutyronitrile
ASA	atomic sphere approximation
CMIP5	Coupled Model Intercomparison Project Phase 5, collection of climate models
COHP	crystal orbital Hamiltonian population
DMSO	dimethyl sulfoxide
DOS	density of states
DSC	differential scanning calorimetry
DTAC	dodecyltrimethylammoniumchloride
E	alkaline earth metal
EDX	energy-dispersive X-ray spectroscopy
EEG	Erneuerbare-Energien-Gesetz, Renewable Energy Sources Act
EELS	electron energy loss spectroscopy
E_F	Fermi level
EN	electronegativity
EPFS	electron-poor framework semiconductor
EV	electric vehicle
H	magnetic field
IPCC	International Panel on Climate Change
IR	infrared
LDA	local density approximation
LGPS	$Li_{10}GeP_2S_{12}$
LIB	lithium ion battery
LISICON	lithium superionic conductor
LMTO	linear muffin-tin orbital
M	metal
M_g	mass magnetization

MAS	magic angle spinning
MO	molecular orbital
NHB	*N*-heterocyclic borane
NHC	*N*-heterocyclic carbene
NMR	nuclear magnetic resonance
OTF	open tetrahedral framework
PDF	pair distribution function
PMMA	poly(methyl methacrylate)
Pn	pnictogen element
PV	photovoltaics
PXRD	powder X-ray diffraction
RT	room temperature
SAED	selected area electron diffraction
SCXRD	single crystal X-ray diffraction
SEM	scanning electron microscopy
*t*BuMA	*tert*-butyl methacrylate
T	tetrel element, typically referring to silicon and germanium
T_1	spin-lattice relaxation time
TB	tight-binding
TEM	transmission electron microscopy
TGA	thermogravimetric analysis
THF	tetrahydrofurane
Tp	template
Tr	triel element
UV	ultraviolet
VEC	valence electron concentration
X_g	mass magnetic susceptibility

Table of Contents

Danksagung II
Zusammenfassung IV
Abstract VI
List of Abbreviations VIII
1 INTRODUCTION 1
1.1 Silicon and Germanium and Their Relevance in the Context of Renewable Energy 2
1.1.1 Anthropogenic Global Warming 2
1.1.2 Renewable Energy Technologies 3
1.1.3 Silicon, Germanium, and Renewable Energy Materials 4
1.2 Zintl phases 8
1.2.1 Definition and Characteristics 8
1.2.2 Alkali Metal Silicides and Germanides 8
1.2.3 Precursors for Novel Materials 11
1.3 Substitution Effects in Zintl Phases 15
1.3.1 General Trends and Issues 15
1.3.2 Cation Substitution 15
1.3.3 Anion Substitution 17
1.4 Scope and Outline 20
1.5 References 22
2 EXPERIMENTAL SECTION 29
2.1 Synthesis 30
2.1.1 Sample Handling 30
2.1.2 Starting Materials 30
2.1.3 High-Temperature Syntheses 30
2.1.4 Flux Synthesis 32
2.1.5 Arc Furnace Reactions 33
2.1.6 Mechanical Alloying and Particle Size Reduction 33
2.1.7 Experimental Contributions of Coauthors 34
2.2 Characterization 35
2.2.1 Single Crystal X-ray Diffraction, Structure Solution, and Refinement 35
2.2.2 Powder X-ray Diffraction and Rietveld Refinement 35
2.2.3 Thermal Analysis 35
2.2.4 Magnetic Measurements 36

2.2.5 Microscopy 36
2.2.6 Energy-Dispersive X-ray Spectroscopy 36
2.2.7 Nuclear Magnetic Resonance Spectroscopy 37
2.2.8 Raman, Infrared, and Photoluminescence Spectroscopy 37
2.2.9 Particle Size Analysis 37
2.2.10 Electrochemical Characterization 37
2.3 Computational Methods 38
2.4 References 39
3 RESULTS AND DISCUSSION 41
3.1 Effects of Alkali Metal Substitution on Alkali Metal Silicides and Germanides 42
3.1.1 $Li_{18}Na_2Ge_{17}$ and Li_3NaGe_2 – Ternary Germanides with Intriguing Structures 42
3.1.2 The $K_{4-x}Na_xSi_4$ System 45
3.1.3 Statistical Alkali Metal Mixing in $Li_{12-y}Na_ySi_7$ 47
3.2 Effects of Tetrel Element Substitution on Alkali Metal Silicides and Germanides 49
3.2.1 Mixed Silicide-Germanides 49
3.2.2 Mixing of Silicon and Boron 52
3.2.3 The Lithium Ion Conductor $Li_6B_{18}(Li_3N)_x$ 53
3.2.4 A Novel Binary Li-C Phase Obtained from Lithium Flux Synthesis 56
3.3 Zintl Phases as Precursors for Novel Materials 58
3.3.1 Amorphous Silicon-based Materials 58
3.3.2 *Allo*-Germanium as an Electrode Material in Lithium Ion Batteries 62
3.3.3 Functionalization of Two-Dimensional Polysilane Sheets Prepared from $CaSi_2$ 65
3.4 References 68
4 SUMMARY AND CONCLUSION 71
5 PUBLICATIONS AND MANUSCRIPTS 77
5.1 $Li_{18}Na_2Ge_{17}$ – A Compound Demonstrating Cation Effects on Cluster Shapes and Crystal Packing in Ternary Zintl Phases 78
5.2 $[Ge_2]^{4-}$ Dumbbells with Very Short Ge–Ge Distances in the Zintl Phase Li_3NaGe_2: A Solid-State Equivalent to Molecular O_2 88
5.3 The Ternary Zintl Phases $K_{4-x}Na_xSi_4$ ($1 \leq x \leq 2.2$) and K_7NaSi_8 – Synthesis, Crystal Structure, and Chemical Bonding 112
5.4 Site-Specific Substitution Preferences in the Solid Solutions $Li_{12}Si_{7-x}Ge_x$, $Li_{12-y}Na_ySi_7$, $Na_7LiSi_{8-z}Ge_z$, and $Li_3NaSi_{6-v}Ge_v$ 138
5.5 The Lithium Ion Conductor $Li_6B_{18}(Li_3N)_x$ – Synthesis, Li Ion Mobility, Topochemical Template Extraction, and Electronic Structure 174
5.6 A Novel Binary Li-C Phase Obtained from Lithium Flux Synthesis 200

5.7 Alkali Metals Extraction Reactions with the Silicides $Li_{15}Si_4$ and Li_3NaSi_6: Amorphous Si *versus* *allo*-Si 210

5.8 Synthesis and Characterization of *a*-*allo*-$Si_{1-x}Ge_x$ 252

5.9 Searching for Open Tetrahedral Frameworks (OTFs) and Electron-Poor Framework Semiconductors (EPFSs) in the (Li-)B-Si System 260

5.10 Electrochemical Synthesis of the Allotrope *allo*-Ge and Investigations on the Use as an Anode Material 274

5.11 Radical-Induced Hydrosilylation Reactions for the Functionalization of Two-Dimensional Hydride Terminated Silicon Nanosheets 294

6 COMPLETE LIST OF PUBLICATIONS 313

Note

This dissertation is written as a publication-based thesis. Several articles published in peer-reviewed journals were selected to be included in this dissertation. Their bibliographic data is compiled in Chapter 5. In case of unpublished work, corresponding manuscripts were prepared for publication and are also included in Chapter 5. All peer-reviewed publications and their bibliographic data are listed in Chapter 6. The relevance of this work, a review of relevant literature, and the scope and outline of the thesis are presented as an introductory part in Chapter 1. The experimental section in Chapter 2 gives details on the synthesis and characterization of materials as well as on computational methods. Contributions from coauthors are explicitly stated therein. The results and discussion in Chapter 3 are presented as summaries of the embedded publications and manuscripts, focusing on the individual contributions in case of joint publications. An overall summary and conclusion is presented in Chapter 4.

1 INTRODUCTION

1.1 Silicon and Germanium and Their Relevance in the Context of Renewable Energy

1.1.1 Anthropogenic Global Warming

"There's one issue that will define the contours of this century more dramatically than any other, and that is the urgent and growing threat of a changing climate."

BARACK OBAMA, UN CLIMATE CHANGE SUMMIT, SEPTEMBER 23, 2014[1]

This warning by U.S. president Barack Obama delivered in a speech at the United Nations Headquarters is in line with more and more alarming news on the global climate. At the United Nations Climate Change Summit in Marrakesh, Morocco, the World Meteorological Organization recently published a provisional statement on the status of the global climate in 2016. It states that 16 out of the warmest 17 years on record have been in the 21st century, sea levels are rising, and annually millions of people are being displaced due to weather-related hazards.[2]

Today, climate scientists widely agree that this global warming event is caused by anthropogenic greenhouse gas emissions, which have led to increasing atmospheric concentrations of trace gases such as carbon dioxide and methane. Greenhouse gases absorb infrared radiation scattered by the Earth which would otherwise escape the atmosphere, offsetting the balance of incoming and outgoing energy. By analyzing ice cores drilled in the Antarctic, paleoclimatologists were able to show that atmospheric CO_2 concentration and temperature have strongly correlated in the past 420 000 years (Figure 1.1a).[3] Additionally, ice core data[4] and direct CO_2 concentration measurements that were started in 1958[5] indicate that recently the atmospheric CO_2 concentration has been increasing steeply. Unsurprisingly, rising CO_2 levels coincide with industrialization when CO_2 emissions started to soar (Figure 1.1b).

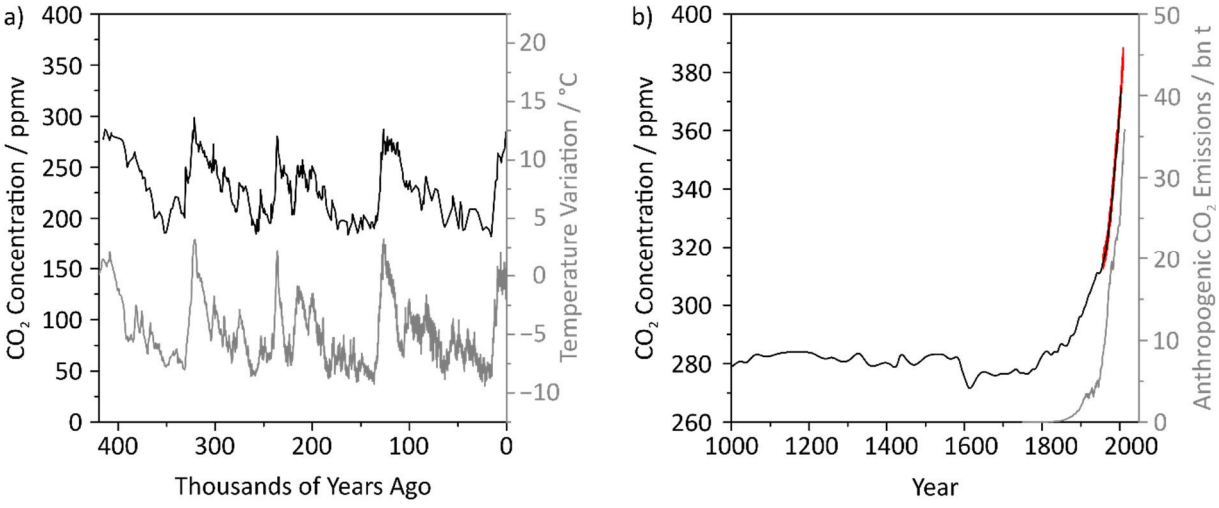

Figure 1.1. a) Atmospheric carbon dioxide concentration and air temperature variations from Vostok ice core data;[6,7] b) more recent carbon dioxide concentrations from Law Dome ice core data (black curve)[8] and atmospheric measurements on Mauna Loa, Hawaii (red curve)[9] showing a significant increase in CO_2 concentration with increasing anthropogenic CO_2 emissions from fossil-fuel burning, cement manufacture, and gas flaring[10] since the beginning of industrialization in the 18th century.

In 1938, Guy Callendar first suggested that global warming is occurring due to increasing carbon dioxide concentrations. He concluded "that the combustion of fossil fuel […] is likely to prove beneficial to mankind in several ways, besides the provision of heat and power" and that "the return of the deadly glaciers should be delayed indefinitely".[11] However, research today shows that global warming has a number of threatening consequences which Callendar did not consider.[12] Ocean warming and

acidification lead to a quickly changing environment to which wildlife can hardly adapt. For example, Australia's famous Great Barrier Reef is greatly endangered and has lost more than half of its coral cover since 1985.[13] Glaciers and ice sheets are losing mass due to rising surface temperatures, resulting in rising sea levels which threaten life in low-altitude regions.[12] Extreme weather and climate events such as droughts, flooding and tropical storms are likely to occur more frequently.

In 2016, CO_2 levels across all measurement stations around the globe surpassed 400 ppm for the first time in a few million years and will not drop below this threshold anytime soon (cf. Figure 1.1).[14] Moreover, 2016 surpassed 2015 as the warmest year on record, exceeding pre-industrial temperatures by 1.1 °C.[15] Thus, effective action to reduce greenhouse gas emissions must be launched urgently.

In the so-called Paris Agreement, 197 countries agreed to "hold[ing] the increase in the global average temperature to well below 2°C above pre-industrial levels and pursuing efforts to limit the temperature increase to 1.5°C above pre-industrial levels".[16] Encouragingly, a majority of the participating countries including the two largest greenhouse gas emitters, China and the United States, have already ratified the Paris Agreement so that it entered into force on November 5, 2016.[17,18] In order to meet its goals, CO_2 emissions due to energy production from fossil fuel burning have to be reduced significantly.[19] Shifting towards alternative energy production from renewable energy sources does not only help to combat climate change, but can also address the finite availability of fossil fuels and the immense risks of nuclear power generation.

1.1.2 Renewable Energy Technologies

The most important technologies used for power generation from renewable energy sources today are wind turbines, hydroelectricity, biomass conversion and solar energy from photovoltaics (solar PV).[20] They are characterized by a number of advantages and disadvantages: Energy production from photovoltaics and wind turbines highly depend on local climate and weather. Therefore, relying more on these technologies will require the implementation of more energy storage facilities. In addition, power distribution will have to be adapted to a less centralized energy production. Decentralization is, however, an advantage for those regions in the world that are not yet connected to conventional electrical grids. In contrast, hydroelectricity and energy from biomass conversion can easily be produced in centralized facilities compatible with the current electrical grid, and their energy output can be adjusted to fit energy demands. The production of biomass for energy means, however, may require additional crop area, which might introduce a dangerous competition with food production.

Today, energy production using traditional energy sources such as coal, natural gas, and nuclear fission is still cheaper than most renewable energy technologies.[21] However, various governmental incentives have already rendered renewable energy sources more attractive. For example, the German Renewable Energy Sources Act (Erneuerbare-Energien-Gesetz EEG) introduced guaranteed feed-in tariffs for renewable energy production facilities in 2000. These feed-in tariffs are financed by an EEG surcharge paid by consumers and decrease regularly to promote innovation.[22] The International Energy Agency has judged the EEG to have "proven very effective in introducing renewable energies" and "in bringing costs down, as reflected in particular in the decrease in feed-in tariffs for PV as a response to the rapid growth in take up of the technology".[23] Consequently, the renewable energy share of the German gross energy production has experienced a dramatic increase from 6.6 % in 2000 (mainly hydroelectricity) to 29.5 % in 2016 (Figure 1.2).[24]

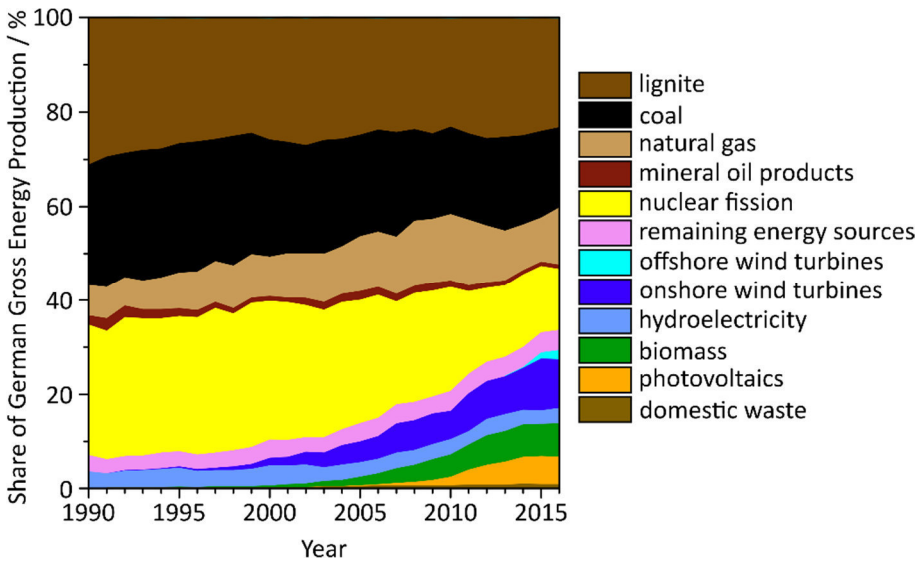

Figure 1.2. Recent development of the German gross energy production by energy source.[24] In the shown time period total energy production has increased by 17.9 %. In 2016, renewable energy sources provided for 32.3 % of the total electricity consumption.

Nevertheless, any technological innovations or potentially disruptive developments making renewable energy production more cost-efficient will facilitate the urgently needed shift towards a more CO_2-neutral society. As will be described below, the elements silicon and germanium play an ever-increasing role in renewable energy technologies.

1.1.3 Silicon, Germanium, and Renewable Energy Materials

As the second-most common element in the Earth's crust, silicon is a virtually unlimited resource (Figure 1.3). In contrast, the share of germanium in the Earth's crust amounts to only 6.7 ppm and the element is only the 53rd-most common element.[25] Naturally, silicon occurs in various silicates and as silicon dioxide (mostly quartz). Germanium is typically found in sulfidic minerals such as argyrodite (Ag_8GeS_6) and germanite ($Cu_{13}Fe_2Ge_2S_{16}$).

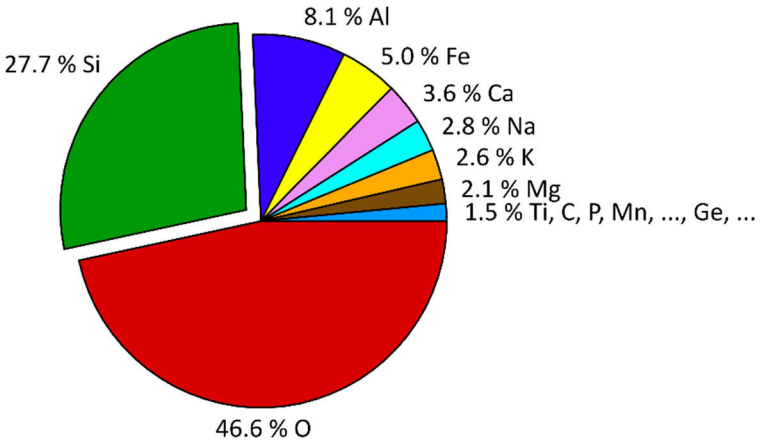

Figure 1.3. Composition of the Earth's crust by element.[26]

Elemental silicon and germanium both crystallize in the diamond structure type and are intrinsic semiconductors characterized by indirect bandgaps of 1.12 eV and 0.67 eV, respectively.[27] Silicon is highly oxophilic and forms a stable SiO_2 passivation layer on any surfaces with air contact. In contrast, germanium is not passivated in air and can be dissolved in oxidizing acids via GeO_2 formation.

These physical and chemical properties determine some of the largest applications of the two elements. Ferrosilicon, for example, is an alloy of iron and silicon, which is available with silicon contents between 15 and 90 %. Exploiting the oxophilicity of silicon, ferrosilicon is largely used in the steel production as a deoxidizing agent. The semiconducting properties of silicon and germanium are exploited in the photovoltaics and electronics industries. Other important applications of silicon include the production of aluminum alloys as well as silanes, silicones, and other silicon-containing compounds. Germanium is further used in fiber and infrared optics as well as in catalysts for the production of polyethylene.[25,28]

Industrially, silicon is typically produced by reducing quartz with coal at > 2000 °C in an electric furnace.[25] The obtained metallurgical grade silicon (98.5–99.7 %) is primarily used in aluminum production and the chemical industry.[25] For the production of ferrosilicon, iron turnings are added to the reactants. Semiconductor application of elemental silicon demands significantly larger purities. The Siemens process is the most important method of silicon purification. Exploiting the reversible reaction of Si with HCl to form trichlorosilane $SiHCl_3$, purity levels of up to 9N to 11N suitable for electronic components can be achieved. Alternatively, silicon can be purified by conversion to highly pure monosilane. This process consumes much less energy than the Siemens process and affords 6N to 9N silicon, which suffices for photovoltaics applications. Due to the increasing demand for solar grade silicon, the market share of this so-called fluidized bed reactor production is growing rapidly.[29]

The Siemens and the fluidized bed reactor processes both produce polycrystalline silicon. However, monocrystalline silicon is necessary for microchips and for some photovoltaics technologies. Thus, polycrystalline Si is converted by growing large single crystals around a seed crystal from molten Si (Czochralski process) or with the floating zone process.[25] The latter technique further purifies silicon, which benefits applications in the electronics industry.

In 2014, 8,200 kilotons of ferrosilicon were produced,[30] rendering it by far the largest application of silicon. Typically, the silicon content in ferrosilicon makes up about 65 % of the total silicon production which was 7,200 megatons in 2016.[31] In addition, 2,700 kt of metallurgical grade Si were produced in 2014, of which 228 kt were converted to highly pure polycrystalline silicon for semiconductor purposes.[30]

Due to its relatively rare occurrence, germanium is quite expensive at about 1500 \$ kg^{-1}. In contrast, ultrapure silicon was sold for 25 \$ kg^{-1} in 2012.[25] Thus, germanium is only used for specialty applications and the total worldwide production in 2013 was 145 t.[28] Industrially, germanium is obtained as a side product during processing of zinc ores. Purification of germanium can be achieved in a floating zone process.[25]

As mentioned earlier, the production of solar photovoltaic (PV) cells is currently rising steeply (Figure 1.4). In 2015, the cumulated global capacity of installed solar PV facilities amounted to 229.3 GW, which can already provide more than 1 % of the global primary energy demand.[32,33] The most probable scenario for the following years predicts a further increase in solar PV capacity of around 20 % per year, yielding 613 GW by 2020.[33]

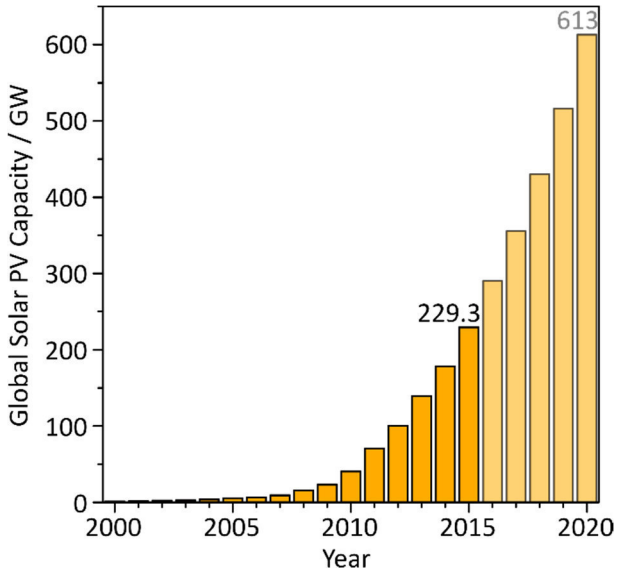

Figure 1.4. Cumulative installed capacity of global solar photovoltaics.[33-35] Projections from 2016 to 2020 represent the most probable scenario according to SolarPower Europe's 2016 Global Market Outlook.[33] For comparison: the total global primary consumption in 2015 corresponds to 17,510 GW.[32]

The vast majority of solar cells uses crystalline or amorphous silicon for the p-n junctions, which are the energy conversion components. However, the maximum efficiency of solar cells based on silicon only is physically restricted by the Shockley-Queisser limit.[36] In AM1.5 solar irradiation[1] the maximum theoretical efficiency for Si p-n junctions is 32 %.[37] The most efficient solar cell based on crystalline Si without sunlight concentration was recently developed by Panasonic and reaches an efficiency of 25.6 %.[38]

Significantly larger energy conversion efficiencies can be achieved using multijunction photovoltaic cells. They employ several p-n junctions fabricated from materials with different band gaps in order to make better use of the whole solar irradiation spectrum. Using concentrator optics, Fraunhofer ISE has recently achieved an energy conversion efficiency of 46.0 % using a quadruple junction cell.[39,40] In order to obtain sets of semiconductor materials with band gaps tuned for the highest possible efficiency, III-V semiconductors such as $Ga_{1-x}In_xAs$ and $Ga_{1-x}In_xP$ deposited on germanium are typically used.[25,40] These compounds are, however, much more expensive so that a widespread use of highly efficient multijunction PV cells is still far away. Therefore, many research groups investigate cheaper semiconductors, ideally with tunable bandgaps, which could eventually disrupt the solar PV market.[41]

Electric vehicles (EVs) using LIBs for energy storage are currently the most promising technology in the attempt to shift the transportation sector away from fossil fuels. Fuel cells have not yet come close to a comparable cost structure and large-scale production of biomass fuels strongly competes with food production in terms of land-use. Thus, many countries support LIB research and have created incentives to increase the demand of EVs. For example, the German Federal Government's National Electromobility Development Plan introduced in 2009 aims for one million EVs sold in Germany by 2020.[42]

However, by December 2015 only 51,600 additional EVs had actually been sold,[2] endangering the implementation of this plan.[43] Evidently, EVs do not yet attract many customers for a variety of economic

[1] Standardized solar irradiation spectrum for sea level at mid-latitude.
[2] The National Development Plan for E-Mobility targetted 100,000 electric vehicles sold by the end of 2014.

and life-style reasons. In EVs, energy storage still represents a large portion of price, weight, and volume and their driving ranges are typically shorter than those of conventional vehicles. Meanwhile, recharging EVs requires much more time than simple refueling at a gas station. Therefore, LIBs still need to be significantly improved in order to be cheap, light, and long-lived while still offering fast recharge options and a long driving range for EVs. Many materials scientists and electrochemists today thus investigate new materials for LIB cathodes, anodes, and electrolytes.

Solid-state electrolytes represent such a heavily investigated class of materials.[44] The flammable organic electrolytes currently used in commercial LIBs pose a significant safety hazard, which can be overcome with solid-state electrolytes. In addition, they could mitigate the stability issues associated with organic electrolytes. However, the biggest challenge here is to find materials with similarly large Li^+ ion diffusivities. Several inorganic Si- and Ge-containing compounds have shown great potential in this context. $Li_{14}Zn(GeO_4)_4$ was the first prominent candidate for a solid Li^+ ion conductor.[45] Its properties were more and more optimized by adjusting the stoichiometry in $Li_{2+2x}Zn_{1-x}GeO_4$ and adding various dopants.[46] More recently, oxides were replaced by sulfides, which exhibit even better Li^+ ion conduction properties. $Li_{10}GeP_2S_{12}$ is currently one of the most promising solid electrolyte materials with Li^+ ion conductivities even exceeding those of liquid organic electrolytes.[47] Additional studies have shown that Ge can also be replaced by Si or Sn in this structure.[48,49]

Both silicon and germanium also attract much attention as potential anode materials.[50,51] Upon formation of $Li_{15}Si_4$, the specific theoretical capacity of Si anodes amounts to 3579 mAh g^{-1},[52] representing an almost ten-fold capacity compared to 372 mAh g^{-1} for graphite anodes (LiC_6 formation) which are commercially used today.[53] Ge anodes are characterized by a specific theoretical capacity of 1385 mAh g^{-1} with isostructural $Li_{15}Ge_4$ as the most lithiated phase.[54] Its high electrical conductivity (10^4 x greater than for Si) and Li^+ ion diffusivity (400 x higher than for Si) render Ge another very interesting LIB anode material.[55] In contrast to graphite anodes, however, lithiation and delithiation of silicon and germanium do not occur via an intercalation/deintercalation mechanism, causing a number of practical difficulties. Most prominently, Si and Ge anodes suffer from extreme volume changes of > 300 % and 230%, respectively, upon charge and discharge.[56] If this issue can be overcome in the upcoming years, silicon and germanium may have a bright future not only in solar cells but also in LIBs.

1.2 Zintl phases

1.2.1 Definition and Characteristics

Zintl phases are intermetallic phases characterized by strongly heteropolar bonding contributions. These salt-like compounds are typically formed by electropositive alkali or alkaline earth metals and more electronegative metals, semimetals, and small band-gap semiconductors of groups III–VI. Their structures can be rationalized by a formal electron transfer from the electropositive to the electronegative components, applying the (8−*N*) rule for the atoms of the anionic substructure.[57]

Thus, in Zintl phases like Na_4Si_4 and $CaSi_2$ each silicon atom formally receives an additional valence electron from the electropositive alkali/alkaline metals, resulting in a valence electron number of $N = 5$. According to the (8−*N*) rule, each silicon atom should form three covalent bonds like elemental pnictides. Indeed, Na_4Si_4 contains $[Si_4]^{4-}$ tetrahedra comparable to white phosphorus[58] (Figure 1.5a) and $CaSi_2$ comprises two-dimensional sheets of puckered hexagonal rings as in grey arsenic[59] (Figure 1.5b). In CaSi, each silicon atom formally receives two electrons. As expected, the anionic substructure of CaSi is related to a chalcogen: CaSi comprises zig-zag chains of two-bonded Si atoms[60] (Figure 1.5c). Unlike in grey selenium, however, these chains are not helical. This is caused by a partially covalent interaction of Ca and Si that also leads to metallic behavior of the compound.[61] Ca_5Si_3 is also an electron-precise Zintl phase, although its structure is somewhat more complicated. Formally, the sum formula can also be written as $[Ca^{2+}]_5[^{3-}Si–Si^{3-}][Si^{4-}]$. As shown in Figure 1.5d, the anionic structure of Ca_5Si_3 contains dimeric $[^{3-}Si–Si^{3-}]$ units, which are valence isoelectronic to molecular halogens, next to isolated $[Si^{4-}]$ with noble gas electron configuration.[62]

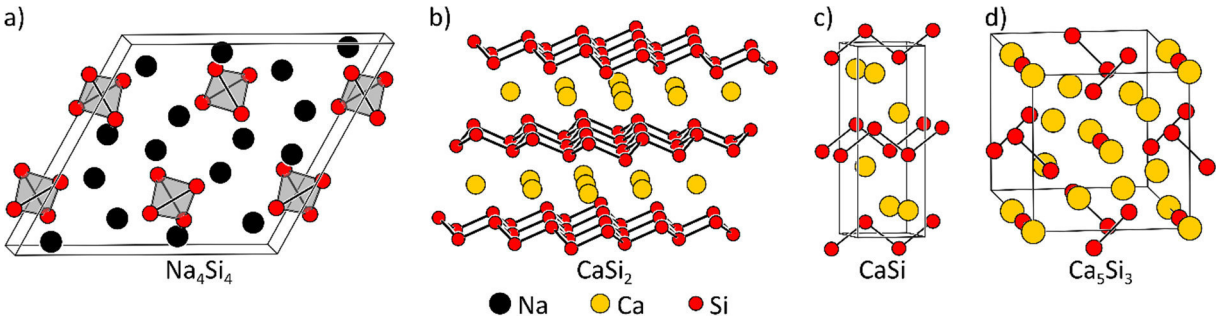

Figure 1.5. Structural excerpts of the Zintl phases a) Na_4Si_4 containing white phosphorus-like $[Si_4]^{4-}$ tetrahedra,[58] b) $CaSi_2$ containing grey arsenic-like puckered hexagonal sheets,[59] c) CaSi containing zig-zag-chains related to grey selenium,[60] and d) Ca_5Si_3 containing halogen like $[^{3-}Si–Si^{3-}]$ next to isolated $[Si^{4-}]$ in noble gas electron configuration.[62]

1.2.2 Alkali Metal Silicides and Germanides

Alkali metal silicides and germanides in particular have received much attention as precursors for novel materials. This group of compounds can be classified by the anionic substructure type into three- and two-dimensional networks, cluster-containing Zintl phases, and lithium-rich phases. This section will focus on binary representatives. Their role as precursors for novel materials is described in Chapter 1.2.3. , whereas ternary and quaternary phases will be covered in Chapter 1.3.

Cluster-containing Zintl Phases

The first and most prominent examples of alkali metal silicides and germanides contain cluster anions and are typical Zintl phases. They are synthesized by melting a stoichiometric mixture of the heavier alkali metals sodium to cesium with silicon or germanium. For example, the Zintl phases A_4T_4 (A = Na–Cs, T = Si, Ge) contain $[T_4]^{4-}$ tetrahedra (Figure 1.6a). Another typical tetrel cluster anion is the

monocapped square antiprism $[T_9]^{4-}$ which is known in the germanides A_4Ge_9 (A = K–Cs, Figure 1.6b)[63,64] as well as in $A_{12}T_{17}$ (A = K–Cs, T = Si, Ge) where it occurs next to $[T_4]^{4-}$ tetrahedra.[64-67] According to the Wade-Mingos rules for structure prediction in clusters,[68,69] $[T_9]^{4-}$ can be described as a *nido*-cluster with 22 skeletal electrons. Most of these cluster compounds are soluble in polar solvents such as liquid ammonia and ethylenediamine, rendering them the foundation of very prolific research on group IV Zintl anions in solution. Starting from intermetallic phases containing $[T_4]^{4-}$ and $[T_9]^{4-}$ clusters, a number of other soluble clusters were obtained and subsequently functionalized.[70]

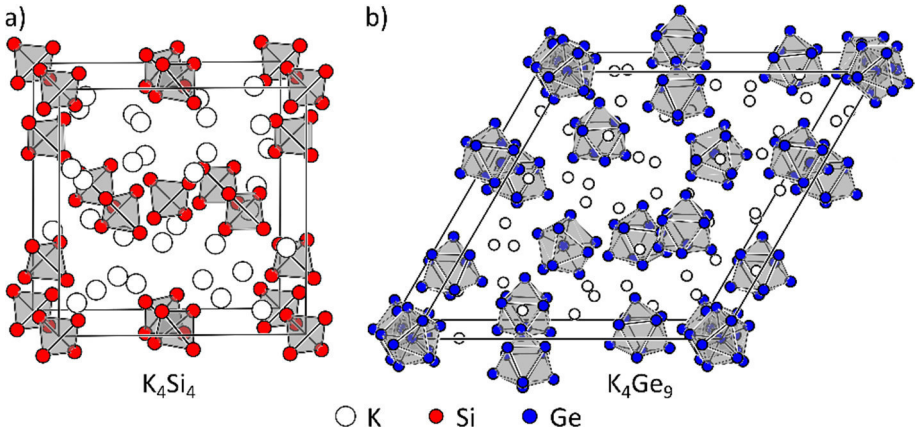

Figure 1.6. Structures of selected binary alkali metal silicides and germanides comprising Zintl clusters: a) K_4Si_4,[71] b) K_4Ge_9.[63]

Lithium-rich Phases

Lithium with its relatively covalent bonding contributions can stabilize more negatively charged tetrelide anions than its heavier homologues. Thus, most lithium tetrelides contain smaller clusters or isolated anions. For instance, $Li_{12}T_7$ (T = Si, Ge) comprises planar five-membered rings as well as planar Y-shaped stars (Figure 1.7a),[72] and dumbbells constitute the polyanions in Li_7T_3 (T = Si, Ge, Figure 1.7b).[73,74] Isolated anions are present in the lithium-richest phases $Li_{13}T_4$ (next to dumbbells),[75-77] $Li_{15}T_4$ (Figure 1.7c),[78,79] high-temperature $Li_{4.1}T_4$,[80,81] and $Li_{17}T_4$ (T = Si, Ge in all cases).[81,82] With the exception of metastable $Li_{15}Si_4$, all lithium-rich silicides and germanides can be synthesized directly by melting a stoichiometric mixture of the respective elements.

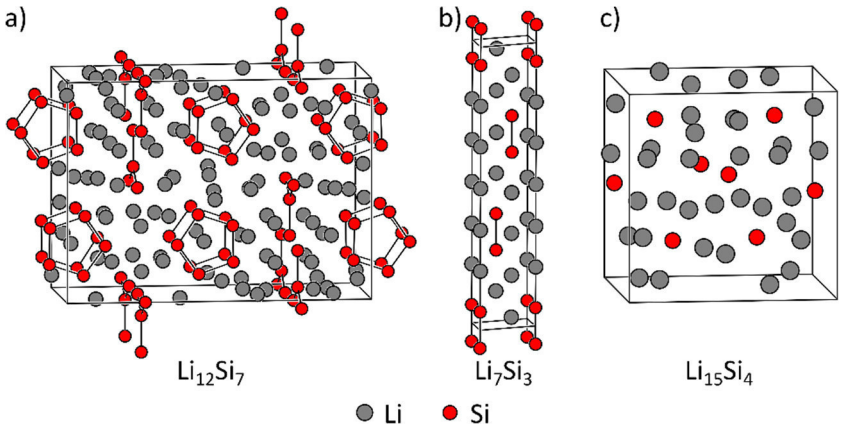

Figure 1.7. Structures of selected Li-rich alkali metal silicides and germanides: a) $Li_{12}Si_7$,[83] b) Li_7Si_3,[73] c) $Li_{15}Si_4$.[78]

In contrast to the electron-precise cluster compounds presented before, the lithium-rich tetrelides do not represent classical Zintl phases. For example, the expected composition according to the Zintl concept for a tetrelide containing only isolated anions (T^{4-}) is Li_4T. However, instead of this electron-precise composition, electron-deficient $Li_{15}T_4$ as well as $Li_{4.1}T$ and $Li_{17}T_4$ with surplus electrons exist.

The dumbbells in Li_7T_3 and $Li_{13}T_4$ have partial multiple bond character, but again they cannot be described in an electron-precise way. NMR spectroscopy proved that the planar five-membered rings in $Li_{12}T_7$ are indeed aromatic,[84,85] while the Y-shaped stars are commonly viewed as carbonate-like.[86] The resulting description of $[T_5]^{6-}$ and $[T_4]^{8-}$ clusters in a 2:1 ratio again does not add up with the number of transferrable Li valence electrons, leaving two electrons per formula unit of $Li_{12}T_7$ unaccounted for.

$Li_{15}Si_4$ and $Li_{15}Ge_4$ as the crystalline products of full lithiation of silicon and germanium anodes play a major role in LIB research.[52,54] $Li_{15}Si_4$ is a metastable phase which slowly decomposes above 170 °C.[78] It was first structurally characterized from the product of the electrochemical lithiation of silicon.[52] The phase can be prepared by mechanical alloying or in flux syntheses with excess Li as a solvent.[78,87] $Li_{15}Ge_4$ is isostructural but thermodynamically stable.[81]

Three- and Two-dimensional Networks

Extended three- or two-dimensional networks are typically found as the anionic substructure of alkali metal-poor silicides and germanides. Already in 1965, the binary phases Na_8Si_{46} and Na_xSi_{136} ($x < 24$) were found via thermal decomposition of Na_4Si_4 (Figure 1.8a, b).[88-90] Isostructural compounds are obtained by thermal decomposition of A_4Si_4 (A = K–Cs) and A_4Ge_4 (A = Na–Rb).[91] Analysis of X-ray diffraction data soon revealed that the compounds both crystallize in structure types which were already known from gas hydrates: type-I and type-II clathrates.[92,93] In these remarkably air- and water-stable intermetallic phases, silicon forms a host structure consisting of different cages which are filled with sodium. Later investigations also demonstrated that either clathrate I-type Na_8Si_{46} or clathrate II-type Na_xSi_{136} is formed selectively when carefully choosing appropriate reaction conditions.[94] Reactions of Na_4Si_4 and K_4Si_4 with gaseous HCl or H_2O also yield the corresponding clathrate compounds.[95]

Thermal decomposition of Na_4Ge_4 in a dynamic vacuum also yielded zeolite-like $Na_{1-x}Ge_{3+z}$. This binary intermetallic is characterized by large open Ge channels which are filled with Na and disordered Ge atoms (Figure 1.8d).[96] In syntheses from the elements at 8 GPa binary $NaSi_6$ was found which crystallizes in the $Eu_4Ga_8Ge_{16}$ structure type.[97] In this compound, the silicon atoms form a three-dimensional network with large open channels, which are filled by the Na guest species (Figure 1.8c).

In contrast to the above-mentioned open framework structures which do not represent electronically balanced Zintl phases, the lithium-poor binaries LiT (T = Si, Ge) and Li_7Ge_{12} are electron-precise. In the LiT compounds, the tetrel atoms form a three-dimensional network of three-connected Si and Ge atoms, respectively, with Li^+ cations distributed throughout (Figure 1.8e).[98,99] Li_7Ge_{12} comprises two-dimensional polygermanide sheets $^2_\infty[Ge_{12}]^{7-}$ which are separated from each other by layers of Li^+ cations (Figure 1.8f).[100,101] While LiGe and Li_7Ge_{12} can be synthesized directly by melting of stoichiometric amounts of the elements, the formation of LiSi under these conditions is kinetically hindered.[98] LiSi can however be obtained at high pressures or via mechanical alloying.[98,102,103] Tetragonal and hexagonal high pressure modifications of LiGe are obtained at 4 GPa.[104]

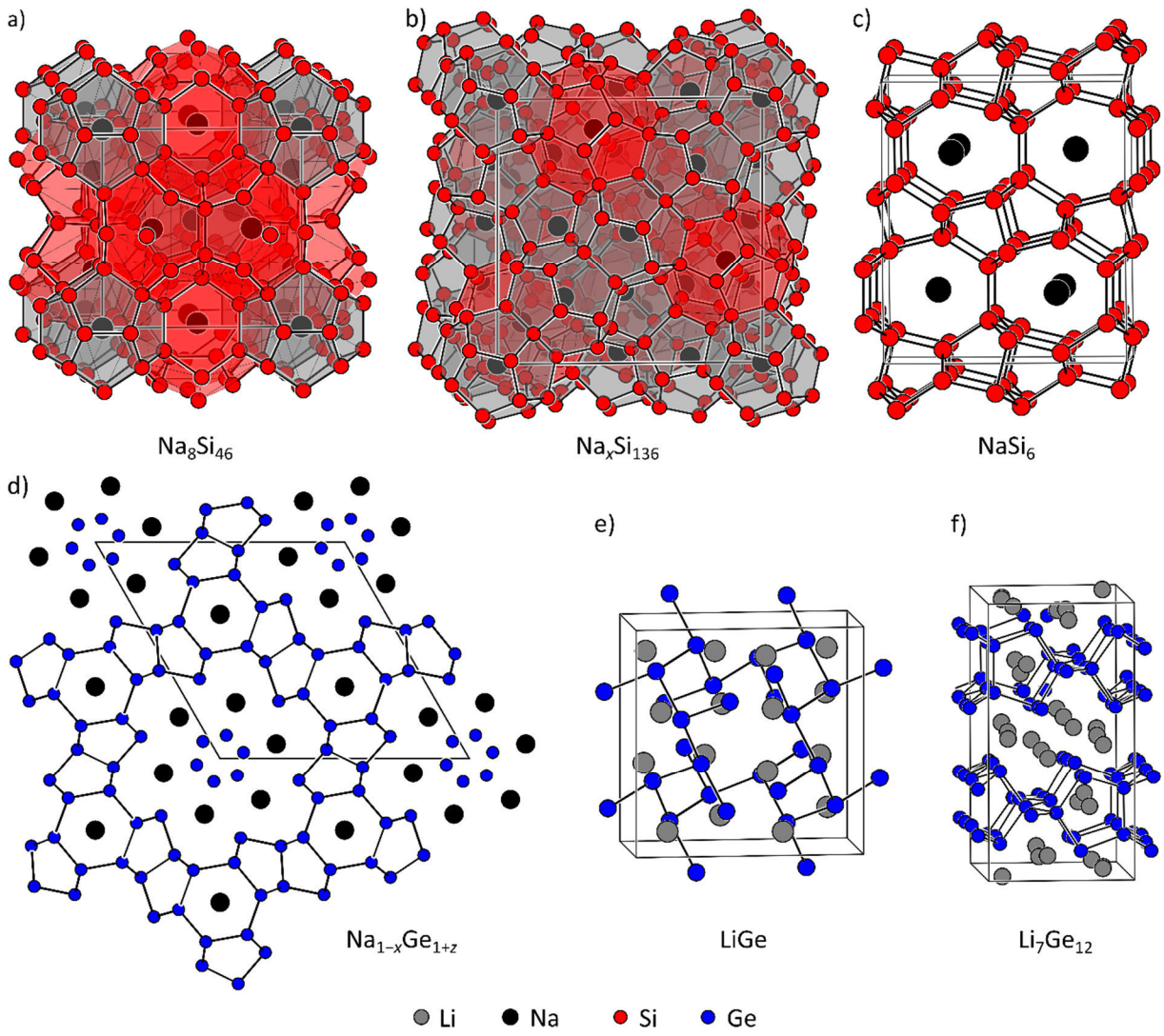

Figure 1.8. Structures of selected binary alkali metal silicides and germanides comprising three- or two-dimensional networks: a) Na_8Si_{46} (clathrate-I type, large and small cages are highlighted in red and grey, respectively),[91] b) Na_xSi_{136} (clathrate-II type, large and small cages are highlighted in red and grey, respectively),[90] c) $NaSi_6$,[105] d) $Na_{1-x}Ge_{3+z}$,[96] e) LiGe,[99] f) Li_7Ge_{12}.[101]

1.2.3 Precursors for Novel Materials

Since the 1980s, several research groups have shown that Zintl phases are suitable precursors for various novel silicon and germanium materials. These materials can be classified as crystalline allotropes, amorphous materials, nanoparticles, and layered structures. Their synthesis and most important properties will be presented below.

Crystalline Allotropes

Li_7Ge_{12} has been reported to undergo a topochemical reaction with protic solvents to a new germanium allotrope, termed *allo*-Ge.[106] Ethanol facilitates the deintercalation of lithium cations from Li_7Ge_{12} according to Equation (1).

$$Li_7Ge_{12} + 7\ EtOH \rightarrow 12\ \textit{m-allo}\text{-Ge} + 7\ LiOEt \quad (1)$$

The microcrystalline product was structurally characterized by powder X-ray diffraction in combination with computational methods, revealing that the two-dimensional sheets of Li_7Ge_{12} are covalently connected to each other in *m-allo*-Ge. This results in a novel three-dimensional network.[107] Upon

heating, *m-allo*-Ge is first converted into 4*H*-Ge, another new Ge modification, which finally transforms to *α*-Ge at even higher temperatures.[106,108,109]

In order to remove the sodium guest atoms from the host structure in Na_xSi_{136}, the clathrate II phase was repeatedly treated with high vacuum at elevated temperatures. By subsequently adding small amounts of elemental iodine to the product, a nearly empty Si clathrate with a remaining Na content of $x \approx 0.0058$ was achieved.[110] Guest-free $\square_{24}Ge_{136}$ ($\square$ denotes the empty alkali metal positions) was obtained via a very different route: Na_4Ge_9 was slowly oxidized in an ionic liquid of dodecyltrimethylammoniumchloride (DTAC) and aluminum trichloride to obtain the empty clathrate II structure.[111] In this reaction, DTAC serves as the oxidant. Unlike the common diamond structure modifications of Si and Ge, the guest-free clathrate materials are characterized by a direct bandgap of 1.9 eV and 0.6 eV, respectively.[111,112] Therefore, they are currently being investigated as potential materials for photovoltaic applications.[113]

Another open framework allotrope of silicon, Si_{24}, was obtained by thermal degassing of $NaSi_6$ in a dynamic vacuum. As in the previously described guest-free clathrates, the open framework structure of the tetrel element is retained (cf. Figure 1.8c), resulting in a promising Si allotrope with a quasidirect bandgap of 1.3 eV.[114]

Amorphous Materials

Ethylenediamine solutions of K_4Ge_9 serve as precursors for inverse opal structures of Ge. The nanomorphology is obtained by spray-coating the cluster solution onto an opal template made from poly(methyl methacrylate) (PMMA) beads and subsequent oxidation with $GeCl_4$. [115] The PMMA beads are then removed by pyrolysis or washing with tetrahydrofurane (THF). This bottom-up approach allows for a very precise control over the shape, size, and arrangement of the resulting mesopores and thus represents a significant improvement with respect to chemical or electrochemical etching procedures.

Alternatively, surfactants can function as templating species for the synthesis of mesoporous Ge materials. The reaction of Mg_2Ge with $GeCl_4$ in a formamide solution containing a surfactant, leads to a mesostructured, amorphous Ge material with cubic pore symmetry.[116] In contrast, the reaction of K_4Ge_9 with $GeCl_4$ under similar conditions yielded a hexagonal mesoporous Ge material.[117] Here, the surfactant was first replaced with ammonium nitrate and then removed thermally. When ethylenediamine is used as a solvent for the latter reaction, it interconnects and oxidizes the Ge clusters without the addition of an external oxidant such as $GeCl_4$. Although the same surfactant was used, a different hexagonal mesoporous Ge structure is obtained, varying in the pore-pore spacing distances.[116]

Although tetrel element-poor compounds naturally do not represent the most suitable precursors for novel tetrel materials, lithium-rich silicides have recently been employed as precursors for amorphous Si. $Li_{12}Si_7$, Li_7Si_3, $Li_{13}Si_4$, and "$Li_{22}Si_5$" (the stoichiometry of this phase has recently been corrected to $Li_{17}Si_4$)[82] were reacted with ethanol, washed with deionized water and hydrochloric acid, and dried at 120 °C.[118] Scanning electron microscopy (SEM) images of the resulting materials show a layered microstructure which was shown to lower volume expansions during cycling in Li-ion half cells. Thus, a significantly improved cycling stability in comparison to bulk crystalline silicon was observed.

Nanoparticles

In heterogeneous reactions, cluster-containing Zintl phases serve as precursors for tetrel element nanoparticles. Reactions of K_4Si_4 or Na_4Si_4 with $SiCl_4$ in high-boiling ethers yield very reactive Si nanoparticles, which can be stabilized by surface termination using methanol or *n*-butyllithium as shown by nuclear magnetic resonance (NMR) spectroscopy.[119,120] Similarly, the oxidation of Na_4Si_4 with NH_4Br yields H-terminated Si nanoparticles.[121] A recent study shows that $A_{12}Si_{17}$ (*A* = K–Cs) compounds also form Si nanoparticles upon reaction with NH_4Br.[122] Analogously, heterogeneous reactions of Na_4Ge_4 with $GeCl_4$ or NH_4Br in high-boiling ethers yield alkyl- and H-capped Ge nanoparticles, respectively, after appropriate work-up.[123,124]

Solution synthesis strategies for tetrel element nanoparticles are characterized by precise particle size control. In addition, different options for surface functionalization offer specific tuning of the particles for specific applications. Due to their small sizes and consequential quantum size effects, tetrel nanoparticles are viewed as potential candidates for optoelectronics and energy conversion technologies.[125,126]

Layered Structures

The alkaline earth metal silicide $CaSi_2$ (cf. Figure 1.5b) was first discovered by Friedrich Wöhler in 1863.[127] He immediately noticed that upon reaction with hydrochloric acid the intermetallic phase forms a yellow compound with sheet-like morphology. This material was later characterized as siloxane $Si_6H_6O_3$ of which two different structures were determined. In the Kautsky siloxane, oxygen atoms are incorporated into the silicon sheets and the Si atoms carry axial bonds to hydrogen atoms.[128] The Weiss siloxane consists of intact sheets of puckered hexagonal Si rings as in $CaSi_2$.[129] Each Si atom carries an equatorial bond to either a hydrogen atom or a hydroxyl group. At −30 °C, the reaction of $CaSi_2$ with hydrochloric acid yields the non-oxidized deintercalation product "Si_6H_6" (Equation 2).[130] The layered polysilane also retains the sheets of puckered hexagonal rings present in $CaSi_2$ and all equatorial positions are occupied by hydrogen atoms only.

$$3\ CaSi_2 + 6\ HCl \rightarrow \text{“}Si_6H_6\text{”} + 3\ CaCl_2 \qquad (2)$$

"Si_6H_6" is a promising two-dimensional material with large potential for (opto-)electronic technologies. By functionalization of the Si–H groups, the material can be stabilized and adjusted for specific applications.[131-133] Preliminary tests of the polysilane as an anode material in lithium ion batteries show that its layered structure may be advantageous in order to overcome volume expansion issues.[134,135]

Analogously, isostructural $CaGe_2$ can be converted to layered polygermane.[136,137] The material possesses a band gap of 1.58 eV and has been shown to be an efficient photocatalyst for hydrogen evolution.[138]

Quantum Chemical Calculations

Both Si and Ge have shown to possess many local minima on the energy landscape, resulting in many different allotropes that have been synthesized to date.[139,140] Some of them have indirect band gaps like diamond-structured *α*-Si and *α*-Ge. Others, like the guest-free clathrates have direct band gaps and thus promise to be much more efficient energy conversion materials.

The search for additional Si and Ge structures is not only performed experimentally but also via quantum chemical calculations. Computational approaches include random searches and swarm methods.[140-142] Alternatively, known tetrahedral structures or anionic substructures of Zintl phases have been used as a starting point. For example, the two-dimensional Ge and Si substructures of Li_7Ge_{12} (cf. Chapter 1.2.2) and Li_3NaSi_6 (cf. Chapter 1.3.2) were combined to three-dimensional, tetrahedral networks, representing possible tetrel allotropes.[143,144] Quantum chemical calculations starting from guest-free clathrate compounds suggest that several clathrate polytypes might be stable under ambient conditions.[145,146]

Recently, a chemically inspired approach proposed to split the diamond structure type into three-atom thick slabs, which can then be recombined. Thus, different tetrahedral networks were found by relaxing the structures from different stacking modes, leading to the discovery of several new tetrel structures.[147] The same method also produced some open framework structures that are already known from Zintl phase substructures.

1.3 Substitution Effects in Zintl Phases

1.3.1 General Trends and Issues

In alkali metal tetrelides, either the alkali metal or the tetrel element can be substituted. Both methods are promising in the attempt to control the anionic substructures of resulting Zintl phases. Partial substitution of the alkali metal cations frequently results in the formation of ternary Zintl phases with intriguing anionic substructures that cannot be obtained in simple binary compounds (see Chapter 1.3.2). Partial substitution of the anionic tetrel element substructure often affords mixed polyanions (see Chapter 1.3.3).

When partially substituting the different components in alkali metal silicides and germanides, the "coloring problem" arises.[148,149] Jeremy K. Burdett translated this concept originating from mathematical graph theory to solid-state chemistry as follows: In a fixed solid-state lattice, there are several ways to distribute different atom types to the various lattice positions. Typically, only one of many combinations yields the energetically most favorable structure. In this context, understanding why a specific distribution of atoms has the lowest energy means solving the "coloring problem".[148] Gordon J. Miller expanded this concept to include the different lattices a solid-state compound with a specific stoichiometry can adopt. Here, solving the "coloring problem" additionally means to predict the lowest energy structure at given conditions.[149]

When moving from binary to ternary and quaternary systems, complexity increases due to the rising number of possible structures and atom distributions. Thus, any knowledge of structural and site preferences for certain compositions would allow for more target-oriented and efficient investigations.[149] With respect to alkali metal silicides and germanides, substitution of one element with a similar one can result in the same or a different structure than corresponding binary phases. In addition, the similar elements may separate onto different atomic sites or they may mix statistically on the same sites, forming solid solutions.

1.3.2 Cation Substitution

Substitutions of the cationic components of alkali metal silicides and germanides can be performed either homologously with other alkali metals or with differently charged cations such as alkaline earth metals. While homologous substitutions mainly change the steric demands of the participating cations, substitutions with multivalent cations introduce additional electronic changes. Both substitution types will be presented below.

Homologous Substitutions

Ternary silicides and germanides comprising two different alkali metals typically form different structures than their binary counterparts. They can be synthesized by simply melting stoichiometric mixtures of the respective elements. Li_3NaSi_6 comprises two-dimensional $^2_\infty[Si_6^{4-}]$ sheets, which are separated by the alkali metal cations (Figure 1.9a).[150] Like Li_7Ge_{12}, the compound was reported to convert topochemically to a novel Si allotrope termed *allo*-Si. However, this work has not been reproduced successfully and *allo*-Si was never structurally characterized. Li_7RbGe_8 comprises the largest Ge Zintl anion known in intermetallic phases: Friauf polyhedra $[Li@Li_4Ge_{12}]^{7-}$ exist next to $[Ge_4]^{4-}$ tetrahedra (Figure 1.9b).[151] In addition, a large variety of phases $A_{4-x}A'_xT_4$ (A = K, Rb, Cs; T = Si, Ge; x = 0.5, 1, 2) comprises silicide or germanide tetrahedra which are connected to dimers or to polymeric chains

via the smaller of the two alkali metals (Figure 1.9c, d).[152-158] In all these examples, the different alkali metals in the ternary compounds occupy separate atomic sites, forming ordered structures.

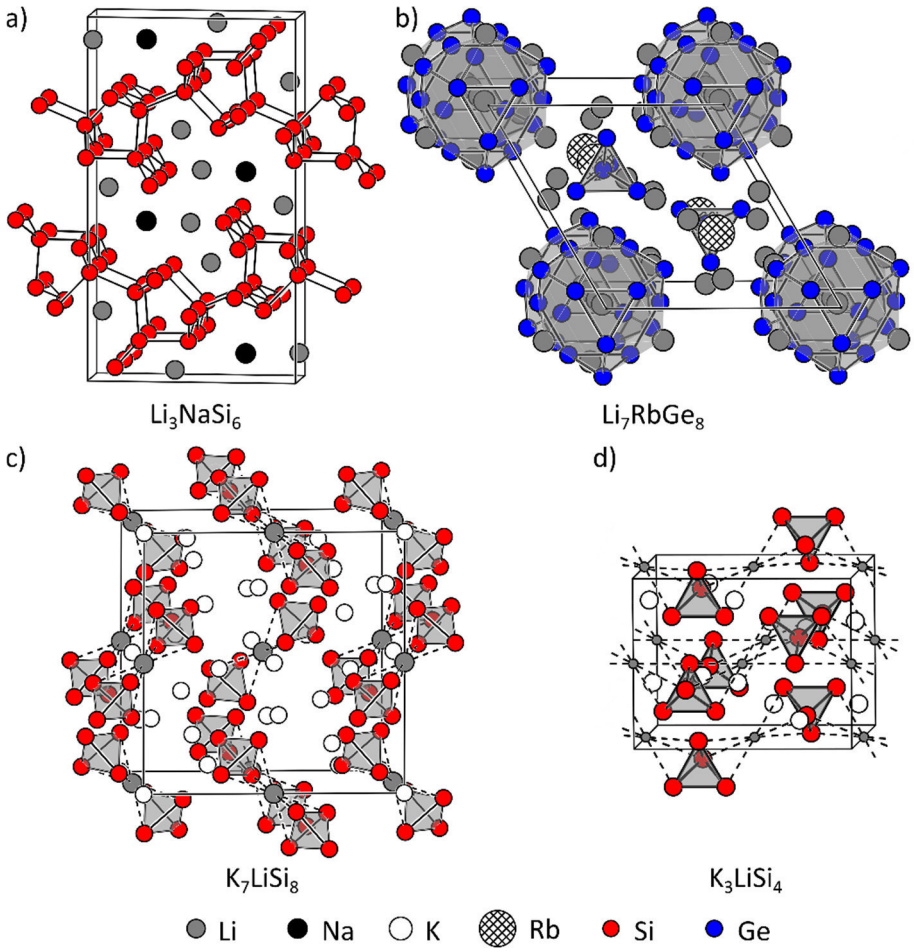

Figure 1.9. Structures of selected mixed-cation alkali metal silicides and germanides: a) Li_3NaSi_6,[150] b) Li_7RbGe_8,[151] c) K_7LiSi_8,[153] and d) K_3LiSi_4.[153]

In addition, compounds $A_8Na_{16}T_{136}$ (A = Rb, Cs; T = Si, Ge) crystallize in the well-known clathrate-II type structure presented in Chapter 1.2.2.[159] The A and Na atoms occupy the larger and smaller cages, respectively (cf. Figure 1.8b). Contrastingly, ternary $K_2Rb_2Si_4$ was found to crystallize isostructurally to binary K_4Si_4 (cf. Figure 1.6a) and Rb_4Si_4 with the two alkali metals mixing statistically.[160]

Substitutions with Alkaline Earth Metals

Ternary alkali metal silicides and germanides containing alkaline earth metals exhibit an even larger structural variety than the products of homologous substitutions presented above. Combinations of alkali metal and alkaline earth metal cations stabilize various intriguing anionic substructures, including nearly planar six-membered rings in $Li_2E_4T_6$ (E = Sr, Ba; T = Si, Ge; Figure 1.10a). [161-163] In addition, various types of one-dimensional chains can be found in compounds LiE_2T_3 (E = Ca, Sr; T = Si, Ge),[162,164] $LiET_2$ (E = Ca, Sr, Br; T = Si, Ge; Figure 1.10b),[165,166] and $Na_xSr_{1-x}Ge_2$.[167]

Other ternary phases comprise anionic substructures which are also known from binary alkali metal silicides such as the superconducting clathrate-I type compounds $A_2Ba_6Si_{46}$ (A = Na, K).[168-170] Again, A and Ba atoms occupy the larger and smaller cages of the open framework structure, respectively. Aromatic five-membered rings (Li_8MgSi_6)[171] and isolated tetrel anions (e.g., Li_2MgT; T = Si, Ge)[172,173] have also been mentioned for binary phases in Chapter 1.2.2.

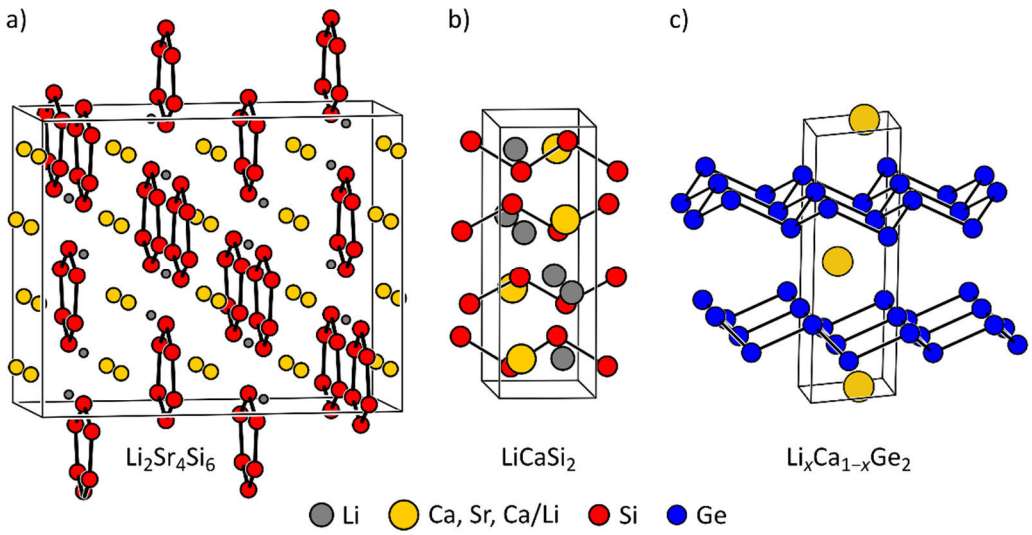

Figure 1.10. Structures of selected alkaline earth metal-containing alkali metal silicides and germanides: a) $Li_2Sr_4Si_6$,[161] b) $LiCaSi_2$,[165] and c) $Li_xCa_{1-x}Ge_2$.[174]

In most of the presented alkaline earth metal-containing structures, the two different cation types occupy distinctly different crystallographic positions. Statistical mixing of alkali metal and alkaline earth metal cations is rare. Examples of statistical mixing include $Na_xSr_{1-x}Ge_2$[167] and $Li_xCa_{1-x}Ge_2$ which crystallizes in the $CaSi_2$ structure polytype 2*H* (Figure 1.10c).[174]

Evidently, the nature and ratio of cations can have a major structure-directing effect on the polyanionic structure. John Corbett describes the stabilization of polyanionic clusters by alkali metals as "cluster solvation" in which the cations typically cap cluster faces, edges, and vertices.[175] Therefore, a mixture of different cations may stabilize a large variety of polyanionic structures, which are yet unknown. Substitutions of alkali metals for alkaline earth or even rare earth metals offers additional possibilities for polyanion stabilization. However, with regard to possible precursors for semiconductor materials, monovalent alkali metals are most promising because they tend to favor less charged polyanions than bi- or trivalent cations.

1.3.3 Anion Substitution

The tetrel component in alkali metal silicides and germanides can also be substituted homologously with germanium and silicon, respectively. In addition, the tetrel atoms can be substituted by elements from neighboring groups of the periodic table, introducing additional electronic effects on the resulting structures. Both substitution types will be discussed below.

Homologous Substitution

The elements silicon and germanium are fully miscible and form solid solutions $Si_{1-x}Ge_x$ across the full range of $0 \leq x \leq 1$.[176] The two atom types mix statistically as shown by Raman spectroscopy and density functional theory calculations.[177-179] Thus, statistical mixing of Si and Ge in mixed alkali metal silicide-germanides seems feasible. Zintl phase silicide-germanides may function as precursors for new $Si_{1-x}Ge_x$ allotropes with interesting (opto-)electronic properties. By varying the Si:Ge ratio these properties could be optimized for electronic, photovoltaic or battery applications.[180-182]

Prior to this work, only few alkali metal tetrelides with mixed anionic substructures containing both silicon and germanium were known. These solid solutions were synthesized by complete melting of stoichiometric amounts of the elements,[155] by using a suitable $Si_{1-x}Ge_x$ alloy prepared by mechanical

alloying,[183] or by annealing of other mixed precursors.[183] $A_4Si_{4-x}Ge_x$ (A = Na, K, Rb),[155,160,184] $Rb_7NaSi_{8-x}Ge_x$,[183] and $K_{12}Si_{17-x}Ge_x$[185] are solid solutions in which the tetrel elements have been confirmed to mix statistically on an atomic level. Thermal decomposition of $Na_4Si_{4-x}Ge_x$ yields the mixed clathrate-II type compounds $Na_ySi_{136-x}Ge_x$ from which the majority of Na atoms can be removed in dynamic high vacuum. [113] The band gaps of the resulting nearly guest-free clathrates $Si_{136-x}Ge_x$ can be tuned between 1.9 and 0.6 eV by changing the Si:Ge ratio. In addition, cell parameters of the solid solutions $Li_{12}Si_{7-x}Ge_x$ and $Li_7Si_{3-x}Ge_x$ were reported.[74]

The mixed alkali metal silicide-germanides known before this work all have in common that both parent phases, i.e. the pure silicide and the pure germanide, exist. Usually, the mixed silicide-germanides and their parent phases crystallize isostructurally. Attempts to substitute silicon or germanium in alkali metal silicides and germanides, which do not have a germanide or silicide counterpart, respectively, have not yet been published.

In ternary alkaline earth metal silicide-germanides, the tetrel elements also tend to mix statistically. For example, $Mg_2Si_{1-x}Ge_x$ forms a solid solution across the full stoichiometric range.[186] Ba_3Si_4 and Ba_3Ge_4 crystallize in different structure types, which both formally contain butterfly-shaped $[T_4]^{6-}$ anions. Silicide-germanides $Ba_3Si_xGe_{4-x}$ with statistically mixed Si and Ge atoms exist in both structures and a phase transition occurs at a Si content of $0.4 \leq x \leq 0.5$.[187] A mixed clathrate-I type structure has been realized in superconducting $Ba_{8-\delta}Si_{46-x}Ge_x$ phases, which were prepared under high pressure and high temperature conditions in the range of $0 \leq x \leq 23$.[188] A thorough analysis of the crystal structures shows that Wyckoff position 24*k* is preferentially but still statistically occupied by Ge, followed by the 16*i* and 6*c* positions.

Epitaxial thin films of mixed $Ca(Si_{1-x}Ge_x)_2$ solid solutions were synthesized via Ca deposition onto $Si_{1-x}Ge_x$ substrates. Upon contact with moisture, they, like $CaSi_2$, convert topochemically, promising alternative tunable $Si_{1-x}Ge_x$ modifications.[189,190]

Substitutions with Triel and Pnictogen Elements

Partial substitutions of alkali metal silicides and germanides with triel (*Tr*) or pnictogen (*Pn*) elements results in a large number of ternary phases, which are usually synthesized directly from the respective elements. The following section presents some general trends, which are observed in these anion substitutions. Silicon and germanium tend to form distinct compounds rather than solid solutions with elements in neighboring groups of the periodic table. Thus, in the respective compounds with alkali metals, a separation of the different elements onto different crystallographic position would generally be expected.

However, in ternary triel element-containing clathrate-I compounds $A_8Tr_xT_{46-x}$ which have been synthesized for a variety of element combinations, statistical mixing of the triel and tetrel elements is frequently observed.[191-193] In addition, Al statistically mixes with Li in a number of compounds related to the NaTl structure type, e.g. $Li_{16}Al_4Ge_7$.[194] Other NaTl-related phases such as LiAl*T* (*T* = Si, Ge) feature a fully ordered zincblende substructure in which Al and *T* alternate strictly.[195,196]

In the ternary *A*-B-*T* systems (*A* = Li – Cs, *T* = Si, Ge) only a few compounds have been published to date. $Li_2B_{12}Si_2$ and $Na_8B_{74.5}Si_{17.5}$ comprise boron icosahedra, which are connected by silicon atoms (Figure 1.11a, b).[197,198] $LiBSi_2$ and the clathrate I phase $K_7B_7Si_{39}$ represent open tetrahedral framework (OTF) structures which are characterized by large open channels ($LiBSi_2$) or pores ($K_7B_7Si_{39}$) filled with alkali metal cations (Figure 1.11c, d).[199,200] The silicon and boron atoms in $LiBSi_2$ and $Li_2B_{12}Si_2$ occupy

distinctly different crystallographic positions so that fully ordered structures are formed. In $Na_8B_{74.5}Si_{17.5}$ and heavily disordered $K_7B_7Si_{39}$, the two elements mix statistically on some positions. Ternary alkali metal boride germanide phases have not yet been reported at all.

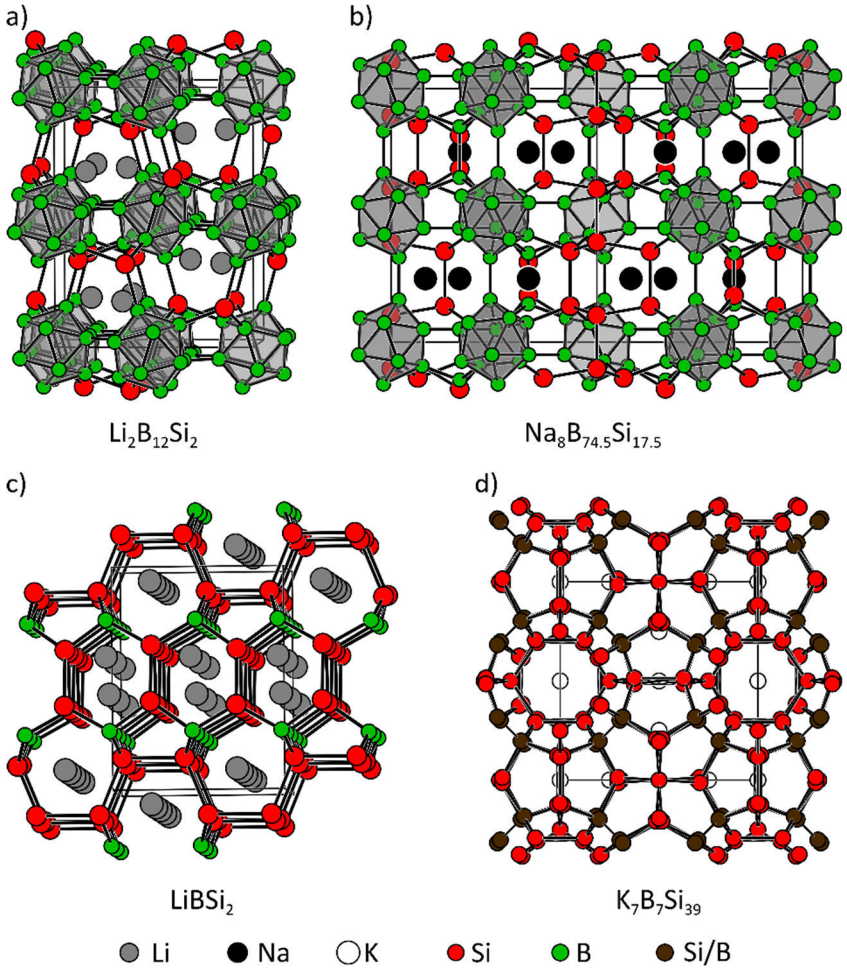

Figure 1.11. Structures of published alkali metal boride silicide structures: a) $Li_2B_{12}Si_2$,[197] b) $Na_8B_{74.5}Si_{17.5}$,[198] c) $LiBSi_2$,[199] and d) $K_7B_7Si_{39}$.[200]

Substitutions of alkali metal silicides and germanides with pnictogen elements have so far always yielded fully ordered structures comprising mixed polyanions. Introduction of N, P, or As, very often results in the formation of nitrido–, phosphido–, and arsenidosilicates or –germanides. The resulting tetrahedral anions can be isolated (Li_8SiP_4)[201] or connected to dimers ($Na_{10}Ge_2P_3$),[202] and one- (K_2SiP_2),[203] two- (KSi_2P_3),[204] and three-dimensional (Li_2SiN_2)[205] frameworks. KSi_3As_3 and $NaGe_3P_3$ contain two-dimensional $^2_\infty[T_3Pt_3]^-$ sheets which are related to the polyanionic substructure of Li_3NaSi_6 (cf. Chapter 1.3.2).[206,207]

Overall, the examples of anion substitution present in this chapter demonstrate the versatility of mixed polyanions that can be achieved. While tetrel/pnictogen mixing always leads to fully ordered structures, the influences of triel elements are more intricate and statistical substitution is sometimes observed. Homologous silicon/germanium substitutions always yield statistically mixed tetrel positions, although some preferentially occupied positions have been observed in mixed clathrates. In all cases, open framework or layered structures have been observed, which could be suitable precursors for the synthesis of new semiconducting materials.

1.4 Scope and Outline

The goal of this work is to investigate substitution effects in alkali metal silicides and germanides. Resulting ternary and quaternary Zintl phases are to be tested as precursors for novel semiconductor materials, which could be interesting for application in the context of renewable energy production or storage (cf. Chapters 1.1–1.4).

In order to find new Zintl phases with unique anionic substructures, the alkali metals were partially substituted. Like Li_3NaSi_6, such compounds might be suitable precursors for new semiconductor materials because the combination of alkali metals can stabilize anion substructures that are not found in simple binary phases. The Li-Na-Ge system had previously not been investigated in detail. Chapter 3.1.1 introduces two novel Zintl phases, which both comprise unique anionic substructures. $Li_{18}Na_2Ge_{17}$ and Li_3NaGe_2 were characterized by X-ray diffraction methods as well as magnetic susceptibility measurements, NMR and Raman spectroscopy, and quantum chemical calculations. Investigations in the K-Na-Si system were aimed at the synthesis of A_4Si_9, the missing link in Zintl anion chemistry. As mentioned in Chapter 1.3.2, mixing different alkali metals might stabilize cluster anions such as $[Si_9]^{4-}$ which are not easily obtained in binary compounds. However, two new ternary Zintl phases containing tetrahedral clusters were found instead. K_7NaSi_8 and $K_{4-x}Na_xSi_4$ ($1 \leq x \leq 2.2$) were characterized using X-ray diffraction methods as well as nuclear magnetic resonance (NMR) spectroscopy (Chapter 3.1.2). In addition, ternary $Li_{12-y}Na_ySi_7$ ($0 \leq y \leq 0.5$) was investigated by X-ray diffraction methods in order to identify the reason for extraordinarily large displacement parameters reported for all known $Li_{12}T_7$ phases (Chapter 3.1.3).

In addition, partial substitution of the tetrel element in several alkali metal silicides and germanides with germanium and silicon, respectively, or with boron was investigated. Resulting mixed silicide-germanide or silicide-boride compounds could function as precursors for $Si_{1-x}Ge_x$ or $Si_{1-x}B_x$ materials. Therefore, this research might provide access to novel materials whose properties can be tuned by optimizing the ratio of the constituting elements.

Previous investigations of tetrel substitution in silicides and germanides were limited to solid solutions in which both side phases exist (cf. Chapter 1.3.3). In this work, substitution of silicon and germanium was attempted in alkali metal tetrelides that are known either only as a silicide or only as a germanide. Being a potential precursor for a new Si allotrope, Li_3NaSi_6 was a prime candidate for this investigation, but $Na_7LiSi_{8-x}Ge_x$ was also examined (Chapter 3.2.1). In addition, the distribution of Si and Ge atoms in $Li_{12}Si_{7-x}Ge_x$, for which "certain site preferences" had previously been mentioned,[74] was closely reviewed. Structures, compositions, and atom distributions of the mixed silicide-germanides were primarily analyzed using X-ray diffraction techniques. Si-Ge ratios were supported by energy-dispersive X-ray spectroscopy (EDX) data. Substitution of silicon with boron was investigated in the Li-Si-B system. Due to the high melting point and stable elemental structures of boron, the synthesis of boride phases typically requires very high temperature, which favor the formation of the thermodynamically most stable phases. Therefore, several boron-containing compounds were tested as reactive starting materials for syntheses under comparatively mild conditions (Chapter 3.2.2). This way, kinetically favorable compounds such as open tetrahedral framework (OTF) structures could be accessible.

Moreover, selected (pseudo-)binary phases in the Li-B and Li-C systems were examined. The potential solid electrolyte $Li_6B_{18}(Li_3N)_x$ with an open framework structure was characterized using X-ray diffraction methods and NMR spectroscopy (Chapter 3.2.3). The electronic structures of the template phase and related open framework structures are analyzed by quantum chemical calculations. Furthermore,

the identity of a novel binary lithium carbide obtained by lithium flux synthesis is analyzed by X-ray diffraction methods, Raman and NMR spectroscopy, thermal analysis by differential scanning calorimetry (DSC), and magnetic susceptibility measurements (Chapter 3.2.4).

Additionally, the reactivities of several Zintl phases were explored in order to produce new semiconductor materials. Broadening the number of functional materials, especially of those with unusual structures, may open up new opportunities for application.[139] In an attempt to reproduce and build on the synthesis of *allo*-Si, Li_3NaSi_6 and its mixed silicide-germanide counterpart $Li_3NaSi_{6-x}Ge_x$ were reacted with protic solvents (Chapter 3.3.1). The products were characterized via Raman spectroscopy, transmission electron microscopy (TEM), and thermal analysis by DSC and compared with amorphous Si synthesized from $Li_{15}Si_4$. Syntheses of mixed tetrel element-boron materials was attempted by reacting various alkali metal silicides and germanides with boron halides in organic solvents. The resulting products were characterized by powder X-ray diffraction (PXRD), thermal analysis via DSC, TEM, and Raman spectroscopy.

Allo-Ge was previously synthesized by chemical deintercalation of Li cations located between polygermanide sheets in Li_7Ge_{12} (cf. Chapter 1.2.3). In this work, the electrochemical deintercalation of Li_7Ge_{12} was investigated. In addition, the cycling stability and phase transformation behavior of *allo*-Ge electrodes was examined in half-cells versus Li (Chapter 3.3.2). The results of electrochemical cycling experiments in combination with in-situ powder X-ray diffraction (PXRD) were compared and analyzed in comparison to *α*-Ge half-cells, which were examined similarly.

Two-dimensional materials such as layered polysilanes extracted from $CaSi_2$ promise interesting properties for application in electronic components. Raw polysilane sheets form a somewhat crystalline stacked structure and are highly labile with respect to air, water, and UV light. Thus, pure $CaSi_2$ was provided for stabilization and separation of the silicon-based nanosheets via surface functionalization (Chapter 3.3.3). Resulting 2D materials were characterized by PXRD, thermogravimetric analysis (TGA) and atomic-force microscopy (AFM).

1.5 References

[1] B. Obama, *Remarks by the President at U.N. Climate Change Summit*, United Nations Headquarters, New York, NY, **September 23, 2014**.

[2] World Meteorological Organization, *Provisional WMO Statement on the Status of the Global Climate in 2016,* http://public.wmo.int/en/media/press-release/provisional-wmo-statement-status-of-global-climate-2016, **2016**.

[3] J. R. Petit, J. Jouzel, D. Raynaud, N. I. Barkov, J. M. Barnola, I. Basile, M. Bender, J. Chappellaz, M. Davis, G. Delaygue, M. Delmotte, V. M. Kotlyakov, M. Legrand, V. Y. Lipenkov, C. Lorius, L. Pepin, C. Ritz, E. Saltzman, M. Stievenard, *Nature* **1999**, *399*, 429–436.

[4] D. M. Etheridge, L. P. Steele, R. L. Langenfelds, R. J. Francey, J. M. Barnola, V. I. Morgan, *J. Geophys. Res.: Atmos.* **1996**, *101*, 4115–4128.

[5] C. D. Keeling, R. B. Bacastow, A. E. Bainbridge, C. A. Ekdahl, P. R. Guenther, L. S. Waterman, J. F. S. Chin, *Tellus* **1976**, *28*, 538–551.

[6] J.-M. Barnola, D. Raydaud, C. Lorius, N. I. Barkov, *Historical CO2 record from the Vostok ice core,* in *Trends: A Compendium of Data on Global Change*, Carbon Dioxide Information Analysis Center, Oak Ridge National Laboratory, U.S. Department of Energy, Oak Ridge, Tenn., USA, **2003**.

[7] J. R. Petit, D. Raynaud, C. Lorius, J. Jouzel, G. Delaygue, N. I. Barkov, V. M. Kotlyakov, *Historical isotopic temperature record from the Vostok ice core,* in *Trends: A Compendium of Data on Global Change*, Carbon Dioxide Information Analysis Center, Oak Ridge National Laboratory, U.S. Department of Energy, Oak Ridge, Tenn. U.S.A., **2000**.

[8] D. M. Etheridge, L. P. Steele, R. L. Langenfelds, R. J. Francey, J. M. Barnola, V. I. Morgan, *Historical CO2 records from the Law Dome DE08, DE08-2, and DSS ice cores,* in *Trends: A Compendium of Data on Global Change*, Carbon Dioxide Information Analysis Center, Oak Ridge National Laboratory, U.S. Department of Energy, Oak Ridge, Tenn., U.S.A., **1998**.

[9] R. F. Keeling, S. C. Piper, A. F. Bollenbacher, J. S. Walker, *Atmospheric CO2 records from sites in the SIO air sampling network,* in *Trends: A Compendium of Data on Global Change*, Carbon Dioxide Information Analysis Center, Oak Ridge National Laboratory, U.S. Department of Energy, Oak Ridge, Tenn., U.S.A., **2009**.

[10] T. A. Boden, G. Marland, R. J. Andres, *Global, Regional, and National Fossil-Fuel CO2 Emissions*, Carbon Dioxide Information Analysis Center, Oak Ridge National Laboratory, Oak Ridge, Tenn., U.S.A., **2016**.

[11] G. S. Callendar, *Q. J. R. Meteorol. Soc.* **1938**, *64*, 223–240.

[12] IPCC, *Climate Change 2013: The Physical Science Basis. Contribution of Working Group I to the Fifth Assessment Report of the Interngovernmental Panel on Climate Change*, Cambridge University Press, Cambridge, United Kingdom and New York, NY, USA, **2013**.

[13] G. De'ath, K. E. Fabricius, H. Sweatman, M. Puotinen, *Proc. Natl. Acad. Sci. U. S. A.* **2012**, *109*, 17995-17999.

[14] R. A. Betts, C. D. Jones, J. R. Knight, R. F. Keeling, J. J. Kennedy, *Nature Clim. Change* **2016**, *6*, 806–810.

[15] World Meteorological Organization, *WMO confirms 2016 as hottest year on record, about 1.1°C above pre-industrial era,* https://public.wmo.int/en/media/press-release/wmo-confirms-2016-hottest-year-record-about-11%C2%B0c-above-pre-industrial-era, **2017**.

[16] UNFCCC. Conference of the Parties (COP), *Report of the Conference of the Parties on its twenty-first session, held in Paris from 30 November to 13 December 2015. Addendum. Part two: Action taken by the Conference of the Parties*, Paris Climate Change Conference, Paris, France, United Nations Office at Geneva, Geneva, Switzerland, **2015**.

[17] United Nations, *Status of Treaties, Paris Agreement,* United Nations Treaty Collection, https://treaties.un.org/Pages/ViewDetails.aspx?src=TREATY&mtdsg_no=XXVII-7-d&chapter=27&clang=_en, **2016**.

[18] UNFCCC, *Landmark Climate Change Agreement to Enter into Force,* http://newsroom.unfccc.int/unfccc-newsroom/landmark-climate-change-agreement-to-enter-into-force/, **2016**.

[19] J. Rogelj, G. Luderer, R. C. Pietzcker, E. Kriegler, M. Schaeffer, V. Krey, K. Riahi, *Nature Clim. Change* **2015**, *5*, 519–527.

[20] International Energy Agency, *Tracking Clean Energy Progress 2016*, OECD, Paris, France, **2016**.

[21] International Energy Agency, Nuclear Energy Agency, *Projected Costs of Generating Electricity*, OECD, Paris, France, **2015**.

[22] S. Jacobsson, V. Lauber, *Energy Policy* **2006**, *34*, 256–276.

[23] International Energy Agency, *Energy Policies of IEA Countries - Germany*, OECD, Paris, France, **2013**.

[24] *Bruttostromerzeugung in Deutschland ab 1990 nach Energieträgern,* AG Energiebilanzen e.V., http://www.ag-energiebilanzen.de/index.php?article_id=29&fileName=20160802_brd_stromerzeugung1990-2015.pdf, **2016**.

[25] M. Bertau, A. Müller, P. Fröhlich, M. Katzberg, *Industrielle Anorganische Chemie*, 4th ed., Wiley-VCH, Weinheim, **2013**.

[26] P. Möller, *Anorganische Geochemie*, Springer-Verlag, Berlin, **1986**.

[27] C. Papadopoulos, *Solid-State Electronic Devices*, Springer, New York, U.S.A., **2014**.

[28] Deutsche Rohstoffagentur, *DERA-Rohstoffliste 2014*, Bundesanstalt für Geowissenschaften und Rohstoffe, Berlin, **2014**.

[29] IHS Inc., *PV Manufacturing Technology Report*, IHS Inc., Englewood, Colorado, U.S.A., **2014**.

[30] Deutsche Rohstoffagentur, *Silizium, Rohstoffwirtschaftliche Steckbriefe*, Bundesanstalt für Geowissenschaften und Rohstoffe, Hannover, **2016**.

[31] U. S. Geological Survey, *Mineral Commodity Summaries 2017*, U.S. Geological Survey, Reston, Virginia, U.S.A., **2016**.

[32] BP, *BP Statistical Review of World Energy 2016,* http://www.bp.com/content/dam/bp/pdf/energy-economics/statistical-review-2016/bp-statistical-review-of-world-energy-2016-full-report.pdf, **2016**.

[33] M. Schmela, *Global Market Outlook for Solar Power 2016–2020*, SolarPower Europe, Brussels, Belgium, **2016**.

[34] M. Rekinger, F. Thies, *Global Market Outlook for Solar Power 2015–2019*, SolarPower Europe, Brussels, Belgium, **2015**.

[35] G. Masson, S. Orlandi, M. Rekinger, *Global Market Outlook for Photovoltaics 2014–2018*, European Photovoltaic Industry Association, Brussels, Belgium, **2014**.

[36] W. Shockley, H. J. Queisser, *J. Appl. Phys.* **1961**, *32*, 510–519.

[37] S. Rühle, *Solar Energy* **2016**, *130*, 139–147.

[38] K. Masuko, M. Shigematsu, T. Hashiguchi, D. Fujishima, M. Kai, N. Yoshimura, T. Yamaguchi, Y. Ichihashi, T. Mishima, N. Matsubara, T. Yamanishi, T. Takahama, M. Taguchi, E. Maruyama, S. Okamoto, *IEEE J. Photovoltaics* **2014**, *4*, 1433–1435.

[39] Fraunhofer ISE, *Press Release,* https://www.ise.fraunhofer.de/en/press-and-media/press-releases/press-releases-2014/new-world-record-for-solar-cell-efficiency-at-46-percent?set_language=en, **2014**.

[40] M. A. Green, K. Emery, Y. Hishikawa, W. Warta, E. D. Dunlop, *Prog. Photovoltaics* **2016**, *24*, 905–913.

[41] N. S. Lewis, *Science* **2016**, *351*, aad1920.

[42] Bundesregierung, *Nationaler Entwicklungsplan Elektromobilität der Bundesregierung,* https://www.bmbf.de/files/nationaler_entwicklungsplan_elektromobilitaet.pdf, **2009**.

[43] Nationale Plattform Elektromobilität, *Wegweiser Elektromobilität*, Gemeinsame Geschäftsstelle Elektromobilität der Bundesregierung, Berlin, Germany, **2016**.

[44] Y. Wang, W. D. Richards, S. P. Ong, L. J. Miara, J. C. Kim, Y. Mo, G. Ceder, *Nat. Mater.* **2015**, *14*, 1026–1031.

[45] P. G. Bruce, A. R. West, *J. Electrochem. Soc.* **1983**, *130*, 662–669.

[46] A. D. Robertson, A. R. West, A. G. Ritchie, *Solid State Ionics* **1997**, *104*, 1–11.

[47] N. Kamaya, K. Homma, Y. Yamakawa, M. Hirayama, R. Kanno, M. Yonemura, T. Kamiyama, Y. Kato, S. Hama, K. Kawamoto, A. Mitsui, *Nat. Mater.* **2011**, *10*, 682–686.

[48] A. Kuhn, O. Gerbig, C. Zhu, F. Falkenberg, J. Maier, B. V. Lotsch, *Phys. Chem. Chem. Phys.* **2014**, *16*, 14669–14674.
[49] Y. Kato, S. Hori, T. Saito, K. Suzuki, M. Hirayama, A. Mitsui, M. Yonemura, H. Iba, R. Kanno, *Nature Energy* **2016**, *1*, 16030.
[50] M. Ashuri, Q. He, L. L. Shaw, *Nanoscale* **2016**, *8*, 74–103.
[51] S. Wu, C. Han, J. Iocozzia, M. Lu, R. Ge, R. Xu, Z. Lin, *Angew. Chem. Int. Ed.* **2016**, *55*, 7898–7922.
[52] M. N. Obrovac, L. Christensen, *Electrochem. Solid-State Lett.* **2004**, *7*, A93–A96.
[53] M. T. McDowell, S. W. Lee, W. D. Nix, Y. Cui, *Adv. Mater.* **2013**, *25*, 4966–4985.
[54] L. Baggetto, P. H. L. Notten, *J. Electrochem. Soc.* **2009**, *156*, A169–A175.
[55] J. Grätz, C. C. Ahn, R. Yazami, B. Fultz, *J. Electrochem. Soc.* **2004**, *151*, A698–A702.
[56] L. Y. Beaulieu, K. W. Eberman, R. L. Turner, L. J. Krause, J. R. Dahn, *Electrochem. Solid-State Lett.* **2001**, *4*, A137–A140.
[57] A. F. Holleman, E. Wiberg, N. Wiberg, *Lehrbuch der anorganischen Chemie*, 102nd ed., de Gruyter, Berlin, **2007**.
[58] J. Witte, H. G. von Schnering, W. Klemm, *Z. Anorg. Allg. Chem.* **1964**, *327*, 260–273.
[59] J. Evers, *J. Solid State Chem.* **1979**, *28*, 369–377.
[60] A. Currao, J. Curda, R. Nesper, *Z. Anorg. Allg. Chem.* **1996**, *622*, 85–94.
[61] I. M. Kurylyshyn, T. F. Fässler, A. Fischer, C. Hauf, G. Eickerling, M. Presnitz, W. Scherer, *Angew. Chem. Int. Ed.* **2014**, *53*, 3029–3032.
[62] B. Eisenmann, H. Schäfer, *Z. Naturforsch. B* **1974**, *29*, 460–463.
[63] S. Ponou, T. F. Fässler, *Z. Anorg. Allg. Chem.* **2007**, *633*, 393–397.
[64] H. G. von Schnering, M. Baitinger, U. Bolle, W. Carrillo-Cabrera, J. Curda, Y. Grin, F. Heinemann, J. Llanos, K. Peters, A. Schmeding, M. Somer, *Z. Anorg. Allg. Chem.* **1997**, *623*, 1037–1039.
[65] C. Hoch, M. Wendorff, C. Röhr, *J. Alloy. Compd.* **2003**, *361*, 206–221.
[66] V. Queneau, S. C. Sevov, *Angew. Chem. Int. Ed. Engl.* **1997**, *36*, 1754–1756.
[67] V. Quéneau, E. Todorov, S. C. Sevov, *J. Am. Chem. Soc.* **1998**, *120*, 3263–3264.
[68] K. Wade, *J. Chem. Soc. D* **1971**, 792–793.
[69] D. M. P. Mingos, *Acc. Chem. Res.* **1984**, *17*, 311–319.
[70] S. Scharfe, F. Kraus, S. Stegmaier, A. Schier, T. F. Fässler, *Angew. Chem. Int. Ed.* **2011**, *50*, 3630–3670.
[71] E. Busmann, *Z. Anorg. Allg. Chem.* **1961**, *313*, 90–106.
[72] H. G. von Schnering, R. Nesper, J. Curda, K.-F. Tebbe, *Angew. Chem. Int. Ed. Engl.* **1980**, *19*, 1033–1034.
[73] H. G. von Schnering, R. Nesper, K.-F. Tebbe, J. Curda, *Z. Metallkd.* **1980**, *71*, 357–363.
[74] R. Nesper, *Prog. Solid State Chem.* **1990**, *20*, 1–45.
[75] U. Frank, W. Müller, H. Schäfer, *Z. Naturforsch. B* **1975**, *30*, 10–13.
[76] M. Zeilinger, T. F. Fässler, *Acta Crystallogr. Sect. E* **2013**, *69*, i81–i82.
[77] R. Nesper, Habilitation, Universität Stuttgart (Stuttgart), **1988**.
[78] M. Zeilinger, V. Baran, L. van Wüllen, U. Häussermann, T. F. Fässler, *Chem. Mater.* **2013**, *25*, 4113–4121.
[79] Q. Johnson, G. S. Smith, D. Wood, *Acta Crystallogr.* **1965**, *18*, 131–132.
[80] M. Zeilinger, I. M. Kurylyshyn, U. Häussermann, T. F. Fässler, *Chem. Mater.* **2013**, *25*, 4623–4632.
[81] M. Zeilinger, T. F. Fässler, *Dalton Trans.* **2014**, *43*, 14959–14970.
[82] M. Zeilinger, D. Benson, U. Häussermann, T. F. Fässler, *Chem. Mater.* **2013**, *25*, 1960–1967.
[83] R. Nesper, H. G. von Schnering, J. Curda, *Chem. Ber.* **1986**, *119*, 3576–3590.
[84] A. Kuhn, P. Sreeraj, R. Pöttgen, H.-D. Wiemhöfer, M. Wilkening, P. Heitjans, *Angew. Chem. Int. Ed.* **2011**, *50*, 12099–12102.
[85] S. Dupke, T. Langer, R. Pöttgen, M. Winter, H. Eckert, *Solid State Nucl. Magn. Res.* **2012**, *42*, 17–25.
[86] R. Nesper, S. Wengert, F. Zürcher, A. Currao, *Chem. Eur. J.* **1999**, *5*, 3382–3389.
[87] R. Tamori, N. Machida, T. Shigematsu, *J. Jpn. Soc. Powder Powder Metall.* **2001**, *48*, 267–273.
[88] C. Cros, M. Pouchard, P. Hagenmuller, *C. R. Hebd. Seances Acad. Sci.* **1965**, *260*, 4764–4767.

[89] J. S. Kasper, P. Hagenmuller, M. Pouchard, C. Cros, *Science* **1965**, *150*, 1713–1714.
[90] M. Beekman, E. N. Nenghabi, K. Biswas, C. W. Myles, M. Baitinger, Y. Grin, G. S. Nolas, *Inorg. Chem.* **2010**, *49*, 5338–5340.
[91] C. Cros, M. Pouchard, P. Hagenmuller, *J. Solid State Chem.* **1970**, *2*, 570–581.
[92] L. Pauling, R. E. Marsh, *Proc. Natl. Acad. Sci. U. S. A.* **1952**, *38*, 112–118.
[93] M. von Stackelberg, H. R. Müller, *J. Chem. Phys.* **1951**, *19*, 1319–1320.
[94] H. Horie, T. Kikudome, K. Teramura, S. Yamanaka, *J. Solid State Chem.* **2009**, *182*, 129–135.
[95] B. Böhme, A. M. Guloy, Z. Tang, W. Schnelle, U. Burkhardt, M. Baitinger, Y. Grin, *J. Am. Chem. Soc.* **2007**, *129*, 5348–5349.
[96] M. Beekman, S. Stefanoski, W. Wong-Ng, J. A. Kaduk, Q. Huang, C. Reeg, C. R. Bowers, G. S. Nolas, *J. Solid State Chem.* **2010**, *183*, 1272–1277.
[97] J. D. Bryan, G. D. Stucky, *Chem. Mater.* **2001**, *13*, 253–257.
[98] J. Evers, G. Oehlinger, G. Sextl, *Angew. Chem. Int. Ed.* **1993**, *32*, 1442–1444.
[99] E. Menges, V. Hopf, H. Schäfer, A. Weiss, *Z. Naturforsch. B* **1969**, *24*, 1351–1352.
[100] A. Grüttner, R. Nesper, H. G. v. Schnering, *Acta Crystallogr. Sect. A* **1981**, *37*, C161.
[101] F. Kiefer, T. F. Fässler, *Solid State Sci.* **2011**, *13*, 636–640.
[102] L. A. Stearns, J. Gryko, J. Diefenbacher, G. K. Ramachandran, P. F. McMillan, *J. Solid State Chem.* **2003**, *173*, 251–258.
[103] W. S. Tang, J.-N. Chotard, R. Janot, *J. Electrochem. Soc.* **2013**, *160*, A1232–A1240.
[104] J. Evers, G. Oehlinger, *Angew. Chem. Int. Ed.* **2001**, *40*, 1050–1053.
[105] O. O. Kurakevych, T. A. Strobel, D. Y. Kim, T. Muramatsu, V. V. Struzhkin, *Cryst. Growth Des.* **2013**, *13*, 303–307.
[106] A. Grüttner, R. Nesper, H. G. von Schnering, *Angew. Chem. Int. Ed. Engl.* **1982**, *21*, 912–913.
[107] F. Kiefer, A. J. Karttunen, M. Döblinger, T. F. Fässler, *Chem. Mater.* **2011**, *23*, 4578–4586.
[108] F. Kiefer, V. Hlukhyy, A. J. Karttunen, T. F. Fässler, C. Gold, E.-W. Scheidt, W. Scherer, J. Nylén, U. Häussermann, *J. Mater. Chem.* **2010**, *20*, 1780–1786.
[109] J. V. Zaikina, E. Muthuswamy, K. I. Lilova, Z. M. Gibbs, M. Zeilinger, G. J. Snyder, T. F. Fässler, A. Navrotsky, S. M. Kauzlarich, *Chem. Mater.* **2014**, *26*, 3263–3271.
[110] A. Ammar, C. Cros, M. Pouchard, N. Jaussaud, J.-M. Bassat, G. Villeneuve, M. Duttine, M. Ménétrier, E. Reny, *Solid State Sci.* **2004**, *6*, 393–400.
[111] A. M. Guloy, R. Ramlau, Z. Tang, W. Schnelle, M. Baitinger, Y. Grin, *Nature* **2006**, *443*, 320–323.
[112] J. Gryko, P. McMillan, R. Marzke, G. Ramachandran, D. Patton, S. Deb, O. Sankey, *Phys. Rev. B* **2000**, *62*, R7707–R7710.
[113] A. D. Martinez, L. Krishna, L. L. Baranowski, M. T. Lusk, E. S. Toberer, A. C. Tamboli, *IEEE J. Photovoltaics* **2013**, *3*, 1305–1310.
[114] D. Y. Kim, S. Stefanoski, O. O. Kurakevych, T. A. Strobel, *Nat. Mater.* **2015**, *14*, 169–173.
[115] M. M. Bentlohner, M. Waibel, P. Zeller, K. Sarkar, P. Müller-Buschbaum, D. Fattakhova-Rohlfing, T. F. Fässler, *Angew. Chem. Int. Ed.* **2016**, *55*, 2441–2445.
[116] G. S. Armatas, M. G. Kanatzidis, *Nature* **2006**, *441*, 1122–1125.
[117] G. S. Armatas, M. G. Kanatzidis, *Science* **2006**, *313*, 817–820.
[118] L. Zhao, D. J. Dvorak, M. N. Obrovac, *J. Power Sources* **2016**, *332*, 290–298.
[119] R. A. Bley, S. M. Kauzlarich, *J. Am. Chem. Soc.* **1996**, *118*, 12461–12462.
[120] D. Mayeri, B. L. Phillips, M. P. Augustine, S. M. Kauzlarich, *Chem. Mater.* **2001**, *13*, 765–770.
[121] D. Neiner, H. W. Chiu, S. M. Kauzlarich, *J. Am. Chem. Soc.* **2006**, *128*, 11016–11017.
[122] B. M. Nolan, T. Henneberger, M. Waibel, T. F. Fässler, S. M. Kauzlarich, *Inorg. Chem.* **2015**, *54*, 396–401.
[123] B. R. Taylor, S. M. Kauzlarich, H. W. H. Lee, G. R. Delgado, *Chem. Mater.* **1998**, *10*, 22–24.
[124] X. Ma, F. Wu, S. M. Kauzlarich, *J. Solid State Chem.* **2008**, *181*, 1628–1633.
[125] C. Eun-Chel, P. Sangwook, H. Xiaojing, S. Dengyuan, C. Gavin, P. Sang-Cheol, A. G. Martin, *Nanotechnology* **2008**, *19*, 245201.
[126] M. L. Mastronardi, E. J. Henderson, D. P. Puzzo, Y. Chang, Z. B. Wang, M. G. Helander, J. Jeong, N. P. Kherani, Z. Lu, G. A. Ozin, *Small* **2012**, *8*, 3647–3654.

[127] F. Wöhler, *Justus Liebigs Ann. Chem.* **1863**, *127*, 257–274.
[128] H. Kautsky, H. Pfleger, *Z. Anorg. Allg. Chem.* **1958**, *295*, 206–217.
[129] A. Weiss, G. Beil, H. Meyer, *Z. Naturforsch. B* **1979**, *34*, 25–30.
[130] S. Yamanaka, H. Matsu, M. Ishikawa, *Mater. Res. Bull.* **1996**, *31*, 307–316.
[131] H. Okamoto, Y. Kumai, Y. Sugiyama, T. Mitsuoka, K. Nakanishi, T. Ohta, H. Nozaki, S. Yamaguchi, S. Shirai, H. Nakano, *J. Am. Chem. Soc.* **2010**, *132*, 2710–2718.
[132] H. Nakano, M. Nakano, K. Nakanishi, D. Tanaka, Y. Sugiyama, T. Ikuno, H. Okamoto, T. Ohta, *J. Am. Chem. Soc.* **2012**, *134*, 5452–5455.
[133] H. Okamoto, Y. Sugiyama, K. Nakanishi, T. Ohta, T. Mitsuoka, H. Nakano, *Chem. Mater.* **2015**, *27*, 1292–1298.
[134] Y. Kumai, S. Shirai, E. Sudo, J. Seki, H. Okamoto, Y. Sugiyama, H. Nakano, *J. Power Sources* **2011**, *196*, 1503–1507.
[135] K. Yoko, N. Hideyuki, *Jpn. J. Appl. Phys.* **2015**, *54*, 035201.
[136] G. Vogg, M. S. Brandt, M. Stutzmann, *Adv. Mater.* **2000**, *12*, 1278–1281.
[137] E. Bianco, S. Butler, S. Jiang, O. D. Restrepo, W. Windl, J. E. Goldberger, *ACS Nano* **2013**, *7*, 4414–4421.
[138] Z. Liu, Z. Lou, Z. Li, G. Wang, Z. Wang, Y. Liu, B. Huang, S. Xia, X. Qin, X. Zhang, Y. Dai, *Chem. Commun.* **2014**, *50*, 11046–11048.
[139] B. Haberl, T. A. Strobel, J. E. Bradby, *Appl. Phys. Rev.* **2016**, *3*, 040808.
[140] M. A. Zwijnenburg, K. E. Jelfs, S. T. Bromley, *Phys. Chem. Chem. Phys.* **2010**, *12*, 8505–8512.
[141] Q. Wang, B. Xu, J. Sun, H. Liu, Z. Zhao, D. Yu, C. Fan, J. He, *J. Am. Chem. Soc.* **2014**, *136*, 9826–9829.
[142] Z. Zhao, F. Tian, X. Dong, Q. Li, Q. Wang, X. Zhong, B. Xu, D. Yu, J. He, H.-T. Wang, Y. Ma, Y. Tian, *J. Am. Chem. Soc.* **2012**, *134*, 12362–12365.
[143] J. C. Conesa, *J. Phys. Chem. B* **2002**, *106*, 3402–3409.
[144] D. Chadi, *Phys. Rev. B* **1985**, *32*, 6485–6489.
[145] A. J. Karttunen, T. F. Fässler, *ChemPhysChem* **2013**, *14*, 1807–1817.
[146] A. J. Karttunen, T. F. Fässler, M. Linnolahti, T. A. Pakkanen, *Inorg. Chem.* **2011**, *50*, 1733–1742.
[147] L.-A. Jantke, S. Stegmaier, A. J. Karttunen, T. F. Fässler, *Chem. Eur. J.* **2016**, DOI: 10.1002/chem.201603406.
[148] J. K. Burdett, S. Lee, T. J. McLarnan, *J. Am. Chem. Soc.* **1985**, *107*, 3083–3089.
[149] G. J. Miller, *Eur. J. Inorg. Chem.* **1998**, *1998*, 523–536.
[150] H. G. von Schnering, M. Schwarz, R. Nesper, *J. Less-Common Met.* **1988**, *137*, 297–310.
[151] S. Bobev, S. C. Sevov, *Angew. Chem. Int. Ed.* **2001**, *40*, 1507–1510.
[152] J. Llanos, R. Nesper, H. G. von Schnering, *Angew. Chem. Int. Ed. Engl.* **1983**, *22*, 998.
[153] H. G. von Schnering, M. Schwarz, R. Nesper, *Angew. Chem. Int. Ed. Engl.* **1986**, *25*, 566–567.
[154] M. Schwarz, Dissertation, Universität Stuttgart **1987**.
[155] J. Llanos, Dissertation, Universität Stuttgart **1984**.
[156] H. G. von Schnering, J. Llanos, G. Yu, W. Carrillo-Cabrera, E.-M. Peters, K. Peters, R. Nesper, *Z. Kristallogr. - New Cryst. Struct.* **1998**, *213*, 661.
[157] T. Goebel, Y. Prots, A. Ormeci, O. Pecher, F. Haarmann, *Z. Anorg. Allg. Chem.* **2011**, *637*, 1982–1991.
[158] O. Pecher, M. Esters, A. Görne, B. Mausolf, A. Ormeci, F. Haarmann, *Z. Anorg. Allg. Chem.* **2014**, *640*, 2169–2176.
[159] S. Bobev, S. C. Sevov, *J. Am. Chem. Soc.* **1999**, *121*, 3795–3796.
[160] M. Waibel, G. Raudaschl-Sieber, T. F. Fässler, *Chem. Eur. J.* **2011**, *17*, 13391–13394.
[161] U. Bolle, W. Carrillo-Cabrera, K. Peters, H. G. v. Schnering, *Z. Kristallogr. - New Cryst. Struct.* **1998**, *213*, 729.
[162] Q. Xie, E. Cuervo Reyes, M. Wörle, R. Nesper, *Z. Anorg. Allg. Chem.* **2011**, *637*, 846–858.
[163] H. G. von Schnering, U. Bolle, J. Curda, K. Peters, W. Carrillo-Cabrera, M. Somer, M. Schultheiss, U. Wedig, *Angew. Chem. Int. Ed. Engl.* **1996**, *35*, 984–986.
[164] W. Müller, H. Schäfer, A. Weiss, *Z. Naturforsch. B* **1971**, *26*, 5–7.

[165] W. Müller, H. Schäfer, A. Weiss, *Z. Naturforsch. B* **1971**, *26*, 534–536.
[166] D. Gon Park, Y. Dong, F. J. DiSalvo, *J. Alloy. Compd.* **2009**, *470*, 90–95.
[167] Q. X. Xie, R. Nesper, *Z. Kristallogr. - New Cryst. Struct.* **2003**, *218*, 291–292.
[168] M. Baitinger, H. G. von Schnering, J.-H. Chang, K. Peters, Y. Grin, *Z. Kristallogr. - New Cryst. Struct.* **2007**, *222*, 87–88.
[169] H. Kawaji, H. Horie, S. Yamanaka, M. Ishikawa, *Phys. Rev. Lett.* **1995**, *74*, 1427–1429.
[170] S. Yamanaka, H. Horie, H. Kawaji, M. Ishikawa, *Eur. J. Solid State Inorg. Chem.* **1995**, *32*, 799–807.
[171] R. Nesper, J. Curda, H. G. von Schnering, *J. Solid State Chem.* **1986**, *62*, 199–206.
[172] J. F. Herbst, M. S. Meyer, *J. Alloy. Compd.* **2010**, *492*, 65–68.
[173] H. Pauly, A. Weiss, H. Witte, *Z. Metallkd.* **1968**, *59*, 414–418.
[174] W. Müller, H. Schäfer, A. Weiss, *Z. Naturforsch. B* **1970**, *25*, 431–432.
[175] J. D. Corbett, *Angew. Chem. Int. Ed.* **2000**, *39*, 670–690.
[176] R. W. Olesinski, G. J. Abbaschian, *Bull. Alloy Phase Diagr.* **1984**, *5*, 180–183.
[177] J. B. Renucci, M. A. Renucci, M. Cardona, *Solid State Commun.* **1971**, *9*, 1651–1654.
[178] M. Alonso, K. Winer, *Phys. Rev. B* **1989**, *39*, 10056–10062.
[179] A. Qteish, R. Resta, *Phys. Rev. B* **1988**, *37*, 1308–1314.
[180] E. Kasper, *J. Cryst. Growth* **1995**, *150*, 921–925.
[181] C. Eisele, M. Berger, M. Nerding, H. P. Strunk, C. E. Nebel, M. Stutzmann, *Thin Solid Films* **2003**, *427*, 176–180.
[182] P. R. Abel, A. M. Chockla, Y. M. Lin, V. C. Holmberg, J. T. Harris, B. A. Korgel, A. Heller, C. B. Mullins, *ACS Nano* **2013**, *7*, 2249–2257.
[183] M. Waibel, O. Pecher, B. Mausolf, F. Haarmann, T. F. Fässler, *Eur. J. Inorg. Chem.* **2013**, *2013*, 5541–5546.
[184] H. Morito, K. Momma, H. Yamane, *J. Alloy. Compd.* **2015**, *623*, 473–479.
[185] M. Waibel, C. B. Benda, B. Wahl, T. F. Fässler, *Chem. Eur. J.* **2011**, *17*, 12928–12931.
[186] R. J. LaBotz, D. R. Mason, D. F. O'Kane, *J. Electrochem. Soc.* **1963**, *110*, 127–134.
[187] F. Zürcher, S. Leoni, R. Nesper, *Z. Kristallogr. - Cryst. Mater.* **2003**, *218*, 171–177.
[188] H. Fukuoka, J. Kiyoto, S. Yamanaka, *J. Solid State Chem.* **2003**, *175*, 237–244.
[189] G. Vogg, A. J.-P. Meyer, C. Miesner, M. S. Brandt, M. Stutzmann, *Appl. Phys. Lett.* **2001**, *78*, 3956–3958.
[190] G. Vogg, C. Miesner, M. S. Brandt, M. Stutzmann, G. Abstreiter, *J. Cryst. Growth* **2001**, *223*, 573–576.
[191] W. Westerhaus, H.-U. Schuster, *Z. Naturforsch. B* **1977**, *32*, 1365–1367.
[192] H. G. von Schnering, H. Menke, R. Kröner, E. M. Peters, K. Peters, R. Nesper, *Z. Kristallogr. - New Cryst. Struct.* **1998**, *213*, 713–714.
[193] H. G. von Schnering, R. Kröner, H. Menke, K. Peters, R. Nesper, *Z. Kristallogr. - New Cryst. Struct.* **1998**, *213*, 717–718.
[194] L. Spina, M. Tillard, C. Belin, *Z. Kristallogr. - New Cryst. Struct.* **2002**, *217*, 453–454.
[195] L. Spina, Z. Jia Yong, B. Ducourant, M. Tillard, C. Belin, *Z. Kristallogr. - Cryst. Mater.* **2003**, *218*, 740–746.
[196] M. Tillard, C. Belin, L. Spina, Y. Z. Jia, *Acta Crystallogr. Sect. C* **2005**, *61*, i51-i53.
[197] N. Vojteer, M. Schroeder, C. Röhr, H. Hillebrecht, *Chem. Eur. J.* **2008**, *14*, 7331–7342.
[198] H. Morito, B. Eck, R. Dronskowski, H. Yamane, *Dalton Trans.* **2010**, *39*, 10197–10202.
[199] M. Zeilinger, L. van Wüllen, D. Benson, V. F. Kranak, S. Konar, T. F. Fässler, U. Häussermann, *Angew. Chem. Int. Ed.* **2013**, *52*, 5978–5982.
[200] W. Jung, J. Lörincz, R. Ramlau, H. Borrmann, Y. Prots, F. Haarmann, W. Schnelle, U. Burkhardt, M. Baitinger, Y. Grin, *Angew. Chem. Int. Ed.* **2007**, *46*, 6725–6728.
[201] L. Toffoletti, H. Kirchhain, J. Landesfeind, W. Klein, L. van Wüllen, H. A. Gasteiger, T. F. Fässler, *Chem. Eur. J.* **2016**, *22*, 17635–17645.
[202] B. Eisenmann, M. Somer, *Z. Naturforsch. B* **1985**, *40*, 886–890.
[203] B. Eisenmann, M. Somer, *Z. Naturforsch. B* **1984**, *39*, 736–738.

[204] K. Feng, L. Kang, W. Yin, W. Hao, Z. Lin, J. Yao, Y. Wu, *J. Solid State Chem.* **2013**, *205*, 129–133.
[205] S. Pagano, M. Zeuner, S. Hug, W. Schnick, *Eur. J. Inorg. Chem.* **2009**, *2009*, 1579–1584.
[206] W. M. Hurng, J. D. Corbett, S. L. Wang, R. A. Jacobson, *Inorg. Chem.* **1987**, *26*, 2392–2395.
[207] K. Feng, W. Yin, R. He, Z. Lin, S. Jin, J. Yao, P. Fu, Y. Wu, *Dalton Trans.* **2012**, *41*, 484–489.

2 EXPERIMENTAL SECTION

2.1 Synthesis

2.1.1 Sample Handling

Most starting materials and products employed in this work are highly sensitive to air and moisture. Therefore, sample preparation, handling and storage were carefully performed under inert conditions inside a glovebox (MBraun, $p(H_2O)$, $p(O_2)$ < 1.0 ppm) or using standard Schlenk techniques. Argon (Westfalen, purity grade 4.8) was used as the inert gas and was dried over P_2O_5, and molecular sieve before use. Argon used in the Schlenk line was additionally dried over a titanium sponge heated to 750 °C in order to remove traces of nitrogen.

2.1.2 Starting Materials

Table 2.1 below lists all starting materials used with their respective specifications. Li, Na, and K were freed from oxide layers prior to use. Si and Ge were often ball-milled in order to obtain a more reactive, fine powder. Ethanol was dried over Na and benzophenone, and tetrahydrofurane (THF) and toluene were taken from a solvent purification system (MBraun, MB-SPS). All solvents were stored over molecular sieve (3 Å).

Table 2.1. Specifications of all starting materials.

Material	Shape	Supplier	Purity
Li	Rods	Rockwood Li	> 99 %
Na	Rods	Chempur	99 %
K	Pieces	Merck	98 %
Ca	Pieces	Alfa Aesar	99.5 %
B (crystalline)	Pieces	Chempur	99.95 %
B (nano)	Powder	Pavezyum	98.5 %
C_{60}	Powder	Hoechst	> 99 %
Si	Pieces	Wacker	99.9 %
Ge	Pieces	EvoChem	99.999 %
LiH	Powder	Alfa Aesar	98 %
NaH	Powder	Sigma Aldrich	95 %
$LiBH_4$	Powder	Acros Organics	95 %
Li_2O	Powder	Alfa Aesar	99.5 %
Li_3N	Powder	Sigma Aldrich	99.5 %
B_2O_3	Powder	Alfa Aesar	99.98 %
BBr_3	Liquid	Sigma Aldrich	99 %
BI_3	Powder	Sigma Aldrich	95 %
$B(C_6H_5)_2I$	Liquid	Sigma Aldrich	97 %
Ethanol	Liquid	-	technical
Dimethyl sulfoxide	Liquid	Sigma Aldrich	> 99.9 %
Tetrahydrofurane	Liquid	Bernd Kraft	99.9 %
Toluene	Liquid	Merck	99.9 %

2.1.3 High-Temperature Syntheses

High-temperature reactions of reactive substances such as alkali metals require careful selection of reaction containers. Glass or silica ampules are unfit for this purpose because alkali metal diffusion

into the container material renders it brittle, thus posing a high threat of breaches. Niobium and tantalum ampules better serve this purpose. Up to 900 °C, tantalum is largely inert with respect to the alkali metals as well as silicon and germanium. In addition, Ta is highly permeable for hydrogen gas, allowing reactions with hydrogen formation. In contrast, niobium preferably forms $NbSi_2$ when in contact with Si at higher temperatures. Because it is much cheaper than Ta, it was used for all reactions containing Ge but not Si as a starting material and without hydrogen formation during the reaction.

Boron reacts readily with both Nb and Ta at elevated temperatures. Reactions using boron or boron-containing compounds were therefore performed in stainless steel ampules or in crucibles custom-built from BN rods by the precision mechanics workshop at TU München. Stainless steel ampules can only be used when no tetrel elements are present in the reaction mixture. Reactions including a tetrel element and boron were thus always performed in BN crucibles.

The Nb and Ta ampules were custom-built from Nb and Ta tubes with outer diameters of 10 or 12.7 mm (wall thickness 0.5 mm). These were cut into shorter tubes of 4–8 cm, depending on the sample size. Fitted caps were punched of Nb and Ta sheets (thickness 0.5 mm) by the precision mechanics workshop at TU München. Examples of such metal ampule sets are shown in Figure 2.1. The prepared tubes and caps were thoroughly cleaned by sonication in acetone, glacial acetic acid, and again acetone. To remove adsorbed water and oxygen, they were pre-dried overnight in a drying oven at 120 °C and then heated to 1000 °C for one hour under dynamic vacuum. Inside the glovebox, all metal ampules were assembled by welding one cap to a tube using an arc furnace (Edmund Bühler, MAM1).

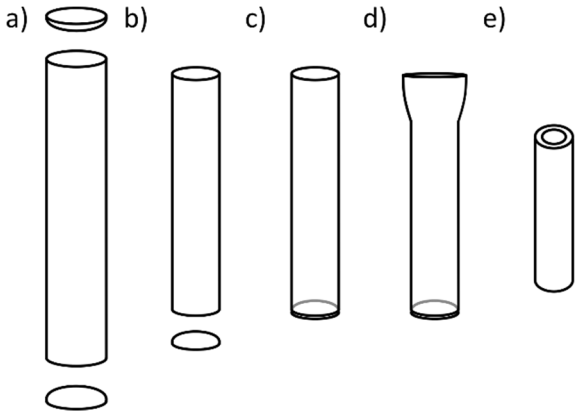

Figure 2.1. Reaction container assemblies used for high-temperature syntheses: a) ø 12.7 mm Nb/Ta tube for large samples with bottom and top cap, b) ø 10 mm Nb/Ta tube for small samples with bottom cap, c) ø 10 mm Nb/Ta ampule with attached bottom cap, d) ø 10 mm Nb/Ta ampule with attached bottom cap and squeezed top, e) ø 8 mm BN crucibles which can be enclosed in ø 10 mm Nb ampules.

The BN crucibles (Figure 2.1e) were characterized by an outer diameter of 8 mm at a length of 30 mm and could thus be enclosed in Nb ampules (inner diameter 9 mm) for synthesis under inert conditions. Stainless steel ampules were custom-built from stainless steel tubes with an outer diameter of 12.7 mm (wall thickness 0.5 mm). Tubes and caps were prepared as described above. To avoid surface oxidation, the stainless steel ampules and caps were cleaned by sonication in acetone and were dried at 120 °C for only a few hours before being transferred to an argon-filled glovebox for storage.

The clean metal ampules were then filled with starting material. When alkali metals were reacted with other reagents, the low-melting metal pieces were placed on the bottom of the reaction container and topped with the higher-melting components. When all starting materials were powders, they were

usually mixed thoroughly by grinding in an agate mortar and then pressed to pellets with a diameter of 6 mm using a manual hydraulic press in the glovebox (Specac, Atlas 15T). This procedure especially benefits solid-state reactions below the melting point of all components by facilitating the rate-limiting diffusion. Ampules filled with starting material were roughly closed using a second metal cap. Alternatively, the top side of the tube can be squeezed together (Figure 2.1d). Accordingly prepared metal ampules were then fixed in a water-cooled copper block and closed tightly by arc welding.

In air, Nb and Ta are both oxidized above 300 °C, so that these reaction containers must be heated under inert conditions. For this purpose, Nb and Ta ampules were enclosed in silica ampules (outer diameter 18 mm, wall thickness 1 mm) or inside larger silica tubes (outer diameter 35 mm) equipped with a 40/45 ground glass joint and a stopcock. The 35 mm silica tubes can hold several metal ampules at a time for parallelized syntheses and were thus also employed for parallel syntheses in stainless steel ampules. All silica ampules and tubes were evacuated and flushed with argon several times before being closed under vacuum in order to prevent both oxidation of the metal ampules and pressure build-up inside the silica container.

Metal ampules enclosed in large silica tubes were then transferred into tube furnaces (HTM Reetz LOBA 1200-40-600, Eurotherm 2416 controller). Metal ampules inside silica ampules were heated in muffle ovens (Nabertherm, P330 controller). The heating programs were adjusted for the specific syntheses and are given in the respective publications and manuscripts in Chapter 5.

2.1.4 Flux Synthesis

Flux syntheses can be an efficient tool for single crystal growth or for the preparation of intermetallic phases rich in low-melting metals. The method requires an excess amount of a low-melting metal, which functions as a solvent in the reaction. Flux syntheses were performed using custom-built stainless steel ampules, which were equipped with a stainless steel sieve, located in the middle of the ampule (Figure 2.2a). The starting materials were loaded onto the sieve with the bottom cap already welded on (Figure 2.2b). Subsequently, the ampules were closed tightly with another metal cap and turned upside down so that the starting materials rest on the bottom of the ampules (Figure 2.2c). The ampules were then enclosed in steel containers lined with silica wool and transferred to a muffle oven (Nabertherm, P330 controller).

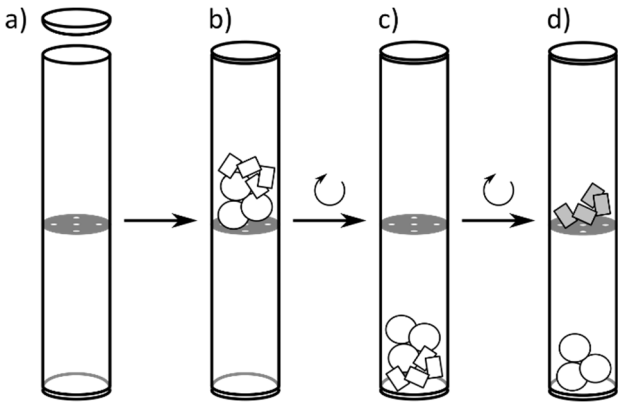

Figure 2.2. Schematic representation of the flux synthesis procedure: a) The stainless ampule is equipped with a stainless steel sieve located in the middle of the ampule; b) the starting materials are loaded onto the sieve and the ampule is closed by welding on caps on both sides; c) the ampule is turned upside down so that the reaction mixture resides on the bottom of the ampule during high-temperature synthesis; d) the ampule is turned upside down again to filter off the flux metal. This last step is facilitated by isothermal centrifugation.

The reaction mixtures were heated to the reaction temperature and then cooled down to the crystallization temperature at which the ampules were typically held for several days. The specific heating programs are given in the respective publications and manuscripts in Chapter 5. After crystallization, the ampules were again turned upside down to filter off the excess low-melting metal. Subsequent centrifugation of the ampules at 3000 rpm for three minutes using a centrifuge (Heraeus Megafuge 1.0) ensures complete removal of the low-melting metal from the reaction product (Figure 2.2d).

2.1.5 Arc Furnace Reactions

Some high-temperature reactions, which did not require extended annealing periods, were performed directly inside the arc furnace. To ensure thorough contact of the starting materials, powders were pressed to pellets enclosing ductile metal reactants (Figure 2.3) using the manual hydraulic press. Such pellets were then positioned inside the arc furnace on top of a water-cooled copper block. Subsequently, pellets was repeatedly melted to reguli in the electric arc until the respective reactions were completed.

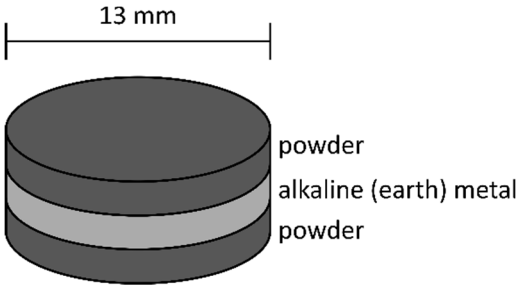

Figure 2.3. Assembly of pellets pressed for arc furnace synthesis of metal reactants with powdered starting materials.

2.1.6 Mechanical Alloying and Particle Size Reduction

Mechanical alloying reactions and particle size reduction of various starting materials were performed in a planetary ball mill (Retsch, PM 100). Depending on the reaction or starting material, 50 mL grinding jars made from tungsten carbide, stainless steel, or zirconia were used with different grinding balls made from the same material (tungsten carbide, stainless steel: diameter 15 mm; zirconia: diameter 5 mm). The exact conditions are given for the respective reactions and procedures in the publications and manuscripts in Chapter 5. To ensure proper function of the ball mill and to minimize abrasion, at least 2 g of material with a particle size of 2 mm or less were used for each run.

2.1.7 Experimental Contributions of Coauthors

Table 2.2. Experimental contributions of coauthors to the included publications.

Publication	Author	Contribution
Li_3NaGe_2 (Chapter 5.2)	Oliver Pecher	NMR spectroscopy
	Antti Karttunen	Quantum chemical calculations
Ternary Zintl Phases $K_{4-x}Na_xSi_4$ (Chapter 5.3)	Oliver Pecher	NMR spectroscopy
	Kent Griffith	Quantum chemical calculations
Mixed Silicide-Germanides (Chapter 5.4)	Nathalie Riphaus	Synthesis of $Li_{12-z}Na_zSi_7$
$Li_6B_{18}(Li_3N)_x$ (Chapter 5.5)	Holger Kirchhain	NMR spectroscopy
Binary Lithium Carbide (Chapter 5.6)	Gabriele Raudaschl-Sieber	NMR spectroscopy
a-Si and *a-allo*-Si (Chapter 5.7)	Michael Zeilinger (first author)	Synthesis of *a*-Si and *a-allo*-Si
	Laura-Alice Jantke	Quantum chemical calculations
	Sumit Konar	Raman spectroscopy
	Gero Neubüser	Transmission electron microscopy
a-allo-$Si_{1-x}Ge_x$ (Chapter 5.8)	Gero Neubüser	Transmission electron microscopy
(Li-)B-Si system (Chapter 5.9)	Nathalie Riphaus	Some solid-state syntheses in the Li-B-Si system
	Gero Neubüser	Transmission electron microscopy
Electrochemistry of *allo*-Ge (Chapter 5.10)	Johannes Hattendorff, Sebastian Geier	Preparation of coin and pouch cells, electrochemical analysis
	Irmgard Buchberger	In-situ PXRD measurements
SiNS Functionalization (Chapter 5.11)	Tobias Helbich (first author)	Synthesis of SiNS-H and SiNS-R; IR, NMR, and PL spectroscopy, AFM, TGA

2.2 Characterization

2.2.1 Single Crystal X-ray Diffraction, Structure Solution, and Refinement

Single crystal X-ray diffraction (SCXRD) is one of the best and most convenient methods to identify the structure and composition of newly found crystalline compounds. Crystals suitable for single crystal X-ray diffraction were selected under a microscope inside a glovebox and transferred into glass capillaries using a glass filament dipped in perfluorinated ether. The capillaries were then sealed airtight and mounted onto a single crystal X-ray diffractometer with Mo K_α radiation (λ = 0.71073 Å). Different diffractometers were used during the course of this work and instrument details are given in the respective publications and manuscripts in Chapter 5.

Data collection was generally controlled with the Bruker APEX software package,[1] and the obtained data was integrated and reduced using SAINT.[2] For absorption correction of untwinned and twinned crystals, SADABS[3] and TWINABS[4] were employed, respectively. Unit cells of twinned components were determined using CELL_NOW.[5] Structures were solved with direct methods (SHELXS) and refined with full-matrix least squares on F^2 (SHELXL).[6]

CIF-Files obtained from structure refinements were prepared for publication using EnCIFer[7] and subsequently validated using the CheckCIF tool offered by the International Union of Crystallography (IUCr).[8] Graphical material was produced with the Diamond software for crystal structure visualization[9] and subsequently enhanced with the vector graphics editor Inkscape.[10]

2.2.2 Powder X-ray Diffraction and Rietveld Refinement

Powder X-ray diffraction (PXRD) is very well suited to identify phases in a crystalline material. Samples for PXRD were ground in an agate mortar and filled into glass capillaries, which were then sealed airtight. A Stoe STADI P diffractometer equipped with a Ge(111) monochromator for Cu $K_{\alpha1}$ radiation (λ = 1.54056 Å) and a Dectris MYTHEN DCS 1K solid-state detector was used to record PXRD patterns. Specific measurement parameters are given in the respective publications and manuscripts in Chapter 5. PXRD patterns were evaluated using the WINXPOW software package, including indexing procedures.[11] An external Si standard was employed to ensure comparability of cell parameters.

Some newly synthesized crystalline materials did not contain single crystals suitable for SCXRD. When they were isostructural to known compounds, their exact structures were determined by Rietveld refinement using JANA2006.[12] Refinement procedures are given in the respective publications and manuscripts in Chapter 5.

2.2.3 Thermal Analysis

Differential Scanning Calorimetry (DSC) allows for thermal analysis of extended solid-state materials. Different phase transitions such as melting, crystallization, phase changes and decompositions can be observed in DSC measurements. Samples for thermal analysis were filled into custom-built, precleaned (s. Chapter 2.1.3 for cleaning procedures) niobium crucibles obtained from the precision mechanics workshop at TU München. An empty niobium crucible served as reference. Both crucibles were then closed by arc welding inside the glovebox.

The prepared crucibles were transferred into the measuring chamber of the DSC machine (Netzsch, DSC 404 Pegasus) which was subsequently evacuated and refilled with argon three times each. Measurements were then carried out under a constant gas flow of 75 mL min^{-1}. The PROTEUS Thermal Analysis software package was employed for measurement control and evaluation.[13]

Thermogravimetric analysis (TGA) was used for the thermal analysis of molecular substances. TGA measurements were performed using a Netzsch TG209F1 Libra under a constant argon flow of 20 mL min^{-1}. Specific details on thermal analyses are given in the respective publications and manuscripts in Chapter 5.

2.2.4 Magnetic Measurements

The magnetic properties of several materials were investigated using a Quantum Design MPMS 5 XL SQUID magnetometer. All data were corrected for sample holder diamagnetism. Ion-core diamagnetism was corrected using Pascal's constants.[14] The magnetic measurements were performed by Andrea Hoffmann, Gergana Nenova, or Marina Boyko at TU München. More detailed experimental procedures are given in the respective publications and manuscripts in Chapter 5.

2.2.5 Microscopy

For characterization of various non-crystalline materials, different microscopic methods were employed. Scanning electron microscopy (SEM) was performed by Sebastian Geier at Ludwig-Maximilians-Universität München. A JEOL JSM-6500F scanning electron microscope equipped with a field emission gun was operated at 5–30 kV.

Transmission electron microscopy (TEM), selected-area electron diffraction (SAED), and electron energy loss spectroscopy (EELS) was performed by Gero Neubüser at Christian-Albrechts-Universität zu Kiel. A Tecnai F30 STwin microscope (field emission gun cathode, spherical aberration coefficient C_S = 1.2 nm) equipped with a Si/Li detector (EDAX) for EDX nanoprobe analysis or a JEM-2100 microscope (JEOL, 200 kV, LaB_6, spherical aberration coefficient C_S = 1.0 nm) equipped with an EDX detector (SDD, Oxford) was used for this purpose.

Atomic-force microscopy (AFM) was performed in contact mode by Tobias Helbich at Wacker-Lehrstuhl für Makromolekulare Chemie (TU München) using an Asylum Research MFP-3D atomic-force microscope with an ARC Controller. Specific details are given in the respective publications and manuscripts in Chapter 5.

2.2.6 Energy-Dispersive X-ray Spectroscopy

Energy-dispersive X-ray (EDX) spectroscopy served to identify the local atomic composition of crystals or powdery samples (only elements with an atomic number > 4 can be detected by this method). EDX spectra were obtained using a scanning electron microscope (JEOL, JSM 7500 F) equipped with an Oxford X-Max EDX analyzer with internal Mn standard. These measurements were performed by Katia Rodewald at Wacker-Lehrstuhl für Makromolekulare Chemie (TU München).

Samples for EDX measurements were mounted onto an aluminum stub using graphite tape. They were prepared inside the glovebox and transferred to the scanning electron microscope facility inside a closed container filled with argon. However, a very short air contact is unavoidable upon loading the aluminum stub into the microscope.

2.2.7 Nuclear Magnetic Resonance Spectroscopy

Solid-state nuclear magnetic resonance (NMR) spectroscopy was performed by Dr. Oliver Pecher at University of Cambridge, Holger Kirchhain at Universität Augsburg, and Dr. Gabriele Raudaschl-Sieber at Lehrstuhl für Anorganische und Metallorganische Chemie (TU München). Static and magic-angle spinning (MAS) NMR experiments were carried out with Bruker Avance III or Bruker Avance 300 spectrometers.

Solution NMR spectra were measured by Tobias Helbich at Wacker-Lehrstuhl für Makromolekulare Chemie (TU München) on a Bruker ARX-300 spectrometer. Additional measurement details are given in the respective publications and manuscripts in Chapter 5.

2.2.8 Raman, Infrared, and Photoluminescence Spectroscopy

Raman spectroscopy was performed by Herta Slavik or Sebastian Geier at TU München using a SENTERRA Raman spectrometer (Bruker) and an inVia Raman microscope (Renishaw, RE04). For sample preparation, both crystalline and powdery substances were filled into glass capillaries, which were sealed airtight inside a glovebox.

Fourier transform infrared spectra were measured by Tobias Helbich at Wacker-Lehrstuhl für Makromolekulare Chemie (TU München) using a Bruker Vertex 70 FTIR equipped with a Bruker Platinum ATR unit. Photoluminescence (PL) spectra were obtained by Tobias Helbich at Wacker-Lehrstuhl für Makromolekulare Chemie (TU München) using an Avantes AVA-Spec 2048 equipped with a Prizmatrix light source.

Detailed measurement parameters of all spectroscopic methods are given in the respective publications and manuscripts in Chapter 5.

2.2.9 Particle Size Analysis

Particle sizes of microcrystalline materials were measured by Johannes Hattendorff at the Chair of Technical Electrochemistry (TU München). Particle size analysis was performed by laser scattering using a Horiba LA-950 instrument. Water-stable samples were suspended in deionized water for this analysis.

2.2.10 Electrochemical Characterization

The electrochemical properties of newly developed materials were investigated by collaborators at the Chair of Technical Electrochemistry (TU München). The investigated materials were each formulated to an ink, which was then coated onto copper foil. From the dried coatings single-side coated electrodes were then punched out and used to assemble half-cells with lithium counter electrodes. For electrochemical cycling and in-situ PXRD experiments, CR2032 coin cells and custom-designed pouch cells, respectively, were prepared.

These half-cells were then run on a battery cycler (Maccor or Biologic VMP3). Concurrently, the pouch cells were monitored by in-situ PXRD using Stoe STADI P diffractometer with Mo K_α radiation (λ = 0.70930 Å, Ge(111) monochromator, Dectris MYTHEN DCS 1K solid state detector). Additional details on the electrochemical characterizations are given in the respective publications and manuscripts in Chapter 5.

2.3 Computational Methods

Many of the experimental findings obtained in this work were supported by quantum chemical calculations. Electronic structure information such as band structure, density of states (DOS), and crystal orbital Hamiltonian population (COHP) was calculated with the linear muffin-tin orbital (LMTO) method in the atomic sphere approximation (ASA), using the tight-binding (TB) program TB-LMTO-ASA (cf. Chapters 5.2 and 5.5).[15]

Optimization of real and theoretical structures was performed with the CRYSTAL09 software package (cf. Chapter 5.7) by Laura-Alice Jantke (TU München) and Antti J. Karttunen (Aalto University, Finland).[16] The latter also investigated vibrational properties of a new Zintl phase using the successor software CRYSTAL14 (cf. Chapter 5.2).[17] In addition, Antti J. Karttunen calculated molecular orbital (MO) diagrams with Gaussian09 (cf. Chapter 5.2).[18]

Solid-state NMR properties of various compounds were investigated by Antti J. Karttunen and Kent J. Griffith (University of Cambridge) using DFT-PBE calculations in the CASTEP program (cf. Chapters 5.2 and 5.3).[19] More detailed information on the computational procedures and parameters employed in this work are given in the indicated publications and manuscripts in Chapter 5.

2.4 References

[1] *APEX Suite of Crystallographic Software*, Bruker AXS Inc., Madison, WI, USA, **2008**.

[2] *SAINT*, Bruker AXS Inc., Madison, WI, USA, **2001**.

[3] *SADABS*, Bruker AXS Inc., Madison, Wisconsin, USA, **2001**.

[4] *TWINABS*, Bruker AXS Inc., Madison, WI, USA, **2001**.

[5] *CELL_NOW*, Bruker AXS Inc., Madison, WI, USA, **2001**.

[6] G. M. Sheldrick, *Acta Crystallogr. Sect. A* **2008**, *64*, 112–122.

[7] F. H. Allen, O. Johnson, G. P. Shields, B. R. Smith, M. Towler, *J. Appl. Crystallogr.* **2004**, *37*, 335–338.

[8] *checkCIF,* International Union of Crystallography, http://checkcif.iucr.org/,

[9] *DIAMOND*, K. Brandenburg, Crystal Impact GbR, Bonn, **2014**.

[10] *Inkscape 0.91*, **2016**.

[11] *WinXPOW*, STOE & Cie GmbH, Darmstadt, **2003**.

[12] V. Petříček, M. Dušek, L. Palatinus, *Z. Kristallogr. - Cryst. Mater.* **2014**, *229*, 345–352.

[13] *PROTEUS Thermal Analysis V4.8.2*, Netzsch-Gerätebau GmbH, Selb, **2006**.

[14] G. A. Bain, J. F. Berry, *J. Chem. Educ.* **2008**, *85*, 532–536.

[15] *The Stuttgart Tight-Binding LMTO-ASA program*, M. v. Schilfgarde, T. A. Paxton, O. Jepsen, O. K. Andersen, G. Krier, Max-Planck-Institut für Festkörperforschung, Stuttgart, Germany, **1998**.

[16] R. Dovesi, R. Orlando, B. Civalleri, C. Roetti, R. Saunders Victor, M. Zicovich-Wilson Claudio, *Z. Kristallogr. - Cryst. Mater.* **2005**, *220*, 571–573.

[17] R. Dovesi, R. Orlando, A. Erba, C. M. Zicovich-Wilson, B. Civalleri, S. Casassa, L. Maschio, M. Ferrabone, M. De La Pierre, P. D'Arco, Y. Noel, M. Causa, M. Rerat, B. Kirtman, *Int. J. Quantum Chem.* **2014**, *114*, 1287–1317.

[18] *Gaussian 09, Revision C.01*, M. J. Frisch, G. W. Trucks, H. B. Schlegel, G. E. Scuseria, M. A. Robb, J. R. Cheeseman, G. Scalmani, V. Barone, B. Mennucci, G. A. Petersson, H. Nakatsuji, M. Caricato, X. Li, H. P. Hratchian, A. F. Izmaylov, J. Bloino, G. Zheng, J. L. Sonnenberg, M. Hada, M. Ehara, K. Toyota, R. Fukuda, J. Hasegawa, M. Ishida, T. Nakajima, Y. Honda, O. Kitao, H. Nakai, T. Vreven, J. A. Montgomery Jr., J. E. Peralta, F. Ogliaro, M. Bearpark, J. J. Heyd, E. Brothers, K. N. Kudin, V. N. Staroverov, R. Kobayashi, J. Normand, K. Raghavachari, A. Rendell, J. C. Burant, S. S. Iyengar, J. Tomasi, M. Cossi, N. Rega, J. M. Millam, M. Klene, J. E. Knox, J. B. Cross, V. Bakken, C. Adamo, J. Jaramillo, R. Gomperts, R. E. Stratmann, O. Yazyev, A. J. Austin, R. Cammi, C. Pomelli, J. W. Ochterski, R. L. Martin, K. Morokuma, V. G. Zakrzewski, G. A. Voth, P. Salvador, J. J. Dannenberg, S. Dapprich, A. D. Daniels, Ö. Farkas, J. B. Foresman, J. V. Ortiz, J. Cioslowski, D. J. Fox, Gaussian, Inc., Wallingford, CT, **2009**.

[19] S. J. Clark, M. D. Segall, C. J. Pickard, P. J. Hasnip, M. I. J. Probert, K. Refson, M. C. Payne, *Z. Kristallogr.* **2005**, *220*, 567–570.

3 RESULTS AND DISCUSSION

3.1 Effects of Alkali Metal Substitution on Alkali Metal Silicides and Germanides

3.1.1 $Li_{18}Na_2Ge_{17}$ and Li_3NaGe_2 – Ternary Germanides with Intriguing Structures

see Chapter 5.1 $Li_{18}Na_2Ge_{17}$ – A Compound Demonstrating Cation Effects on Cluster Shapes and Crystal Packing in Ternary Zintl Phases
L. M. Scherf, M. Zeilinger, T. F. Fässler, *Inorg. Chem.* **2014**, *53*, 2096–2101.

see Chapter 5.2 $[Ge_2]^{4-}$ Dumbbells with Very Short Ge–Ge Distances in the Zintl Phase Li_3NaGe_2: A Solid-State Equivalent to Molecular O_2
L. M. Scherf, A. J. Karttunen, O. Pecher, P. C. M. M. Magusin, C. P. Grey, T. F. Fässler, *Angew. Chem. Int. Ed.* **2016**, *55*, 1075–1079.

Prior to this work, the Li-Na-Ge system had not been investigated in detail so that no ternary phase was known. In the related Li-Na-Si only one compound had been published before.[1] As described in Chapter 1.3.2, Li_3NaSi_6 comprises a unique anionic substructure of two-dimensional polysilicide sheets which have been reported to form a new Si allotrope upon treatment with various oxidants.[2] Due to the similar behavior of silicon and germanium in alkali metal tetrelides, the Li-Na-Ge system was searched for new Zintl phases with intriguing anionic substructures.

Overall, three new Zintl phases were discovered during these investigations. Na_7LiGe_8 contains common tetrahedral $[Ge_4]^{4-}$ clusters and is isostructural to the other $A_7A'T_8$ phases. The compound will be discussed in more detail in Chapter 3.2.1 in the context of Si/Ge substitution. $Li_{18}Na_2Ge_{17}$ and Li_3NaGe_2 crystallize in new structure types and will be presented below.

$Li_{18}Na_2Ge_{17}$

$Li_{18}Na_2Ge_{17}$ can easily be synthesized by melting a stoichiometric mixture of the corresponding elements. Its structure was determined by single crystal X-ray diffraction. The compound is a rare representative of a Zintl phase comprising three different Zintl anions of the same element (Figure 3.1a). Other examples include $Ba_6Mg_{10.8}Li_{1.2}Si_{12}$,[3] $E_{31}Sn_{20}$ (E = Ca, Sr, Yb),[4] $Yb_{36}Sn_{23}$,[5] and $Na_{23}K_9Tl_{15.3}$.[6]

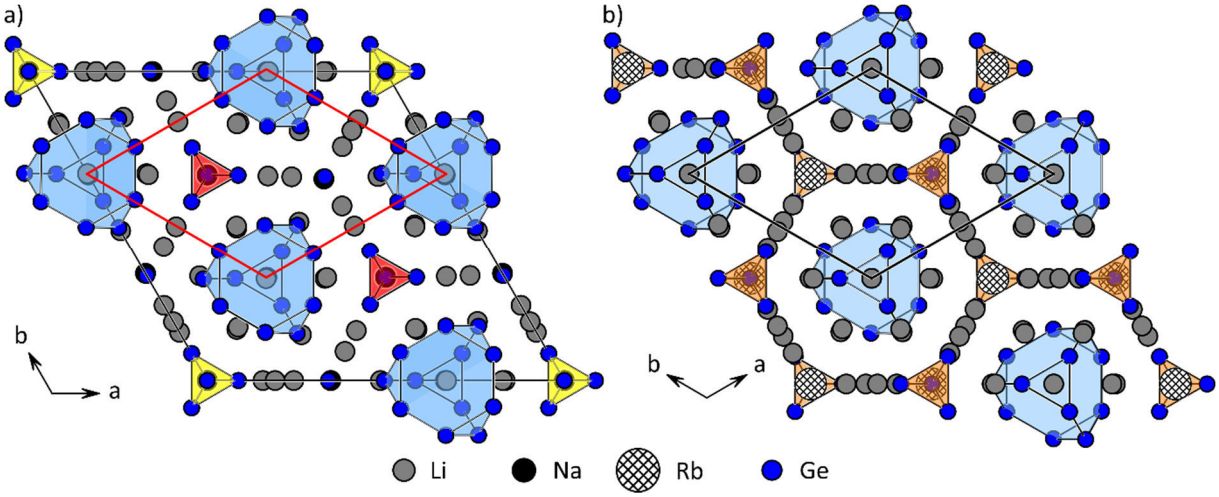

Figure 3.1. a) Projection of the structure of $Li_{18}Na_2Ge_{17}$. Colored polyhedra denote the different anionic Ge clusters (blue: truncated tetrahedra $[Ge_{12}]^{12-}$, red/yellow: tetrahedra $[Ge_4]^{4-}$). Na atoms are located below isolated Ge^{4-} anions and $[Ge_4]^{4-}$ clusters. A red rhombus highlights the hexagonal primitive packing of truncated tetrahedra. b) Projection of the structure of Li_7RbGe_8. Colored polyhedra denote the anionic Ge clusters (Ge: truncated tetrahedra $[Ge_{12}]^{12-}$, orange: tetrahedra $[Ge_4]^{4-}$).

One of these Zintl anions is a truncated tetrahedron $[Ge_{12}]^{12-}$ – the largest Ge cluster in Zintl phases yet. It has only been observed once before in Li_7RbGe_8[7] (Figure 3.1b) which was presented in Chapter 1.3.2. The cluster is filled with one Li cation and four additional Li cations cap the hexagonal faces, constructing a filled, 16-vertex Friauf polyhedron $[Li@Li_4Ge_{12}]^{7-}$.[8] The Friauf polyhedra arrange in a hexagonal primitive fashion, and isolated Ge^{4-} anions with noble gas configuration and two crystallographically different tetrahedral $[Ge_4]^{4-}$ clusters fill the resulting voids. Li and Na cations separate the Ge anions from each other. The three different cluster types occur in a 1:1:1 ratio, so that the sum formula $Li_{18}Na_2Ge_{17}$ can be rewritten as $(Li^+)_{13}(Na^+)_2[Li@Li_4Ge_{12}]^{7-}[Ge_4]^{4-}(Ge^{4-})$. Thus, all charges are balanced and $Li_{18}Na_2Ge_{17}$ can be considered a Zintl phase.

Remarkably, the hexagonally primitive arrangement of Friauf polyhedra is already known from Li_7RbGe_8 in which the voids are filled by tetrahedral $[Ge_4]^{4-}$ clusters only (Figure 3.1b). In $Li_{18}Na_2Ge_{17}$, the isolated Ge^{4-} anions replace 50 % of the tetrahedral $[Ge_4]^{4-}$ clusters present in Li_7RbGe_8, resulting in the change in stoichiometry. Although it has the same four-fold negative charge, the small isolated anion cannot encompass the same number of coordinating alkali metal cations in its coordination sphere. Furthermore, crystal packing along *c* varies between the related Zintl phases. All these structural changes are induced by very different sizes of the Na and Rb cations which make up only 5.41 ($Li_{18}Na_2Ge_{17}$) and 6.25 atom % (Li_7RbGe_8) of the compounds. Thus, the nature of the heavier alkali metal has a dramatic effect on both stoichiometry and crystal structure by changing the requirements for efficient cluster solvation and packing.

Li_3NaGe_2

Li_3NaGe_2 can be synthesized by melting a stoichiometric mixture of the elements or by annealing a mixture of binary precursors according to Equation (3).

$$12\ Li_{17}Ge_4 + 17\ Na_4Ge_4 + 20\ Ge \rightarrow 68\ Li_3NaGe_2 \qquad (3)$$

The melting procedure yields metallic red single crystals suitable for single crystal X-ray diffraction, which were employed to determine the crystal structure of the novel compound. The annealing procedure produces nearly phase pure material containing only small traces of Li_7Ge_3[9] and Na_7LiGe_8 (cf. Chapter 3.2.1).

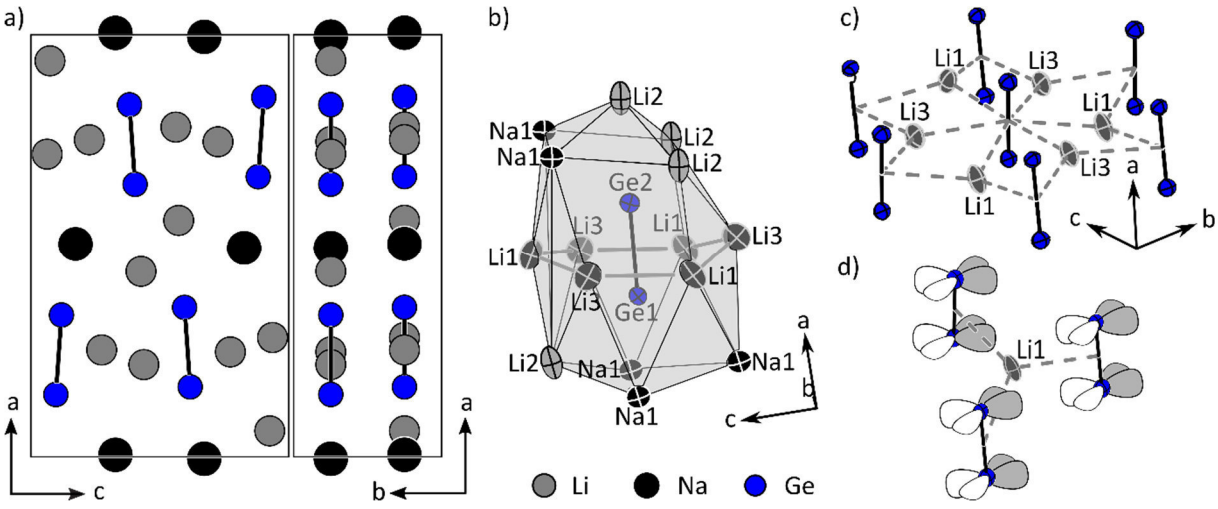

Figure 3.2. a) Projections of the unit cell of Li_3NaGe_2 onto the *ac* and *ab* planes; b) coordination sphere of the $[Ge{=}Ge]^{4-}$ dumbbells; c) coordination sphere of Li1 and Li3; d) Li1 surrounded by π-bonding Ge p orbitals (thermal ellipsoids at 90 % probability at 123 K).

Li_3NaGe_2 consists of Ge dimers, which are separated by Li and Na cations (Figure 3.2a, b). According to the Zintl Klemm concept (cf. Chapter 1.2.1), these dimers have an overall charge of −4, suggesting a double bond as in molecular O_2. Indeed, the Ge–Ge bond length amounts to 2.390(1) Å which is significantly shorter than a Ge–Ge single bond in elemental Ge (2.44 Å)[10] and in a similar range as in molecular $[RGe{=}GeR]^{2-}$ anions (*R* = organic ligand).[11] Germanium dumbbell clusters are already known, i.e. from the binary lithium germanides $Li_{13}Ge_4$,[12] Li_7Ge_3,[9] and Li_9Ge_4.[13] However, these Ge dimers all carry a higher negative charge[3] and thus do not represent true double bonds. The corresponding bond lengths are in the range of a Ge–Ge single bond or larger due to electrostatic repulsion.

Like molecular O_2, the symmetrically unperturbed $[Ge_2]^{4-}$ clusters are characterized by two degenerate π* orbitals which are singly occupied (Figure 3.3c). For O_2 molecules in the gas phase, the occupation of the degenerate orbital set with two electrons leads to paramagnetism while in the extended solid Li_3NaGe_2 partially occupied antibonding states at the Fermi level result in metallic properties. Analysis of the electronic structure of Li_3NaGe_2 using TB-LMTO-ASA[14] confirms this (Figure 3.3). Ge p states dominate the density of states near the Fermi level whereas Li and Na states barely contribute to it.

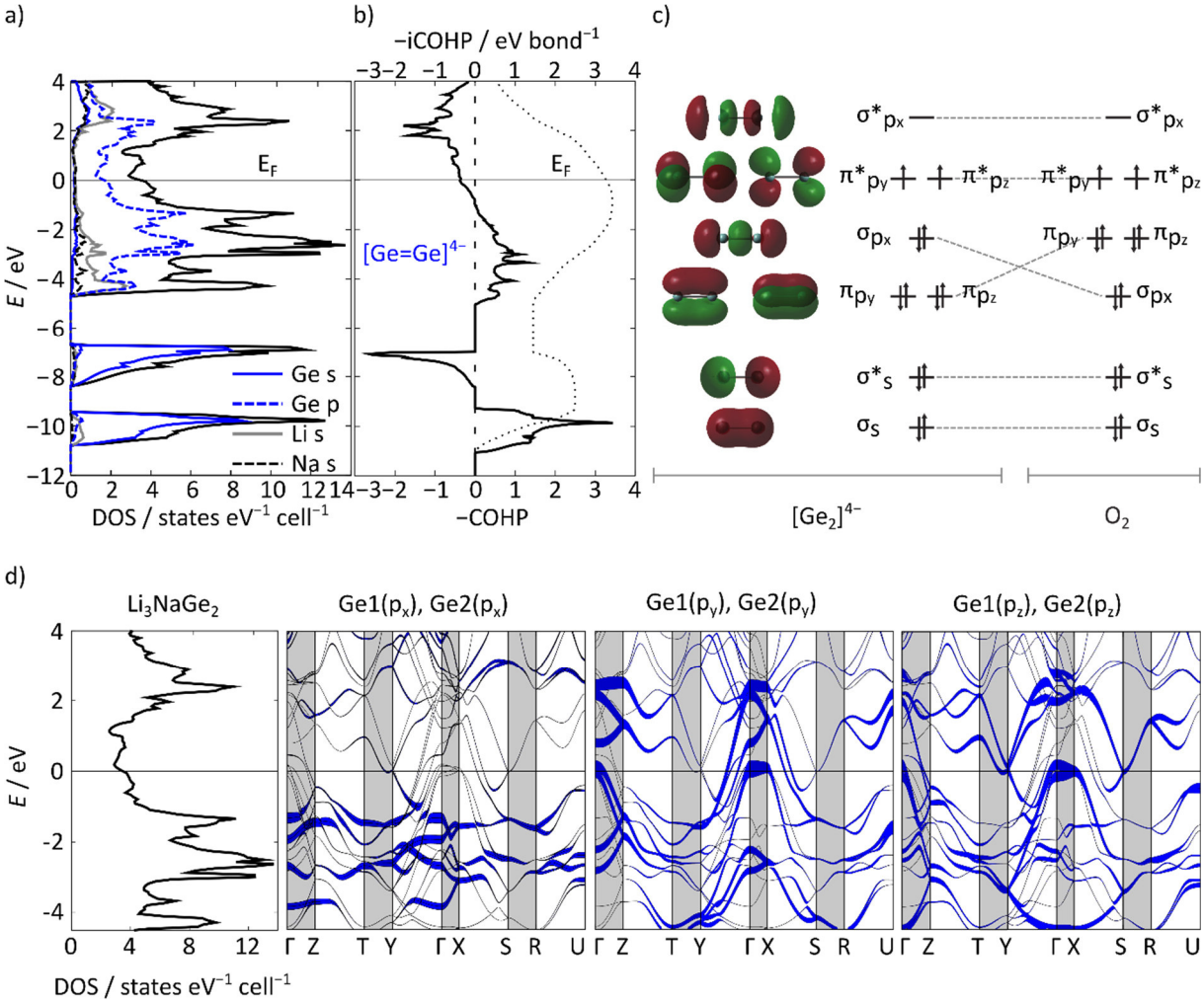

Figure 3.3. a) Total and partial density of states (DOS) curves for Li_3NaGe_2; b) crystal orbital Hamiltonian population (COHP, solid line) and integrated COHP (dotted line) of the Ge1–Ge2 bond; c) molecular orbitals of free $[Ge_2]^{4-}$ and molecular orbital diagrams for free $[Ge_2]^{4-}$ and O_2; d) total DOS curve as well as band structures containing the Ge(p) fat bands.

[3] Formal charges are derived by simple electron counting according to the Zintl Klemm concept (cf. Chapter 1.2.1).

The π-bond character of the $[Ge_2]^{4-}$ dumbbells was also observed by solid-state NMR spectroscopy of a ^{6}Li-enriched sample of Li_3NaGe_2. The ^{6}Li MAS NMR spectrum (Figure 3.4a) contains two signals corresponding to Li_3NaGe_2 at −10.0 and 94.5 ppm in a 2 : 1 ratio. These signals can be assigned to the three different Li sites considering their surroundings. Li1 and Li3 are encompassed by the π-bonding p orbitals of three Ge dumbbells each (Figure 3.2c, d) and the respective NMR signal is shifted upfield to −10.0 ppm. A significant upfield shift of Li NMR signals is also known from Li cations located in the π cloud of aromatic $[Ge_5]^{6-}$ clusters in $Li_{12}Ge_7$ (−17 ppm).[15] Contrastingly, Li2 and Na1 (Figure 3.4b) experience significant downfield Knight shifts due to the metallic character of Li_3NaGe_2.Thus, the NMR experiment further supports the multiple bond character postulated for the $[Ge_2]^{4-}$ dimer.

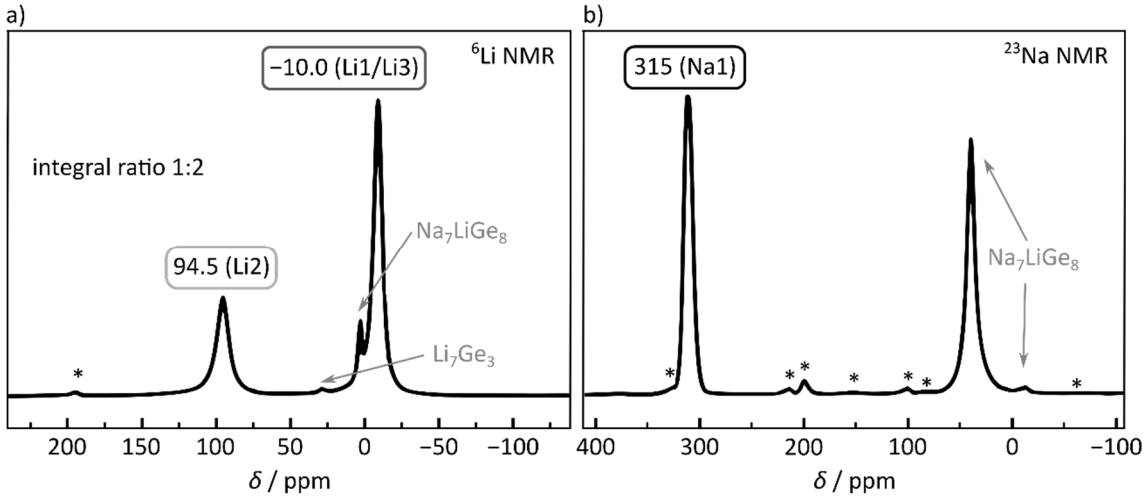

Figure 3.4. a) ^{6}Li and b) ^{23}Na MAS NMR spectra of $^6Li_3NaGe_2$. Impurity signals are marked in grey and asterisks denote rotational sidebands.

Overall, Li_3NaGe_2 can be considered a Zintl phase because its double bond character and Li/Na pseudo band gap at the Fermi level agree well with the salt-like electron distribution of $(Li^+)_3(Na^+)[Ge_2]^{4-}$. Unlike most Zintl phases, the novel compound exhibits typical metallic properties due to its unique anionic substructure. The analogy between double-bonded $[Ge_2]^{4-}$ and molecular O_2 can easily be understood using the (8−*N*) rule. Again, a mixture of two different alkali metals can stabilize anionic structures that are not available in simple binary phases.

3.1.2 The $K_{4-x}Na_xSi_4$ System

see Chapter 5.3 The Ternary Zintl Phases $K_{4-x}Na_xSi_4$ ($1 \leq x \leq 2.2$) and K_7NaSi_8 – Synthesis, Crystal Structure, and Chemical Bonding
L. M. Scherf, O. Pecher, K. J. Griffith, F. Haarmann, C. P. Grey, T. F. Fässler, *Eur. J. Inorg. Chem.* 2016, *2016*, 4674–4682.

Zintl phases of the general formula A_4T_9 (*A* = Na–Cs, *T* = Ge, Sn, Pb) have proven to be efficient precursors for prolific functionalization of Zintl clusters in solution.[16] They are easy to synthesize and characterize, and dissolve well in a number of polar solvents such as ammonia, ethylenediamine, and dimethylformamide. However, phases A_4Si_9 have yet eluded successful synthesis and, thus, the chemistry of Si cluster anions in solution is still very limited. Therefore, the mixed cation approach was employed using different ratios of Na and K as the alkali metals to potentially stabilize the comparatively small $[Si_9]^{4-}$ clusters. Synthesis attempts of $K_{4-x}Na_xSi_9$, however, only yielded various phases $K_{4-x}Na_xSi_4$ comprising tetrahedral $[Si_4]^{4-}$ clusters, which represent another very common tetrelide cluster (cf. Chapter 1.2.2).

Previously, binary K_4Si_4 (space group $P\bar{4}3n$)[17] and Na_4Si_4 (space group $C2/c$)[18] were the only phases known in the $K_{4-x}Na_xSi_4$ system. In the present experiments, the ternary phases $K_{3.5}Na_{0.5}Si_4$ (space group $Pa\bar{3}$) and the solid solution $K_{4-x}Na_xSi_4$ with $1 \leq x \leq 2.2$ (space group $P2_1/n$) were newly discovered (Figure 3.5a).

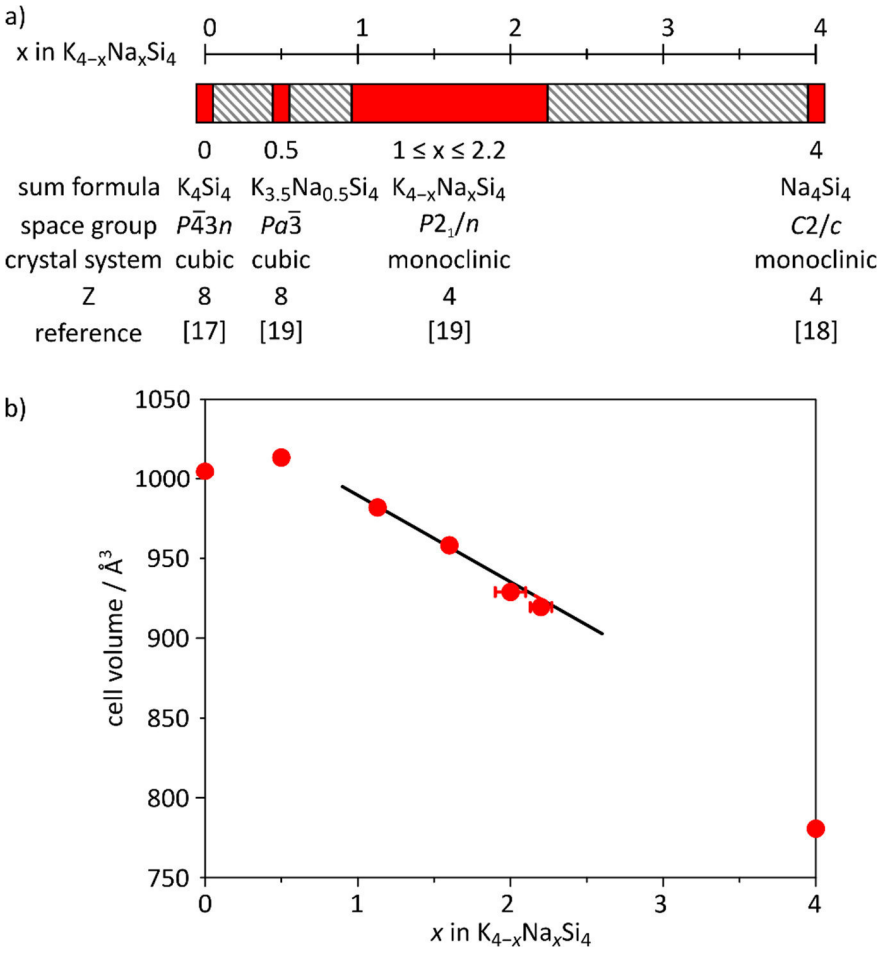

Figure 3.5. a) Phases in the $K_{4-x}Na_xSi_4$ system: red blocks denote single-phase regions while two-phase regions are shaded; b) unit cell volumes of all $K_{4-x}Na_xSi_4$ phases normalized to $Z = 4$. Vertical error bars are too small to be visible.[19]

$K_{3.5}Na_{0.5}Si_4$ (space group $Pa\bar{3}$) is isostructural to the $A_7A'T_8$ phases presented in Chapter 1.3.2 and will therefore be termed K_7NaSi_8 from now on. In this cubic structure, $[Si_4]^{4-}$ tetrahedra are bridged to dimers by face-capping Na cations (Figure 3.6a). The dimers are coordinated by K cations, so that the two alkali metal species are clearly separated onto different crystallographic positions. In contrast to all other $A_7A'T_8$ compounds, K_7NaSi_8 cannot be synthesized by melting a stoichiometric mixture of the corresponding elements. This reaction yields a mixture of K_4Si_4 and $K_{4-x}Na_xSi_4$ (space group $P2_1/n$). Instead, K_7NaSi_8 is obtained via annealing of binary precursors according to Equation (4).

$$7\ K_4Si_4 + Na_4Si_4 \rightarrow 4\ K_7NaSi_8 \qquad (4)$$

Solid-state NMR experiments on K_7NaSi_8 coupled with quantum chemical calculations reveal anisotropic chemical bonding for all atom types. This is in good agreement with previous investigations on Rb_7NaSi_8 and Cs_7NaSi_8.[20,21]

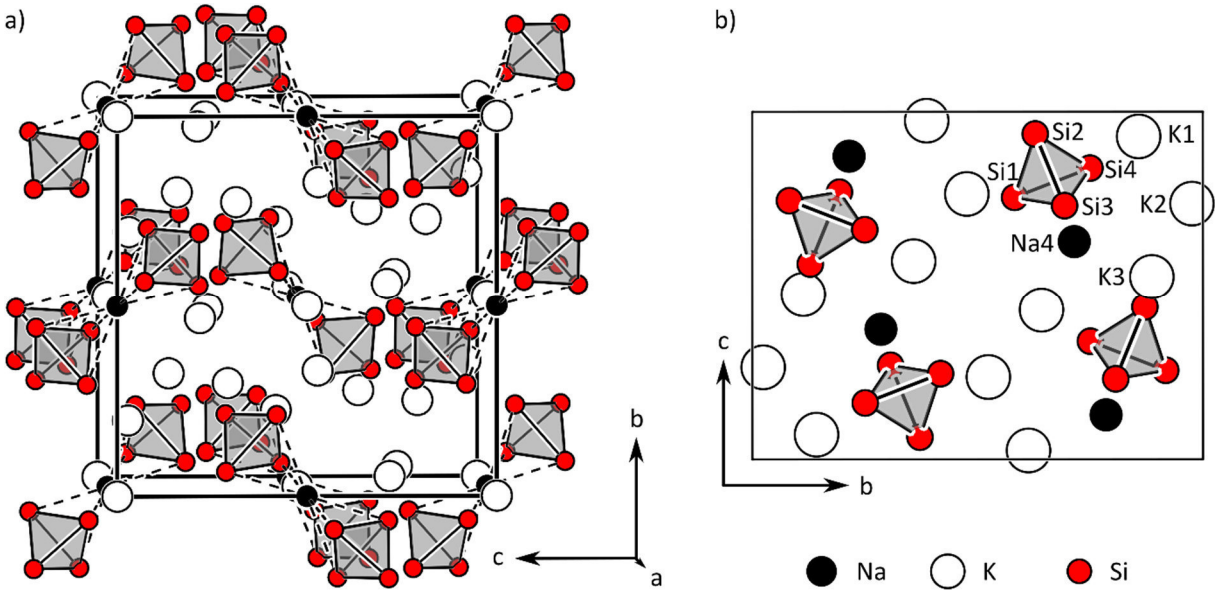

Figure 3.6. Projections of the unit cells of a) K_7NaSi_8 and b) K_3NaSi_4.

$K_{4-x}Na_xSi_4$ (space group $P2_1/n$) can be prepared with $1 \leq x \leq 2.2$ from a stoichiometric melt of the corresponding elements or via annealing of binary precursors. The solid solution crystallizes in a new structure type as determined by single crystal X-ray diffraction of a $K_{4-x}Na_xSi_4$ crystal with $x = 1$. The structure comprises $[Si_4]^{4-}$ tetrahedra which are coordinated by K and Na cations on four different alkali metal positions K1, K2, K3, and Na4 (Figure 3.6b). In the K_3NaSi_4 single crystal, the alkali metals are clearly separated. However, Rietveld analysis of Na-richer $K_{4-x}Na_xSi_4$ (space group $P2_1/n$) samples clearly demonstrates a significant phase width. The unit cell volumes of $K_{4-x}Na_xSi_4$ (space group $P2_1/n$) decrease linearly with increasing Na content, which is in good agreement with Vegard's rule for solid solutions (Figure 3.5b).[22]

In the Na-richer samples, increasing statistical substitution of the K2 and K3 positions for Na is observed. K1 and Na4 remain pure K and Na sites, respectively, in all samples. These site preferences of the alkali metals correlate with the space available for the different alkali metal positions. With respect to the coloring problem, mixing of K and Na cations obviously leads to the formation of different structures than those known from the related binary phases. Interestingly, the distribution of alkali metals onto the different sites in this new structure occurs in a partially ordered fashion including some statistical cation mixing.

3.1.3 Statistical Alkali Metal Mixing in $Li_{12-y}Na_ySi_7$

see Chapter 5.4 Site-Specific Substitution Preferences in the Solid Solutions $Li_{12}Si_{7-x}Ge_x$, $Li_{12-y}Na_ySi_7$, $Na_7LiSi_{8-z}Ge_z$, and $Li_3NaSi_{6-v}Ge_v$
L. M. Scherf, N. Riphaus, T. F. Fässler, *Z. Anorg. Allg. Chem.* **2016**, *642*, 1143–1151.

During investigation of mixed silicide-germanides $Li_{12}Si_{7-x}Ge_x$ (cf. Chapter 3.2.1), significantly enlarged displacement parameters were observed for exactly two of the thirteen lithium positions (Li1 and Li9) in all members of the solid solution series. Large displacement parameters could be caused by partial occupation of the crystallographic positions or by the presence of larger cavities in which the Li cations can move significantly. Free refinement of the respective site occupancies demonstrated that all Li sites are fully occupied.

Larger Li cavities could potentially encompass larger cations. Thus, this hypothesis was probed by synthesis attempts of mixed cation compounds $Li_{12-y}A_ySi_7$ using the larger alkali metals Na, K, Rb, and Cs as well as Ag. The latter has been shown to interchange with Li in several compounds.[23,24] Reactions including K, Rb, Cs, and Ag only afforded $Li_{12}Si_7$ in addition to other known binary and ternary phases. In contrast, the synthesis of $Li_{12-y}Na_ySi_7$ resulted in a ternary compound with $y \approx 0.5$ as shown by single crystal XRD, Rietveld refinement, and EDX analysis. Larger Na contents could not be obtained.

When refining the structure of $Li_{12-y}Na_ySi_7$ [y = 0.443(9)] from single crystal XRD data, all 13 Li positions were carefully tested for Na substitution. However, only the alkali metal positions *A*1 and *A*9 characterized by large displacement parameters exhibit significant partial Na occupation (Figure 3.7a) of 15.2(7) % and 36.8(5) %, respectively. An inspection of the coordination spheres of all alkali metal positions demonstrates that only three Si atoms and four/five Li atoms coordinate *A*1 and *A*9, whereas all other alkali metal positions are surrounded by four to ten Si atoms and four to six Li atoms. As depicted in Figures 3.7b and c, the thermal ellipsoids of *A*1 and *A*9 are elongated along those directions providing the most space.

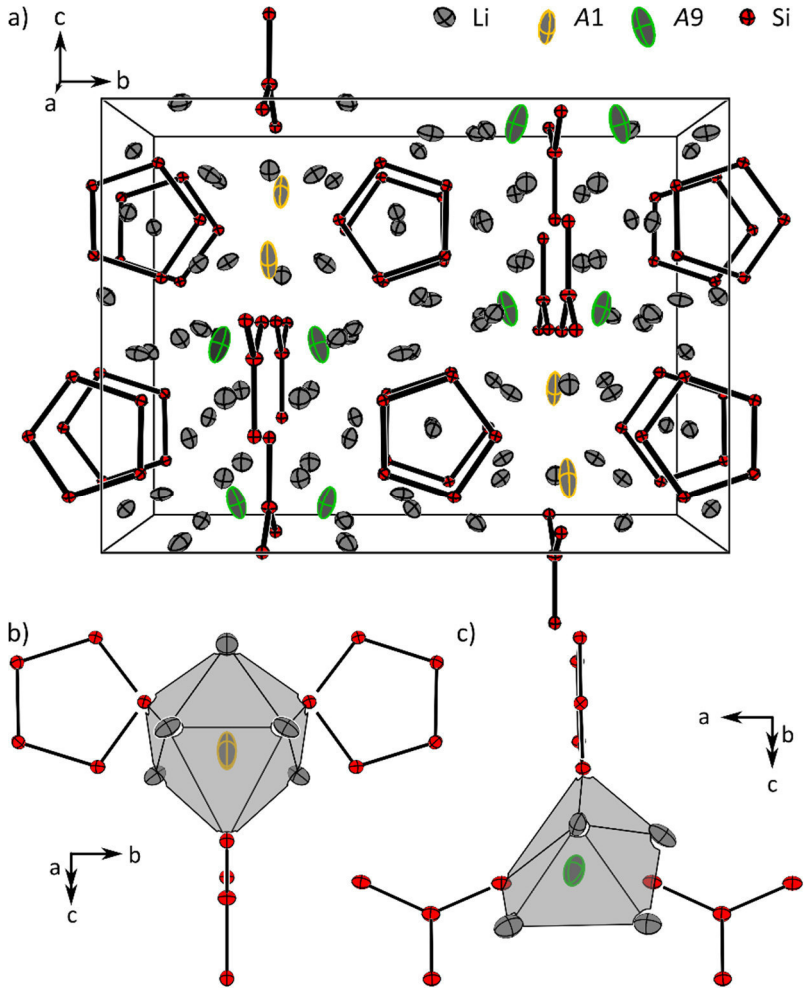

Figure 3.7. a) Unit cell of $Li_{12-y}Na_ySi_7$ [y = 0.443(9)] showing the large anisotropic displacement parameters (thermal ellipsoids at 90 % probability at 123 K) of the mixed alkali metal positions *A*1 [15.2(7) % Na] and *A*9 [36.8(5) % Na); coordination spheres of b) *A*1 and c) *A*9.

Overall, the compounds $Li_{12}Si_{7-x}Ge_x$ comprise two relatively large and flexible alkali metal atom cavities that can accommodate the presence of limited amounts of larger Na cations in the mixed cation phase $Li_{12-y}Na_ySi_7$. The Li and Na cations on these two crystallographic positions mix statistically.

3.2 Effects of Tetrel Element Substitution on Alkali Metal Silicides and Germanides

3.2.1 Mixed Silicide-Germanides

see Chapter 5.4 Site-Specific Substitution Preferences in the Solid Solutions $Li_{12}Si_{7-x}Ge_x$, $Li_{12-y}Na_ySi_7$, $Na_7LiSi_{8-z}Ge_z$, and $Li_3NaSi_{6-v}Ge_v$
L. M. Scherf, N. Riphaus, T. F. Fässler, *Z. Anorg. Allg. Chem.* **2016**, *642*, 1143–1151.

Prior to this work, substitution of silicon for germanium and vice versa in alkali metal tetrelides had not been investigated in detail. All previous examples exhibit statistical mixing of the two elements in compounds, which were already known both as pure silicides and pure germanides (cf. Chapter 1.3.3). Certain site preferences have been mentioned but not further examined. Thus, investigation of mixed silicide-germanides was extended to the $Na_7LiSi_{8-z}Ge_z$ and $Li_3NaSi_{6-v}Ge_v$ systems, in which either only the silicide or only the germanide structure exists. A previous Master's Thesis demonstrated that no Si/Ge substitution can be achieved in Li_7Ge_{12}.[25] In addition, the coloring problem with respect to mixed silicide-germanides was addressed via a thorough analysis of the Si and Ge distribution onto the crystallographic tetrel sites in $Li_{12}Si_{7-x}Ge_x$, $Na_7LiSi_{8-z}Ge_z$ and $Li_3NaSi_{6-v}Ge_v$. Below, the examined silicide-germanides will be described in more detail.

$Li_{12}Si_{7-x}Ge_x$

$Li_{12}Si_{7-x}Ge_x$ can be easily synthesized in different Si/Ge ratios ($0 \le x \le 7$) by melting a stoichiometric mixture of the elements. Si and Ge are typically premixed via grinding in an agate mortar. $Li_{12}Si_7$ and $Li_{12}Ge_7$ were both previously known[9,26,27] so that the formation of a solid solution across the full range of possible Si/Ge ratios does not surprise. All members of the solid solution crystallize in the same structure type (space group *Pnma*) characterized by aromatic five-membered rings[28] and carbonate-like Y-shaped stars[29] in a 2:1 ratio (Figure 3.8a). As expected from Vegard's law,[22] the unit cell volumes of $Li_{12}Si_{7-x}Ge_x$ samples which were acquired both from single crystal and powder X-ray diffraction data increase linearly with increasing Ge content *x* (Figure 3.8b).

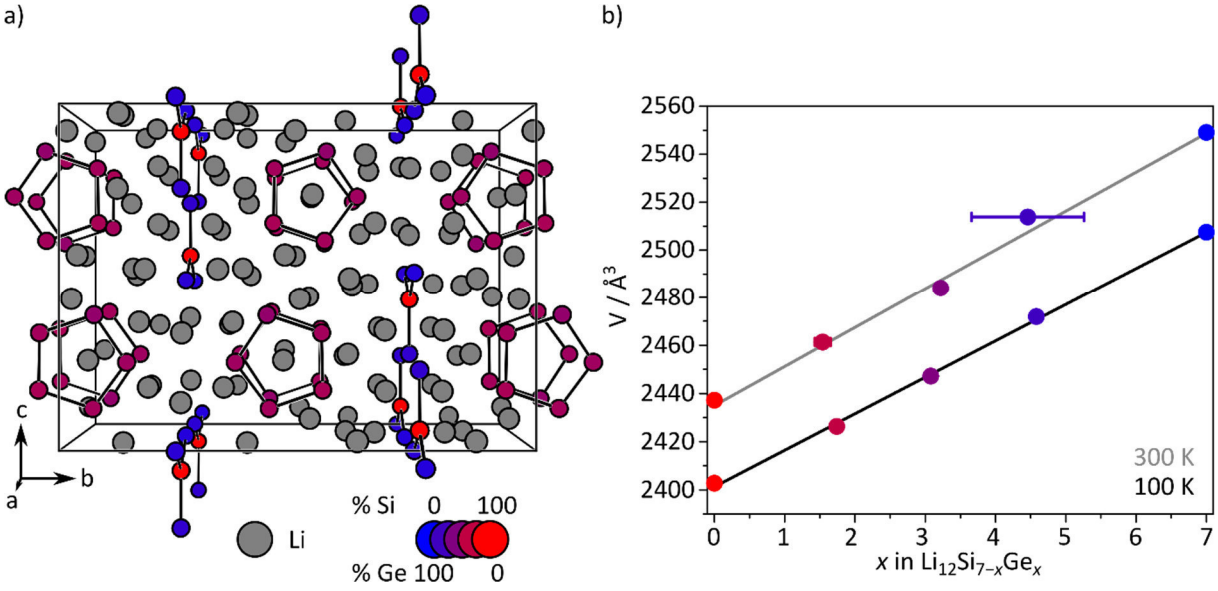

Figure 3.8. a) Unit cell of $Li_{12}Si_{7-x}Ge_x$ [x = 3.08(2)] showing the preferential occupation of the mixed tetrel positions. b) Vegard plot[22] illustrating the linearly increasing unit cell volumes of $Li_{12}Si_{7-x}Ge_x$ with increasing x. 300 K data is obtained from powder diffraction data, 100 K data from single crystal measurements. Vertical error bars are within the symbols.

Remarkably, Si and Ge mix statistically but exhibit strong preferences for the occupation of certain crystallographic sites. In $Li_{12}Si_{3.92(2)}Ge_{3.08}$ (Figure 3.8a), the central atom of the $[T_4]^{8-}$ stars is only occupied by Si while the outer atoms are occupied by 80.6(5)–86.1(5) % Ge. The five-membered rings $[T_5]^{6-}$ have medium Ge contents of 33.3(3)–41.8(4) %. All other members of the solid solution series follow the same trend.

The clear site preferences of Si and Ge in $Li_{12}Si_{7-x}Ge_x$ can be explained by the different electronegativities (EN) of Ge (EN = 2.02) and Si (EN = 1.74).[30] According to the formal cluster charges assigned above, the outer star positions are most highly negative charged at −2.33, followed by the members of the five-membered ring at −1.2 and the central star position at 0. Calculated Bader charges show the same trend.[31] Thus, the more electronegative Ge clearly prefers the crystallographic positions characterized by the higher negative charges while Si preferably occupies the less negatively charged sites in $Li_{12}Si_{7-x}Ge_x$.

Similar effects have also been observed in molecular main group chemistry: When reacting *N*-heterocyclic carbene (NHC) coordinated $GeCl_2$ **1** with a disilenide **2** (Scheme 3.1), the resulting transient disilenyl-substituted chlorogermylene **3** instantly rearranges to the NHC-coordinated silagermenylidene **4**.[32] This rearrangement is formally associated with a intramolecular disproportionation in which the Ge atom is reduced at the expense of an oxidation of a silicon atom, so that Ge eventually occupies the most negatively charged of the heavy tetrel element positions.

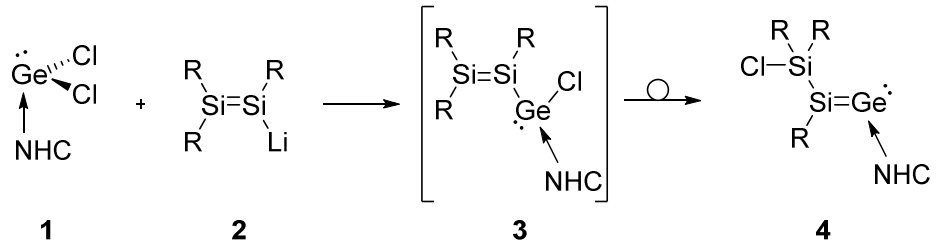

Scheme 3.1. The reaction of NHC-coordinated $GeCl_2$ and a disilenide (R = 2,4,6-triisopropylphenyl) affords a NHC-coordinated silagermanylidene via 1,3-migration of a chlorine atom; NHC = 1,3-diisopropyl-4,5-dimethylimidazol-2-ylidene.[32]

$Na_7LiSi_{8-z}Ge_z$

Na_7LiGe_8 is one of three new Zintl phases in the Li-Na-Ge system (cf. Chapter 3.1.1). It can be synthesized by melting a stoichiometric mixture of the elements. Na_7LiGe_8 crystallizes in the common $A_7A'T_8$ structure type (space group $Pa\bar{3}$) comprising tetrahedral clusters $[Ge_4]^{4-}$ which are bridged to dimers by η^3-capping Li atoms (Figure 3.9a, b, cf. Chapter 1.3.2).[33,34] Its silicide counterpart Na_7LiSi_8, however, could not be obtained although a very similar quaternary phase, KNa_6LiSi_8 is known.[1] Thus, the substitution of Ge for Si was investigated in order to gain more information on why Na_7LiSi_8 cannot be easily synthesized.

By synthesis of various phases $Na_7LiSi_{8-z}Ge_z$ and subsequent Rietveld refinement of PXRD data, the existence of a solid solution in the range of $1.3 \leq z \leq 8$ was established. As expected, the unit cell volume of $Na_7LiSi_{8-z}Ge_z$ increases linearly with increasing Ge content *z* (Figure 3.9c). Site occupancy factors show that position *T*1, which is not η^3-coordinated by Li, is preferentially occupied by Si. The formation of Na_7LiSi_8 appears to be thermodynamically or kinetically unfavorable in a reaction from the elements or from the binary reactants Na_4Si_4 and LiSi. Yet, either the substitution of small amounts of Na for K to yield KNa_6LiSi_8 or the substitution of small amounts of Si for Ge to yield $Na_7LiSi_{6.7(1)}Ge_{1.3}$ sufficiently stabilizes the compounds so that they do form under the same conditions.

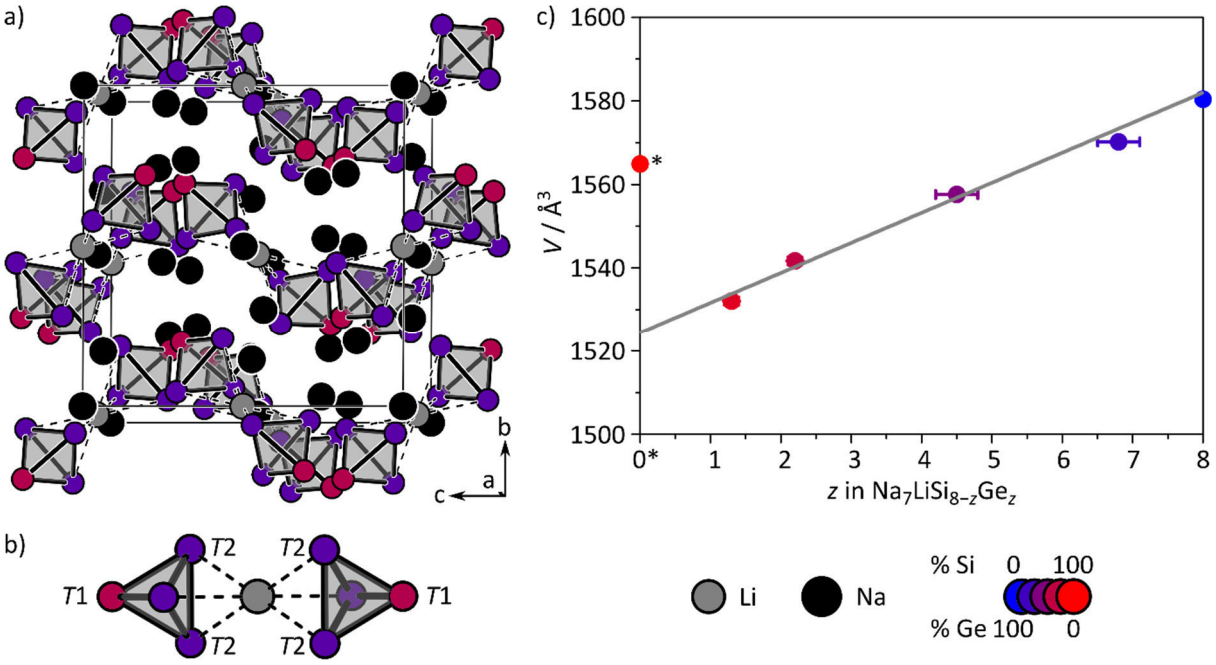

Figure 3.9. a) Unit cell and b) anionic substructure of $Na_7LiSi_{8-x}Ge_x$ [x = 4.5(3)] showing the preferential occupation of the mixed tetrel positions *T*. c) Vegard plot[22] illustrating the linear increase of the unit cell volume of $Na_7LiSi_{8-x}Ge_x$ with increasing x. * All data are obtained from Rietveld refinements with the exception of x = 0 which is taken from room temperature single crystal diffraction data of KNa_6LiSi_8,[1] in which Na2 is replaced by K. Vertical error bars are within the symbols.

$Li_3NaSi_{6-v}Ge_v$

Li_3NaSi_6 has been reported to act as a precursor for the formation of a new silicon allotrope which was named *allo*-Si.[2] Although this modification is yet to be reproduced and structurally characterized, Si/Ge substitution was investigated to find a potential precursor for mixed $Si_{1-x}Ge_x$ materials. As known for Li_3NaSi_6,[35] the synthesis of $Li_3NaSi_{6-v}Ge_v$ was attempted by mixing Si (and Ge) with LiH and NaH in stoichiometric ratio according to Equation (5).

$$3\ LiH + NaH + (6-v)\ Si + v\ Ge \rightarrow Li_3NaSi_{6-v}Ge_v + 2\ H_2 \quad (5)$$

This synthesis methods yields crystals, which are nicely suitable for single crystal XRD, but the resulting products are not phase pure. Thus, a second synthesis method was developed which reverses the peritectic decomposition of Li_3NaSi_6 to $Li_{12}Si_7$, Na_4Si_4, and Si at elevated temperatures. To improve the substitution of Si for Ge in the diffusion controlled annealing synthesis, ternary silicide-germanides were employed to introduce Ge into the product according to Equation (6).

$$Li_{12}Si_{7-x}Ge_x + Na_4Si_4 + 13\ Si \rightarrow 4\ Li_3NaSi_{6-v}Ge_v \quad (6)$$

Using these two synthesis methods, mixed silicide-germanides $Li_3NaSi_{6-v}Ge_v$ with $0 \leq v \leq 0.5$ were obtained. Therefore, the substitution of Si for Ge in this compound is very limited but the presence of small amounts of Ge was proven by EDX and single crystal XRD.

The two-dimensional polytetrelide sheets $^2_\infty[T_6]^{4-}$ in $Li_3NaSi_{6-v}Ge_v$ consist of three different types of tetrel sites (Figure 3.10): four-bonded (4b) *T*1, *T*5, and *T*6; 3b-*T*3 and -*T*4; and 2b-*T*2 which are characterized by formal charges of 0, −1, and −2, respectively. As observed for $Li_{12}Si_{7-x}Ge_x$, more electronegative Ge preferably occupies the more negatively charged tetrel positions: 2b-*T*2 exhibits by far the largest Ge occupancy at 24.3(7) % in $Li_3NaSi_{5.56(1)}Ge_{0.44}$, followed by 3b-*T*3 and -*T*4 at 8.9(5) % and 6.8(5) %, respectively. The four-bonded sites *T*1, *T*5, and *T*6 exhibit no significant Ge occupation.

Thus, only limited amounts of Si can be substituted for Ge in $Li_3NaSi_{6-v}Ge_v$ and the tetrel atoms mix statistically on selected negatively charged tetrel sites.

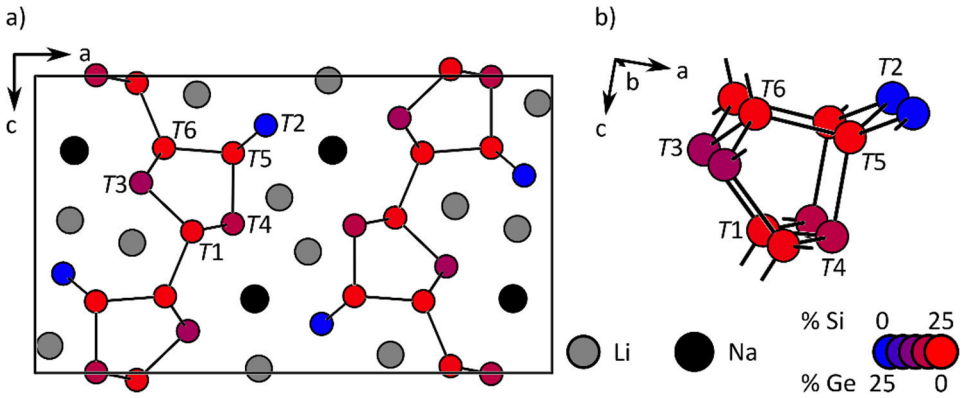

Figure 3.10. a) Unit cell and b) anionic substructure of $Li_3NaSi_{6-v}Ge_v$ [v = 0.44(1)] showing the preferential occupation of the mixed tetrel positions *T*2, *T*3, and *T*4. Note the different coloring range compared to Figures 3.8 and 3.9.

3.2.2 Mixing of Silicon and Boron

see Chapter 5.9 Searching for Open Tetrahedral Frameworks (OTFs) and Electron-Poor Framework Semiconductors (EPFSs) in the (Li-)B-Si System
L. M. Scherf, N. Riphaus, G. Neubüser, L. Kienle, T. F. Fässler, *manuscript for publication*.

Ternary alkali metal silicon boride compounds are relatively scarce (cf. Chapter 1.3.3). However, the element combination *A*-B-Si is well suited for Zintl phase OTFs as the alkali metal can donate its valence electrons to B such that all B and Si atoms are four-coordinated according to the general formula $A_xB_xSi_y$. The resulting open frameworks contain large voids or channels, which are filled by the alkali metal cations. With respect to the coloring problem, Si and B can either share mixed crystallographic positions as in $K_7B_7Si_{39}$ and $Na_8B_{74.5}Si_{17.5}$ or form an ordered structure in which B and Si are strictly separated ($Li_2B_{12}Si_2$ and $LiBSi_2$).[36-39]

Synthesis of *A*-Si-B phases is challenging because the three elements are characterized by very different melting points. Therefore, reaction temperatures of 900 °C and above are typically necessary to obtain phase-pure, crystalline products. Thus, $K_7B_7Si_{39}$, $Na_8B_{74.5}Si_{17.5}$, and $Li_2B_{12}Si_2$ were obtained from the respective elements at 900 °C, 1000 °C, and 1500 °C, respectively.[36-38] $LiBSi_2$ can so far only be obtained in very small amounts from the starting materials LiB and Si via high-pressure high-temperature synthesis at 10 GPa and 1000 °C.[39] At high temperatures, the three components readily react with a variety of reaction container materials. In addition, thermodynamically stable phases are heavily favored over any potential metastable phases under such conditions. This work focuses on the Li-B-Si phase system because $LiBSi_2$ is being considered as a potential Li ion conductor.[39]

As mentioned above, ternary A-B-Si phases have so far mostly been prepared directly from the respective elements. The synthesis of $LiBSi_2$ using LiB as a starting material[39] demonstrates that other boron containing compounds may be applicable as precursors for ternary phases. More reactive starting materials could even facilitate the synthesis of potentially metastable compounds under significantly milder conditions. In this work, different B-containing reagent were tested as starting materials for syntheses of ternary Li-Si-B at temperatures of 400–900 °C. BN crucibles were used as inert reaction containers to avoid any side reactions.

Syntheses were attempted using the following B reagents: a) nanoparticles of amorphous boron (nano-B), b) LiB, c) $LiBH_4$, d) α-SiB_3, and e) B_2O_3. Mehmet Somer and coworkers had previously shown that nano-B is more reactive than other elemental forms of boron and thus facilitates the synthesis of superconducting MgB_2.[40] LiB comprises linear strands of B atoms which should be easier to break than the icosahedral B units in elemental B.[41] $LiBH_4$ was selected because, according to literature,[42] it decomposes at 370 °C and should thus form reactive boron species in-situ. α-SiB_3 had been proven to be metastable[43] and B_2O_3 should be reduced by excess Li so that these reagents also promise to form reactive B species. The B-containing starting materials were reacted with various lithium silicides as well as with elemental Li and Si. In this context, LiSi and $Li_{15}Si_4$ are especially promising because they also decompose at relatively low temperatures.[44,45]

Nanoparticles of amorphous boron (nano-B) were found to readily react with elemental lithium and silicon as well as lithium-rich silicides under moderate conditions. However, only mixtures of previously known lithium borides and silicides and $Li_2B_{12}Si_2$ were obtained. Similarly, LiB and α-SiB_3 are adequate boron reagents for mild condition syntheses. Reactions with LiSi and $Li_{15}Si_4$ yield binary and ternary borides and silicides at temperatures as low as 500 °C. Again, neither $LiBSi_2$ nor any novel ternary compounds were found. In contrast, reactions of $LiBH_4$ and B_2O_3 with various lithium silicides or with elemental lithium and silicon afford only Si and lithium silicides as crystalline reaction products.

Overall, nano-B, LiB, and α-SiB_3 were identified as reactive boron precursors for mild condition syntheses in the Li-B-Si system. However, neither the target compound $LiBSi_2$ nor novel ternary compounds were obtained with this method.

3.2.3 The Lithium Ion Conductor $Li_6B_{18}(Li_3N)_x$

see Chapter 5.5 The Lithium Ion Conductor $Li_6B_{18}(Li_3N)_x$ – Synthesis, Li Ion Mobility, Topochemical Template Extraction, and Electronic Structure
L. M. Scherf, H. Kirchhain, L. van Wüllen, T. F. Fässler, *manuscript for publication*.

During investigations in the Li-B-Si system, the template phase $Li_6B_{18}(Tp)_x$ was observed as a side product. It comprises an open framework structure constructed by interconnected B_6-octahedra, which form large hexagonal pores (Figure 3.11a and b). The phase was reported to form only in the presence of template species such as Li_2O or $LiBH_4$.[46,47] The template atoms are located inside the open channels and form one-dimensional strands that resemble a cutout of the hexagonal Li_3N structure (Figure 3.11b and c).[48]

Li_3N is an excellent Li ion conductor (ionic conductivity of $6 \cdot 10^{-3}$ S cm^{-1} at room temperature)[49,50] but it cannot be applied as a solid electrolyte in lithium ion batteries due to its low theoretical decomposition potential. In this work, the outstanding ionic conductivity of Li_3N was combined with the stable boron framework of $Li_6B_{18}(Tp)_x$ by using Li_3N as the template species. The reaction of elemental lithium, boron, and Li_3N affords the desired product. Dark red $Li_6B_{18}(Li_3N)_x$ differs from orange $Li_6B_{18}(Li_2O)_x$ not only in color but also by significantly larger cell parameters. According to Rietveld refinement, the Li2 and N1 positions located inside the large pores are not fully occupied. The obtained sum formula of $Li_{6.35(7)}B_{18}N_{0.94(1)}$ demonstrates a significant Li deficiency with respect to electron-precise $Li_6B_{18}(Li_3N)_x$.

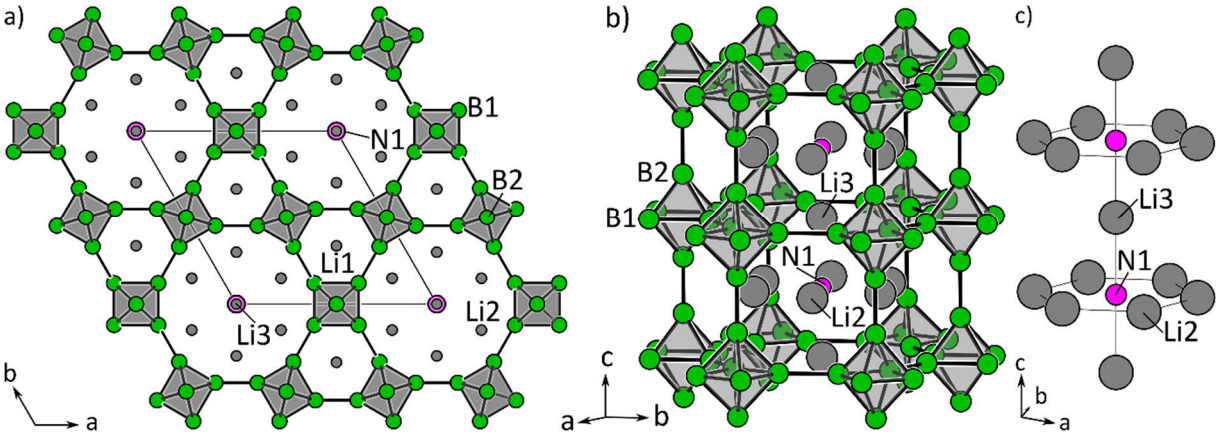

Figure 3.11. a) Hexagonal open framework structure of $Li_6B_{18}(Li_3N)_x$; Li2 and N1 are only partially occupied. b) Depiction of the large hexagonal pore formed by the interconnected B_6-octahedra. c) Depiction of the $^1_\infty[Li_7N]$ strands representing a structural cutout of the Li_3N structure.

The presence of the template Li_3N inside the open channels in combination with a large number of Li vacancies suggests Li ion mobility along the pores. Static ^{7}Li solid-echo NMR spectra of $Li_6B_{18}(Tp)_x$ at room temperature exhibit one narrow signal with quadrupole coupling (Figure 3.12a). Variable temperature measurements suggest fully mobile Li ions above 200 K. Only below 200 K line broadening is observed (Figure 3.12b). The "rigid lattice regime" characterized by the absence of fast motional processes was not reached even at 112 K. Using temperature-dependent linewidths and relaxation times T_1, the activation energy for Li motion in $Li_6B_{18}(Tp)_x$ was determined to be between 5 and 20 kJ mol^{-1}. This very low activation energy is comparable with that of LGPS-type compounds, which represent the best Li ion conductors known to date.[51,52] Quadrupole coupling at room temperature indicates that Li mobility in $Li_6B_{18}(Li_3N)_x$ is anisotropic, which is in good agreement with presumed Li hopping inside the open channels.

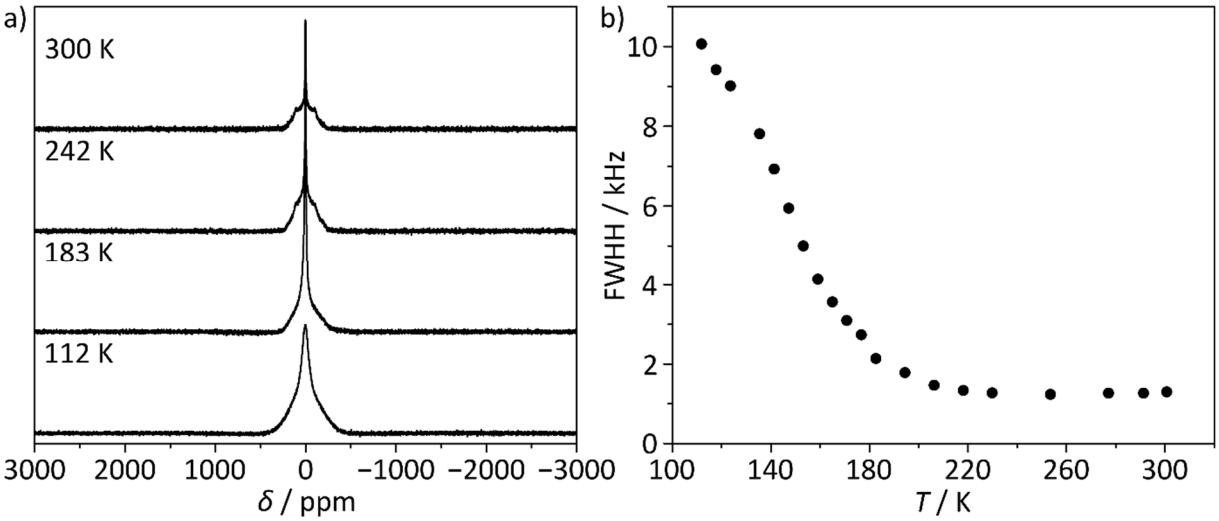

Figure 3.12. a) Static ^{7}Li solid-echo NMR spectra of $Li_6B_{18}(Tp)_x$. b) Evolution of the linewidth of the ^{7}Li central transition in the measured temperature range from 112 K to 300 K.

Previous investigations on $Li_6B_{18}(Tp)_x$ phases mentioned that the template phase can be extracted under retention of the stable boron framework in reactions with water.[46,53] However, the extraction products were never analyzed in detail. In this work, the template extraction was performed under more controlled reaction conditions using ethanol as the extracting agent. As reported previously, the red starting materials turns green immediately after contact with ethanol. Washing and drying of the

solid product affords a mixture of the extracted template phase and a new tetragonal phase.[4] The latter can be removed by further treatment with a mixture of ethanol and water. Evaporation of the clear filtrate in air affords lithium carbonate, proving that a lithium species was extracted from the template phase. Rietveld refinement of the extracted template phase yields a sum formula of $Li_{4.12(8)}B_{17.01(8)}N_{0.42(1)}$, indicating not only a loss of Li and N atoms inside the large hexagonal channels but also a significant boron-deficiency in the open framework. This observation is confirmed by Raman spectra, which demonstrate a significant shift of the three Raman modes characteristic for the inter-connected B_6 framework (Figure 3.13).

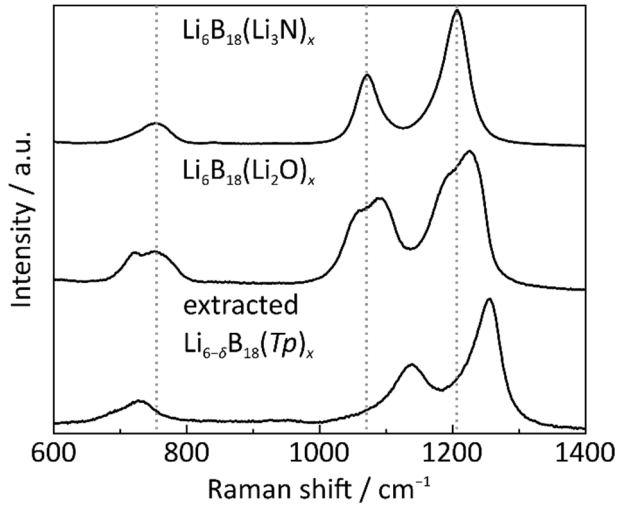

Figure 3.13. Raman spectra of $Li_6B_{18}(Li_3N)_x$, $Li_6B_{18}(Li_2O)_x$, and extracted $Li_{6-\delta}B_{18}(Tp)_x$. The Raman shifts of $Li_6B_{18}(Li_3N)_x$ are marked by dotted lines to illustrate the large deviations of the extracted phase.

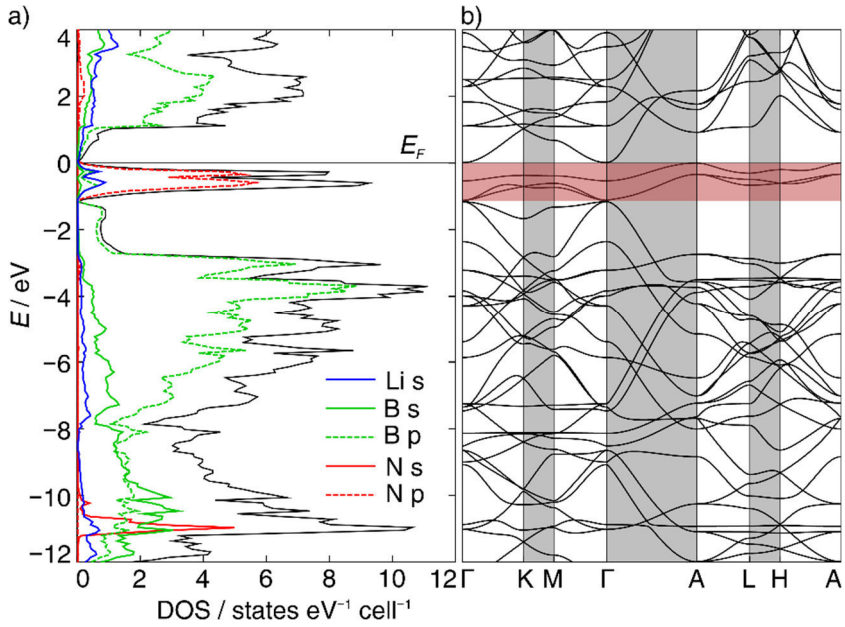

Figure 3.14. a) Total and partial DOS curves in the range of −12 eV to 4 eV for $Li_6B_{18}(Li_3N)$; b) band structure of $Li_6B_{18}(Li_3N)$ in the range of −12 eV to 4 eV, the bands marked in red correspond to states of the atoms situated in the large pores of the structure.

[4] Elemental analysis suggests the sum formula $LiBC_8H_{20}O_4$ for the new tetragonal phase, consistent with lithium tetraethoxyborate.

The electronic structure of $Li_6B_{18}(Li_3N)_x$ was calculated using the TB-LMTO-ASA program,[14] assuming full occupation of all atomic positions. According to the calculated band structure (Figure 3.14), the conduction and valence bands touch the Fermi level E_F, but do not cross E_F or touch each other. Since the local density approximation (LDA) method tends to underestimate band gaps significantly,[54] semi-conducting behavior with an indirect band gap can be assumed. Interestingly, the top three conduction bands between 0 and −1.11 eV correspond almost exclusively to Li(s) and N(p) states of the atoms located inside the large pores, whereas the boron framework and Li1 contribute only to valence bands and conduction bands below −1.15 eV. Thus, a similar open framework without guest species located inside the channels is expected to exhibit a larger, direct band gap.

Therefore, the template phase structure was employed as the starting point for a chemically inspired construction of empty pore structures. Template-free structures Li_6B_{18} still comprise some Li atoms inside the hexagonal pore, which result in in-gap valence bands. Completely guest-free structures were constructed by substituting one third of the boron framework positions by carbon. The latter brings along the additional electrons that are otherwise contributed by Li host species. The resulting $B_{12}C_6$ structures indeed exhibit direct band gaps ranging from 2.4 eV to 3.2 eV (Figure 3.15).

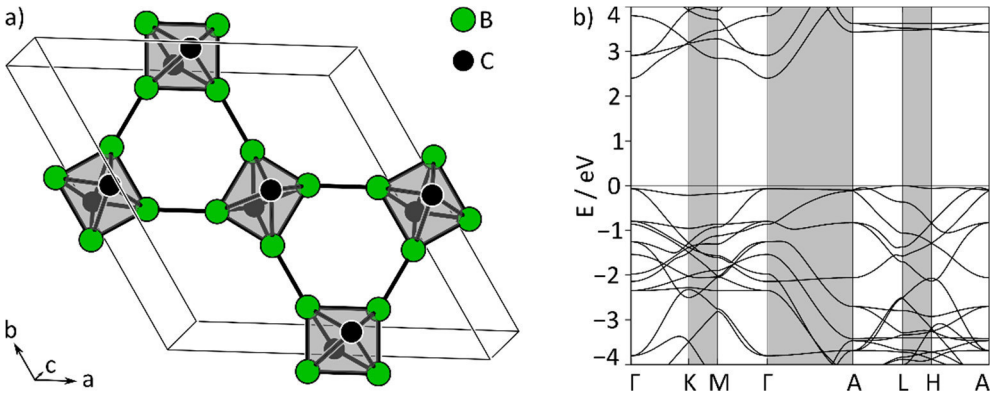

Figure 3.15. a) Structure of $B_{12}C_6$ in *P*6/*mmm*, empty circles represent the void Li2 positions. b) Band structure of *P*6/*mmm*-$B_{12}C_6$ in the range of −4 to 4 eV.

In conclusion, the combination of the excellent Li ion conductor Li_3N with a stable B framework in $Li_6B_{18}(Li_3N)_x$ yields a very promising solid electrolyte material characterized by outstanding Li ion mobility. Theoretical guest-free $B_{12}C_6$ structures which are chemically inspired by the open framework structure of $Li_6B_{18}(Li_3N)_x$ anticipate a direct band gap semiconductor material.

3.2.4 A Novel Binary Li-C Phase Obtained from Lithium Flux Synthesis

see Chapter 5.6 A Novel Binary Li-C Phase Obtained from Lithium Flux Synthesis
L. M. Scherf, G. Neubüser, L. Kienle, T. F. Fässler, *manuscript for publication*.

Unlike silicon and germanium, which behave very similar in binary alkali and alkaline earth metal compounds, the lighter and much more electronegative tetrel analogue carbon forms very different structures. Binary carbides contain either very small or very large (poly-)anions. Thus, methanides (Be_2C, Mg_2C),[55,56] diatomic acetylides (A_2C_2, EC_2),[57-63] and triatomic allenides (Li_4C_3, Mg_2C_3)[64-67] are the only small carbon anions found in binary alkali or alkaline earth carbides. Large carbon anions comprise graphite intercalation compounds and alkali metal fullerides.[68,69] Medium-sized carbon anions as in the binary silicide and germanide cluster compounds, however, have not been reported yet.

In this work, lithium flux synthesis was performed using fullerene C_{60} as a reactive carbon precursor. The flux method was selected facilitate the synthesis of lithium-rich carbides. At a reaction temperature of 575 °C, a novel binary Li-C phase was obtained next to the side phase Li_2C_2 (Figure 3.16a). Reaction temperatures above 700 °C produce single-phase Li_2C_2. Carbon is not soluble in liquid lithium, so that the diffusion-controlled reaction of Li and C_{60} does not produce any single crystals of the newly discovered compound. Indexing of the PXRD pattern, however, yields a monoclinic unit cell in space group *P*2/*m* with cell parameters with a = 8.298(2) Å, b = 6.327(3) Å, c = 10.424(3) Å, β = 109.33(1)°, and V = 516.4(3) Å^3 (Figure 3.16a).

First attempts to solve the structure of LiC_x directly from the powder pattern have not been successful, but further investigations are underway. Meanwhile, a variety of other characterization methods have shed some light onto the identity of the binary carbide. Elemental analysis suggests a composition of LiC_2 or lithium-poorer. Raman and ^{13}C MAS NMR spectra (Figure 3.16b) of LiC_x exhibit signals, which could be assigned to carbon species with conjugated double bonds or even fused aromatic rings. The latter could represent fragments of the C_{60} precursor. Decomposition of LiC_x with ethanol yields a brown solid product, further indicating the presence of at least medium-sized carbon polyanions.

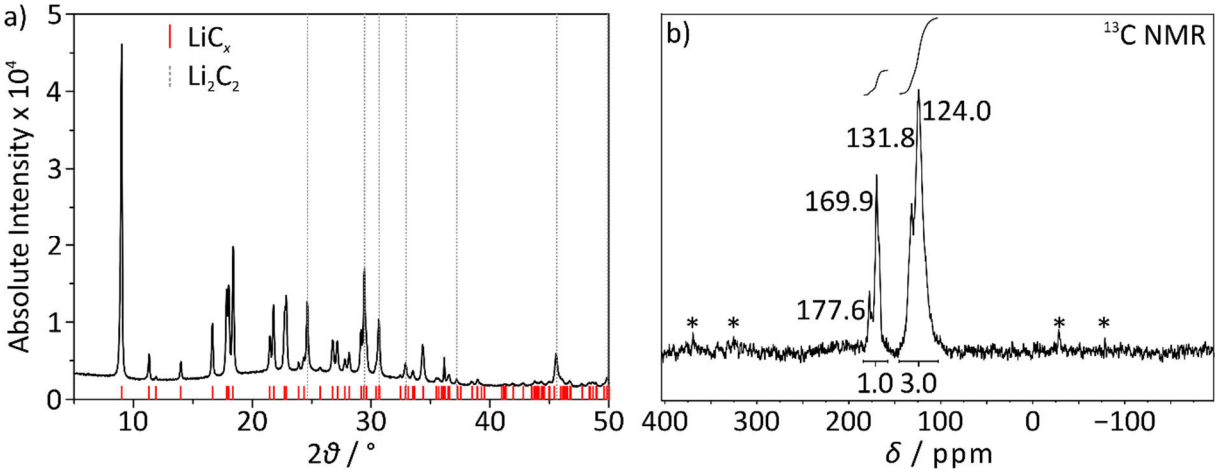

Figure 3.16. a) Experimental powder diffraction pattern of a LiC_x sample; reflections of Li_2C_2 are marked by grey dotted lines, reflection positions of the monoclinic unit cell of LiC_x with a = 8.298(2) Å, b = 6.327(3) Å, c = 10.424(3) Å, β = 109.33(1)°, and V = 516.4(3) Å^3 are marked in red. b) ^{13}C MAS NMR spectrum of LiC_x; rotational side bands are marked with asterisks.

Thermal analysis of LiC_x shows that the binary carbide decomposes exothermically at 710 °C. Annealing experiments additionally demonstrate a slow decomposition at lower temperatures, suggesting that LiC_x is metastable. Magnetic measurements of LiC_x indicate Pauli paramagnetic behavior, which is typically observed in metallic compounds. Unlike in alkali metal fullerides and alkali metal-doped polycyclic aromatic hydrocarbons, superconductivity was not detected down to 2 K.

Overall, the novel binary lithium carbide could represent the missing link between small and large carbon anions in binary metal carbides, opening up a completely new class of compounds.

3.3 Zintl Phases as Precursors for Novel Materials

3.3.1 Amorphous Silicon-based Materials

see Chapter 5.7 Alkali Metals Extraction Reactions with the Silicides $Li_{15}Si_4$ and Li_3NaSi_6: Amorphous Si *versus allo*-Si
M. Zeilinger, L. A. Jantke, L. M. Scherf, F. J. Kiefer, G. Neubüser, L. Kienle, A. J. Karttunen, S. Konar, U. Häussermann, T. F. Fässler, *Chem. Mater.* 2014, *26*, 6603–6612.

see Chapter 5.8 Synthesis and Characterization of *a-allo*-$Si_{1-x}Ge_x$
L. M. Scherf, G. Neubüser, L. Kienle, T. F. Fässler, *manuscript for publication.*

see Chapter 5.9 Searching for Open Tetrahedral Frameworks (OTFs) and Electron-Poor Framework Semiconductors (EPFSs) in the (Li-)B-Si System
L. M. Scherf, N. Riphaus, G. Neubüser, L. Kienle, T. F. Fässler, *manuscript for publication*.

The substitution reactions presented in Chapters 3.1 and 3.2 offered only few mixed Zintl phases which, judging by their structure, are well suited as precursors for novel materials. Thus, the reaction of Li_3NaSi_6 and $Li_3NaSi_{6-v}Ge_v$ with protic solvents was studied in detail. Novel ternary Li-Si-B phases were not found, so that the synthesis of Si-B materials was studied in heterogeneous reactions of alkali metal silicides (and germanides) with boron halide solutions. All these reactions resulted in amorphous Si-based materials, which will be presented below.

a-allo-Si and a-allo-$Si_{1-x}Ge_x$

Nearly 30 years ago, the topochemical conversion of the Zintl phase Li_3NaSi_6 comprising polyanionic Si sheets to a new Si allotrope termed *allo*-Si was reported.[2] The new allotrope was not structurally characterized but an experimental powder diffraction pattern was published. Since then, no additional reports were published on this material. However, after the structure of *allo*-Ge had recently been successfully clarified,[70] the formation of *allo*-Si was reinvestigated in a collaborative effort. In addition, the analogous reaction of the mixed silicide-germanide $Li_3NaSi_{6-v}Ge_v$ with ethanol was examined.

The starting materials $Li_3NaSi_{6-v}Ge_v$ with $v = 0$ and 0.5 were prepared by annealing binary precursors as shown in Equation (6) in Chapter 3.2.1. To render $Li_3NaSi_{6-v}Ge_v$ more reactive, it was finely ground using a planetary ball mill and then subjected to dry ethanol. The reaction proceeds vigorously according to the formal Equation (7) with significant heat and gas formation.

$$Li_3NaSi_{6-v}Ge_v + 4\ EtOH \rightarrow a\text{-}allo\text{-}Si_{1-x}Ge_x + 3\ LiOEt + NaOEt + 2\ H_2 \quad (7)$$

The resulting materials appear fully amorphous in PXRD patterns and are thus termed *a-allo*-Si and *a-allo*-$Si_{1-x}Ge_x$ ($x \approx 0.083$). In addition, the amorphous materials obtained from $Li_3NaSi_{6-v}Ge_v$ with $v = 0$ and 0.5 were compared with amorphous Si (*a*-Si) prepared by extraction of $Li_{15}Si_4$ with liquid ammonia.

The three materials were thermally analyzed by differential scanning calorimetry (DSC). The resulting DSC curves all contain one exothermic signal in the first heating cycle (Figure 3.17), which can be attributed to crystallization of *α*-Si by subsequent PXRD analysis. In case of *a-allo*-$Si_{1-x}Ge_x$ the *α*-Si reflections in the post-DSC diffraction pattern do not indicate increased cell parameters for a solid

solution. Crystallization of the materials occurs at very different temperatures. *a-allo*-Si and *a-allo*-$Si_{1-x}Ge_x$ crystallize at 565 °C and 579 °C, respectively, whereas *a*-Si does not crystallize until 658 °C.

To find the cause of the different crystallization temperatures, the materials were closely examined using Raman spectroscopy and transmission electron microscopy (TEM). *a*-Si and *a-allo*-Si additionally underwent IR spectroscopy and synchrotron radiation PXRD from which pair distribution functions (PDFs) were subsequently determined.

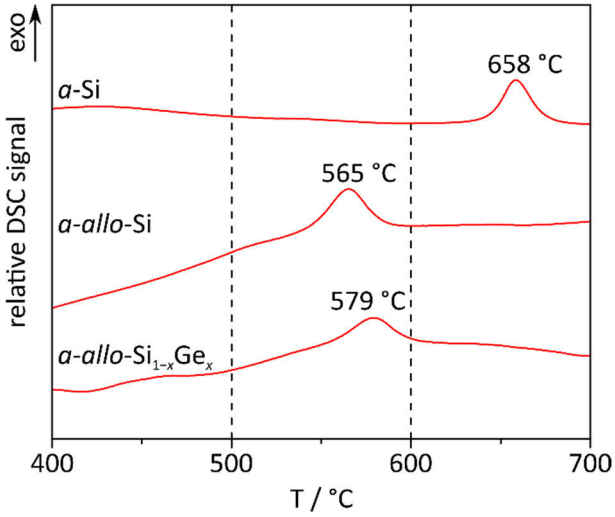

Figure 3.17. DSC heating traces of *a*-Si,[71] *a-allo*-Si,[71] and *a-allo*-$Si_{1-x}Ge_x$[72] measured with a heating rate of 10 °C min^{-1}.

The TEM investigations (Figure 3.18) show that all materials comprise amorphous and nanocrystalline particles, which can be assigned to amorphous and *α*-Si using the diffuse rings and discrete reflections observed in selected area electron diffraction (SAED) patterns. For *a-allo*-$Si_{1-x}Ge_x$, the cell parameters seem to be slightly enlarged. EDX measurements performed inside the transmission electron microscope prove the presence of Ge in the material. In addition, *a*-Si contains significantly fewer and smaller crystalline Si particles than *a-allo*-Si. This finding is supported by PDF analysis. The larger crystalline particles in *a-allo*-Si could function as seed crystals for the crystallization of the material in the DSC measurements and could thus lower its crystallization temperature.

The formation of a new crystalline Si allotrope from Li_3NaSi_6 could however not be reproduced. In contrast, quantum chemical calculations on Si structures potentially resulting from a topotactic recombination of the polysilicide sheets in Li_3NaSi_6 show that even the lowest energy structure of the TON zeolite type are energetically unfavorable with respect to stable clathratic and zeolitic frameworks. In addition, the published PXRD pattern for crystalline *allo*-Si could be assigned to the reflections of $NbSi_2$, which could well have been formed during the synthesis of the starting material Li_3NaSi_6 in Nb ampules.

Raman spectra of *a*-Si and *a-allo*-Si also exhibit signals of amorphous and nanocrystalline Si particles (Figure 3.19). Upon more intense irradiation of the laser beam, the materials crystallize inside the Raman spectrometer and subsequent Raman spectra show the typical signals for Si–Si vibrations in crystalline *α*-Si around 520 cm^{-1}. *a-allo*-$Si_{1-x}Ge_x$ behaves similarly and is also easily crystallized by the laser beam. However, the spectra before and after intense laser beam irradiation contain bands corresponding to Ge–Ge and Si–Ge vibrations next to the Si–Si bands. This clearly proves that Ge is not just present next to Si in the material but that it also substitutes Si on an atomic level.

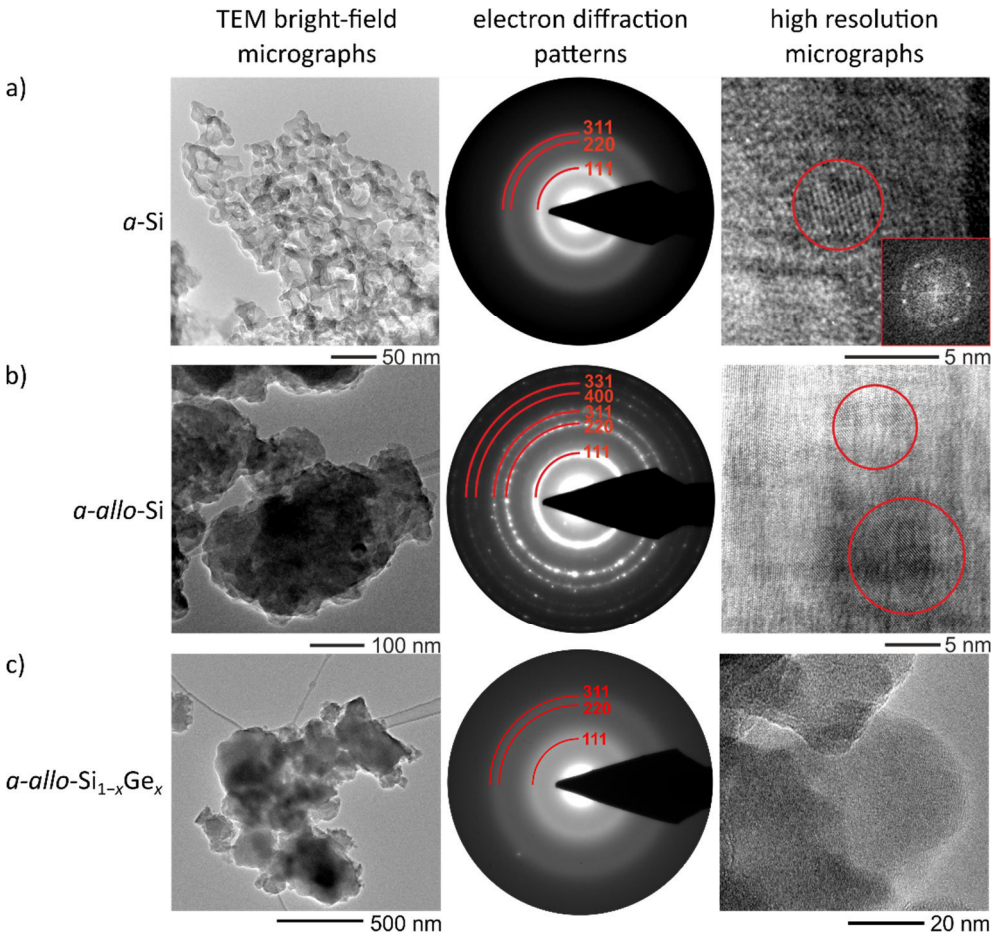

Figure 3.18. TEM bright-field micrographs, SAED patterns, and high resolution micrographs of a) *a*-Si synthesized by liquid ammonia extraction of $Li_{15}Si_4$,[71] b) *a-allo*-Si synthesized by ethanol extraction of Li_3NaSi_6,[71] and c) *a-allo*-$Si_{1-x}Ge_x$ synthesized by ethanol extraction of $Li_3NaSi_{6-v}Ge_v$.[72] Red circles mark nanocrystalline areas.

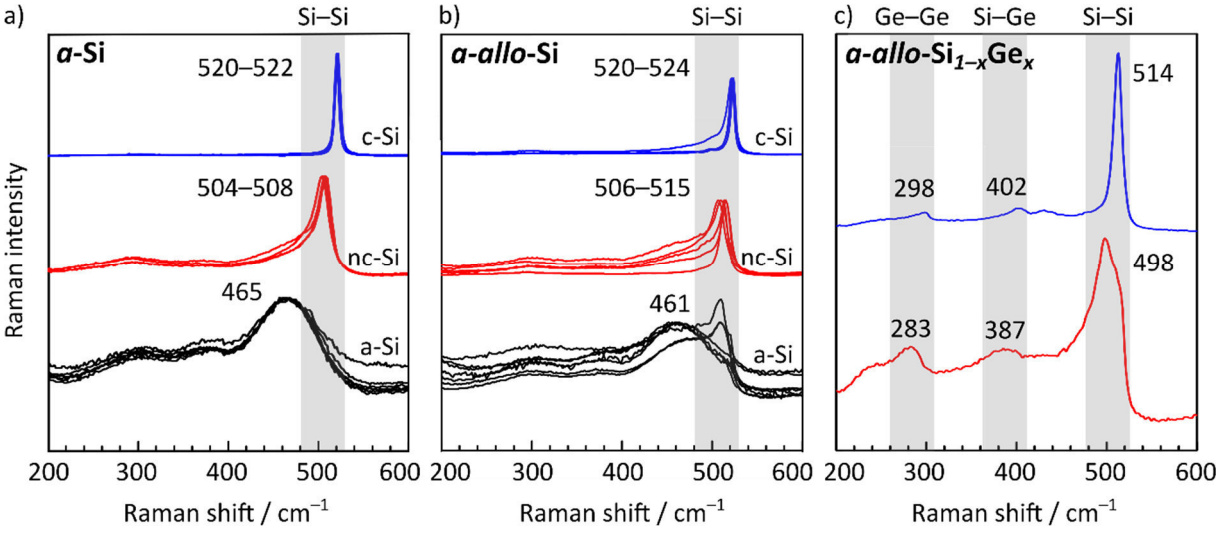

Figure 3.19. Raman spectra of a) *a*-Si synthesized by liquid ammonia extraction of $Li_{15}Si_4$,[71] b) *a-allo*-Si synthesized by ethanol extraction of Li_3NaSi_6,[71] and c) *a-allo*-$Si_{1-x}Ge_x$ synthesized by ethanol extraction of $Li_3NaSi_{6-v}Ge_v$ (measured on a different Raman spectrometer than a and b).[72] Black and red spectra are obtained from various positions of the sample characterized by a more amorphous (black) or nanocrystalline (Si, red) nature. Blue spectra were measured after increasing the laser power, which resulted in crystallization of the samples. Grey shaded areas denote the typical Raman shifts of Si–Si, Si–Ge, and Ge–Ge bonds in (nano-)crystalline samples.

Recently, Obrovac and coworkers prepared amorphous Si from $Li_{12}Si_7$, Li_7Si_3, $Li_{13}Si_4$ and "$Li_{22}Si_5$"[5] by reaction with ethanol.[74] Some of their products exhibited layered structures on the µm scale, which could originate from sintering processes during their drying procedure at 120 °C under Ar flow. They were able to show that due to large void spaces their samples are promising anode materials for lithium ion batteries because of lower volume expansions. Therefore, *α-allo*-Si and *α-allo*-$Si_{1-x}Ge_x$ are currently being tested as LIB anode materials.

Amorphous Si-B materials

Silicon borides are typical representatives of electron-poor framework semiconductors (EPFSs). This class of compounds which encompasses *α*-SiB_3 as well as the excellent thermoelectric material *β*-Zn_4Sb_3,[75,76] is characterized by weakly polar bonding, small band gaps, and valence electron concentrations between three and four. The latter results in highly complicated structures with multi-center bond contributions, rendering all EPFSs promising candidates for thermoelectric materials.[77]

Due to the high melting points of the elements, the synthesis of silicon borides typically requires very high temperatures. It is, however, well-known that alkali metal silicides are excellent precursors for the synthesis of Si nanoparticles (cf. Chapter 1.2.3).[78] In addition, B nanoparticles are accessible via the reduction of boron tribromide.[79] Thus, the synthesis of Si-B materials was attempted by combining the two procedures according to Equation (8).

$$3/x\ A_xSi_y + BX_3 \rightarrow \text{“}BSi_{3y/x}\text{”} + 3\ AX \qquad (8)$$

Several alkali metal silicides A_xSi_y (and some germanides) were subjected to boron halides BX_3 in organic solvents. The exothermic formation of alkali metals *AX* drives the reactions, which proceeded sluggishly. $Li_{12}Si_7$, $Li_{17}Si_4$, Li_7Ge_{12}, and $Li_{18}Na_2Ge_{17}$ hardly reacted with excess amounts of BBr_3, even after stirring at 100 °C in toluene for one week as shown by PXRD. In contrast, Na_4Si_4, Na_4Ge_4, $Li_{15}Si_4$, $Li_{15}Ge_4$, and Li_3NaSi_6 demonstrate complete conversion of the starting material, indicated by the absence of starting material reflections and the presence of alkali metal bromide reflections in the respective PXRD patterns.

To analyze the mostly amorphous reaction products, the alkali metal bromides were removed by washing with THF (LiBr) and DMSO (NaBr). Subsequently, thermal analyses using DSC, Raman spectroscopy and transmission electron microscopy (TEM) were performed on the samples. The reaction product of $Li_{15}Si_4$ and BBr_3 was demonstrated to convert to crystalline $Li_{12}Si_7$ and Si at 429 °C in a DSC measurement. Thus, the fully amorphous reaction product must contain a mixture of lithium silicides and Si, which was supported by TEM measurements. The reaction product of $Li_{15}Ge_4$ and BBr_3 was crystalline Li_7Ge_3 and LiGe next to largely amorphous Ge. The latter was shown to crystallize in a DSC measurement. Finely ground Li_3NaSi_6 was oxidized by BBr_3 to amorphous Si with traces of starting material remaining. Raman spectroscopy and TEM support this finding (Figure 3.20). Crystallization of the amorphous material occurs already at 378 °C, suggesting that the sample contained many nanocrystalline particles, which serve as seed crystals for the crystallization process. Exchanging BBr_3 for BI_3 facilitates the alkali metal bromide removal from the reaction products because unlike NaBr, NaI is soluble in THF. This, however, does not influence the identity of the reaction product.

[5] The stoichiometry of this phase has recently been corrected to $Li_{17}Si_4$.[73]

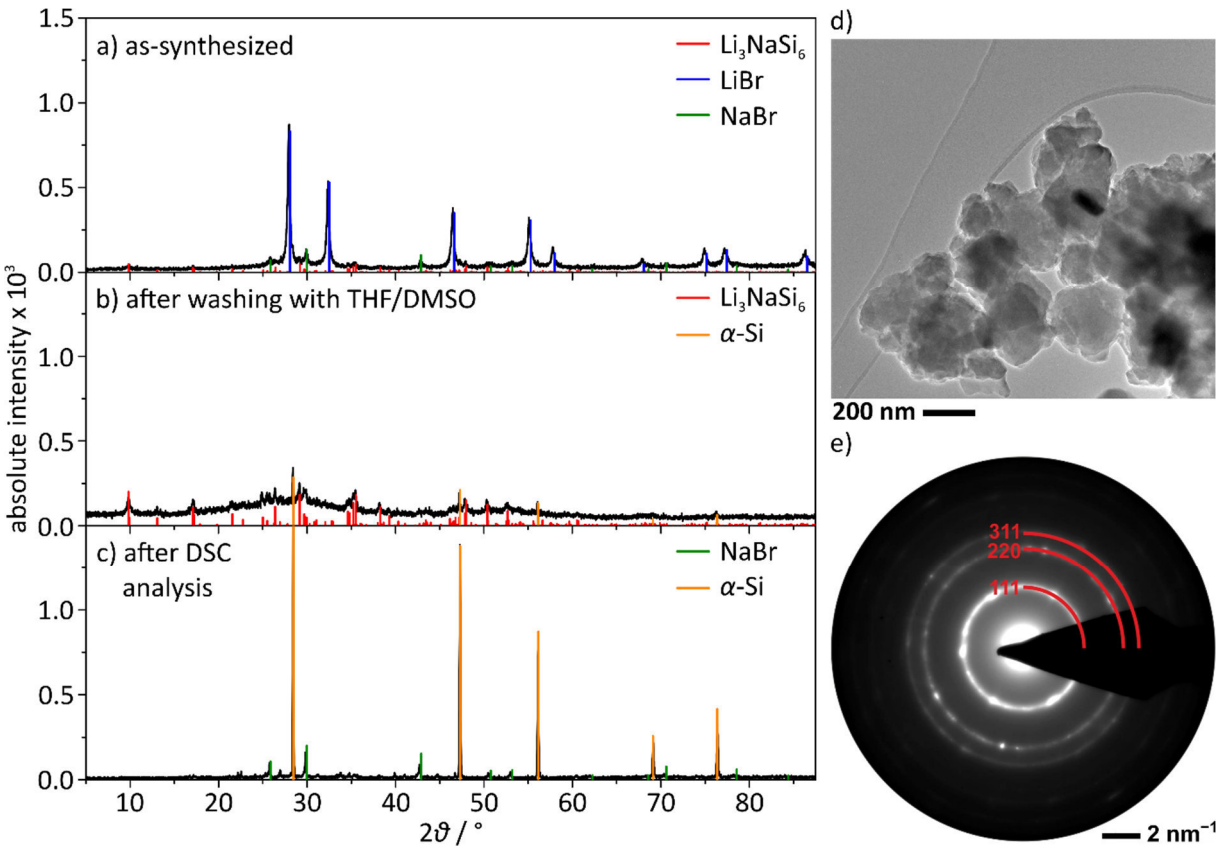

Figure 3.20. Powder diffraction patterns of the reaction product of Li_3NaSi_6 and BBr_3 in toluene a) as-synthesized, b) after removal of LiBr and NaBr with THF and DMSO, and c) after DSC analysis; d) TEM micrograph of the washed reaction product showing porous particles of 100–500 nm; e) SAED pattern of the washed reaction product displaying diffuse rings and some discrete reflections (*α*-Si).

In addition, Li_3NaSi_6 was reacted with the boron monohalides dicyclohexyliodoborane (BCy_2I) and the *N*-heterocyclic bromoborane *N,N'*-bis(2,6-diisopropylphenyl)-2-bromo-2,3-dihydro-1*H*-1,3,2-diazaborole (NHB-Br). This could lead to the functionalization and exfoliation of the two-dimensional polysilicide sheets in Li_3NaSi_6, in analogy to polysilane sheets prepared from $CaSi_2$ (cf. Chapter 3.3.3). However, NHB-Br did not react with Li_3NaSi_6. The reaction of Li_3NaSi_6 and BCy_2I yielded similar products to those with BBr_3, and no C–C or C–H bands were observed in the respective Raman spectra.

In conclusion, boron halides oxidize alkali metal silicides and germanides under very mild reaction conditions. However, the reduced boron species is not incorporated into the resulting amorphous silicon-based materials, which is confirmed by electron energy loss spectroscopy (EELS).

3.3.2 *Allo*-Germanium as an Electrode Material in Lithium Ion Batteries

see Chapter 5.10 Electrochemical Synthesis of the Allotrope *allo*-Ge and Investigations on the Use as an Anode Material
L. M. Scherf, J. Hattendorff, I. Buchberger, S. Geier, H. A. Gasteiger, T. F. Fässler, *submitted for publication.*

The topochemical synthesis of metastable *allo*-Ge via oxidation of the Zintl phase Li_7Ge_{12} with benzophenone or protic solvents (Figure 3.21) was first published in 1982.[80] Since then, the Ge allotrope has been structurally characterized[70] and its thermal behavior was studied in detail.[81,82] Similar to Li_3NaSi_6, Li_7Ge_{12} comprises two-dimensional polygermanide sheets, which are separated by Li cations.

In analogy to the reversible intercalation and deintercalation of lithium in graphite electrodes, *allo*-Ge could potentially be synthesized by electrochemical delithiation.

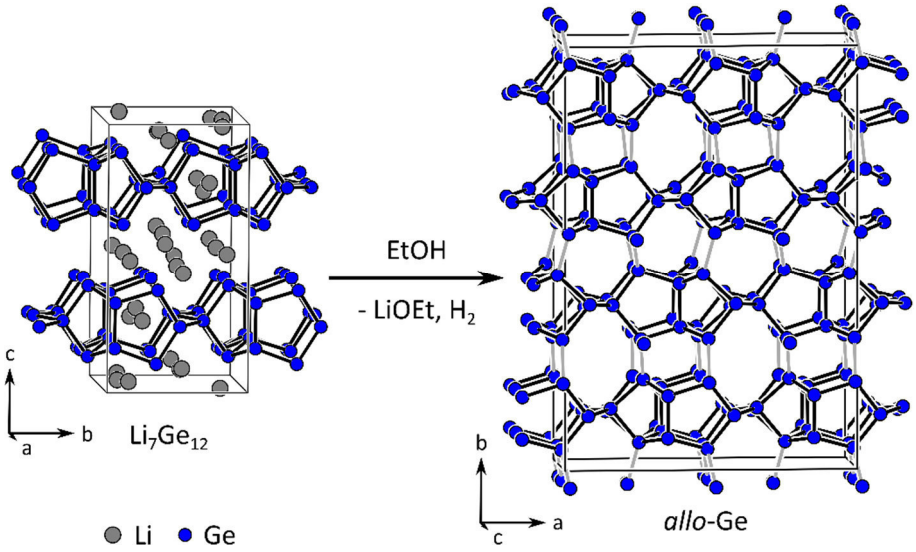

Figure 3.21. Upon reaction with ethanol, the Zintl phase Li_7Ge_{12} converts topotactically to *allo*-Ge. Newly formed bonds are marked in grey.

Therefore, Li_7Ge_{12}-containing electrodes were prepared using carbon black and polyethyleneoxide as a binder.[6] The electrodes were used to assemble CR2032 coin half-cells with a Li counter electrode and an organic $LiPF_6$-containig electrolyte. Such coin cells were then delithiated at a rate of C/80. PXRD analysis of the electrode materials before and after delithiation shows that *allo*-Ge can indeed be prepared by electrochemical delithiation of Li_7Ge_{12}.

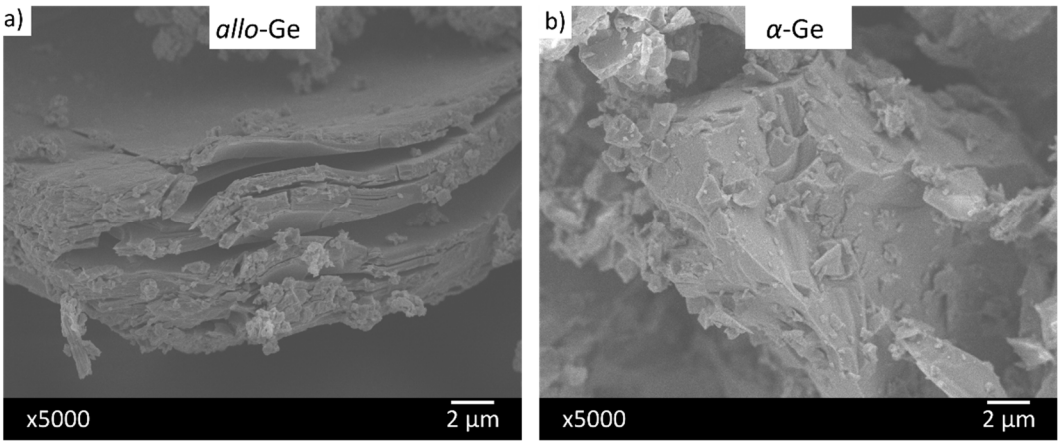

Figure 3.22. Scanning electron microscopy images of a) *allo*-Ge and b) *α*-Ge particles.

As described in the introduction (cf. Chapter 1.1.3), Ge is currently being heavily investigated as an anode material in LIBs due to its large theoretical capacity, electrical conductivity and Li^+ ion diffusivity. The main problem of Ge anodes today is the large volume change during charge and discharge. A (de-)in-tercalation mechanism, which is feasible for *allo*-Ge, could mitigate this issue. Unlike graphite, *allo*-Ge consists of a three-dimensional framework of Ge atoms, which during electrochemical lithiation may or may not separate into the two-dimensional sheets known from Li_7Ge_{12}. Yet, scanning electron

[6] The common binder polyvinylidene fluoride cannot be used for Li_7Ge_{12} because the *N*-methyl-pyrrolidone solution readily reacts with the anode material.

microscopy (SEM) images of *allo*-Ge exhibit a stacked sheets morphology (Figure 3.22). In case of a reversible reaction, *allo*-Ge could offer an alternative (de-)lithiation mechanism to conventional *α*-Ge, which undergoes an alloying mechanism upon charge and discharge in lithium ion batteries.[83,84] Accordingly, the electrochemical behavior of chemically synthesized *allo*-Ge as an anode material in Li half-cells was investigated in comparison with *α*-Ge.

allo-Ge and *α*-Ge electrodes were prepared with carbon black and polyvinylidene fluoride as a binder. Subsequently, CR2032 coin and Al pouch half-cells with Li foil counter electrodes were assembled. The coin cells were used to test the cycling behavior of the different electrode materials at C/20. *allo*-Ge exhibits similar lithiation capacities to *α*-Ge upon first lithiation and the potential curves of the materials also resemble one another, suggesting a similar (de-)lithiation mechanism. However, in the long run *α*-Ge exhibits a significantly better cycling stability.

In order to clarify the electrochemical behavior of *allo*-Ge, in-situ PXRD experiments of pouch cells with *allo*-Ge and *α*-Ge electrodes were performed. Figure 3.23 exemplarily shows the in-situ XRD data for *allo*-Ge. For both materials, the crystalline Ge modification is initially amorphized. Upon full lithiation, crystalline $Li_{15}Ge_4$ is formed. Delithiation of the materials affords amorphous Ge via a crystalline Li_7Ge_3 step. In the second and third cycles, crystalline Li_7Ge_3 is formed during lithiation of the amorphous material and traces of Li_7Ge_3 remain present throughout further *allo*-Ge cycling (Figure 3.23).

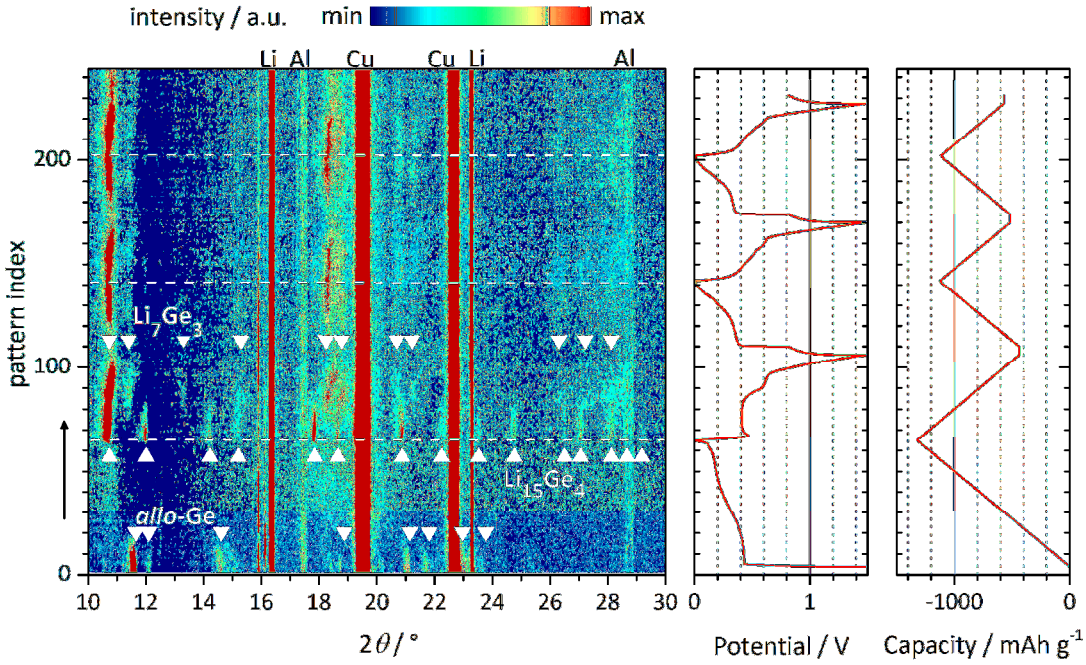

Figure 3.23. *allo*-Ge in-situ diffraction patterns next to potential and capacity for the first three lithiation and delithiation cycles. The main reflections of observed crystalline phases are marked with triangles.

Taking into account the extensive phase transition studies on *α*-Ge anodes reported by Grey et al. and Notten et al.,[83,84] the same (de-)lithiation mechanism in Figure 3.24 is postulated for both Ge modifications.

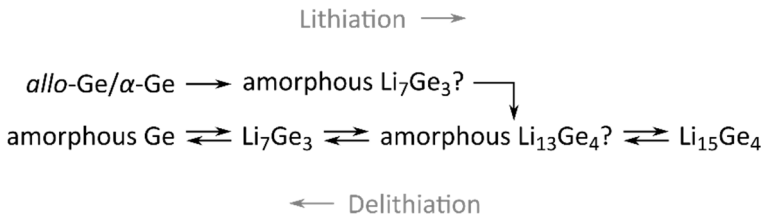

Figure 3.24. Postulated (de-)lithiation mechanisms for *allo*-Ge and *α*-Ge as anode materials in LIBs.

The decreasing cycling stabilities observed for *allo*-Ge and *α*-Ge are accompanied by increasing amounts of crystalline Li_7Ge_3, which remain in the electrodes and are not affected by lithiation and delithiation. This effect is observed more strongly for the *allo*-Ge cell, which was shown to deteriorate more quickly. According to the in-situ PXRD analysis, the poor cycling stability of *allo*-Ge is not caused by different (de-)lithiation mechanisms and is also independent of particle size effects. Maybe the very different morphologies of a*llo*-Ge and *α*-Ge particles are responsible for the different cycling stabilities.

3.3.3 Functionalization of Two-Dimensional Polysilane Sheets Prepared from $CaSi_2$

see Chapter 5.11 Radical-Induced Hydrosilylation Reactions for the Functionalization of Two-Dimensional Hydride Terminated Silicon Nanosheets
T. Helbich, A. Lyuleeva, I. M. D. Höhlein, P. Marx, L. M. Scherf, J. Kehrle, T. F. Fässler, P. Lugli, B. Rieger, *Chem. Eur. J.* 2016, *22*, 6194–6198.

As mentioned in Chapter 1.2.3, the Zintl phase $CaSi_2$ can be chemically deintercalated by reaction with concentrated hydrochloric acid. Depending on the reaction temperature, layered siloxene or polysilane is formed.[85,86] Layered polysilane is a very promising two-dimensional material for various microelectronics applications. However, the hydrogen-capped silicon nanosheets (SiNS) are relatively labile and form a crystalline structure of stacked layers (Figure 3.25).

Functionalization of the Si-H groups via reactions with aminoalkanes[87,88] and Grignard reagents[89] as well as Pt-catalyzed hydrosilylation[90] exfoliates and stabilizes the 2D material. In contrast to Pt-catalyzed hydrosilylation, radical-induced hydrosilylation enables the functionalization of Si materials without the addition of transition metals. Because transition metals are known to alter the interesting photoluminescense properties of Si nanomaterials, radical-induced hydrosilylation represents a promising alternative in the functionalization of SiNS. In a collaborative effort, this method was therefore investigated in detail.

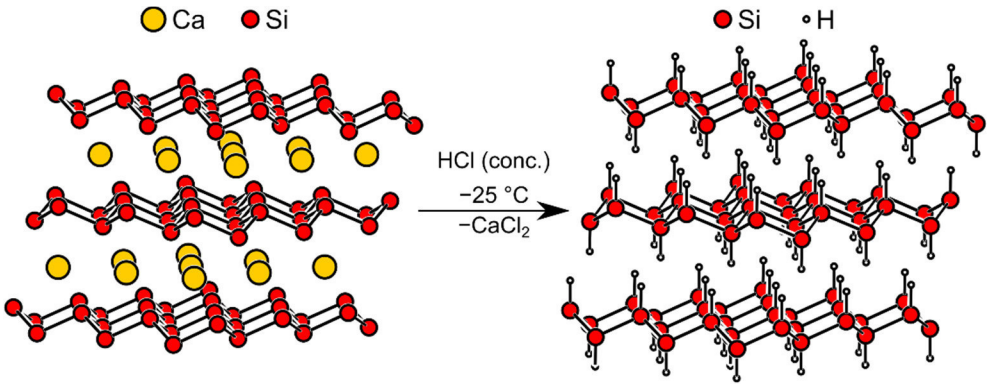

Figure 3.25. In a topochemical reaction, $CaSi_2$ is deintercalated to layered polysilane using concentrated hydrochloric acid at −25 °C.

Commercially available $CaSi_2$ usually contains substantial amounts of crystalline α-Si as an impurity, which remains present after subsequent steps of synthesis. Therefore, the synthesis of $CaSi_2$ was optimized at first. Stoichiometric amounts of Ca metal and Si powder were pressed to a pellet (cf. Chapter 2.1.5) and repeatedly fused using an arc furnace located inside a glovebox. This procedure affords a phase-pure starting material (Figure 3.26a). The subsequent reaction with concentrated hydrochloric acid at −25 °C produces layered polysilane (SiNS-H) without contaminating α-Si. The SiNS-H stack regularly, forming an almost crystalline structure which can be indexed by a hexagonal unit cells with a = 3.8331 Å and c = 6.3751 Å (Figure 3.26b). The a parameter which describes the Si sheet planes is almost identical with that of $CaSi_2$ [3.855(5) Å],[91] proving that a topochemical reaction has occurred. The distance between two polysilane sheets is described by the c parameter and increases significantly with respect to $CaSi_2$ [5.10(2) Å]. These results agree very well with the findings of Yamanaka and coworkers.[86] However, the SiNS-H prepared in this work appear to arrange even more regularly.

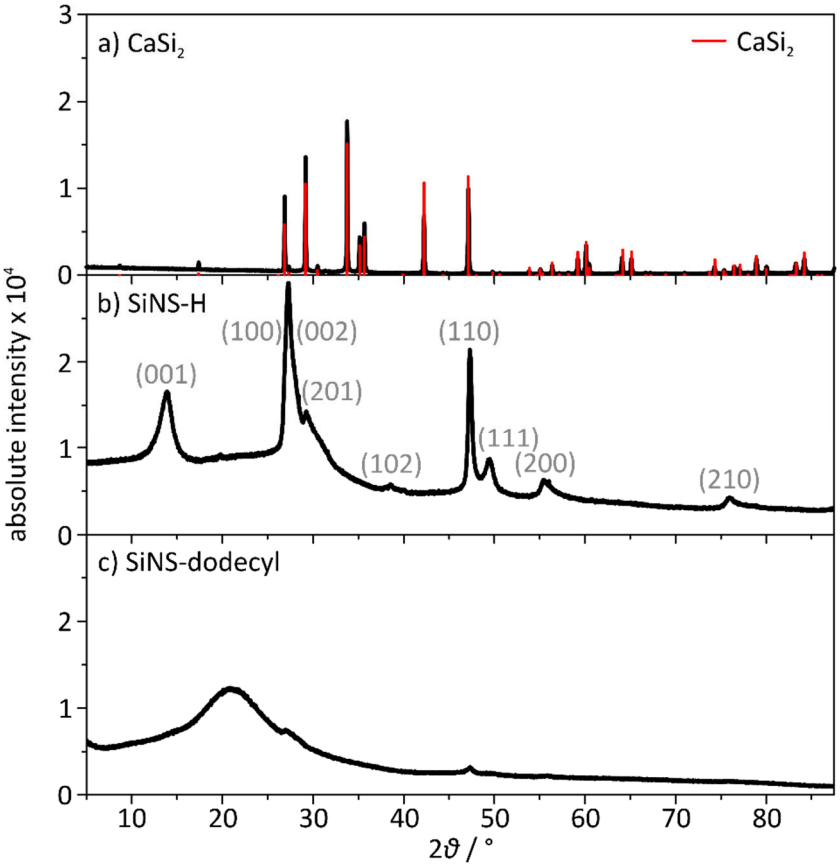

Figure 3.26. Powder X-ray patterns of a) phase-pure $CaSi_2$ obtained from arc-melting synthesis, b) layered polysilane, and c) dodecene-functionalized SiNS obtained using 3-DDB as an initiator. The grey, bracketed numbers in b represent the *hkl* indices of the hexagonal unit cell description. The background signal around 21° visible in c is caused by the capillary material.

Radical hydrosilylation (Scheme 3.2) was investigated using 1-dodecene as a model substrate. In addition, functionalization of the SiNS was performed with 10-undecenoic acid, 9-decen-1-ol, *tert*-butyl methacrylate (*t*BuMA), and 1-dodecyne. The radical chain reaction was induced by heat (stirring at 130 °C) or by catalytic amounts of 4-decylbenzene diazonium tetrafluoroborate (4-DDB). Although polymerization of the alkenes is obviously a possible side reaction in the presence of radical species, only in thermally induced hydrosilylation with *t*BuMA significant amounts of polymerization products were observed. In 4-DDB-induced hydrosilylations, polymerization products were not observed at all.

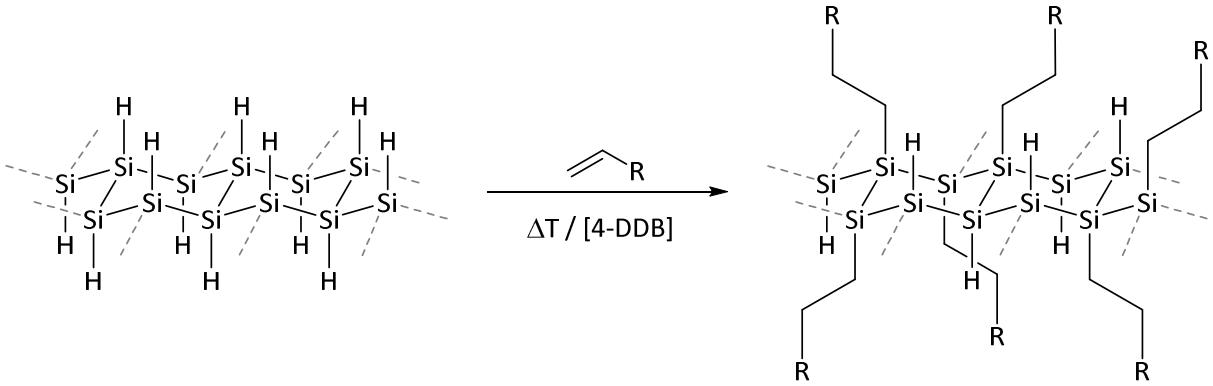

Scheme 3.2. The layered polysilane is functionalized by radical hydrosilylation with alkenes. The radical chain reaction is induced by heat (130 °C) or catalytic amounts of 4-decylbenzene diazonium tetrafluoroborate (4-DDB).

Infrared and NMR spectra of the functionalized Si sheets (SiNS) demonstrate that the functionalization reactions were successful with both radical induction methods. In addition, atomic force microscopy (AFM) images exhibit single layers of SiNS-dodecyl proving successful exfoliation. This is supported by PXRD patterns, which do not exhibit reflections of any crystalline material (Figure 3.26c). In contrast, amine-functionalized SiNS still exhibit a regular stacking behavior.[87,88] The photoluminescence properties of the layered polysilane remain largely unaltered by functionalization.

In additional investigations on radical hydrosilylation of layered polysilane using azobisisobutyronitrile (AIBN) as the radical starter, polymeric nanocomposites containing functionalized SiNS were prepared in one-pot reactions.[92] These materials combine the beneficial properties of SiNS and the polymer matrix while further stabilizing the two-dimensional SiNS against basic conditions and UV light. Lewis acid-catalyzed hydrosilylation of SiNS afforded alkene-functionalized SiNS, which enabled the construction of a functioning, nanoscale solution-gated field-effect transistor.[93]

3.4 References

[1] M. Schwarz, Dissertation, Universität Stuttgart **1987**.
[2] H. G. von Schnering, M. Schwarz, R. Nesper, *J. Less-Common Met.* **1988**, *137*, 297–310.
[3] S. Wengert, R. Nesper, *Z. Anorg. Allg. Chem.* **2000**, *626*, 246–252.
[4] A. K. Ganguli, A. M. Guloy, E. A. Leon-Escamilla, J. D. Corbett, *Inorg. Chem.* **1993**, *32*, 4349–4353.
[5] E. A. Leon-Escamilla, J. D. Corbett, *Inorg. Chem.* **1999**, *38*, 738–743.
[6] Z.-C. Dong, J. D. Corbett, *Inorg. Chem.* **1996**, *35*, 3107–3112.
[7] S. Bobev, S. C. Sevov, *Angew. Chem. Int. Ed.* **2001**, *40*, 1507–1510.
[8] J. B. Friauf, *J. Am. Chem. Soc.* **1927**, *49*, 3107–3114.
[9] A. Grüttner, R. Nesper, H. G. v. Schnering, *Acta Crystallogr. Sect. A* **1981**, *37*, C161.
[10] M. E. Straumanis, E. Z. Aka, *J. Appl. Phys.* **1952**, *23*, 330–334.
[11] L. Pu, A. D. Phillips, A. F. Richards, M. Stender, R. S. Simons, M. M. Olmstead, P. P. Power, *J. Am. Chem. Soc.* **2003**, *125*, 11626–11636.
[12] R. Nesper, Habilitation, Universität Stuttgart (Stuttgart), **1988**.
[13] V. Hopf, H. Schäfer, A. Weiss, *Z. Naturforsch. B* **1970**, *25*, 653.
[14] *The Stuttgart Tight-Binding LMTO-ASA program*, M. v. Schilfgarde, T. A. Paxton, O. Jepsen, O. K. Andersen, G. Krier, Max-Planck-Institut für Festkörperforschung, Stuttgart, Germany, **1998**.
[15] S. Dupke, T. Langer, R. Pöttgen, M. Winter, H. Eckert, *Solid State Nucl. Magn. Res.* **2012**, *42*, 17–25.
[16] S. Scharfe, F. Kraus, S. Stegmaier, A. Schier, T. F. Fässler, *Angew. Chem. Int. Ed.* **2011**, *50*, 3630–3670.
[17] R. Schäfer, W. Klemm, *Z. Anorg. Allg. Chem.* **1961**, *312*, 214–220.
[18] J. Witte, H. G. von Schnering, W. Klemm, *Z. Anorg. Allg. Chem.* **1964**, *327*, 260–273.
[19] L. M. Scherf, O. Pecher, K. J. Griffith, F. Haarmann, C. P. Grey, T. F. Fässler, *Eur. J. Inorg. Chem.* **2016**, *2016*, 4674–4682.
[20] T. Goebel, Y. Prots, A. Ormeci, O. Pecher, F. Haarmann, *Z. Anorg. Allg. Chem.* **2011**, *637*, 1982–1991.
[21] O. Pecher, M. Esters, A. Görne, B. Mausolf, A. Ormeci, F. Haarmann, *Z. Anorg. Allg. Chem.* **2014**, *640*, 2169–2176.
[22] L. Vegard, *Z. Physik* **1921**, *5*, 17–26.
[23] H.-J. Deiseroth, S.-T. Kong, H. Eckert, J. Vannahme, C. Reiner, T. Zaiß, M. Schlosser, *Angew. Chem. Int. Ed.* **2008**, *47*, 755–758.
[24] A. Henze, T. F. Fässler, *Inorg. Chem.* **2016**, *55*, 822–827.
[25] L. M. Scherf, Master's Thesis, Technische Universität München **2013**.
[26] H. G. von Schnering, R. Nesper, J. Curda, K.-F. Tebbe, *Angew. Chem. Int. Ed. Engl.* **1980**, *19*, 1033–1034.
[27] R. Nesper, H. G. von Schnering, J. Curda, *Chem. Ber.* **1986**, *119*, 3576–3590.
[28] A. Kuhn, P. Sreeraj, R. Pöttgen, H.-D. Wiemhöfer, M. Wilkening, P. Heitjans, *Angew. Chem. Int. Ed.* **2011**, *50*, 12099–12102.
[29] R. Nesper, S. Wengert, F. Zürcher, A. Currao, *Chem. Eur. J.* **1999**, *5*, 3382–3389.
[30] A. L. Allred, E. G. Rochow, *J. Inorg. Nuc. Chem.* **1958**, *5*, 264–268.
[31] V. L. Chevrier, J. W. Zwanziger, J. R. Dahn, *J. Alloy. Compd.* **2010**, *496*, 25–36.
[32] A. Jana, M. Majumdar, V. Huch, M. Zimmer, D. Scheschkewitz, *Dalton Trans.* **2014**, *43*, 5175–5181.
[33] J. Llanos, R. Nesper, H. G. von Schnering, *Angew. Chem. Int. Ed. Engl.* **1983**, *22*, 998.
[34] H. G. von Schnering, M. Schwarz, R. Nesper, *Angew. Chem. Int. Ed. Engl.* **1986**, *25*, 566–567.
[35] M. Zeilinger, Master's Thesis, Technische Universität München **2010**.
[36] W. Jung, J. Lörincz, R. Ramlau, H. Borrmann, Y. Prots, F. Haarmann, W. Schnelle, U. Burkhardt, M. Baitinger, Y. Grin, *Angew. Chem. Int. Ed.* **2007**, *46*, 6725–6728.
[37] H. Morito, B. Eck, R. Dronskowski, H. Yamane, *Dalton Trans.* **2010**, *39*, 10197–10202.
[38] N. Vojteer, M. Schroeder, C. Röhr, H. Hillebrecht, *Chem. Eur. J.* **2008**, *14*, 7331–7342.

[39] M. Zeilinger, L. van Wüllen, D. Benson, V. F. Kranak, S. Konar, T. F. Fässler, U. Häussermann, *Angew. Chem. Int. Ed.* **2013**, *52*, 5978–5982.
[40] A. Bateni, S. Repp, R. Thomann, S. Acar, E. Erdem, M. Somer, *Appl. Phys. Lett.* **2014**, *105*, 202605.
[41] M. Wörle, R. Nesper, T. K. Chatterji, *Z. Anorg. Allg. Chem.* **2006**, *632*, 1737–1742.
[42] P. Mauron, F. Buchter, O. Friedrichs, A. Remhof, M. Bielmann, C. N. Zwicky, A. Züttel, *J. Phys. Chem. B* **2008**, *112*, 906–910.
[43] T. L. Aselage, *J. Mater. Res.* **1998**, *13*, 1786–1794.
[44] J. Evers, G. Oehlinger, G. Sextl, *Angew. Chem. Int. Ed.* **1993**, *32*, 1442–1444.
[45] M. Zeilinger, V. Baran, L. van Wüllen, U. Häussermann, T. F. Fässler, *Chem. Mater.* **2013**, *25*, 4113–4121.
[46] M. Wörle, R. Nesper, G. Mair, H. G. von Schnering, *Solid State Sci.* **2007**, *9*, 459–464.
[47] M. Wörle, Dissertation, ETH Zürich **1995**.
[48] E. Zintl, G. Brauer, *Z. Elektrochem. Angew. Phys. Chem.* **1935**, *41*, 102–107.
[49] U. von Alpen, A. Rabenau, G. H. Talat, *Appl. Phys. Lett.* **1977**, *30*, 621–623.
[50] T. Lapp, S. Skaarup, A. Hooper, *Solid State Ionics* **1983**, *11*, 97–103.
[51] N. Kamaya, K. Homma, Y. Yamakawa, M. Hirayama, R. Kanno, M. Yonemura, T. Kamiyama, Y. Kato, S. Hama, K. Kawamoto, A. Mitsui, *Nat. Mater.* **2011**, *10*, 682–686.
[52] A. Kuhn, O. Gerbig, C. Zhu, F. Falkenberg, J. Maier, B. V. Lotsch, *Phys. Chem. Chem. Phys.* **2014**, *16*, 14669–14674.
[53] G. Mair, Dissertation, Universität Stuttgart **1984**.
[54] J. P. Perdew, *Int. J. Quantum Chem.* **1985**, *28*, 497–523.
[55] E. Staritzky, *Anal. Chem.* **1956**, *28*, 915.
[56] O. O. Kurakevych, T. A. Strobel, D. Y. Kim, G. D. Cody, *Angew. Chem. Int. Ed.* **2013**, *52*, 8930–8933.
[57] U. Ruschewitz, R. Pöttgen, *Z. Anorg. Allg. Chem.* **1999**, *625*, 1599–1603.
[58] S. Hemmersbach, B. Zibrowius, U. Ruschewitz, *Z. Anorg. Allg. Chem.* **1999**, *625*, 1440–1446.
[59] U. Ruschewitz, P. Müller, W. Kockelmann, *Z. Anorg. Allg. Chem.* **2001**, *627*, 513–522.
[60] P. Karen, A. Kjekshus, Q. Huang, V. L. Karen, *J. Alloy. Compd.* **1999**, *282*, 72–75.
[61] M. Knapp, U. Ruschewitz, *Chem. Eur. J.* **2001**, *7*, 874-880.
[62] V. Vohn, M. Knapp, U. Ruschewitz, *J. Solid State Chem.* **2000**, *151*, 111–116.
[63] V. Vohn, W. Kockelmann, U. Ruschewitz, *J. Alloy. Compd.* **1999**, *284*, 132–137.
[64] R. West, P. A. Carney, I. C. Mineo, *J. Am. Chem. Soc.* **1965**, *87*, 3788-3789.
[65] R. West, P. C. Jones, *J. Am. Chem. Soc.* **1969**, *91*, 6156-6161.
[66] H. Fjellvaag, P. Karen, *Inorg. Chem.* **1992**, *31*, 3260–3263.
[67] T. A. Strobel, O. O. Kurakevych, D. Y. Kim, Y. Le Godec, W. Crichton, J. Guignard, N. Guignot, G. D. Cody, A. R. Oganov, *Inorg. Chem.* **2014**, *53*, 7020–7027.
[68] M. S. Dresselhaus, G. Dresselhaus, *Adv. Phys.* **2002**, *51*, 1–186.
[69] Y. Iwasa, T. Takenobu, *J. Phys.: Condens. Matter* **2003**, *15*, R495–R519.
[70] F. Kiefer, A. J. Karttunen, M. Döblinger, T. F. Fässler, *Chem. Mater.* **2011**, *23*, 4578–4586.
[71] M. Zeilinger, L.-A. Jantke, L. M. Scherf, F. J. Kiefer, G. Neubüser, L. Kienle, A. J. Karttunen, S. Konar, U. Häussermann, T. F. Fässler, *Chem. Mater.* **2014**, *26*, 6603–6612.
[72] L. M. Scherf, G. Neubüser, L. Kienle, T. F. Fässler, *manuscript for publication*.
[73] M. Zeilinger, D. Benson, U. Häussermann, T. F. Fässler, *Chem. Mater.* **2013**, *25*, 1960–1967.
[74] L. Zhao, D. J. Dvorak, M. N. Obrovac, *J. Power Sources* **2016**, *332*, 290–298.
[75] T. Caillat, J. P. Fleurial, A. Borshchevsky, *J. Phys. Chem. Solids* **1997**, *58*, 1119–1125.
[76] G. J. Snyder, M. Christensen, E. Nishibori, T. Caillat, B. B. Iversen, *Nat. Mater.* **2004**, *3*, 458–463.
[77] U. Häussermann, A. S. Mikhaylushkin, *Dalton Trans.* **2010**, *39*, 1036–1045.
[78] R. A. Bley, S. M. Kauzlarich, *J. Am. Chem. Soc.* **1996**, *118*, 12461–12462.
[79] A. L. Pickering, C. Mitterbauer, N. D. Browning, S. M. Kauzlarich, P. P. Power, *Chem. Commun.* **2007**, 580–582.
[80] A. Grüttner, R. Nesper, H. G. von Schnering, *Angew. Chem. Int. Ed. Engl.* **1982**, *21*, 912–913.

[81] F. Kiefer, V. Hlukhyy, A. J. Karttunen, T. F. Fässler, C. Gold, E.-W. Scheidt, W. Scherer, J. Nylén, U. Häussermann, *J. Mater. Chem.* **2010**, *20*, 1780–1786.
[82] J. V. Zaikina, E. Muthuswamy, K. I. Lilova, Z. M. Gibbs, M. Zeilinger, G. J. Snyder, T. F. Fässler, A. Navrotsky, S. M. Kauzlarich, *Chem. Mater.* **2014**, *26*, 3263–3271.
[83] H. Jung, P. K. Allan, Y.-Y. Hu, O. J. Borkiewicz, X.-L. Wang, W.-Q. Han, L.-S. Du, C. J. Pickard, P. J. Chupas, K. W. Chapman, A. J. Morris, C. P. Grey, *Chem. Mater.* **2015**, *27*, 1031–1041.
[84] L. Baggetto, P. H. L. Notten, *J. Electrochem. Soc.* **2009**, *156*, A169–A175.
[85] J. R. Dahn, B. M. Way, E. Fuller, J. S. Tse, *Phys. Rev. B* **1993**, *48*, 17872–17877.
[86] S. Yamanaka, H. Matsu, M. Ishikawa, *Mater. Res. Bull.* **1996**, *31*, 307–316.
[87] H. Okamoto, Y. Sugiyama, K. Nakanishi, T. Ohta, T. Mitsuoka, H. Nakano, *Chem. Mater.* **2015**, *27*, 1292–1298.
[88] H. Okamoto, Y. Kumai, Y. Sugiyama, T. Mitsuoka, K. Nakanishi, T. Ohta, H. Nozaki, S. Yamaguchi, S. Shirai, H. Nakano, *J. Am. Chem. Soc.* **2010**, *132*, 2710–2718.
[89] Y. Sugiyama, H. Okamoto, T. Mitsuoka, T. Morikawa, K. Nakanishi, T. Ohta, H. Nakano, *J. Am. Chem. Soc.* **2010**, *132*, 5946–5947.
[90] H. Nakano, M. Nakano, K. Nakanishi, D. Tanaka, Y. Sugiyama, T. Ikuno, H. Okamoto, T. Ohta, *J. Am. Chem. Soc.* **2012**, *134*, 5452–5455.
[91] J. Evers, *J. Solid State Chem.* **1979**, *28*, 369–377.
[92] T. Helbich, A. Lyuleeva, T. Ludwig, L. M. Scherf, T. F. Fässler, P. Lugli, B. Rieger, *Adv. Funct. Mater.* **2016**, *26*, 6711–6718.
[93] T. Helbich, A. Lyuleeva, P. Marx, L. M. Scherf, T. Purkait, T. F. Fässler, J. G. C. Veinot, P. Lugli, B. Rieger, *Adv. Funct. Mater.* **2017**, *accepted*.

4 SUMMARY AND CONCLUSION

In the light of a threatening climate change, research on materials for conversion and storage of renewable energy has become more important than ever before. The tetrel elements silicon and germanium promise to play a decisive role in the necessary technologies. Due to their semiconductor properties, Si and Ge are already used in several large-scale applications in the semiconductor and solar cell industries. In addition, the two elements offer immensely increased lithium ion battery (LIB) capacities when employed as anode materials. However, the physical efficiency limit of simple Si solar cells is nearly exhausted and silicon and germanium LIB anodes suffer greatly from large volume expansion during charge and discharge. Thus, new materials, which retain the advantages of the elements while alleviating some of the mentioned problems, could heavily disrupt the energy market.

The goal of this thesis was to find new approaches to Si- and Ge-containing semiconductor materials. For this purpose, substitutions of the cationic and anionic components of alkali metal silicides and germanides were investigated. Alkali metal silicides and germanides as well as other Zintl phases had previously been shown to be suitable precursors for novel element modifications and morphologies. Mixing of alkali metal cations in ternary silicides and germanides can lead to the stabilization of anionic substructures, which are not accessible in binary compounds. Mixing of the anionic tetrel element with boron or the other respective tetrel element offers the formation of precursors of mixed element materials with intriguing structures and morphologies.

Effects of Alkali Metal Substitution

During the course of this thesis, several ternary Zintl phases with mixed alkali metal cations were discovered. The ternary Li-Na-Ge system was found to contain at least three Zintl phases: Na_7LiGe_8, $Li_{18}Na_2Ge_{17}$, and Li_3NaGe_2. Na_7LiGe_8 comprises tetrahedral $[Ge_4]^{4-}$ clusters, which are bridged to dimers by η^3-coordination Li cations. This structure type is well known from several other ternary silicides and germanides of the general sum formula $A_7A'T_8$. $Li_{18}Na_2Ge_{17}$ represents a rare example of a ternary Zintl phase containing three different Zintl anions (Figure 4.1a). Its anionic substructure consists of isolated Ge^{4-} anions next to $[Ge_4]^{4-}$ tetrahedra and truncated tetrahedra $[Ge_{12}]^{12-}$. The latter cluster is filled with one Li cation and four additional Li cation cap the hexagonal faces, forming a Friauf polyhedron $[Li@Li_4Ge_{12}]^{4-}$. The compound demonstrates the important role of the cations for cluster solvation and packing. Li_3NaGe_2 is the first Zintl phase which comprises truly double-bonded $[Ge=Ge]^{4-}$ dimers (Figure 4.1b). According to the Zintl-Klemm concept, the $[Ge=Ge]^{4-}$ dimers thus represent an unprecedented solid-state equivalent of molelecular oxygen. In analogy to paramagnetic O_2, Li_3NaGe_2 is characterized by a partially filled π-antibonding band around the Fermi level, which results in metallic conductivity.

K_7NaSi_8 and $K_{4-x}Na_xSi_4$ ($1 \leq x \leq 2.2$) are the first known phases in the ternary K-Na-Si system. K_7NaSi_8 is another representative of the common $A_7A'T_8$ structure type (Figure 4.1c). Unlike the other mentioned mixed alkali metal compounds, it can only be obtained via annealing of binary precursors. $K_{4-x}Na_xSi_4$ ($1 \leq x \leq 2.2$) contains tetrahedral $[Si_4]^{4-}$ clusters and represents a solid solution of the two alkali metals in a confined region. As the previous examples have shown, mixed alkali metal silicides and germanides typically represent stoichiometric compounds without any phase width. This is caused by a strict distribution of the two alkali metals onto different crystallographic positions. $K_{4-x}Na_xSi_4$ ($1 \leq x \leq 2.2$) comprises four different alkali metal positions. One of these is occupied by K only, one is occupied by Na only, and the two remaining positions can be shared by K and Na. $Li_{12-y}Na_ySi_7$ ($0 \leq y \leq 0.5$) also exhibits statistical mixing of the alkali metals on two out of thirteen alkali metal positions. The ternary phase is isostructural with binary $Li_{12}Si_7$ and proves that the consistently enlarged displacement

parameters of the exact same alkali metal positions in $Li_{12}Si_7$ and all related phases is caused by enlarged alkali metal cavities.

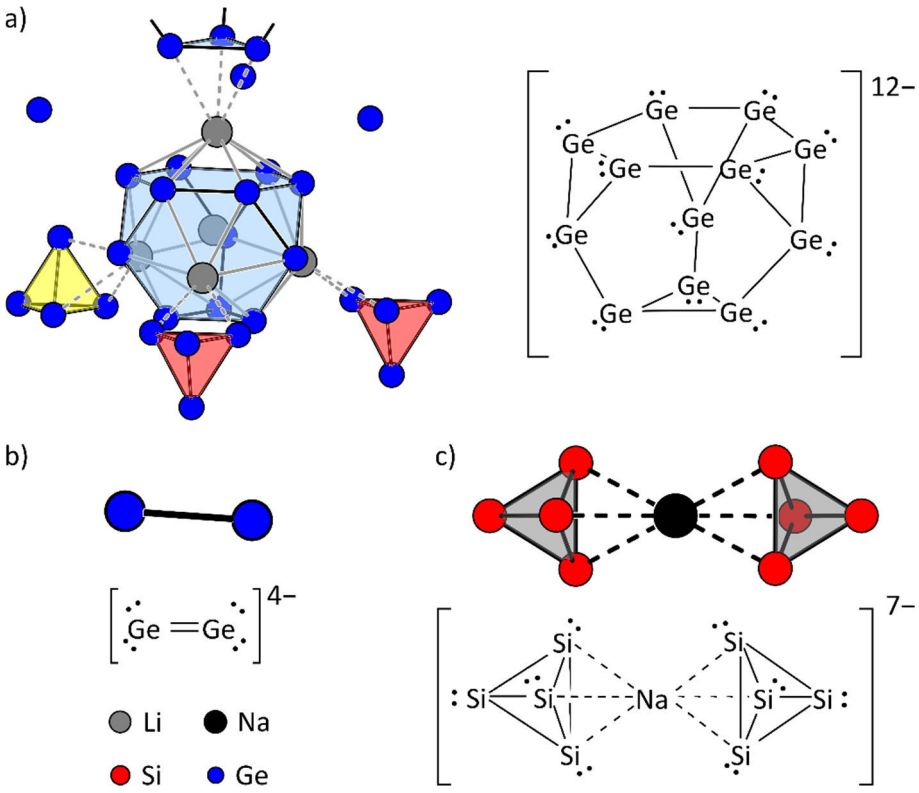

Figure 4.1. Selected anionic substructures of alkali metal silicides and germanides obtained by alkali metal substitution in this work: a) The Zintl phase $Li_{18}Na_2Ge_{17}$ contains three different Zintl anions: isolated Ge^{4-}, tetrahedra $[Ge_4]^{4-}$ (highlighted in red and yellow), and Friauf polyhedra $[Li@Li_4Ge_{12}]^{7-}$ (highlighted in blue); b) the Zintl phase Li_3NaGe_2 comprises double-bonded $[Ge=Ge]^{4-}$dimers, representing a solid-state equivalent of molecular O_2; c) the Zintl phase K_7NaSi_8 comprises $[Si_4]^{4-}$ tetrahedra that are bridged to dimers by η^3-ccordinating Na cations.

Effects of Tetrel Element Substitution

Partial substitution of the anionic component of several Zintl phases yielded solid Si/Ge solutions. As their binary relatives $Li_{12}Si_7$ and $Li_{12}Ge_7$ crystallize isostructurally, the existence of $Li_{12}Si_{7-x}Ge_x$ phases across the whole substitution range of $0 \leq x \leq 7$ does not come as a surprise. Although Si and Ge mix statistically, intriguing site preferences of the two tetrel elements were observed (Figure 4.2a). The more electronegative Ge atoms exhibit a strong preference to occupy the formally more negatively charged tetrel atom positions, whereas formally uncharged sites are largely occupied by more electro-positive Si. A similar trend is observed in the two additional solid Si/Ge solutions that were closely investigated in the present thesis. However, $Na_7LiSi_{8-z}Ge_z$ and $Li_3NaSi_{6-v}Ge_v$ differ from the $Li_{12}Si_{7-x}Ge_x$ system because either only the ternary germanide (Na_7LiGe_8) or only the silicide (Li_3NaSi_6) exist. The miscibilities of Si and Ge in the two systems were found to be very different. For $Na_7LiSi_{8-z}Ge_z$ a large substitution range of $1.3 \leq z \leq 8$ was observed which is in line with the existence of closely related KNa_6LiSi_8 (Figure 4.2b). In $Li_3NaSi_{6-v}Ge_v$, however, only minor amounts of Si can be substituted for Ge, amounting to a substitution range of $0 \leq v \leq 0.5$ (Figure 4.2c).Substitutions of silicon for boron were attempted under comparatively mild conditions using reactive boron compounds as starting materials. However, only previously known binary and ternary lithium borides and silicides were obtained.

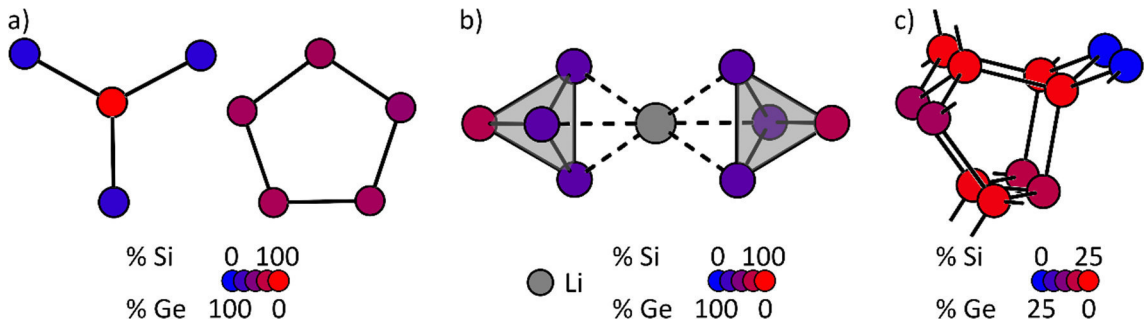

Figure 4.2. Site preferences of Si and Ge in alkali metal silicide-germanides obtained during the course of this work: a) In the solid solution $Li_{12}Si_{7-x}Ge_x$ ($0 \le x \le 7$), Ge preferentially occupies the formally more negatively charged positions in the vertices of the Y-shaped star and in the planar, five-membered ring; b) in the solid solution $Na_7LiSi_{8-z}Ge_z$ ($1.3 \le z \le 8$), Si preferentially occupies the atomic position that is not coordinated by Li; c) in the solid solution $Li_3NaSi_{6-v}Ge_v$ ($0 \le v \le 0.5$), in which very little Si can be substituted by Ge, the formally more negatively charged 2b- and 3b-positions in the two-dimensional polyanion are preferentially occupied by Ge.

Complete substitution of the tetrel elements by boron afforded the promising Li ion conductor $Li_6B_{18}(Li_3N)_x$. The template phase combines the outstanding Li ion mobility of Li_3N with a stable open boron framework (Figure 4.3). A large number of Li vacancies inside the hexagonal channels of the structure combined with a very low activation energy for Li motion of 5–20 kJ mol^{-1} promises excellent Li ion conductivity, rendering $Li_6B_{18}(Li_3N)_x$ interesting for applications as a solid electrolyte in lithium ion batteries. Extraction reactions with ethanol show that the template species can be partially removed from the open hexagonal pores. Concurrently, some boron is extracted from the compound but the overall framework structure is retained. Electronic structure calculations suggest that $Li_6B_{18}(Li_3N)_x$ is a semiconductor with a small indirect band gap. In contrast, $B_{12}C_6$ structures which were chemically inspired by the template phase structure are expected to be direct band gap semiconductors with band gaps of 2.4–3.2 eV. Substitution of silicon and germanium with their lighter counterpart carbon yielded a novel binary lithium carbide, whose structure could not be solved yet. Elemental analysis, Raman and NMR spectroscopy, however, suggest at least medium-sized carbon polyanions containing cumulated double bonds or fused aromatic rings.

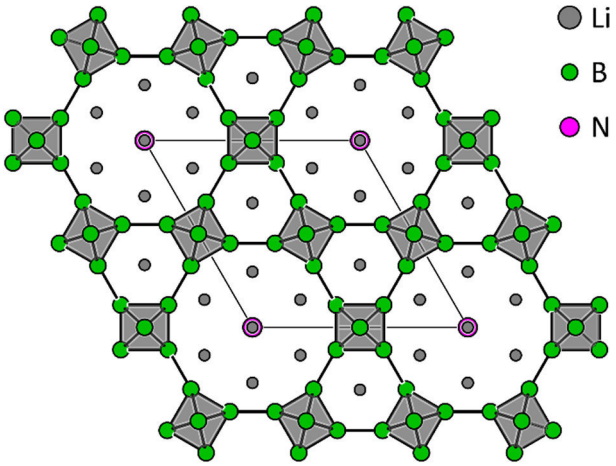

Figure 4.3. The template phase $Li_6B_{18}(Li_3N)_x$ comprises an open framework structure of interconnected B_6 octahedra, whose large open channels are filled with lithium cations and the template species.

Overall, several new ternary and quaternary phases were discovered in the substitution experiments performed in this work. With the exception of $Li_3NaSi_{6-v}Ge_v$ ($0 \le v \le 0.5$) the alkali metal silicides and germanides cannot be classified as particularly rich in the anionic components and, thus, do not represent ideal precursors for the synthesis of novel semiconductor materials. Nevertheless, some of the new phases as well as other tetrel-rich Zintl phases were reacted with various oxidizing agents and the resulting products were characterized in-depth in highly collaborative projects.

Li_3NaSi_6 and the mixed silicide-germanide $Li_3NaSi_{6-v}Ge_v$ ($0 \le v \le 0.5$) were oxidized with ethanol. Unlike previous investigations suggesting a crystalline but structurally not yet characterized Si allotrope termed *allo*-Si, the present experiments only yielded amorphous materials, which were compared with amorphous Si synthesized by liquid ammonia extraction of $Li_{15}Si_4$. The materials exhibit different crystallization temperatures, which can be attributed to different numbers and sizes of nanocrystalline particles in the samples. Careful analysis of the $Li_3NaSi_{6-v}Ge_v$ reaction product shows that the two tetrel elements indeed mix on an atomic level. Unfortunately, the properties of this material cannot be easily tuned by varying Si/Ge ratios because the starting material does not allow higher Ge contents. Electrochemical investigations of *a-allo*-Si and *a-allo*-$Si_{1-x}Ge_x$ are underway. Mild-condition synthesis of mixed tetrel-boron materials was attempted by reacting alkali metal silicides and germanides with boron halides, using the exothermic formation of alkali metal halides as a driving force for the heterogeneous reactions. The resulting products were demonstrated to comprise amorphous tetrel and alkali metal tetrelide phases. Incorporation of boron into these amorphous structures was not observed, so that the boron halides seem to function only as oxidizing agents.

The Zintl phase Li_7Ge_{12} has been known to convert topochemically to the crystalline Ge allotrope termed *allo*-Ge. Similar to graphite intercalation compounds, the Li cations in this compound are located between sheets of polygermanide anions so that an electrochemical delithiation of Li_7Ge_{12} to form *allo*-Ge is feasible. Experiments with Li_7Ge_{12} in Li half-cells confirm that *allo*-Ge can be synthesized electrochemically. In addition, *allo*-Ge was studied as an anode material for lithium ion batteries. In-situ experiments in Li half-cells show that *allo*-Ge and common *α*-Ge behave very similarly and undergo the same phase transitions upon battery cycling. The poorer cycling stability of *allo*-Ge may be caused by the different morphology, making *allo*-Ge more prone to loss of electrical contact.

For the preparation of pure layered polysilane, the synthesis of $CaSi_2$ was optimized. Phase-pure $CaSi_2$ served as an efficient precursor for stacked Si nanosheets (SiNS). Via radical hydrosilylation of the SiNS with various alkenes exfoliation of the layers was achieved. Reactions with polymerizable substrates yielded a very stable polymer-composite material, which facilitates further handling of the two-dimensional material.

Conclusion

The investigations on substitution effects in alkali metal silicides and germanides performed in this work shed light onto the possibilities that substitutions offer in intermetallic phases. The discovery of the first solid-state equivalent of molecular O_2, Li_3NaGe_2, via cation substitution demonstrates the power of cationic stabilization of unique Zintl anions and will most likely spark a new search for similar double-bonded species. With respect to the coloring problem, the present results suggest no simple solution for the observed phase systems. In both cation and anion substitutions, site preferences and statistical mixing of the different elements were observed. Complete substitutions with boron and

carbon, respectively, afforded the promising Li ion conductor $Li_6B_{18}(Li_3N)_x$ and a new binary lithium carbide that could open up a completely new class of metal carbides. Using alkali metal silicides and germanides as precursors, different semiconducting materials were obtained. Unfortunately, *allo*-Ge did not fulfill the promise of a (de-)intercalation material for lithium ion batteries. However, the successful functionalization of Si nanosheets renders them much easier to handle so that most certainly broad research on electronic and other applications will follow.

5 PUBLICATIONS AND MANUSCRIPTS

5.1 $Li_{18}Na_2Ge_{17}$ – A Compound Demonstrating Cation Effects on Cluster Shapes and Crystal Packing in Ternary Zintl Phases

Inorganic Chemistry

Article

pubs.acs.org/IC

$Li_{18}Na_2Ge_{17}$—A Compound Demonstrating Cation Effects on Cluster Shapes and Crystal Packing in Ternary Zintl Phases

Lavinia M. Scherf, Michael Zeilinger, and Thomas F. Fässler*

Department Chemie, Technische Universität München, Lichtenbergstraße 4, 85747 Garching b. München, Germany

Supporting Information

ABSTRACT: The novel ternary Zintl phase $Li_{18}Na_2Ge_{17}$ was synthesized from a stoichiometric melt and characterized crystallographically. It crystallizes in the trigonal space group $P31m$ (No. 157) with a = 17.0905(4) Å, c = 8.0783(2) Å, and V = 2043.43(8) Å^3 (final R indices R1 = 0.0212 and wR2 = 0.0420 for all data). The structure contains three different Zintl anions in a 1:1:1 ratio: isolated anions Ge^{4-}, tetrahedra $[Ge_4]^{4-}$, and truncated, Li-centered tetrahedra $[Li@Ge_{12}]^{11-}$, whose hexagonal faces are capped by four Li cations, resulting in the Friauf polyhedra $[Li@Li_4Ge_{12}]^{7-}$. According to the Zintl–Klemm concept, $Li_{18}Na_2Ge_{17}$ is an electronically balanced Zintl phase, as experimentally verified by its diamagnetism. The compound is structurally related to Li_7RbGe_8, which also contains $[Ge_4]^{4-}$ and $[Li@Li_4Ge_{12}]^{7-}$ in its anionic substructure. However, exchanging the heavier alkali metal cation Rb for Na in the mixed-cation germanides leads to drastic changes in stoichiometry and crystal packing, demonstrating the great effects that cations exert on such Zintl phases through optimized cluster sheathing and space filling.

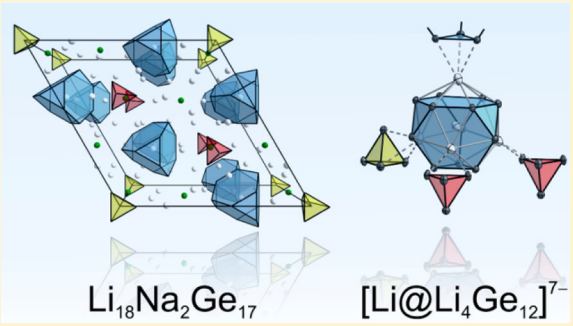

INTRODUCTION

Zintl phases are commonly defined as saltlike intermetallic compounds with highly heteropolar bonds. Formally, they can be described by a complete valence electron transfer from electropositive elements such as alkali or alkaline-earth metals to the more electronegative p-block metals of groups 13–16. Resulting Zintl anions typically behave like elements with the same number of valence electrons N according to the octet (8 − N) rule.[1] Just like the corresponding elements, Zintl anions may take the form of extensive polymeric structures as well as few-atom clusters or isolated atoms. Ge cluster anions range from Br_2-like $[Ge_2]^{6-}$ dumbbells in $BaMg_2Ge_2$[2] and P_4-analogous $[Ge_4]^{4-}$ tetrahedra in A_4Ge_4 (A = Na, K, Rb, Cs)[3] to truncated tetrahedra $[Ge_{12}]^{12-}$ in Li_7RbGe_8.[4] Some examples of such Ge Zintl anions are depicted in Figure 1. Isolated Ge^{4-} anions with noble-gas configurations are frequently observed as well: for example, in compounds E_2Ge (E = Mg, Ca, Sr, Ba).[5] Examples of polymeric germanides are $CaGe_2$ ($^3_\infty[Ge^-]$, As_{gray} structure),[6] CaGe ($^1_\infty[Ge^{2-}]$, polymeric Se structure),[7] Li_7Ge_{12} ($^2_\infty[Ge_{24}^{14-}]$),[8] and clathrate-type compounds Ba_6Ge_{25},[9] A_xGe_{46} (A = K, Rb, Cs, Ba),[10] and A_xGe_{136} (A = Na, K, Rb).[11]

The formation of the novel allotrope *m-allo*-Ge as a microcrystalline bulk material[14] in a topotactic reaction of Li_7Ge_{12} triggered our interest in looking for other allotropes of Ge and Si.[15] In the course of our investigations, we considered Li_3NaSi_6 as a potential precursor because it has a two-dimensional Si substructure similar to that of Li_7Ge_{12} and a topotactic conversion to *allo*-Si has been reported.[16] During our attempts to synthesize a solid solution Li_3NaSi_6/Li_3NaGe_6 as a precursor of a new modification of binary Si–Ge, we serendipitously obtained the new compound $Li_{18}Na_2Ge_{17}$.

A single-crystal X-ray structure determination shows that the novel Zintl phase $Li_{18}Na_2Ge_{17}$ contains the largest known anionic cluster unit, $[Ge_{12}]^{12-}$, which has been observed in only one other compound—the structurally related Li_7RbGe_8.[4] Moreover, $Li_{18}Na_2Ge_{17}$ features three different Ge Zintl anions. Reports of compounds comprised of three or more different Zintl anions are extremely rare. The few examples include $Ba_6Mg_{10.8}Li_{1.2}Si_{12}$ (Si^{4-}, $[Si_2]^{6-}$ dumbbells, bent $[Si_3]^{7.4-}$ chains),[17] $E_{31}Sn_{20}$ (E = Ca, Sr, Yb; Sn^{4-}, $[Sn_2]^{6-}$ dumbbells, linear $[Sn_5]^{12-}$ chains),[18] $Yb_{36}Sn_{23}$ (Sn^{4-}, $[Sn_2]^{6-}$ dumbbells, linear $[Sn_6]^{14-}$ chains)[19] and $Na_{23}K_9Tl_{15.3}$ (Tl^{5-}, linear $[Tl_3]^{7-}$ chains, $[Tl_4]^{8-}$ tetrahedra, trigonal-bipyramidal $[Tl_5]^{7-}$).[20]

Rather complex Zintl phases with various anions of different sizes require an equally complex and efficient coordination by cations. Corbett described the concepts and effects of this cluster "solvation" in detail.[21] In short, surrounding cations stabilize anionic clusters by bridging and separating them. Stable Zintl phases require an optimized balance of specific cluster sheathing and efficient space filling. Interestingly, some Ge Zintl anions (e.g., $[Ge_2]^{6-}$ in $BaMg_2Ge_2$,[2] $[Ge_{12}]^{12-}$ in Li_7RbGe_8[4]) have only been obtained in ternary compounds with mixed cations. Others (e.g., $[Ge_4–Na–Ge_4]^{7-}$ in A_7NaGe_8 with A = K, Rb)[22] show packing schemes very different from those of their binary analogues. These examples along with extensive studies on mixed cation trielides performed by Dong

Received: October 27, 2013
Published: January 31, 2014

   dx.doi.org/10.1021/ic4027046 | *Inorg. Chem.* 2014, 53, 2096–2101

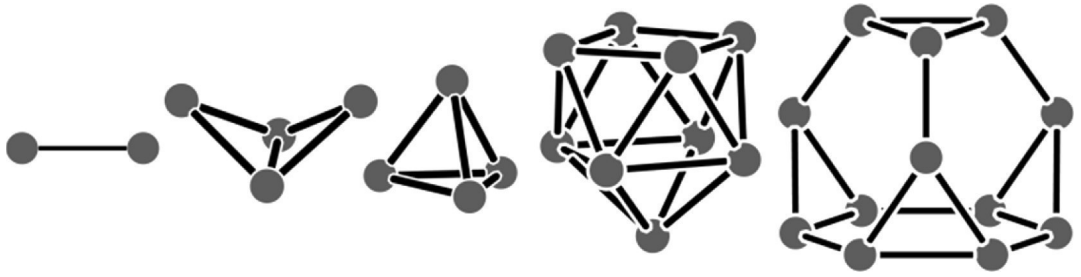

Figure 1. Selected Ge cluster anions from left to right: $[Ge_2]^{6-}$ dumbbell ($BaMg_2Ge_2$),[2] butterfly-shaped $[Ge_4]^{6-}$ (β-Ba_3Ge_4),[12] $[Ge_4]^{4-}$ tetrahedron (A_4Ge_4; A = Na, K, Rb, Cs),[3] monocapped-quadratic-antiprismatic $[Ge_9]^{4-}$ (K_4Ge_9),[13] truncated-tetrahedral $[Ge_{12}]^{12-}$ (Li_7RbGe_8).[4]

and Corbett[20,23] demonstrated that mixing cations of different sizes can be a very useful tool for achieving this balance.[21] Ab initio calculations on the structural differences in NaTl and KTl[24] as well as Li_2AuBi and Na_2AuBi[25] support the frequently observed structure-directing effect of cations in Zintl compounds. The new Zintl phase $Li_{18}Na_2Ge_{17}$ presented here clearly illustrates the influence of cations on cluster shapes and crystal packing in ternary Zintl phases.

EXPERIMENTAL SECTION

Synthesis of $Li_{18}Na_2Ge_{17}$. All steps of synthesis and sample preparation were carried out in an Ar-filled glovebox (MBraun, H_2O level <0.1 ppm, O_2 level <0.1 ppm). $Li_{18}Na_2Ge_{17}$ was prepared from the pure elements (99% Li rods, Rockwood-Lithium; 99% Na rods, Chempur; 99.999% Ge pieces, Chempur) in a tantalum ampule. The sealed ampule containing the stoichiometric reaction mixture with a total mass of 1 g was placed inside a silica reaction container, which was then evacuated and heated to 750 °C for 1 h. The resulting melt was cooled at a rate of 0.5 °C min^{-1} to 300 °C, at which temperature annealing of the reaction product was allowed for 3 h.

Single-Crystal Structure Determination. Crystals of $Li_{18}Na_2Ge_{17}$ were selected in an Ar-filled glovebox and sealed in 0.3 mm glass capillaries. For the best specimen, intensity data were collected at 123 K using a Bruker AXS X-ray diffractometer equipped with a CCD detector (APEX II, κ-CCD), a rotating anode FR591 with Mo Kα radiation (λ = 0.71073 Å), and a MONTEL optic monochromator. Data collection was controlled with the Bruker APEX software package.[26] Integration, data reduction, and absorption correction were performed with the SAINT[27] and SADABS[28] packages. The structure was solved with direct methods (SHELXS-97) and refined with full-matrix least squares on F^2 (SHELXL-97).[29] Details of the single-crystal data collection and refinement are given in Table 1. Further details on the crystal structure investigation may be obtained as Supporting Information (atomic coordinates and isotropic displacement parameters in Table S1, CIF file) and from Fachinformationszentrum Karlsruhe, 76344 Eggenstein-Leopoldshafen, Germany (fax (+49)7247-808-666; e-mail crysdata@fiz-karlsruhe.de; http://www.fiz-karlsruhe.de/request_for_deposited_data.html) on quoting the deposition number CSD-426692.

Powder X-ray Diffraction Analysis. A PXRD pattern of $Li_{18}Na_2Ge_{17}$ was recorded using a Stoe STADI P diffractometer equipped with a Ge(111) monochromator for Cu Kα radiation (λ = 1.54056 Å) and a Dectris MYTHEN DCS 1K solid-state detector. A crystalline sample of a $Li_{18}Na_2Ge_{17}$ synthesis product was ground in an agate mortar and filled into a 0.3 mm glass capillary, which was then sealed. The sample was measured within a 2θ range of 5–89° (PSD steps, 0.075°; time/step, 45 s). The diffraction pattern is shown in Figure S2 in the Supporting Information.

Magnetic Measurements. Using a Quantum Design MPMS 5 XL SQUID magnetometer, the magnetization of 39 mg of a $Li_{18}Na_2Ge_{17}$ synthesis product was measured at applied fields of 5000 and 10000 Oe over the temperature range 2–300 K. The data were corrected for the sample holder and for ion-core diamagnetism using Pascal's constants.[30] The molar susceptibility X_m is negative in the range of $-(1.44–1.55) \times 10^{-3}$ emu mol^{-1} and temperature independent, as expected for a diamagnetic compound. The corresponding graph is shown in Figure S3 in the Supporting Information.

Table 1. Crystallographic Data and Structure Refinement for $Li_{18}Na_2Ge_{17}$

T (K)	123(2)
formula wt	1404.93
cryst size (mm^3)	0.11 × 0.13 × 0.28
cryst color	metallic black
cryst shape	block
space group	$P31m$
unit cell dimens (Å)	
a	17.0905(4)
c	8.0783(2)
Z	3
V ($Å^3$)	2043.43(8)
ρ(calcd) (g cm^{-3})	3.425
μ (mm^{-1})	18.459
F(000)	1860
θ range (deg)	2.38–33.16
index range	$-26 \le h \le 26$
	$-25 \le k \le 23$
	$-12 \le l \le 12$
no. of rflns collected	47691
no. of indep rflns	5466 (R_{int} = 0.0407)
no. of rflns with $I > 2\sigma(I)$	5150 (R_σ = 0.0250)
abs cor	multiscan
no. of data/restraints/params	5466/1/191
goodness of fit on F^2	1.041
final R indices ($I > 2\sigma(I)$)[a,b]	
R1	0.0185
wR2	0.0412
R indices (all data)[a,b]	
R1	0.0212
wR2	0.0420
Flack param	0.01(2)
largest diff peak, hole (e $Å^{-3}$)	0.88, −0.99

[a] $R1 = \sum||F_o| - |F_c||/\sum|F_o|$. [b] $wR2 = [\sum w(F_o^2 - F_c^2)^2/\sum w(F_o^2)^2]^{1/2}$.

RESULTS AND DISCUSSION

Structure of $Li_{18}Na_2Ge_{17}$. $Li_{18}Na_2Ge_{17}$ was serendipitously identified from a reaction intended to yield $Li_3NaSi_3Ge_3$, a derivative of the known Zintl phase Li_3NaSi_6.[16] Subsequently, the air- and moisture-sensitive compound was synthesized directly from the pure elements and characterized crystallographically. $Li_{18}Na_2Ge_{17}$ crystallizes in the trigonal space group $P31m$ (No. 157) with a = 17.0905(4) Å, c = 8.0783(2) Å. and Z

dx.doi.org/10.1021/ic4027046 | Inorg. Chem. 2014, 53, 2096–2101

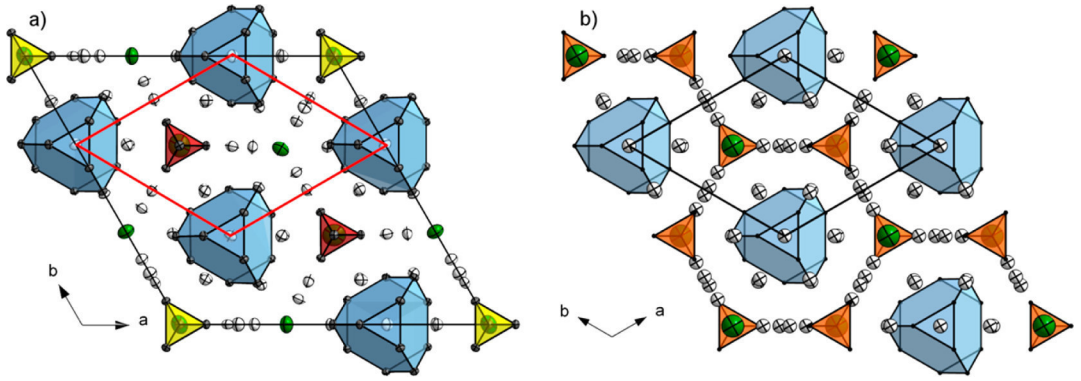

Figure 2. (a) Projection of the structure of $Li_{18}Na_2Ge_{17}$ onto the *ab* plane (Li, white; Na, green; Ge, gray; thermal ellipsoids at 90% probability at 123 K). The anionic Ge clusters are highlighted as colored polyhedra (truncated tetrahedra $[Ge_{12}]^{12-}$, blue; crystallographically different tetrahedra $[Ge_4]^{4-}$ (**A**) red, (**B**) yellow). The hexagonal primitive packing of truncated tetrahedra is indicated by red lines. (b) Projection of the structure of Li_7RbGe_8[4] onto the *ab* plane (Li, white; Rb, green; Ge, gray). The anionic Ge clusters are highlighted as colored polyhedra (truncated tetrahedra $[Ge_{12}]^{12-}$, blue; tetrahedra $[Ge_4]^{4-}$, orange).

= 3. All atoms were refined anisotropically with final reliability factors of R1 = 0.0212 and wR2 = 0.0420 for all data (Table 1).

Interestingly, the structure of $Li_{18}Na_2Ge_{17}$ incorporates three different Zintl anions in a 1:1:1 ratio: truncated Ge tetrahedra $[Ge_{12}]^{12-}$, Ge tetrahedra $[Ge_4]^{4-}$, and isolated Ge anions Ge^{4-} (Figure 2a). Thus, to the best of our knowledge, it is the first germanide containing three different Zintl anions with each of them observing the $(8 - N)$ rule. In addition, the new Zintl phase $Li_{18}Na_2Ge_{17}$ is only the second compound containing the largest known anionic Ge cluster unit, $[Ge_{12}]^{12-}$. Such $[Ge_{12}]^{12-}$ truncated tetrahedra have been reported once before in the related Zintl phase Li_7RbGe_8, in which they occur next to tetrahedral $[Ge_4]^{4-}$.[4] Similar $[Sn_{12}]^{12-}$ clusters are observed in $ENa_{10}Sn_{12}$ (E = Ca, Sr).[31] Larger Ge polyanions have only been isolated via soluble $[Ge_9]^{4-}$, with $[Ge_{45}]^{12-}$ being the largest example of covalently linked Ge atoms.[32]

The shape of the large $[Ge_{12}]^{12-}$ unit, a polyhedron with four triangular and four hexagonal faces, derives from a large tetrahedron with truncated vertices. Four Li atoms cap the hexagonal faces of the truncated tetrahedron and thus constitute the 16-vertex Friauf[33] polyhedron $[Li_4Ge_{12}]^{8-}$. In addition, the Friauf polyhedron is centered by one Li atom (Figure 3). Due to the lower crystal symmetry, Ge−Ge bond lengths (2.4840(5)−2.6948(5) Å) vary in a greater range than in Friauf polyhedra in Li_7RbGe_8 (2.505(2)−2.603(2) Å).[4] However, average Ge−Ge bond lengths are identical (2.567(1) Å for $Li_{18}Na_2Ge_{17}$, 2.569(2) Å for Li_7RbGe_8). Similarly, the average interatomic distances of Ge and capping Li atoms (2.91(1) Å for $Li_{18}Na_2Ge_{17}$, 2.96(2) Å for Li_7RbGe_8) as well as the interatomic distances of centering Li1 to all 16 surrounding atoms (2.99(1) Å for $Li_{18}Na_2Ge_{17}$, 3.02(2) Å for Li_7RbGe_8) fall in the same ranges (Table 2). In addition, the Friauf polyhedron $[Li@Li_4Ge_{12}]^{7-}$ is coordinated by another 30 alkali-metal cations, forming an approximately spherical "solvation" environment (Figure S1 in the Supporting Information).

The four capping Li atoms link the Friauf polyhedron to neighboring Zintl anions (Figure 3). Li2 is coordinated by a triangular face of a neighboring Friauf polyhedron along *c*, whereas Li4 coordinates one edge of crystallographically distinguishable tetrahedra **A** and Li3 coordinates a face of the second tetrahedron type **B**.

Ge tetrahedra **A** and **B** (ratio 2:1) are both located on 3-fold rotation axes (Figure 2a) and differ in their relative orientations

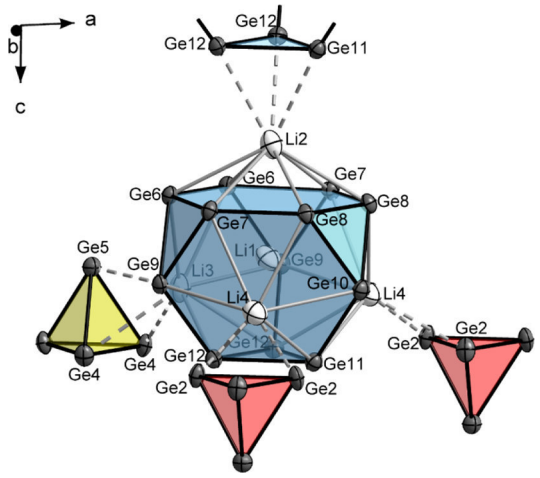

Figure 3. Structure of the Li-centered Friauf polyhedron $[Li@Li_4Ge_{12}]^{7-}$ (Li, white; Ge, gray; truncated tetrahedron $[Ge_{12}]^{12-}$, blue; crystallographically different tetrahedra $[Ge_4]^{4-}$ (**A**) red, (**B**) yellow; thermal ellipsoids at 90% probability at 123 K). Ge−Ge bonds are marked in black, whereas capping Li atoms are connected with gray lines. Interactions of capping Li atoms with edges (**A**) or triangular faces (**B** and $[Li@Li_4Ge_{12}]^{7-}$) of neighboring clusters are shown with broken lines. Relevant interatomic distances are given in Table 2.

as well as their coordination environments (Figure 4a,b). Nevertheless, their Ge−Ge bond lengths of 2.5610(5)−2.5818(6) Å agree well with those in A_4Ge_4 (A = Na, K, Rb, Cs).[3] Tetrahedron **A** has a coordination environment similar to that of $[Ge_4]^{4-}$ tetrahedra in Li_7RbGe_8,[4] containing 12 Li and 2 Na atoms (Figure 4a; Ge−Li distances 2.575(5)−3.114(6) Å, Ge−Na distances 2.980(2)−3.320(2) Å). In contrast, tetrahedron **B** is coordinated by 15 Li and 2 Na atoms (Figure 4b; Ge−Li distances 2.703(7)−3.095(6) Å, Ge−Na distances 3.020(3)−3.335(2) Å). For both tetrahedron types, Li atoms cap trigonal faces or bridge edges or coordinate *exo* at vertices. These coordination modes commonly occur in Zintl cluster sheathing.[21]

The isolated Ge atom Ge1 is coordinated by nine Li atoms and Na1 (Figure 4c) with a Ge−Na distance of 2.877(2) Å. Coordinating Li atoms (Ge−Li distance 2.514(6)−2.903(5) Å) are clearly differentiated from next-nearest neighbors with Ge−Li distances >4.8 Å. All relevant interatomic distances in $Li_{18}Na_2Ge_{17}$ are given in Table 2.

dx.doi.org/10.1021/ic4027046 | *Inorg. Chem.* 2014, 53, 2096−2101

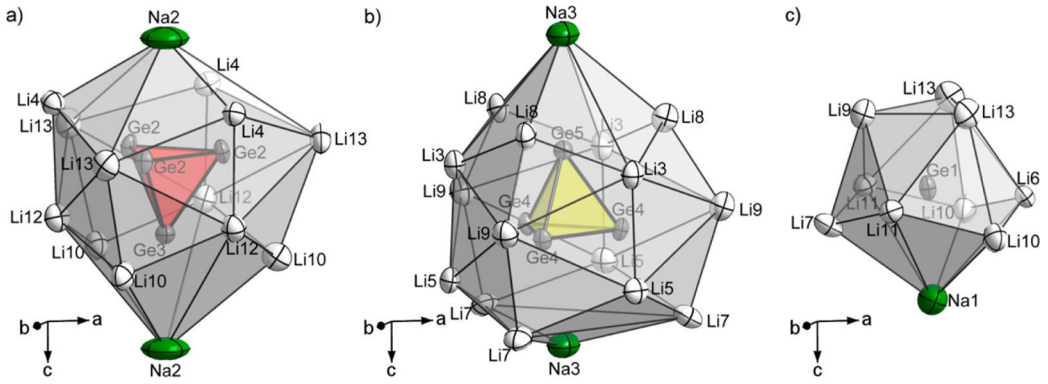

Figure 4. Coordination environments of (a) the Ge tetrahedron **A**, (b) the Ge tetrahedron **B**, (c) and the isolated Ge atom Ge1 (Li, white; Na, green; Ge, gray; thermal ellipsoids at 90% probability at 123 K). Relevant interatomic distances are given in Table 2.

Table 2. Relevant Interatomic Distances in $Li_{18}Na_2Ge_{17}$ ($P31m$, $Z = 3$, Estimated Standard Deviations in Parentheses)

atom pair		d (Å)	atom pair		d (Å)	atom pair		d (Å)
Ge1	Li6	2.514(6)	Ge6	Ge6	2.4883(5)	Ge9	Li8	2.856(4)
	Li11 × 2	2.543(5)		Ge9	2.5980(4)		Li13	2.921(5)
	Li9	2.560(7)		Ge7	2.6596(4)		Li3	2.935(3)
	Li13 × 2	2.643(5)		Li11	2.708(4)		Li4	2.978(4)
	Li7	2.709(7)		Li7	2.740(3)		Li1	3.058(3)
	Na1	2.877(2)		Li8	2.752(3)		Na1	3.161(1)
	Li10 × 2	2.902(5)		Li5	2.836(6)	Ge10	Ge11	2.4840(5)
Ge2	Ge2 × 2	2.5610(5)		Li3	2.906(6)		Ge8 × 2	2.5596(4)
	Ge3	2.5753(4)		Li2	2.974(6)		Li13 × 2	2.826(5)
	Li13	2.575(5)		Li1	2.995(6)		Li4 × 2	2.946(4)
	Li4	2.854(5)	Ge7	Ge8	2.4952(4)		Na1	2.978(2)
	Li4	2.885(5)		Ge9	2.5651(4)		Li1	3.042(6)
	Li12	2.924(5)		Li11	2.618(5)	Ge11	Ge10	2.4839(5)
	Li12	2.932(5)		Ge6	2.6596(4)		Li6	2.585(6)
	Li10	3.114(6)		Li10	2.767(5)		Ge12 × 2	2.5921(4)
	Na2	3.335(2)		Li4	2.882(5)		Li4 × 2	2.871(5)
Ge3	Ge2 × 3	2.5753(4)		Li12	2.951(6)		Li12 × 2	2.903(5)
	Li12 × 3	2.862(5)		Li2	2.980(4)		Li2	2.960(8)
	Li10 × 3	2.975(6)		Li1	2.997(4)		Li1	2.964(7)
	Na2	2.980(2)	Ge8	Ge7	2.4952(4)	Ge12	Ge9	2.5000(4)
Ge4	Ge5	2.5688(6)		Ge10	2.5597(4)		Li11	2.567(5)
	Ge4 × 2	2.5818(6)		Li6	2.659(5)		Ge11	2.5921(4)
	Li9	2.703(7)		Ge8	2.6948(5)		Ge12	2.5992(5)
	Li5 × 2	2.823(6)		Li10	2.768(5)		Li5	2.766(6)
	Li7	2.902(7)		Li4	2.851(5)		Li4	2.857(5)
	Li3 × 2	3.035(6)		Li12	2.912(6)		Li3	2.875(6)
	Li8	3.095(6)		Li2	2.916(6)		Li12	2.942(5)
	Na3	3.320(2)		Li1	2.969(6)		Li1	2.945(7)
Ge5	Ge4 × 3	2.5688(6)	Ge9	Ge12	2.5000(4)		Li2	3.018(7)
	Li8 × 3	2.770(6)		Ge7	2.5651(4)	Li1	Li2	2.94(1)
	Li3 × 3	2.838(6)		Ge6	2.5980(4)		Li3	2.981(9)
	Na3	3.020(3)		Li9	2.855(4)		Li4 × 2	3.009(6)

Electron Count. According to the Zintl–Klemm concept,[1a,34] the truncated Ge tetrahedron may be viewed as a $[Ge_{12}]^{12-}$ anion with one negative charge for every three-connected Ge atom. Adding the four capping Li atoms and Li1 in the center with one positive charge each results in an overall electron count of −7 for $[Li@Li_4Ge_{12}]^{7-}$. $Li_{18}Na_2Ge_{17}$ contains the Friauf polyhedron, tetrahedral $[Ge_4]^{4-}$, and isolated Ge^{4-} in a 1:1:1 ratio. Thus, $(Li^+)_{13}(Na^+)_2[Li@Li_4Ge_{12}]^{7-}[Ge_4]^{4-}(Ge^{4-})$ is an appropriate notation for this novel Zintl phase, in which all Zintl anions obey the $(8 - N)$ rule. A magnetic measurement of $Li_{18}Na_2Ge_{17}$ clearly reveals diamagnetism of the metallic black and brittle compound (Figure S3 in the Supporting Information), which is consistent with a semiconducting Zintl phase.

Cation Effects. The crystal structure of $Li_{18}Na_2Ge_{17}$ is closely related to the structure of Li_7RbGe_8.[4] In both compounds, the Li-centered Friauf polyhedra $[Li@Li_4Ge_{12}]^{7-}$ arrange in a hexagonally primitive fashion, as demonstrated in Figure 2. The resulting voids are filled by $[Ge_4]^{4-}$ tetrahedra and in the case of $Li_{18}Na_2Ge_{17}$ also by isolated Ge anions.

dx.doi.org/10.1021/ic4027046 | Inorg. Chem. 2014, 53, 2096–2101

Alkali-metal cations Li^+ as well as Na^+ and Rb^+, respectively, stabilize the Zintl anions by counterbalancing the negative charge, filling voids and providing cluster sheathing that keeps clusters separated.

Although the heavier alkali-metal content in the two ternary germanides only amounts to 5.41 ($Li_{18}Na_2Ge_{17}$) and 6.25 atom % (Li_7RbGe_8), the exchange of the heavier alkali-metal cation induces a dramatic difference in the crystal structures. A comparison of cell dimensions of the hexagonally primitive framework of Friauf polyhedra in both compounds shows a slight cell contraction upon utilization of Na instead of Rb (Table 3), changing the requirements for effective space filling.

Table 3. Cell Dimensions a', c', and V' of the Hexagonally Primitive Friauf Polyhedron Framework in $Li_{18}Na_2Ge_{17}$ (Room-Temperature Powder Data; $a' = (1/3)^{1/2}a$; $c' = c$; $V' = (1/3)^{1/2}V$) and Li_7RbGe_8 (Room-Temperature Single-Crystal Data;[4] $a' = a$; $c' = (1/2)c$; $V' = (1/2)V$)

	$Li_{18}Na_2Ge_{17}$	Li_7RbGe_8
a' (Å)	9.899(2)	9.8946(7)
c' (Å)	8.100(1)	8.135(2)
V' (Å^3)	679.74(4)	689.74(2)

An isolated Ge^{4-} anion replaces one of the two $[Ge_4]^{4-}$ tetrahedra in each primitive cell. However, the isolated anion, which has the same 4-fold negative charge as the larger $[Ge_4]^{4-}$ tetrahedron, cannot encompass the same number of cations in its coordination environment. Therefore, $[Ge_4]^{4-}$ tetrahedron **B** accommodates three additional Li cations, resulting in decreased overall symmetry and a greater a parameter. The lowered symmetry is accompanied by a slight distortion of the hexagonally primitive Friauf polyhedron framework in $Li_{18}Na_2Ge_{17}$. Whereas the distances of one Friauf polyhedron center to the centers of each of the six neighboring polyhedra in the ab plane are all equal in Li_7RbGe_8 (9.8946(7) Å, room-temperature single-crystal data), these center-to-center distances slightly differ in $Li_{18}Na_2Ge_{17}$ (4 × 9.931(6) Å, 2 × 9.742(6) Å, 123 K single-crystal data).

In addition, the introduction of Na as the heavier alkali-metal cation evokes a drastic change of the crystal packing along the c direction (Figure 5). In Li_7RbGe_8, two $[Ge_4]^{4-}$ tetrahedra are separated by two Rb cations and Friauf polyhedra are staggered due to a 6_3 screw axis. However, in $Li_{18}Na_2Ge_{17}$ a single Na cation alternates with each tetrahedron and isolated Ge anion, respectively. Concomitantly, the length of the c axis is halved (Table 3) because $[Li@Li_4Ge_{12}]^{7-}$ clusters stack in an eclipsed manner in the lower symmetry.

CONCLUSIONS

Mixing cations of different size or even different charge in syntheses of Zintl phases has been shown to be an efficient tool to stabilize rare cluster shapes. The novel compound $Li_{18}Na_2Ge_{17}$ presented here and the related Li_7RbGe_8[4] illustrate this concept well. Although the heavier alkali-metal content only amounts to 5−6 atom % in these compounds, the exchange of Rb by Na introduces a dramatic structural difference. In the case of $Li_{18}Na_2Ge_{17}$ an intriguing structure with three different Zintl anions is obtained. It is therefore easy to imagine that many more novel structures may be stabilized as mixed-cation compounds which are not available in binary systems. Thus, cation ratios must be carefully selected in order to obtain electronically balanced structures with favorable cluster sheathing and efficient space filling. However, owing to the multitude of Zintl anion geometries and countless possible combinations thereof, predicting new ternary Zintl phases remains difficult.

ASSOCIATED CONTENT

Supporting Information

Atomic coordinates and isotropic displacement parameters of $Li_{18}Na_2Ge_{17}$ (Table S1), coordination environment of the Friauf polyhedron $[Li@Li_4Ge_{12}]^{7-}$ in $Li_{18}Na_2Ge_{17}$ (Figure S1), a powder X-ray diffraction pattern of $Li_{18}Na_2Ge_{17}$ (Figure S2), results of magnetic susceptibility measurements (Figure S3), and a CIF file giving crystallographic data. This material is available free of charge via the Internet at http://pubs.acs.org.

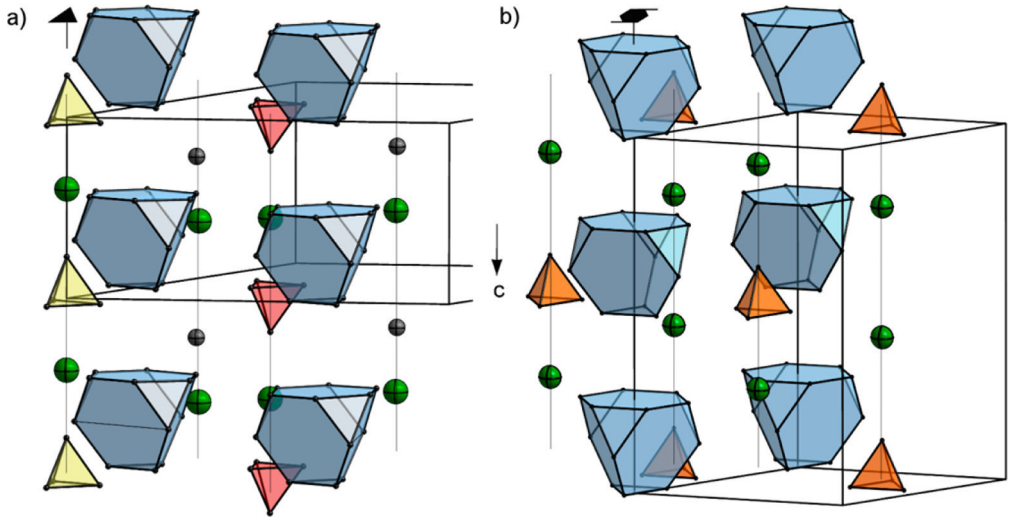

Figure 5. Fragments of the structures of (a) $Li_{18}Na_2Ge_{17}$ (Na, green, Ge, gray; truncated tetrahedra $[Ge_{12}]^{12-}$, blue; crystallographically different tetrahedra $[Ge_4]^{4-}$ (**A**) red, (**B**) yellow) and (b) Li_7RbGe_8[4] (Rb, green; Ge, gray; truncated tetrahedra $[Ge_{12}]^{12-}$, blue; tetrahedra $[Ge_4]^{4-}$, orange), demonstrating the packing of Zintl anions and Na and Rb cations, respectively, along c. The main symmetry elements are indicated by their symbols. Li atoms are omitted for enhanced clarity.

dx.doi.org/10.1021/ic4027046 | Inorg. Chem. 2014, 53, 2096−2101

AUTHOR INFORMATION

Corresponding Author

*E-mail for T.F.F.: thomas.faessler@lrz.tum.de.

Notes

The authors declare no competing financial interest.

ACKNOWLEDGMENTS

The authors thank A. V. Hoffmann for the SQUID measurement and for financial support from the SolTech (Solar Technologies go Hybrid) program of the State of Bavaria. L.M.S. is further grateful to the Studienstiftung des Deutschen Volkes for her fellowship.

REFERENCES

(1) (a) Zintl, E. *Angew. Chem.* **1939**, *52*, 1−6. (b) *Zintl Phases: Principles and Recent Developments*; Fässler, T. F., Ed.; Springer-Verlag: Heidelberg, Germany, 2011; Structure and Bonding Vol. *139*.

(2) (a) Eisenmann, B.; May, N.; Müller, W.; Schäfer, H.; Weiss, A.; Winter, J.; Ziegleder, G. *Z. Naturforsch., B* **1970**, *25*, 1350−1352. (b) Eisenmann, B.; Schäfer, H. *Z. Anorg. Allg. Chem.* **1974**, *403*, 163−172.

(3) (a) Witte, J.; von Schnering, H. G.; Klemm, W. *Z. Anorg. Allg. Chem.* **1964**, *327*, 260−273. (b) Busmann, E. *Z. Anorg. Allg. Chem.* **1961**, *313*, 90−106.

(4) Bobev, S.; Sevov, S. C. *Angew. Chem.* **2001**, *113*, 1555−1558; *Angew. Chem., Int. Ed.* **2001**, *40*, 1507−1510.

(5) (a) Zintl, E.; Kaiser, H. *Z. Anorg. Allg. Chem.* **1933**, *211*, 113−131. (b) Eckerlin, P.; Wölfel, E. *Z. Anorg. Allg. Chem.* **1955**, *280*, 321−331. (c) Eisenmann, B.; Schäfer, H.; Turban, K. *Z. Naturforsch., B* **1975**, *30*, 677−680. (d) Turban, K.; Schäfer, H. *Z. Naturforsch., B* **1973**, *28*, 220−222.

(6) (a) Wallbaum, H. J. *Naturwissenschaften* **1944**, *32*, 76. (b) Tobash, P. H.; Bobev, S. *J. Solid State Chem.* **2007**, *180*, 1575−1581.

(7) Eckerlin, P.; Meyer, H. J.; Wölfel, E. *Z. Anorg. Allg. Chem.* **1955**, *281*, 322−328.

(8) (a) Kiefer, F.; Fässler, T. F. *Solid State Sci.* **2011**, *13*, 636−640. (b) Grüttner, A.; Nesper, R.; von Schnering, H. G. *Angew. Chem.* **1982**, *94*, 933; *Angew. Chem., Int. Ed. Engl.* **1982**, *21*, 912−913.

(9) (a) Fukuoka, H.; Iwai, K.; Yamanaka, S.; Abe, H.; Yoza, K.; Häming, L. *J. Solid State Chem.* **2000**, *151*, 117−121. (b) Kim, S.-J.; Hu, S.; Uher, C.; Hogan, T.; Huang, B.; Corbett, J. D.; Kanatzidis, M. G. *J. Solid State Chem.* **2000**, *153*, 321−329. (c) Carrillo-Cabrera, W.; Curda, J.; von Schnering, H. G.; Paschen, S.; Grin, Y. *Z. Kristallogr.-New Cryst. Struct.* **2000**, *215*, 207−208.

(10) (a) Cros, C.; Pouchard, M.; Hagenmuller, P. *J. Solid State Chem.* **1970**, *2*, 570−581. (b) Liang, Y.; Böhme, B.; Ormeci, A.; Borrmann, H.; Pecher, O.; Haarmann, F.; Schnelle, W.; Baitinger, M.; Grin, Y. *Chem. Eur. J.* **2012**, *18*, 9818−9822. (c) Veremchuk, I.; Wosylus, A.; Böhme, B.; Baitinger, M.; Borrmann, H.; Prots, Y.; Burkhardt, U.; Schwarz, U.; Grin, Y. *Z. Anorg. Allg. Chem.* **2011**, *637*, 1281−1286.

(11) (a) Simon, P.; Tang, Z.; Carrillo-Cabrera, W.; Chiong, K.; Böhme, B.; Baitinger, M.; Lichte, H.; Grin, Y.; Guloy, A. M. *J. Am. Chem. Soc.* **2011**, *133*, 7596−7601. (b) Bobev, S.; Sevov, S. C. *J. Am. Chem. Soc.* **1999**, *121*, 3795−3796.

(12) Zürcher, F.; Nesper, R. *Angew. Chem.* **1998**, *110*, 3451−3454; *Angew. Chem., Int. Ed.* **1998**, *37*, 3314−3318.

(13) Ponou, S.; Fässler, T. F. *Z. Anorg. Allg. Chem.* **2007**, *633*, 393−397.

(14) Kiefer, F.; Karttunen, A. J.; Döblinger, M.; Fässler, T. F. *Chem. Mater.* **2011**, *23*, 4578−4586.

(15) (a) Karttunen, A. J.; Fässler, T. F.; Linnolahti, M.; Pakkanen, T. A. *Inorg. Chem.* **2011**, *50*, 1733−1742. (b) Karttunen, A. J.; Fässler, T. F. *ChemPhysChem* **2013**, *14*, 1807−1817.

(16) von Schnering, H. G.; Schwarz, M.; Nesper, R. *J. Less-Common Met.* **1988**, *137*, 297−310.

(17) Wengert, S.; Nesper, R. *Z. Anorg. Allg. Chem.* **2000**, *626*, 246−252.

(18) Ganguli, A. K.; Guloy, A. M.; Leon-Escamilla, E. A.; Corbett, J. D. *Inorg. Chem.* **1993**, *32*, 4349−4353.

(19) Leon-Escamilla, E. A.; Corbett, J. D. *Inorg. Chem.* **1999**, *38*, 738−743.

(20) Dong, Z.-C.; Corbett, J. D. *Inorg. Chem.* **1996**, *35*, 3107−3112.

(21) Corbett, J. D. *Struct. Bonding (Berlin)* **1997**, *87*, 157−194. (b) Corbett, J. D. *Angew. Chem.* **2000**, *112*, 682−704; *Angew. Chem., Int. Ed.* **2000**, *39*, 670−690.

(22) Llanos, J.; Nesper, R.; von Schnering, H. G. *Angew. Chem.* **1983**, *95*, 1026−1027; *Angew. Chem., Int. Ed. Engl.* **1983**, *22*, 998.

(23) (a) Dong, Z.-C.; Corbett, J. D. *J. Am. Chem. Soc.* **1994**, *116*, 3429−3435. (b) Dong, Z. C.; Corbett, J. D. *J. Am. Chem. Soc.* **1995**, *117*, 6447−6455. (c) Cordier, G.; Müller, V. *Z. Naturforsch., B* **1994**, *49*, 935−938.

(24) Wang, F.; Miller, G. J. *Inorg. Chem.* **2011**, *50*, 7625−7636.

(25) Wang, F.; Miller, G. J. *Eur. J. Inorg. Chem.* **2011**, *2011*, 3989−3998.

(26) *APEX 2: APEX Suite of Crystallographic Software, 2008.4*; Bruker AXS Inc., Madison, WI, USA, 2008.

(27) *SAINT*; Bruker AXS Inc., Madison, WI, USA, 2001.

(28) *SADABS*; Bruker AXS Inc., Madison, WI, USA, 2001.

(29) Sheldrick, G. M. *Acta Crystallogr.* **2008**, *A64*, 112−122.

(30) Bain, G. A.; Berry, J. F. *J. Chem. Educ.* **2008**, *85*, 532−536.

(31) Bobev, S.; Sevov, S. C. *Inorg. Chem.* **2001**, *40*, 5361−5364.

(32) (a) Scharfe, S.; Kraus, F.; Stegmaier, S.; Schier, A.; Fässler, T. F. *Angew. Chem.* **2011**, *123*, 3712−3754; *Angew. Chem., Int. Ed.* **2011**, *50*, 3630−3670. (b) Spiekermann, A.; Hoffmann, S. D.; Fässler, T. F.; Krossing, I.; Preiss, U. *Angew. Chem.* **2007**, *119*, 5404−5407; *Angew. Chem., Int. Ed.* **2007**, *46*, 5310−5313.

(33) Friauf, J. B. *J. Am. Chem. Soc.* **1927**, *49*, 3107−3114.

(34) (a) Klemm, W. *Proc. Chem. Soc.* **1958**, 329−341. (b) Klemm, W.; Busmann, E. *Z. Anorg. Allg. Chem.* **1963**, *319*, 297−311.

SUPPORTING INFORMATION

$Li_{18}Na_2Ge_{17}$ – a Compound Demonstrating Cation Effects on Cluster Shapes and Crystal Packing in Ternary Zintl Phases

*Lavinia M. Scherf, Michael Zeilinger, Thomas F. Fässler**

Table S1. Fractional atomic coordinates and equivalent isotropic atomic displacement parameters for $Li_{18}Na_2Ge_{17}$ ($P31m$, $Z = 3$, $T = 123$ K, estimated standard deviations in parentheses).

atom	Wyckoff position	x	y	z	U_{eq} /Å$^2\cdot10^3$
Ge1	3*c*	0.33940(2)	0	0.20480(5)	9.55(7)
Ge2	6*d*	0.58056(2)	0.24642(1)	0.97870(4)	10.08(5)
Ge3	2*b*	2/3	1/3	0.23971(5)	9.61(9)
Ge4	3*c*	0.08722(2)	0	0.02877(6)	9.46(7)
Ge5	1*a*	0	0	0.76979(8)	9.2(1)
Ge6	6*d*	0.23988(2)	0.15581(2)	0.48856(3)	7.70(5)
Ge7	6*d*	0.41951(2)	0.24371(2)	0.49600(3)	8.40(5)
Ge8	6*d*	0.50333(2)	0.41229(2)	0.49809(3)	8.29(5)
Ge9	6*d*	0.32803(1)	0.15256(2)	0.74800(3)	8.43(5)
Ge10	3*c*	0.49594(2)	0	0.74910(4)	9.31(6)
Ge11	3*c*	0.41729(2)	0.41729(2)	0.99578(4)	8.84(6)
Ge12	6*d*	0.32997(1)	0.24217(2)	0.99415(3)	8.68(5)
Na1	3*c*	0.3462(1)	0	0.5607(2)	26.6(4)
Na2	2*b*	2/3	1/3	0.6086(3)	43.1(7)
Na3	1*a*	0	0	0.3960(3)	28.5(6)
Li1	3*c*	0.3291(3)	0.3291(3)	0.6799(9)	17(2)
Li2	3*c*	0.3333(3)	0.3333(3)	0.316(1)	15(1)
Li3	3*c*	0.1651(4)	0.1651(4)	0.8062(9)	15(1)
Li4	6*d*	0.4944(3)	0.3294(3)	0.8091(7)	16(1)
Li5	3*c*	0.1726(4)	0.1726(4)	0.1776(9)	16(1)
Li6	3*c*	0.4855(3)	0	0.2409(8)	13(1)
Li7	3*c*	0.1897(4)	0	0.3152(8)	19(1)
Li8	3*c*	0.1556(4)	0	0.6740(8)	16(1)
Li9	3*c*	0.2423(4)	0	0.9634(9)	18(1)
Li10	6*d*	0.4987(3)	0.1619(4)	0.3216(7)	18(1)
Li11	6*d*	0.3382(3)	0.1476(3)	0.2332(6)	14.0(9)
Li12	6*d*	0.5013(3)	0.3324(3)	0.1786(7)	17(1)
Li13	6*d*	0.4331(3)	0.0943(3)	0.9449(7)	19(1)

Figures S1 – S3

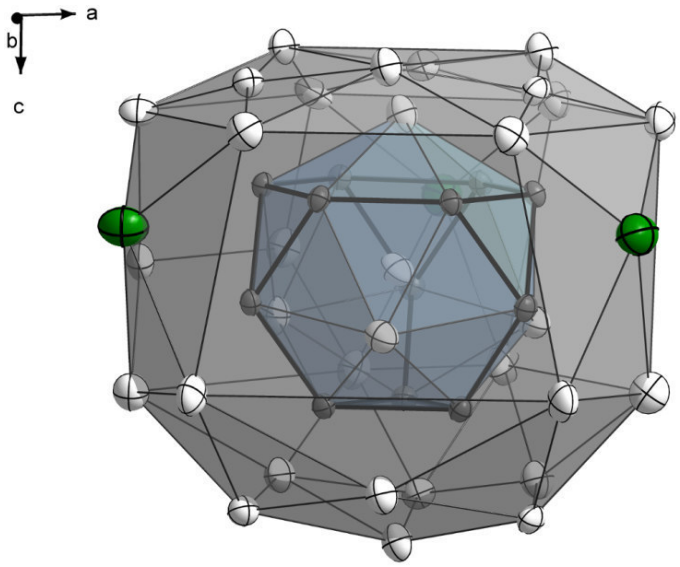

Figure S1. Coordination sphere of the Friauf polyhedron $[Li@Li_4Ge_{12}]^{7-}$ (blue) in $Li_{18}Na_2Ge_{17}$ (Li = white, Na = green, Ge = grey; thermal ellipsoids at 90 % probability at 123 K).

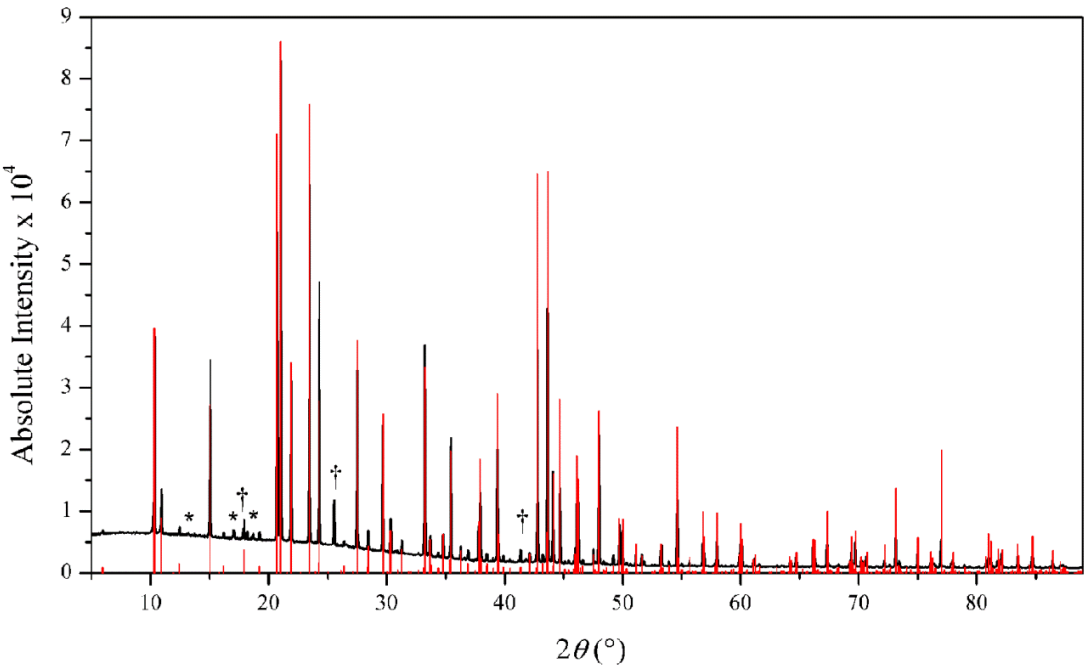

Figure S2. Experimental X-ray powder diffraction pattern of $Li_{18}Na_2Ge_{17}$ (black) referenced with its theoretical powder pattern (red; † = LiGe, * = unknown compound).

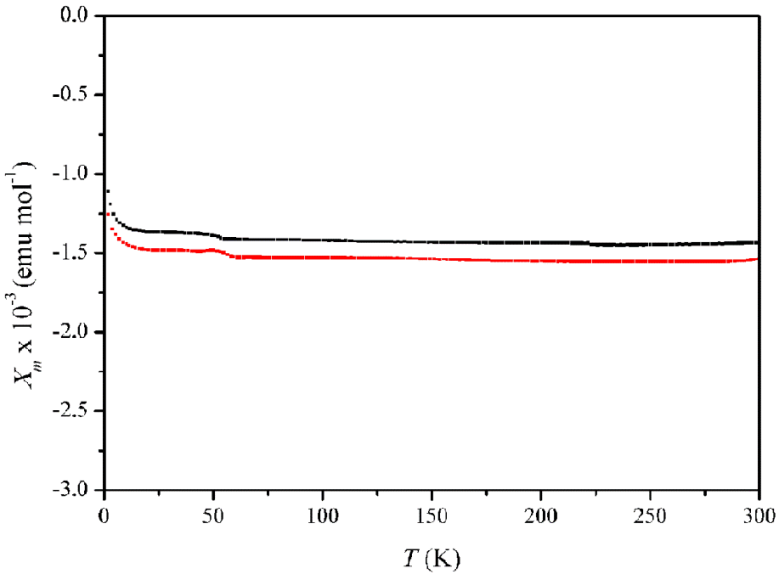

Figure S3. Molar susceptibilities X_m of $Li_{18}Na_2Ge_{17}$ at field intensities H of 5 000 Oe (black) and 10 000 Oe (red) over the temperature range of 2–300 K. The data were corrected for the sample holder and for ion-core diamagnetism using Pascal's constants.[1] Slight deviations from ideal diamagnetic behavior at low temperatures are caused by small sample impurities.

REFERENCES

1. Bain, G. A.; Berry, J. F. *J. Chem. Educ.* **2008,** *85*, 532–536.

5.2 $[Ge_2]^{4-}$ Dumbbells with Very Short Ge–Ge Distances in the Zintl Phase Li_3NaGe_2: A Solid-State Equivalent to Molecular O_2

VIP Zintl Phases Very Important Paper

International Edition: DOI: 10.1002/anie.201508044
German Edition: DOI: 10.1002/ange.201508044

$[Ge_2]^{4-}$ Dumbbells with Very Short Ge–Ge Distances in the Zintl Phase Li_3NaGe_2: A Solid-State Equivalent to Molecular O_2

*Lavinia M. Scherf, Antti J. Karttunen, Oliver Pecher, Pieter C. M. M. Magusin, Clare P. Grey, and Thomas F. Fässler**

Abstract: *The novel ternary Zintl phase Li_3NaGe_2 comprises alkali-metal cations and $[Ge_2]^{4-}$ dumbbells. The diatomic $[Ge_2]^{4-}$ unit is characterized by the shortest Ge–Ge distance (2.390(1) Å) ever observed in a Zintl phase and thus represents the first Ge=Ge double bond under such conditions, as also suggested by the (8–N) rule. Raman measurements support these findings. The multiple-bond character is confirmed by electronic-structure calculations, and an upfield ^{6}Li NMR shift of −10.0 ppm, which was assigned to the Li cations surrounded by the π systems of three Ge dumbbells, further underlines this interpretation. For the unperturbed, ligand-free dumbbell in Li_3NaGe_2, the π-bonding p_y and p_z orbitals are degenerate as in molecular oxygen, which has singly occupied orbitals. The partially filled π-type bands of the neat solid Li_3NaGe_2 cross the Fermi level, resulting in metallic properties. Li_3NaGe_2 was synthesized from the elements as well as from binary reactants and subsequently characterized crystallographically.*

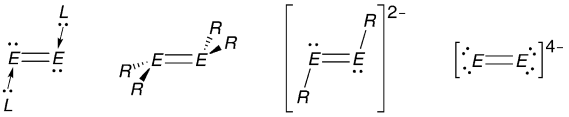

E = Si	2.23 Å[14a]	2.14-2.29 Å[2]	-	(≥ 2.34 Å[15])
E = Ge	2.35 Å[14b]	2.21-2.51 Å[2]	2.39-2.46 Å[6]	(≥ 2.44 Å[10])

Scheme 1. Types of double-bonded heavier tetrel systems and their respective E=E bond lengths. Values in parentheses correspond to the tetrel dumbbells in $Li_{14}Si_6$ and Li_9Ge_4, which are closest to a double-bond system.

Multiple bonds of the heavier homologues of boron, carbon, and nitrogen have been intensively investigated during the last decades.[1–3] Among those, the heavier tetrel homologues all adopt a *trans*-bent structure in contrast to planar ethylene. The pyramidalization at the E atom in $R_2E{=}ER_2$ drastically influences the possibility of forming a classical π bond between the two metal atoms for E = Ge, Sn, and Pb.

The CGMT model proposed by Trinquier and Malrieu[4] traces the deviation from planarity in $R_2E{=}ER_2$ molecules back to the relative values of the singlet and triplet energies of the monomeric units ER_2 (E_S and E_T, respectively) and the energy of the double-bonded system: For $E_{\sigma+\pi} > 2\Delta E_{S-T}$ a classical planar structure is obtained, whereas $E_{\sigma+\pi} < 2\Delta E_{S-T}$ favors the *trans*-bent structure. $E_{\sigma+\pi} < \Delta E_{S-T}$ results in monomeric ER_2 fragments without E–E bonding.[1,5]

The interatomic E–E distance is another strong indicator for the bond order. Scheme 1 gives an overview of several homonuclear double-bonded Si and Ge species. For second-row elements, double bonds are considerably shorter than the sum of the covalent radii, whereas for the heavier homologues, deviations occur owing to the strict requirements of the bulky ligands that are often used to stabilize the reactive bonds or owing to electrostatic repulsion in the case of charged systems. For example, in $R_2Ge{=}GeR_2$, the Ge–Ge bond lengths are in the range of 2.21 to 2.51 Å,[2] most of them being shorter than a Ge–Ge single bond (2.44 Å), but for $[RGe{=}GeR]^{2-}$, greater bond lengths are observed.[6]

In general, *trans*-bent structures are energetically favored over planar structures. Ligand-free and thus symmetrically unperturbed germanide dumbbells have been observed in Zintl phases.[7] Assuming a complete valence electron transfer in $BaMg_2Ge_2$, a 14 valence electron $[Ge{-}Ge]^{6-}$ dumbbell should be obtained. However, the Ge–Ge bond (2.58 Å)[8] is significantly longer than a typical Ge single bond, which was sketchily explained by Coulombic repulsion of the negatively charged atoms. Recently, the strong interaction of alkaline-earth metal d states with anions in Zintl phases was experimentally established, hinting at a less effective electron transfer with alkaline-earth metal counterions.[9]

Ge dumbbells also occur in binary lithium germanides, Li_xGe_{1-x} $(0.692 \le x \le 0.778)$.[10–13] However, assuming the formal electron transfer according to the Zintl–Klemm concept, they never contain a truly double-bonded dumbbell, $[Ge{=}Ge]^{4-}$. Instead, more highly charged species, such as $(Li^+)_{13}(Ge^{4-})_2[Ge_2]^{5-}$ for $Li_{13}Ge_4$ and $(Li^+)_9([Ge_2]^{4.5-})_2$ for Li_9Ge_4 have been considered, or alternatively $[Ge_2]^{4-}$ units with one or 0.5 excess electrons per dimer, respectively, have been proposed. Yet, with decreasing Li content, π-bonding contributions are expected to increase, and the Ge–Ge bond lengths accordingly decrease from 2.62 Å ($Li_{13}Ge_4$)[12,13] to 2.44 Å (Li_9Ge_4),[10] but in all cases, they remain longer than a typical Ge–Ge single bond.

For silicides, stannides, and plumbides[12] as well as pnicogenides,[16] the situation is similar; quite a few com-

[*] L. M. Scherf, Prof. Dr. T. F. Fässler
Department of Chemistry, Technische Universität München
Lichtenbergstrasse 4, 85747 Garching/München (Germany)
E-mail: thomas.faessler@lrz.tum.de
Prof. Dr. A. J. Karttunen
Department of Chemistry, Aalto University
00076 Aalto (Finland)
Dr. O. Pecher, Dr. P. C. M. M. Magusin, Prof. Dr. C. P. Grey
Department of Chemistry, University of Cambridge
Lensfield Road, Cambridge, CB2 1EW (UK)

Supporting information for this article is available on the WWW under http://dx.doi.org/10.1002/anie.201508044.

pounds containing dumbbells are known but their electron counts never suggest a true double bond, and the bond lengths are at least in the range of the elemental single bond.[17]

Herein, we report on the new Zintl phase, Li_3NaGe_2, which contains anionic dumbbells $[Ge_2]^{4-}$ with a short Ge–Ge bond that can be characterized as a true double bond. To the best of our knowledge, this is the first time that a true Ge=Ge bond has been observed in a neat solid. Furthermore, we show the first Raman spectrum of a solid-state Ge=Ge double bond. As it does not possess covalently bonded ligands, it can be considered as an analogue to molecular O_2. After the recently discovered $Li_{18}Na_2Ge_{17}$,[18] Li_3NaGe_2 is only the second ternary Li/Na/Ge compound to be reported.

Red, lustrous single crystals of Li_3NaGe_2 were initially found as a product of a flux synthesis in the Li/Na/Ge system with excess Na. Subsequently, the air- and moisture-sensitive compound was synthesized directly from the pure elements by heating to 750 °C and characterized crystallographically. Nearly phase-pure samples of Li_3NaGe_2 were obtained from thoroughly mixed $Li_{17}Ge_4$, NaGe, and Ge precursors by dwelling at 400 °C.

Li_3NaGe_2 crystallizes with a new structure type in the orthorhombic space group *Pnma* (No. 62) with $a = 12.706(3)$ Å, $b = 4.4571(9)$ Å, and $c = 7.7715(16)$ Å (Figure 1a).[20] The structure contains Ge–Ge dumbbells that are coordinated by 15 alkali metal cations (Figure 1b). Three Li1 and three Li3 atoms form a six-membered ring in envelope configuration that surrounds the dimer. Four Li2 and five Na1 atoms coordinate the Ge atoms in a terminal fashion. Selected distances for the Ge–Ge coordination sphere are given in Ref. [19]. Remarkably, the Ge–Ge bond (2.390(1) Å) is significantly shorter than a Ge single bond (2.44 Å) and shorter than the Ge–Ge bonds in known intermetallic compounds. For molecular digermenes, the Ge=Ge bond-length reduction varies significantly depending on the competing influences of steric and electrostatic repulsion. However, in dianions, $[RGe{=}GeR]^{2-}$, the bond lengths are in a similar range (2.39–2.45 Å).[6]

According to the Zintl–Klemm concept,[21] Li_3NaGe_2 can also be described as $(Li^+)_3(Na^+)[Ge_2]^{4-}$, suggesting a true double bond for the Ge dumbbell. This description and the very short bond length demand a large p–p π-bonding contribution to the Ge–Ge bond. Typically, for Zintl phases, a small band gap at the Fermi level is expected. In this case, however, the Li_3NaGe_2 structure formally contains a double-bonded dimer (a formal charge of −2 for each Ge atom), and the compound should thus behave similarly to molecular O_2 according to the $(8-N)$ rule. Unlike other double-bonded π systems such as ethylene, O_2 does not have a preferred orientation for π bonding because two sets of perpendicular p orbitals are available for π bonding as in triple-bonded systems. This results in the single occupation of degenerate antibonding molecular orbitals (MOs) and paramagnetism. The coordination sphere of the Ge dumbbell in Li_3NaGe_2 does not show any preferred orientation, and hypothetical $[Ge_2]^{4-}$ in vacuum is also paramagnetic (Figure 2c). Thus, Li_3NaGe_2 may be viewed as a solid-state equivalent to O_2. Li_3NaGe_2 is not, however, paramagnetic, the partially filled bands in the solid state resulting in metallic properties. A

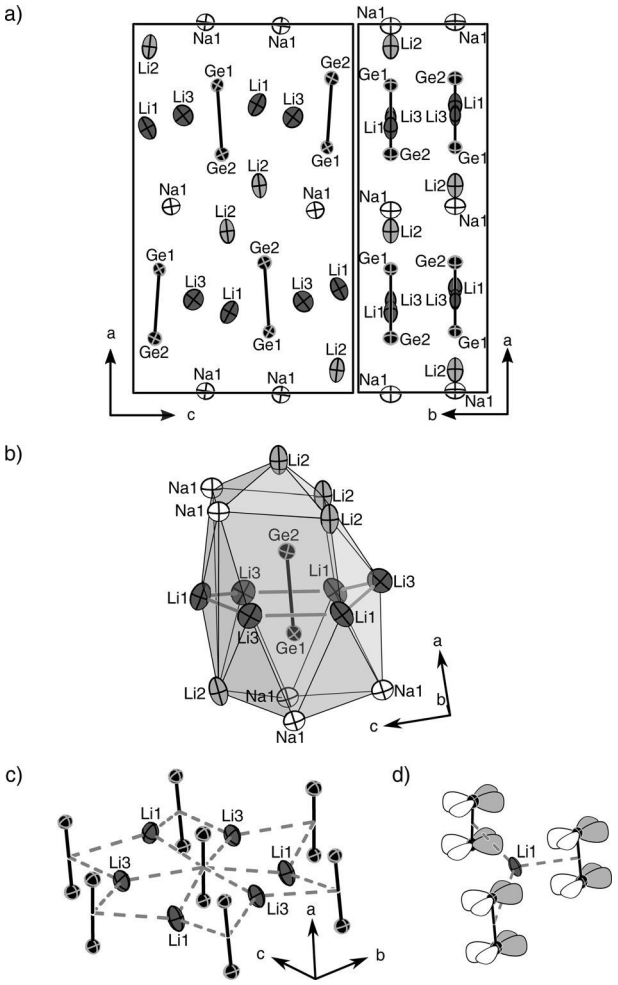

Figure 1. a) Projections of the unit cell of Li_3NaGe_2 onto the *ac* (left) and *ab* planes (right). b, c) Coordination spheres of a Ge–Ge dumbbell (b) and of Li1 and Li3 (c). d) Li1 surrounded by π-bonding Ge p orbitals (thermal ellipsoids set at 90% probability at 123 K).[19]

significant density of states at the Fermi level, partially occupied π-antibonding Ge(p) orbitals, and thus metallic behavior were confirmed by a thorough electronic-structure analysis by TB-LMTO-ASA[22] (for details on the calculations, see the Supporting Information). The total and partial densities of states (DOS) are depicted in Figure 2a. Indeed, Li_3NaGe_2 does not have a band gap at the Fermi level (E_F). The Ge(s) states are largely situated below −6 eV and thus do not contribute significantly to the bonding in Li_3NaGe_2. In the range of −5 to 4 eV, the total DOS is dominated by the Ge(p) states involved in Ge–Ge bonding. The Li(s) and Na(s) states are also partially occupied in this region and therefore play a non-negligible role in the overall bonding and stability of Li_3NaGe_2.

To analyze the Ge p–p π bonding in Li_3NaGe_2 more closely, the crystal orbital Hamilton population (COHP) of the Ge–Ge bond was calculated and a detailed band structure analysis performed. The COHP (Figure 2b) indicates that as expected, some π-antibonding Ge(p) states are occupied at the Fermi level. The −iCOHP value at the Fermi level yields 3.27 eV per bond, affirming the large p–p π bonding contri-

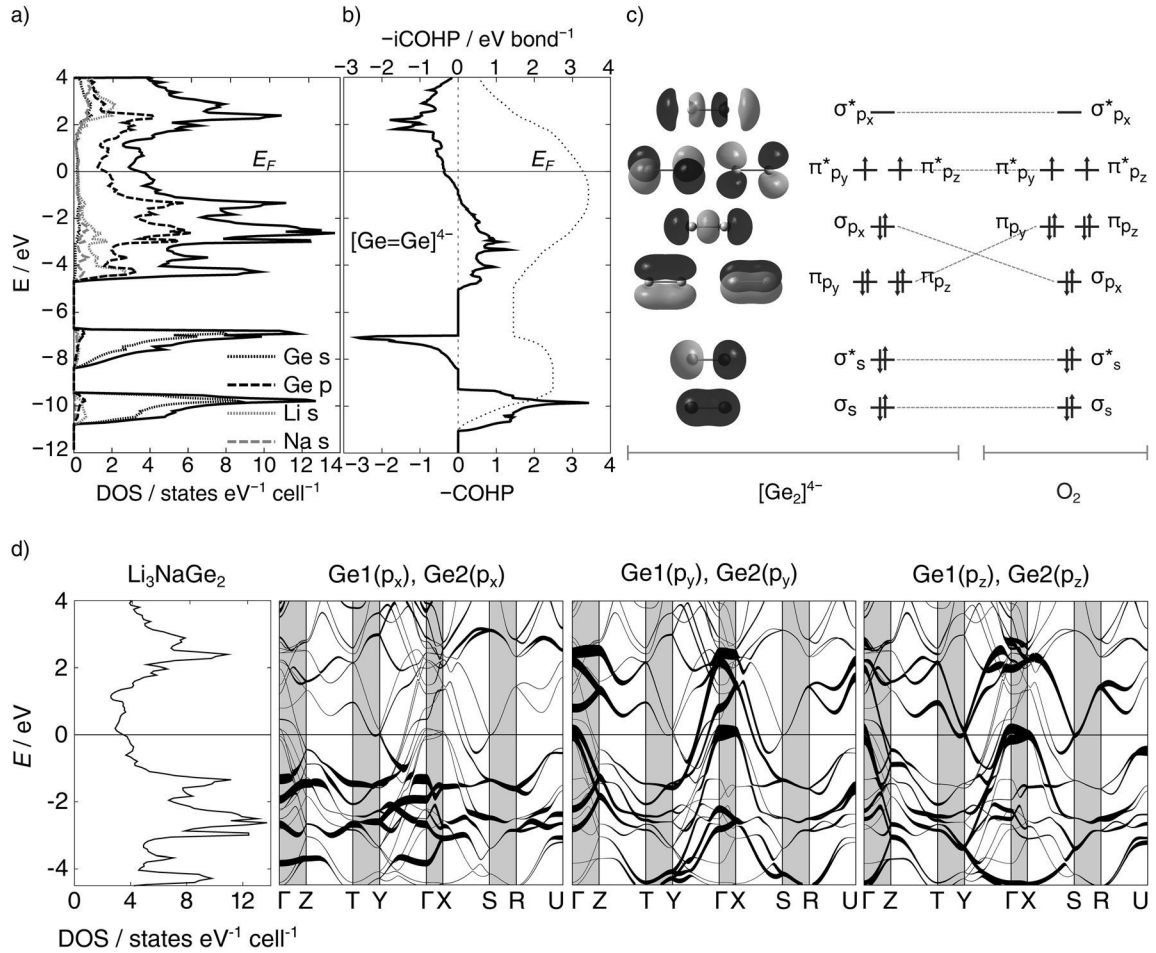

Figure 2. a) Total and partial DOS curves in the range of −12 eV to 4 eV for Li_3NaGe_2. b) COHP (——) and integrated COHP (•••••) of the Ge1−Ge2 bond in Li_3NaGe_2, iCOHP at $E_F = 3.27$ eV per bond. c) Molecular orbitals of free $[Ge_2]^{4-}$ and MO diagrams for free $[Ge_2]^{4-}$ and O_2 calculated at the DFT-PBE0/def2-TZVP level of theory (see the Supporting Information; the p_x orbital was chosen to be parallel to the bond axis as in Li_3NaGe_2). d) Total DOS curve as well as band structures including the Ge(p) fat bands in the range of −4.5 eV to 4 eV for Li_3NaGe_2.

bution. For comparison, Ge dumbbells in M_7Ge_6 (M = Ca, Sr, Ba), which have been shown to feature significant π bonding, exhibit −iCOHP values of 2.48 to 2.92 eV.[23]

A fat-band analysis of the Ge(p) states served to clarify the π-bonding situation of $[Ge_2]^{4-}$ (Figure 2d). Although the Ge dumbbell is not aligned exactly with any cell parameter, a separate view of the p_x, p_y, and p_z orbital contributions clearly shows that the Ge anion may justifiably be related to molecular O_2: The p_x orbitals are oriented almost parallel to the Ge–Ge bond. The corresponding bands representing the Ge–Ge σ bond are clearly separated with bonding bands below and antibonding bands well above E_F. The p_y and p_z orbitals are oriented nearly perpendicular to the bond axis and are therefore available for π bonding. The corresponding bands are located around E_F, demonstrating a significant π-bonding contribution. As also seen in the COHP analysis, the π-antibonding p_y and p_z bands are partially occupied, similar to those in molecular O_2.

According to magnetic measurements (see the Supporting Information), Li_3NaGe_2 is diamagnetic with a molar magnetic susceptibility of -4.0×10^{-5} emu mol^{-1} at 5000 Oe, suggesting that the diamagnetic contributions of Li^+, Na^+, and the Ge core and 3d electrons superimpose Pauli paramagnetic contributions from the conduction electrons of the metal.[24]

The Raman spectrum of Li_3NaGe_2 is shown in Figure 3. We assigned the Raman bands by utilizing density functional calculations (DFT-PBE/TZVP level of theory, see the Supporting Information for full computational details). It was not possible to calculate Raman intensities because Li_3NaGe_2 shows metallic conductivity, but by calculating the wavenumbers of the Raman-active modes and inspecting the corresponding normal modes, the spectrum could still be fully interpreted (Supporting Information, Table S1). The broad

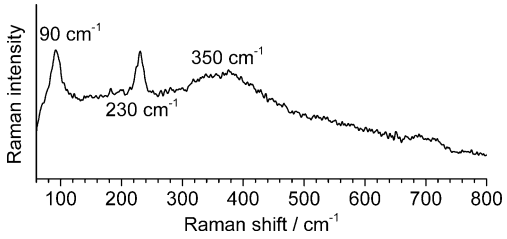

Figure 3. Raman spectrum of a Li_3NaGe_2 single crystal.

band centered at about 350 cm^{-1} arises from vibrational motion of the Li atoms. The 230 cm^{-1} band is due to Ge=Ge stretching vibrations of the Ge dumbbell. The calculated wavenumbers are slightly overestimated in comparison to experiment, showing one symmetric Ge=Ge stretching mode at 251 cm^{-1} and two asymmetric stretching modes at 230 and 224 cm^{-1}.[25] This stretching frequency is in the range typical for Zintl polyanions, such as $[Ge_9]^{4-}$ (220–222 cm^{-1}) and $[Ge_4]^{4-}$ (274 cm^{-1}).[26] Finally, the band centered at 90 cm^{-1} is due to tilting and low-energy motions of the Ge dumbbell and falls in the range of libration modes of $[Ge_9]^{4-}$ clusters.[27]

^{6}Li and ^{23}Na magic angle spinning (MAS) NMR spectra were recorded for ^{6}Li-enriched Li_3NaGe_2 (Figure 4). The spectra can be consistently interpreted with the aid of 2D ^{6}Li spin exchange, ^{7}Li 1D, and ^{23}Na multiple-quantum (MQ) MAS NMR spectroscopy (Figures S8–S10) in combination with DFT-PBE calculations of the chemical shifts and quadrupolar NMR parameters for Na_7LiGe_8 and $Li_{14}Ge_6$ (see the Supporting Information for details and Tables S2, S3).

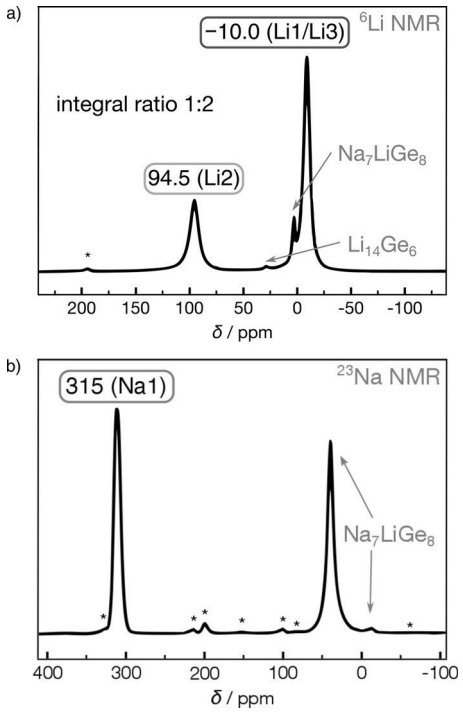

Figure 4. a) ^{6}Li and b) ^{23}Na MAS NMR spectra of $^{6}Li_3NaGe_2$ (15 kHz MAS spinning speed, 11.7 T, ambient temperature). Signal assignments for the main phase and the respective crystallographic positions are given in black, those for the impurity phases are shown in gray. Rotational sidebands are marked by asterisks.

The ^{6}Li NMR spectrum contains two major resonances at 94.5 and −10.0 ppm with an integral ratio of 1:2, which belong to Li_3NaGe_2. ^{6}Li spin-exchange NMR spectroscopy confirms that the corresponding Li atoms are in close proximity and originate from the same phase (Figure S9). Negative shifts have been reported for Li^+ located in π electron clouds, such as in aromatic $[Ge_5]^{6-}$ in $Li_{12}Ge_7$ (−17 ppm)[28] or in the Li cyclopentadienide (Cp) monomer (−7.6 ppm).[29] Li1 and Li3 are surrounded by the π electrons of three Ge dumbbells (Figure 1). Therefore, we assign the signal at −10.0 ppm to these two atom positions (Figure 4 a). The two Li sites cannot be resolved owing to their similar coordination spheres. The Knight-shifted ^{6}Li signal at 94.5 ppm can be attributed to Li2, which coordinates the Ge dumbbells terminally (Figure 1 b). Minor signals at 1.9 and 28.1 ppm belong to Na_7LiGe_8[30] and $Li_{14}Ge_6$[12,31] impurities, respectively (Figure S11 and Table S2).

Apart from minor spinning sidebands, the ^{23}Na NMR spectrum shows two major and one minor center-band resonances (Figure 4 b), of which the highest at 315 ppm belongs to Na1 in Li_3NaGe_2. As for Li2, this Na environment has a Knight shift well outside the diamagnetic shift range, which is explained by the fact that it possesses a similar atomic environment and experiences the same local electronic band structure (see the Supporting Information). The signals at −8.0 and 38.0 ppm were assigned to the impurity Na_7LiGe_8, which had also been observed by ^{6}Li NMR analysis. The interpretation of the 1D NMR spectra was corroborated by ^{23}Na MQMAS NMR spectroscopy and DFT-PBE calculations (Figure S10 and Tables S2, S3).

In conclusion, we have discovered that the novel phase Li_3NaGe_2 contains $[Ge_2]^{4-}$ dumbbells. The Ge–Ge distance and electronic-structure calculations clearly indicate a true Ge=Ge double bond, with a strong influence of its π electron system on the ^{6}Li NMR shifts. Li_3NaGe_2 can be viewed as a model system for heavier-element multiple bonds in molecular compounds without preferential orientation of the π bonds, rendering it an example of a solid-state equivalent to molecular O_2. The resulting degeneracy of the π-bonding p orbitals, which is well known for paramagnetic O_2, leads to metallic behavior in the title compound.

Acknowledgements

We thank Michael Zeilinger for help in treating the twinned crystal, Herta Slavik for the Raman measurement, and Gergana Nenova for the SQUID measurement. We gratefully acknowledge the help of Steffen Emge during NMR sample preparation. We thank Dr. Michal Leskes, Dr. Andrew J. Pell, and Raphaële Clément for fruitful discussions. O.P. acknowledges support from a Marie Skłodowska-Curie Individual Fellowship. L.M.S. is grateful to the Fonds der Chemischen Industrie and the Studienstiftung des deutschen Volkes for fellowships. A.J.K. gratefully acknowledges funding from the Alfred Kordelin Foundation and computational resources from CSC—the Finnish IT Center for Science.

Keywords: double bonds · germanium dumbbells · lithium · sodium · Zintl phases

How to cite: *Angew. Chem. Int. Ed.* **2016**, *55*, 1075–1079
Angew. Chem. **2016**, *128*, 1087–1091

[1] P. P. Power, *Chem. Rev.* **1999**, *99*, 3463–3504.
[2] Y. Wang, G. H. Robinson, *Chem. Commun.* **2009**, 5201–5213.

[3] V. Y. Lee, A. Sekiguchi, *Organometallic Compounds of Low-Coordinate Si, Ge, Sn and Pb*, Wiley, Hoboken, **2010**.
[4] G. Trinquier, J. P. Malrieu, *J. Am. Chem. Soc.* **1987**, *109*, 5303 – 5315.
[5] M. Driess, H. Grützmacher, *Angew. Chem. Int. Ed. Engl.* **1996**, *35*, 828 – 856; *Angew. Chem.* **1996**, *108*, 900 – 929.
[6] L. Pu, A. D. Phillips, A. F. Richards, M. Stender, R. S. Simons, M. M. Olmstead, P. P. Power, *J. Am. Chem. Soc.* **2003**, *125*, 11626 – 11636.
[7] Zintl phases are polar intermetallic compounds that can be described by a salt-like complete valence-electron transfer from electropositive Group 1 or 2 metals to more electronegative Group 13 to 16 p block metals.
[8] a) B. Eisenmann, N. May, W. Müller, H. Schäfer, A. Weiss, J. Winter, G. Ziegleder, *Z. Naturforsch. B* **1970**, *25*, 1350 – 1352; b) B. Eisenmann, H. Schäfer, *Z. Anorg. Allg. Chem.* **1974**, *403*, 163 – 172.
[9] I. M. Kurylyshyn, T. F. Fässler, A. Fischer, C. Hauf, G. Eickerling, M. Presnitz, W. Scherer, *Angew. Chem. Int. Ed.* **2014**, *53*, 3029 – 3032; *Angew. Chem.* **2014**, *126*, 3073 – 3077.
[10] A. Grüttner, R. Nesper, H. G. von Schnering, *Acta Crystallogr. Sect. A* **1981**, *37*, C161.
[11] V. Hopf, H. Schäfer, A. Weiss, *Z. Naturforsch. B* **1970**, *25*, 653.
[12] R. Nesper, *Prog. Solid State Chem.* **1990**, *20*, 1 – 45.
[13] R. Nesper, Habilitation, Universität Stuttgart (Stuttgart), **1988**.
[14] a) Y. Wang, Y. Xie, P. Wei, R. B. King, H. F. Schaefer, P. v. R. Schleyer, G. H. Robinson, *Science* **2008**, *321*, 1069 – 1071; b) A. Sidiropoulos, C. Jones, A. Stasch, S. Klein, G. Frenking, *Angew. Chem. Int. Ed.* **2009**, *48*, 9701 – 9704; *Angew. Chem.* **2009**, *121*, 9881 – 9884.
[15] H. G. von Schnering, R. Nesper, K.-F. Tebbe, J. Curda, *Z. Metallkd.* **1980**, *71*, 357.
[16] a) H. G. Von Schnering, W. Hönle, *Chem. Rev.* **1988**, *88*, 243 – 273; b) S. C. Sevov in *Intermetallic Compounds—Principles and Practice* (Eds.: J. H. Westbrook, R. L. Fleischer), Wiley, New York, **2002**, pp. 113 – 132; c) R. Pöttgen, D. Johrendt, *Intermetallics*: *Synthesis, Structure, Function*, de Gruyter, Berlin, **2014**; d) F. Gascoin, S. C. Sevov, *J. Am. Chem. Soc.* **2000**, *122*, 10251 – 10252.
[17] Si dumbbells with a rather short Si–Si distance were observed in the recently discovered $Ba_{26}B_{12}Si_5N_{27}$. The Si–Si bond length of 2.177(5) Å is shorter than a typical Si single bond (2.35 Å). However, the Si positions were not fully occupied and the N atoms were disordered; thus a charge-balanced description was not possible; see: H. Takayuki, H. Yamane, N. Becker, R. Dronskowski, *J. Solid State Chem.* **2015**, *230*, 390 – 396.
[18] L. M. Scherf, M. Zeilinger, T. F. Fässler, *Inorg. Chem.* **2014**, *53*, 2096 – 2101.
[19] Selected distances in Å: Ge1–Ge2 2.3900(10), Ge1–Li 2.718(7)–2.891(13), Ge1–Na 3.038(3)–3.133(2), Ge2–Li 2.658(14)–3.072(10), Ge2–Na 3.385(2), Li1–Li2 2.80(2), Li1–Li3 2.600(10)–2.65(2), Li2–Li2 2.954(18), Li2–Li3 3.458(15).
[20] Data collection, solution, and refinement for Li_3NaGe_2 are shortly described in the Supporting Information. Further details on the crystal-structure investigation may be obtained from the Fachinformationszentrum Karlsruhe, 76344 Eggenstein-Leopoldshafen, Germany (fax (+49) 7247-7808-666; crysdata@fiz-karlsruhe.de; http://www.fiz-karlsruhe.de/request for deposited data.html) on quoting the deposition number CSD 429881.
[21] a) E. Zintl, *Angew. Chem.* **1939**, *52*, 1 – 6; b) W. Klemm, *Proc. Chem. Soc.* **1958**, 329 – 341; c) W. Klemm, E. Busmann, *Z. Anorg. Allg. Chem.* **1963**, *319*, 297 – 311.
[22] *The Stuttgart Tight-Binding LMTO-ASA program*, M. v. Schilfgarde, T. A. Paxton, O. Jepsen, O. K. Andersen, G. Krier, Max-Planck-Institut für Festkörperforschung, Stuttgart, Germany, **1998**.
[23] L. Siggelkow, V. Hlukhyy, T. F. Fässler, *J. Solid State Chem.* **2012**, *191*, 76 – 89.
[24] The metals Cu, Ag, Zn, Cd, Ga, and In, which feature completely filled valence d shells, are also diamagnetic.
[25] For molecular compounds containing Ge double bonds, Raman vibrational data for characterization of the double bond is very scarce. The vibrations of the Ge=Ge stretches in $Me_2Ge=GeMe_2$, determined in an Ar matrix at 5 K, in RBrGe=GeRBr (R = Bbt, Bbt = 2,6-bis[bis(trimethylsilyl)methyl]-4-[tris(trimethylsilyl)methyl]phenyl) and in proposed $R_2Ge=GeR_2$ (R = CH-$(SiMe_3)_2$) were found at 404 cm^{-1}, 355 cm^{-1}, and 300 cm^{-1}, respectively; see: a) P. Bleckmann, R. Minkwitz, W. P. Neumann, M. Schriewer, M. Thubud, B. Watta, *Tetrahedron Lett.* **1984**, *25*, 2467 – 2470; b) Y. Sugiyama, T. Sasamori, Y. Hosoi, Y. Furukawa, N. Takagi, S. Nagase, N. Tokitoh, *J. Am. Chem. Soc.* **2006**, *128*, 1023 – 1031; c) P. J. Davidson, D. H. Harris, M. F. Lappert, *J. Chem. Soc. Dalton Trans.* **1976**, 2268 – 2274.
[26] a) W. Carrillo-Cabrera, R. Cardoso Gil, M. Somer, Ö. Persil, H. G. von Schnering, *Z. Anorg. Allg. Chem.* **2003**, *629*, 601 – 608; b) H. G. von Schnering, M. Baitinger, U. Bolle, W. Carrillo-Cabrera, J. Curda, Y. Grin, F. Heinemann, J. Llanos, K. Peters, A. Schmeding, M. Somer, *Z. Anorg. Allg. Chem.* **1997**, *623*, 1037 – 1039.
[27] V. Hlukhyy, T. F. Fässler, *Angew. Chem. Int. Ed.* **2012**, *51*, 742 – 747; *Angew. Chem.* **2012**, *124*, 766 – 771.
[28] S. Dupke, T. Langer, R. Pöttgen, M. Winter, H. Eckert, *Solid State Nucl. Magn. Reson.* **2012**, *42*, 17 – 25.
[29] L. A. Paquette, W. Bauer, M. R. Sivik, M. Buehl, M. Feigel, P. v. R. Schleyer, *J. Am. Chem. Soc.* **1990**, *112*, 8776 – 8789.
[30] Na_7LiGe_8 is a ternary Zintl phase that will be dicussed in more detail in an upcoming publication.
[31] H. Jung, P. K. Allan, Y.-Y. Hu, O. J. Borkiewicz, X.-L. Wang, W.-Q. Han, L.-S. Du, C. J. Pickard, P. J. Chupas, K. W. Chapman, A. J. Morris, C. P. Grey, *Chem. Mater.* **2015**, *27*, 1031.

Received: August 27, 2015
Published online: December 2, 2015

Angewandte Chemie
Eine Zeitschrift der Gesellschaft Deutscher Chemiker

Supporting Information

$[Ge_2]^{4-}$ Dumbbells with Very Short Ge–Ge Distances in the Zintl Phase Li_3NaGe_2: A Solid-State Equivalent to Molecular O_2

*Lavinia M. Scherf, Antti J. Karttunen, Oliver Pecher, Pieter C. M. M. Magusin, Clare P. Grey, and Thomas F. Fässler**

anie_201508044_sm_miscellaneous_information.pdf

Supporting Information

Contents

Experimental Section **2**
Synthesis 2
Powder X-ray Diffraction 2
Single Crystal X-ray Diffraction 2
Magnetic Measurements 2
Raman Spectroscopy 3
Solid State NMR Spectroscopy 3
Electronic Structure Calculations 3
X-Ray Powder Diffraction Patterns **5**
Electronic Structure Analysis **6**
Magnetic Properties **8**
Vibrational Analysis **9**
MAS NMR Spectra **10**
NMR/QM Data Summary **14**
Full basis set listings in CRYSTAL14 input format **15**
References **17**

Experimental Section

All steps of synthesis and sample preparation were performed inside an Ar-filled glove box (MBraun, $p(H_2O,O_2)$ < 0.1 ppm). Li rods (99 %, Rockwood-Li) and Na pieces (99 %, Chempur) were freed from their oxidic layers before use. Ge (99.999 %, Evochem) was used without further purification.

Synthesis. Li_3NaGe_2 was prepared from a stoichiometric mixture of the corresponding elements which was sealed in a Ta ampule. The ampule was transferred into a silica tube which was then evacuated. Inside a tube furnace, the mixture was heated to 750 °C at a rate of 5 °C min^{-1} at which temperature it was kept for 1 h. The ampule was subsequently cooled to 300 °C at 0.5 °C min^{-1}, and after dwelling for 3 h cooled down rapidly. To obtain purer products, Li_3NaGe_2 can also be prepared according to Equation (1).

$$3\ Li_{17}Ge_4 + 17\ NaGe + 5\ Ge \rightarrow 17\ Li_3NaGe_2 \quad (1)$$

In this case, a stoichiometric mixture of the reactants that is prepared similarly is rapidly heated to 400 °C, dwelled for 7 days and cooled down slowly. The preparation of reaction mixtures of about 0.5 g and product recovery were performed in an Ar-filled glove box. Products were analyzed by powder X-ray diffraction (PXRD), single crystal X-ray diffraction (SCXRD), Raman, ^{7}Li- and ^{23}Na-MAS NMR spectroscopy.

Powder X-ray Diffraction. Samples for PXRD were ground, filled into 0.3 mm glass capillaries, and measured using a STOE STADI P diffractometer equipped with a Ge(111) monochromator for CuK_α radiation (λ = 1.54056 Å) and a Dectris MYTHEN DCS 1K solid-state detector.

Single Crystal X-ray Diffraction. Crystals of Li_3NaGe_2 were sealed in 0.3 mm glass capillaries. For the best specimen, intensity data were collected at 123 K using a Bruker AXS X-ray diffractometer equipped with a CCD detector (APEX II, κ-CCD), a rotating anode FR591 with Mo K_α radiation (λ = 0.71073 Å), and a MONTEL optic monochromator. Data collection was controlled with the Bruker APEX software package.[1] Integration, data reduction, and absorption correction for the pseudomerohedrically twinned crystal (BASF = 0.1827) were performed with the SAINT[2], CELL_NOW[3] and TWINABS[4] packages. The structure was solved with direct methods (SHELXS-97) and refined with full-matrix least squares on F^2 (SHELXL-97).[5]

Crystal data for Li_3NaGe_2: M_r = 188.99 g mol^{-1}, crystal size 0.18 x 0.13 x 0.09 mm^3, orthorhombic, space group *Pnma* (No. 62), a = 12.706(3) Å, b = 4.4571(9) Å, c = 7.7715(16) Å, V = 440.10(15) $Å^3$, Z = 4, $\rho_{calc.}$ = 2.852 g cm^{-1}, μ = 13.527 mm^{-1}, Mo-K_α radiation, λ = 0.71073 Å, T = 123(2) K, $2\theta_{max.}$ = 66.326°, 2713 reflections measured, 1152 independent reflections, R_{int} = 0.1231, least-squares refinement on F^2, R factors (all data/$I > 2\sigma(I)$): R_1 = 0.0471/0.0426, wR_2 = 0.1186/0.1123, largest difference peak/hole = 1.240/−2.055 e $Å^{-3}$. Further details on the crystal structure investigation may be obtained from the Fachinformationszentrum Karlsruhe, 76344 Eggenstein-Leopoldshafen, Germany (fax: (+49) 7247-808-666; e-mail: crysdata@fiz-karlsruhe.de) on quoting the deposition number CSD-429881.

Magnetic Measurements. Using a Quantum Design MPMS 5 XL SQUID magnetometer, the magnetization of 37 mg of a Li_3NaGe_2 synthesis product was measured at an applied field of 5000 Oe over the temperature range 2–300 K. The data were corrected for the sample holder diamagnetism to −4.0 x 10^{-5} emu/mol. Correction for ion-core diamagnetism of Li^+ and Na^+ using Pascal's constants[6] yields a magnetic susceptibility of –3.0 x 10^{-5} emu/mol. In addition, the

magnetization of Li_3NaGe_2 was measured at 300 K over the field range of 0–50000 Oe, indicating fully diamagnetic behavior.

Raman Spectroscopy. Single crystals for Raman spectroscopy were sealed in a 0.3 mm glass capillary. Measurements were performed at 1 mW laser power and 5x 60 s exposure time using a Senterra Raman spectrometer (Bruker) equipped with a laser diode (λ = 785 nm), an objective lens for 50-fold magnification and a 1200a grid.

Solid-State NMR Spectroscopy. Powder samples of ^{6}Li-enriched $^6Li_3NaGe_2$ and $Li_{14}Ge_6$ were diluted with fine GeO_2 powder (high vacuum dried at 100°C for 24 h) in a 1:1 ratio, packed into 4.0 mm ZrO_2 rotors (Bruker), topped with a thin layer of pure GeO_2 powder and finally closed with Kel-F rotor caps.[7] The dilution with GeO_2 suppresses potential sample heating due to eddy currents during sample spinning. This is furthermore beneficial for the *Q* value of the NMR probehead while measuring metallically conductive powder materials.[8] All sample handling was done under Argon atmosphere in a glove box with $p(H_2O,O_2)$ < 0.1 ppm.

Ambient temperature $^{6;7}$Li, ^{23}Na and ^{6}Li spin-exchange magic angle spinning (MAS) NMR experiments were performed at 11.7 T and ^{23}Na MQMAS NMR experiments at 4.7 T on Bruker Avance III HD consoles using Bruker double resonance 4.0 mm NMR probeheads. Pulse optimization was done on $^6Li_2CO_3$ (^{6}Li), LiF (^{7}Li), and NaCl (^{23}Na) powders, respectively. The $^{6;7}$Li and ^{23}Na shifts are referenced to 1M LiCl and NaCl solutions in D_2O, respectively.[9] NMR data acquisition, processing and analysis was done using Bruker Topspin and the Dmfit program.[10]

$^6Li_3NaGe_2$: ^{6}Li, ^{7}Li, and ^{23}Na NMR signal line shapes were determined at 15 kHz MAS speed by one-pulse experiments with high power pulses of 4.50 μs (repetition time 32 s), 0.95 μs (repetition time 8 s), and 1.40 μs (repetition time 1 s), respectively. A saturation recovery pulse sequence was applied to determine spin-lattice relaxation time constants (T_1) for all the isotopes mentioned above. ^{6}Li spin-exchange NMR experiments were done at 11.7 T using the $90°-t_1-90°-t_{mix}-90°-t_2$ pulse sequence with 90° pulses of 4.0 μs (repetition time 4.0 s) at 7.7 kHz MAS speed for mixing times t_{mix} of 1 ms, 10 ms, 100 ms, and 1 s. ^{23}Na MQMAS NMR spectra were recorded at 4.7 T by use of the three-pulse sequence $p_1–t_1–p_2–t–p_3–t_2$ for triple-quantum generation and zero-quantum filtering (strong pulses p_1= 6 μs and p_2= 2 μs at ν_1=100 kHz; soft pulse p_3=20 μs at ν_1 = 12.5 kHz; filter time t = 40 μs; interscan delay 0.3 s). The $^6Li_3NaGe_2$ sample used in NMR experiments was recovered after measurements and respective PXRD patterns show that the material remains unaltered.

$Li_{14}Ge_6$: ^{6}Li and ^{7}Li NMR signal line shapes were determined at 10 kHz and 15 kHz MAS speed by one-pulse experiments with high power pulses of 4.50 μs (repetition time 40 s) and 0.95 μs (repetition time 3 s), respectively.

Electronic Structure Calculations. Computational studies on the electronic structure of the title compound employed the linear muffin-tin orbital (LMTO) method in the atomic sphere approximation (ASA) using the tight-binding (TB) program TB-LMTO-ASA.[11] The exchange-correlation term was calculated within the local density approximation (LDA) and was parameterized according to von Barth and Hedin.[12] The radii of the muffin-tin spheres and empty spheres were determined after Jepsen and Andersen.[13] The basis set of short-ranged[14] atom-centered TB-LMTOs contained s, p valence functions for Ge and s valence functions for Li and Na. Li p, Na p and Ge d orbitals were included using a downfolding technique.

The vibrational properties of Li_3NaGe_2 were investigated using the CRYSTAL14 program package.[15] PBE density functional method and Gaussian-type, all-electron triple-zeta-valence + polarization (TZVP) level basis sets derived from the molecular Karlsruhe def2-TZVP basis sets were applied in the calculations (the basis sets are listed on page 15).[16] The reciprocal space was sampled using a 3x9x6 Monkhorst-Pack-type *k*-point grid. For the evaluation of the Coulomb and exchange integrals (TOLINTEG), tight tolerance factors of 8, 8, 8, 8, and 16 were used. Default optimization convergence thresholds and an extra-large integration grid (XLGRID) for the density-functional part were applied in all calculations. Both the atomic positions and lattice constants of Li_3NaGe_2 were fully optimized, resulting in lattice constants of a = 12.71 Å, b= 4.45 Å, and c = 7.77 Å (differences between the theoretical and experimental lattice constants are smaller than 0.5%). The harmonic vibrational frequencies were obtained by using the computational scheme implemented in CRYSTAL.[17]

The NMR properties were investigated by means of DFT-PBE calculations. The Electric Field Gradients required for the prediction of Quadrupolar Coupling Constants were calculated at the PBE/TZVP level of theory using the CRYSTAL program package. Because Li_3NaGe_2 is conducting, the NMR shielding tensor and NMR chemical shifts could not be predicted. However, the Na_7LiGe_8 impurity is not conducting, enabling first-principles NMR calculations with the CASTEP program package.[18] Ultrasoft pseudopotentials generated with the on-the-fly scheme[19] and a plane-wave basis set cut-off of 460 eV were applied. 4x4x4 Monkhorst-Pack sampling was used for integrations in the reciprocal space, corresponding to a *k*-point grid spacing of approximately 0.03 $Å^{-1}$. The NMR shielding tensor and chemical shifts for $^{6,7}Li$ and ^{23}Na in Na_7LiGe_8 were obtained using the GIPAW formalism as implemented in CASTEP-NMR.[20] The chemical shifts (δ_{iso}) were evaluated with respect to aqueous Li^+ and Na^+ ions described as $[M(H_2O)_4]^+$ (σ_{ref} = 89.7 and 556.5 ppm for Li and Na, respectively). The calculations for the molecular $[M(H_2O)_4]^+$ reference systems were carried out in a primitive cubic cell (a = 15 Å) using a plane-wave basis set cut-off of 610 eV and 2x2x2 *k*-point sampling (grid spacing of approximately 0.03 $Å^{-1}$).

The molecular orbital diagrams for O_2 and $[Ge_2]^{4-}$ were calculated at the DFT-PBE0/def2-TZVP level of theory using the Gaussian09 program package.[16, 21] Restricted Open-Shell formalism was applied. The geometries of the molecules were optimized within the $D_{\infty h}$ point group. The anionic charge of $[Ge_2]^{4-}$ was countered by using a Polarizable Continuum Model solvent field (SCRF=(PCM, Solvent=Water)).

X-ray Powder Diffraction Patterns

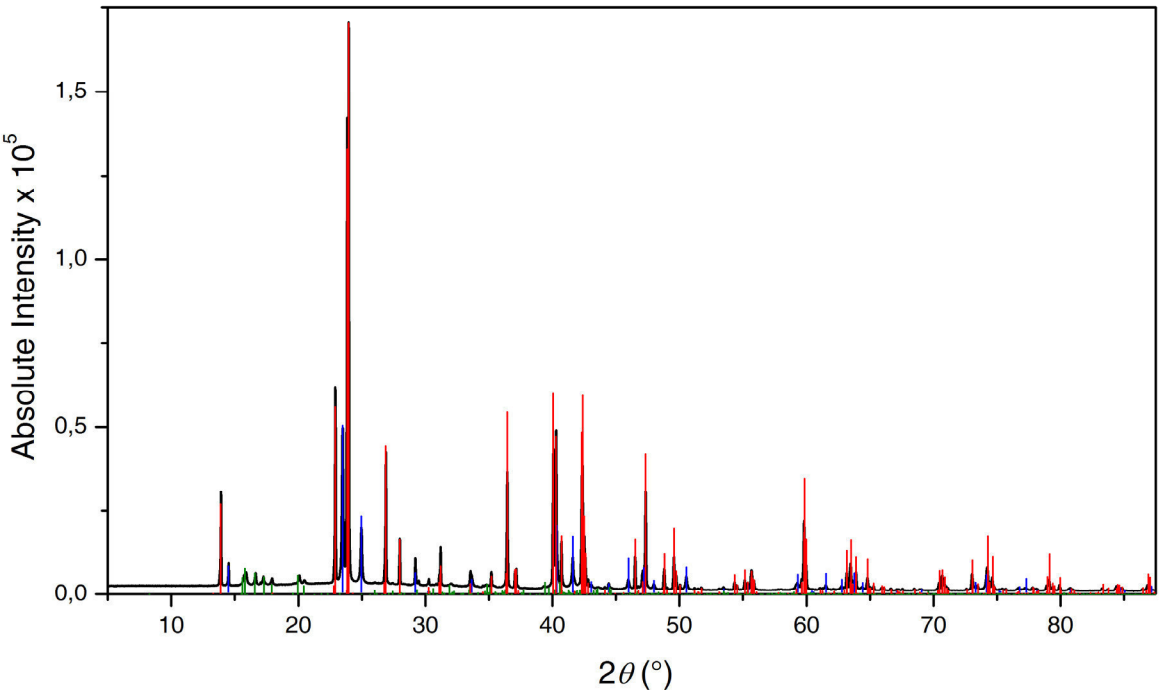

Figure S1. Experimental X-ray powder diffraction pattern of Li_3NaGe_2 synthesized from the elements (black) referenced with theoretical powder patterns of Li_3NaGe_2 (red), $Li_{14}Ge_6$ (blue) and Na_4Ge_4 (green).

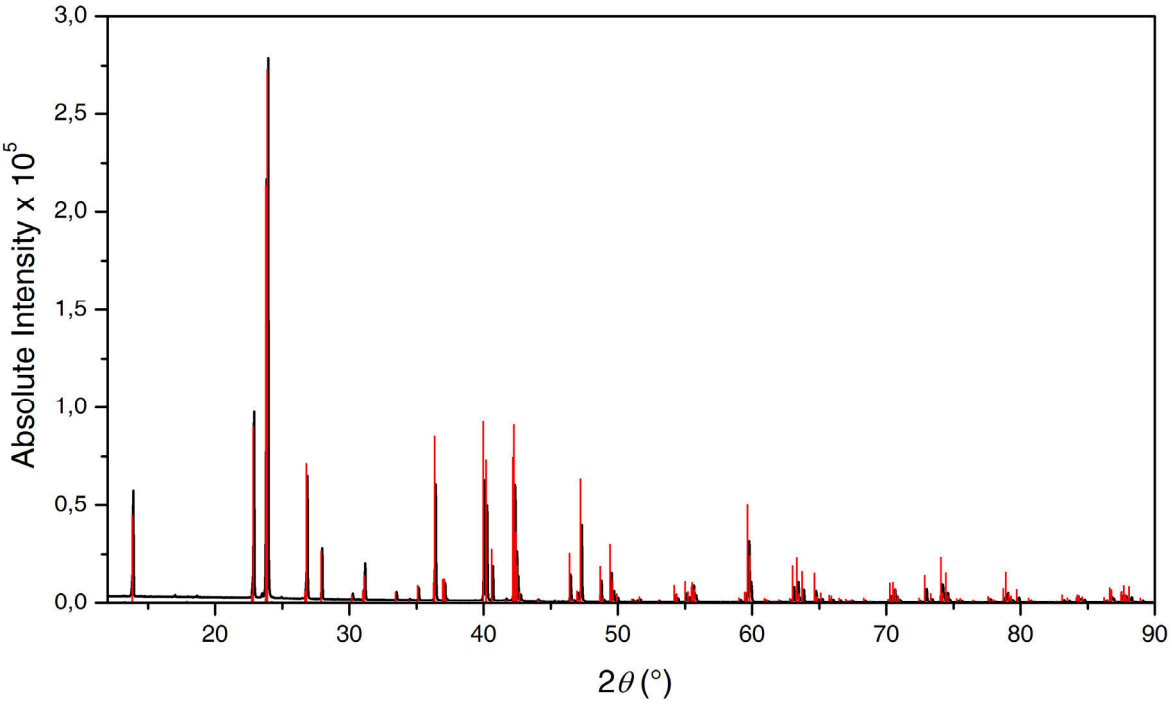

Figure S2. Experimental X-ray powder diffraction pattern of Li_3NaGe_2 synthesized from the binary compounds $Li_{17}Ge_4$ and NaGe as well as elemental Ge (black) referenced with its theoretical powder patterns (red). Slight impurities of $Li_{14}Ge_6$ and Na_7LiGe_8 are barely detectable.

Electronic Structure Analysis

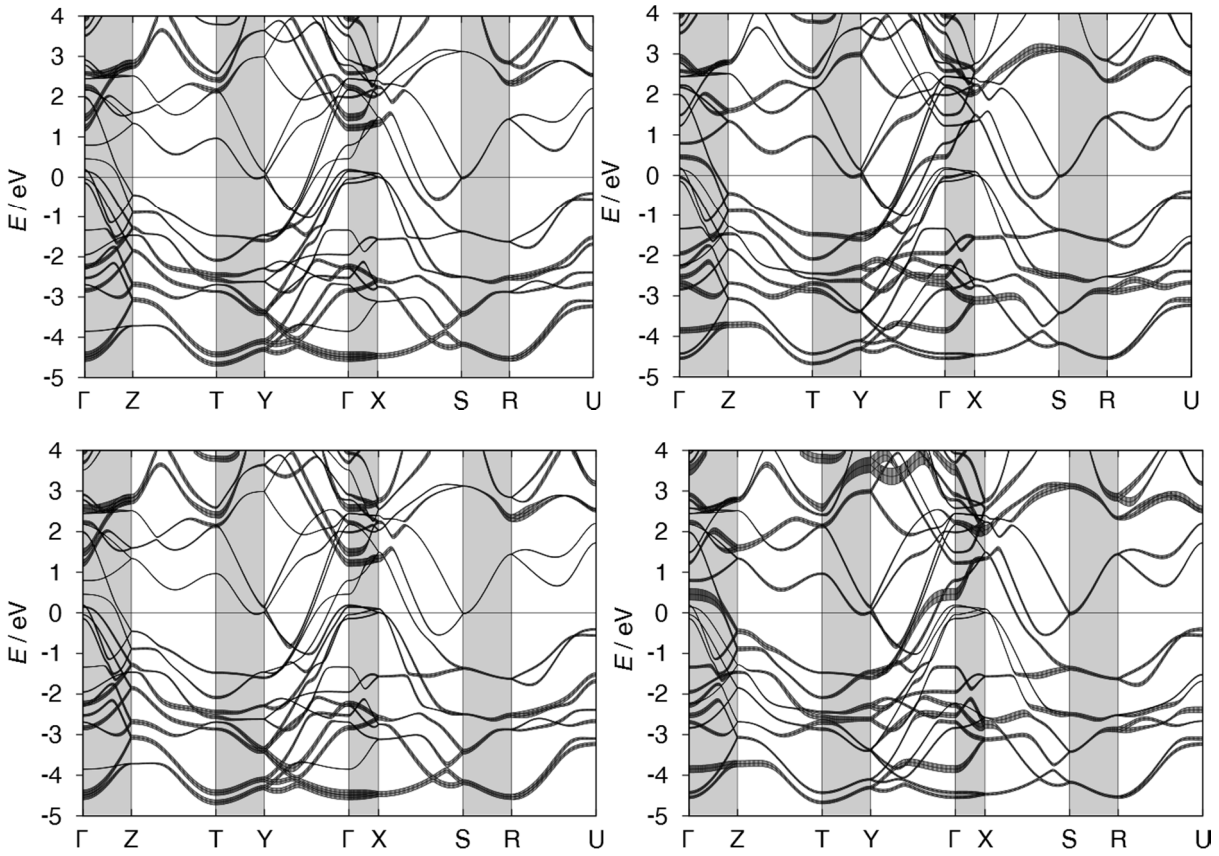

Figure S3. Band structures of Li_3NaGe_2 calculated using the TB-LMTO-ASA program including Li1 (top left), Li2 (top right), Li3 (bottom left) and Na1 (bottom right) fatbands in the range of −5 eV to 4 eV for Li_3NaGe_2.

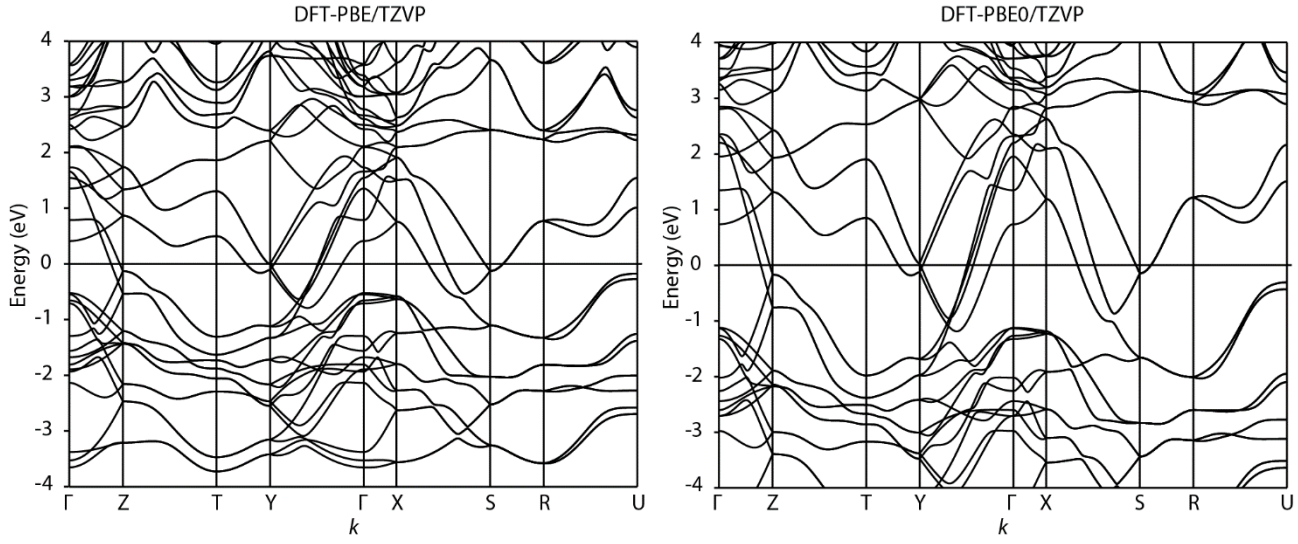

Figure S4. Band structure of Li_3NaGe_2 calculated at the DFT-PBE/TZVP and DFT-PBE0/TZVP levels of theory (CRYSTAL program package). The Fermi level is at 0 eV.

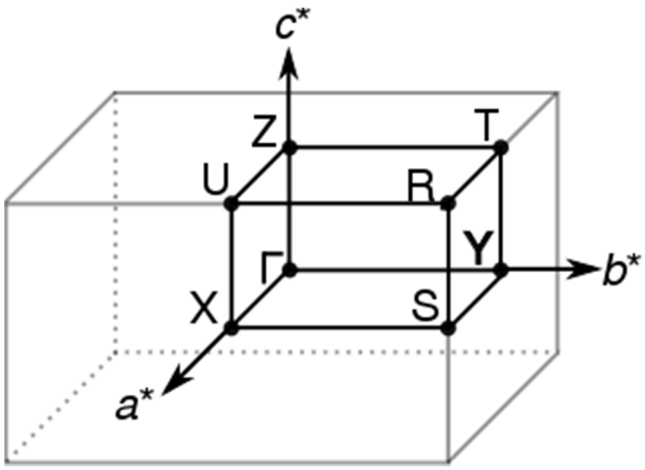

Figure S5. Brillouin zone for Li_3NaGe_2 in *Pnma*, showing symmetry points in *k* space with respect to the reciprocal conventional vectors.

Magnetic Properties

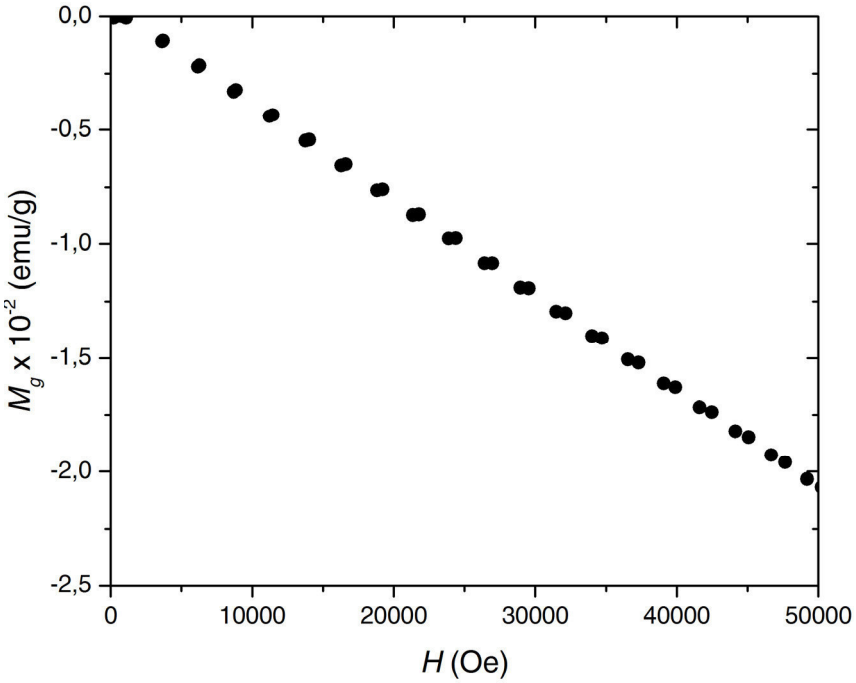

Figure S6. Mass magnetization M_g of Li_3NaGe_2 at 300 K over the field intensity range of 0–50000 Oe. The data were corrected for the sample holder diamagnetism.

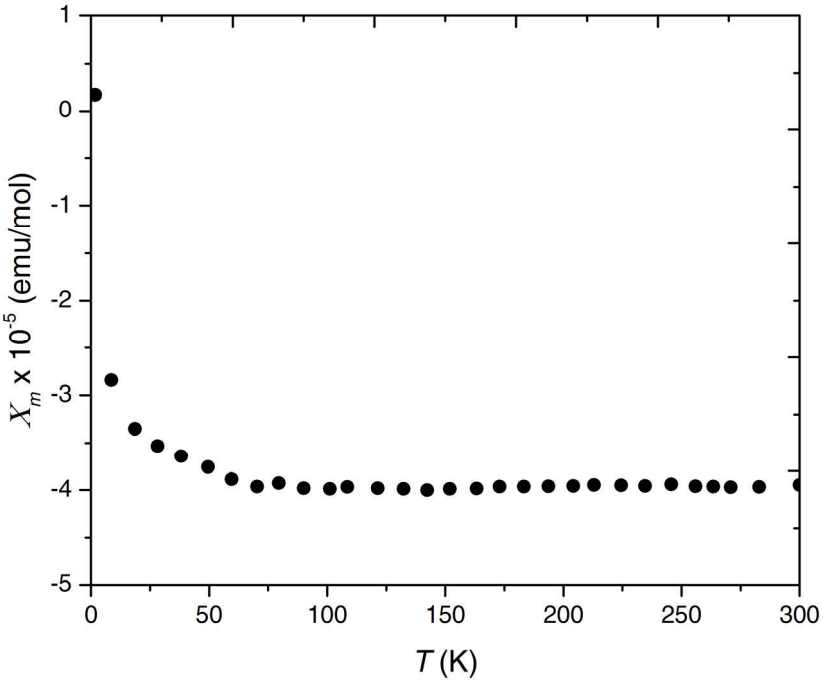

Figure S7. Molar susceptibility X_m of Li_3NaGe_2 at a field intensity H of 5000 Oe over the temperature range of 2–300 K. The data were corrected for the sample holder diamagnetism.

Vibrational analysis

Table S1. Assignment of the Raman-active vibrational modes of Li_3NaGe_2 (DFT-PBE/TZVP level of theory). The assignment of the peaks was carried out by visual inspection of the normal modes (Jmol program package[22]).

Frequency (cm^{-1})	Irrep	Assignment
40	A_g	Ge_2, Na, Li, lattice vibration[a], *ac*-plane
48	B_{2g}	Ge_2, Na, Li, lattice vibration, *b*-direction
81	B_{3g}	Ge_2, Na, Li, lattice vibration, *ac*-plane
84	B_{1g}	Ge_2 lattice vibration, *b*-direction
87	A_g	Ge_2 lattice vibration, *ac*-plane
98	A_g	Ge_2 lattice vibration, *ac*-plane
100	B_{3g}	Ge_2 lattice vibration, *ac* -plane
102	B_{2g}	Ge_2 tilting, Na, Li motion, in *ab*-plane
106	B_{1g}	Ge_2 tilting in *ab*-plane
111	B_{3g}	Ge_2 tilting in *ac*-plane
131	A_g	Na, Li1, Li2, Li3, *ac*-plane
139	B_{2g}	Na, *b*-direction
142	B_{3g}	Na, *ac*-plane
144	B_{1g}	Na, *b*-direction
150	A_g	Na, *ac*-plane
162	B_{3g}	Na, *ac*-plane
186	B_{3g}	Li1, Li2, Li3, Na, *ac*-plane
202	A_g	Li1, Li2, Li3, Na, *ac*-plane
224	B_{3g}	Asymmetric Ge=Ge stretch, Li motion in *ac*-plane
230	B_{3g}	Asymmetric Ge=Ge stretch, Li motion in *ac*-plane
235	A_g	Li1, Li3, *ac*-plane
248	B_{1g}	Li1, Li3, *b*-direction
251	A_g	Symmetric Ge=Ge stretch, Li motion in *ac*-plane
281	A_g	Li1, Li2, Li3, *ac*-plane
282	B_{3g}	Li1, Li2, Li3, *ac*-plane
286	A_g	Li1, Li2, Li3, *ac*-plane
288	B_{2g}	Li1, Li3, *b*-direction
301	B_{2g}	Li2, *b*-direction
303	B_{1g}	Li2, *b*-direction
320	B_{3g}	Li1, Li3, *ac*-plane
353	A_g	Li2 *ac*-plane
357	B_{3g}	Li1, Li2, *ac*-plane
373	B_{3g}	Li1, Li3, *ac*-plane
405	A_g	Li1, Li3, *ac*-plane
416	B_{2g}	Li1, Li3, *b*-direction
430	B_{1g}	Li1, Li3, *b*-direction

[a] Lattice vibration = low-frequency motion spanning the whole lattice

MAS NMR Spectra

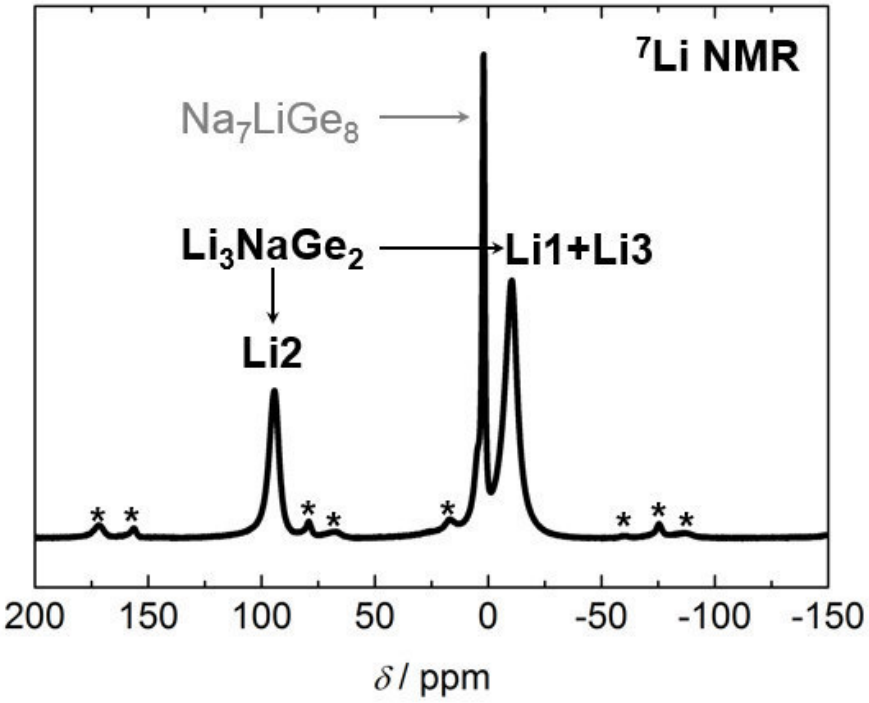

Figure S8. ^{7}Li MAS spectra of $^6Li_3NaGe_2$ (MAS 15 kHz, 11.7 T, RT). Rotational sidebands are marked by asterisks.

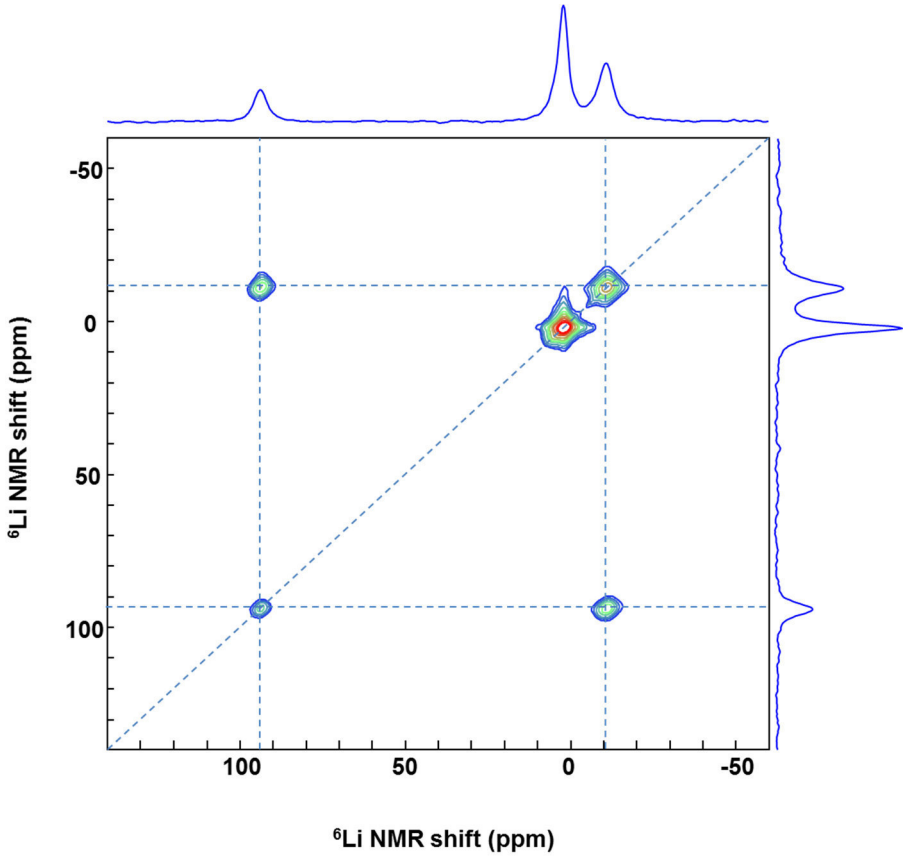

Figure S9. ^{6}Li spin-exchange spectra of Li_3NaGe_2 (mixing time 10 ms, MAS 7.7 kHz, 11.7 T, RT). Crosspeaks between the signals at -10 and 96 ppm show that the corresponding Li sites are close together in the unit cell.

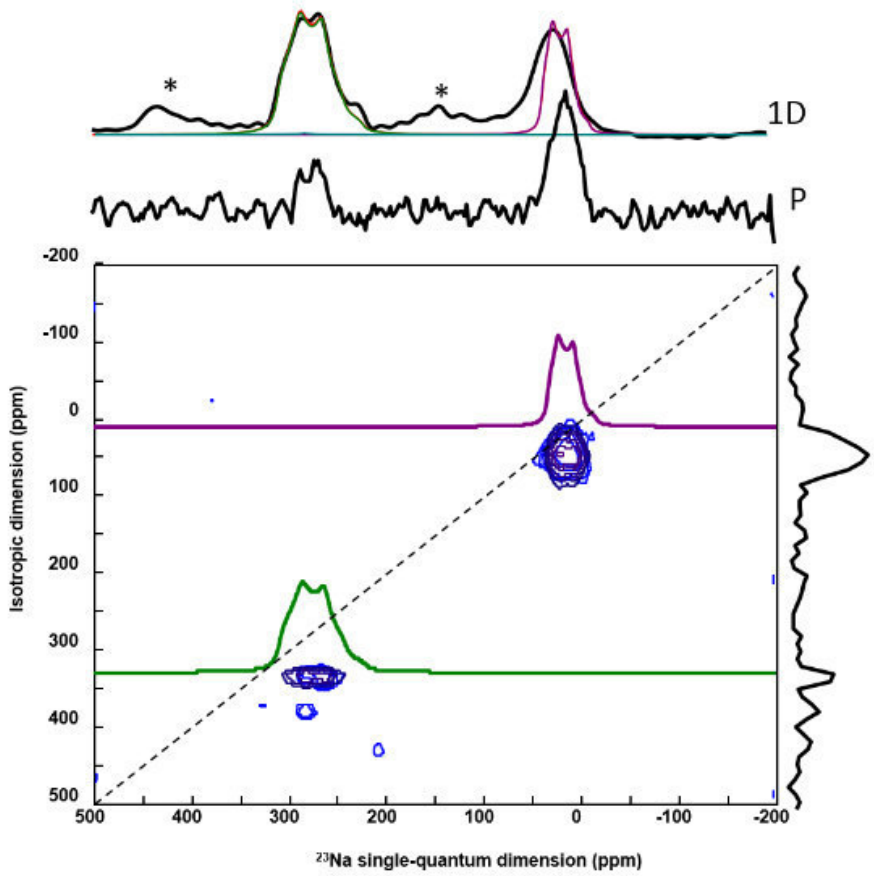

Figure S10. ^{23}Na MQMAS NMR spectra of $^{6}Li_3NaGe_2$ (MAS 5 kHz, 4.7 T, RT) along with lineshape simulation. At the relatively low magnetic field of 4.7 T, the quadrupole-induced shift and quadrupolar lineshape of the two signals is more pronounced. Lineshape parameters extracted from the simulation are given in Table S2.

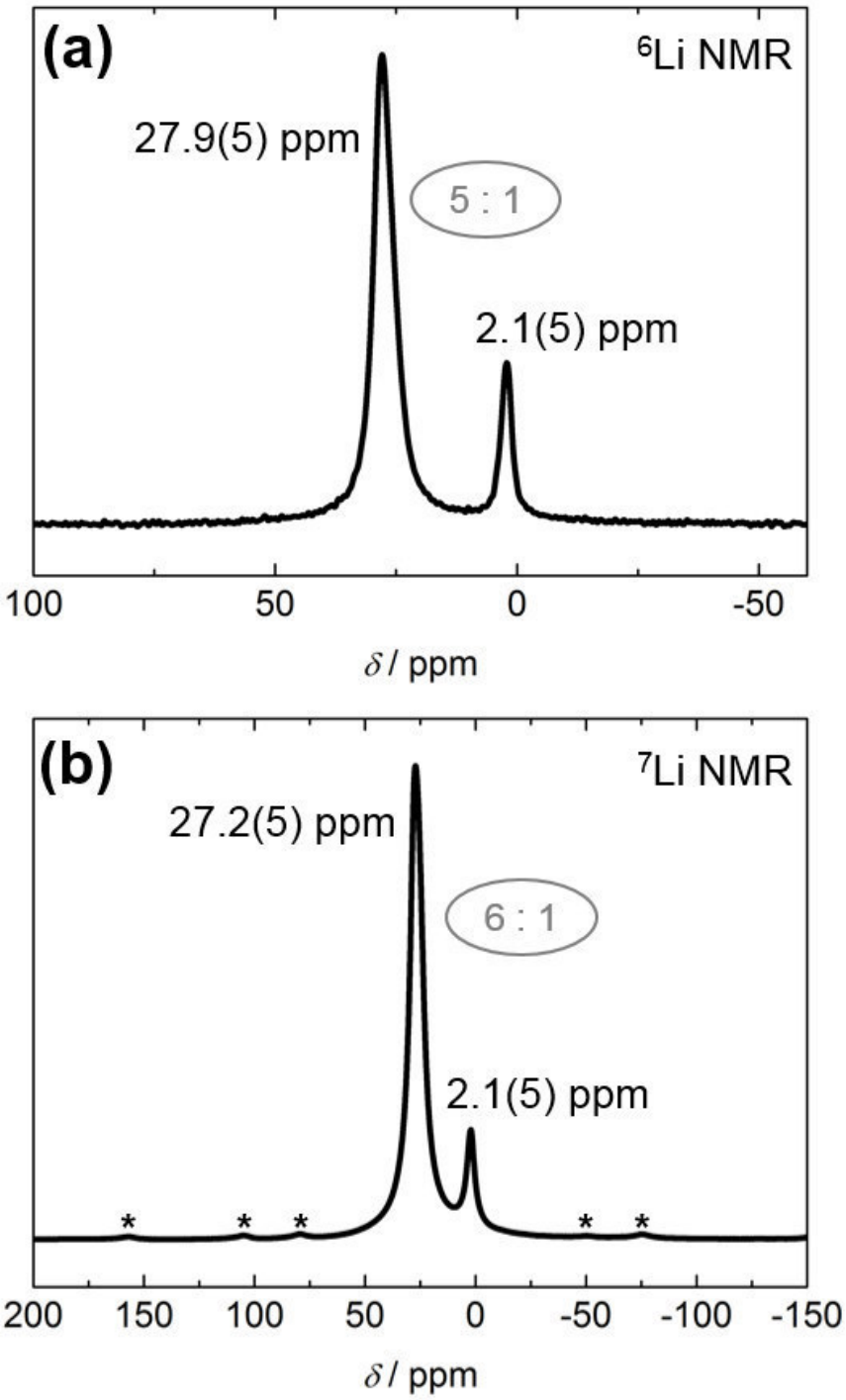

Figure S11. (a) ^{6}Li MAS (15 kHz) and **(b)** ^{7}Li MAS (15 kHz) NMR spectra of $Li_{14}Ge_6$ (RT, 11.7 T). The respective shift values are given in black and the integral intensities in grey. Rotational sidebands are marked by asterisks.

NMR/QM Data Summary

Table S2. [6;7]Li and [23]Na NMR parameters of Li_3NaGe_2 and Na_7LiGe_8 (impurity phase) derived from NMR signal line shape analysis. Furthermore, the spin-lattice relaxation time constants (T_1) at ambient temperature are given for the cases where they have been measured (otherwise denoted as not determined, n.d.).

Phase	Isotope	Assignment	δ_{iso} [1)] / ppm	$\Delta\delta_{aniso}$ [2)] / ppm	η_δ [3)]	C_Q [4)] / MHz	η_Q [5)]	T_1 [6)] / s
Li_3NaGe_2	^{6}Li	Li1+Li3	-10.0	70.0	0.0	$2.0\cdot10^{-3}$	0.1	10.67
		Li2	94.5	92.0	0.0	$1.0\cdot10^{-3}$	0.2	10.43
	^{7}Li	Li1+Li3	-10.4	30.0	0.0	0.10	0.1	1.32
		Li2	94.5	92.0	0.0	0.07	0.2	1.26
	^{23}Na	Na1[7)]	315.0	-70	0.0	2.00	0.4	0.11
		Na1[8)]	313.0	n.d.	n.d.	2.0	0.45	n.d.
Na_7LiGe_8	^{6}Li	Li1	1.9	-52.0	0.0	$3.0\cdot10^{-3}$	0.0	> 18.0
	^{7}Li	Li1	2.1	-52.0	0.0	0.15	0.0	n.d.
	^{23}Na	Na1	-8.0	-800.0	1.0	1.50	1.0	n.d.
		Na2	38.0	25.0	0.0	0.08	0.0	n.d.

[1] isotropic chemical/Knight shift; [2] chemical/Knight shift anisotropy; [3] chemical/Knight shift asymmetry parameter; [4] quadrupole coupling constant; [5] quadrupole asymmetry parameter; [6] spin-lattice relaxation time; [7] from 1D MAS NMR at 11.7 T; [8] from 2D MQMAS NMR at 4.7 T.

Table S3. [7]Li and [23]Na NMR parameters of Li_3NaGe_2 and Na_7LiGe_8 derived from DFT-PBE calculations. The Quadrupolar Coupling Constants (C_Q) and NMR chemical shifts have been calculated using the CRYSTAL and CASTEP program packages, respectively (see details for Electronic Structure Calculations above). The chemical shifts for Li_3NaGe_2 could not be calculated due to the metallic conductivity of the material.

Phase	Isotope	Atom	Wyckoff	δ_{iso} / ppm	δ_{aniso} / ppm	η_δ	C_Q / MHz	η_Q
Li_3NaGe_2	^{7}Li	Li1	4*c*	-	-	-	0.04	0.70
		Li2	4*c*	-	-	-	0.05	0.15
		Li3	4*c*	-	-	-	0.01	0.43
	^{23}Na	Na1	4*c*	-	-	-	-2.27	0.44
Na_7LiGe_8	^{7}Li	Li1	4*b*	1.3	-52.3	0	0.15	0
	^{23}Na	Na1	4*a*	6.7	-47.5	0.20	1.42	0.98
		Na2	24*d*	54	21.6	0	-0.08	0

Full basis set listings in CRYSTAL14 input format

```
Li
3 6
0 0 6 2.0 1.0
  6269.2628010      0.20540968826E-03
  940.31612431      0.15916554089E-02
  214.22107528      0.82869829707E-02
  60.759840184      0.33856374249E-01
  19.915152032      0.11103225876
  7.3171509797      0.27449383329
0 0 2 1.0 1.0
  2.9724674216      0.23792456411
  1.2639852314      0.30765411924
0 0 1 0.0 1.0
 0.51427489953      1.0000000000
0 1 1 0.0 1.0
 0.16               1.0 1.0
0 2 1 0.0 1.0
  3.327             1.0000000000
0 2 1 0.0 1.0
 0.40               1.0000000000

Na
11 9
0 0 7 2.0 1.0
  26041.109927      0.61806342811E-03
  3906.1268548      0.47748604414E-02
  888.97454993      0.24471684829E-01
  251.45497961      0.94755394977E-01
  81.650143512      0.26867496920
  28.904158401      0.47925475440
  10.625782932      0.33248591469
0 0 3 2.0 1.0
  53.769410179      0.19527731872E-01
  16.308243025      0.92648010794E-01
  2.3730384125     -0.39938670172
0 0 2 1.0 1.0
  0.95730772603     1.6428595391
  0.40806460959     0.55692596966
0 1 1 0.0 1.0
  0.20              1.0 1.0
0 1 1 0.0 1.0
  0.10              1.0 1.0
0 2 5 6.0 1.0
  138.07979989      0.57951891929E-02
  32.232700393      0.41620846251E-01
  9.9816075360      0.16281916885
  3.4822033928      0.36011784647
  1.2299134620      0.44858979889
0 2 1 0.0 1.0
  0.41743959423     1.0
0 3 1 0.0 1.0
  2.609             1.0
0 3 1 0.0 1.0
  0.207             1.0

Ge
32 14
0 0 8 2.0 1.0
  466115.00592      0.22487264660E-03
  69875.420762      0.17435426729E-02
  15903.276716      0.90691482206E-02
  4501.8233453      0.36906174685E-01
  1466.0570924      0.12050167907
  527.07841728      0.28748641703
  205.00395074      0.41622321885
  81.251596065      0.22397845695
0 0 4 2.0 1.0
  505.74661282     -0.25184609291E-01
  156.96593744     -0.11898929721
  25.761448176      0.54930135870
  11.106654687      0.52939309129
0 0 2 2.0 1.0
  17.272059104     -0.22854595728
  2.9438289048      0.68377930317
```

```
0 0 1 2.0 1.0
  1.2852272293       1.0000000000
0 0 1 0.0 1.0
 0.30110831584       1.0000000000
0 1 1 0.0 1.0
 0.11000000000       1.0 1.0
0 2 6 6.0 1.0
  2633.9346241      0.22143925310E-02
  624.00161628      0.18140899141E-01
  200.58528404      0.86632184922E-01
  75.097081525      0.25649020592
  30.214388474      0.42658611262
  12.440087567      0.26200527313
0 2 3 6.0 1.0
  45.981316002     -0.20321767678E-01
  6.9945654416      0.32013744527
  2.9686001327      0.59051014555
0 2 1 2.0 1.0
 1.2452540491        1.0000000000
0 2 1 0.0 1.0
 0.36766682938       1.0000000000
0 3 5 10.0 1.0
  122.93850231      0.10586544521E-01
  36.242755203      0.69601280945E-01
  13.191062921      0.22807035287
  5.2163136729      0.40301067220
  2.0927838749      0.41304847015
0 3 1 0.0 1.0
 0.81259117944       1.0000000000
0 3 1 0.0 1.0
 0.24600000000       1.0000000000
0 4 1 0.0 1.0
 0.36210645          1.0
```

References

[1] *APEX Suite of Crystallographic Software*, Bruker AXS Inc., Madison, WI, USA, **2008**.

[2] *SAINT*, Bruker AXS Inc., Madison, WI, USA, **2001**.

[3] *CELL_NOW*, Bruker AXS Inc., Madison, WI, USA, **2001**.

[4] *TWINABS*, Bruker AXS Inc., Madison, WI, USA, **2001**.

[5] G. M. Sheldrick, *Acta Crystallogr. Sect. A* **2008**, *64*, 112–122.

[6] G. A. Bain, J. F. Berry, *J. Chem. Educ.* **2008**, *85*, 532.

[7] a) T. Goebel, Y. Prots, A. Ormeci, O. Pecher, F. Haarmann, *Z. Anorg. Allg. Chem.* **2011**, *637*, 1982–1991; b) M. Waibel, O. Pecher, B. Mausolf, F. Haarmann, T. F. Fässler, *Eur. J. Inorg. Chem.* **2013**, *2013*, 5541-5546.

[8] F. Haarmann, in *eMagRes* (Eds.: R. K. Harris, R. E. Wasylishen), John Wiley & Sons, Ltd, Chichester, **2007**.

[9] R. K. Harris, E. D. Becker, *J. Magn. Reson.* **2002**, *156*, 323-326.

[10] D. Massiot, F. Fayon, M. Capron, I. King, S. Le Calvé, B. Alonso, J.-O. Durand, B. Bujoli, Z. Gan, G. Hoatson, *Magn. Reson. Chem.* **2002**, *40*, 70-76.

[11] *The Stuttgart Tight-Binding LMTO-ASA program*, M. v. Schilfgarde, T. A. Paxton, O. Jepsen, O. K. Andersen, G. Krier, Max-Planck-Institut für Festkörperforschung, Stuttgart, Germany, **1998**.

[12] U. v. Barth, L. Hedin, *J. Phys. C: Solid State Phys.* **1972**, *5*, 1629.

[13] O. Jepsen, O. K. Andersen, *Z. Phys. B: Condens. Matter* **1995**, *97*, 35-47.

[14] O. Andersen, O. Jepsen, *Phys. Rev. Lett.* **1984**, *53*, 2571-2574.

[15] a) R. Dovesi, R. Orlando, A. Erba, C. M. Zicovich-Wilson, B. Civalleri, S. Casassa, L. Maschio, M. Ferrabone, M. De La Pierre, P. D'Arco, Y. Noel, M. Causa, M. Rerat, B. Kirtman, *Int. J. Quantum Chem.* **2014**, *114*, 1287-1317; b) R. Dovesi, V. R. Saunders, C. Roetti, R. Orlando, C. M. Zicovich-Wilson, F. Pascale, B. Civalleri, K. Doll, N. M. Harrison, I. J. Bush, P. D'Arco, M. Llunell, M. Causa, Y. Noel, (Ed.: C. U. s. Manual), University of Torino, Torino, **2014**.

[16] a) J. P. Perdew, K. Burke, M. Ernzerhof, *Phys. Rev. Lett.* **1996**, *77*, 3865-3868; b) F. Weigend, R. Ahlrichs, *Phys. Chem. Chem. Phys.* **2005**, *7*, 3297-3305.

[17] a) F. Pascale, C. M. Zicovich-Wilson, F. Lopez Gejo, B. Civalleri, R. Orlando, R. Dovesi, *J. Comput. Chem.* **2004**, *25*, 888-897; b) C. M. Zicovich-Wilson, F. Pascale, C. Roetti, V. R. Saunders, R. Orlando, R. Dovesi, *J. Comput. Chem.* **2004**, *25*, 1873-1881.

[18] S. J. Clark, M. D. Segall, C. J. Pickard, P. J. Hasnip, M. I. J. Probert, K. Refson, M. C. Payne, *Z. Kristallogr.* **2005**, *220*, 567.

[19] D. Vanderbilt, *Phys. Rev. B* **1990**, *41*, 7892-7895.

[20] a) C. J. Pickard, F. Mauri, *Phys. Rev. B* **2001**, *63*, 245101; b) J. R. Yates, C. J. Pickard, F. Mauri, *Phys. Rev. B* **2007**, *76*, 024401.

[21] a) *Gaussian 09, Revision C.01*, M. J. Frisch, G. W. Trucks, H. B. Schlegel, G. E. Scuseria, M. A. Robb, J. R. Cheeseman, G. Scalmani, V. Barone, B. Mennucci, G. A. Petersson, H. Nakatsuji, M. Caricato, X. Li, H. P. Hratchian, A. F. Izmaylov, J. Bloino, G. Zheng, J. L. Sonnenberg, M. Hada, M. Ehara, K. Toyota, R. Fukuda, J. Hasegawa, M. Ishida, T. Nakajima, Y. Honda, O. Kitao, H. Nakai, T. Vreven, J. A. Montgomery Jr., J. E. Peralta, F. Ogliaro, M. Bearpark, J. J. Heyd, E. Brothers, K. N. Kudin, V. N. Staroverov, R. Kobayashi, J. Normand, K. Raghavachari, A. Rendell, J. C. Burant, S. S. Iyengar, J. Tomasi, M. Cossi, N. Rega, J. M. Millam, M. Klene, J. E. Knox, J. B. Cross, V. Bakken, C. Adamo, J. Jaramillo, R. Gomperts, R. E. Stratmann, O. Yazyev, A. J. Austin, R. Cammi, C. Pomelli, J. W. Ochterski, R. L. Martin, K. Morokuma, V. G. Zakrzewski, G. A. Voth, P. Salvador, J. J. Dannenberg, S. Dapprich, A. D. Daniels, Ö. Farkas, J. B. Foresman, J. V. Ortiz, J. Cioslowski, D. J. Fox, Gaussian, Inc., Wallingford, CT, **2009**; b) C. Adamo, V. Barone, *The Journal of Chemical Physics* **1999**, *110*, 6158-6170.

[22] Jmol: an open-source Java viewer for chemical structures in 3D. http://www.jmol.org

5.3 The Ternary Zintl Phases $K_{4-x}Na_xSi_4$ ($1 \leq x \leq 2.2$) and K_7NaSi_8 – Synthesis, Crystal Structure, and Chemical Bonding

ChemPubSoc Europe

DOI: 10.1002/ejic.201600735

EurJIC European Journal of Inorganic Chemistry

Full Paper

Zintl Phases

Zintl Phases $K_{4-x}Na_xSi_4$ ($1 \le x \le 2.2$) and K_7NaSi_8: Synthesis, Crystal Structures, and Solid-State NMR Spectroscopic Investigations

Lavinia M. Scherf,[a] Oliver Pecher,[b] Kent J. Griffith,[b] Frank Haarmann,[c,d] Clare P. Grey,[b] and Thomas F. Fässler*[a]

Abstract: The Zintl phases $K_{4-x}Na_xSi_4$ ($1 \le x \le 2.2$) and K_7NaSi_8 are the first representatives of the K–Na–Si system, and both contain tetrahedral $[Si_4]^{4-}$ clusters and a charge-balancing number of K^+ and Na^+ cations. All phases of $K_{4-x}Na_xSi_4$ ($1 \le x \le 2.2$) crystallize in a new structure type with space group $P2_1/n$, as determined by single-crystal X-ray diffraction analysis of the parent phase K_3NaSi_4. Rietveld refinement of the X-ray diffraction data showed that the solid solutions follow Vegard's rule. K_7NaSi_8 can only be synthesized by diffusion-controlled reaction of binary precursors and is isostructural with known $A_7A'T_8$ (A = Na–Cs; A' = Li, Na; T = Si, Ge) phases. A combination of solid-state NMR investigations and quantum mechanical calculations served to show the anisotropic chemical bonding behavior of all the atoms in K_7NaSi_8, which is additionally compared with the related phases A_7NaSi_8 (A = Rb, Cs).

Introduction

Most binary alkali-metal silicides and germanides in the phase systems A–T (A = Li–Cs; T = Si, Ge) are typical examples of Zintl phases. These polar intermetallic compounds can be described by a formal electron transfer from the electropositive alkali metal (A) to the more electronegative tetrel (T) atoms. The resulting tetrel anions form substructures that can often be rationalized by using the octet or (8 – N) rule.[1]

In lithium tetrelides, the Li cations can stabilize a large variety of polyanions of the tetrel elements[2] as a result of strong covalent contributions to the Li–T bonds. Such polyanions include 3D substructures in the compounds LiT[3] and 2D slabs of T atoms in Li_7Ge_{12} and Li_3NaSi_6.[4,5] Often, small anionic tetrel clusters are observed, such as dumbbells in Li_7T_3[6] and Li_3NaGe_2[7] and Friauf polyhedra $[Li@Li_4Ge_7]^{12-}$ in $Li_{18}Na_2Ge_{17}$ and Li_7RbGe_8.[8] The latter two Zintl phases also contain tetrahedral $[Ge_4]^{4-}$ clusters. Li-rich binary tetrelides, such as $Li_{17}T_4$, $Li_{4.1}T_4$, and $Li_{15}T_4$, seem to evade compositions such as Li_4T, which would allow a salt-like and valence-electron-precise situation.[9]

In contrast, alkali metals heavier than lithium only form less alkali-metal-rich silicides and germanides with binary A_4T_4 (A = Na–Cs)[10,11] being the most alkali-metal-rich phases. Aside from clathrate-type phases,[12] their anionic substructures comprise either only tetrahedral $[T_4]^{4-}$ or deltahedral $[T_9]^{4-}$ clusters or both. These clusters are separated and balanced by an appropriate number of alkali-metal cations, resulting in various binary and ternary Zintl phases with differing structure types. Binary phases include A_4T_4 (A = Na–Cs),[10,11] A_4Ge_9 (A = K–Cs)[13] and $A_{12}T_{17}$ (A = Na, K),[14] and the ternary phases A_7NaSi_8 (A = Rb, Cs),[15–18] A_7NaGe_8 (A = K–Cs),[19,20] $Cs_2Na_2Ge_4$[21] and $K_6Rb_6Si_{17}$[22] have also been reported. Additionally, the semiconductor Ba_2Si_4 with slightly distorted $[Si_4]^{4-}$ units[23,24] as well as the metallic Zintl phase Ba_3Si_4 comprising butterfly-like $[Si_4]^{6-}$ anions[25] have been prepared.

Alkali-metal silicides and germanides have proven to be suitable precursors for a broad range of new Si and Ge materials. For example, the thermal decomposition of Na_4Si_4 under vacuum yields the guest-free clathrate $\square_{24}Si_{136}$.[26] Guest-free Ge clathrates $\square_{24}Ge_{136}$ can be prepared by the oxidation of Na_4Ge_9 in ionic liquids.[27] The oxidation of Li_7Ge_{12} with protic solvents leads to the topochemical formation of *allo*-Ge, a crystalline Ge allotrope.[4,5,28] Amorphous Si is obtained upon both the oxidation of Li_3NaSi_6 with protic solvents and the extraction of $Li_{15}Si_4$ with liquid ammonia.[29] Using surfactants, elemental nanostructures such as hexagonal mesoporous Ge can be synthesized from K_4Ge_9 and polymeric $^1{}_\infty[Ge_9]^{2-}$ solutions.[30] Poly(methyl methacrylate) (PMMA) opals can function as templates for the synthesis of inverse opal-structured Ge from solutions of $[Ge_9]^{4-}$ clusters.[31]

In addition, Zintl phases containing tetrahedral $[Si_4]^{4-}$ and $[Ge_4]^{4-}$ anions have been shown to be efficient precursors for

[a] *Department of Chemistry, Technical University of Munich, Lichtenbergstraße 4, 85747 Garching/München, Germany*
E-mail: Thomas.faessler@lrz.tum.de
http://www.ch.tum.de/faessler/
[b] *Department of Chemistry, University of Cambridge, Lensfield Road, Cambridge CB2 1EW, UK*
[c] *Institute of Inorganic Chemistry, RWTH Aachen University, Landoltweg 1, 52073 Aachen, Germany*
[d] *Max Planck Institute for Chemical Physics of Solids, Nöthnitzer Str. 40, 01187 Dresden, Germany*
Supporting information and ORCID(s) from the author(s) for this article are available on the WWW under http://dx.doi.org/10.1002/ejic.201600735.

nanocrystalline Si and Ge. Kauzlarich and co-workers have shown that binary Na_4Si_4, K_4Si_4, and Na_4Ge_4 as well as ternary Rb_7NaSi_8 can be reduced to Si and Ge nanoparticles upon reaction with TCl_4 or NH_4Br.[32] Depending on the workup procedure, the particle surfaces can be capped with different functional groups.[33,34] In addition, it was possible to monitor the synthesis of alkyl-capped Si nanoparticles from Na_4Si_4 and $SiCl_4$ by NMR spectroscopy.[34] Furthermore, the binary compounds A_4T_4, A_4Ge_9, and $A_{12}T_{17}$ are frequently used as precursors for the preparation and modification of Zintl clusters in solution.[35,36]

The combined application of NMR spectroscopy and quantum mechanical (QM) calculations allows the chemical bonding in intermetallic phases and the anisotropy of the charge distribution to be investigated and rationalized.[37,38] Anisotropy is a result of the so-called quadrupole coupling, that is, the interaction of the electric field gradient (EFG) with the nuclear quadrupole moment.[37] Some of us have recently applied this approach to gain insights into the chemical bonding in the Zintl phases A_4Si_4 (A = Na–Cs) and A_7NaSi_8 (A = Rb, Cs), which all contain tetrahedral $[Si_4]^{4-}$ clusters.[15,16,23] In the solid solutions $Rb_7NaSi_{8-x}Ge_x$, the presence of mixed $(Si_{4-x}Ge_x)^{4-}$ clusters could be proven by using these techniques.[36]

To broaden the selection of possible precursors for Zintl ions in solution and the synthesis of novel materials we have been searching for new alkali-metal tetrelides by mixing different alkali-metal cations. As seen in the various ternary phases, employing cations of different sizes such as Na and K can stabilize different structure types and polyanions. Herein, we present the synthesis of two new Zintl phases of the $K_{4-x}Na_xSi_4$ system comprising tetrahedral $[Si_4]^{4-}$ clusters: The solid solutions $K_{4-x}Na_xSi_4$ ($1 \le x \le 2.2$) and K_7NaSi_8 were structurally characterized by X-ray diffraction (XRD) and solid-state NMR spectroscopy, and QM calculations were utilized to gain insights into the chemical bonding of K_7NaSi_8 in a comparative study with A_7NaSi_8 (A = Rb, Cs).

Results and Discussion

The $K_{4-x}Na_xSi_4$ System

Figure 1 shows the different phases identified in the $K_{4-x}Na_xSi_4$ system as part of this study. Prior to this work only the binary phases K_4Si_4 ($P\bar{4}3n$)[11] and Na_4Si_4 ($C2/c$)[39] were known, with K_3NaSi_4 and $K_{3.5}Na_{0.5}Si_4$, which crystallize in the space groups $P2_1/n$ and $Pa\bar{3}$, respectively, being identified for the first time.

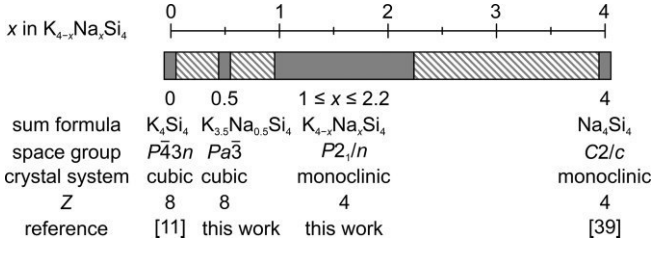

Figure 1. Zintl phases in the $K_{4-x}Na_xSi_4$ system and their structure types. Gray blocks symbolize single-phase regions and shaded areas are two-phase regions.

K_4Si_4, $K_{3.5}Na_{0.5}Si_4$, and Na_4Si_4 are stoichiometrically exact phases, whereas solid solutions such as K_3NaSi_4 exist for $1 \le x \le 2.2$. The four phases crystallize in four different structure types and space groups. $K_{3.5}Na_{0.5}Si_4$ is isostructural with the known phases A_7NaSi_8 (A = Rb, Cs),[15,16] K_7LiGe_8,[18] A_7NaGe_8 (A = K–Cs),[19,20] and A_7LiSi_8 (A = K–Cs)[17,18] and will therefore be denoted as K_7NaSi_8 from now on.

Synthesis of K_3NaSi_4

In an initial experiment aimed at the synthesis of "K_3NaSi_9", the novel ternary Zintl phase K_3NaSi_4 was obtained in addition to unreacted Si. Nearly phase-pure K_3NaSi_4 can be synthesized from the binary precursors K_4Si_4 and Na_4Si_4 according to Equation (1) or from a stoichiometric mixture of the pure elements at 600 °C in sealed Nb ampoules. The latter synthesis method yielded single crystals suitable for X-ray diffraction analysis.

$$3\ K_4Si_4 + Na_4Si_4 \rightarrow 4\ K_3NaSi_4 \quad (1)$$

K_3NaSi_4 crystallizes in the monoclinic space group $P2_1/n$ (Table 1) with a new structure type comprising three K, one Na, and four Si positions (all Wyckoff positions 4*e*, Figure 2a). The Si atoms form a slightly distorted $[Si_4]^{4-}$ tetrahedron with typical Si distances (2.38–2.46 Å) and angles (58.6–61.6°). Its coordination sphere (Figure 2b) consists of three face-capping η^3-K ligands, two η^2-Na and η^2-K ligands each, and eight terminal ligands (seven K and one Na). The corresponding K–Si and Na–Si distances of 3.30–3.86 and 2.98–3.11 Å, respectively (see Table S2 in the Supporting Information), are comparable to those in K_4Si_4 and Na_4Si_4.[11,39]

Table 1. Crystal structure data for K_3NaSi_4.

Empirical formula	K_3NaSi_4
M_r [g mol^{-1}]	252.65
Crystal size [mm]	0.31 × 0.20 × 0.14
Crystal shape	block
Crystal system	monoclinic
Space group	$P2_1/n$ (no. 14)
a [Å]	6.6791(5)
b [Å]	13.685(1)
c [Å]	10.7427(9)
β [°]	100.667(4)
V [Å^3]	965.0(1)
Z	4
$d_{calcd.}$ [g cm^{-3}]	1.739
μ(Mo-K_α) [mm^{-1}]	1.868
F(000) [e]	496
Θ range [°]	2.44–31.62
hkl range	±8, ±16, ±12
Refl. measured	22693
Refl. unique	1753
R_{int}	0.0526
Parameters refined	73
Restraints	0
$R(F)/wR(F^2)$[a] [$I > 2\sigma(I)$]	0.0346/0.0920
$R(F)/wR(F^2)$[a] (all reflections)	0.0395/0.0961
GoF (F^2)[b]	1.244
$\Delta\varrho_{fin}$ (max/min) [e Å^{-3}]	0.443/–0.448

[a] $R(F) = ||F_o| - |F_c||/\Sigma|F_o|$, $wR(F^2) = [\Sigma w(F_o^2 - F_c^2)^2/\Sigma w(F_o^2)^2]^{1/2}$, $w = [\sigma^2(F_o^2) + (0.0318P)^2 + 3.4316]^{-1}$ in which $P = (F_o^2 + 2F_c^2)/3$. [b] GoF = $[\Sigma w(F_o^2 - F_c^2)^2/(n_{obs} - n_{param})]^{1/2}$.

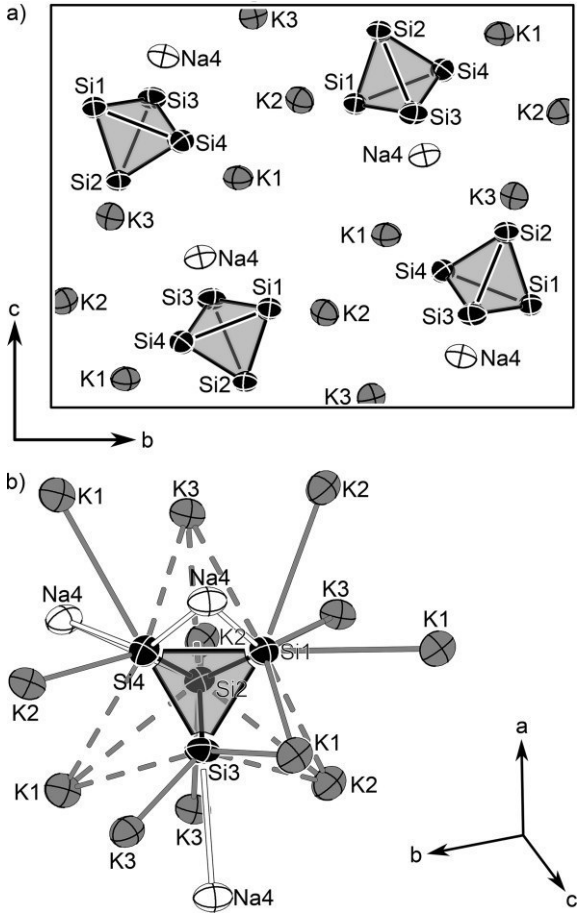

Figure 2. (a) Projection of the unit cell of K_3NaSi_4 onto the *bc* plane. (b) Coordination sphere of the $[Si_4]^{4-}$ tetrahedra. Anisotropic displacement parameters are shown at the 90 % probability level at 100 K.

Solid Solutions $K_{4-x}Na_xSi_4$ ($1 \le x \le 2.2$)

Further experiments on the K–Na–Si system revealed that K_3NaSi_4 is not a stoichiometrically exact phase but rather a solid solution $K_{4-x}Na_xSi_4$ with $1 \le x \le 2.2$ in which the K cations can be partially substituted by more Na cations.[40]

The solid solution range was obtained from Rietveld analysis (see Table S4 in the Supporting Information) of powder X-ray diffraction patterns obtained from a series of products obtained by the mixing of binary phases [Equation (2)]. Rietveld-refined diffraction patterns of $K_{4-x}Na_xSi_4$ with $1 \le x \le 2.2$ are shown in Figures S2–S5.

$$(4 - x)\ K_4Si_4 + x\ Na_4Si_4 \rightarrow 4\ K_{4-x}Na_xSi_4\ (x = 1, 1.5, 2, 2.5) \quad (2)$$

While higher Na contents in the initial reaction mixture led to the appearance of Na_4Si_4 as a side-phase, reaction mixtures with Na contents of $x \le 1$ contain the new ternary phase K_7NaSi_8, which will be discussed in a later section.

In accordance with Vegard's rule,[41] the unit-cell volume of the solid solution $K_{4-x}Na_xSi_4$ in the space group $P2_1/n$ decreases approximately linearly with increasing Na content (Figure 3a). As expected, these unit-cell volumes are between those of K_4Si_4 and $K_{3.5}Na_{0.5}Si_4$ on the one hand and Na_4Si_4 on the other. The cell parameters *a*, *b*, and *c* for the monoclinic solid solutions ($1 \le x \le 2.2$) also change linearly but not uniformly (Figure 3b): *a* decreases slightly, *b* decreases significantly, and *c* increases with increasing Na content.

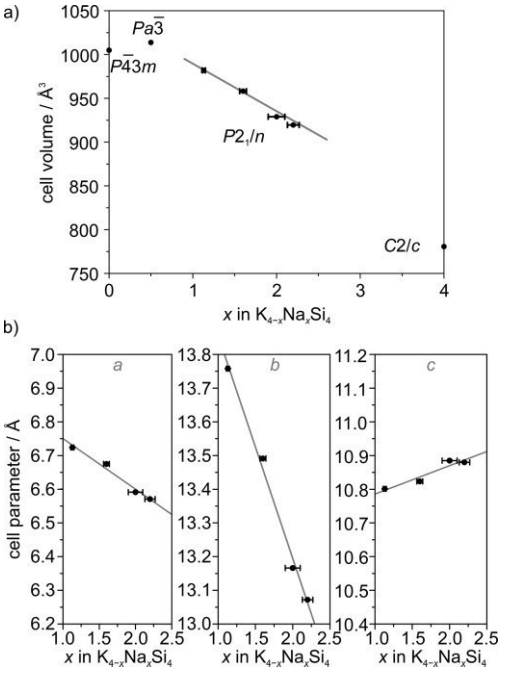

Figure 3. (a) Cell volumes of all $K_{4-x}Na_xSi_4$ phases normalized to $Z = 4$. (b) Vegard plots[41] illustrating the linear change in cell parameters in space group $P2_1/n$ with increasing Na content in solid solutions $K_{4-x}Na_xSi_4$ ($1 \le x \le 2.2$; alkali-metal ratios *x* from Rietveld refinement). Vertical error bars are too small to be visible.

These different changes in cell parameters appear reasonable when taking into account the non-random substitution behavior of Na in $P2_1/n$ solid solutions (Table 2): The crystallographic positions K1 and Na4 are exclusively occupied by K and Na, respectively. K2 and K3 can, however, be substituted by Na, but substitution of K3 is clearly preferred up to full Na occupancy. In contrast, K2 is only partially substituted by Na with a maximum Na content of 0.22(4) at this position.

Table 2. Site occupancy factors (s.o.f.) of the four alkali-metal positions K1/Na1 to K4/Na4 in solid solutions $K_{4-x}Na_xSi_4$ in space group $P2_1/n$ (*x* from Rietveld refinement).

x in $K_{4-x}Na_xSi_4$	1.13(2)	1.60(4)	2.0(1)	2.20(7)
s.o.f. K1	1	1	1	1
s.o.f. Na1	0	0	0	0
s.o.f. K2	1	0.85(2)	0.87(6)	0.78(4)
s.o.f. Na2	0	0.15	0.13	0.22
s.o.f. K3	0.87(2)	0.55(2)	0.09(5)	0.02(3)
s.o.f. Na3	0.13	0.45	0.91	0.98
s.o.f. K4	0	0	0	0
s.o.f. Na4	1	1	1	1

This substitution behavior can be rationalized by a closer inspection of the coordination spheres around the different al-

kali-metal sites in K_3NaSi_4 (see Figure S1 in the Supporting Information). The first coordination spheres contain five to seven Si atoms with interatomic distances of up to 3.856(2) Å (all *A*–Si distances are given in Table S2). A second coordination sphere is clearly distinguished with *A*–Si distances starting from 4.034(2) Å. We used average *A*–Si distances as a measure of the space available at the different alkali-metal sites. Whereas atom K1 has the longest average distance of 3.603(1) Å to Si atoms, the K2 and K3 sites are significantly smaller with average K–Si distances of 3.475(1) and 3.468(1) Å, respectively. The average Na4–Si distance of 3.050(2) Å is again much shorter, as is expected for the smaller alkali-metal cation. Therefore, the largest alkali-metal site K1 can only stabilize K atoms, whereas K/Na mixing can occur at the smaller K2 and K3 sites. Concurrently, the average *A*–Si distances for K2 and K3 decrease significantly with increasing Na content (see Table S3).

Synthesis of K_7NaSi_8

Experiments aimed at the synthesis of the Na-poor phases $K_{4-x}Na_xSi_4$ with $x \leq 1$ always yielded mixtures of K_3NaSi_4 and K-richer side-phases. However, the identities of the side-product phases depend on the method of synthesis. Although all high-temperature syntheses and those starting from the elements simply yielded binary K_4Si_4, a different side-phase was obtained by using the binary reactants route. This side-phase was identified as K_7NaSi_8 by Rietveld refinement. Purer samples were obtained from the reaction of a stoichiometric mixture of the binary reactants K_4Si_4 and Na_4Si_4 [Equation (3)], as described for Rb_7NaSi_8 and Cs_7NaSi_8,[15,16,42] allowing reliable characterization by Rietveld refinement (Table 3 and Table S4 in the Supporting Information).

$$7\ K_4Si_4 + Na_4Si_4 \rightarrow 4\ K_7NaSi_8 \quad (3)$$

Table 3. Crystallographic data of K_7NaSi_8 obtained from powder diffraction data by Rietveld refinement, adapted from K_7LiSi_8.[17]

Empirical formula	K_7NaSi_8[a]
M_r [g mol^{-1}]	521.4
T [K]	293
Powder color	gray
Crystal system	cubic
Space group	$Pa\bar{3}$ (no. 205)
Lattice parameters	
a [Å]	12.6563(7)
V [Å^3]	2027.3(2)
Z	4
$d_{calcd.}$ [g cm^{-3}]	1.7082
μ(Cu-K_α) [mm^{-1}]	18.308
Θ range [°]	5.00–89.76
R [$I > 3\sigma(I)$]	0.0307
wR [$I > 3\sigma(I)$]	0.0317
R (all)	0.0364
wR (all)	0.0324
Goodness of fit	1.38

[a] Sample contains 29.2(5) % K_4Si_4. Slight traces of $K_{4-x}Na_xSi_4$ ($x \approx 1$) could not be quantified.

As mentioned earlier, K_7NaSi_8 is isostructural with the known $A_7A'T_8$ phases. Its bright-red color is typical of the silicides $A_7A'Si_8$, which, in contrast to the black $A_7A'Ge_8$ phases, have been described as red and transparent.[18] K_7NaSi_8 crystallizes in the cubic space group $Pa\bar{3}$ with a = 12.6563(7) Å, similar to the cell parameters of cubic K_4Si_4 (a = 12.62 Å; $P\bar{4}3n$).[11] Although the cell parameters of the two cubic phases are so similar, they can be clearly distinguished by Rietveld refinement (see Figure S6 in the Supporting Information). The Zintl phase comprises tetrahedral $[Si_4]^{4-}$ units that are connected to form dimers through η^3-capping Na cations (Figure 4a,b). η^3-Coordination of the tetrahedron yields a K_3NaSi_4 heterocubane in which each Si atom is further coordinated by three terminal K atoms (Figure 4c).

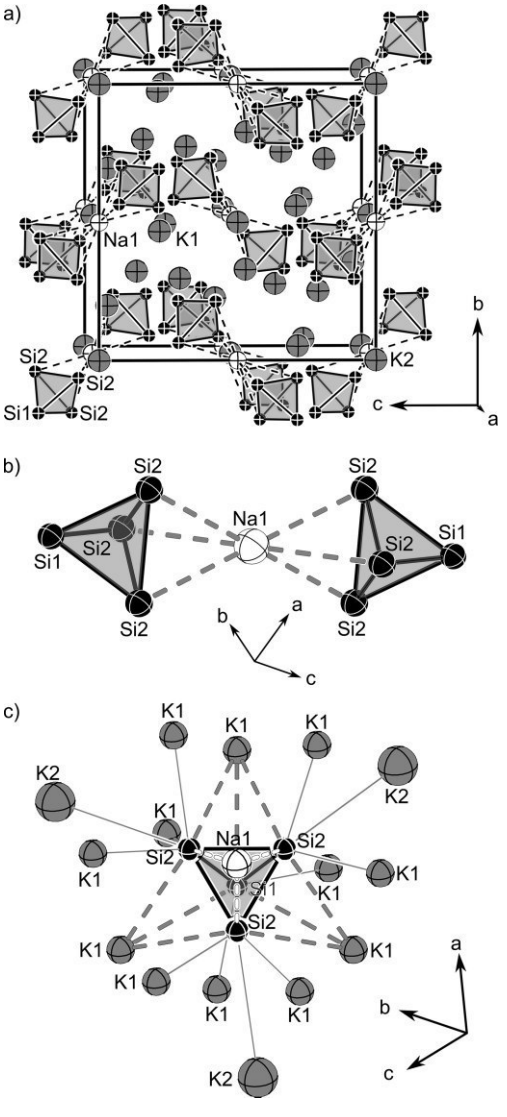

Figure 4. (a) Projection of the unit cell of K_7NaSi_8 onto the *bc* plane. (b) $[Na(Si_4)_2]^{7-}$ unit with two clusters linearly coordinating Na. (c) Coordination sphere of $[Si_4]^{4-}$ tetrahedra. Isotropic displacement parameters are shown at the 70 % probability level at 293 K. K atoms are shown in gray, Na atoms in white, and Si atoms in black.

The Si–Si distances in the slightly distorted tetrahedra are in the range of 2.38–2.48 Å with the longest bonds surrounding

the triangular face capped by Na. The Na–Si distance of 2.919(5) Å is in the range of those in A_7NaSi_8 (A = Rb, Cs).[15,16] The K1–Si distances are also typical and in the range of 3.36–3.69 Å, whereas K2 is very distant from its six neighboring Si atoms at 3.905(4) Å. Previous studies have shown that the alkali-metal cation in this large cavity can be substituted by larger alkali metal atoms to yield the quaternary $AA'_6A''T_8$ aristotype. One such quaternary example is CsK_6NaSi_8,[18] which is closely related to the phase described here. Substitution of the K2 position by the larger Cs atom also seems to stabilize the quaternary phase. Attempts to synthesize K_7NaSi_8 directly from the elements only yielded mixtures of K_4Si_4 and K_3NaSi_4. Thus, K_7NaSi_8 is only accessible from a diffusion-controlled solid-state reaction of the binary starting materials, whereas CsK_6NaSi_8 is readily available from a stoichiometric melt of the constituent elements.

Solid-State NMR Analysis and QM Calculations on K_7NaSi_8

In agreement with the Rietveld refinement, solid-state NMR investigations of a K_7NaSi_8 sample showed that this phase is the majority phase showing one Na and two Si signals at δ = 91.0, –369.7, and –357.2 ppm from the respective crystallographic Na1, Si1, and Si2 positions (Figures 4 and 5, Tables 4 and 5). Although second-order quadrupole coupling results in broad ^{23}Na NMR MAS and static signal line shapes, comparably high-resolution ^{29}Si NMR signals are visible for the anions (Figure 5). Additional signals and line-shape features are due to the minority phases of K_3NaSi_4, Na_4Si_4, K_4Si_4, and Na metal (Figure 5 and Figures S7–S9 in the Supporting Information).[43] The assignment of the ^{23}Na metal signal is straightforward due to the Knight-shifted metal resonance at δ = 1120 ppm (see Figure S7 and Table 5). An unambiguous assignment of all other impurity signals is possible through fits of the NMR line shapes by consideration of NMR coupling parameters derived from QM calculations as starting values (Figure 5, Tables 4 and 5), with the calculations based on both the known crystal structures of the binary precursor phases as well as the ones for K_3NaSi_4 and K_7NaSi_8 (Tables 1 and 3–5, and Exp. Sect.). The parameters derived from the NMR data and calculations show reasonable agreement within experimental error and support the application of NMR spectroscopy in combination with theory to gain insights into materials on the local atomic scale even for these multiphase samples.

Interestingly, no ^{29}Si NMR signals from Na_4Si_4 (Si1 and Si2) or K_3NaSi_4 (Si1–Si4) were detected in the measurements, although these minority phases are visible in the ^{23}Na NMR spectra (Figure 5). Presumably, this is due to the very small amounts of these phases in the investigated K_7NaSi_8 sample, which is furthermore in agreement with the 7:1 ratio of the binary precursor phases [Equation (3)]. Calculations showed that the ^{29}Si NMR chemical shifts of K_3NaSi_4 span a range of δ = –366.4 to –316.9 ppm for Si1–Si4 and lie in the same frequency range as the signals of K_4Si_4 and K_7NaSi_8, which suggests that our inability to detect K_3NaSi_4 resonances is either a signal-to-noise ratio or possibly a relaxation issue rather than our inability to locate the resonance due to the choice of an inappropriate frequency offset.

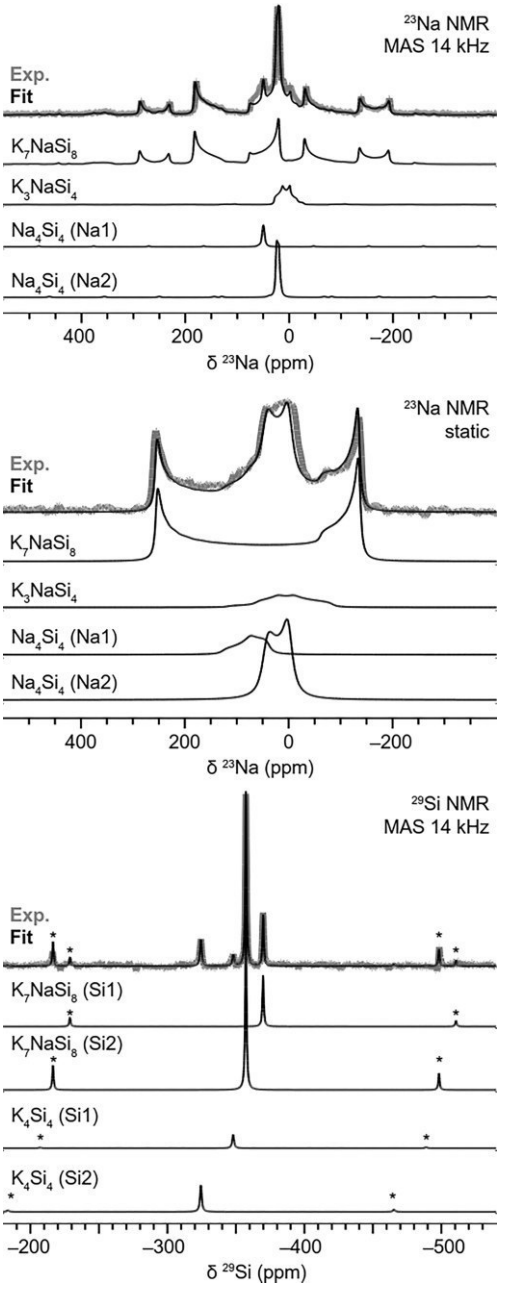

Figure 5. (a) ^{23}Na MAS, (b) ^{23}Na static, and (c) ^{29}Si MAS NMR spectra of K_7NaSi_8. MAS speeds of 14 kHz were applied; rotational side-bands are marked by asterisks. Experimental data in thick gray, the line-shape fit and its contributions in black lines. Signal contributions from different phases are highlighted and labelled in the figure.

We now focus on a discussion of the NMR parameters of K_7NaSi_8, all of which have been derived by the combined application of solid-state NMR experiments and QM calculations, thereby enabling a discussion of the chemical bonding within the series A_7NaSi_8 with A = K, Rb,[15] and Cs[16] (see Table S7 in the Supporting Information). With increasing alkali-metal atomic number an increase in the ^{29}Si chemical shift is seen for Si1 and Si2 with the same trend of δ_{iso}(Si2) > δ_{iso}(Si1) for all three phases (see Table S7 and Figure S10). This tendency is in agreement with the order of the shifts in signals of A_4Si_4 (A =

Table 4. ^{29}Si NMR coupling parameters derived from NMR signal line-shape analysis (exp.) and QM calculations (calcd.).[a]

Atom		δ_{iso} [ppm]	δ_{aniso} [ppm]	η_δ[b]	Integral
K_7NaSi_8 (maj.)					
Si1	exp.	−369.7	150.0	0.00	1.0
	calcd.	−353.6	160.1	0.00	1
Si2	exp.	−357.2	150.0	0.00	3.4
	calcd.	−343.9	161.8	0.26	3
K_4Si_4 (min.)					
Si1	exp.	−348.0	150.0	0.00	1.0
	calcd.[23]	−339.0	149.3	0.00	1
Si2	exp.	−324.2	153.0	0.00	2.4
	calcd.[23]	−313.4	152.9	0.06	3
K_3NaSi_4 (min.)					
Si1	calcd.	−366.4	157.3	0.10	1
Si2	calcd.	−333.9	176.8	0.11	1
Si3	calcd.	−316.9	133.1	0.21	1
Si4	calcd.	−325.5	142.0	0.22	1

[a] Majority and minority phases are indicated by maj. and min., respectively. [b] Asymmetry parameter of the chemical shielding.

Table 5. ^{23}Na NMR coupling parameters derived from NMR signal line-shape analysis (exp.) and QM calculations (calcd.).[a]

Atom		δ_{iso} [ppm]	δ_{aniso} [ppm]	η_δ[b]	C_Q[c] [MHz]	η_Q[d]
K_7NaSi_8 (maj.)						
Na	exp.	91.0	−150.0	0	5.80	0
	calcd.	91.7	−167.6	0	−5.60	0
Na_4Si_4 (min.)						
Na1	exp.	52.3	31.0	0.60	1.26	0.93
	calcd.[23]	62.3	31.0	0.60	1.26	0.93
Na2	exp.	26.7	−31.0	0.86	1.90	0.26
	calcd.[23]	43.9	−31.0	0.86	2.38	0.26
K_3NaSi_4 (min.)						
Na	exp.	29.7	−55.0	0.5	4.00	0.5
	calcd.	40.0	−51.4	0.49	3.65	0.78
Na metal (min.)						
Na	exp.[44]	1120	–	–	–	–

[a] The sign of C_Q is provided only by the calculations. Majority and minority phases are indicated by maj. and min., respectively. [b] Asymmetry parameter of the chemical shielding. [c] Quadrupole coupling constant. [d] Asymmetry parameter of the quadrupole coupling.

Na, K, Rb, Cs).[23] The chemical shift anisotropy (CSA, δ_{aniso}) values for Si1 and Si2 in K_7NaSi_8 are identical to those of Rb_7NaSi_8 in which δ_{iso}(Si1) is smaller and δ_{aniso}(Si2) is larger than in Cs_7NaSi_8 (see Table S7 and Figure S10). The asymmetry parameters for both Si environments and all three phases are in agreement with the site symmetry and thus zero for Si1 and unequal to zero for Si2 (see Table S8).

The isotropic ^{23}Na shift decreases from K_7NaSi_8 to Rb_7NaSi_8 to Cs_7NaSi_8. On the other hand, the CSA values for Na are identical, the asymmetry parameters of zero indicating no difference in the anisotropies of the chemical shift in all three compounds (see Table S7 and Figure S10 in the Supporting Information). The Na atoms in A_7NaSi_8 (A = K, Rb, Cs) possess a negative value of the EFG's main component V_{ZZ}, which reveals a prolate charge distribution around the nuclei with the largest principal axis along the three-fold axis.

The $|V_{ZZ}|$ values slightly decrease within the series A = K, Rb, and Cs, which indicates a less pronounced anisotropy of charge distribution around the Na atoms with increasing atomic number and radius of the alkali-metal ion (see Table S7 and Figure S10 in the Supporting Information). Interestingly, this finding contrasts the slight increase in the interatomic Na–Si2 distances of 2.92(1), 2.94(1), and 2.97(1) Å for A = K, Rb,[15] and Cs,[16] respectively. This indicates that the dimeric linear $[Na(Si_4)_2]^{7-}$ arrangement in A_7NaSi_8 is quite rigid with respect to the alkali metal atom (Figure 4b). Further support for this is given by the minor changes in the alkali-metal bonding (see below). Furthermore, a similar structural motif has been observed in the isotypic A_7NaGe_8 compounds.[19,20]

The difference between the $A1$ and $A2$ isotropic shifts is 81, 177, and 308 ppm for A = K, Rb, and Cs, respectively. The CSA for $A1$ ($\eta_\delta \neq 0$) decreases, whereas the values slightly increase for $A2$ ($\eta_\delta = 0$). More significant differences are visible by comparing the sign and value of V_{ZZ} as a measure of the anisotropy of charge distribution, which is oblate for $A1$ ($\eta_Q \neq 0$) and prolate for $A2$ ($\eta_Q = 0$). The $|V_{ZZ}|$ values increase for both environments with increasing alkali-metal radius, with $|V_{ZZ}|(A1) > |V_{ZZ}|(A2)$. The $|V_{ZZ}|(A1)/|V_{ZZ}|(A2)$ ratios of 2.9, 2.5, and 2.5 for A = K, Rb, and Cs, respectively, indicate similar bonding situations for the alkali metal atoms in A_7NaSi_8 (A = K, Rb, and Cs). Nevertheless, the significant difference and increase in the absolute values of $|V_{ZZ}|$ for both sites of K, Rb, and Cs clearly reveal larger anisotropies of charge distribution with increasing alkali-metal atomic numbers and radii. This is in agreement with the higher polarizability of the cations.

Conclusions

During the search for suitable precursors for the preparation of Zintl ions in solution and nanoparticulate material by the mixed cation approach, we discovered two new Zintl phases containing silicide tetrahedra $[Si_4]^{4-}$. K_3NaSi_4 crystallizes with a new structure type comprising isolated tetrahedra and forms solid solutions $K_{4-x}Na_xSi_4$ with $1 \leq x \leq 2.2$ that obey Vegard's rule. K_7NaSi_8 is isostructural with A_7NaSi_8 (A = Rb, Cs) and can only be synthesized by a diffusion-controlled reaction of binary starting materials. The combined application of solid-state NMR investigations and QM calculations revealed anisotropic chemical bonding for all the atoms in A_7NaSi_8 with A = K, Rb, and Cs. With increasing atomic number and polarizability of the alkali metal, the anisotropies of charge distribution significantly increase. A comparable slight decrease is found for the Na atoms. This indicates that the dimeric linear $[Na(Si_4)]^{7-}$ structural motif in A_7NaSi_8 is a quite rigid atomic arrangement. Hence, further studies on similar materials, for example, the isotypic Ge compounds, are envisioned.

Experimental Section

General: All steps of the synthesis and sample preparation were performed inside an argon-filled glovebox (MBraun, H_2O level

< 0.1 ppm, O_2 level < 0.1 ppm.). Na (99 %, Chempur) and K (98 %, Merck) pieces were freed from oxide layers before use. Ge (99.999 %, Evochem) and Si (99.99 %) pieces were ground to powder before use. ***CAUTION:*** Na, K, and the synthesized alkali-metal silicides react vigorously with water! The heat generated in the exothermic reaction may ignite the hydrogen formed. Therefore, the alkali metals and their silicides must be handled under the exclusion of air and water at all times. For disposal, very small portions must be carefully deactivated with copious amounts of water in a fireproof container.

Synthesis of K_4Si_4 and Na_4Si_4: K_4Si_4 and Na_4Si_4 were synthesized from stoichiometric amounts of the elements with a total mass of 2 g in tantalum ampoules. The ampoules were sealed and placed inside silica reaction containers, which were then evacuated. The reaction mixtures were heated up to 500 °C at 5 °C min^{-1}. After 1 h of pre-dwelling, the ampoules were further heated to 600 °C at 5 °C min^{-1} at which temperature dwelling was allowed for 30 h, followed by cooling at 5 °C min^{-1}.

Synthesis of $K_{4-x}Na_xSi_4$ ($1 \le x \le 2.2$): Solid solutions $K_{4-x}Na_xSi_4$ were synthesized from stoichiometric amounts (x = 1, 1.5, 2, 2.5) of K_4Si_4 and Na_4Si_4 with a total mass of 200–250 mg. The starting materials were thoroughly mixed by grinding in an agate mortar and subsequently pressed into pellets (diameter 6 mm). The pellets were then sealed inside tantalum ampoules, which were treated as described above. The reaction mixture was heated to 450 °C at 5 °C min^{-1} and dwelled for 7 d. Finally, the samples were cooled to room temperature at 0.1 °C min^{-1}. Alternatively, K_3NaSi_4 was prepared directly from stoichiometric amounts of the elements with a total mass of 500 mg in tantalum ampoules by using the same heating sequence as used for K_4Si_4 and Na_4Si_4.

Synthesis of K_7NaSi_8: K_7NaSi_8 was synthesized from stoichiometric amounts of K_4Si_4 and Na_4Si_4 with a total mass of 500 mg. The starting materials were thoroughly mixed by grinding in an agate mortar and subsequently pressed into pellets (diameter 6 mm). The pellets were then sealed inside tantalum ampoules, which were treated as described above. The reaction mixture was heated to 450 °C at 5 °C min^{-1} and dwelled for 7 d. Finally, the samples were cooled to room temperature at 0.1 °C min^{-1}.

X-ray Structure Determination: Crystals of K_3NaSi_4 were sealed in 0.3 mm glass capillaries. Intensity data were collected at 100(2) K by using a Bruker AXS X-ray diffractometer equipped with a CCD detector (APEX II, κ-CCD), a rotating anode FR591 with Mo-K_α radiation (λ = 0.71073 Å), and a MONTEL optic monochromator. Data collection was controlled with the Bruker APEX software package.[45] Integration, data reduction, and multi-scan absorption correction were performed with the SAINT[46] and SADABS[47] packages. The structure was solved by direct methods (SHELXS-2014) and refined with full-matrix least-squares on F^2 (SHELXL_2014).[48] Details of the single-crystal data collection and refinement are given in Table 1. Further details of the crystal structure investigation may be obtained from Fachinformationszentrum Karlsruhe, 76344 Eggenstein-Leopoldshafen, Germany (fax: +49-7247-808-666; e-mail: crysdata@fiz-karlsruhe.de), on quoting the deposition number CSD-431197.

Powder X-ray Diffraction Analysis: All PXRD patterns were recorded by using a Stoe STADI P diffractometer equipped with a Ge(111) monochromator for Cu-K_α radiation (λ = 1.54056 Å) and a Dectris MYTHEN DCS 1 K solid-state detector. Samples were prepared by grinding in an agate mortar and transferring the powders to 0.3 mm glass capillaries inside the glovebox, which were then sealed. All measured diffraction patterns were angle-corrected with an external α-Si standard.

Rietveld Refinement: Rietveld refinements were performed by using Jana2006.[49] The crystal structures of K_3NaSi_4 and K_7LiSi_8[17] were used as initial structural models. All cell parameters and atom positions as well as site occupancies for mixed positions were refined with the sum of mixed-site occupancies set to 1. Isotropic displacement parameters were refined whenever possible.

Solid-State NMR Spectroscopy: Static and magic-angle spinning (MAS) NMR experiments were performed on powder samples of K_7NaSi_8 and K_4Si_4 as a reference sample with a Bruker Avance III spectrometer with an 11.7 T magnet. The respective resonance frequencies of ^{29}Si and ^{23}Na were 99.3 and 132.3 MHz, respectively. The signals were acquired by using a Bruker 4.0 mm triple-resonance probehead with 4.0 mm ZrO_2 rotors at MAS frequencies of 7.5, 12.5, and 14.0 kHz. The ^{29}Si and ^{23}Na NMR shifts are referenced to TMS and NaCl, respectively.[50] A one-pulse sequence with hard pulses of 1.30 µs duration, corresponding to approximately 30° pulses, and a recycle delay of 170 s was used for the ^{29}Si NMR measurements. ^{23}Na NMR signals were acquired with hard pulses of 1.40 µs duration and a recycle delay of 10 s in MAS-frequency-synchronized Hahn-echo pulse sequences and by applying an interpulse delay of 60 µs for static measurements, respectively. All sample handling was carried out in an MBraun argon glovebox with O_2 and H_2O levels < 0.1 ppm to prevent the samples from reacting with moisture and/or air. The powder samples were mixed with vacuum-dried GeO_2 in a 4:1 ratio and pressed into a ZrO_2 rotor. The mixture was topped with a thin layer of pure GeO_2 as well as a Teflon tape seal before closing the rotor with the cap. NMR raw data handling and signal line-shape analysis were carried out by using the SOLA program implemented in Bruker Topspin (version 2.1). The expressions $\delta_{iso} = (\delta_{XX} + \delta_{YY} + \delta_{ZZ})/3$, $\delta_{aniso} = (\delta_{ZZ} - \delta_{iso})$, and $\eta_\delta = (\delta_{YY} - \delta_{XX})/\delta_{aniso}$ refer to the isotropic chemical shift, the chemical shift anisotropy, and the asymmetry parameter of the chemical shielding, respectively.[16] The order of the principal axes of the shielding tensor is defined by $|\delta_{ZZ} - \delta_{iso}| \ge |\delta_{XX} - \delta_{iso}| \ge |\delta_{YY} - \delta_{iso}|$, which results in $0 \le \eta_\delta \le 1$. The quadrupole coupling constant is defined as $C_Q = (V_{ZZ}eQ)/h$ in which V_{ZZ} is the main component of the electric field gradient (EFG), e is the elementary charge, Q is the quadrupole moment (5.85, 13.35, and –0.343 fm^2 for ^{39}K, ^{87}Rb, and ^{133}Cs, respectively),[50] and h is Planck's constant.[16,37] The asymmetry parameter of the quadrupole coupling is defined as $\eta_Q = (V_{YY} - V_{XX})/V_{ZZ}$ with $|V_{ZZ}| \ge |V_{XX}| \ge |V_{YY}|$ and $0 \le \eta_Q \le 1$.[16,37] Asymmetry parameters of $\eta = 0$ and $\eta \ne 0$ correspond to axial and nonaxial symmetry for the atom under investigation, respectively. Symmetry constraints for the NMR coupling parameters/line-shape due to the site symmetries of the atoms in A_7NaSi_8 (A = K, Rb, and Cs) are summarized in Table S8 in the Supporting Information.

QM Calculations: QM calculations of the NMR parameters[51] were performed in the gauge-including projector augmented wave (GIPAW) method implemented in the periodic density functional theory (DFT) code CASTEP.[52] The gradient-corrected PBE exchange-correlation functional[53] was used for all calculations. Core electrons were described with Vanderbilt ultrasoft pseudopotentials generated "on-the-fly" in CASTEP 8.0. Shielding and quadrupole tensor calculations were performed for each compound with a plane wave basis set truncation energy of 800 eV. The Brillouin zone was sampled with a Monkhorst–Pack grid[54] with k-point sampling finer than 2π•0.02 $Å^{-1}$. Convergence of the basis-set energy and k-point sampling were examined and confirmed. In the discussion of experimentally derived and calculated NMR coupling parameters

we refer to a good agreement, which can be achieved within the ranges of ±10 ppm for δ_{iso} and δ_{aniso}, ±0.1 MHz for C_Q, and $\pm 0.1 \times 10^{21}$ V m^{-2} for V_{ZZ}, as has recently been discussed for Zintl phases.[16]

Acknowledgments

We gratefully acknowledge fruitful discussions with Dr. Rachel N. Kerber (Cambridge). L. M. S. is grateful for financial support by the Fonds der Chemischen Industrie and a fellowship from the Studienstiftung des deutschen Volkes. This work was performed using the Darwin Supercomputer of the University of Cambridge High Performance Computing Service (http://www.hpc.cam.ac.uk/), provided by Dell Inc. using Strategic Research Infrastructure Funding from the Higher Education Funding Council for England and funding from the Science and Technology Facilities Council. K. J. G. thanks the Winston Churchill Foundation of the United States and the Herchel Smith Scholarship for financial support.

Keywords: Alkali metals · Silicon · Zintl phases · NMR spectroscopy · Density functional calculations

[1] a) E. Zintl, *Angew. Chem.* **1939**, *51*, 1–6; b) T. F. Fässler in *Structure and Bonding*, vol. 139 (Ed. D. M. P. Mingos), Springer, Heidelberg, **2011.**
[2] R. Nesper, *Prog. Solid State Chem.* **1990**, *20*, 1–45.
[3] a) E. Menges, V. Hopf, H. Schäfer, A. Weiss, *Z. Naturforsch. B* **1969**, *24*, 1351–1352; b) J. Evers, G. Oehlinger, G. Sextl, *Angew. Chem. Int. Ed. Engl.* **1993**, *32*, 1442–1444; *Angew. Chem.* **1993**, *105*, 1532–1534.
[4] A. Grüttner, R. Nesper, H. G. von Schnering, *Angew. Chem. Int. Ed. Engl.* **1982**, *21*, 912–913; *Angew. Chem.* **1982**, *94*, 933.
[5] a) F. Kiefer, T. F. Fässler, *Solid State Sci.* **2011**, *13*, 636–640; b) H. G. von Schnering, M. Schwarz, R. Nesper, *J. Less-Common Met.* **1988**, *137*, 297–310.
[6] a) A. Grüttner, R. Nesper, H. G. von Schnering, *Acta Crystallogr., Sect. A* **1981**, *37*, C161; b) H. G. von Schnering, R. Nesper, K.-F. Tebbe, J. Curda, *Z. Metallkd.* **1980**, *71*, 357–363.
[7] L. M. Scherf, A. J. Karttunen, O. Pecher, P. C. M. M. Magusin, C. P. Grey, T. F. Fässler, *Angew. Chem. Int. Ed.* **2016**, *55*, 1075–1079; *Angew. Chem.* **2016**, *128*, 1087–1091.
[8] a) L. M. Scherf, M. Zeilinger, T. F. Fässler, *Inorg. Chem.* **2014**, *53*, 2096–2101; b) S. Bobev, S. C. Sevov, *Angew. Chem. Int. Ed.* **2001**, *40*, 1507–1510; *Angew. Chem.* **2001**, *113*, 1555–1558.
[9] a) M. Zeilinger, D. Benson, U. Häussermann, T. F. Fässler, *Chem. Mater.* **2013**, *25*, 1960–1967; b) M. Zeilinger, T. F. Fässler, *Dalton Trans.* **2014**, *43*, 14959–14970; c) M. Zeilinger, V. Baran, L. van Wüllen, U. Häussermann, T. F. Fässler, *Chem. Mater.* **2013**, *25*, 4113–4121; d) E. I. Gladyshevskii, P. I. Kripyakevich, *Kristallografiya* **1960**, *5*, 574–576; e) Q. Johnson, G. S. Smith, D. Wood, *Acta Crystallogr.* **1965**, *18*, 131–132; f) M. Zeilinger, I. M. Kurylyshyn, U. Häussermann, T. F. Fässler, *Chem. Mater.* **2013**, *25*, 4623–4632.
[10] E. Hohmann, *Z. Anorg. Chem.* **1948**, *257*, 113–126.
[11] R. Schäfer, W. Klemm, *Z. Anorg. Allg. Chem.* **1961**, *312*, 214–220.
[12] a) J. S. Kasper, P. Hagenmuller, M. Pouchard, C. Cros, *Science* **1965**, *150*, 1713–1714; b) C. Cros, M. Pouchard, P. Hagenmuller, *J. Solid State Chem.* **1970**, *2*, 570–581; c) S. Bobev, S. C. Sevov, *J. Am. Chem. Soc.* **1999**, *121*, 3795–3796; d) S. Bobev, S. C. Sevov, *J. Solid State Chem.* **2000**, *153*, 92–105.
[13] a) S. Ponou, T. F. Fässler, *Z. Anorg. Allg. Chem.* **2007**, *633*, 393–397; b) V. Queneau, S. C. Sevov, *Angew. Chem. Int. Ed. Engl.* **1997**, *36*, 1754–1756; *Angew. Chem.* **1997**, *109*, 1818–1820.
[14] a) C. Hoch, M. Wendorff, C. Röhr, *J. Alloys Compd.* **2003**, *361*, 206–221; b) W. Carrillo-Cabrera, R. Cardoso Gil, M. Somer, Ö. Persil, H. G. von Schnering, *Z. Anorg. Allg. Chem.* **2003**, *629*, 601–608.
[15] a) T. Goebel, Y. Prots, A. Ormeci, O. Pecher, F. Haarmann, *Z. Anorg. Allg. Chem.* **2011**, *637*, 1982–1991.
[16] O. Pecher, M. Esters, A. Görne, B. Mausolf, A. Ormeci, F. Haarmann, *Z. Anorg. Allg. Chem.* **2014**, *640*, 2169–2176.
[17] H. G. von Schnering, M. Schwarz, R. Nesper, *Angew. Chem. Int. Ed. Engl.* **1986**, *25*, 566–567; *Angew. Chem.* **1986**, *98*, 558–559.
[18] M. Schwarz, Dissertation, University of Stuttgart, **1987**.
[19] J. Llanos, R. Nesper, H. G. von Schnering, *Angew. Chem. Int. Ed. Engl.* **1983**, *22*, 998; *Angew. Chem.* **1983**, *95*, 1026–1027.
[20] J. Llanos, Dissertation, University of Stuttgart, **1984**.
[21] H. G. von Schnering, J. Llanos, G. Yu, W. Carrillo-Cabrera, E.-M. Peters, K. Peters, R. Nesper, *Z. Kristallogr. - New Cryst. Struct.* **1998**, *213*, 661.
[22] V. Quéneau, E. Todorov, S. C. Sevov, *J. Am. Chem. Soc.* **1998**, *120*, 3263–3264.
[23] T. Goebel, A. Ormeci, O. Pecher, F. Haarmann, *Z. Anorg. Allg. Chem.* **2012**, *638*, 1437–1445.
[24] T. Goebel, Y. Prots, F. Haarmann, *Z. Kristallogr. - New Cryst. Struct.* **2009**, *224*, 7–8.
[25] U. Aydemir, A. Ormeci, H. Borrmann, B. Böhme, F. Zürcher, B. Uslu, T. Goebel, W. Schnelle, P. Simon, W. Carrillo-Cabrera, F. Haarmann, M. Baitinger, R. Nesper, H. G. von Schnering, Y. Grin, *Z. Anorg. Allg. Chem.* **2008**, *634*, 1651–1661.
[26] A. Ammar, C. Cros, M. Pouchard, N. Jaussaud, J.-M. Bassat, G. Villeneuve, M. Duttine, M. Ménétrier, E. Reny, *Solid State Sci.* **2004**, *6*, 393–400.
[27] A. M. Guloy, R. Ramlau, Z. Tang, W. Schnelle, M. Baitinger, Y. Grin, *Nature* **2006**, *443*, 320–323.
[28] F. Kiefer, A. J. Karttunen, M. Döblinger, T. F. Fässler, *Chem. Mater.* **2011**, *23*, 4578–4586.
[29] M. Zeilinger, L.-A. Jantke, L. M. Scherf, F. J. Kiefer, G. Neubüser, L. Kienle, A. J. Karttunen, S. Konar, U. Häussermann, T. F. Fässler, *Chem. Mater.* **2014**, *26*, 6603–6612.
[30] a) G. S. Armatas, M. G. Kanatzidis, *Science* **2006**, *313*, 817–820; b) G. S. Armatas, M. G. Kanatzidis, *Adv. Mater.* **2008**, *20*, 546–550; c) D. Sun, A. E. Riley, A. J. Cadby, E. K. Richman, S. D. Korlann, S. H. Tolbert, *Nature* **2006**, *441*, 1126–1130.
[31] M. M. Bentlohner, M. Waibel, P. Zeller, K. Sarkar, P. Müller-Buschbaum, D. Fattakhova-Rohlfing, T. F. Fässler, *Angew. Chem. Int. Ed.* **2016**, *55*, 2441–2445; *Angew. Chem.* **2016**, *128*, 2487–2491.
[32] a) R. A. Bley, S. M. Kauzlarich, *J. Am. Chem. Soc.* **1996**, *118*, 12461–12462; b) D. Neiner, H. W. Chiu, S. M. Kauzlarich, *J. Am. Chem. Soc.* **2006**, *128*, 11016–11017; c) B. R. Taylor, S. M. Kauzlarich, H. W. H. Lee, G. R. Delgado, *Chem. Mater.* **1998**, *10*, 22–24; d) B. M. Nolan, T. Henneberger, M. Waibel, T. F. Fässler, S. M. Kauzlarich, *Inorg. Chem.* **2015**, *54*, 396–401.
[33] D. Neiner, S. M. Kauzlarich, *Chem. Mater.* **2010**, *22*, 487–493.
[34] D. Mayeri, B. L. Phillips, M. P. Augustine, S. M. Kauzlarich, *Chem. Mater.* **2001**, *13*, 765–770.
[35] S. Scharfe, F. Kraus, S. Stegmaier, A. Schier, T. F. Fässler, *Angew. Chem. Int. Ed.* **2011**, *50*, 3630–3670; *Angew. Chem.* **2011**, *123*, 3712–3754.
[36] M. Waibel, O. Pecher, B. Mausolf, F. Haarmann, T. F. Fässler, *Eur. J. Inorg. Chem.* **2013**, 5541–5546.
[37] F. Haarmann in *eMagRes* (Eds.: R. K. Harris, R. E. Wasylishen), Wiley, Chichester, **2011**.
[38] O. Pecher, B. Mausolf, K. Lamberts, D. Oligschläger, C. Niewieszol (née Merkens), U. Englert, F. Haarmann, *Chem. Eur. J.* **2015**, *21*, 13971–13982.
[39] J. Witte, H. G. von Schnering, W. Klemm, *Z. Anorg. Allg. Chem.* **1964**, *327*, 260–273.
[40] Free refinement of the site-occupancy factors for all K positions in the single-crystal X-ray diffraction experiment shows full occupation for all three sites.
[41] L. Vegard, *Z. Phys.* **1921**, *5*, 17–26.
[42] T. Goebel, Dissertation, Technische University of Dresden, **2011**.
[43] The Na and Na_4Si_4 impurities could not be detected in the respective powder diffraction pattern and must therefore be minute. The main reflections of K_3NaSi_4 are barely visible in the powder diffraction pattern and could not be reasonably included in the Rietveld refinement.
[44] O. Pecher, P. M. Bayley, H. Liu, Z. Liu, N. M. Trease, C. P. Grey, *J. Magn. Reson.* **2016**, *265*, 200–209.
[45] *APEX Suite of Crystallographic Software*, Bruker AXS Inc., Madison, WI, **2008**.
[46] *SAINT*, Bruker AXS Inc., Madison, WI, **2001**.
[47] *SADABS*, Bruker AXS Inc., Madison, WI, **2001**.
[48] G. M. Sheldrick, *Acta Crystallogr., Sect. A* **2008**, *64*, 112–122.

[49] V. Petříček, M. Dušek, L. Palatinus, *Z. Kristallogr. - Cryst. Mater.* **2014**, *229*, 345–352.
[50] a) R. K. Harris, E. D. Becker, *J. Magn. Reson.* **2002**, *156*, 323–326; b) R. K. Harris, E. D. Becker, S. M. C. De Menezes, P. Granger, R. E. Hoffman, K. W. Zilm, *Magn. Reson. Chem.* **2008**, *46*, 582–598; c) R. K. Harris, E. D. Becker, S. M. Cabral de Menezes, R. Goodfellow, P. Granger, *Magn. Reson. Chem.* **2002**, *40*, 489–505.
[51] a) C. J. Pickard, F. Mauri, *Phys. Rev. B* **2001**, *63*, 245101; b) J. R. Yates, C. J. Pickard, F. Mauri, *Phys. Rev. B* **2007**, *76*, 024401; c) M. Profeta, F. Mauri, C. J. Pickard, *J. Am. Chem. Soc.* **2003**, *125*, 541–548.
[52] S. J. Clark, M. D. Segall, C. J. Pickard, P. J. Hasnip, M. I. J. Probert, K. Refson, M. C. Payne, *Z. Kristallogr.* **2005**, *220*, 567–570.
[53] J. P. Perdew, K. Burke, M. Ernzerhof, *Phys. Rev. Lett.* **1996**, *77*, 3865–3868.
[54] H. J. Monkhorst, J. D. Pack, *Phys. Rev. B* **1976**, *13*, 5188–5192.

Received: June 20, 2016
Published Online: August 29, 2016

Eur. J. Inorg. Chem. **2016** · ISSN 1099–0682

SUPPORTING INFORMATION

DOI: 10.1002/ejic.201600735
Title: Zintl Phases $K_{4-x}Na_xSi_4$ ($1 \leq x \leq 2.2$) and K_7NaSi_8: Synthesis, Crystal Structures, and Solid-State NMR Spectroscopic Investigations
Author(s): Lavinia M. Scherf, Oliver Pecher, Kent J. Griffith, Frank Haarmann, Clare P. Grey, Thomas F. Fässler*

Contents

Crystal structure determination of $K_{4-x}Na_xSi_4$ ($1 \le x \le 2.2$) 2

Single crystal X-ray diffraction of K_3NaSi_4 2

Powder X-ray diffraction and Rietveld refinement for solid solutions $K_{4-x}Na_xSi_4$ ($1 \le x \le 2.2$) 4

Crystal structure determination of K_7NaSi_8 8

Solid State NMR data of K_7NaSi_8 9

Comparison of A_7NaSi_8 (A = K, Rb, Cs) 13

References 14

Crystal structure determination of $K_{4-x}Na_xSi_4$ ($1 \leq x \leq 2.2$)

Single crystal X-ray diffraction of K_3NaSi_4

Table S1. Atomic coordinates and isotropic displacement parameters for K_3NaSi_4.

		x	*y*	*z*	U_{iso}
K1	4*e*	0.9425(1)	0.14204(6)	0.07121(8)	0.0194(2)
K2	4*e*	0.5319(1)	0.02392(6)	0.26432(8)	0.0197(2)
K3	4*e*	0.1920(1)	0.11316(6)	0.47457(8)	0.0190(2)
Na4	4*e*	0.3068(2)	0.2149(1)	0.8731(1)	0.0182(3)
Si1	4*e*	0.9678(2)	0.08232(8)	0.7455(1)	0.0144(2)
Si2	4*e*	0.7164(2)	0.12840(8)	0.5634(1)	0.0138(2)
Si3	4*e*	0.6964(2)	0.19343(8)	0.7695(1)	0.0176(3)
Si4	4*e*	0.9559(2)	0.24973(8)	0.6616(1)	0.0162(3)

Table S2. Selected atomic distances (Å) and bond angles (°) for K_3NaSi_4 with estimated standard deviations in parentheses.

K_3NaSi_4					
Distances				K3–Si2	3.400(1)
Si1–Si2	2.414(1)	K1–Si2	3.644(1)	K3–Si3	3.447(1)
Si1–Si3	2.416(1)	K1–Si4	3.696(1)	K3–Si2	3.462(1)
Si1–Si4	2.458(2)	K1-Si4	3.856(1)	K3–Si2	3.488(1)
Si2–Si3	2.412(1)	K2–Si4	3.296(1)	K3–Si1	3.536(1)
Si2–Si4	2.409(1)	K2–Si3	3.331(1)	K3–Si1	3.599(1)
Si3–Si4	2.384(2)	K2–Si2	3.414(1)	Na4–Si4	2.985(2)
K1–Si3	3.338(1)	K2–Si2	3.524(1)	Na4–Si1	3.025(2)
K1–Si3	3.425(1)	K2–Si1	3.624(1)	Na4–Si3	3.028(2)
K1–Si1	3.627(1)	K2–Si1	3.663(1)	Na4–Si2	3.099(2)
K1–Si1	3.637(1)	K3–Si4	3.345(1)	Na4–Si4	3.113(2)
Angles					
Si2–Si1–Si3	59.92(4)	Si4–Si2–Si1	61.27(4)	Si2–Si3–Si1	60.00(4)
Si2–Si1–Si4	59.26(4)	Si3–Si2–Si1	60.08(4)	Si3–Si4–Si2	60.43(4)
Si3–Si1–Si4	58.56(4)	Si4–Si3–Si2	60.29(4)	Si3–Si4–Si1	59.85(4)
Si4–Si2–Si3	59.27(4)	Si4–Si3–Si1	61.59(5)	Si2–Si4–Si1	59.47(4)

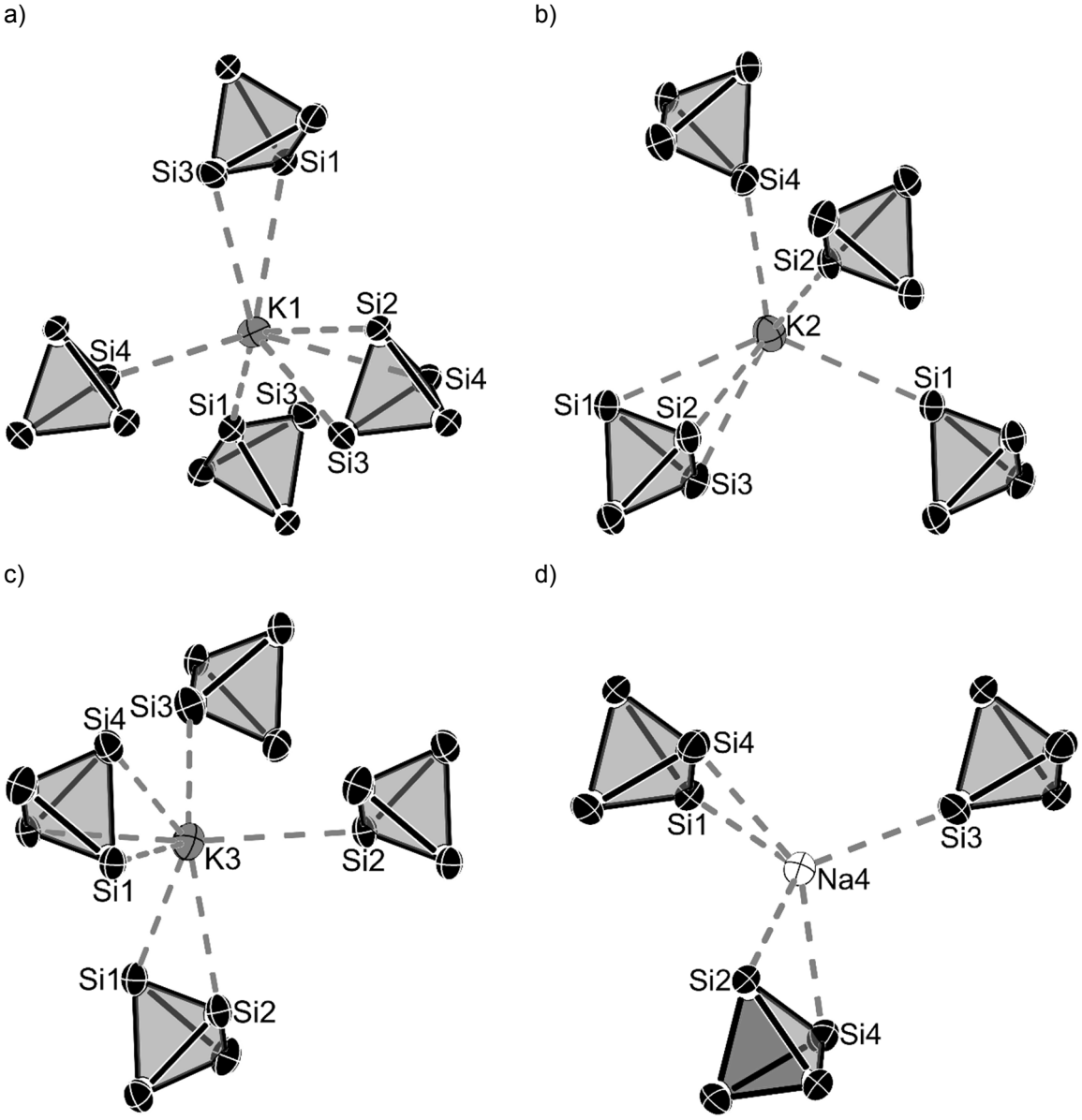

Figure S1. Si coordination spheres of the alkali metal positions in K_3NaSi_4.

Table S3. Average *A*-Si distances / Å in the coordination spheres of the different alkali metal sites in $K_{4-x}Na_xSi_4$ ($1 \leq x \leq 2.2$).

	K_3NaSi_4[a]	$K_{2.87(2)}Na_{1.13}Si_4$[b]	$K_{2.40(4)}Na_{1.60}Si_4$[b]	$K_{2.0(1)}Na_{2.0}Si_4$[b]	$K_{1.80(7)}Na_{2.20}Si_4$[b]
K1	3.603(1)	3.62(1)	3.61(1)	3.58(3)	3.57(2)
K2/Na2	3.475(1)	3.50(1)	3.46(1)	3.44(3)	3.42(2)
K3/Na3	3.468(1)	3.49(1)	3.43(1)	3.32(3)	3.31(2)
Na4	3.050(2)	3.07(1)	3.07(1)	3.07(3)	3.07(2)

[a] Data from single crystal X-ray diffraction at 100 K.
[b] Data from Rietveld refinement of powder X-ray diffraction patterns at room temperature.

Powder X-ray diffraction and Rietveld refinement for solid solutions $K_{4-x}Na_xSi_4$ ($1 \leq x \leq 2.2$)

Table S4. Crystallographic data of several $K_{4-x}Na_xSi_4$ ($1 \leq x \leq 2.2$) phases obtained from powder diffraction data via Rietveld refinement.

x	**1**	**1.5**	**2**	**2.5**
Stoichiometry	$K_{2.87(2)}Na_{1.13}Si_4$[a]	$K_{2.40(4)}Na_{1.60}Si_4$	$K_{2.0(1)}Na_{2.0}Si_4$	$K_{1.80(7)}Na_{2.20}Si_4$[b]
T / K	293 K			
M_r / g mol^{-1}	250.5	242.9	236.0	233.3
Powder color	Grey			
Crystal system	Monoclinic			
Space group	$P2_1/n$			
Lattice parameters				
a / Å	6.7240(4)	6.6749(5)	6.591(2)	6.571(2)
b / Å	13.7577(8)	13.4912(9)	13.166(5)	13.072(4)
c / Å	10.8011(6)	10.8231(7)	10.885(4)	10.880(3)
β / Å	100.658(2)	100.545(1)	100.301(7)	100.299(6)
V / Å^3	981.9(2)	958.2(2)	929(1)	919.5(8)
Z	4			
$\rho_{calc.}$ / g cm^{-3}	1.694	1.684	1.687	1.685
μ / mm^{-1}	16.71	15.474	14.394	13.923
Θ range / °	4.94–89.76	4.96–89.79	5.01–89.80	5.01–89.80
R [$I > 3\sigma(I)$]	0.0289	0.0564	0.595	0.0502
wR [$I > 3\sigma(I)$]	0.0296	0.0497	0.0674	0.0432
R (all)	0.0293	0.0753	0.0600	0.0517
wR (all)	0.0297	0.0527	0.0675	0.0435
Goodness of fit	1.28	1.01	2.52	1.10

[a] sample contains 16.2(3) % K_7NaSi_8.
[b] sample contains 17(1) % Na_4Si_4.

Table S5. Atomic coordinates and isotropic displacement parameters for $K_{4-x}Na_xSi_4$ ($1 \leq x \leq 2.2$) from Rietveld refinement (structural model K_7LiSi_8).[1]

		$K_{2.87(2)}Na_{1.13}Si_4$		$K_{2.40(4)}Na_{1.60}Si_4$		$K_{2.0(1)}Na_{2.0}Si_4$		$K_{1.80(7)}Na_{2.20}Si_4$	
		x, y, z	***U_{eq}*, % Na**	***x, y, z***	***U_{eq}*, % Na**	***x, y, z***	***U_{eq}*, % Na**	***x, y, z***	***U_{eq}*, % Na**
*A*1	4*e*	0.9424(9) 0.1409(4) 0.0712(5)	0.028(3) 0	0.9374(9) 0.1408(4) 0.0700(5)	0.056(6) 0	0.946(3) 0.141(1) 0.432(2)	0.063(9) 0	0.942(2) 0.1405(8) 0.065(1)	0.060(6) 0
*A*2	4*e*	0.5316(9) 0.0246(4) 0.2632(6)	0.032(3) 0	0.525(1) 0.0260(4) 0.2670(7)	0.064(5) 15(2)	0.519(3) 0.026(1) 0.267(1)	0.07(1) 13(6)	0.514(2) 0.0272(9) 0.269(1)	0.07(1) 22(4)
*A*3	4*e*	0.1946(9) 0.1135(4) 0.4749(5)	0.014(3) 14(2)	0.192(1) 0.1107(5) 0.4734(7)	0.050(4) 45(2)	0.188(4) 0.098(2) 0.477(2)	0.05(2) 91(5)	0.189(3) 0.097(2) 0.474(2)	0.06(1) 98(3)
*A*4	4*e*	0.309(1) 0.2135(8) 0.8742(9)	0.021(4) 100	0.310(2) 0.2145(7) 0.8703(9)	0.052(4) 100	0.314(4) 0.219(2) 0.860(2)	0.03(1) 100	0.318(3) 0.220(1) 0.860(2)	0.050(8) 100
Si1	4*e*	0.968(1) 0.0814(5) 0.7480(8)	0.22(3) -	0.972(1) 0.0794(5) 0.7420(9)	0.054(4) -	0.981(3) 0.074(1) 0.730(2)	0.03(1) -	0.982(2) 0.075(1) 0.731(2)	0.056(8) -
Si2	4*e*	0.719(1) 0.1279(6) 0.5639(7)	0.019(3) -	0.713(1) 0.1276(6) 0.5641(8)	0.048(4) -	0.718(3) 0.127(2) 0.565(2)	0.04(1) -	0.715(2) 0.127(1) 0.567(2)	0.046(7) -
Si3	4*e*	0.695(1) 0.1934(5) 0.7705(8)	0.023(4) -	0.691(1) 0.1961(6) 0.7672(8)	0.061(5) -	0.225(3) 0.204(1) 0.763(2)	0.03(1) -	0.733(2) 0.206(1) 0.764(2)	0.039(8) -
Si4	4*e*	0.956(1) 0.2491(5) 0.6657(7)	0.021(3) -	0.961(1) 0.248(6) 0.6558(7)	0.054(4) -	0.976(3) 0.247(2) 0.638(2)	0.05(1) -	0.978(2) 0.250(1) 0.640(1)	0.047(7) -

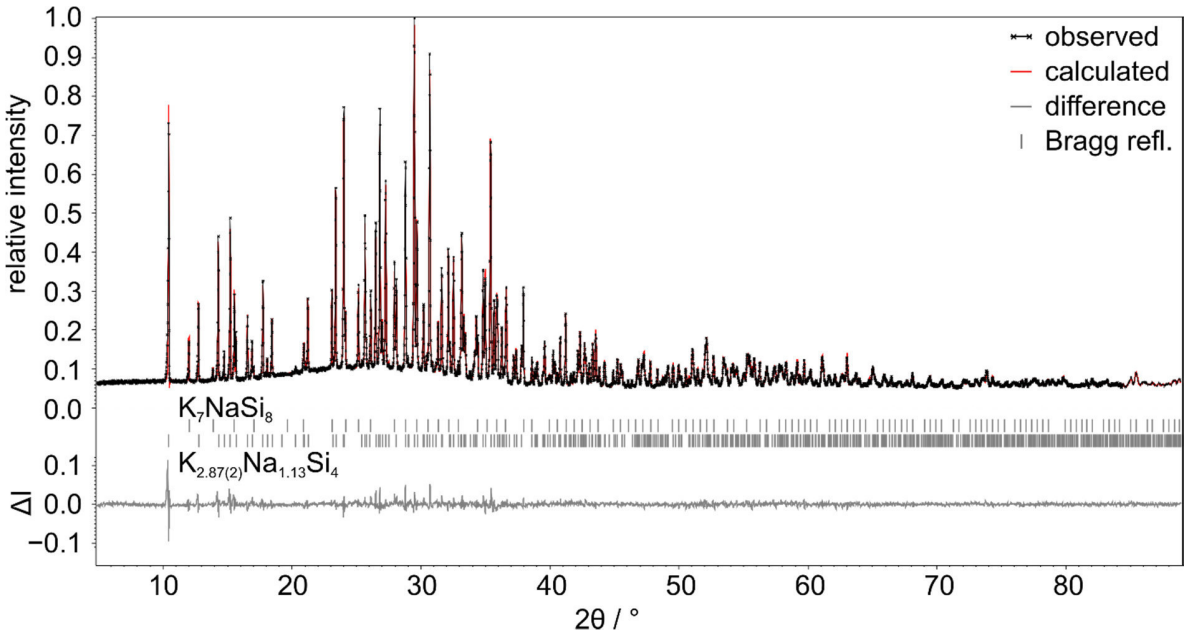

Figure S2. Rietveld refined powder diffraction pattern of $K_{2.87(2)}Na_{1.13}Si_4$ with K_7NaSi_8 impurity. Corresponding refinement data is listed in Table S3.

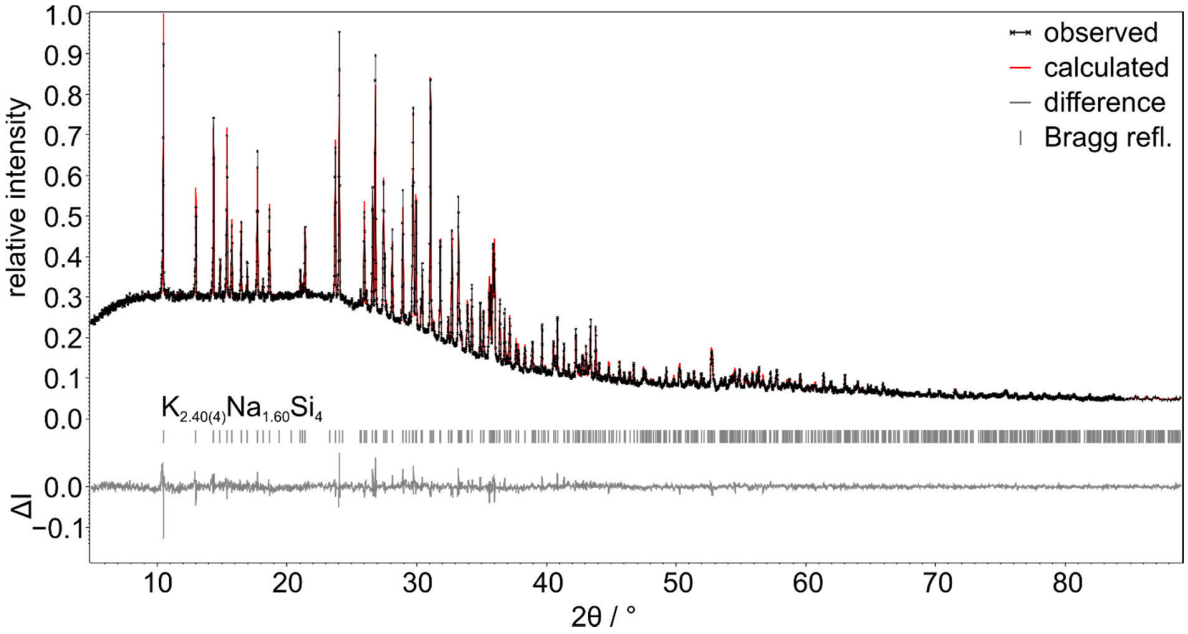

Figure S3. Rietveld refined powder diffraction pattern of $K_{2.40(4)}Na_{1.60}Si_4$. Corresponding refinement data is listed in Table S3.

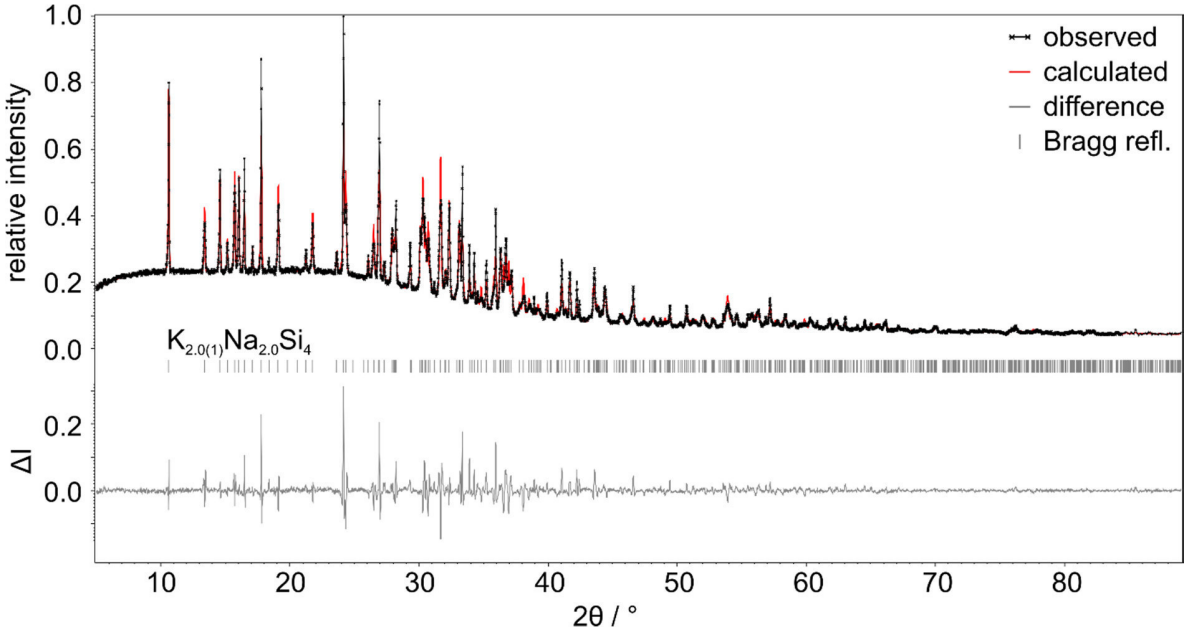

Figure S4. Rietveld refined powder diffraction pattern of $K_{2.0(1)}Na_{2.0}Si_4$. Corresponding refinement data is listed in Table S3.

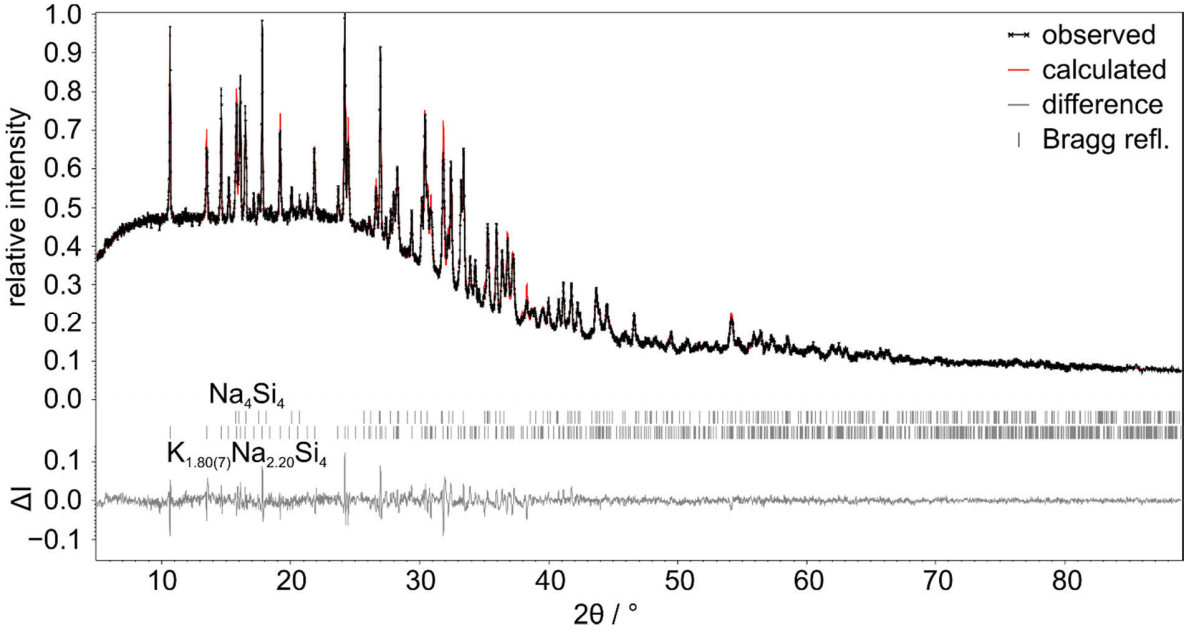

Figure S5. Rietveld refined powder diffraction pattern of $K_{1.80(7)}Na_{2.20}Si_4$ with Na_4Si_4 impurity. Corresponding refinement data is listed in Table S3.

Crystal structure determination of K_7NaSi_8

Table S6. Atomic coordinates and isotropic displacement parameters for K_7NaSi_8 from Rietveld refinement (structural model K_7LiSi_8).[1]

		x	*y*	*z*	U_{iso}
K1	24*d*	0.424(3)	0.2266(3)	0.3146(3)	0.035(2)
K2	4*a*	0	0	0	0.072(5)
Si1	8*c*	0.2974(4)	0.2974(4)	0.2974(4)	0.022(3)
Si2	24*d*	0.2080(4)	0.9216(4)	0.4384(3)	0.024(2)
Na1	4*b*	0.5	0.5	0.5	0.040(6)

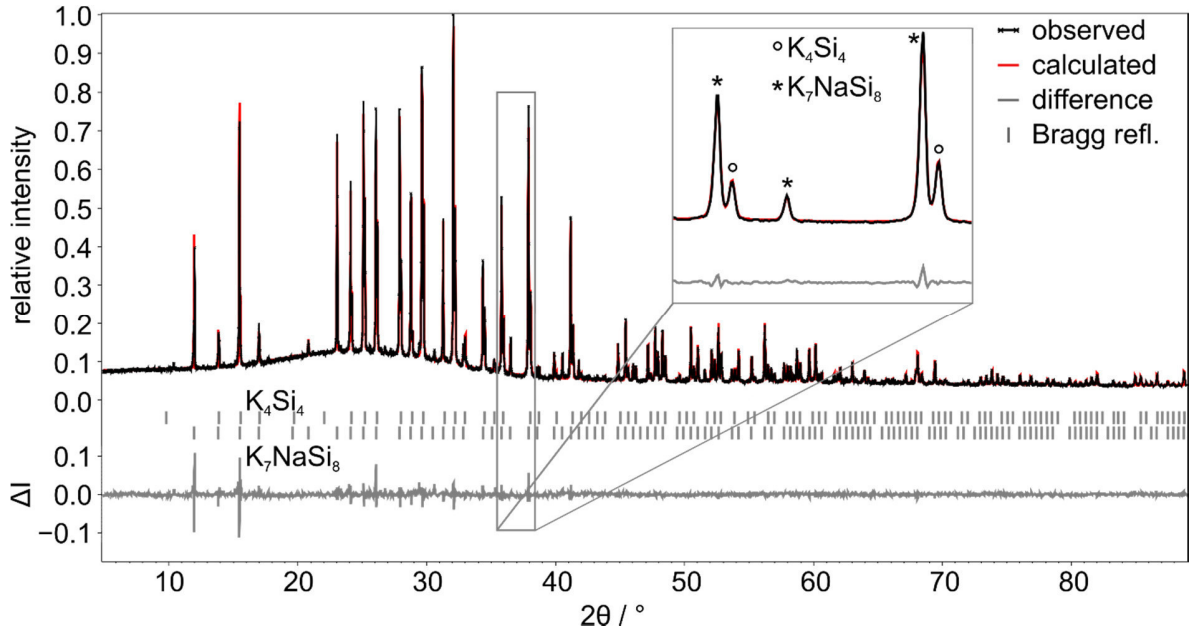

Figure S6. Rietveld refined powder diffraction pattern of K_7NaSi_8 (structural model K_7LiSi_8)[1] with K_4Si_4 impurity. Slight traces of $K_{4-x}Na_xSi_4$ ($x \approx 1$) could not be refined.

Solid state NMR data of K_7NaSi_8

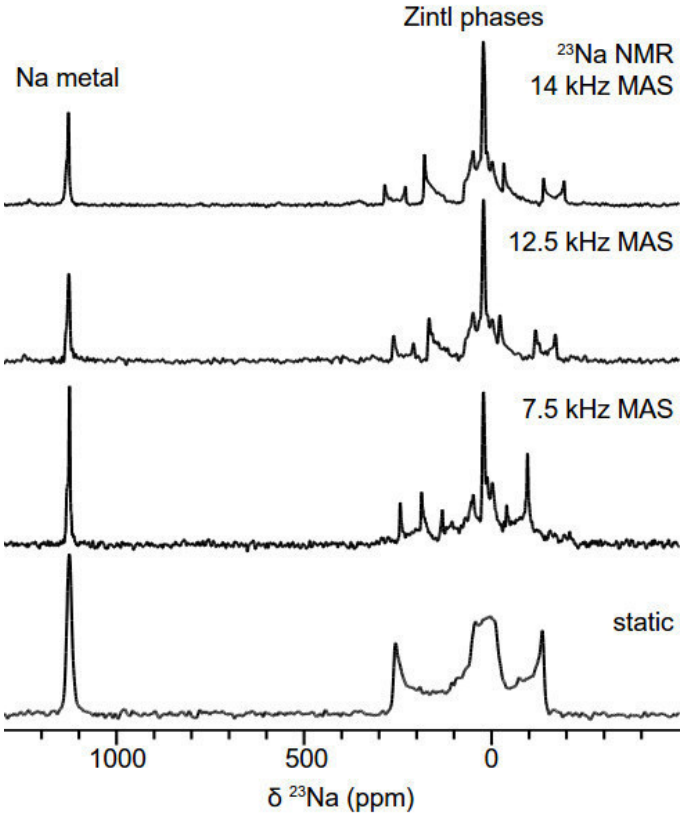

Figure S7. ^{23}Na NMR spectra of K_7NaSi_8 under MAS frequencies of 14, 12.5, 7.5 kHz and under static conditions, respectively (from top to bottom). The signal of a Na metal impurity at high shifts as well as the frequency range of the Zintl phases (majority K_7NaSi_8 as well as Na_4Si_4 and K_3NaSi_4 minorities) are highlighted in the figure.

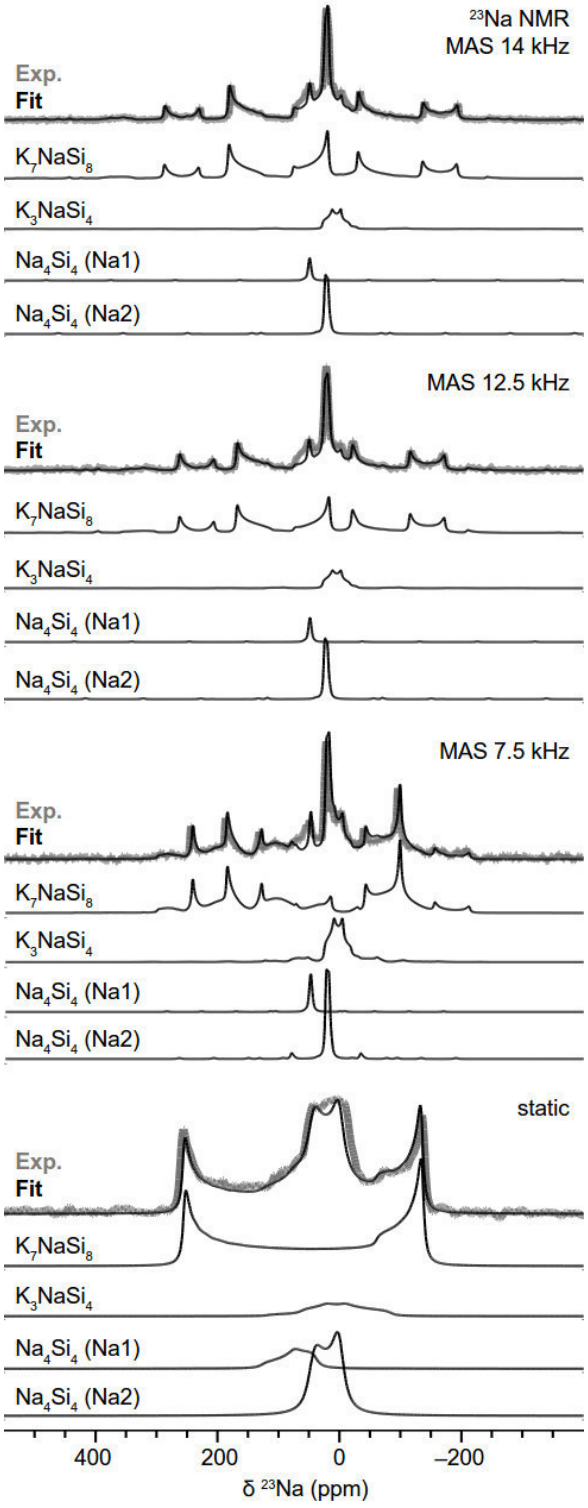

Figure S8. ^{23}Na NMR spectra of K_7NaSi_8 under MAS frequencies of 14, 12.5, 7.5 kHz and under static conditions, respectively (from top to bottom). Rotational sidebands are marked by asterisks. Na signal contributions of K_7NaSi_8, Na_4Si_4 (Na1 and Na2) as well as K_3NaSi_4 determined by signal line shape analysis are highlighted and labelled in the figure.

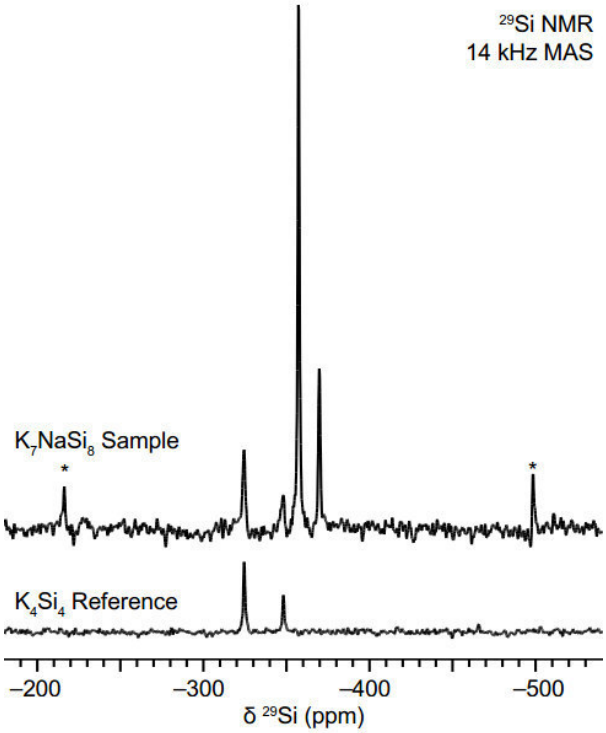

Figure S9. ^{29}Si MAS NMR spectra of K_7NaSi_8 and K_4Si_4 at MAS speeds of 14 kHz; rotational sidebands are marked by asterisks.

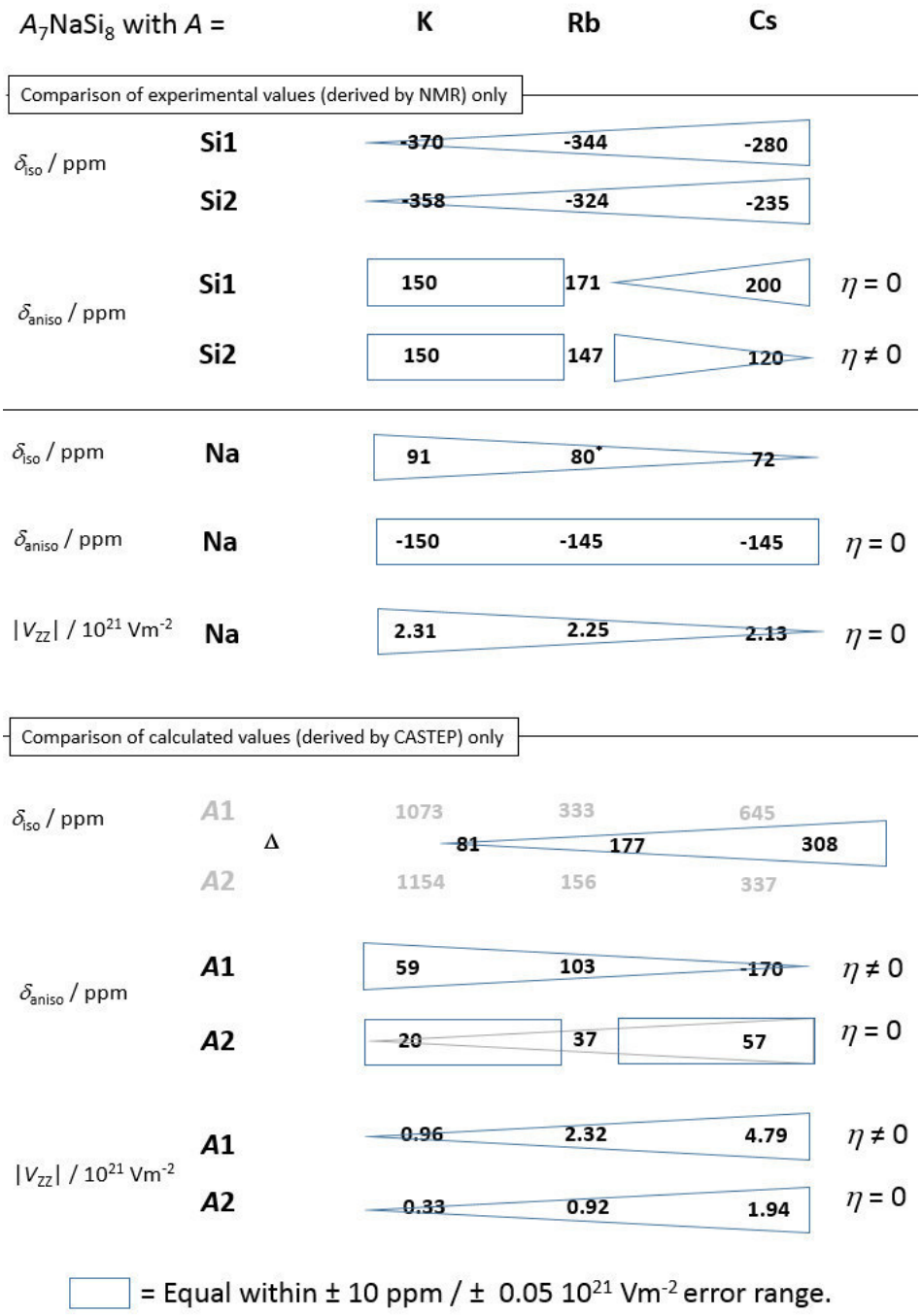

Figure S10. Schematic comparison of the NMR coupling parameters of A_7NaSi_8 with *A* = K, Rb, and Cs. The parameters derived by NMR experiments are discussed for the Si and Na atoms while for the *A*1 and *A*2 atoms (*A* = K, Rb, and Cs), the values derived by QM calculations are shown/discussed. The isotropic shift for Na in Rb_7NaSi_8 was re-calculated within this work and is exclusively shown here as the only calculated value in the upper section (marked with an asterisk). The sign for V_{ZZ} is provided by QM calculations only and $V_{ZZ}(Na) < 0$, $V_{ZZ}(A1) > 0$, and $V_{ZZ}(A2) < 0$, respectively; please refer to Table S5 and the main text for further details.

Comparison of A_7NaSi_8 (A = K, Rb, Cs)

Table S7. ^{29}Si and ^{23}Na NMR coupling parameters for A_7NaSi_8 with A = K, Rb, and Cs derived by NMR signal line shape analysis (exp.) and QM calculations using the CASTEP program (calc.). An error estimation for the given values can be found in reference [3]. The sign of C_Q and V_{ZZ} is provided by the calculations and the V_{ZZ} calculation with respect to the C_Q values considering the Q value of the respective isotope. Further details can be found in the given references and Experimental Section.

		A_7NaSi_8 with A = K[a]				**A_7NaSi_8 with A = Rb[2]**				**A_7NaSi_8 with A = Cs[3]**			
		δ_{iso} / ppm	**δ_{aniso} / ppm**	**η_δ**	**Int.**	**δ_{iso} / ppm**	**δ_{aniso} / ppm**	**η_δ**	**Int.**	**δ_{iso} / ppm**	**δ_{aniso} / ppm**	**η_δ**	**Int.**
Si1	exp.	-369.7	150.0	0.00	1	-344.0	171.4	0	1	-279.4	200.4	0	1
	calc.	-353.6	160.1	0.00	1	-348.9	180.7	0	1	-307.9	205.3	0	1
Si2	exp.	-357.2	150.0	0.25	3.4	-324.3	147.1	0.28	3	-234.6	120.2	0.38	3
	calc.	-343.9	161.8	0.26	3	-319.4	147.3	0.24	3	-244.9	120.1	0.44	3
Na	exp.	91.0	-150.0	0	1	157.2	-145.1	0	1	72.2	-145.1	0	1
	calc.	91.7	-167.6	0.00	1	85.7[c]	-160.5	0	1	64.0	-140.3	0	1
***A*1**	exp.	-	-	-	-	329.1	-108.5	0.76	6.7	649.6	-170.0	0.99	6
	calc.	1073.4[b]	59.0	0.52	6	333.4	-102.7	0.80	6	645.4	-170.4	0.95	6
***A*2**	exp.	-	-	-	-	159.7	27.2	0	1	332.6	56.5	0	1
	calc.	1154.1[b]	19.8	0.00	1	155.7	36.5	0	1	336.8	56.8	0	1
		C_Q / MHz	**V_{ZZ} / 10^{21} Vm^{-2}**	**η_Q**		**C_Q / MHz**	**V_{ZZ} / 10^{21} Vm^{-2}**	**η_Q**		**C_Q / MHz**	**V_{ZZ} / 10^{21} Vm^{-2}**	**η_Q**	
Na	exp.	5.80	2.31	0		5.66	2.25	0		5.36	2.13	0	
	calc.	-5.60	-2.23	0		-5.554	-2.21	0		-5.360	-2.13	0	
***A*1**	exp.	-	-	-		7.88	2.44	0.71		0.35	4.22	0.99	
	calc.	1.354	0.96	0.60		7.475	2.32	0.65		0.350	4.79	0.99	
***A*2**	exp.	-	-	-		2.79	0.86	0		0.15	1.81	0	
	calc.	-0.4635	-0.33	0		-2.897	-0.92	0		-0.142	-1.94	0	

[a] This work.

[b] Absolute shielding, rather than a chemical shift, is reported for the ^{39}K resonance as the potassium NMR literature is limited and the ^{39}K NMR is not the focus of this work. Absolute shielding is known to have a linear negative correlation with shift, which is consistent with what is observed for the two potassium sites in K_7NaSi_8.

[c] Re-calculated within this work.

Table S8. Site symmetry and symmetry constraints for the lineshape of the NMR signals[4] of the isotypic phases A_7NaSi_8 (*A* = K, Rb,[2][and Cs[3]) in space group $Pa\bar{3}$.

Atom	Site	Site symmetry	Relative intensity	Constraints
*A*1	24*d*	1	6	none
*A*2	4*b*	$\bar{3}$	1	$\eta = 0$
Na	4*a*	3	1	$\eta = 0$
Si1	8*c*	3	1	$\eta = 0$
Si2	24*d*	1	3	none

References

[1] H. G. von Schnering, M. Schwarz, R. Nesper, *Angew. Chem.* **1986**, *98*, 558–559; *Angew. Chem. Int. Ed. Engl.* **1986**, *25*, 566-567.

[2] T. Goebel, Y. Prots, A. Ormeci, O. Pecher, F. Haarmann, *Z. Anorg. Allg. Chem.* **2011**, *637*, 1982–1991.

[3] O. Pecher, M. Esters, A. Görne, B. Mausolf, A. Ormeci, F. Haarmann, *Z. Anorg. Allg. Chem.* **2014**, *640*, 2169-2176.

[4] a) K. R. Jeffrey, G. H. Penner, in *NMR Crystallography, Part E: Properties of the Crystalline State* (Eds.: R. K. Harris, R. E. Wasylishen, M. J. Duer), John Wiley & Sons, Chichester, West Sussex, **2009**; b) S. E. Ashbrook, S. Wimperis, in *NMR Crystallography, Part C: Coupling Interactions* (Eds.: R. K. Harris, R. E. Wasylishen, M. J. Duer), John Wiley & Sons, Chichester, West Sussex, **2009**.

5.4 Site-Specific Substitution Preferences in the Solid Solutions $Li_{12}Si_{7-x}Ge_x$, $Li_{12-y}Na_ySi_7$, $Na_7LiSi_{8-z}Ge_z$, and $Li_3NaSi_{6-v}Ge_v$

Journal of Inorganic and General Chemistry
ZAAC
Zeitschrift für anorganische und allgemeine Chemie
www.zaac.wiley-vch.de
ARTICLE

DOI: 10.1002/zaac.201600259

Site-Specific Substitution Preferences in the Solid Solutions $Li_{12}Si_{7-x}Ge_x$, $Li_{12-y}Na_ySi_7$, $Na_7LiSi_{8-z}Ge_z$, and $Li_3NaSi_{6-v}Ge_v$

Lavinia M. Scherf,[a] Nathalie Riphaus,[a] and Thomas F. Fässler*[a]

Keywords: Solid solution; Lithium; Silicon; Germanium; Electronegativity

Abstract. The mixed silicide-germanides $Li_{12}Si_{7-x}Ge_x$, $Na_7LiSi_{8-z}Ge_z$, and $Li_3NaSi_{6-v}Ge_v$ which could serve as potential precursors for $Si_{1-x}Ge_x$ materials were synthesized and characterized by X-ray diffraction methods. The full solid solution series $Li_{12}Si_{7-x}Ge_x$ ($0 \le x \le 7$) is easily accessible from the elements and features preferential occupation of the more negatively charged crystallographic tetrel positions by Ge, which is the more electronegative element. In case of $Na_7LiSi_{8-z}Ge_z$ a broad solid solution range of $1.3 \le x \le 8$ is available but the ternary silicide Na_7LiSi_8 could not be obtained by the tested methods of synthesis. The solubility of Ge in $Li_3NaSi_{6-v}Ge_v$ is highly limited to a maximum of $v \approx 0.5$, and again the formally more negatively charged tetrel positions are preferred by Ge. Additionally, the two crystallographic Li positions in $Li_{12}Si_7$ with unusually large displacement parameters can be partially substituted by Na in $Li_{12-y}Na_ySi_7$ with $0 \le y \le 0.6$. The statistical mixing of Li and Na in this solid solution contrasts the typical ordering of Li and Na in most ternary tetrelides.

Introduction

In the global struggle to switch from fossil fuels to renewable energy sources, power generation with photovoltaic technologies can play an important role.[1] However, commercial implementation, which is primarily based on crystalline silicon has not yet become truly economical in comparison to power generation from coal, natural gas, and petroleum.[2] A significant increase in solar cell efficiency achieved by a disruptive technology could significantly lower costs. However, due to the indirect band structure of crystalline silicon, solar energy absorption of solar cells based on pure silicon is limited. Therefore, many other materials such as $Cu_2ZnSnS_{4-x}Se_x$[3] and organic-inorganic perovskites[4] are currently being investigated. Alternatively, the advantages of silicon (abundant, low price, non-hazardous) can be combined with higher efficiencies in new silicon-based materials such as $Si_{1-x}Ge_x$.[5] In such materials, silicon and germanium form a solid solution, whose electronic properties are tunable by stoichiometry.[6]

Alkali metal silicides and germanides have been established as precursors for novel Si and Ge materials and allotropes. Partial oxidation of Na_4Si_4 and K_4Si_4 with gaseous HCl or H_2O leads to Si-rich clathrate structures[7] and thermal decomposition of Na_4Si_4 under vacuum even yields the guest-free clathrate $\square_{24}Si_{136}$.[8] The analogous Ge clathrate $\square_{24}Ge_{136}$ can be prepared by oxidation of Na_4Ge_9 in ionic liquids.[9] A variety of alkali metal tetrelides comprising tetrahedral $[Si_4]^{4-}$ and $[Ge_4]^{4-}$ anions have been shown to be efficient precursors for nanocrystalline Si and Ge[10] and hexagonal mesoporous Ge can be synthesized by comproportionation of K_4Ge_9 and $GeCl_4$ or by oxidation of $^1_\infty[Ge_9^{2-}]$ with ferrocenium hexafluorophosphate.[11] In 1982, single crystals of *allo*-Ge were obtained in a topochemical reaction of Li_7Ge_{12} crystals with benzophenone.[12] A similar reaction of microcrystalline Li_7Ge_{12} yielded slightly different *m-allo*-Ge, whose structure was established in 2010.[13] It consists of the two-dimensional sheets present in Li_7Ge_{12} ($^2_\infty[Ge_{24}^{14-}]$), which are statistically connected. Li_3NaSi_6, also containing two-dimensional polyanions ($^2_\infty[Si_6^{4-}]$) has been reported to be a precursor for "*allo*-Si", which has never been structurally characterized.[14] However, we have recently found the formation of amorphous Si under the same reaction conditions.[15] In addition, the formation of amorphous and crystalline germanium from K_4Ge_9 providing high surface areas in form of an inverse opal structure was reported lately.[16]

Alkali metal tetrelides, in which silicon and germanium form solid solutions, may serve as precursors, potentially giving easy access to $Si_{1-x}Ge_x$ materials. However, alkali metal silicide-germanides have been very scarcely investigated. Phases $A_4Si_{4-x}Ge_x$ (A = Na, K, Rb) and $Rb_7NaSi_{8-x}Ge_x$ were characterized crystallographically[17–20] and cell parameters of the solid solutions $Li_{12}Si_{7-x}Ge_x$ and $Li_7Si_{3-x}Ge_x$ were reported.[21] The mentioned solid solution systems have in common that both side phases, the pure silicide and the germanide, exist. Although the *A*-Si and *A*-Ge phase diagrams are very similar, there are some compounds, which are only known as either silicide or germanide, including Li_3NaSi_6 and Li_7Ge_{12}. Such phases could allow partial substitution of one tetrel element by the other, or any mixing could be impossible.

* Prof. Dr. T. F. Fässler
E-Mail: Thomas.faessler@lrz.tum.de
[a] Department of Chemistry
Technical University of Munich
Lichtenbergstraße 4
85747 Garching/München, Germany
Supporting information for this article is available on the WWW under **http://dx.doi.org/10.1002/zaac.201600259** or from the author.

For solid solutions in general, the "coloring problem" becomes an issue:[22] In structures, in which similar elements (Si/Ge or Li/Na) can occupy the same crystallographic positions, the distribution of those elements may or may not be statistical. Various factors such as coordination environment or local charges can influence site preferences.[22,23] For the mentioned alkali metal silicide-germanides both tetrel atoms statistically mix, sometimes showing specific site preferences. The alkali metals Li and Na however, typically form ordered structures as in the ternary phases Li_3NaSi_6, $Li_{18}Na_2Ge_{17}$, and Li_3NaGe_2.[24–26]

Herein we report the synthesis and characterization of solid solutions $Li_{12}Si_{7-x}Ge_x$, $Li_{12-y}Na_ySi_7$, $Na_7LiSi_{8-z}Ge_z$, and $Li_3NaSi_{6-v}Ge_v$ as potential precursors for $Si_{1-x}Ge_x$ materials. They all show site preferences of the statistically mixed atoms.

Results and Discussion

$Li_{12}Si_{7-x}Ge_x$

Since the binary lithium tetrelides $Li_{12}Si_7$ and $Li_{12}Ge_7$ crystallize isostructurally, it is not surprising that the solid solution $Li_{12}Si_{7-x}Ge_x$ exists. *Nesper* has briefly mentioned it before and also noted "certain site preferences for the different metametal components" in $Li_{12}Si_{7-x}Ge_x$,[21] but no detailed investigation has been published since. We therefore synthesized a series $Li_{12}Si_{7-x}Ge_x$ in the range of $0 \leq x \leq 7$ by high temperature syntheses from stoichiometric mixtures of the pure elements and characterized them crystallographically.

Analyses of the Si/Ge ratio in the solid solution products with starting mixtures $x = 2$, 3.5, 5 were performed with single-crystal X-ray diffraction and energy-dispersive X-ray spectroscopy. In all cases the actual substitution amount x was smaller than expected from the initial stoichiometry (Table S2, Supporting Information). In addition, these products contained increasing amounts of impurities such as Li_7Ge_3[27] and elemental Si with increasing Ge contents (Figure 1), indicating that the formation of $Li_{12}Si_{7-x}Ge_x$ becomes less favored. Yet, Si and Ge seem to be fully miscible in $Li_{12}Si_{7-x}Ge_x$.

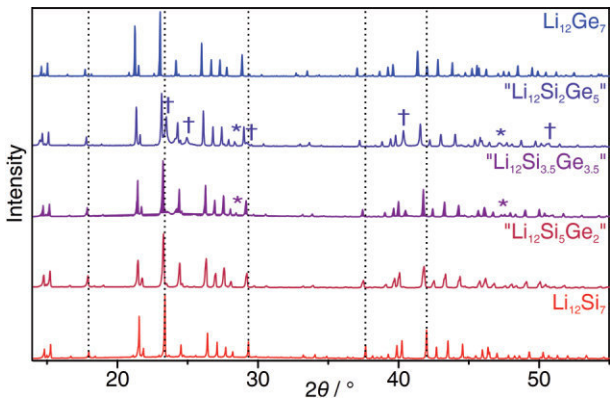

Figure 1. Experimental powder diffraction patterns of $Li_{12}Si_{7-x}Ge_x$ (starting $x = 0$, 2, 3.5, 5, 7). Small impurities are marked with * (Si) and † (Li_7Ge_3).

As expected, all phases $Li_{12}Si_{7-x}Ge_x$ crystallize isostructurally in space group *Pnma*[28,29] and show a proportional increase of cell parameters with increasing Ge content $x = 0$, 2, 3.5, 5, and 7 according to Vegard's law (Figure 2).[30]

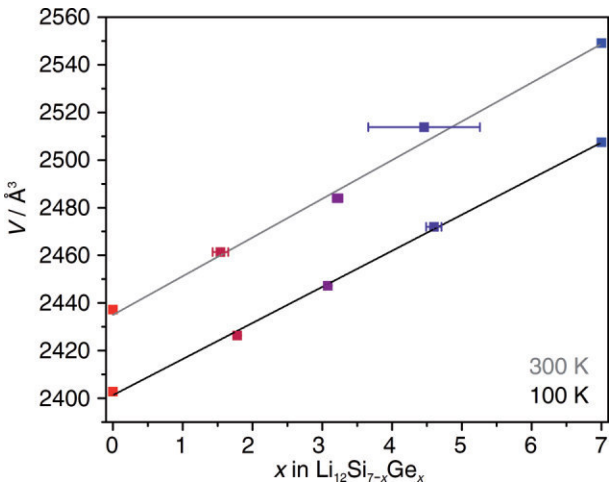

Figure 2. Vegard plot[30] illustrating an approximately linear increase of the unit cell volume of $Li_{12}Si_{7-x}Ge_x$ with increasing x at 300 and 100 K. The volumes were taken from powder diffraction (300 K) and single crystal (100 K) measurements (Tables S1 and S2). x was determined by EDX (300 K, Figures S1–S3) and the single crystal measurements (100 K). Vertical error bars are within the symbols.

The anionic substructure of the $Li_{12}Si_{7-x}Ge_x$ phases contains five-membered rings and Y-shaped stars in a 2:1 ratio (Figure 3). For the following analysis we will employ the most recent model of the anionic clusters as aromatic, cyclopentadienide-like $[T_5]^{6-}$ and carbonate-like $[T_4]^{8-}$ (T = Si, Ge).[31]

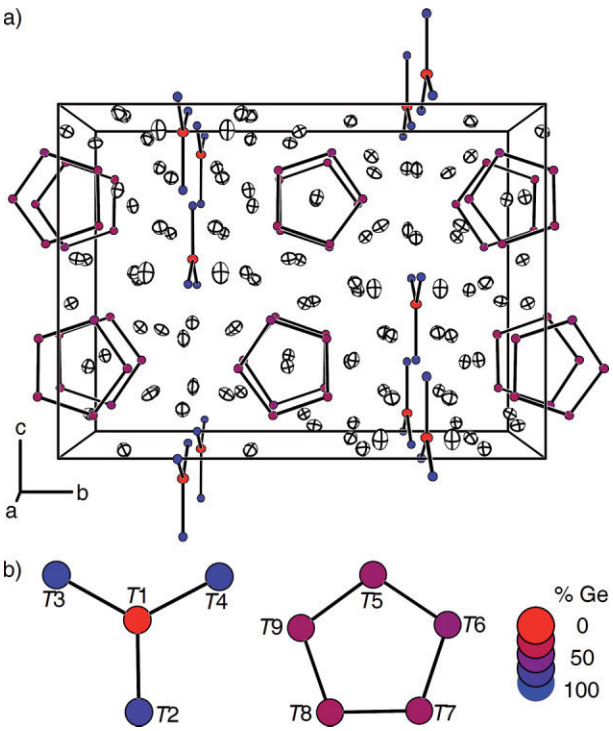

Figure 3. (a) Unit cell (thermal ellipsoids at 90 % probability at 100 K) and b) polyanionic tetrel clusters $[T_5]^{6-}$ and $[T_4]^{8-}$ of $Li_{12}Si_{7-x}Ge_x$ [$x = 3.08(2)$] showing preferential substitution on the mixed Si/Ge positions T.

Table 1. Partial occupations of the mixed Si/Ge positions *T* in $Li_{12}Si_{7-x}Ge_x$ according to single-crystal X-ray diffraction in relation to their respective formal[31] and Bader charges.[34]

Atom	% Ge in $Li_{12}Si_{7-x}Ge_x$			Formal charge[a)]	Bader charge[b)]
	x = 1.74(2)	x = 3.09(2)	x = 4.58(8)		
*T*1	0.4(2)	0.9(3)	0.8(7)	0	–0.663
*T*2	61.4(4)	80.6(5)	93.8(14)	–2.67	–1.694
*T*3	70.9(4)	86.1(5)	95.4(14)	–2.67	–1.841
*T*4	65.6(4)	83.1(5)	94.1(14)	–2.67	–1.906
*T*5	14.8(2)	37.3(3)	63.4(11)	–1.2	–1.215
*T*6	17.7(2)	41.8(4)	70.6(11)	–1.2	–1.162
*T*7	14.2(2)	35.5(4)	62.0(11)	–1.2	–1.244
*T*8	13.3(2)	33.3(3)	59.0(11)	–1.2	–1.199
*T*9	14.6(2)	35.5(3)	60.9(11)	–1.2	–1.194

a) Assuming an electron distribution[31] of $[T_5]^{6-}$ and $[T_4]^{8-}$. b) As calculated by *Chevrier* et al.[34]

In this interpretation $Li_{12}T_7$ cannot be treated as typical Zintl phases due to two additional electrons per unit cell: $(Li^+)_{12}[T_5]^{6-}([T_4]^{8-})_{0.5}(e^-)_2$. This is in good agreement with the one-dimensional metallicity that has been observed for $Li_{12}Si_7$.[32]

Interestingly, the Si/Ge occupancy ratios on the different tetrel sites in $Li_{12}Si_{7-x}Ge_x$ vary tremendously (Table 1). Atoms *T*2 to *T*4, which form the vertices of the Y-shaped star (Figure 3b; formal charge –2.67), have the highest Ge contents, and atoms *T*5 to *T*9, forming the five-membered ring (formal charge –1.2), are occupied by medium amounts of Ge. In contrast, the central atom of $[T_4]^{8-}$, *T*1 (formal charge 0), contains no significant or very small amounts of Ge in the mixed silicide-germanides. These variations in Ge content correlate strongly with formal charges of the different tetrel sites: the greater the negative charge of a tetrel site, the more Ge, which is more electronegative, prefers the respective sites.[33] The formal charges derived from our description of the anionic clusters agree qualitatively with Bader charges that have been calculated for $Li_{12}Si_7$ by *Chevrier* et al.[34]

$Li_{12-y}Na_ySi_7$

For all members of the $Li_{12}Si_{7-x}Ge_x$ series we noticed particularly large atomic displacement parameters for Li1 and Li9 (Table S3, Supporting Information).[35] This could be explained by either partial occupation of these positions or by a larger cavity for Li atoms on these sites.

Partial occupation of Li positions in $Li_{12}T_7$ would lower the number of extra electrons per formula unit, potentially resulting in an electron-precise Zintl phase. Therefore, we first attempted free refinement of the respective site occupancy factors. However, both Li1 and Li9 are fully occupied in all cases. In order to test the hypothesis of a larger cavity for Li1 and Li9 we attempted to substitute these two positions by the larger alkali metal cations Na^+, K^+, Rb^+, and Cs^+ as well as Ag^+, which is known to be able to replace Li^+ in various compounds.[36] Reactions including K, Rb, Cs, and Ag afforded only pure $Li_{12}Si_7$ next to known binary and ternary phases. In a reaction aimed at "$Li_{10.5}Na_{1.5}Si_7$", however, we were able to obtain a solid solution $Li_{12-y}Na_ySi_7$. This is again clearly indicated in powder diffraction patterns by a shift of all reflections toward smaller angles 2θ and significantly larger cell parameters obtained from indexing (Figure 4).

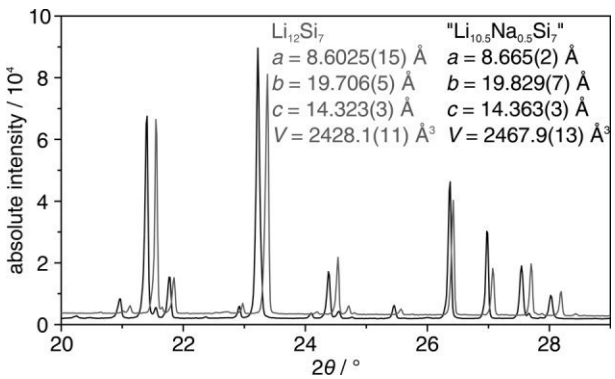

Figure 4. Powder diffraction patterns of $Li_{12}Si_7$ (grey) and "$Li_{10.5}Na_{1.5}Si_7$" (black) showing a shift in diffraction angles. Both patterns were referenced with an external Si standard. Cell parameters were determined by indexing the patterns using TREOR[37] as implemented in WinXPOW.[38]

Additionally, suitable single crystals were selected from $Li_{12-y}Na_ySi_7$ samples with y = 0 and y = 1.5, which were characterized by X-ray diffraction. The "$Li_{10.5}Na_{1.5}Si_7$" crystal yields a crystallographic composition of $Li_{11.56(1)}Na_{0.44}Si_7$, whereas Rietveld refinement of the corresponding powder diffraction pattern results in a bulk stoichiometry of $Li_{11.39(3)}Na_{0.61}Si_7$ (Figure S6, Table S7, Supporting Information). EDX measurements were performed on a single crystal of "$Li_{10.5}Na_{1.5}Si_7$", further proving that Na is incorporated into the structure (Figure S5). The Na:Si ratio obtained by EDX translates to a sum formula of $Li_{12-y}Na_ySi_7$ with y = 0.48(1). The significantly lower Na content than in the starting mixture obtained from three independent methods suggests that Li substitution by Na is very limited. In addition, the powder diffraction pattern (Figure S4) also shows traces of the Na-containing side phase Na_4Si_4. We therefore conclude a maximum Na content in $Li_{12-y}Na_ySi_7$ of approximately $y < 0.6$.

To test for possible substitutions of Li by Na, the site occupancy factors of all Li positions were freely refined in structure determinations from single crystal diffraction and Rietveld refinement. However, only Li1 and Li9 contain significant amounts of Na (Table 2), proving larger cavities for the alkali

metal cations there. The partial incorporation of Na on these sites leads to increased Si–*A* (*A* = Li/Na) distances with respect to binary $Li_{12}Si_7$ (Table S4).

Table 2. Partial occupations of Li positions in $Li_{12-y}Na_ySi_7$ with Na (mixed Li/Na positions are abbreviated as *A*) according to single-crystal X-ray diffraction (SCXRD) and Rietveld refinement (RV).

Atom	% Na SCXRD [*y* = 0.443(8)]	% Na RV [*y* = 0.61(3)]	Coordination number[a)] (Si + Li/*A*)
*A*1	15.2(7)	25(2)	3 + 5
Li2	0	0	5 + 5
Li3	0	0	5 + 5
Li4	0	0	5 + 5
Li5	0	0	5 + 5
Li6	0	0	5 + 5
Li7	0	0	5 + 5
Li8	0	0	10 + 5
*A*9	36.8(5)	48(2)	3 + 4
Li10	0	0	4 + 6
Li11	0	0	5 + 6
Li12	0	0	4 + 6
Li13	0	0	4 + 4

a) All neighboring atoms with interatomic distances of up to 3.1 Å are considered.

A closer look at the coordination numbers of all Li positions shows why exactly two Li positions are partially substituted by Na (Table 2). Since the structure does not allow clear distinction of the first and second coordination spheres, a maximum interatomic distance of 3.1 Å was arbitrarily chosen for comparison. Pure Li positions have four to ten Si and four to six Li neighbors. In contrast, the mixed positions *A*1 and *A*9 are coordinated by only three Si atoms as well as five and four Li atoms, respectively. The resulting coordination spheres are displayed in Figure 5. Clearly, the *A*1 and *A*9 atoms are more agile and their thermal ellipsoids are elongated along the direction providing the most space. However, the $Li_{12}Si_7$ structure can apparently not compensate a full occupation of these positions by Na only.

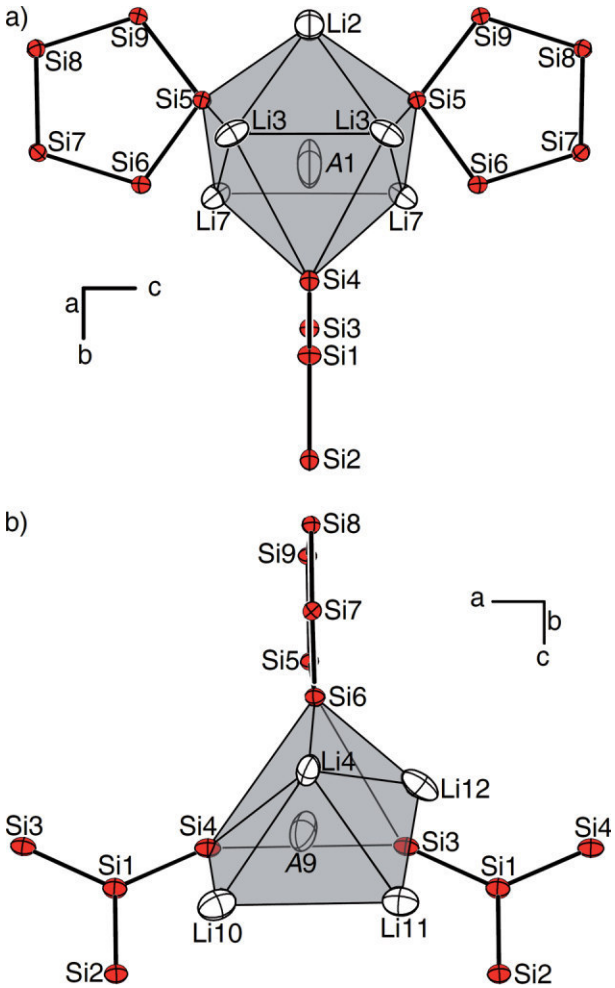

Figure 5. Coordination spheres of (a) *A*1 [15.2(7) % Na] and (b) *A*9 [36.8(5) % Na] in $Li_{12-x}Na_xSi_7$ [$x = 0.443(9)$; thermal ellipsoids at 90 % probability at 123 K]. All neighboring atoms with interatomic distances of up to 3.1 Å are included (Table S4).

$Na_7LiSi_{8-z}Ge_z$

During our investigations in the Li-Na-Ge system,[25,26] the new compound Na_7LiGe_8 was frequently observed as a side phase. The Zintl phase is readily available from a stoichiometric melt of the elements. Rietveld refinement (Table S8, Supporting Information) shows that it is isostructural to the known $A_7A'T_8$ phases, crystallizing in the cubic space group $Pa\bar{3}$.[17,24,39–41] Na_7LiGe_8 comprises tetrahedral $[Ge_4]^{4-}$ clusters, which are bridged to $[Ge_4–Li–Ge_4]^{7-}$ dimers by η^3-coordinating Li^+ cations (Figure 6). Na^+ cations on two different atomic positions (Na1 on 24*d*, Na2 on 4*a*) balance the charge of the Zintl phase.

For $Rb_7NaSi_{8-x}Ge_x$, another representative of this structure type, both ternary phases Rb_7NaSi_8 and Rb_7NaGe_8 as well as solid solution phases with $x = 1–3$ have been characterized previously,[20,40] and the solid solution was shown to be soluble in liquid ammonia.[20] In the context of a search for suitable precursors for new $Si_{1-x}Ge_x$ materials, we therefore first attempted to prepare the analogous silicide, Na_7LiSi_8. However, it is not available with this synthesis route or from the binary starting materials Na_4Si_4 and LiSi.[42] Nevertheless, solid solution phases $Na_7LiSi_{8-z}Ge_z$ with low Ge contents of as little as $z = 1.3(1)$ were obtained from stoichiometric melts of the elements. The grey powders obtained were characterized by Rietveld analyses (Tables S7 and S9; Figures S7–S11, Supporting Information), and in all samples the side phase $Na_4Si_{4-w}Ge_w$ is also present.

In accordance with Vegard's rule,[30] the cell volume of the cubic structure decreases linearly with increasing Si content (Figure 7). The site occupancy factors obtained from Rietveld refinement (Table 3) show that the Ge1 position, which is not coordinated by η^3-capping Li1 (cf. Figure 6b), is preferentially substituted by Si. Yet, partial substitution of Ge2 also occurs.

In order to rationalize the non-existence of Na_7LiSi_8 we analyzed the interatomic distances in $Na_7LiSi_{8-z}Ge_z$ in comparison with those reported for the closely related compound KNa_6LiSi_8,[24] in which Na2 is replaced by K (Figure S12, Supporting Information). Most interatomic distances change inconspicuously and only the large increase of the *T*2–Na1 dis-

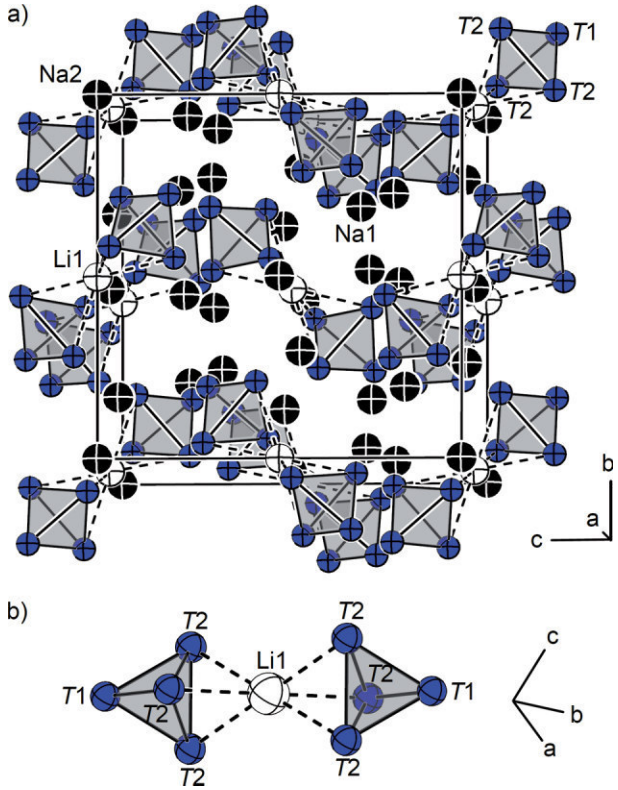

Figure 6. (a) Projection of the unit cell of $Na_7LiSi_{8-z}Ge_z$ (here: $z = 8$); (b) dimeric $[T_4–Li–T_4]^{7-}$ unit. Na atoms are shown in black, Li atoms in white, and mixed Si/Ge positions *T* in blue.

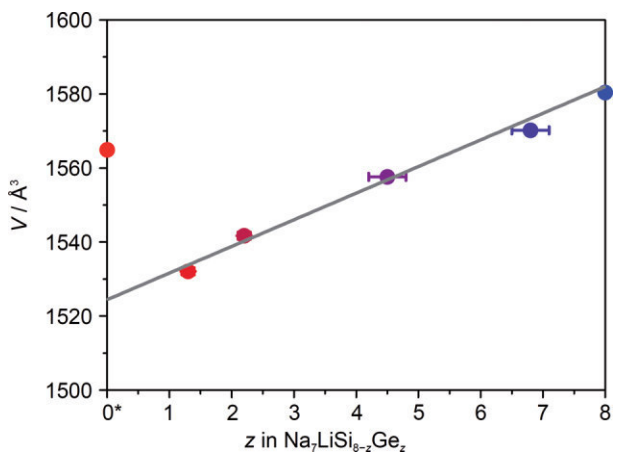

Figure 7. Vegard plot[30] illustrating the linear reduction of the cubic cell volume in solid solution phases $Na_7LiSi_{8-z}Ge_z$. Vertical error bars are within the symbols, * data for $z = 0$ from KNa_6LiSi_8,[24] in which Na2 is replaced by K.

Table 3. Partial occupations of the mixed Si/Ge positions *T* in $Na_7LiSi_{8-z}Ge_z$ according to Rietveld refinements.

Atom	% Ge in $Na_7LiSi_{8-z}Ge_z$				
	$z = 1.3(1)$	$z = 2.2(1)$	$z = 4.5(3)$	$z = 6.8(3)$	$z = 8$
*T*1	6(2)	10(2)	30 (4)	68(4)	100
*T*2	19(1)	34(2)	65(4)	91(4)	100

tance from $Na_7LiSi_{6.7(1)}Ge_{1.3}$ to KNa_6LiSi_8 is somewhat peculiar. Therefore, a reason for the non-existence of Na_7LiSi_8 could be that the resulting *T*2–Na1 contacts (three per *T*2 atom) would be too short in the silicide. In any case, the substitution of Na2 by K in KNa_6LiSi_8 stabilizes the structure compared to Na_7LiSi_8.

$Li_3NaSi_{6-v}Ge_v$

Syntheses of $Li_3NaSi_{6-v}Ge_v$ with varying *v* were attempted using two different approaches (a) and (b), which were proven to be successful synthesis routes for Li_3NaSi_6:[15]

(a) $Li_{12}Si_{7-x}Ge_x + Na_4Si_{4-w}Ge_w + 13Si \rightarrow 4Li_3NaSi_{6-v}Ge_v$

(b) $3LiH + NaH + (6-v)Si + vGe \rightarrow Li_3NaSi_{6-v}Ge_v + 2H_2$

Route (a) employs silicide-germanides $Li_{12}Si_{7-x}Ge_x$ ($0 \le x \le 7$) and $Na_4Si_{4-w}Ge_w$ ($0 \le w \le 4$), which are both readily available with different Si/Ge ratios.[18,21] These reactants were characterized by X-ray diffraction (XRD), Rietveld refinements, energy-dispersive X-ray spectroscopy or single-crystal X-ray diffraction. We chose this synthesis approach because Si/Ge mixing on an atomic level in the precursor compounds could facilitate the formation of a solid solution of Si and Ge in the diffusion-controlled solid state reaction. XRD powder patterns of route (a) syntheses show that "$Li_3NaSi_{5.5}Ge_{0.5}$" (reactants $Li_{12}Si_7$, $Na_4Si_2Ge_2$, α-Si) contains only minor impurities (Figure S14, Supporting Information). All reflections for "$Li_3NaSi_{5.5}Ge_{0.5}$" are shifted towards smaller diffraction angles 2θ with respect to Li_3NaSi_6, indicating a successful incorporation of Ge into the anionic Si substructure (Figure 8). A comparison of cell parameters from indexing powder diffraction patterns confirms this.

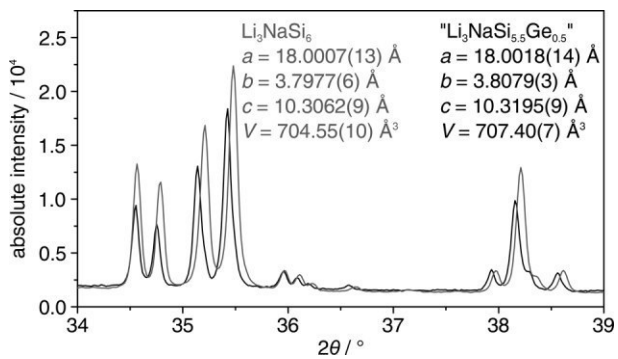

Figure 8. Powder diffraction patterns of Li_3NaSi_6 (grey) and "$Li_3NaSi_{5.5}Ge_{0.5}$" (black) from synthesis (a) showing a slight shift in diffraction angles. Both patterns were referenced with an external Si standard. Cell parameters were determined by indexing the patterns using DICVOL04[43] as implemented in WinXPOW.[38]

All materials synthesized with route (a) are microcrystalline and do not yield single crystals suitable for X-ray diffraction studies. Instead, from route (b) employing the alkali metal hydrides LiH and NaH, needle-shaped single crystals were obtained, allowing the structure determination of $Li_3NaSi_{5.56(1)}Ge_{0.44(1)}$. However, products from this route contain larger amounts of side products.

$Li_3NaSi_{6-v}Ge_v$ syntheses were attempted with varying overall Ge contents ($0 \le v \le 3$; cf. Table 6). Product analyses by

Table 4. Si/Ge ratios in $Li_3NaSi_{6-v}Ge_v$ and resulting empirical formulae from synthesis attempts with $x = 0.5$.

Route	% Si	% Ge	Sum formula	Method of analysis
(a)	92.5(2)	7.5(2)	$Li_3NaSi_{5.55(1)}Ge_{0.45}$	Rietveld refinement
(b)	92.7(2)	7.3(2)	$Li_3NaSi_{5.56(1)}Ge_{0.44}$	single-crystal XRD
(b)	92.1(4)	7.9(4)	$Li_3NaSi_{5.53(3)}Ge_{0.47}$	EDX

indexing of XRD powder patterns show that the greatest possible incorporation of Ge into the anionic substructure is reached for $v \approx 0.5$ in both synthesis routes. Greater overall Ge contents of reactants only lead to greater amounts of more Ge-rich side products such as $Li_{12}Si_{7-x}Ge_x$, $Na_7LiGe_{8-z}Si_z$ and $Li_{18}Na_2Ge_{17}$.[25] Therefore, the purest samples of $Li_3NaSi_{6-v}Ge_v$ with a maximum v were obtained with overall Ge contents of $v = 0.5$. The resulting products were analyzed for their Si/Ge ratios with Rietveld refinement [route (a) product, Figure S16, Table S13, Supporting Information], single-crystal X-ray diffraction [route (b) product, Tables S10–S12, Supporting Information], and EDX of a single crystal [route (b) product, Figure S13, Supporting Information]. The results for all methods are summarized in Table 4 and agree well, indicating a maximum Ge content of $0.4 \leq v \leq 0.5$ or 6.7 to 8.3 % in the anionic substructure of $Li_3NaSi_{6-v}Ge_v$.

$Li_3NaSi_{5.56(1)}Ge_{0.44}$ crystallizes isostructurally with Li_3NaSi_6[14] in space group *Pnma* with $a = 17.949(2)$ Å, $b = 3.8085(3)$ Å, $c = 10.2947(8)$ Å and $Z = 8$ (Table S11). It contains two-dimensional sheets of $^2_\infty[T_6]^{4-}$ (T = Si, Ge) which are separated by Li and Na cations (Figure 9a). The tetrel sheets are constructed from four-valent *T*1, *T*5, and *T*6, three-valent *T*3 and *T*4, as well as two-valent *T*2, resulting in the alternative formulation $^2_\infty[(4b\text{-}T^0)_3(3b\text{-}T^-)_2(2b\text{-}T^{2-})]$ for the polyanion (Figure 9b).

As in $Li_{12}Si_{7-x}Ge_x$, the Si/Ge occupancy ratios on the different tetrel sites in $Li_3NaSi_{5.56(1)}Ge_{0.44(1)}$ vary tremendously (Table 5). The formally neutral, four-valent sites 4b-T^0 contain no significant amount of Ge, whereas 3b-T^- sites have Ge contents of 6.8(6) and 8.9(5) %, and 2b-T^{2-} shows a Ge occupancy of 24.3(7) % in the single crystal measurements. Rietveld refinement gives similar results. Again, these variations in Ge content correlate with formal charges of the different tetrel sites, and the greater the negative charge of a tetrel site, the more Ge, which is more electronegative, prefers the respective sites.[33]

Table 5. Partial occupations of the mixed Si/Ge positions *T* in $Li_3NaSi_{6-v}Ge_v$ according to single-crystal X-ray diffraction (SCXRD) and Rietveld refinement (RV) and their respective formal charges.

Position	% Ge SCXRD [$v = 0.44(1)$]	% Ge RV [$v = 0.45(2)$]	Formal charge
*T*1	1.6(5)	0	0
*T*2	24.3(7)	28.3(3)	–2
*T*3	8.9(5)	9.1(3)	–1
*T*4	6.8(6)	7.4(4)	–1
*T*5	1.2(5)	0	0
*T*6	1.3(5)	0	0

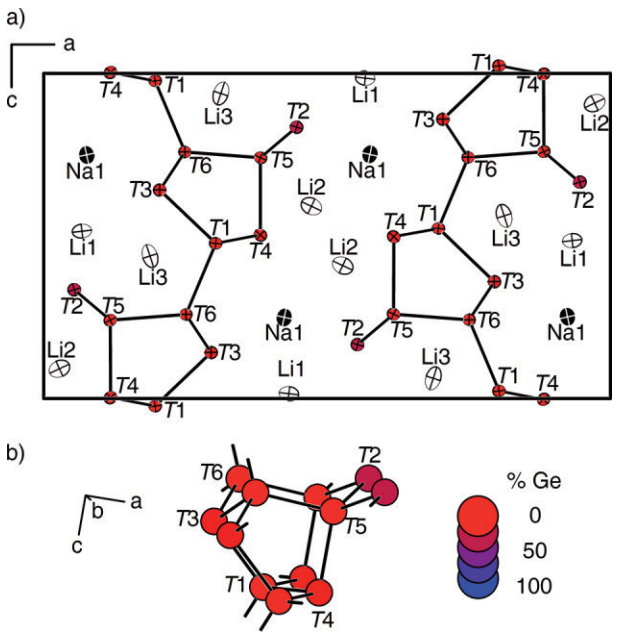

Figure 9. (a) Projection of the unit cell of $Li_3NaSi_{5.56(1)}Ge_{0.44}$ onto the *ac* plane (thermal ellipsoids at 90 % probability at 100 K), mixed Si/Ge positions are abbreviated as *T*; (b) subunit of the $^2_\infty[T_6]^{4-}$ polyanion showing preferential substitution of the *T*2, *T*3, and *T*4 positions by Ge.

Conclusions

We have shown that both constituents of the Zintl-like phase $Li_{12}Si_7$ can be substituted by the related elements Na and Ge, respectively. Since $Li_{12}Si_7$ and $Li_{12}Ge_7$ exist isostructurally, the full solid solution series $Li_{12}Si_{7-x}Ge_x$ is accessible. The distribution of Si and Ge in $Li_{12}Si_{7-x}Ge_x$ onto the various positions in cyclopentadienide-like $[T_5]^{6-}$ and carbonate-like $[T_4]^{8-}$ clusters varies greatly. These preferences can be explained by the respective electronegativities, with more electronegative Ge atoms preferring the more negatively charged positions. This statistical mixing behavior is typical for the two neighboring tetrel elements. The alkali metals Li and Na typically form ordered structures with clearly separated Li and Na positions. Remarkably, a solid solution $Li_{12-y}Na_ySi_7$ with a maximum Na content of $y < 0.6$ was obtained, explaining the large isotropic displacement parameters for the two partially substitutable Li positions in all $Li_{12}Si_{7-x}Ge_x$ phases.

In addition, Na_7LiGe_8 and its solid solution $Na_7LiSi_{8-z}Ge_z$ are readily available from stoichiometric melts of the constituting elements. Although we observe a large solution range ($1.3 \leq z \leq 8$), ternary Na_7LiSi_8 cannot be obtained under these conditions. When attempting to prepare $Li_3NaSi_{6-v}Ge_v$ we discovered that the synthesis of this solid solution is limited to a

maximum Ge content of $v \approx 0.5$. The distribution of Si and Ge atoms onto the different crystallographic positions in the two-dimensional polyanions can also be explained by the more electronegative Ge preferring the formally more negatively charged atomic positions.

Overall, we have shown that it is possible to synthesize various mixed alkali metal silicide-germanides that may serve as precursors for novel $Si_{1-x}Ge_x$ materials. However, the miscibility of Si and Ge strongly differs between the different compounds. Thus, there remains a lot to be learned about the mixing behavior of similar elements in Zintl and Zintl-like phases. Further investigations on such systems could give more insight on the existence and extent of substitution in different solid solutions.

Experimental Section

General Remarks: All steps of synthesis and sample preparation were carried out in an argon-filled glove box (MBraun, H_2O level <0.6 ppm, O_2 level <1.2 ppm). >99 % Li rods (Rockwood-Lithium) and >99 % Na rods (Chempur) were freed from oxidic layers before use, whereas 99.9 % Si powder (Wacker), 99.999 % Ge pieces (Chempur), 98 % LiH powder (Alfa Aesar) and 95 % NaH powder (Sigma Aldrich) were utilized without further purification.

Synthesis of LiSi: LiSi was synthesized by mechanical alloying.[44] A stoichiometric mixture of the pure elements (total mass 2.0 g) and three WC grinding balls (diameter 15 mm) were placed inside a 50 mL WC milling jar which was then sealed airtight. Using a planetary ball mill (Retsch, PM 100) the jar was rotated for 12 h at 300 rpm with 2 min breaks and inversion of the rotation direction after each 30 min interval.

Synthesis of $Li_{12}Si_{7-x}Ge_x$: Compounds $Li_{12}Si_{7-x}Ge_x$ (x = 0, 2, 3.5, 5, 7) were synthesized from the pure elements in Ta ampules. Sealed ampules containing stoichiometric reaction mixtures with a total mass of 0.5 g, respectively, were placed inside a silica reaction container, which was evacuated and heated to 750 °C for 1 h. The resulting melt was cooled down at a rate of 0.5 K·min^{-1} to 400 °C, at which temperature annealing of the product was allowed for 6 h.

Synthesis of $Li_{12-y}Na_ySi_7$: Compounds $Li_{12-y}Na_ySi_7$ (y = 0, 1.5) were synthesized from of LiSi, Li (and Na) in Ta ampules. Sealed ampules containing a stoichiometric reaction mixture with a total mass of 0.4 g, respectively, were placed inside a silica reaction container which was evacuated and heated to 750 °C for 1 h. The resulting melt was cooled down at a rate of 0.5 K·min^{-1} to 400 °C, at which temperature annealing of the product was allowed for 6 h.

Synthesis of $Na_7LiSi_{8-z}Ge_z$: $Na_7LiGe_{8-z}Si_z$ was synthesized from stoichiometric amounts (z = 1, 2, 4, 6, 8) of the elements with a total mass of 1 g in tantalum ampules which were treated as described above. The reaction mixture was heated to 750 °C at 5 K min^{-1} and after 1 h of dwelling cooled to 300 °C at 0.5 K·min^{-1}. Subsequent dwelling for 3 h afforded the desired products.

Synthesis of $Na_4Si_{4-w}Ge_w$: Compounds $Na_4Si_{4-w}Ge_w$ (w = 0, 2, 3, 4) were synthesized in 1 g batches from the pure elements in Ta ampules. Sealed ampules containing stoichiometric reaction mixtures were placed inside a silica reaction container which was then evacuated and preheated to 500 °C for 1 h. The reaction mixture was brought to a reaction at 600 °C for 30 h.

Synthesis of $Li_3NaSi_{6-v}Ge_v$: Synthesis attempts of compounds $Li_3NaSi_{6-v}Ge_v$ ($0 \le v \le 3$) were performed in 0.5 g batches using two different synthesis routes (Table 6). To obtain single phase product, $Li_3NaSi_{6-v}Ge_v$ was synthesized using stoichiometric amounts of $Li_{12}Si_{7-x}Ge_x$ (x = 0, 3.5), $Na_4Si_{4-w}Ge_w$ (w = 0, 2, 3, 4) and α-Si, which were mixed thoroughly by grinding in an agate mortar. The reaction mixtures were pressed to pellets and sealed in Ta ampules. For single crystals of $Li_3NaSi_{6-v}Ge_v$, stoichiometric amounts of LiH, NaH, α-Si, and α-Ge were mixed thoroughly in an agate mortar and sealed in Ta ampules. All ampules were placed inside silica reaction containers which were evacuated and heated to 550 °C for 24–72 h. The reaction mixtures were cooled down very slowly at a rate of 0.075 K·min^{-1}.

Structure Determination: Crystals of, $Li_{12}Si_{7-x}Ge_x$, $Li_{12-y}Na_ySi_7$, and $Li_3NaSi_{6-v}Ge_v$ were selected in an argon-filled glove box and sealed in 0.3 mm glass capillaries. For the best specimens intensity data were collected at 100 K with a Bruker AXS X-ray diffractometer equipped with a CCD detector (APEX II, κ-CCD), a MONTEL optic monochromator. A fine-focused sealed tube ($Li_{12}Si_{7-x}Ge_x$ and $Li_{12-y}Na_ySi_7$) and a rotating anode FR591 ($Li_3NaSi_{6-v}Ge_v$) with Mo-K_α radiation (λ = 0.71073 Å), respectively, were used as X-ray sources. Data collection was controlled with the Bruker APEX Software package.[45] Integration, data reduction and absorption correction were performed with the SAINT[46] and SADABS[47] packages. The structures were solved with direct methods (SHELXS-2014/7) and refined with full-matrix least-squares on F^2 (SHELXL-2014/7).[48] For the refinement of mixed occupancies, the respective sites were split. Atom coordinates and atomic displacement parameters were constrained to be identical for both atom types. Free refinement of site occupation factors resulted in similar results as after constraining to a total occupancy of one.

Further details of the crystal structures investigations may be obtained from the Fachinformationszentrum Karlsruhe, 76344 Eggenstein-Leopoldshafen, Germany (Fax: +49-7247-808-666; E-Mail: crysdata@fiz-karlsruhe.de, http://www.fiz-karlsruhe.de/request for deposited data.html) on quoting the depository numbers CSD-430491

Table 6. Product mixtures from various synthesis attempts of $Li_3NaSi_{6-v}Ge_v$. Main products are marked in bold.

Reactants	x	Products
$Li_{12}Si_7$, Na_4Si_4, Si	0	**Li_3NaSi_6**, $Li_{12}Si_{7-x}Ge_x$, Si
LiH, NaH, Si	0	**Li_3NaSi_6**
$Li_{12}Si_7$, $Na_4Si_2Ge_2$, Si	0.5	**$Li_3NaSi_{6-v}Ge_v$**, Si
LiH, NaH, Si, Ge	0.5	**$Li_3NaSi_{6-v}Ge_v$**, $Li_{12}Si_{7-x}Ge_x$, Si
$Li_{12}Si_7$, Na_4SiGe_3, Si	0.75	**$Li_3NaSi_{6-v}Ge_v$**, $Li_{12}Si_{7-x}Ge_x$, Si, $Na_7LiGe_{8-z}Si_z$
$Li_{12}Si_{3.5}Ge_{3.5}$, Na_4Si_4, Si	0.875	**$Li_3NaSi_{6-v}Ge_v$**, **$Li_{12}Si_{7-x}Ge_x$**, Si, $Na_7LiGe_{8-z}Si_z$
$Li_{12}Si_7$, Na_4Ge_4, Si	1.0	**$Li_3NaSi_{6-v}Ge_v$**, **$Li_{12}Si_{7-x}Ge_x$**, Si, $Na_7LiGe_{8-z}Si_z$
$Li_{12}Si_{3.5}Ge_{3.5}$, $Na_4Si_2Ge_2$, Si	1.375	**$Li_{12}Si_{7-x}Ge_x$**, Si, $Na_7LiGe_{8-z}Si_z$
$Li_{12}Si_{3.5}Ge_{3.5}$, $Na_4Si_2Ge_2$, Si, Ge	3.0	**$Li_{12}Si_{7-x}Ge_x$**, Si, $Si_{1-w}Ge_w$, $Na_7LiGe_{8-z}Si_z$, $Li_{18}Na_2Ge_{17}$
LiH, NaH, Si, Ge	3.0	$Li_{12}Si_{7-x}Ge_x$, Si, **$Na_7LiGe_{8-z}Si_z$**, **$Li_{18}Na_2Ge_{17}$**

($Li_{12}Si_7$ at 100 K), CSD-430492 ($Li_{12}Si_{5.22(2)}Ge_{1.78}$), CSD-430493 ($Li_{12}Si_{3.92(2)}Ge_{3.08}$), CSD-430494 ($Li_{12}Si_{2.40(11)}Ge_{4.60}$), CSD-430495 ($Li_{12}Ge_7$), CSD-430496 ($Li_{12}Si_7$ at 123 K), CSD-430497 ($Li_{11.56(1)}Na_{0.44}Si_7$), and CSD-430490 ($Li_3NaSi_{5.56(1)}Ge_{0.44}$).

Powder X-ray Diffraction (PXRD): PXRD patterns of $Li_{12}Si_{7-x}Ge_x$ (x = 0, 2, 3.5, 5, 7), $Li_{12-y}Na_ySi_7$ (y = 1.5), $Na_7LiSi_{8-z}Ge_z$ (z = 1, 2, 4, 6, 8), and $Li_3NaSi_{6-v}Ge_v$ (v = 0, 0.5; from binary compounds and hydride routes) were recorded with a Stoe STADI P diffractometer equipped with a Ge(111) monochromator for Cu-K_α radiation (λ = 1.54056 Å) and a Dectris MYTHEN DCS 1 K solid state detector. Crystalline samples of these synthesis products were ground in an agate mortar and filled into 0.3 mm glass capillaries, which were then sealed. The samples were measured within a 2θ range of 5–89° (PSD steps: 0.075°; time/step: 45 s). For indexing, selected PXRD patterns were angle-corrected with external α-silicon[49] standards.

Rietveld Refinement: Rietveld refinements were performed using Jana2006.[50] 15th order Chebychev functions were used to fit the background and the zero point error was refined freely. Reflections were fitted with the Pseudo Voigt function and the Berar Baldinozzi model with four refined parameters for peak asymmetry. Crystal structures of $Li_{12}Si_7$,[29] K_7LiSi_8,[41] and Li_3NaSi_6,[14] respectively, were used as initial structural models. All cell parameters and atom positions as well as site occupancies for mixed positions were refined. Displacement parameters were refined when possible. Detailed results of Rietveld refinements are given in the Supporting Information.

Energy-Dispersive X-ray Spectroscopy (EDX): EDX spectra of crystalline materials were obtained with a JSM 7500F scanning electron microscope (JEOL) and an Oxford X-Max EDX analyzer with internal Mn standard. Single crystals were mounted onto an Al stub using graphite tape. Ratios of Na, Si and Ge in the single crystals were determined from several EDX measurements (elements with an atomic number <4 cannot be detected by this method).

Supporting Information (see footnote on the first page of this article): Detailed single crystal and powder X-ray diffraction data, Rietveld refinement results and EDX data of the investigated solid solutions $Li_{12}Si_{7-x}Ge_x$, $Li_{12-y}Na_ySi_7$, $Na_7LiSi_{8-z}Ge_z$, and $Li_3NaSi_{6-v}Ge_v$.

Acknowledgements

The authors thank *K. Rodewald* for EDX measurements. *L. M. S* and *N. R.* are grateful to the Studienstiftung des Deutschen Volkes for their fellowships *L. M. S* thanks the Fonds der Chemischen Industrie for her fellowship and the TUM Graduate School for support.

References

[1] International Energy Agency, *World Energy Outlook*, OECD, Paris, **2014**.
[2] S. Chu, A. Majumdar, *Nature* **2012**, *488*, 294–303.
[3] S. Delbos, *EPJ Photovolt.* **2012**, *3*, 35004.
[4] S. D. Stranks, P. K. Nayak, W. Zhang, T. Stergiopoulos, H. J. Snaith, *Angew. Chem.* **2015**, *127*, 3288–3297; *Angew. Chem. Int. Ed.* **2015**, *54*, 3240–3248.
[5] a) C. Eisele, M. Berger, M. Nerding, H. P. Strunk, C. E. Nebel, M. Stutzmann, *Thin Solid Films* **2003**, *427*, 176–180; b) R. Lechner, M. Buschbeck, M. Gjukic, M. Stutzmann, *Phys. Status Solidi C* **2004**, *1*, 1131–1143.
[6] J. S. Kline, F. H. Pollack, M. Cardona, *Helv. Phys. Acta* **1968**, *41*, 968–977.
[7] B. Böhme, A. M. Guloy, Z. Tang, W. Schnelle, U. Burkhardt, M. Baitinger, Y. Grin, *J. Am. Chem. Soc.* **2007**, *129*, 5348–5349.
[8] A. Ammar, C. Cros, M. Pouchard, N. Jaussaud, J.-M. Bassat, G. Villeneuve, M. Duttine, M. Ménétrier, E. Reny, *Solid State Sci.* **2004**, *6*, 393–400.
[9] A. M. Guloy, R. Ramlau, Z. Tang, W. Schnelle, M. Baitinger, Y. Grin, *Nature* **2006**, *443*, 320–323.
[10] a) R. A. Bley, S. M. Kauzlarich, *J. Am. Chem. Soc.* **1996**, *118*, 12461–12462; b) D. Neiner, H. W. Chiu, S. M. Kauzlarich, *J. Am. Chem. Soc.* **2006**, *128*, 11016–11017; c) B. R. Taylor, S. M. Kauzlarich, H. W. H. Lee, G. R. Delgado, *Chem. Mater.* **1998**, *10*, 22–24; d) B. M. Nolan, T. Henneberger, M. Waibel, T. F. Fässler, S. M. Kauzlarich, *Inorg. Chem.* **2015**, *54*, 396–401.
[11] a) G. S. Armatas, M. G. Kanatzidis, *Science* **2006**, *313*, 817–820; b) G. S. Armatas, M. G. Kanatzidis, *Adv. Mater.* **2008**, *20*, 546–550; c) D. Sun, A. E. Riley, A. J. Cadby, E. K. Richman, S. D. Korlann, S. H. Tolbert, *Nature* **2006**, *441*, 1126–1130.
[12] A. Grüttner, R. Nesper, H. G. von Schnering, *Angew. Chem.* **1982**, *94*, 933; *Angew. Chem. Int. Ed. Engl.* **1982**, *21*, 912–913.
[13] F. Kiefer, A. J. Karttunen, M. Döblinger, T. F. Fässler, *Chem. Mater.* **2011**, *23*, 4578–4586.
[14] H. G. von Schnering, M. Schwarz, R. Nesper, *J. Less-Common Met.* **1988**, *137*, 297–310.
[15] M. Zeilinger, L.-A. Jantke, L. M. Scherf, F. J. Kiefer, G. Neubüser, L. Kienle, A. J. Karttunen, S. Konar, U. Häussermann, T. F. Fässler, *Chem. Mater.* **2014**, *26*, 6603–6612.
[16] M. M. Bentlohner, M. Waibel, P. Zeller, K. Sarkar, P. Müller-Buschbaum, D. Fattakhova-Rohlfing, T. F. Fässler, *Angew. Chem. Int. Ed.* **2016**, *55*, 2441–2445.
[17] J. Llanos, Dissertation, Universität Stuttgart, Germany **1984**.
[18] H. Morito, K. Momma, H. Yamane, *J. Alloys Compd.* **2015**, *623*, 473–479.
[19] M. Waibel, G. Raudaschl-Sieber, T. F. Fässler, *Chem. Eur. J.* **2011**, *17*, 13391–13394.
[20] M. Waibel, O. Pecher, B. Mausolf, F. Haarmann, T. F. Fässler, *Eur. J. Inorg. Chem.* **2013**, *2013*, 5541–5546.
[21] R. Nesper, *Prog. Solid State Chem.* **1990**, *20*, 1–45.
[22] G. J. Miller, *Eur. J. Inorg. Chem.* **1998**, *1998*, 523–536.
[23] M. Jehle, I. Dürr, S. Fink, B. Lang, M. Langenmaier, J. Steckhan, C. Röhr, *J. Solid State Chem.* **2015**, *221*, 351–363.
[24] M. Schwarz, Dissertation, Universität Stuttgart, Germany **1987**.
[25] L. M. Scherf, M. Zeilinger, T. F. Fässler, *Inorg. Chem.* **2014**, *53*, 2096–2101.
[26] L. M. Scherf, A. J. Karttunen, O. Pecher, P. C. M. M. Magusin, C. P. Grey, T. F. Fässler, *Angew. Chem.* **2016**, *128*, 1087–1091; *Angew. Chem. Int. Ed.* **2016**, *55*, 1075–1079.
[27] a) A. Grüttner, R. Nesper, H. G. v. Schnering, *Acta Crystallogr., Sect. A* **1981**, *37*, C161; b) A. Grüttner, Dissertation, Universität Stuttgart **1982**.
[28] H. G. von Schnering, R. Nesper, J. Curda, K.-F. Tebbe, *Angew. Chem.* **1980**, *92*, 1070; *Angew. Chem. Int. Ed. Engl.* **1980**, *19*, 1033–1034.
[29] R. Nesper, H. G. von Schnering, J. Curda, *Chem. Ber.* **1986**, *119*, 3576–3590.
[30] L. Vegard, *Z. Phys.* **1921**, *5*, 17–26.
[31] a) A. Kuhn, P. Sreeraj, R. Pöttgen, H.-D. Wiemhöfer, M. Wilkening, P. Heitjans, *Angew. Chem.* **2011**, *123*, 12305–12308; *Angew. Chem. Int. Ed.* **2011**, *50*, 12099–12102; b) R. Nesper, S. Wengert, F. Zürcher, A. Currao, *Chem. Eur. J.* **1999**, *5*, 3382–3389.
[32] S. Wengert, Dissertation, ETH Zürich , Switzerland **1997**.
[33] Electronegativities: 2.02 (Ge) and 1.74 (Si). A. L. Allred, E. G. Rochow, *J. Inorg. Nucl. Chem.* **1958**, *5*, 264–268.
[34] V. L. Chevrier, J. W. Zwanziger, J. R. Dahn, *J. Alloys Compd.* **2010**, *496*, 25–36.
[35] *von Schnering et al.* also mentioned this in Ref. [29].
[36] a) H.-J. Deiseroth, S.-T. Kong, H. Eckert, J. Vannahme, C. Reiner, T. Zaiß, M. Schlosser, *Angew. Chem.* **2008**, *120*, 767–770; *Angew. Chem. Int. Ed.* **2008**, *47*, 755–758; b) A. Henze, T. F. Fässler, *Inorg. Chem.* **2016**, *55*, 822–827.

[37] P.-E. Werner, L. Eriksson, M. Westdahl, *J. Appl. Crystallogr.* **1985**, *18*, 367–370.
[38] *WinXPOW*, STOE & Cie GmbH, Darmstadt, Germany, **2003**.
[39] a) L. M. Scherf, O. Pecher, K. J. Griffith, F. Haarmann, C. P. Grey, T. F. Fässler, *Eur. J. Inorg. Chem.* **2016**, published online, DOI:10.1002/ejic.201600735; b) O. Pecher, M. Esters, A. Görne, B. Mausolf, A. Ormeci, F. Haarmann, *Z. Anorg. Allg. Chem.* **2014**, *640*, 2169–2176.
[40] a) T. Goebel, Y. Prots, A. Ormeci, O. Pecher, F. Haarmann, *Z. Anorg. Allg. Chem.* **2011**, *637*, 1982–1991; b) J. Llanos, R. Nesper, H. G. von Schnering, *Angew. Chem.* **1983**, *95*, 1026–1027; *Angew. Chem. Int. Ed. Engl.* **1983**, *22*, 998.
[41] H. G. von Schnering, M. Schwarz, R. Nesper, *Angew. Chem.* **1986**, *98*, 558–559; *Angew. Chem. Int. Ed. Engl.* **1986**, *25*, 566–567.
[42] The isostructural phase K_7LiSi_8 can only be synthesized from binary precursors (Ref. [39a]). Stoichiometric mixtures of the elements yield a product mix of K_3NaSi_4 and K_4Si_4.
[43] A. Boultif, D. Louer, *J. Appl. Crystallogr.* **2004**, *37*, 724–731.
[44] W. S. Tang, J.-N. Chotard, R. Janot, *J. Electrochem. Soc.* **2013**, *160*, A1232–A1240.
[45] *APEX Suite of Crystallographic Software*, Bruker AXS Inc., Madison, WI, USA, **2008**.
[46] *SAINT*, Bruker AXS Inc., Madison, WI, USA, **2001**.
[47] *SADABS*, Bruker AXS Inc., Madison, WI, USA, **2001**.
[48] G. M. Sheldrick, *Acta Crystallogr., Sect. A* **2008**, *64*, 112–122.
[49] C. R. Hubbard, H. E. Swanson, F. A. Mauer, *J. Appl. Crystallogr.* **1975**, *8*, 45–48.
[50] V. Petříček, M. Dušek, L. Palatinus, *Z. Kristallogr. Cryst. Mater.* **2014**, *229*, 345.

Received: July 21, 2016
Published Online: September 5, 2016

Z. Anorg. Allg. Chem. **2016** · ISSN 0044–2313

SUPPORTING INFORMATION

Title: Site-Specific Substitution Preferences in the Solid Solutions $Li_{12}Si_{7-x}Ge_x$, $Li_{12-y}Na_ySi_7$, $Na_7LiSi_{8-z}Ge_z$, and $Li_3NaSi_{6-v}Ge_v$

Author(s): L. M. Scherf, N. Riphaus, T. F. Fässler*

Ref. No.: Z201600259

SUPPORTING INFORMATION

Site-Specific Substitution Preferences in the Solid Solutions $Li_{12}Si_{7-x}Ge_x$, $Li_{12-y}Na_ySi_7$, $Na_7LiSi_{8-z}Ge_z$, and $Li_3NaSi_{6-v}Ge_v$

Lavinia M. Scherf, Nathalie Riphaus, Thomas F. Fässler*

Table of Contents

Characterization of $Li_{12}Si_{7-x}Ge_x$ **S2**
Cell parameters S2
EDX data S2
Single crystal data S4
Characterization of $Li_{12-y}Na_ySi_7$ **S9**
Powder diffraction patterns S9
EDX data S9
Single crystal data S10
Rietveld refinement S13
Characterization of $Na_7LiSi_{8-z}Ge_z$ **S14**
Rietveld refinement S14
Characterization of $Li_3NaSi_{6-v}Ge_v$ **S19**
EDX data S19
Powder diffraction patterns S20
Single crystal data S21
Rietveld refinement S23
References **S24**

Characterization of $Li_{12}Si_{7-x}Ge_x$

Cell parameters

Table S1. Cell parameters of $Li_{12}Si_{7-x}Ge_x$ determined by indexing powder diffraction patterns using TREOR[1] as implemented in WinXPOW.[2] Previously, all patterns were referenced with an external Si standard. *x* is given as the stoichiometry used in the syntheses of $Li_{12}Si_{7-x}Ge_x$.

***x* in $Li_{12}Si_{7-x}Ge_x$**	***a* / Å**	***b* / Å**	***c* / Å**	***V* / Å^3**
0	8.605(1)	19.736(2)	14.351(1)	2437.2(3)
2	8.634(1)	19.800(4)	14.398(3)	2461.4(5)
3.5	8.654(1)	19.875(1)	14.442(1)	2484.0(1)
5	8.684(2)	19.948(2)	14.512(4)	2513.8(5)
7	8.720(1)	20.044(3)	14.585(2)	2549.1(4)

EDX data

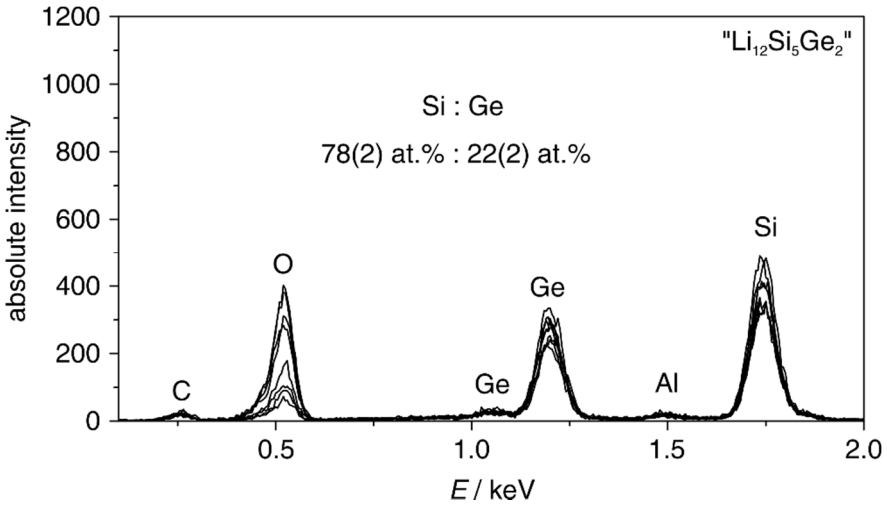

Figure S1. EDX spectra of a "$Li_{12}Si_5Ge_2$" single crystal (acceleration voltage 15 kV). The carbon and aluminum signals are induced by the graphite tape used to fix the crystal on the aluminum holder. The oxygen impurity stems from a short transfer through air into the scanning electron microscope.

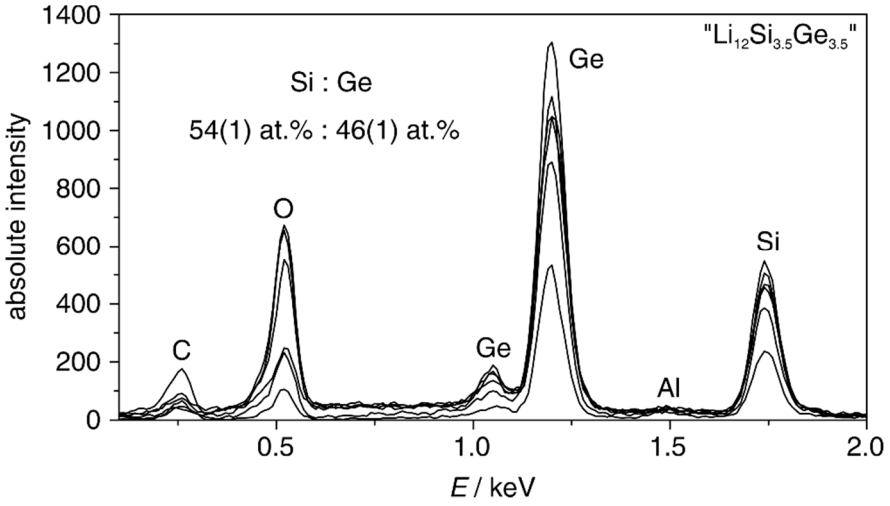

Figure S2. EDX spectra of a "$Li_{12}Si_{3.5}Ge_{3.5}$" single crystal (acceleration voltage 5 kV). The carbon and aluminum signals are induced by the graphite tape used to fix the crystal on the aluminum holder. The oxygen impurity stems from a short transfer through air into the scanning electron microscope.

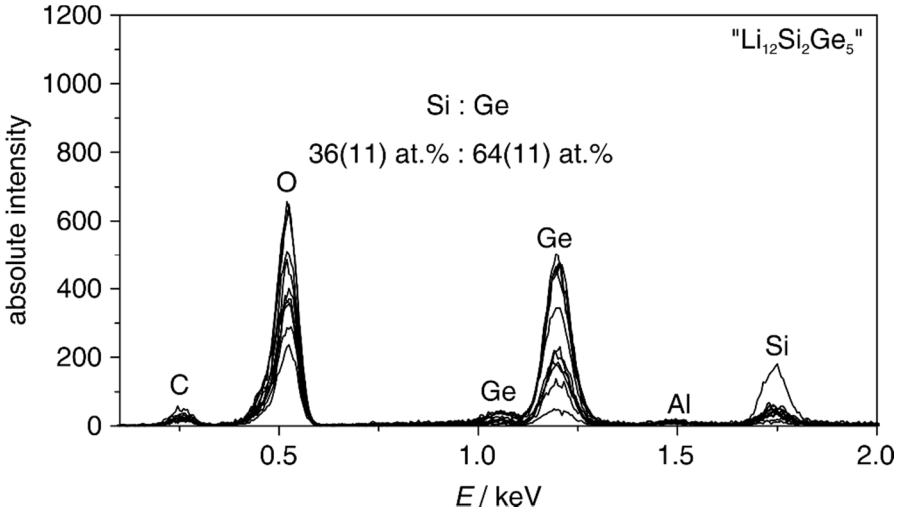

Figure S3. EDX spectra of a "$Li_{12}Si_2Ge_5$" single crystal (acceleration voltage 15 kV). The carbon and aluminum signals are induced by the graphite tape used to fix the crystal on the aluminum holder. The oxygen impurity stems from a short transfer through air into the scanning electron microscope.

Single crystal data

Table S2. Crystallographic Data and Structure Refinement of $Li_{12}Si_{7-x}Ge_x$ (x = 0, 1.74, 3.09, 4.58, 7).

	$Li_{12}Si_7$	**$Li_{12}Si_{5.26(2)}Ge_{1.74}$**	**$Li_{12}Si_{3.91(2)}Ge_{3.09}$**	**$Li_{12}Si_{2.42(8)}Ge_{4.58}$**	**$Li_{12}Ge_7$**
T (K)	100(2)	100(2)	100(2)	100(2)	100(2)
formula weight (g·mol^{-1})	279.91	357.17	417.42	483.72	591.41
crystal size (mm^3)	0.28 × 0.29 × 0.85	0.26 × 0.28 × 0.48	0.15 × 0.20 × 0.35	0.17 × 0.26 × 0.34	0.32 × 0.37 × 0.55
crystal color	metallic grey	metallic grey	metallic grey	metallic grey	metallic grey
crystal shape	block	block	block	Block	block
space group	*Pnma*	*Pnma*	*Pnma*	*Pnma*	*Pnma*
unit cell dimensions	a = 8.5576(6)	a = 8.5783(4)	a = 8.6025(2)	a = 8.6263(4)	a = 8.6667(4)
(Å)	b = 19.6735(14)	b = 19.7420(8)	b = 19.7744(5)	b = 19.8579(8)	b = 19.9310(9)
	c = 14.2841(11)	c = 14.3274(5)	c = 14.3863(4)	c = 14.4307(7)	c = 14.5161(6)
Z	8	8	8	8	8
V (Å^3)	2404.8(3)	2426.39(17)	2447.24(11)	2471.98(19)	2507.5(2)
ρ (calc.) (g·cm^{-3})	1.546	1.956	2.266	2.599	3.133
μ (mm^{-1})	0.731	4.772	7.860	11.190	16.491
F(000)	1072	1322	1517	1732	2080
ϑ range (deg)	1.76–36.32	1.76–33.14	1.75–33.13	1.74–33.14	1.74–30.51
index range	$-14 \le h \le 14$	$-13 \le h \le 13$	$-10 \le h \le 13$	$-13 \le h \le 13$	$-12 \le h \le 12$
	$-32 \le k \le 32$	$-29 \le k \le 30$	$-28 \le k \le 30$	$-30 \le k \le 30$	$-28 \le k \le 28$
	$-23 \le l \le 23$	$-22 \le l \le 22$	$-21 \le l \le 22$	$-22 \le l \le 22$	$-20 \le l \le 20$
reflections collected	162921	127509	55084	127565	112603
independent reflections	5955 (R_{int} = 0.0316)	4734 (R_{int} = 0.0434)	4773 (R_{int} = 0.0405)	4822 (R_{int} = 0.0998)	3928 (R_{int} = 0.0805)
reflections with $I > 2\sigma(I)$	5106 (R_σ = 0.0093)	3962 (R_σ = 0.0151)	3679 (R_σ = 0.0187)	3232 (R_σ = 0.0335)	3229 (R_σ = 0.0286)
absorption correction	multi-scan	multi-scan	multi-scan	multi-scan	multi-scan
data / restraints / parameters	5955 / 0 / 181	4734 / 0 / 190	4773 / 0 / 190	4822 / 0 / 190	3928 / 0 / 182
goodness-of-fit on F^2	1.119	1.059	1.023	1.111	1.137
final R indices	R_1 = 0.0154	R_1 = 0.0183	R_1 = 0.0204	R_1 = 0.0390	R_1 = 0.0221
$[I > 2\sigma(I)]^{a, b}$	wR_2 = 0.0358	wR_2 = 0.0426	wR_2 = 0.0339	wR_2 = 0.688	wR_2 = 0.0509
R indices (all data)^{a,b}	R_1 = 0.0212	R_1 = 0.0266	R_1 = 0.0351	R_1 = 0.0749	R_1 = 0.0318
	wR_2 = 0.0383	wR_2 = 0.0465	wR_2 = 0.0372	wR_2 = 0.0800	wR_2 = 0.0547
largest diff. peak and hole (e·Å^{-3})	0.490 and −0.371	0.782 and −0.541	0.523 and −0.577	1.075 and −1.456	0.864 and −0.661

Table S3. Atom coordinates, Wyckoff positions, isotropic displacement factors / Å^2 and Ge content on tetrel positions *T* for $Li_{12}Si_{7-x}Ge_x$ at 100 K.

		$Li_{12}Si_7$		$Li_{12}Si_{5.26(2)}Ge_{1.74}$		$Li_{12}Si_{3.91(2)}Ge_{3.09}$		$Li_{12}Si_{2.42(8)}Ge_{4.58}$		$Li_{12}Ge_7$	
		x, y, z	***U_{eq}*, % Ge**	***x, y, z***	***U_{eq}*, % Ge**	***x, y, z***	***U_{eq}*, % Ge**	***x, y, z***	***U_{eq}*, % Ge**	***x, y, z***	***U_{eq}*, % Ge**
*T*1	4*c*	0.13264(2) 0.25 0.43093(2)	0.00682(3) -	0.13342(4) 0.25 0.43112(2)	0.00773(11) 0.4(2)	0.13284(6) 0.25 0.43054(3)	0.00656(13) 0.9(3)	0.13350(16) 0.25 0.43015(9)	0.0069(4) 0.8(7)	0.13477(4) 0.25 0.42907(2)	0.00631(8) 100
*T*2	4*c*	0.12786(2) 0.25 0.26594(2)	0.00658(3) -	0.12799(2) 0.25 0.26348(2)	0.00711(7) 61.4(5)	0.12791(2) 0.25 0.26286(2)	0.00492(6) 80.6(5)	0.12824(7) 0.25 0.26260(3)	0.00624(14) 93.8(14)	0.12884(4) 0.25 0.25699(2)	0.00480(8) 100
*T*3	4*c*	0.37552(2) 0.25 0.51142(2)	0.00618(3) -	0.38043(2) 0.25 0.51202(2)	0.00631(5) 70.9(4)	0.37910(2) 0.25 0.51239(2)	0.00479(5) 86.1(5)	0.37933(6) 0.25 0.51194(4)	0.00552(15) 95.4(14)	0.38705(4) 0.25 0.51251(2)	0.00435(8) 100
*T*4	4*c*	0.38614(2) 0.25 0.99114(2)	0.00619(3) -	0.38401(2) 0.25 0.98931(2)	0.00638(5) 65.6(4)	0.38312(2) 0.25 0.99080(2)	0.00474(6) 83.2(5)	0.38367(6) 0.25 0.99100(4)	0.00537(15) 94.1(14)	0.37876(4) 0.25 0.98996(2)	0.00433(7) 100
*T*5	8*d*	0.12508(2) 0.13169(2) 0.74830(2)	0.00576(3) -	0.12535(2) 0.13256(2) 0.74823(2)	0.00610(7) 14.8(2)	0.12469(2) 0.13364(2) 0.74802(2)	0.00510(6) 37.3(3)	0.12502(6) 0.13455(2) 0.74793(3)	0.00542(12) 63.3(11)	0.12440(3) 0.13530(2) 0.74815(2)	0.00369(6) 100
*T*6	8*d*	0.10913(2) 0.06450(2) 0.88530(2)	0.00616(3) -	0.10971(2) 0.06486(2) 0.88658(2)	0.00656(6) 17.7(2)	0.10870(2) 0.06539(2) 0.88790(2)	0.00544(6) 41.8(4)	0.10896(5) 0.06582(2) 0.88880(3)	0.00639(13) 70.6(11)	0.10959(3) 0.06596(2) 0.88956(2)	0.00413(6) 100
*T*7	8*d*	0.38145(2) 0.05035(2) 0.33320(2)	0.00594(3) -	0.38101(2) 0.05100(2) 0.33356(2)	0.00628(6) 14.2(2)	0.38160(2) 0.05189(2) 0.33458(2)	0.00521(6) 35.5(3)	0.38149(5) 0.05248(2) 0.33508(3)	0.00588(14) 62.0(11)	0.38158(3) 0.05295(2) 0.33555(2)	0.00393(6) 100
*T*8	8*d*	0.37970(2) 0.05260(2) 0.16868(2)	0.00597(3) -	0.37883(2) 0.05319(2) 0.16754(2)	0.00645(7) 13.3(2)	0.37946(2) 0.05421(2) 0.16716(2)	0.00530(6) 33.4(3)	0.37916(6) 0.05475(2) 0.16650(3)	0.00593(14) 59.0(11)	0.37873(3) 0.05545(2) 0.16580(2)	0.00404(6) 100
*T*9	8*d*	0.13071(2) 0.06069(2) 0.61468(2)	0.00579(2) -	0.13096(2) 0.06102(2) 0.61373(2)	0.00613(6) 14.6(2)	0.13076(2) 0.06107(2) 0.61262(2)	0.00501(6) 35.6(3)	0.13092(5) 0.06141(2) 0.61183(3)	0.00533(13) 60.9(11)	0.13035(3) 0.06194(2) 0.61095(2)	0.00356(6) 100
Li1	4*c*	0.1627(2) 0.25 0.83273(11)	0.0235(3)	0.1608(4) 0.25 0.8348(2)	0.0238(6)	0.1625(5) 0.25 0.8333(2)	0.0211(8)	0.1618(15) 0.25 0.8354(8)	0.027(3)	0.1570(9) 0.25 0.8380(5)	0.0209(15)
Li2	4*c*	0.11396(15) 0.25 0.63175(10)	0.0144(2)	0.1148(3) 0.25 0.63218(18)	0.0143(5)	0.1136(4) 0.25 0.6308(2)	0.0130(6)	0.1137(11) 0.25 0.6293(8)	0.017(2)	0.1142(7) 0.25 0.6299(5)	0.0141(13)
Li3	8*d*	0.37805(10) 0.16549(5) 0.65892(7)	0.01401(17)	0.3781(2) 0.16536(10) 0.65924(12)	0.0141(4)	0.3781(3) 0.16558(12) 0.65967(15)	0.0133(5)	0.3784(8) 0.1653(3) 0.6597(5)	0.0140(13)	0.3775(5) 0.1657(2) 0.6588(3)	0.0137(9)

		0.12903(10)		0.12880(19)		0.1294(3)		0.1297(8)		0.1293(5)	
Li4	8*d*	0.02778(5)	0.01269(16)	0.02726(10)	0.0128(4)	0.02753(12)	0.0119(4)	0.0269(3)	0.0108(12)	0.0251(2)	0.0120(9)
		0.06534(6)		0.06552(12)		0.06582(14)		0.0658(4)		0.0653(3)	
		0.12977(10)		0.12968(19)		0.1302(3)		0.1306(8)		0.1305(5)	
Li5	8*d*	0.11318(5)	0.01254(16)	0.11324(10)	0.0135(4)	0.11295(11)	0.0117(4)	0.1131(3)	0.0121(12)	0.1132(2)	0.0127(9)
		0.26387(7)		0.26305(13)		0.26310(15)		0.2628(4)		0.2625(3)	
		0.13204(10)		0.13185(19)		0.1320(3)		0.1319(8)		0.1323(5)	
Li6	8*d*	0.00548(5)	0.01179(16)	0.00548(9)	0.0122(3)	0.00542(11)	0.0105(4)	0.0054(3)	0.0129(13)	0.0058(2)	0.0093(8)
		0.43308(6)		0.43337(12)		0.43257(14)		0.4325(5)		0.4318(3)	
		0.37351(10)		0.37377(19)		0.3734(3)		0.3740(8)		0.3728(5)	
Li7	8*d*	0.14601(5)	0.01284(16)	0.14577(10)	0.0128(4)	0.14566(11)	0.0115(4)	0.1454(3)	0.0122(12)	0.1468(2)	0.0111(9)
		0.86076(7)		0.86076(12)		0.86062(15)		0.8612(4)		0.8601(3)	
		0.37133(11)		0.3718(2)		0.3713(3)		0.3727(8)		0.3715(5)	
Li8	8*d*	0.03153(5)	0.01326(17)	0.03162(10)	0.0133(4)	0.14566(11)	0.0130(4)	0.0316(3)	0.0141(12)	0.0321(2)	0.0135(10)
		0.74395(6)		0.74417(11)		0.86062(15)		0.7429(5)		0.7428(3)	
		0.13804(12)		0.1398(2)		0.1386(3)		0.1397(9)		0.1413(6)	
Li9	8*d*	0.17202(6)	0.0219(2)	0.17140(11)	0.0255(5)	0.17145(13)	0.0204(5)	0.1715(4)	0.0253(17)	0.1696(3)	0.0237(11)
		0.02294(9)		0.02569(18)		0.02419(18)		0.0262(6)		0.0310(4)	
		0.36151(12)		0.3630(3)		0.3631(3)		0.3645(9)		0.3670(6)	
Li10	8*d*	0.18909(5)	0.01751(19)	0.18915(13)	0.0263(5)	0.18940(13)	0.0156(5)	0.1894(4)	0.0186(15)	0.1896(3)	0.0181(10)
		0.16233(7)		0.16213(15)		0.16420(15)		0.1627(5)		0.1627(3)	
		0.39104(11)		0.3893(2)		0.3898(3)		0.3909(8)		0.3883(5)	
Li11	8*d*	0.18739(5)	0.01387(17)	0.18708(10)	0.0146(4)	0.18725(12)	0.0131(5)	0.1874(3)	0.0141(14)	0.1873(2)	0.0121(9)
		0.34208(7)		0.34124(13)		0.34280(15)		0.3423(5)		0.3417(3)	
		0.34052(12)		0.3413(2)		0.3419(3)		0.3418(8)		0.3421(6)	
Li12	8*d*	0.11228(5)	0.01491(17)	0.11250(9)	0.0160(4)	0.11229(12)	0.0146(5)	0.1126(3)	0.0155(14)	0.1135(2)	0.0145(9)
		0.49404(7)		0.49384(12)		0.49485(16)		0.4948(5)		0.4944(3)	
		0.49252(13)		0.4935(2)		0.4941(3)		0.4951(9)		0.4909(6)	
Li13	8*d*	0.12493(5)	0.01806(19)	0.12564(10)	0.0199(4)	0.12512(13)	0.0170(5)	0.1256(4)	0.0185(16)	0.1260(2)	0.0186(10)
		0.02793(7)		0.02889(13)		0.02742(16)		0.0274(5)		0.0269(3)	

Table S4. Relevant interatomic distances in $Li_{12}Si_{7-x}Ge_x$ and $Li_{12-y}Na_ySi_7$ (*Pnma, Z* = 8, estimated standard deviations in parentheses).

Atom pair			*d* / Å						
			$Li_{12}Si_{7-x}Ge_x$ (100 K)					$Li_{12-y}Na_ySi_7$ (123 K)	
			***x* = 0**	***x* = 1.74(2)**	***x* = 3.09(2)**	***x* = 4.58(8)**	***x* = 7**	***y* = 0**	***y* = 0.44(1)**
*T*1	*T*2		2.3571(3)	2.4023(4)	2.4126(5)	2.4184(14)	2.4984(5)	2.3583(3)	2.3754(9)
*T*1	*T*3		2.3752(3)	2.4152(4)	2.4237(5)	2.4269(15)	2.4995(5)	2.3743(3)	2.3670(9)
*T*1	*T*4		2.3851(3)	2.4243(4)	2.4281(5)	2.4370(15)	2.5109(5)	2.3852(3)	2.3718(9)
*T*5	*T*6		2.3654(2)	2.3945(3)	2.4269(3)	2.4524(6)	2.4779(4)	2.3648(2)	2.3673(6)
*T*6	*T*7		2.3803(2)	2.4113(3)	2.4442(3)	2.4751(6)	2.4975(4)	2.3786(2)	2.3783(6)
*T*7	*T*8		2.3505(3)	2.3791(3)	2.4090(3)	2.4332(6)	2.4649(4)	2.3510(2)	2.3567(6)
*T*8	*T*9		2.3601(2)	2.3845(3)	2.4124(3)	2.4394(7)	2.4726(4)	2.3588(2)	2.3641(6)
*T*9	*T*5		2.3656(2)	2.3898(3)	2.4201(3)	2.4432(6)	2.4713(4)	2.3653(2)	2.3685(6)
*A*1	*T*5	×2	2.6412(8)	2.6466(14)	2.628(2)	2.637(6)	2.647(4)	2.6418(9)	2.735(2)
	*T*4		2.9626(16)	2.927(3)	2.956(4)	2.950(11)	2.926(7)	2.9594(19)	2.946(4)
Li2	*T*4		2.6234(14)	2.636(2)	2.645(3)	2.636(10)	2.681(6)	2.6237(15)	2.623(4)
	*T*3		2.8222(14)	2.856(3)	2.849(3)	2.849(10)	2.914(7)	2.8210(16)	2.799(5)
	*T*5	×2	2.8634(9)	2.8545(15)	2.854(2)	2.863(6)	2.860(4)	2.8632(10)	2.889(3)
	*T*1		2.8730(15)	2.885(3)	2.886(3)	2.879(11)	2.920(7)	2.8733(17)	2.886(5)
Li3	*T*5		2.5822(9)	2.5837(17)	2.581(2)	2.583(7)	2.602(4)	2.5827(10)	2.604(3)
	*T*5		2.5997(9)	2.5972(17)	2.601(2)	2.602(7)	2.619(4)	2.5996(11)	2.607(3)
	*T*3		2.6839(10)	2.6910(18)	2.697(2)	2.717(6)	2.709(5)	2.6843(11)	2.707(3)
	*T*6		2.8736(10)	2.8837(19)	2.886(2)	2.889(7)	2.914(5)	2.8739(11)	2.901(3)
	*T*9		3.0218(10)	3.0269(19)	3.042(2)	3.048(7)	3.058(5)	3.0191(11)	3.018(3)
Li4	*T*7		2.6052(9)	2.6131(17)	2.613(2)	2.625(6)	2.644(4)	2.6051(10)	2.624(3)
	*T*8		2.6494(9)	2.6456(17)	2.652(2)	2.655(7)	2.678(4)	2.6479(10)	2.676(3)
	*T*6		2.6766(10)	2.6741(17)	2.673(2)	2.674(6)	2.683(5)	2.6780(11)	2.695(3)
	*T*9		2.7845(9)	2.7859(18)	2.789(2)	2.789(6)	2.791(4)	2.7844(10)	2.777(3)
	*T*6		2.8191(9)	2.8221(18)	2.831(2)	2.838(7)	2.830(4)	2.8180(11)	2.793(3)
Li5	*T*8		2.6322(9)	2.6504(18)	2.647(2)	2.662(7)	2.677(4)	2.6349(10)	2.648(3)
	*T*7		2.6734(9)	2.6793(18)	2.682(2)	2.687(6)	2.702(4)	2.6718(10)	2.681(3)
	*T*2		2.6919(10)	2.700(2)	2.710(2)	2.719(6)	2.729(5)	2.6905(11)	2.706(3)
	*T*8		2.8006(9)	2.8010(18)	2.802(2)	2.805(7)	2.814(5)	2.7987(11)	2.816(3)
	*T*7		2.8224(9)	2.8242(18)	2.829(2)	2.839(6)	2.850(5)	2.8224(11)	2.829(3)
Li6	*T*9		2.6862(9)	2.6948(17)	2.695(2)	2.703(7)	2.719(4)	2.6860(10)	2.693(3)
	*T*6		2.6958(9)	2.7005(17)	2.711(2)	2.719(7)	2.725(4)	2.6942(10)	2.697(3)
	*T*7		2.7148(9)	2.7241(17)	2.728(2)	2.736(7)	2.739(4)	2.7155(10)	2.746(3)
	*T*8		2.7632(9)	2.7729(17)	2.777(2)	2.785(7)	2.796(4)	2.7635(10)	2.782(3)
	*T*9		2.8124(9)	2.8070(17)	2.814(2)	2.817(6)	2.831(4)	2.8110(11)	2.817(3)
Li7	*T*5		2.6723(9)	2.6766(17)	2.678(2)	2.686(7)	2.697(4)	2.6721(10)	2.674(3)
	*T*5		2.6794(9)	2.6849(17)	2.694(2)	2.707(6)	2.707(4)	2.6778(10)	2.698(3)
	*T*4		2.7687(10)	2.7629(18)	2.788(2)	2.799(6)	2.790(5)	2.7670(11)	2.791(3)
	*T*9		2.7902(9)	2.7930(18)	2.802(2)	2.801(6)	2.826(4)	2.7897(10)	2.804(3)
	*T*6		2.7952(9)	2.7964(18)	2.803(2)	2.808(7)	2.831(6)	2.7939(11)	2.827(3)
Li8	*T*6		2.8232(9)	2.8472(17)	2.860(2)	2.868(7)	2.899(5)	2.8259(11)	2.840(3)
	*T*9		2.8245(9)	2.8454(17)	2.856(2)	2.877(7)	2.895(5)	2.8239(11)	2.841(3)
	*T*7		2.8784(10)	2.8980(18)	2.921(2)	2.924(7)	2.958(5)	2.8799(11)	2.893(3)
	*T*5		2.8857(10)	2.9057(19)	2.923(2)	2.958(7)	2.970(5)	2.8831(11)	2.900(3)
	*T*8		2.9173(10)	2.9376(18)	2.961(2)	2.980(7)	3.000(5)	2.9148(11)	2.933(3)
	*T*5		2.9343(10)	2.9523(19)	2.967(2)	2.989(7)	3.008(5)	2.9346(11)	2.946(3)
	*T*8		2.9727(10)	2.9969(18)	3.026(2)	3.038(7)	3.082(5)	2.9734(11)	2.998(3)
	*T*7		2.9832(10)	3.0003(18)	3.034(2)	3.061(7)	3.082(5)	2.9799(11)	3.001(3)
	*T*9		3.0550(9)	3.0699(17)	3.098(2)	3.116(7)	3.146(5)	3.0550(11)	3.066(3)
	*T*6		3.0873(9)	3.1062(17)	3.140(2)	3.173(7)	3.186(5)	3.0830(11)	3.086(3)

Atom pair		*d* / Å						
		$Li_{12}Si_{7-x}Ge_x$ (100 K)					$Li_{12-y}Na_ySi_7$ (123 K)	
		***x* = 0**	***x* = 1.74(2)**	***x* = 3.09(2)**	***x* = 4.58(8)**	***x* = 7**	***y* = 0**	***y* = 0.44(1)**
*A*9	*T*4	2.6585(10)	2.659(2)	2.659(3)	2.668(7)	2.675(5)	2.6572(12)	2.8226(17)
	*T*3	2.7643(11)	2.766(2)	2.770(3)	2.789(8)	2.797(5)	2.7675(13)	2.9642(18)
	*T*6	2.8985(12)	2.909(2)	2.883(3)	2.899(8)	2.925(6)	2.9030(14)	3.0540(18)
Li10	*T*8	2.6913(11)	2.689(3)	2.678(3)	2.678(7)	2.675(5)	2.6929(13)	2.694(3)
	*T*4	2.7312(11)	2.758(2)	2.749(2)	2.760(7)	2.784(5)	2.7319(12)	2.736(3)
	*T*2	2.7611(10)	2.760(2)	2.760(2)	2.771(7)	2.754(5)	2.7601(12)	2.772(4)
	*T*2	2.7715(11)	2.783(2)	2.790(2)	2.790(8)	2.821(5)	2.7706(12)	2.778(3)
	*T*1	2.9315(10)	2.934(2)	2.934(2)	2.938(8)	2.935(5)	2.9304(12)	2.913(3)
Li11	*T*7	2.7002(10)	2.6897(19)	2.680(2)	2.683(7)	2.680(5)	2.6995(11)	2.704(3)
	*T*3	2.7177(10)	2.7452(19)	2.739(2)	2.747(7)	2.777(5)	2.7190(11)	2.728(3)
	*T*2	2.7879(10)	2.7945(18)	2.818(2)	2.829(7)	2.821(5)	2.7830(11)	2.769(3)
	*T*2	2.8293(10)	2.8260(18)	2.836(2)	2.833(7)	2.851(5)	2.8298(11)	2.863(3)
	*T*1	2.8316(10)	2.8320(19)	2.832(2)	2.843(7)	2.828(4)	2.8290(11)	2.816(3)
Li12	*T*7	2.6240(10)	2.6199(18)	2.619(2)	2.618(7)	2.625(4)	2.6238(11)	2.632(3)
	*T*9	2.6878(10)	2.6906(18)	2.682(2)	2.683(7)	2.700(4)	2.6884(11)	2.703(3)
	*T*3	2.7371(10)	2.7476(19)	2.753(2)	2.759(6)	2.760(5)	2.7352(11)	2.737(3)
	*T*6	3.0229(11)	3.020(2)	2.996(2)	2.999(7)	3.018(5)	3.0272(12)	3.092(4)
Li13	*T*8	2.6456(10)	2.6381(19)	2.642(2)	2.647(7)	2.643(5)	2.6440(11)	2.659(3)
	*T*9	2.6732(10)	2.6819(19)	2.654(2)	2.653(7)	2.664(5)	2.6776(11)	2.672(3)
	*T*4	2.6757(10)	2.689(19)	2.699(2)	2.702(7)	2.710(5)	2.6728(11)	2.679(3)
	*T*1	2.7996(11)	2.792(2)	2.809(3)	2.811(8)	2.842(5)	2.7969(12)	2.807(4)

Characterization of $Li_{12-y}Na_ySi_7$

Powder diffraction pattern

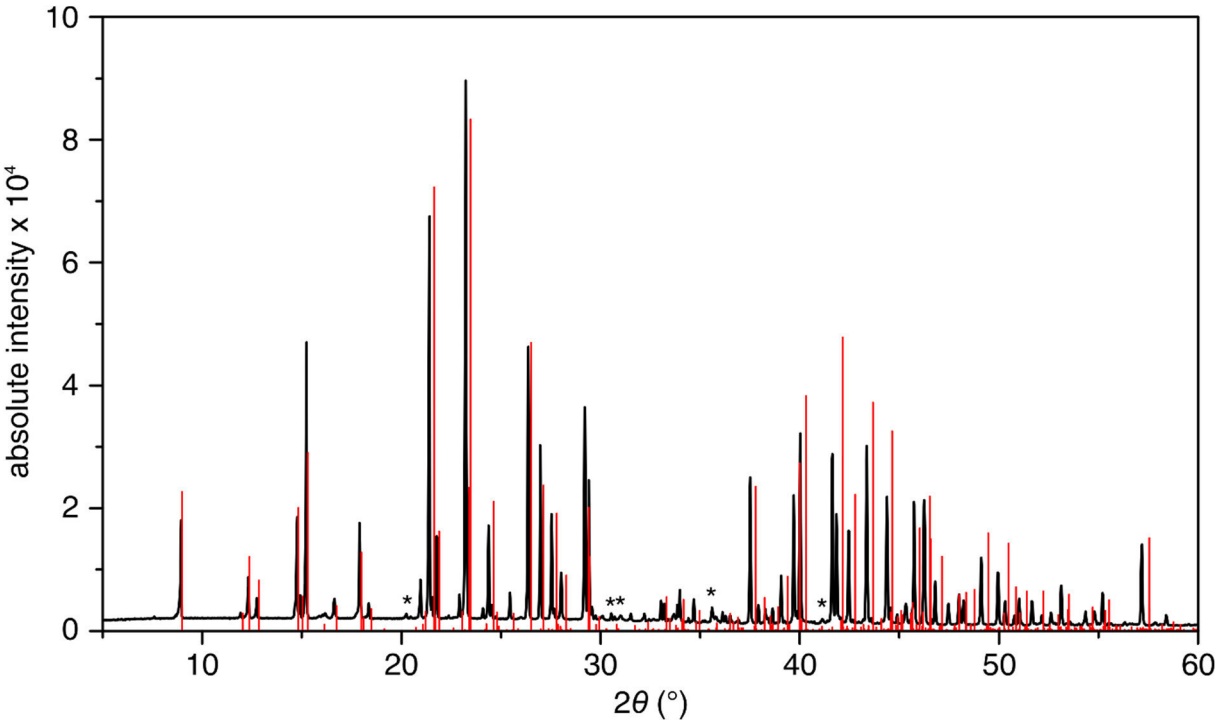

Figure S4. Experimental powder diffraction pattern of "$Li_{10.5}Na_{0.5}Si_7$" (black) prepared. A calculated reference pattern for $Li_{12}Si_7$ is shown in red. Reflections of the impurity Na_4Si_4 (*) are marked.

EDX data

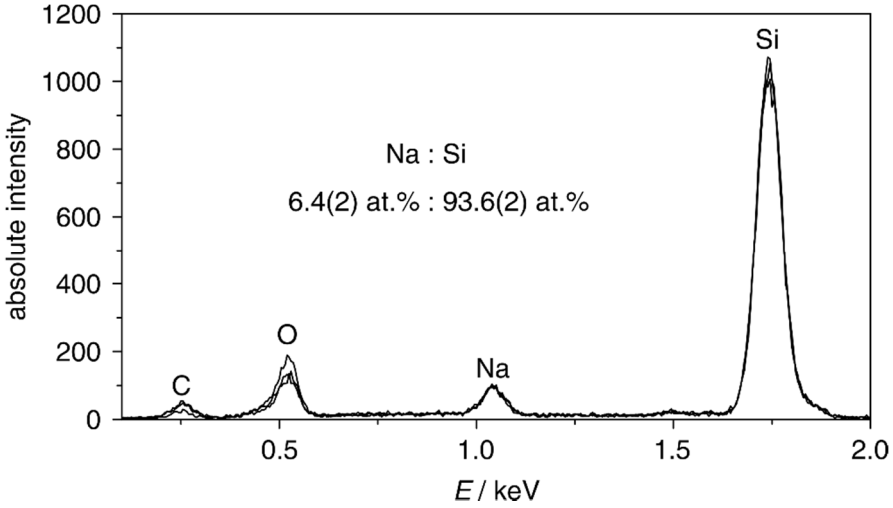

Figure S5. EDX spectra of a $Li_{12-y}Na_ySi_7$ single crystal (acceleration voltage 10 kV). The carbon signal is induced by the graphite tape used to fix the crystal. The oxygen impurity stems from a short transfer through air into the scanning electron microscope.

Single crystal data

Table S5. Crystallographic Data and Structure Refinement of $Li_{12-y}Na_ySi_7$ (y = 0, 0.44).

	$Li_{12}Si_7$	**$Li_{11.56(1)}Na_{0.44}Si_7$**
T (K)	123(2)	123(2)
formula weight (g·mol^{-1})	279.91	287.03
crystal size (mm^3)	0.29 × 0.43 × 0.78	0.17 × 0.19 × 0.52
crystal color	metallic grey	metallic grey
crystal shape	block	block
space group	*Pnma*	*Pnma*
unit cell dimensions (Å)	a = 8.5553(4)	a = 8.6265(3)
	b = 19.6667(9)	b = 19.7512(7)
	c = 14.2868(7)	c = 14.3149(5)
Z	8	8
V (Å^3)	2403.8(2)	2439.03(15)
ρ (calc.) (g·cm^{-3})	1.547	1.563
μ (mm^{-1})	0.731	0.737
F(000)	1072	1100
ϑ range (deg)	1.76–33.14	1.76–30.51
index range	−13 ≤ h ≤ 13	−12 ≤ h ≤ 12
	−30 ≤ k ≤ 30	−28 ≤ k ≤ 28
	−21 ≤ l ≤ 21	−20 ≤ l ≤ 20
reflections collected	123113	117190
independent reflections	4695 (R_{int} = 0.0258)	3819 (R_{int} = 0.0746)
reflections with $I > 2\sigma(I)$	4147 (R_σ = 0.0083)	3062 (R_σ = 0.0206)
absorption correction	multi-scan	multi-scan
data / restraints / parameters	4695 / 0 / 181	3819 / 0 / 183
goodness-of-fit on F^2	1.122	1.127
final R indices	R_1 = 0.0145	R_1 = 0.0363
$[I > 2\sigma(I)]$[a, b]	wR_2 = 0.0359	wR_2 = 0.0724
R indices (all data)[a,b]	R_1 = 0.0189	R_1 = 0.0488
	wR_2 = 0.0382	wR_2 = 0.0796
largest diff. peak and hole (e·Å^{-3})	0.516 and −0.293	0.638 and −0.719

Table S6. Atom coordinates, Wyckoff positions, isotropic displacement factors / Å^2 and Na content on mixed alkali metal positions *A* for $Li_{12-y}Na_ySi_7$ at 123 K.

		$Li_{12}Si_7$		$Li_{11.558(8)}Na_{0.443}Si_7$	
		x, y, z	***U_{eq}*, % Na**	***x, y, z***	***U_{eq}*, % Na**
Si1	4*c*	0.13262(2) 0.25 0.43095(2)	0.00756(4)	0.13273(7) 0.25 0.43013(4)	0.00969(12)
Si2	4*c*	0.12782(2) 0.25 0.26591(2)	0.00728(4)	0.12973(7) 0.25 0.26420(4)	0.00828(12)
Si3	4*c*	0.37553(2) 0.25 0.51133(2)	0.00667(6)	0.37166(7) 0.25 0.51143(4)	0.00878(12)
Si4	4*c*	0.38616(2) 0.25 0.99100(2)	0.00669(4)	0.39036(7) 0.25 0.99164(4)	0.00917(12)
Si5	8*d*	0.12517(2) 0.13168(2) 0.74835(2)	0.00624(3)	0.12453(5) 0.13092(2) 0.74848(3)	0.00622(9)
Si6	8*d*	0.10943(2) 0.06445(2) 0.88526(2)	0.00676(3)	0.11015(5) 0.06336(2) 0.88480(3)	0.00695(9)
Si7	8*d*	0.38128(2) 0.05035(2) 0.33314(2)	0.00645(3)	0.38223(5) 0.05094(2) 0.33268(3)	0.00649(9)
Si8	8*d*	0.37953(2) 0.05255(2) 0.16862(2)	0.00651(3)	0.37925(5) 0.05301(2) 0.16808(3)	0.00644(9)
Si9	8*d*	0.13072(2) 0.06072(2) 0.61471(2)	0.00627(3)	0.12994(4) 0.06022(2) 0.61487(3)	0.00620(9)
*A*1	4*c*	0.1625(3) 0.25 0.83297(13)	0.0263(4) -	0.1515(5) 0.25 0.8447(3)	0.0363(13) 15.2(7)
Li2	4*c*	0.11423(17) 0.25 0.63177(12)	0.0157(3) -	0.1156(5) 0.25 0.6315(3)	0.0171(8) -
Li3	8*d*	0.37805(12) 0.16543(6) 0.65881(8)	0.0151(2) -	0.3762(3) 0.16403(16) 0.6587(2)	0.0151(6) -
Li4	8*d*	0.12888(12) 0.02774(6) 0.06539(7)	0.0134(2) -	0.1281(3) 0.02529(17) 0.0653(2)	0.0164(6) -
Li5	8*d*	0.12984(11) 0.11320(6) 0.26374(8)	0.0136(2) -	0.1300(3) 0.11298(15) 0.2645(2)	0.0131(5) -
Li6	8*d*	0.13193(11) 0.00550(5) 0.43324(7)	0.0126(2) -	0.1319(3) 0.00539(15) 0.4332(2)	0.0128(5) -
Li7	8*d*	0.37354(11) 0.14607(6) 0.86067(8)	0.0138(2) -	0.3744(3) 0.14608(15) 0.8599(2)	0.0134(5) -

		$Li_{12}Si_7$		$Li_{11.558(8)}Na_{0.443}Si_7$	
		x, y, z	***U_{eq}*, % Na**	***x, y, z***	***U_{eq}*, % Na**
Li8	8*d*	0.37118(12) 0.03154(6) 0.74403(7)	0.0140(2) -	0.3709(3) 0.03113(15) 0.7441(2)	0.0130(5) -
*A*9	8*d*	0.13841(13) 0.17198(7) 0.02338(10)	0.0242(3) -	0.14075(18) 0.16566(8) 0.04371(14)	0.0303(6) 36.8(5)
Li10	8*d*	0.36145(14) 0.18918(6) 0.16228(8)	0.0198(2) -	0.3665(4) 0.18926(17) 0.1628(2)	0.0221(7) -
Li11	8*d*	0.39053(13) 0.18740(6) 0.34187(8)	0.0150(2) -	0.3870(4) 0.18768(16) 0.3417(2)	0.0188(6) -
Li12	8*d*	0.34041(14) 0.11234(6) 0.49391(8)	0.0162(2) -	0.3370(4) 0.11289(17) 0.4932(2)	0.0200 (6) -
Li13	8*d*	0.49224(15) 0.12505(6) 0.02814(8)	0.0198(2) -	0.4950(4) 0.12494(17) 0.0274(2)	0.0215(7) -

Rietveld refinement

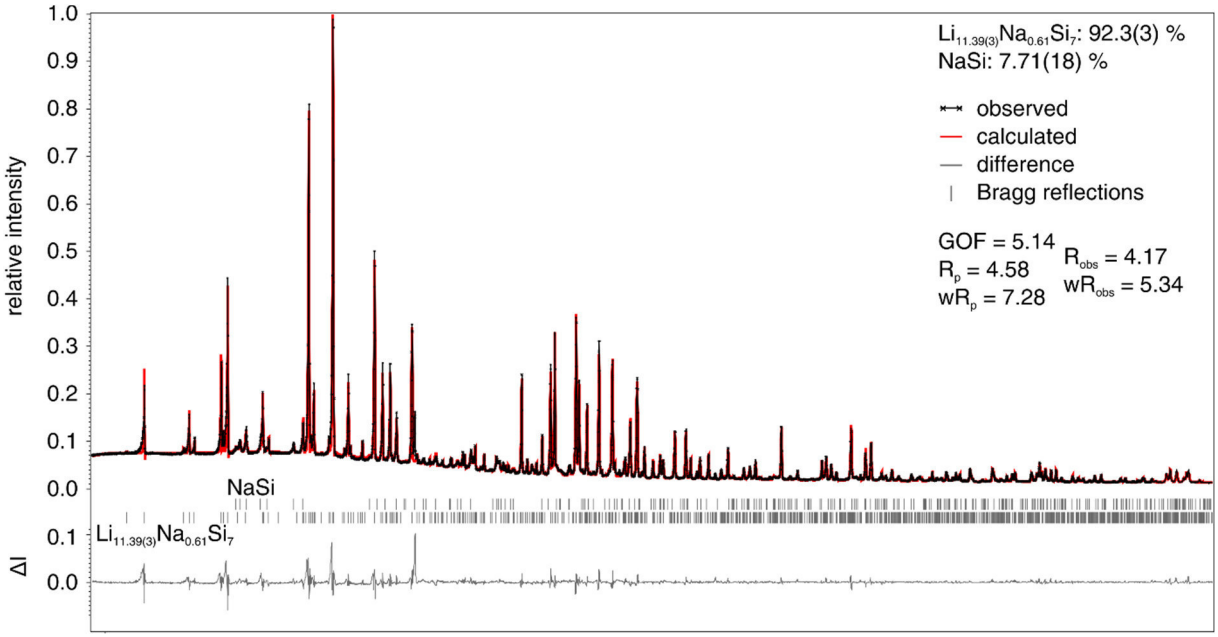

Figure S6. Rietveld-refined powder diffraction pattern of $Li_{11.39(3)}Na_{0.61}Si_7$ (structural model $Li_{12}Si_7$).[3] Obtained cell parameters in *Pnma*: *a* = 8.6620(3) Å, *b* = 19.8012(6) Å, *c* = 14.3586(4) Å, V = 2462.8(2) Å^3.

Table S7. Structural data for $Li_{11.39(3)}Na_{0.61}Si_7$ from Rietveld refinement (structural model $Li_{12}Si_7$).[3]

atom		*x*	*y*	*z*	% Na	U_{iso} / Å^2
Si1	4*c*	0.1289(11)	0.25	0.44278(5)		0.027(3)
Si2	4*c*	0.130(2)	0.25	0.2618(9)		0.025(3)
Si3	4*c*	0.365(2)	0.25	0.5123(9)		0.02
Si4	4*c*	0.391(2)	0.25	0.9932(8)		0.02
Si5	8*d*	0.123(2)	0.13119(19)	0.7487(8)		0.0138(13)
Si6	8*d*	0.1075(12)	0.0629(4)	0.8833(6)		0.014(3)
Si7	8*d*	0.3807(15)	0.0504(4)	0.3328(6)		0.02
Si8	8*d*	0.3757(15)	0.0538(4)	0.1690(5)		0.015(2)
Si9	8*d*	0.1272(14)	0.0607(3)	0.6124(6)		0.019(3)
*A*1	4*c*	0.184(5)	0.25	0.831(3)	25(2)	0.085
Li2	4*c*	0.104 (9)	0.25	0.638(4)	0	0.03
Li3	8*d*	0.349(6)	0.1639(17)	0.637(3)	0	0.03
Li4	8*d*	0.153(5)	0.027(2)	0.063(3)	0	0.027(13)
Li5	8*d*	0.110(9)	0.1149(12)	0.264(3)	0	0.03
Li6	8*d*	0.145(6)	0.0010(16)	0.442(3)	0	0.03
Li7	8*d*	0.351(6)	0.1519(17)	0.841(3)	0	0.03
Li8	8*d*	0.353(7)	0.0317(13)	0.741(4)	0	0.033(13)
*A*9	8*d*	0.142(4)	0.1685(7)	0.0390(13)	48(2)	0.089(10)
Li10	8*d*	0.380(9)	0.1938(18)	0.167(3)	0	0.03
Li11	8*d*	0.376(10)	0.181(2)	0.345(3)	0	0.043(13)
Li12	8*d*	0.324(5)	0.115(2)	0.487(3)	0	0.03
Li13	8*d*	0.490(5)	0.127(2)	0.024(4)	0	0.03

Characterization of $Na_7LiSi_{8-z}Ge_z$

Rietveld refinement

Table S8. Crystallographic data of several $Na_7LiGe_{8-z}Si_z$ phases obtained from powder diffraction data via Rietveld refinement (structural model K_7LiSi_8).[4]

z	8	6	4	2	1
stoichiometry	Na_7LiGe_8[a]	$Na_7LiSi_{1.2(3)}Ge_{6.8}$[b]	$Na_7LiSi_{3.5(3)}Ge_{4.5}$[c]	$Na_7LiSi_{5.8(1)}Ge_{2.2}$[d]	$Na_7LiSi_{6.7(1)}Ge_{1.3}$[e]
T / K			293 K		
M_r / g mol^{-1}	748.6	695.6	591.9	492.2	448.2
Powder color			Grey		
Crystal system			Cubic		
Space group			$Pa\bar{3}$		
Lattice parameters					
a / Å	11.648(1)	11.624(1)	11.5918(8)	11.5522(4)	11.5282(4)
V / Å^3	1580.4(2)	1570.4(2)	1557.6(1)	1541.68(5)	1532.08(6)
Z			4		
$\rho_{calc.}$ / g cm^{-3}	3.146	2.9422	2.524	2.121	1.943
μ / mm^{-1}	18.57	17.136	14.21	11.38	10.126
Θ range / °	5.00–88.99	5.00–88.99	5.00–88.99	5.00–88.99	5.00–89.96
R [$I > 3\sigma(I)$]	0.0438	0.0263	0.0444	0.0879	0.0638
wR [$I > 3\sigma(I)$]	5.620.0562	0.0367	0.0631	0.1061	0.0765
R (all)	0.0438	0.0263	0.0444	0.0922	0.0638
wR (all)	0.0562	0.0367	0.0631	0.1068	0.0765
Goodness of fit	1.66	2.74	3.84	3.54	3.18

[a] Sample contains 9.4(5) % Na_4Ge_4.
[b] Sample contains 30(3) % $Na_4Si_{0.67(8)}Ge_{3.33}$.
[c] Sample contains 55(5) % $Na_4Si_{1.4(2)}Ge_{2.6}$ and 1.1(2) % Li_7Ge_3.[5]
[d] Sample contains 28(3) % $Na_4Si_{2.6(2)}Ge_{1.4}$.
[e] Sample contains 56(2) % $Na_4Si_{3.40(7)}Ge_{0.60}$.

Table S9. Atomic coordinates and isotropic displacement parameters for $Na_7LiGe_{8-z}Si_z$ from Rietveld refinement (structural model K_7LiSi_8).[4]

		Na_7LiGe_8		$Na_7LiSi_{1.2(3)}Ge_{6.8}$		$Na_7LiSi_{3.5(3)}Ge_{4.5}$		$Na_7LiSi_{5.8(1)}Ge_{2.2}$		$Na_7LiSi_{6.7(1)}Ge_{1.3}$	
		x, y, z	***U_{eq}*, % Si**	***x, y, z***	***U_{eq}*, % Si**	***x, y, z***	***U_{eq}*, % Si**	***x, y, z***	***U_{eq}*, % Si**	***x, y, z***	***U_{eq}*, % Si**
Na1	24*d*	0.039(1) 0.227(1) 0.3126(7)	0.076(4) -	0.041(1) 0.226(1) 0.3129(9)	0.036(9) -	0.040(3) 0.229(3) 0.315(2)	0.076 -	0.041(1) 0.223(1) 0.313(1)	0.313(1) -	0.040(1) 0.224(1) 0.315(1)	0.315(1) -
Na2	4*a*	0 0 0	0.13(2) -	0 0 0	0.09(2) -	0 0 0	0.13 -	0 0 0	0.13 -	0 0 0	0.13 -
*T*1	8*c*	0.2888(3) 0.2888(3) 0.2888(3)	0.059(3) 0	0.2901(5) 0.2901(5) 0.2901(5)	0.033(5) 32(4)	0.289(2) 0.289(2) 0.289(2)	0.060 70(4)	0.291(1) 0.291(1) 0.291(1)	0.060 90(2)	0.294(1) 0.294(1) 0.294(1)	0.060 94(2)
*T*2	24*d*	0.2164(3) 0.9314(2) 0.4524(3)	0.064(2) 0	0.2148(4) 0.9320(3) 0.4523(4)	0.032(2) 9(4)	0.214(1) 0.9313(1) 0.4513(9)	0.064 35(4)	0.2151(6) 0.9315(6) 0.4505(6)	0.064 66(2)	0.2145(8) 0.9313(7) 0.4499(7)	0.064 81(1)
Li1	4*b*	0.5 0.5 0.5	0.12 -	0.5 0.5 0.5	0.05 -	0.5 0.5 0.5	0.12 -	0.5 0.5 0.5	0.05 -	0.5 0.5 0.5	0.05 -

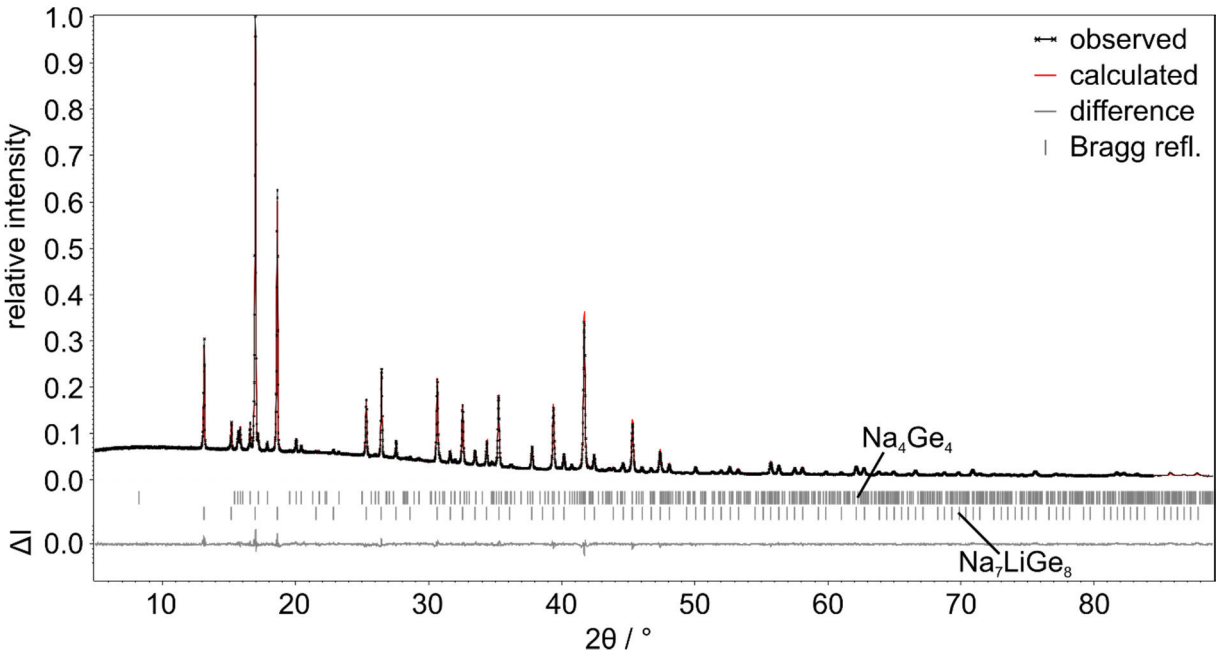

Figure S7. Rietveld refined powder diffraction pattern of Na_7LiGe_8 (structural model K_7LiSi_8)[4] with Na_4Ge_4 impurity. Corresponding refinement data is listed in Table S5.

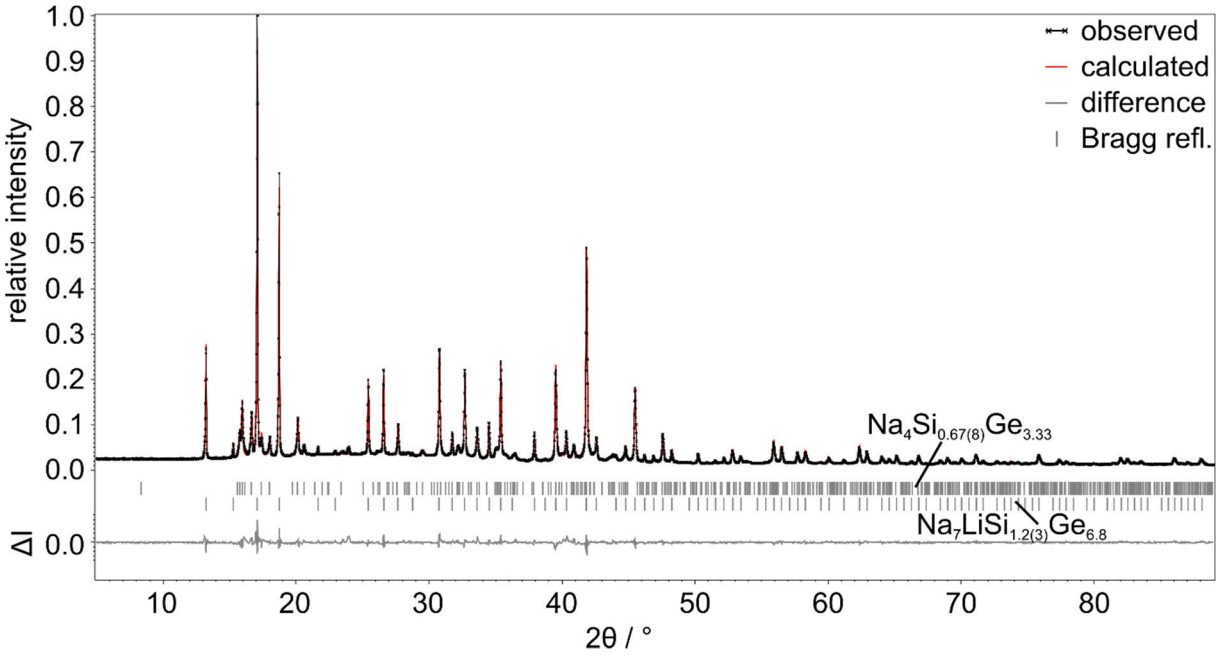

Figure S8. Rietveld refined powder diffraction pattern of $Na_7LiSi_{1.2(3)}Ge_{6.8}$ with $Na_4Si_{0.67(8)}Ge_{3.33}$ impurity. Corresponding refinement data is listed in Table S5.

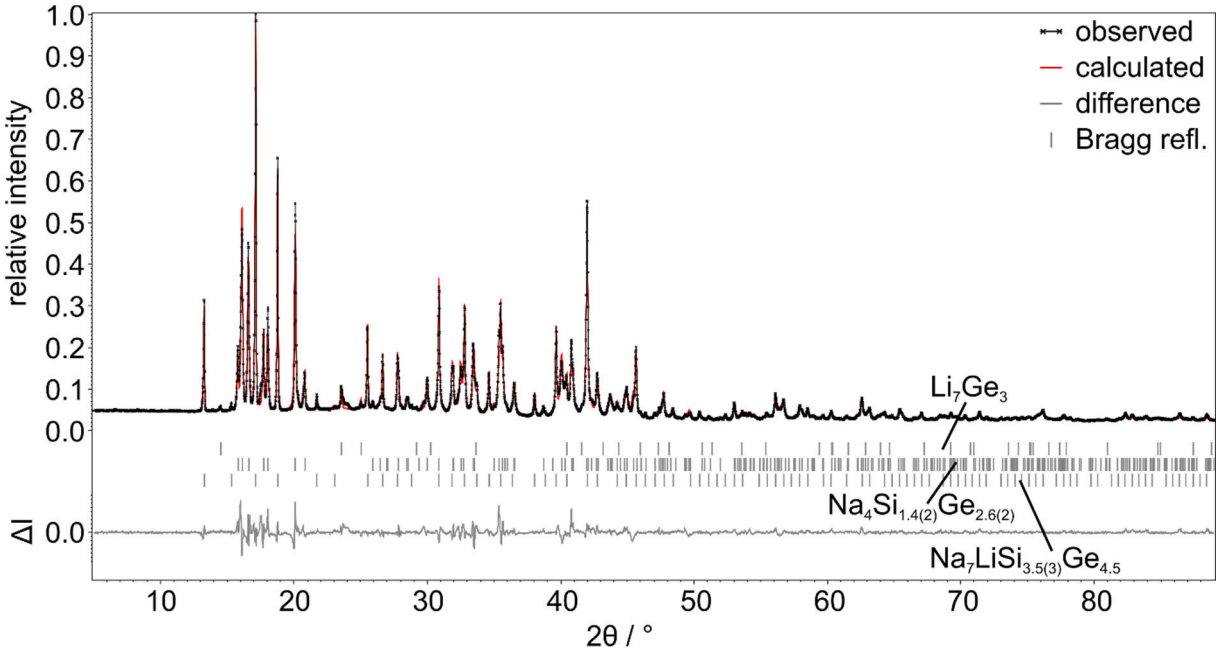

Figure S9. Rietveld refined powder diffraction pattern of $Na_7LiSi_{3.5(3)}Ge_{4.5}$ with $Na_4Si_{1.4(2)}Ge_{2.6}$ and Li_7Ge_3 impurities. Corresponding refinement data is listed in Table S5.

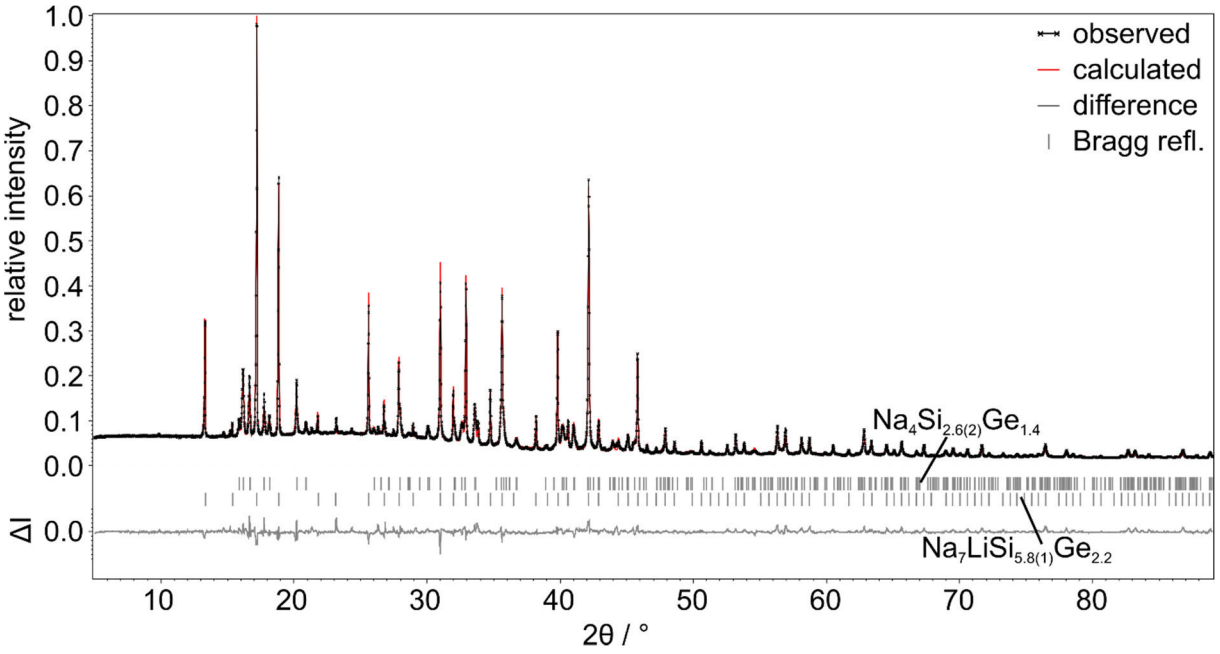

Figure S10. Rietveld refined powder diffraction pattern of $Na_7LiSi_{5.8(1)}Ge_{2.2}$ with $Na_4Si_{2.6(2)}Ge_{1.4}$ impurity. Corresponding refinement data is listed in Table S5.

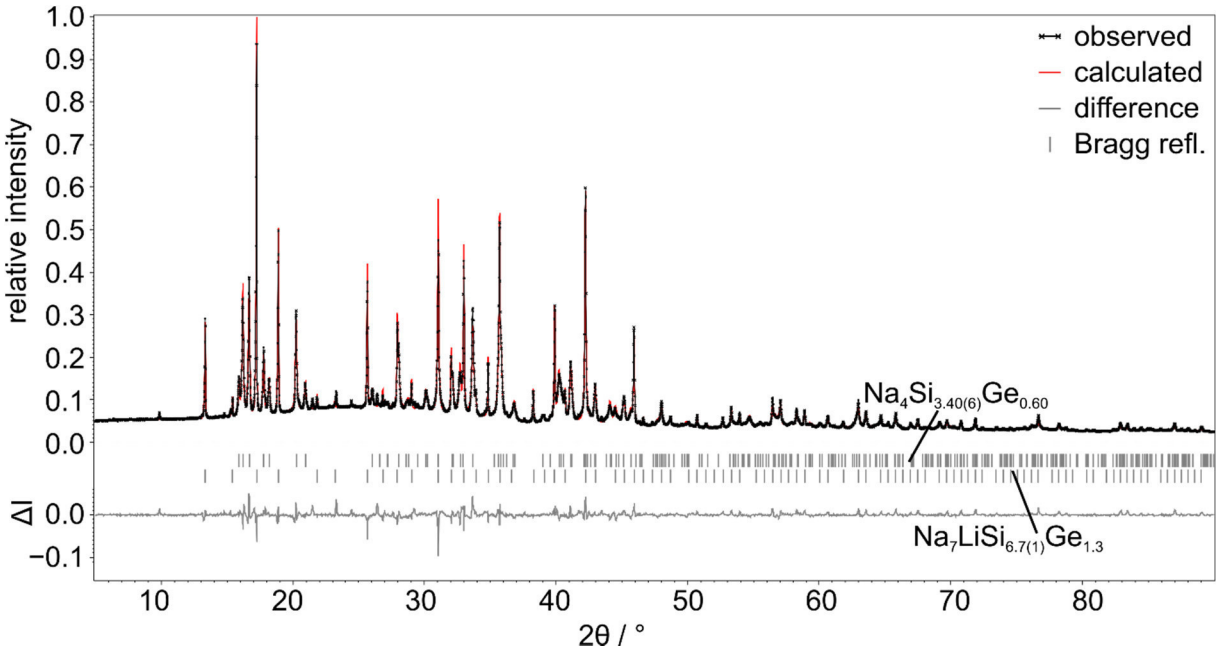

Figure S11. Rietveld refined powder diffraction pattern of $Na_7LiSi_{6.7(1)}Ge_{1.3}$ with $Na_4Si_{3.40(7)}Ge_{0.60}$ impurity. Corresponding refinement data is listed in Table S5.

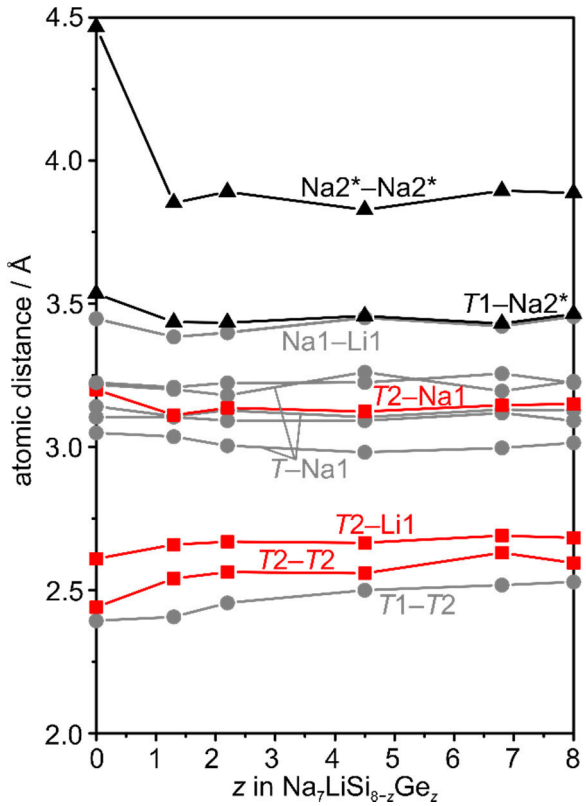

Figure S12. Changes of interatomic distances in $Na_7LiSi_{8-z}Ge_z$ with increasing Si content; tetrel element ratios *z* from Rietveld refinement, * data for *z* = 0 from KNa_6LiSi_8[6] in which Na2 is replaced by K. The interatomic distances including Na2/K (shown in black) change significantly due to the changed alkali metal. The interatomic distances between Na1, Li1 and *T*1 (shown in grey) display only slight changes with composition. In contrast, the interatomic distances including position *T*2 (shown in red) which is preferentially occupied by Ge in $Na_7LiSi_{8-z}Ge_z$ change more dramatically from $Na_7LiSi_{8-z}Ge_z$ to KNa_6LiSi_8.

Characterization of $Li_3NaSi_{6-v}Ge_v$

EDX data

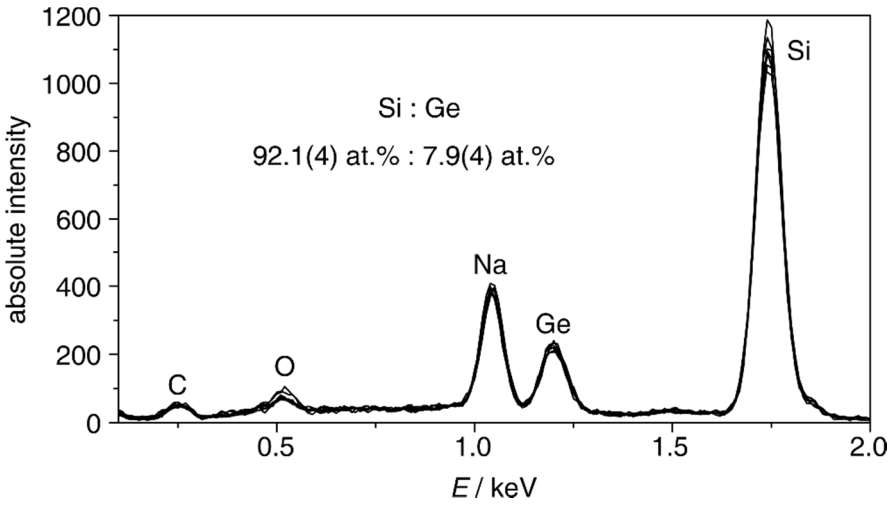

Figure S13. EDX spectra of a "$Li_3NaSi_{5.5}Ge_{0.5}$" single crystal (acceleration voltage 5 kV). The carbon signal is induced by the graphite tape used to fix the crystal. The oxygen impurity stems from a short transfer through air into the scanning electron microscope.

Powder diffraction patterns

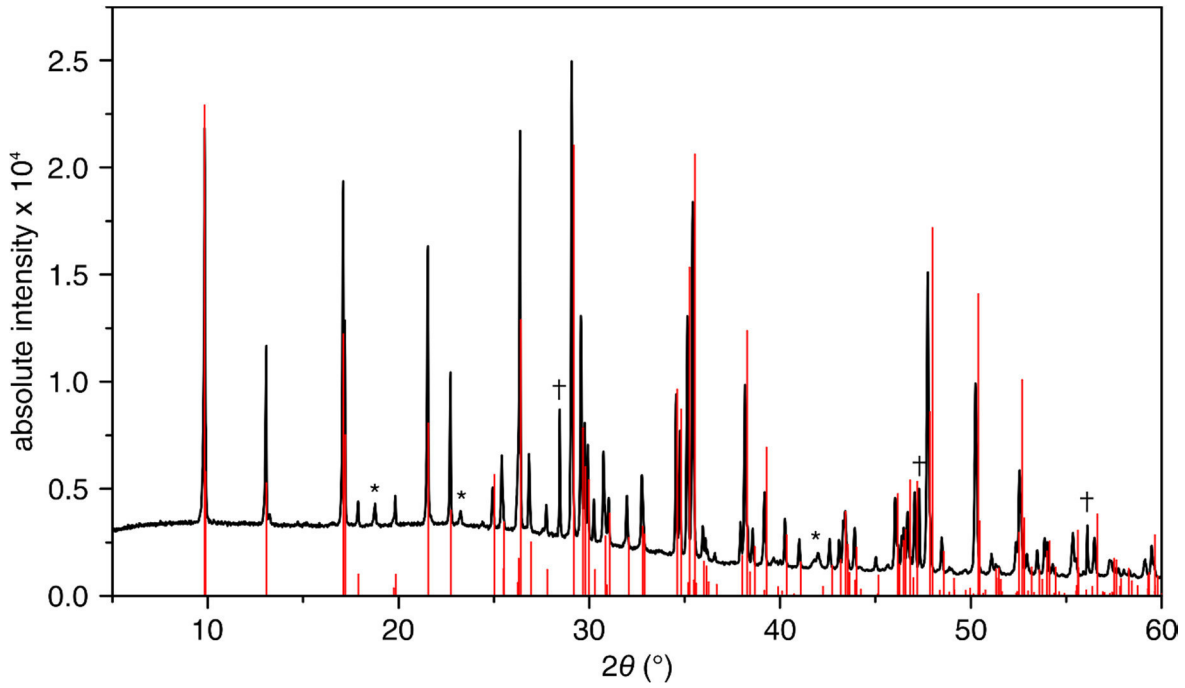

Figure S14. Experimental powder diffraction pattern of "$Li_3NaSi_{5.5}Ge_{0.5}$" (black) prepared via route (a). A calculated reference pattern for Li_3NaSi_6 is shown in red. Reflections of impurities Si (†) and $Li_{12}Si_{7-x}Ge_x$ (*) are marked.

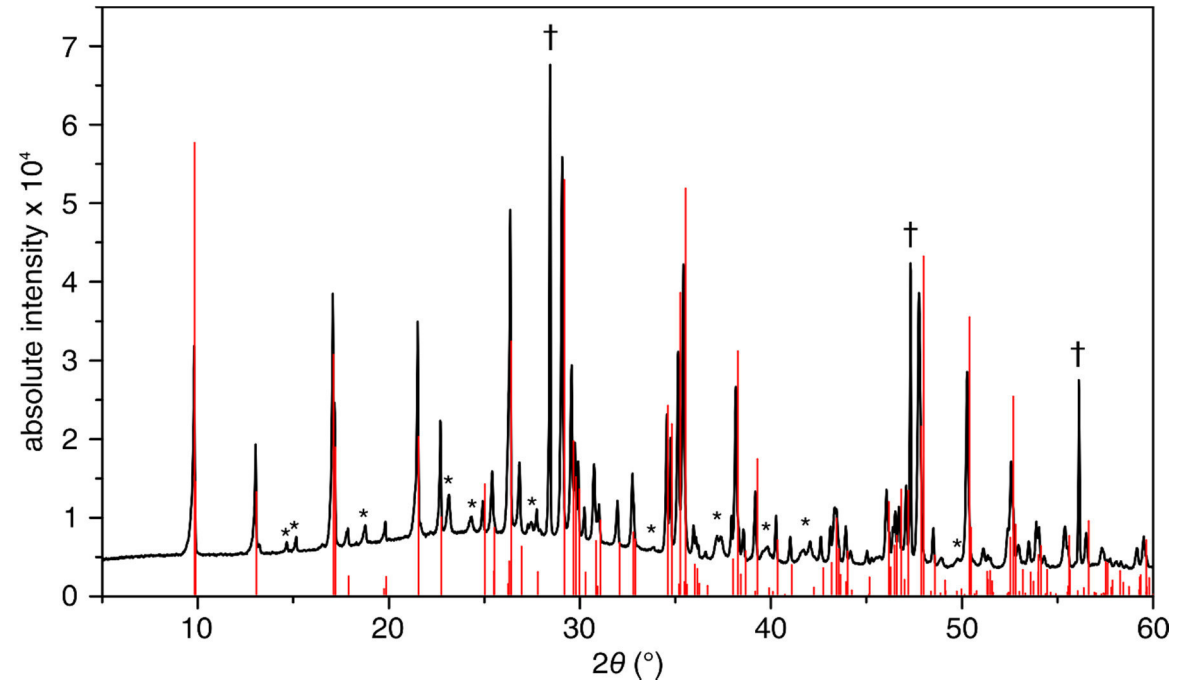

Figure S15. Experimental powder diffraction pattern of "$Li_3NaSi_{5.5}Ge_{0.5}$" (black) prepared via route (b). A calculated reference pattern for Li_3NaSi_6 is shown in red. Reflections of impurities Si (†) and $Li_{12}Si_{7-x}Ge_x$ (*) are marked.

Single crystal data

Table S10. Crystallographic Data and Structure Refinement of $Li_3NaSi_{5.56(1)}Ge_{0.44}$.

	$Li_3NaSi_{5.56(1)}Ge_{0.44}$
T (K)	100(2)
formula weight (g·mol^{-1})	231.93
crystal size (mm^3)	0.10 × 0.10 × 0.35
crystal color	metallic silver
crystal shape	needle
space group	*Pnma*
unit cell dimensions (Å)	a = 17.949(2)
	b = 3.8085(3)
	c = 10.2947(8)
Z	8
V (Å^3)	707.7(1)
ρ (calc.) (g·cm^{-3})	2.189
μ (mm^{-1})	2.895
F(000)	448
ϑ range (deg)	2.28–28.28
index range	−21 ≤ h ≤ 23
	−5 ≤ k ≤ 5
	−13 ≤ l ≤ 13
reflections collected	9604
independent reflections	996 (R_{int} = 0.0824)
reflections with $I > 2\sigma(I)$	899 (R_σ = 0.0403)
absorption correction	multi-scan
data / restraints / parameters	996 / 0 / 67
goodness-of-fit on F^2	1.101
final R indices [$I > 2\sigma(I)$][a,b]	R_1 = 0.0327
	wR_2 = 0.0796
R indices (all data)[a,b]	R_1 = 0.0372
	wR_2 = 0.0829
largest diff. peak and hole (e·Å^{-3})	0.940 and −0.516

Table S11. Atom coordinates, Wyckoff positions, isotropic displacement factors / Å^2 and Ge content on tetrel positions *T* for $Li_3NaSi_{5.56(1)}Ge_{0.44}$ at 100 K.

		x	***y***	***z***	U_{eq}	**% Ge**
*T*1	4*c*	0.19647(4)	0.25	0.02333(7)	0.0073(3)	1.6(5)
*T*2	4*c*	0.05414(3)	0.25	0.66546(5)	0.0076(2)	24.3(7)
*T*3	4*c*	0.29527(4)	0.25	0.85883(6)	0.0075(3)	8.9(5)
*T*4	4*c*	0.38210(4)	0.25	0.49713(7)	0.0076(2)	6.8(6)
*T*5	4*c*	0.38241(4)	0.25	0.25923(7)	0.0074(3)	1.2(5)
*T*6	4*c*	0.24910(4)	0.25	0.24173(7)	0.0070(3)	1.3(5)
Na1	4*c*	0.07572(7)	0.25	0.2506(1)	0.0144(4)	
Li1	4*c*	0.4325(3)	0.25	0.9852(5)	0.014(1)	
Li2	4*c*	0.0278(3)	0.25	0.9086(5)	0.015(1)	
Li3	4*c*	0.1875(3)	0.25	0.5620(6)	0.017(1)	

Table S12. Relevant interatomic distances in $Li_3NaSi_{5.56(1)}Ge_{0.44}$ (*Pnma*, *Z* = 8, estimated standard deviations in parentheses).

Atom			***d*** **(Å)**	**Atom**			***d*** **(Å)**	**Atom pair**			***d*** **(Å)**
*T*1	*T*4	×2	2.3849(7)	*T*3	*T*6	×2	2.3903(6)	*T*5	*T*2	×2	2.4197(6)
	*T*6		2.439(1)		*T*1		2.452(1)		*T*4		2.449(1)
	*T*3		2.452(1)		Li1		2.785(5)		Li2	×2	2.930(4)
	Li3	×2	2.850(4)		Li3	×2	2.845(4)		Li1		2.960(5)
	Na1		3.189(2)		Na1	×2	3.199(1)		Li3		3.054(4)
*T*2	*T*5	×2	2.4197(6)	*T*4	*T*1	×2	2.3849(7)	*T*6	*T*3	×2	2.3903(6)
	Li2		2.547(5)		*T*5		2.449(1)		*T*1		2.439(1)
	Li3		2.620(6)		Li2	×2	2.659(4)		Li3	×2	2.889(5)
	Li1	×2	2.670(4)		Li2		2.790(6)		Na1		3.113(2)
	Li1		2.679(5)		Na1	×2	3.318(1)	Na1	Li1	×2	3.080(4)
	Na1	×2	3.132(1)	*T*5	*T*6		2.400(1)		Li2	×2	3.125(4)

Rietveld refinement

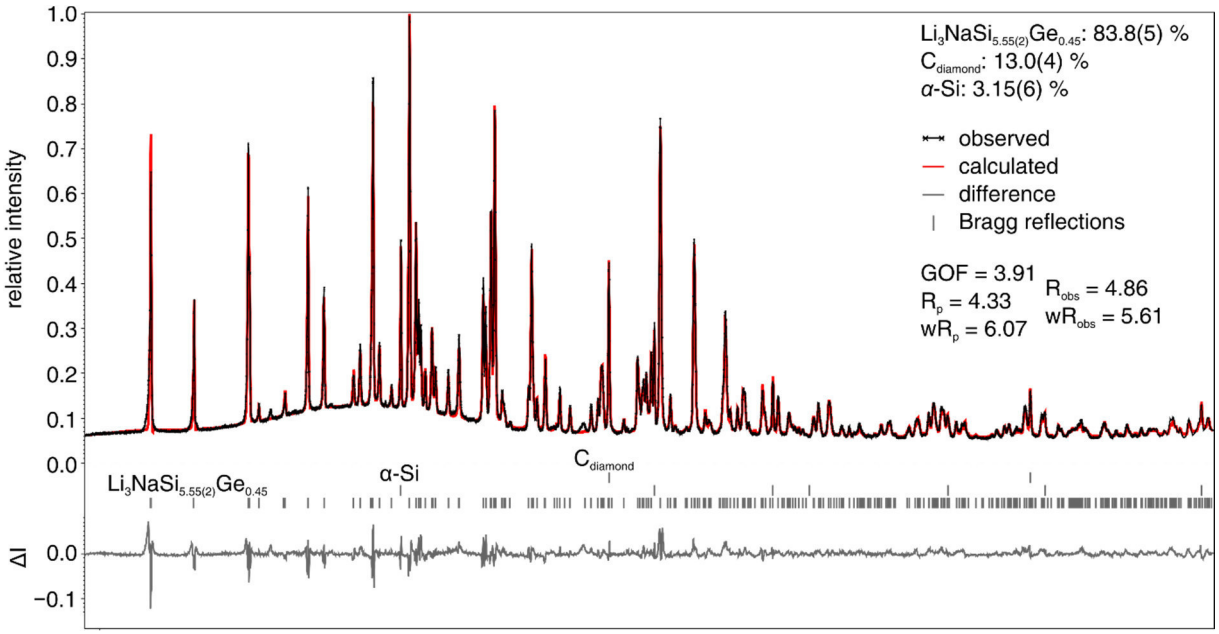

Figure S16. Rietveld-refined powder diffraction pattern of $Li_3NaSi_{5.55(2)}Ge_{0.45}$ (structural model Li_3NaSi_6).[7] Obtained cell parameters in *Pnma*: *a* = 17.9879(15) Å, *b* = 3.8038(3) Å, *c* = 10.3113(8) Å, V = 705.53(17) Å^3.

Table S13. Structural data for $Li_3NaSi_{5.55(2)}Ge_{0.45}$ from Rietveld refinement (structural model Li_3NaSi_6).[7]

atom		*x*	*y*	*z*	% Ge	U_{iso} / Å^2
*T*1	4*c*	0.1963(2)	0.25	0.0228(3)	0	0.02
*T*2	4*c*	0.05486(13)	0.25	0.8349(2)	28.3(3)	0.02
*T*3	4*c*	0.29731(16)	0.25	0.8592(3)	9.2(3)	0.02
*T*4	4*c*	0.38310(17)	0.25	0.4957(3)	7.4(4)	0.02
*T*5	4*c*	0.38165(17)	0.25	0.2576(4)	0	0.02
*T*6	4*c*	0.2482(2)	0.25	0.2393(4)	0	0.02
Na1	4*c*	0.0746(2)	0.25	0.2507(4)		0.0151(15)
Li1	4*c*	0.4378(14)	0.25	0.975(2)		0.06
Li2	4*c*	0.0189(13)	0.25	0.912(2)		0.06
Li3	4*c*	0.1870(15)	0.25	0.551(2)		0.06

References

[1] P.-E. Werner, L. Eriksson, M. Westdahl, *J. Appl. Crystallogr.* **1985**, *18*, 367-370.
[2] *WinXPOW*, STOE & Cie GmbH, Darmstadt, **2003**.
[3] R. Nesper, H. G. von Schnering, J. Curda, *Chem. Ber.* **1986**, *119*, 3576–3590.
[4] H. G. von Schnering, M. Schwarz, R. Nesper, *Angew. Chem.* **1986**, *98*, 558–559; *Angew. Chem. Int. Ed. Engl.* **1986**, *25*, 566-567.
[5] A. Grüttner, R. Nesper, H. G. v. Schnering, *Acta Crystallogr.* **1981**, *A37*, C161.
[6] M. Schwarz, Dissertation, Universität Stuttgart **1987**.
[7] H. G. von Schnering, M. Schwarz, R. Nesper, *J. Less-Common Met.* **1988**, *137*, 297–310.

5.5 The Lithium Ion Conductor $Li_6B_{18}(Li_3N)_x$ – Synthesis, Li Ion Mobility, Topochemical Template Extraction, and Electronic Structure

Lavinia M. Scherf, Holger Kirchhain, Leo van Wüllen, Thomas F. Fässler*, *manuscript for publication*.

Abstract

The open framework template phase $Li_6B_{18}(Li_3N)_x$ was synthesized from elemental Li, crystalline B and Li_3N. It can be clearly distinguished from the previously known oxide phase $Li_6B_{18}(Li_2O)_x$ by its larger cell parameters of a = 8.2709(7) Å, c = 4.1832(3) Å, V = 247.82(3) Å^3 in space group $P6/mmm$. Rietveld refinement suggests a sum formula of $Li_{6.35(7)}B_{18}N_{0.94(1)}$ containing more Li vacancies than expected for an electron-precise compound. The open framework structure comprises large hexagonal pores filled with $^1_\infty[Li_7N]$ strands which represent a cutout from the structure of the lithium ion conductor Li_3N. Variable-temperature ^{7}Li NMR spectroscopy yields a very high Li mobility in the template phase $Li_6B_{18}(Tp)_x$ with an activation energy between 5 and 20 kJ mol^{-1}. By reaction with ethanol, the template species can be partially extracted from red $Li_6B_{18}(Tp)_x$. The resulting green powder largely retains its boron framework structure, although Raman spectroscopy suggests that some changes (e.g. substitution or partial oxidation) do occur. The band structure of fully occupied $Li_6B_{18}(Li_3N)$, determined with TB-LMTO-ASA, is typical for a host-guest compound: only the host atoms located in the large pores contribute to the bands just below the Fermi level, whereas the B framework bands exhibit set up a direct band gap at the Γ point. Template-free Li_6B_{18} structures still have in-gap states corresponding to Li atoms inside the pore. In contrast, chemically inspired $B_{12}C_6$ structures with completely empty pores are predicted to be direct band gap semiconductors.

Introduction

In times of an ongoing shift from continuous energy production from fossil fuels to weather-dependent generation of energy from renewable sources, efficient energy storage becomes more and more important. In order to run on renewable energy, mobile applications such as electronic devices and electric vehicles require safe and lightweight batteries. Currently, lithium ion batteries (LIBs) are widely used for this purpose because they are characterized by large gravimetric and volumetric capacities.[1] However, the combination of reactive inorganic species, large voltages and organic electrolytes as well as the possibility of short circuits by dendrite formation still pose significant safety issues. Therefore, solid-state batteries in which the liquid organic electrolytes are replaced by solid electrolytes have become a major focus of LIB research.[2]

In order to compete with liquid electrolytes, solid electrolytes for LIBs must be characterized by a large Li ion conductivity. This can be achieved by a low activation energy for ion mobility and the presence of sufficient vacancies to which the Li ions can move.[3] At the same time, low electric conductivity and good electrochemical stability are necessary. Already in the 1970s, Li_3N was found to be an excellent Li ion conductor with an ionic conductivity of $6 \cdot 10^{-3}$ S cm^{-1} at room temperature.[4,5] This conductivity is only one order of magnitude lower than that of organic liquid electrolytes.[6] Due to its insufficient electrochemical stability, however, Li_3N is not suitable for application as a solid electrolyte.

The LISICON compounds $Li_{2+2x}ZnGeO_4$ were soon found to be much more stable Li ion conductors, albeit exhibiting much a much lower ionic conductivity of around 10^{-6} S cm^{-1}.[7,8] Further improvements of Li ion conductivity were achieved by turning to sulfide compounds such as the thio-LISICONs[9,10] and recently discovered LGPS-type superionic conductors $Li_{10}GeP_2S_{12}$[11] and $Li_{11}Si_2PS_{12}$.[12] The latter possess ionic conductivities in the range of organic liquid electrolytes at around 10^{-2} S cm^{-1}. The activation energies for Li diffusion in LGPS-type compounds amount to about 20 kJ mol^{-1}.[11,12]

In addition to crystalline Li ion conductors like those presented above, glassy mixtures of various binary sulfides have been investigated as potential solid-state electrolytes. Amorphous phases prepared by the combination of Li_2S with B_2S_3/LiI, SiS_2/LiBr, and P_2S_5/LiI have exhibited large ionic conductivities of up to 10^{-3} S cm^{-1}.[13-17] Boron-containing solid electrolytes offer the great advantage of containing mostly very light elements and thus promise solid-state batteries with exceptionally large gravimetric capacities. Recently, the crystalline compound $LiBSi_2$ was discovered by high-temperature high-pressure synthesis.[18] Its tetrahedral open framework structure comprises large open channels, which are filled with Li^+ cations. Due to the difficult synthesis, the ion conductivity of $LiBSi_2$ could not yet be determined, but its pore structure suggests great Li mobility.

Similarly, large open channels are found in the template phase $Li_6B_{18}(Tp)_x$ (Figure 1a). Li_2O and $LiBH_4$ have been shown to function as templates (*Tp*) in the formation of this hexagonal phase comprising a $3^2.4^8.6^2$ network of interconnected B_6 octahedra.[19-21] Small and large pores of the structure, which run along the *c* direction, are filled with Li cations and the template species *Tp*, rendering it a typical example of an inorganic open framework structure. Previous impedance measurements suggest semiconducting behavior at room temperature and ion conductivity with an activation energy of 38.5 kJ mol^{-1} above 150 °C.[22]

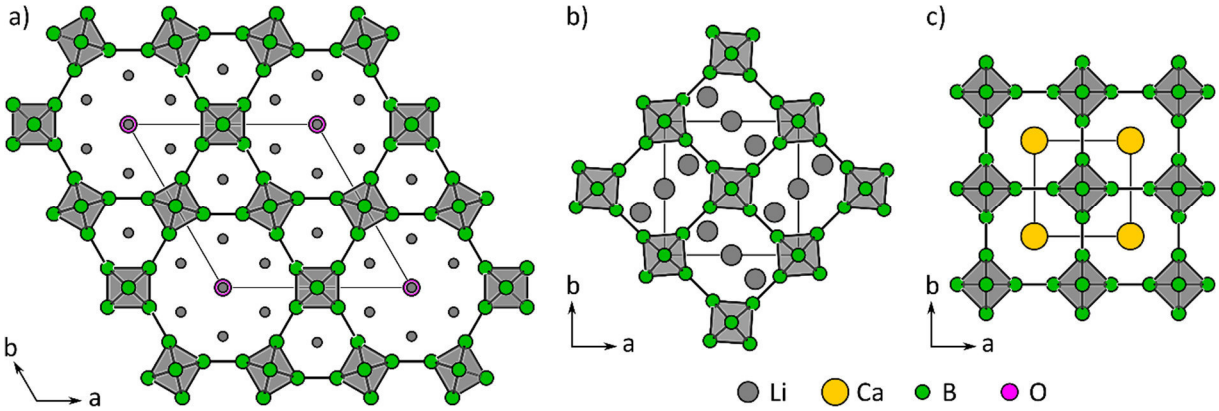

Figure 1. a) Hexagonal open framework structure of $Li_6B_{18}(Li_2O)_{0.26}$. The boron octahedra form a $3^2.4^8.6^2$ network in which the lithium and oxygen positions located in the channels are only partially occupied.[21] b) Tetragonal 4^{12} structure of Li_2B_6 comprising only small channels. Again, the Li positions are only partially occupied.[23] c) Cubic 4^{12} structure of CaB_6 and related rare earth metal borides.[24]

$Li_6B_{18}(Tp)_x$ is structurally related to the cubic MB_6 compounds[24] as well as to tetragonal Li_2B_6, which forms without the presence of a template species under otherwise similar conditions.[23] These compounds consist of a 4^{12} framework of interconnected B_6-octahedra whose cubic voids are filled with metal cations (Figure 1b, c). The existence of the very stable, cubic MB_6 structure for monovalent (KB_6),[25] divalent (e.g., MgB_6, CaB_6),[24,26] trivalent (e.g., LaB_6, YB_6),[24] and even mixed-valent (SmB_6)[27] metals *M* demonstrate the structural and electronic flexibility of the boron framework. Electronic structure calculations suggest semiconducting behavior for the electron-precise hexaborides with

divalent cations, whereas the electron-deficient or excess-electron hexaborides should be metallic.[28,29]

Using Li_3N as the template species for the formation of $Li_6B_{18}(Tp)_x$, we have now prepared a novel crystalline phase with extraordinary Li ion mobility as shown by solid state NMR spectroscopy. $Li_6B_{18}(Li_3N)_x$ combines the very stable open framework structure of $Li_6B_{18}(Tp)_x$ with the outstanding Li ion conduction properties of Li_3N. In order to find out whether the host species *Tp* can be removed from the boron framework, the reactivity of $Li_6B_{18}(Tp)_x$ with ethanol is examined. Furthermore, we analyze the electronic structure of fully occupied $Li_6B_{18}(Li_3N)$ and use the open framework structure as a starting point for the chemically inspired construction of an open framework boron carbide $B_{12}C_6$, which we demonstrate to be a direct band gap semiconductor.

Experimental Section

All steps of synthesis and sample preparation were performed inside an argon-filled glovebox (MBraun, $p(H_2O)$, $p(O_2)$ < 1.0 ppm) or using standard Schlenk procedures. Li (> 99 %) was freed from oxide layers before use. Ethanol was dried over sodium. Crystalline B (99.95 %, Chempur), nano-B (98.5 %, Pavezyum), Li_3N (99.5 %, Sigma Aldrich), and Li_2O (99.5 %, Alfa Aesar) were used as purchased.

Synthesis of $Li_6B_{18}(Tp)_x$. The open framework phases $Li_6B_{18}(Tp)_x$ were synthesized from Li, B, and the template species Li_3N or Li_2O. As previously mentioned for $Li_6B_{18}(Li_2O)_x$, a slight excess of lithium promotes the formation of the crystalline template phase.[21] In case of crystalline B as the B source, B (136.5 mg/139.0 mg; 18 equiv.) was placed inside the ampules first, followed by Li (39.2 mg/40.3 mg; 8 equiv.) and Li_3N (24.6 mg; 1 equiv.) or Li_2O (21.5 mg; 1 equiv.). In case of nano-B, the B material (337.7 mg; 18 equiv.) was thoroughly mixed with Li_3N (60.8 mg; 1 equiv.) by grinding in an agate mortar. Then, Li (108.0 mg; 9 equiv.) and the B/Li_3N mixture were placed in stainless steel ampules. The ampules were enclosed in silica reaction containers, which were then evacuated. The reaction mixtures were heated up to 900 °C at 5 °C min^{-1} and dwelled for 24 h. Subsequent cooling to room temperature at 1 °C min^{-1} afforded the orange or dark red reaction products.

Template extraction. For the extraction of the template species out of the open framework structure, 6 mL ethanol was added to 178 mg $Li_6B_{18}(Tp)_x$ in a Schlenk tube. Immediately, gas formation and heating of the reaction mixture was observed. In addition, the reddish brown solid rapidly changes to a green color. To ensure a complete reaction, the suspension was stirred at room temperature for 24 hours. Then, the colorless solution was removed by filtration and the green solid was washed with ethanol. To remove the tetragonal, boron-containing side product, the green solid was subsequently stirred with a 1:1 mixture of ethanol and deionized water for 24 hours, after which the resulting stable, light brown suspension was removed from the green solid by repeated filtration and washing with ethanol. The extracted template compound was then dried under dynamic vacuum for at least 2 hours.

Powder X-ray diffraction. Powder X-ray diffraction (PXRD) was carried out to determine the crystalline phases present in all synthesis products. Thus, the samples were finely ground in an agate mortar and then sealed inside 0.5 mm glass capillaries. The PXRD patterns were measured using a Stoe STADI P diffractometer equipped with a Ge(111) monochromator for Cu $K_{\alpha1}$ radiation (λ = 1.54056 Å) and a Dectris MYTHEN DCS 1K solid-state detector. A 5–89° 2ϑ range was irradiated for 30 s each in 0.07° steps of the position sensitive detector.

Rietveld refinement. Rietveld refinements were performed using Jana2006.[30] The crystal structure of $Li_6B_{18}(Li_2O)_{0.90}$ was used as initial structural model.[21] All cell parameters and atom positions as well as site occupancies for all Li and template atom N and O positions were refined freely. Isotropic displacement parameters were refined whenever possible.

Raman spectroscopy. Raman spectra were measured using an inVia Raman microscope (Renishaw, RE04). The powdery samples were filled into a 0.5 mm glass capillary and irradiated with a 532 nm laser beam for 1 s at 0.5 % ($Li_6B_{18}(Li_3N)_x$ and $Li_6B_{18}(Li_2O)_x$) or 1 % ($Li_{6-\delta}B_{18}(Tp)_x$) laser power using a microscope equipped with a 50-fold magnifying objective and a grating with 1800 lines mm^{-1}. 150 such measurements were averaged to yield the final Raman spectra.

NMR spectroscopy. Solid-state NMR experiments were performed using a Bruker Avance III-spectrometer equipped with a 4mm WVT MAS probe. The resonance frequencies of the measured nuclei at the operating field of 7 T are 116.6 MHz, 300.13 MHz and 96.3 MHz for ^{7}Li, ^{1}H and ^{11}B. Sample preparation was conducted under argon while the measurements were performed under a permanent nitrogen flow. The static ^{7}Li single-pulse, solid-echo (90-τ-90), and T_1-inversion-recovery experiments were conducted in a temperature range from 112 K to 300 K with 4, 8 and 8 scans, respectively, and recycle delays between 10s at 112 K and 3 s at 300 K for the single-pulse and solid-echo measurements. ^{11}B single-pulse measurements were performed under MAS at 10 kHz with 1024 scans and a recycle delay of 2 s using 15°-pulses for excitation at room temperature (294 K). ^{1}H-Spin-echo measurements were performed at room temperature under MAS 10 at kHz and under static conditions with 16 and 64 scans respectively and a recycle delay of 5 s. The spectra were referenced to LiCl (aq), adamantane (s) and H_3BO_3 (aq) for ^{7}Li, ^{1}H and ^{11}B.

Transmission electron microscopy (TEM). TEM and selected-area electron diffraction (SAED) experiments were performed using a JEM-2100 microscope (JEOL, 200 kV, LaB_6, spherical aberration coefficient C_S = 1.0 nm) equipped with an EDX detector (SDD, Oxford).

Elemental analysis. Elemental analysis was performed by the microanalytical laboratory at TU München.

Differential scanning calorimetry (DSC). Thermal analyses were performed in order to assess the thermal stability of different $Li_6B_{18}(Tp)_x$ phases. The samples were sealed in Nb ampules and measured on a DSC machine (Netzsch, DSC 404 Pegasus) under a constant gas flow of 75 mL min^{-1}. The samples were heated to 1000 °C and cooled back down to 150 °C twice at a rate of 10 °C min^{-1}. The PROTEUS Thermal Analysis software was used to determine onset temperatures of the various DSC signals.[31]

Electronic Structure Calculations. Computational studies on the electronic structures of $Li_6B_{18}(Li_3N)$, Li_6B_{18}, and B_4C_2 employed the linear muffin-tin orbital (LMTO) method in the atomic sphere approximation (ASA) using the tight-binding (TB) program TB-LMTO-ASA.[32] The exchange-correlation term was calculated within the local density approximation (LDA) and was parameterized according to von Barth and Hedin.[33] The radii of the muffin-tin spheres and empty spheres were determined after Jepsen and Andersen.[34] The basis set of short-ranged,[35] atom-centered TB-LMTOs contained s and p valence functions for B, C, and N and s valence functions for Li. Li p, B d, C d, and N d orbitals were included using a downfolding technique. For Li_6B_{18} and B_4C_2 several different atom distributions were obtained from symmetry reduction of *P*6/*mmm*. The utilized structures are listed in the Supporting Information (Tables S4–S9).

Results and Discussion

Synthesis and characterization of $Li_6B_{18}(Li_3N)_x$. We have synthesized $Li_6B_{18}(Li_3N)_x$ using Li_3N as the template species from elemental Li, crystalline B, and Li_3N. A stoichiometric ratio of 8:18:1 heated to 900 °C in steel ampules yielded the best $Li_6B_{18}(Li_3N)_x$ sample, which contains only small amounts of LiB (cf. Figure 2). Previous experiments by Wörle and Mair have shown that impurities contained in Li and B can also function as template species,[19,20] allowing the formation of $Li_6B_{18}(Tp)_x$ without the addition of any template species. A control experiment using a 8:18 ratio of Li and B yields Li_2B_6 as the main product (Figure 2c) next to LiB and only traces of $Li_6B_{18}(Tp)_x$. Therefore, we can be certain that in addition to Li_2O and $LiBH_4$, Li_3N indeed functions as a template for $Li_6B_{18}(Tp)_x$.

For comparison, we also synthesized $Li_6B_{18}(Li_2O)_x$ via the same synthesis route. The PXRD patterns of $Li_6B_{18}(Li_3N)_x$ and $Li_6B_{18}(Li_2O)_x$ show a slight shift of the template phase reflections, suggesting different unit cell sizes for the structures crystallizing in space group *P*6/*mmm*. Incorporation of the larger Li_3N unit in $Li_6B_{18}(Li_3N)_x$ gives rise to larger lattice parameters of a = 8.2709(7) Å, c = 4.1832(3) Å, V = 247.82(3) Å^3. The lattice parameters of $Li_6B_{18}(Li_2O)_x$ are significantly smaller with a = 8.223(2) Å, c = 4.148(1) Å, V = 242.90(8) Å^3. In addition, the template phases based on Li_3N and Li_2O templates, respectively, differ in color (dark red vs. orange) and the intensity ratio of reflections (100) and (200) in the powder diffraction patterns (Figure 2). Calculated diffraction patterns of the P6/mmm structure reveal that the intensity ratio of the (100) and (200) reflections mainly depends on the occupancies of the atoms located inside the large hexagonal pores. The intensity of (100) with respect to (200) decreases with increasing pore atom occupancies.

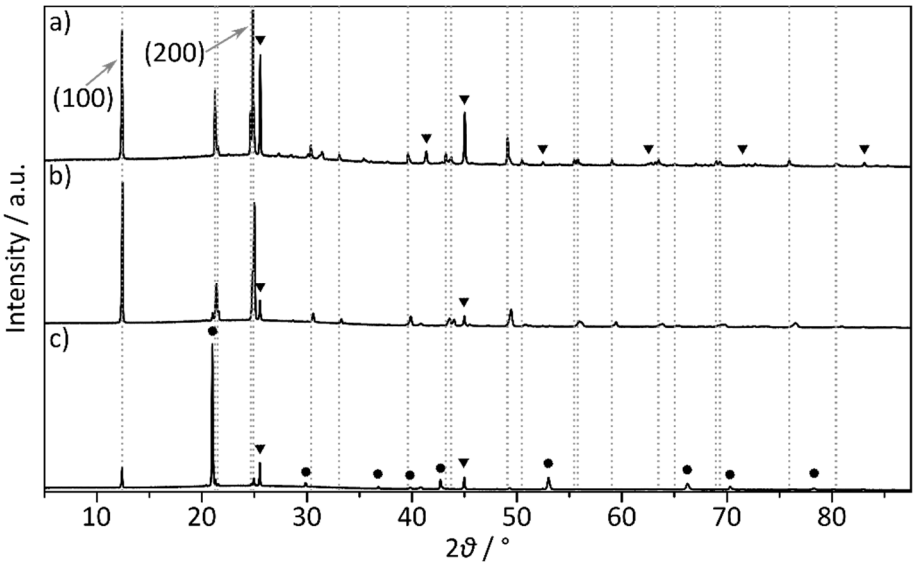

Figure 2. Experimental powder X-ray diffraction (PXRD) patterns of a) $Li_6B_{18}(Li_3N)_x$, b) $Li_6B_{18}(Li_2O)_x$, and c) the reaction product without added template species. The characteristic reflections of $Li_6B_{18}(Tp)_x$ are marked by dotted lines, Li_2B_6 and LiB are denoted by ● and ▼, respectively. For comparability, all diffraction patterns were angle-corrected using an external standard.

Thus, Rietveld refinements of the powder diffraction patterns were performed for both $Li_6B_{18}(Li_3N)_x$ and $Li_6B_{18}(Li_2O)_x$, using the published structure of $Li_6B_{18}(Li_2O)_{0.90}$ as the structural model. Complete data of the Rietveld refinements and the refined diffraction patterns are given in the Supporting Information (Tables S1 and S2, Figures S1 and S2). As shown in Figure 3a, the structure of $Li_6B_{18}(Tp)_x$ comprises a boron-framework consisting of two boron positions B1 and B2, which represent the four atoms making up the distorted square in the *ab* plane and the atoms capping the square in *c* direction, respectively. The small pores along *c*, which are constructed by three interconnected B_6-octahedra,

are filled with one Li position, Li1. The larger pores along *c* constructed by six interconnected B_6-octahedra are filled with the template atom N1/O1 that alternates with Li3 in the *c* direction. In addition, six Li2 atoms surround N1/O1 (Figure 3b).

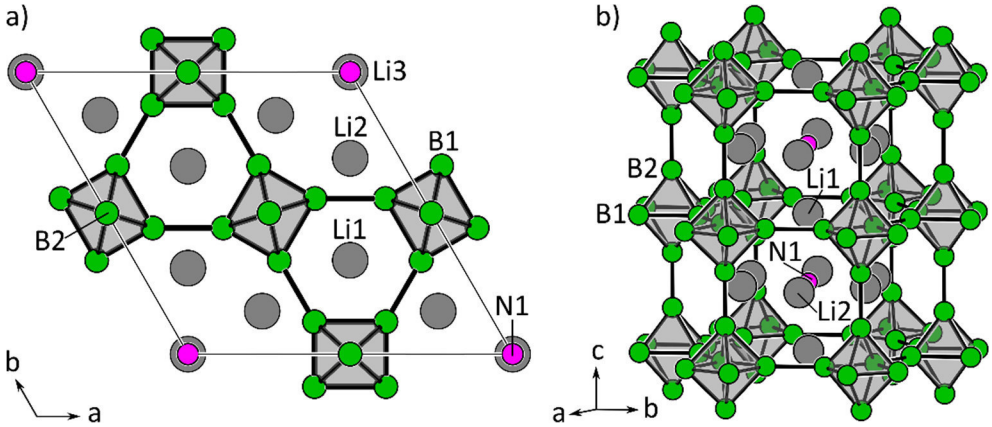

Figure 3. a) Projection of the unit cell of $Li_{6.35(7)}B_{18}N_{0.94(1)}$ onto the *ab* plane. b) Depiction of the large hexagonal pore formed by interconnected B_6-octahedra. The formal Li_7N-unit inside the pore represents a structural excerpt from the hexagonal *P*6/*mmm* structure of *α*-Li_3N.[36]

According to Rietveld refinement, atomic positions B1, B2, Li1, and Li3 are fully occupied for both $Li_6B_{18}(Li_3N)_x$ and $Li_6B_{18}(Li_2O)_x$. Li2 and N1/O1 however exhibit partial occupation, as listed in Table 1. The template atom position *Tp*1 is almost fully occupied by N in $Li_6B_{18}(Li_3N)_x$, whereas a significantly smaller site occupancy factor (s.o.f.) of 0.765(5) is found for O1 in $Li_6B_{18}(Li_2O)_x$. Furthermore, $Li_6B_{18}(Li_2O)_x$ contains an additional Li position, Li2b, inside the larger pores (Figure 4).[37] Li2b is located at a distance of only 1.09(4) Å from two Li2 positions, so that no neighboring Li2 and Li2b sites can be occupied at the same time. Thus, Li2b allows for a more even distribution of underoccupied Li around the template atom.

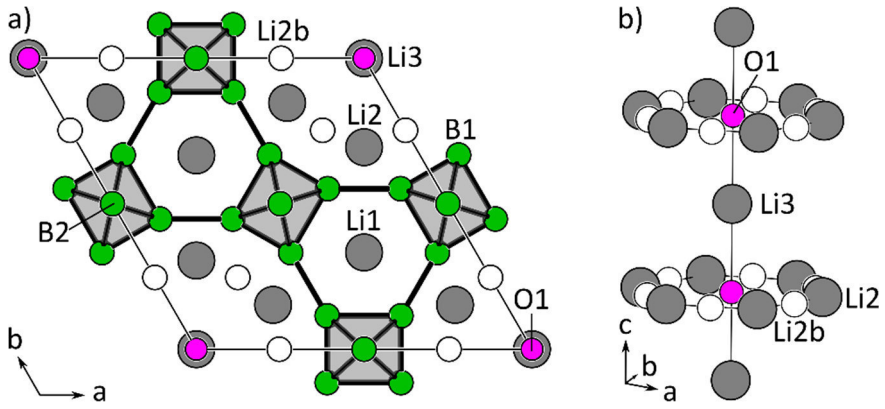

Figure 4. a) Projection of the unit cell of $Li_{6.9(1)}B_{18}O_{0.76(5)}$ onto the *ab* plane. b) Content of the large hexagonal pore formed by interconnected B_6-octahedra.

Overall, our Rietveld results for $Li_6B_{18}(Li_2O)_x$ agree qualitatively with the single crystal data obtained by Wörle et al. for $Li_6B_{18}(Li_2O)_{0.70}$ (Table 1), although they observed an underoccupation of Li3.[21] However, the stoichiometry of the two phases examined in this work results to $Li_{6.35(7)}B_{18}N_{0.94(1)}$ and $Li_{6.9(1)}B_{18}O_{0.765(5)}$. These sum formulae suggest a significant Li deficiency compared to expected electron-precise $Li_6B_{18}(Tp)_x$ (Table 1), which has not yet been described elsewhere. In the Li_3N-based phase, the difference between the actual Li content per formula unit of 6.35(7) and the expected Li content of 8.82(3) is strikingly large and much greater than in the Li_2O-based phase [6.9(1) vs. 7.53(2) Li per

formula unit]. So far, we do not have a consistent explanation for this Li deficiency. However, cubic MB_6 has been shown to accommodate not only divalent but also monovalent cations as in KB_6, which is also electron-deficient with respect to electron-precise $M^{II}B_6$.[25] Semiconducting KB_6 has been shown to be nonmetallic due to localized spin states.[25,38,39] Similarly, electron-deficient $Li_6B_{18}(Tp)_x$ seems to be stable as well.

Table 1. Site occupancy factors of the atomic positions in $Li_6B_{18}(Tp)_x$ with Tp = Li_3N, Li_2O in comparison with single crystal data of $Li_6B_{18}(Li_2O)_{0.70}$.[21] The total Li content of the template phases is compared with the expected values derived from the $Tp1$ occupancy.

		$Li_{6.35(7)}B_{18}N_{0.94(1)}$	$Li_{6.9(1)}B_{18}O_{0.765(5)}$	$Li_{7.3(2)}B_{18}O_{0.70(1)}$[21]
B1	12*q*	1	1	1
B2	6*i*	1	1	1
*Tp*1	1*a*	0.94(1) N	0.765(5) O	0.70(1) O
Li1	2*c*	1	1	1
Li2	6*l*	0.56(1)	0.489(9)	0.56(2)
Li2b	6*j*	-	0.16(1)	0.22(1)
Li3	1*b*	1	1	0.59(6)
Total Li content		6.35(7)	6.9(1)	7.3(2)
Expected Li content		8.82(3)	7.53(2)	7.4(2)

A closer look at the structure of $Li_6B_{18}(Li_3N)_x$ reveals that, if fully occupied, the contents of the larger pore constitute a structural cutout from the α-Li_3N structure (Figure 5): The coordination sphere of the N atom in $Li_6B_{18}(Li_3N)_x$ is the same as in α-Li_3N and, overall, a $^1_\infty[Li_7N]$ strand fills the large pores of the B framework. Due to the pore size, the Li_7N unit in $Li_6B_{18}(Li_3N)_x$ expands slightly in comparison to α-Li_3N, resulting in larger interatomic Li-Li and Li-N distances (Figure 5).

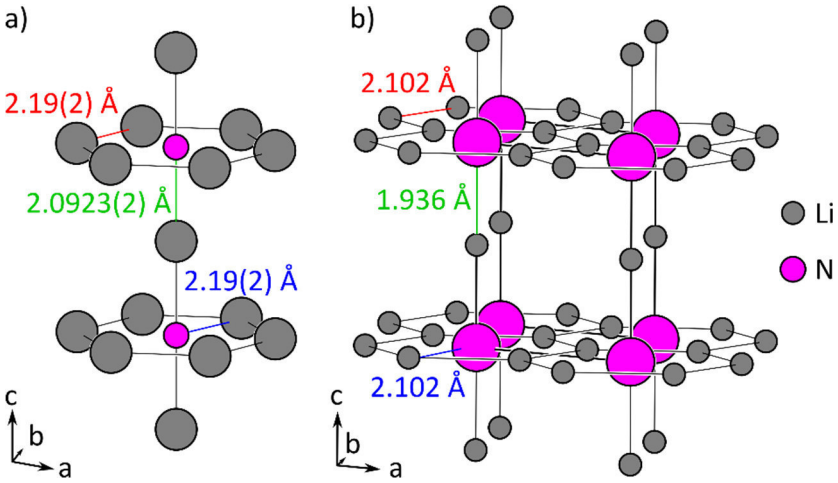

Figure 5. a) Depiction of the formal Li_7N unit inside the large hexagonal pore of $Li_6B_{18}(Li_3N)_x$. b) Structure of α-Li_3N.[40]

α-Li_3N has been shown to be a very efficient Li ion conductor with a room temperature Li-ion conductivity of 10^{-3} Ω^{-1} cm^{-1}.[41] Containing a structural cutout from the α-Li_3N structure with a significant amount of Li vacancies, $Li_6B_{18}(Li_3N)_x$ could also represent a good Li-ion conductor along *c*. Thus, we performed NMR spectroscopy to investigate the mobility of the Li ions.

Investigation of the Li ion mobility via solid state NMR experiments. Crystallographically single-phase $Li_6B_{18}(Tp)_x$ material was synthesized using nano-B as the boron source (Figure S3a). However, due to

its immense surface area, nano-boron (cf. Figure S5) contains significant amounts of impurities. Even without the addition of a template phase, $Li_6B_{18}(Tp)_x$ is obtained quantitatively from this boron precursor (Figure S3b), so that the identity of the template species cannot be controlled with this method. Li_3N, Li_2O, and $LiBH_4$ are candidates for the template species here and could all be present in the sample. Nevertheless, the single-phase material is ideally suited for the investigation of Li ion mobility via NMR spectroscopy.

The ^{11}B MAS NMR spectrum of a $Li_6B_{18}(Tp)_x$ sample prepared from nano-B as the boron source exhibits only one signal at 5.2 ppm with a linewidth of the central transition of 2.6 kHz (Figure S6). The signal is accompanied by a large quadrupolar powder pattern, yielding a sizeable coupling constant C_q of 1.1 MHz. No motional processes, e.g rotational diffusion of the boride-polyeders, which would result in an averaging of the (first order) quadrupolar interaction, are observed.

The temperature-dependent evolution of ^7Li solid-echo NMR spectra is depicted in Figure 6a. Only one signal is visible, which at 300 K is comprised of the central transition and a quadrupolar powder pattern with a coupling constant C_q of 50 kHz. The central transition is only affected by homo- and heteronuclear dipolar interactions. Scaling with the second Legendrian $3\cos^2\beta-1$, the (first order) quadrupolar and dipole interactions should be averaged by any fast motional process of the measured nuclei. Thus, an isotropic diffusional motion of the Li cations would cause a vanishing of the electric field gradient when the corresponding inverse correlation time is greater than the magnitude of the quadrupolar interaction (motional narrowing). In case of anisotropic motion of the Li cations, the effective electric field gradient would not be completely averaged, resulting in a residual quadrupolar powder pattern even if lithium is highly mobile. This can happen, for example, when Lithium moves through defined positions in the crystal lattice by a hopping process.

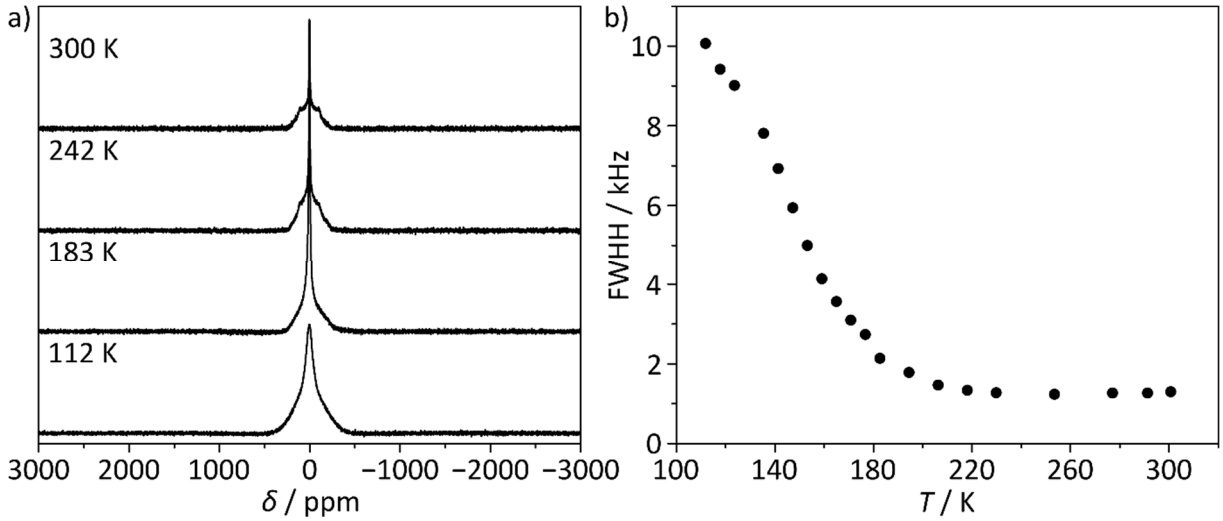

Figure 6. a) Static ^7Li solid-echo spectra of $Li_6B_{18}(Tp)_x$. b) Evolution of the linewidth of the ^7Li central transition in the measured temperature range from 112 K to 300 K.

Cooling the sample down, the linewidth of the ^7Li central transition remains constant at approximately 1 kHz until a temperature of 200 K is reached. Further lowering of the temperature results in an advancing increase of the central transition's linewidth to a value of 10 kHz at 112 K, which is the lowest temperature reached in the conducted measurements. Furthermore, the quadrupolar powder pattern also shows a gradual increase in linewidth between 200 K and 112 K as can be seen in the depicted spectra.

Figure 6b shows the temperature dependent evolution of the linewidth (FWHH) of the static ^{7}Li single-pulse measurements. Again, the linewidth of the central transition remains almost constant between 300 K and 200 K before it starts to increase steadily. Thus, until 200 K the lithium cations are in the so-called "regime of motional narrowing" with the lithium being extremely mobile in the crystal structure. Upon further cooling, a second and final plateau should appear, the "rigid lattice regime", where the linewidth of the ^{7}Li signal remains constant again, reflecting the absence of any fast motional processes. It is remarkable, that this point was not reached in the investigated sample even at 112 K. A rough estimation of the activation energy of the motional process can usually be given employing the empirical Waugh-Fedin relation, $E_A = 0.156 \times T_{onset}$, where T_{onset} represents the temperature where the motional narrowing starts. Since we did not reach the rigid lattice regime experimentally, we can only give an upper limit for the activation energy of 20 kJ/mol.

In addition, the inverse-spin lattice relaxation times of the ^{7}Li-nucleus in the measured temperature range was determined through an inversion-recovery pulse sequence (Figure S7). The T_1-minimum is reached at 195 K. Assuming an Arrhenius behavior of the inverse relaxation time, a linear fit of the low temperature flank results in an activation energy of 5 kJ/mol. The linear low temperature flank of the inverse spin lattice relaxation time is in solids generally biased towards lower activation energies and represents a lower limit for the activation of the dynamic processes.

Thus, we find the activation energy for Li motion in $Li_6B_{18}(Tp)_x$ to be very low between 5 and 20 kJ/mol. Due to the pronounced quadrupolar coupling observed even in room temperature spectra where Li atoms are fully mobile, the Li motion must occur anisotropically. Considering the presence of numerous Li vacancies inside the large pores of the structure, Li hopping across the pores seems feasible. As a great Li-ionic and a poor electric conductor,[22] this open framework phase is thus very promising for solid electrolyte applications.

In addition, ^{1}H spin-echo spectra were recorded with a spinning speed of 10 kHz and under static conditions at room temperature (Figure S8). They clearly prove the presence of H in the $Li_6B_{18}(Tp)_x$ sample, suggesting that H impurities are introduced when using nano-B is used in the synthesis. The static signal is comprised of two components, a broad Gaussian peak at 5.2 ppm comprising 92 % of the signal intensity and a smaller Lorentzian signal at 1 ppm (8 %).

Template extraction from $Li_6B_{18}(Tp)_x$ with ethanol. Von Schnering et al. have reported that the template in $Li_6B_{18}(Tp)_x$ can be removed or substituted by simple washing with water, yielding a dark green product.[21] They observed a retention of the rigid boron framework but did not present additional structural characterization of the resulting material. We have now treated $Li_6B_{18}(Tp)_x$ (prepared using nano-B as the B source) with ethanol instead of water to ensure a more controlled reaction. While the reaction of $Li_6B_{18}(Tp)_x$ with water proceeds very violently, we observed a similar but milder reaction accompanied by slight gas formation and an immediate color change towards a dark green suspension. Washing with ethanol and drying in dynamic vacuum affords an olive green powder consisting of the template phase $Li_6B_{18}(Tp)_x$ next to a novel tetragonal phase with cell parameters a = 11.417(2) Å and c = 5.052(1) Å (Figure S4a).[42] The clear filtrate removed from the green solid was allowed to evaporate in air. PXRD analysis of the remaining white powder shows pure lithium carbonate (Figure S4c), proving that significant amounts of lithium were extracted from $Li_6B_{18}(Tp)_x$.

The tetragonal phase can be removed from the extracted template phase $Li_{6-\delta}B_{18}(Tp)_x$ by overnight treatment with a 1:1 mixture of ethanol and deionized water and subsequent washing and drying. PXRD analysis of the resulting product shows single-phase $Li_{6-\delta}B_{18}(Tp)_x$. The intensity ratio of reflections

(100) and (200) significantly differs from those in $Li_6B_{18}(Li_3N)_x$ and $Li_6B_{18}(Li_2O)_x$ (cf. Figure 2), suggesting more vacancies for the atomic positions located inside the large hexagonal pores. Thus, Rietveld refinements were performed in order to determine the site occupancy factors (Figures 7 and S4b, Tables S1 and S2).

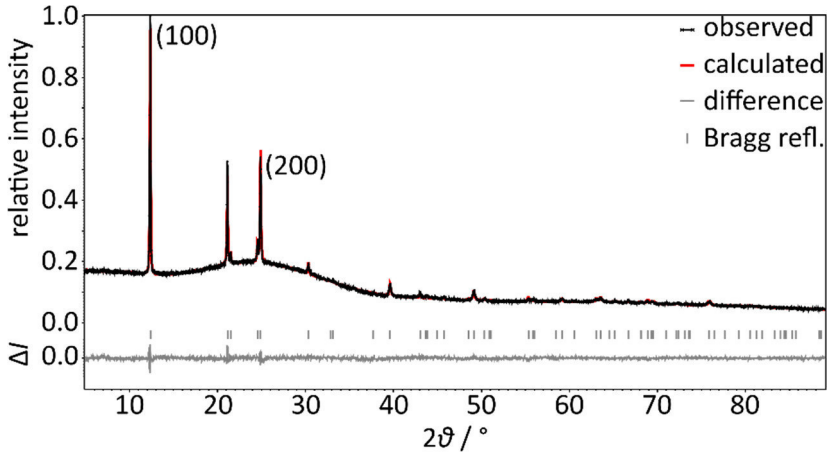

Figure 7. Refined powder X-ray diffraction product of the EtOH extraction product of $Li_6B_{18}(Tp)_x$.

Due to the unclear identity of the template species, we used both N and O as the *Tp* atom in Rietveld refinements (Table 2). Slightly better R values were obtained in case of N as the template species (cf. Table S1). The structure proposed for $Li_6B_{18}(LiBH_4)$ by Wörle did not yield useful results in our refinements of the extracted framework structure.[20] A careful inspection of the site occupancy factors obtained from the Rietveld refinement (Table 2) demonstrates that, as expected, positions *Tp*1 and Li2 are much less occupied than before the extraction experiment. In contrast, position Li3, which is also located inside the large pores, remains fully occupied. In addition, we observe a significant underoccupation of the boron framework position B2, leading to overall sum formulae of $Li_{4.12(8)}B_{17.01(8)}N_{0.42(1)}$ and $Li_{4.00(8)}B_{17.21(5)}O_{0.35(1)}$, respectively. This suggests that the extraction of template atoms is in part compensated by voids or substitutions of the B framework, which help to retain the overall framework structure. The observation of the most likely boron-containing tetragonal phase as a product of the extraction reaction supports this. Again, the number of Li atoms per formula unit is less than expected for an electron-precise compound.

Table 2. Site occupancy factors for extracted $Li_{6-\delta}B_{18}(Tp)_x$ from Rietveld refinements using N or O as the *Tp* atom.

		$\mathbf{Li_{4.12(8)}B_{17.01(8)}N_{0.42(1)}}$	$\mathbf{Li_{4.00(8)}B_{17.21(5)}O_{0.35(1)}}$
B1	12*q*	1	1
B2	6*i*	0.84(1)	0.87(1)
*Tp*1	1*a*	0.42(1) N	0.35(1) O
Li1	2*c*	1	1
Li2	6*l*	0.19(1)	0.17(1)
Li3	1*b*	1	1

The octahedral B frameworks of $Li_6B_{18}(Tp)_x$ as well as Li_2B_6 and MB_6 exhibit distinct Raman bands, which are very characteristic for the respective phases.[21,43] For example, Raman experiments are sensitive to the presence of a di- or trivalent metal in MB_6.[43] In the cubic MB_6 symmetry the three bands correspond to the A_{1g}, E_g, and T_{2g} modes (Figure S9). Figure 8 depicts the Raman spectra of the

$Li_6B_{18}(Tp)_x$ phases investigated in this work. The Raman shifts observed for $Li_6B_{18}(Li_2O)_x$ are similar to those observed by Wörle et al.[21] The Raman bands of extracted $Li_{6-\delta}B_{18}(Tp)_x$ are significantly shifted with respect to the other two phases. Apparently, the extraction of template species with ethanol induces a change in the boron framework. Whether framework atoms are partially substituted or whether a partial oxidation of B occurs is yet to be determined.

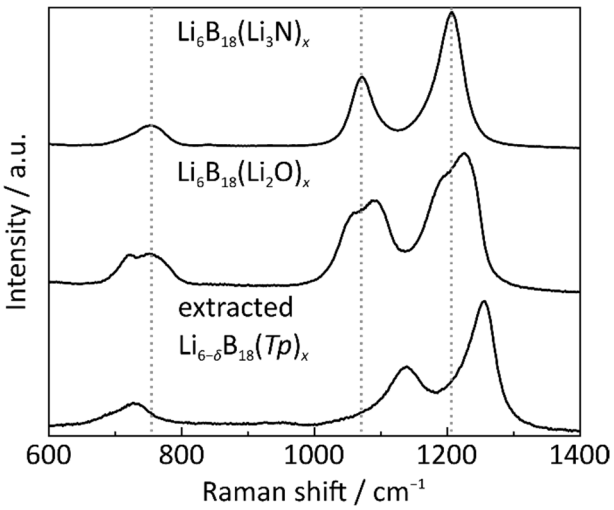

Figure 8. Raman spectra of $Li_6B_{18}(Li_3N)_x$, $Li_6B_{18}(Li_2O)_x$, and extracted $Li_{6-\delta}B_{18}(Tp)_x$. The Raman shifts of $Li_6B_{18}(Li_3N)_x$ are marked by dotted lines to illustrate the large deviations of the extracted phase. Exact Raman shifts are listed in Table S3.

Thermal analysis of extracted $Li_{6-\delta}B_{18}(Tp)_x$ via DSC measurements (Figure S10a) suggest that the phase decomposes to an amorphous product at 459 °C. In contrast, the starting material $Li_6B_{18}(Li_3N)_x$ is stable up to at least 884 °C (Figure S10b).

Electronic structure of $Li_6B_{18}(Li_3N)$. The electronic structure of the open framework structure was determined using the TB-LMTO-ASA program,[32] assuming full occupation of all atomic positions in $Li_6B_{18}(Li_3N)$. Density of states and band structure of $Li_6B_{18}(Li_3N)$ are depicted in Figure 9a and 9b. Conducting and valence bands touch the Fermi level E_F at the A and Γ points, respectively (cf. Figure S11 for a depiction of the Brillouin zone). However, they neither touch each other nor cross E_F. Since local density approximation (LDA) methods tend to underestimate band gaps in solids,[44] we can assume semiconducting behavior.

Interestingly, the top three conducting bands situated between 0 and −1.11 eV correspond only to atoms located inside the large pores of the open framework structure, as shown by a fat-band analysis (Figure 9c). The Li3 and N1 atoms alternate along the *c* direction so that the corresponding Li3(s) and N1(p_z) orbitals mix to form the topmost conduction band. The Li2 atoms surround N1 in the *ab* plane and therefore the corresponding Li2(s), N1(p_x) and N1(p_y) contribute to the following two partially degenerate conduction bands. The boron framework states (and Li1) contribute only to the valence states and the conduction states below −1.15 eV, as is expected for a true host-guest compound. Without the host species in the large hexagonal pores, the open framework structure would possess a direct band gap, rendering the structure type an interesting candidate for optoelectronic applications.

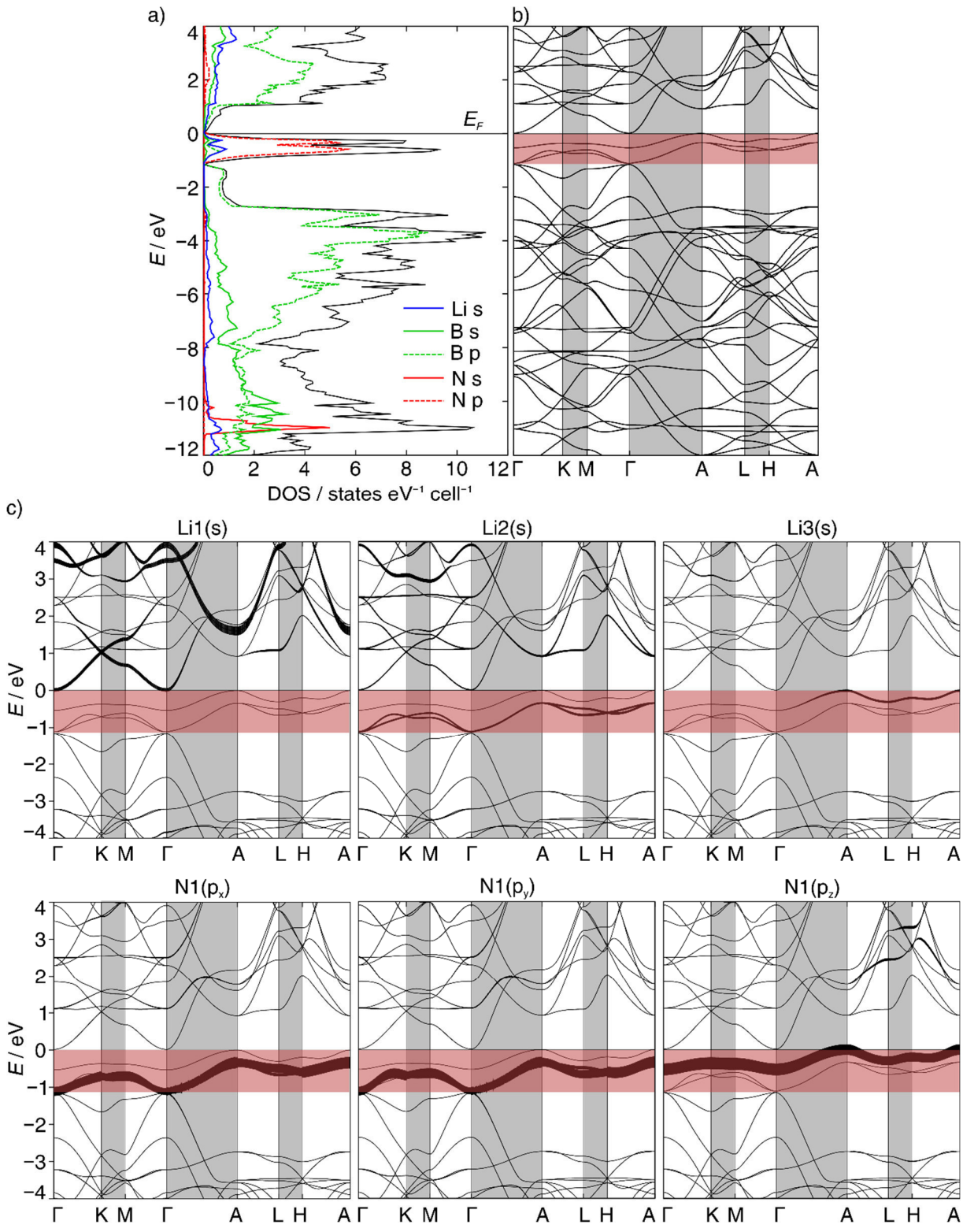

Figure 9. a) Total and partial DOS curves in the range of −12 eV to 4 eV for $Li_6B_{18}(Li_3N)$; b) band structure of $Li_6B_{18}(Li_3N)$ in the range of −12 eV to 4 eV, the bands marked in red correspond to states of the atoms situated in the large pores of the structure; c) band structures including Li(s) and N(p) fat bands in the range of −4 eV to 4 eV for $Li_6B_{18}(Li_3N)$.

Since our extraction experiments have shown that the template species can be at least partially removed by reaction with ethanol, we determined a variety of hexagonal, template-free structures and calculated their electronic structures. For TB-LMTO-ASA calculations we decided to keep the boron framework intact. In addition, atomic positions Li1 and Li3 were maintained because, according to

Rietveld refinement, they remain fully occupied even in the extracted $Li_{6-\delta}B_{18}(Tp)_x$. For the template-free structures, position *Tp*1 was removed completely and the overall symmetry was reduced in order to split Li2 into a fully occupied and an empty position, yielding a sum formula of Li_6B_{18}. Three different symmetry reduction methods were selected to construct three different Li atom configurations inside the large pore of the structure: Symmetry reduction to $P\bar{6}m2$-Li_6B_{18} affords a stacked configuration in which every other Li2 position is occupied, whereas doubling of the *c* axis in $P6_3/mmc$ constructs a staggered Li2 configuration. Additionally, a $P\bar{6}2m$ configuration was considered, in which every other Li2b position is occupied in a stacked fashion. The starting configurations for these electronic structure calculations as well as corresponding structure images are given in the supporting information (Tables S4–S6, Figure S12).

The band structures calculated for the different Li_6B_{18} structures show that removal of the template species alone does not result in true semiconductors. The direct band gap at the Γ point set up by the octahedral boron framework is always filled with Li(s) states corresponding to the Li atoms remaining in the large pores (Figures 10 and S12). Thus, the pores must be completely free of any host species to obtain a true semiconductor without any gap states.

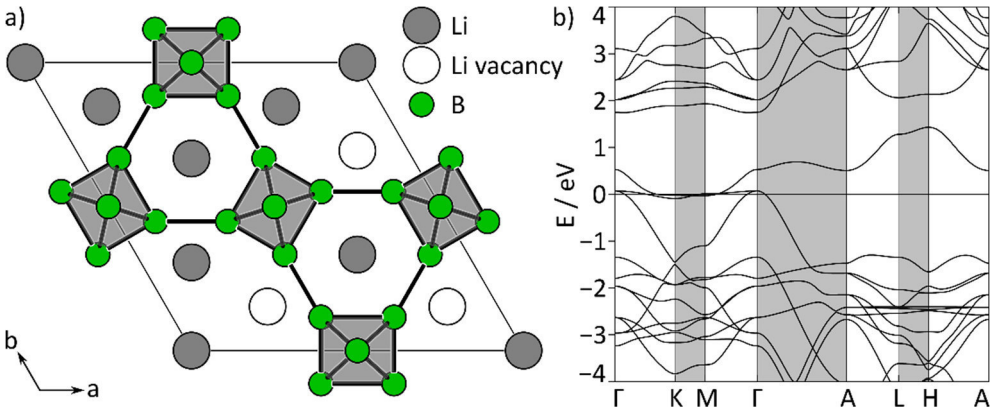

Figure 10. a) Structure of template-free Li_6B_{18} in $P\bar{6}2m$, empty circles represent the void Li2 positions. b) Band structure of $P\bar{6}m2$-Li_6B_{18} in the range of −4 to 4 eV.

Therefore, we used the template structure $Li_6B_{18}(Tp)_x$ as the starting point for the theoretical construction of chemically inspired, semiconducting boron carbide structures.[45] A similar chemically inspired structure investigation has already been performed for the cubic MB_6 structure after isostructural NaB_5C had been found experimentally.[46] In the latter, B and C mix statistically. Ivanovskii and Medvedeva calculated the electronic structures of CaB_6, NaB_5C, and B_4C_2 without specifying their B-C configurations.[47] They find a direct band gap for CaB_6 (0.7 eV), whereas NaB_5C and B_4C_2 exhibit indirect band gaps of 1.63 eV and 1.77 eV, respectively.

To obtain a neutral, electron-precise boron carbide structure with empty pores, the template species and all lithium cations are removed from the $Li_6B_{18}(Tp)_x$ structure. To compensate for the loss of framework electrons donated by lithium, six of the 18 B atoms per formula unit must be replaced by carbon. The tetrel element brings along the additional electrons needed to construct open framework structures $B_{12}C_6$. We have selected three different distributions of boron and carbon in the structure: Substitution of B2 for carbon results in $P6/mmm$-$B_{12}C_6$. Alternatively, substituting two opposite or two adjacent B1 positions yields $P6/m$- and $P\bar{6}2m$-$B_{12}C_6$, respectively. The starting configurations to determine the electronic structures of $B_{12}C_6$ using TB-LMTO-ASA[32] and corresponding structure images are given in the supporting information (Tables S7–S9, Figure S13).

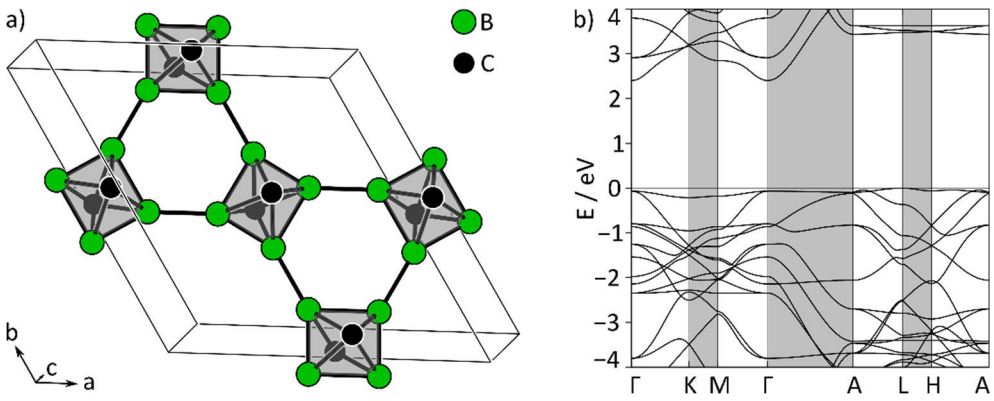

Figure 11. a) Structure of $B_{12}C_6$ in *P*6/*mmm*, empty circles represent the void Li2 positions. b) Band structure of *P*6/*mmm*-$B_{12}C_6$ in the range of −4 to 4 eV.

$B_{12}C_6$ is determined to be a direct band gap semiconductor in all three configurations with band gaps ranging from 2.4 eV (*P*6/*mmm*) to 3.2 eV ($P\bar{6}2m$) (Figures 11 and S13). These calculations, however, do not take into account any changes in geometry, which would most likely be induced by the substitutions of boron with carbon. In order to find the energetically most stable among our and other possible hexagonal $B_{12}C_6$ structures and to assess its stability with respect to the only known boron carbide $B_{12}C_3$,[48] similar calculations should be performed with initial geometry optimization using DFT methods. Due to the large empty pores in $B_{12}C_6$, its synthesis could require a similar template approach as is necessary to synthesize $Li_6B_{18}(Tp)_x$.

Conclusions

The previously known template structure $Li_6B_{18}(Tp)_x$ was shown to also form around Li_3N as the template species. $Li_6B_{18}(Li_3N)_x$ significantly differs from $Li_6B_{18}(Li_2O)_x$ in cell parameters, its dark red color, and the characteristic ratio of (100) and (200) reflections in powder X-ray diffraction patterns. In both compounds, we observe significantly less Li than would be expected from an electron-precise stoichiometry. The large hexagonal pores in $Li_6B_{18}(Li_3N)_x$ contain a cutout strand from the Li_3N structure, resulting in very high Li ion mobility as shown by variable-temperature NMR spectroscopy. The activation energy for Li motion was determined to be between 5 and 20 kJ/mol. Quadrupolar coupling at room temperature suggest that the Li movement occurs anisotropically. Therefore, $Li_6B_{18}(Li_3N)_x$ is an interesting candidate for solid electrolyte applications.

Reaction of $Li_6B_{18}(Tp)_x$ with ethanol allows the controlled extraction of template species from the large hexagonal pores. The resulting green phase is characterized by a reduced occupation of in-pore positions as well as B2. Significant shifts in the Raman spectra suggest a change in the boron framework induced by the extraction reaction.

Electronic structure calculations of fully occupied $Li_6B_{18}(Li_3N)$ demonstrate that it is a typical host-guest compound, in which the host framework sets up a direct band gap which is filled by the guest species inside the large pore. Removal of only the template Li_3N in Li_6B_{18} structures do not yield energy bands typical for a semiconductor because the remaining Li atoms inside the large pores still generate in-gap bands. The chemically inspired construction of $B_{12}C_6$ structures with completely empty pores, however, leads to semiconductors with large direct band gaps of 2.4–3.2 eV, depending on the exact structural configuration.

Associated Content

Supporting Information. Rietveld refinement data of all investigated $Li_6B_{18}(Tp)_x$ phases (Tables S1, S2) and refined PXRD patterns of $Li_6B_{18}(Li_3N)_x$ and $Li_6B_{18}(Li_2O)_x$ (Figures S1, S2); PXRD patterns of $Li_6B_{18}(Tp)_x$ prepared from nano-B (Figure S3), of extraction products $Li_{6-\delta}B_{18}(Tp)_x$, and the evaporated filtrate (Figure S4); TEM micrographs and SAED pattern of nano-B (Figure S5); ^{11}B and ^{1}H NMR spectra and the temperature-dependency of ^{7}Li spin lattice relaxation time (Figures S6–S8); Raman modes and shifts of $Li_6B_{18}(Tp)_x$ (Figure S9, Table S3); DSC curves of $Li_6B_{18}(Li_3N)_x$ and $Li_{6-\delta}B_{18}(Tp)_x$ (Figure S10); Brillouin zone of hexagonal space groups (Figure S11); structural data of Li_6B_{18} and $B_{12}C_6$ for electronic structure calculations (Tables S4–S9); structural images and band structures of Li_6B_{18} and $B_{12}C_6$ (Figures S12, S13).

Author Information

Corresponding Author. * E-mail: Thomas.Faessler@lrz.tum.de

Notes. The authors declare no competing financial interest.

Acknowledgments

The authors thank Sebastian Geier for measuring the Raman spectra. L.M.S. thanks Technische Universität München for financial support through the Laura Bassi-Prize as well as Fonds der Chemischen Industrie and Studienstiftung des deutschen Volkes for her fellowships.

References

[1] A. Patil, V. Patil, D. Wook Shin, J.-W. Choi, D.-S. Paik, S.-J. Yoon, *Mater. Res. Bull.*, *43*, 1913–1942.
[2] J. G. Kim, B. Son, S. Mukherjee, N. Schuppert, A. Bates, O. Kwon, M. J. Choi, H. Y. Chung, S. Park, *J. Power Sources* **2015**, *282*, 299–322.
[3] N. A. Anurova, V. A. Blatov, G. D. Ilyushin, O. A. Blatova, A. K. Ivanov-Schitz, L. N. Dem'yanets, *Solid State Ionics* **2008**, *179*, 2248–2254.
[4] U. von Alpen, A. Rabenau, G. H. Talat, *Appl. Phys. Lett.* **1977**, *30*, 621–623.
[5] T. Lapp, S. Skaarup, A. Hooper, *Solid State Ionics* **1983**, *11*, 97–103.
[6] P. E. Stallworth, J. J. Fontanella, M. C. Wintersgill, C. D. Scheidler, J. J. Immel, S. G. Greenbaum, A. S. Gozdz, *J. Power Sources* **1999**, *81–82*, 739-747.
[7] P. G. Bruce, A. R. West, *J. Electrochem. Soc.* **1983**, *130*, 662–669.
[8] H. Y. P. Hong, *Mater. Res. Bull.* **1978**, *13*, 117–124.
[9] R. Kanno, M. Murayama *J. Electrochem. Soc.* **2001**, *148*, A742–A746.
[10] M. Murayama, R. Kanno, M. Irie, S. Ito, T. Hata, N. Sonoyama, Y. Kawamoto, *J. Solid State Chem.* **2002**, *168*, 140–148.
[11] N. Kamaya, K. Homma, Y. Yamakawa, M. Hirayama, R. Kanno, M. Yonemura, T. Kamiyama, Y. Kato, S. Hama, K. Kawamoto, A. Mitsui, *Nat. Mater.* **2011**, *10*, 682–686.
[12] A. Kuhn, O. Gerbig, C. Zhu, F. Falkenberg, J. Maier, B. V. Lotsch, *Phys. Chem. Chem. Phys.* **2014**, *16*, 14669–14674.
[13] H. Wada, M. Menetrier, A. Levasseur, P. Hagenmuller, *Mater. Res. Bull.* **1983**, *18*, 189–193.
[14] M. Menetrier, A. Hojjaji, C. Estournes, A. Levasseur, *Solid State Ionics* **1991**, *48*, 325–330.
[15] M. Ménétrier, C. Estournès, A. Levasseur, K. J. Rao, *Solid State Ionics* **1992**, *53*, 1208–1213.
[16] S. Sahami, S. W. Shea, J. H. Kennedy, *J. Electrochem. Soc.* **1985**, *132*, 985–986.

[17] J. P. Malugani, G. Robert, *Solid State Ionics* **1980**, *1*, 519–523.
[18] M. Zeilinger, L. van Wüllen, D. Benson, V. F. Kranak, S. Konar, T. F. Fässler, U. Häussermann, *Angew. Chem. Int. Ed.* **2013**, *52*, 5978–5982.
[19] G. Mair, Dissertation, Universität Stuttgart **1984**.
[20] M. Wörle, Dissertation, ETH Zürich **1995**.
[21] M. Wörle, R. Nesper, G. Mair, H. G. von Schnering, *Solid State Sci.* **2007**, *9*, 459–464.
[22] M. Panda, Dissertation, Universität Hamburg **2006**.
[23] G. Mair, H. G. von Schnering, M. Wörle, R. Nesper, *Z. Anorg. Allg. Chem.* **1999**, *625*, 1207–1211.
[24] M. von Stackelberg, F. Neumann, *Z. Phys. Chem., Abt. B* **1932**, *19*, 314–320.
[25] R. Naslain, J. Étourneau, *C. R. Seances Acad. Sci., Ser. C* **1966**, *263*, 484–487.
[26] H. Moissan, P. Williams, *C. R. Hebd. Seances Acad. Sci.* **1897**, *125*, 629–634.
[27] T. Kasuya, *Europhys. Lett.* **1994**, *26*, 283–287.
[28] P. G. Perkins, D. R. Armstrong, A. Breeze, *J. Phys. C: Solid State Phys.* **1975**, *8*, 3558–3570.
[29] P. G. Perkins, A. V. J. Sweeney, *J. Less-Common Met.* **1976**, *47*, 165–173.
[30] V. Petříček, M. Dušek, L. Palatinus, *Z. Kristallogr. - Cryst. Mater.* **2014**, *229*, 345–352.
[31] *PROTEUS Thermal Analysis V4.8.2*, Netzsch-Gerätebau GmbH, Selb, **2006**.
[32] *The Stuttgart Tight-Binding LMTO-ASA program*, M. v. Schilfgarde, T. A. Paxton, O. Jepsen, O. K. Andersen, G. Krier, Max-Planck-Institut für Festkörperforschung, Stuttgart, Germany, **1998**.
[33] U. von Barth, L. Hedin, *J. Phys. C: Solid State Phys.* **1972**, *5*, 1629–1642.
[34] O. Jepsen, O. K. Andersen, *Z. Phys. B: Condens. Matter* **1995**, *97*, 35–47.
[35] O. Andersen, O. Jepsen, *Phys. Rev. Lett.* **1984**, *53*, 2571–2574.
[36] E. Zintl, G. Brauer, *Z. Elektrochem. Angew. Phys. Chem.* **1935**, *41*, 102–107.
[37] To ensure that the absence of Li2b in $Li_6B_{18}(Li_3N)_x$ is not an artefact, we performed a Rietveld refinement with O as the *Tp* atom. In this refinement, Li2b was not observed either.
[38] A. Ammar, M. Ménétrier, A. Villesuzanne, S. Matar, B. Chevalier, J. Etourneau, G. Villeneuve, J. Rodríguez-Carvajal, H. J. Koo, A. I. Smirnov, M. H. Whangbo, *Inorg. Chem.* **2004**, *43*, 4974–4987.
[39] J. Etourneau, A. Ammar, A. Villesuzanne, G. Villeneuve, B. Chevalier, M. H. Whangbo, *Inorg. Chem.* **2003**, *42*, 4242–4244.
[40] H. Schulz, K. Schwarz, *Acta Crystallogr. Sect. A* **1978**, *34*, 999–1005.
[41] U. von Alpen, *J. Solid State Chem.* **1979**, *29*, 379–392.
[42] Elemental analysis suggests the sum formula $LiBC_8H_{20}O_4$, consistent with lithium tetraethoxyborate. Its structure will be published elsewhere.
[43] N. Ogita, S. Nagai, N. Okamoto, F. Iga, S. Kunii, T. Akamtsu, J. Akimitsu, M. Udagawa, *J. Solid State Chem.* **2004**, *177*, 461–465.
[44] J. P. Perdew, *Int. J. Quantum Chem.* **1985**, *28*, 497–523.
[45] L.-A. Jantke, S. Stegmaier, A. J. Karttunen, T. F. Fässler, *Chem. Eur. J.* **2016**, DOI: 10.1002/chem.201603406.
[46] B. Albert, K. Schmitt, *Chem. Commun.* **1998**, 2373–2374.
[47] A. L. Ivanovskii, S. V. Okatov, *Mendeleev Commun.* **2001**, *11*, 8–10.
[48] M. M. Balakrishnarajan, P. D. Pancharatna, R. Hoffmann, *New J. Chem.* **2007**, *31*, 473-485.

SUPPORTING INFORMATION

Table S1. Crystallographic data of template phases $Li_6B_{18}(Tp)_x$ obtained from powder diffraction data by Rietveld refinement.

	1	**2**	**3**[a]	
Empirical formula	$Li_{6.35(7)}B_{18}N_{0.94(1)}$[b]	$Li_{6.9(1)}B_{18}O_{0.765(5)}$[c]	$Li_{4.12(8)}B_{17.01(8)}N_{0.42(1)}$	$Li_{4.00(8)}B_{17.21(5)}O_{0.35(1)}$
M_r / g mol^{-1}	251.8	254.6	218.4	219.4
T / K	293			
Powder color	dark red	orange	green	
Crystal system	hexagonal			
Space Group	*P*6/*mmm*			
Cell parameters				
a / Å	8.2735(7)	8.2237(6)	8.2603(1)	
c / Å	4.1846(3)	4.1520(3)	4.2046(1)	
V / Å^3	248.06(3)	243.18(3)	248.458(8)	
Z	1			
$d_{calcd.}$ / g cm^{-3}	1.686	1.739	1.459	1.4664
μ(Cu-K_α) / mm^{-1}	0.351	0.387	0.297	0.313
Θ range / °	5.01–89.02	5.00–89.02	4.98–89.00	
R [$I > 3\sigma(I)$]	0.0870	0.0532	0.0501	0.0647
wR [$I > 3\sigma(I)$]	0.0893	0.0622	0.0368	0.0450
R (all)	0.0896	0.0553	0.0745	0.0792
wR (all)	0.0895	0.0624	0.0405	0.0474
Goodness of fit	2.71	2.25	0.95	0.95

[a] Two different Rietveld refinements were performed of sample **3** using N and O as the *Tp* species, respectively.

[b] Sample contains 31(5) % LiB.

[c] Sample contains 9(4) % LiB and 2.0(2) % Li_2B_6.

Table S2. Atomic coordinates, isotropic displacement parameters / Å², and site occupancy factors (*s.o.f.*) for template phases $Li_6B_{18}(Tp)_x$ obtained from powder diffraction data by Rietveld refinement.

			x	***y***	***z***	U_{iso}	***s.o.f.***
B1	12*q*	$Li_{6.35(7)}B_{18}N_{0.94(1)}$	0.4478(4)	0.1152(4)	0.5	0.014(1)	1
		$Li_{6.9(1)}B_{18}O_{0.765(5)}$	0.4478(2)	0.1179(2)	0.5	0.0205(7)	1
		$Li_{4.12(8)}B_{17.01(8)}N_{0.42(1)}$	0.4499(4)	0.1139(5)	0.5	0.009	1
		$Li_{4.00(8)}B_{17.21(5)}O_{0.35(1)}$	0.4505(4)	0.1140(5)	0.5	0.009	1
B2	6*i*	$Li_{6.35(7)}B_{18}N_{0.94(1)}$	0.5	0	0.798(1)	0.014	1
		$Li_{6.9(1)}B_{18}O_{0.765(5)}$	0.5	0	0.8010(6)	0.0130(9)	1
		$Li_{4.12(8)}B_{17.01(8)}N_{0.42(1)}$	0.5	0	0.803(2)	0.009	0.84(1)
		$Li_{4.00(8)}B_{17.21(5)}O_{0.35(1)}$	0.5	0	0.800(2)	0.009	0.868(9)
*Tp*1	1*a*	$Li_{6.35(7)}B_{18}N_{0.94(1)}$	0	0	0	0.076(3)	0.94(1) N
		$Li_{6.9(1)}B_{18}O_{0.765(5)}$	0	0	0	0.041(1)	0.765(5) O
		$Li_{4.12(8)}B_{17.01(8)}N_{0.42(1)}$	0	0	0	0.061	0.42(1) N
		$Li_{4.00(8)}B_{17.21(5)}O_{0.35(1)}$	0	0	0	0.061	0.35(1) O
Li1	2*c*	$Li_{6.35(7)}B_{18}N_{0.94(1)}$	1/3	2/3	0	0.076	1
		$Li_{6.9(1)}B_{18}O_{0.765(5)}$	1/3	2/3	0	0.041	1
		$Li_{4.12(8)}B_{17.01(8)}N_{0.42(1)}$	1/3	2/3	0	0.061	1
		$Li_{4.00(8)}B_{17.21(5)}O_{0.35(1)}$	1/3	2/3	0	0.061	1
Li2	6*l*	$Li_{6.35(7)}B_{18}N_{0.94(1)}$	0.1527(9)	0.3055	0	0.076	0.56(1)
		$Li_{6.9(1)}B_{18}O_{0.765(5)}$	0.152(1)	0.304	0	0.041	0.489(9)
		$Li_{4.12(8)}B_{17.01(8)}N_{0.42(1)}$	0.138(3)	0.277	0	0.061	0.19(1)
		$Li_{4.00(8)}B_{17.21(5)}O_{0.35(1)}$	0.134(3)	0.267	0	0.061	0.17(1)
Li2b	6*j*	$Li_{6.35(7)}B_{18}N_{0.94(1)}$	-	-	-	-	-
		$Li_{6.9(1)}B_{18}O_{0.765(5)}$	0.247(5)	0	0	0.041	0.16(1)
		$Li_{4.12(8)}B_{17.01(8)}N_{0.42(1)}$	-	-	-	-	-
		$Li_{4.00(8)}B_{17.21(5)}O_{0.35(1)}$	-	-	-	-	-
Li3	1*b*	$Li_{6.35(7)}B_{18}N_{0.94(1)}$	0	0	0.5	0.076	1
		$Li_{6.9(1)}B_{18}O_{0.765(5)}$	0	0	0.5	0.041	1
		$Li_{4.12(8)}B_{17.01(8)}N_{0.42(1)}$	0	0	0.5	0.061	1
		$Li_{4.00(8)}B_{17.21(5)}O_{0.35(1)}$	0	0	0.5	0.061	1

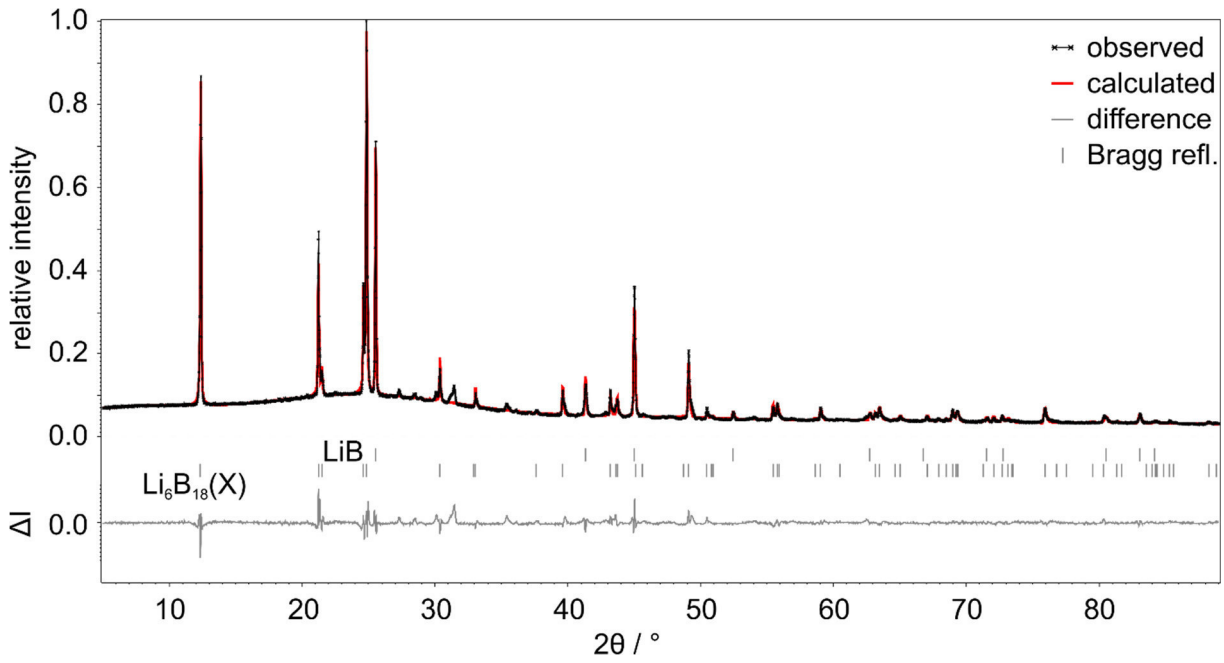

Figure S1. Refined powder X-ray diffraction pattern of $Li_{6.35(7)}B_{18}N_{0.94(1)}$.

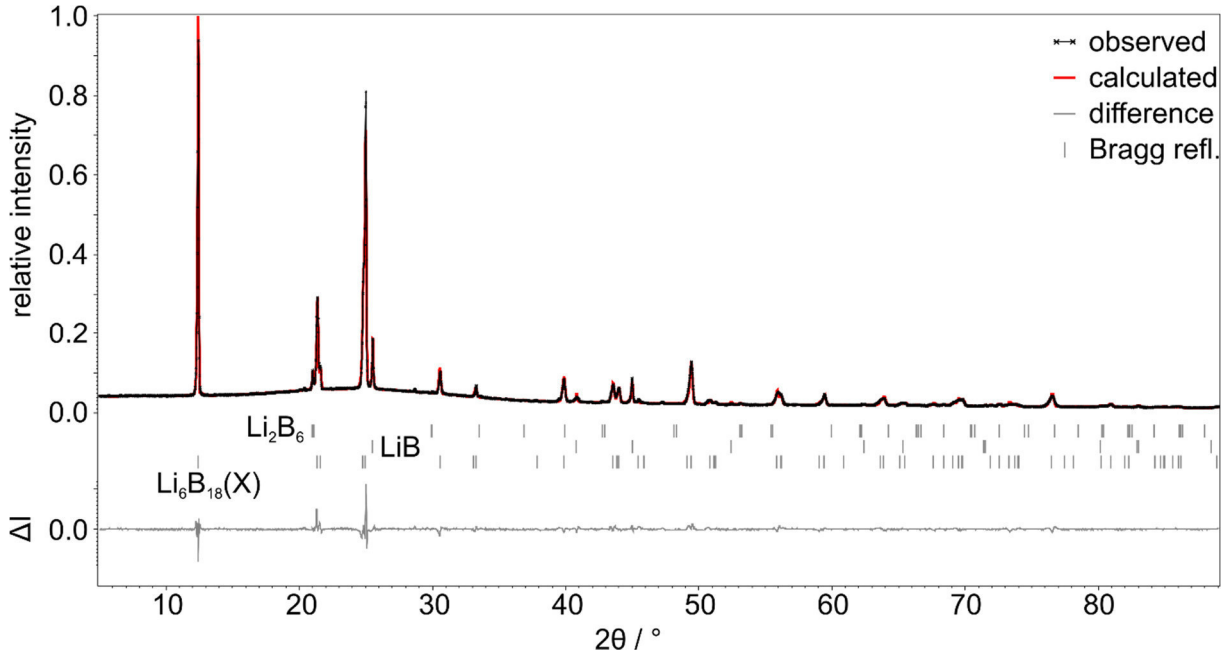

Figure S2. Refined powder X-ray diffraction pattern of $Li_{6.9(1)}B_{18}O_{0.765(5)}$.

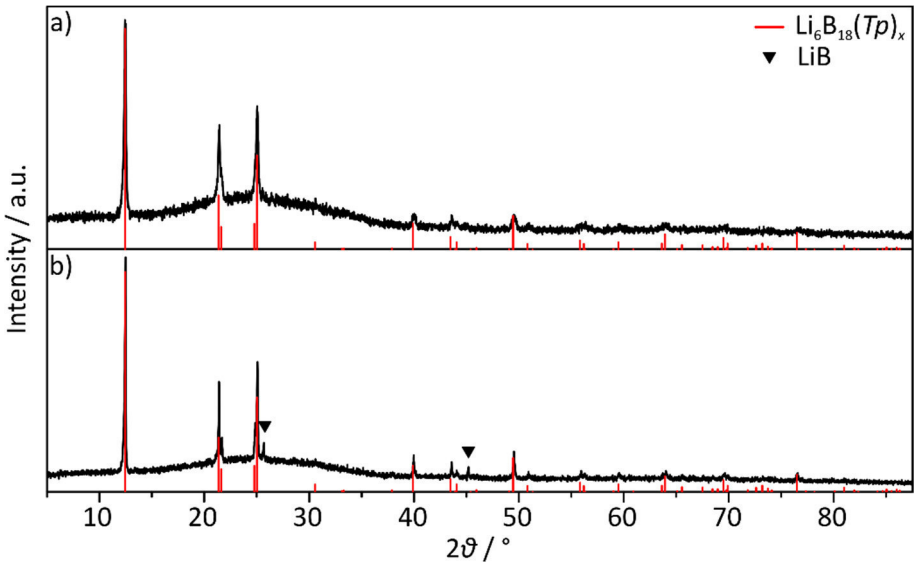

Figure S3. Experimental powder X-ray diffraction patterns of a) the product of the reaction 8 Li + 18 nano-B + Li_3N at 900 °C, b) the product of the reaction 8 Li + 18 nano-B without template species at 900 °C.

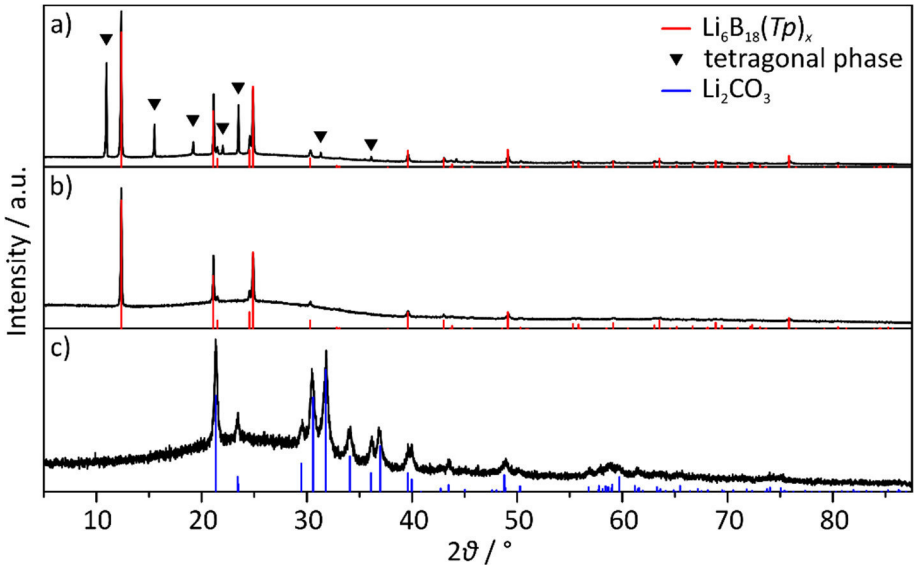

Figure S4. Experimental powder X-ray diffraction patterns of a) the reaction product of the extraction of $Li_6B_{18}(Tp)_x$ with ethanol, b) the extraction product after treatment with deionized water, c) the solid obtained by evaporating the clear ethanol solution separated from the solid reaction product.

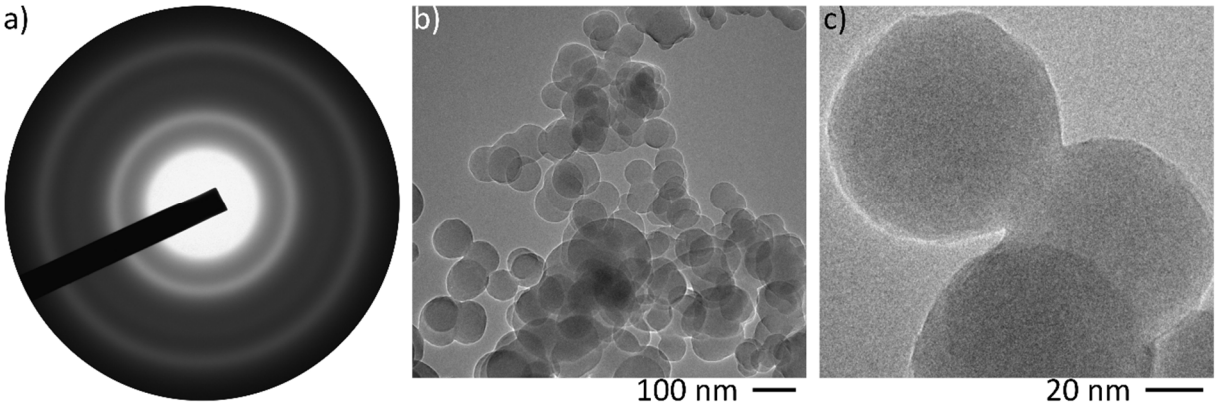

Figure S5. a) Selected area electron diffraction (SAED) pattern, b) transmission electron micrograph, and c) high resolution micrograph of nano-boron. EDX measurements yield the following composition: 97.97 % B, 1.07 % C, 0.60 % N, 0.31 % O.

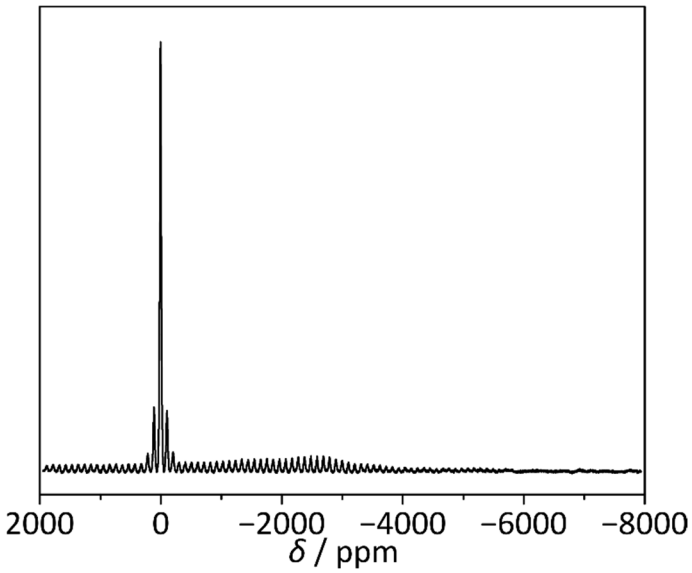

Figure S6. ^{11}B single-pulse MAS NMR spectrum of $Li_6B_{18}(Tp)_x$, recorded at room temperature. The spectrum contains one signal and its rotational side bands.

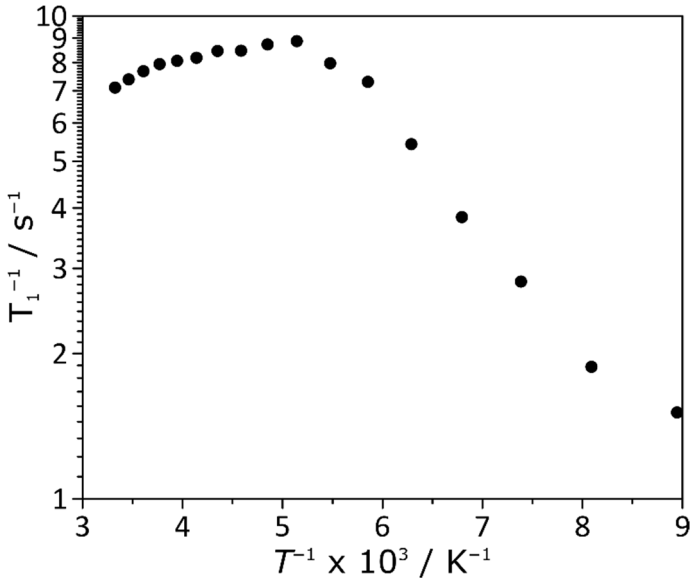

Figure S7. Evolution of the inverse ^{7}Li spin lattice relaxation time as a function of the inverse temperature.

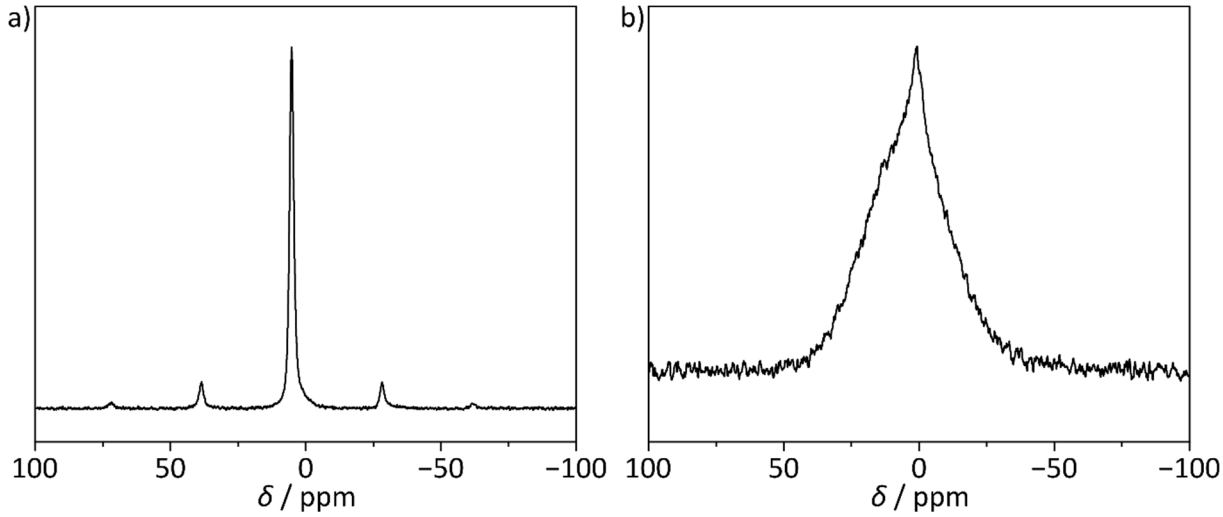

Figure S8. a) Room temperature ^{1}H spin-echo spectrum recorded at 10 kHz spinning speed. b) Static ^{1}H spin-echo spectrum recorded at room temperature.

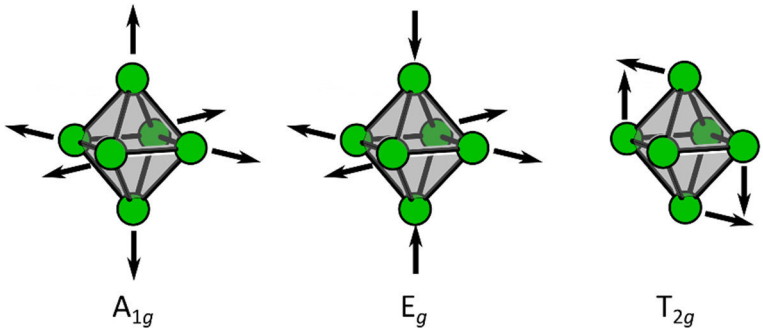

Figure S9. Raman modes in cubic MB_6.[1]

Table S3. Raman shifts of the examined $Li_6B_{18}(Tp)_x$ in comparison with those of Li_2B_6 and CaB_6. The bands are assigned to the Raman modes of cubic MB_6 (cf. Figure S9).

	$Li_6B_{18}(Li_3N)_x$	$Li_6B_{18}(Li_2O)_x$	$Li_{6-\delta}B_{18}(Tp)_x$	Li_2B_6	CaB_6[2]
A_{1g}	1206	1225	1255	1206	1270
E_g	1072	1091	1138	1074	1154
T_{2g}	754	752/723	730	791/727	775

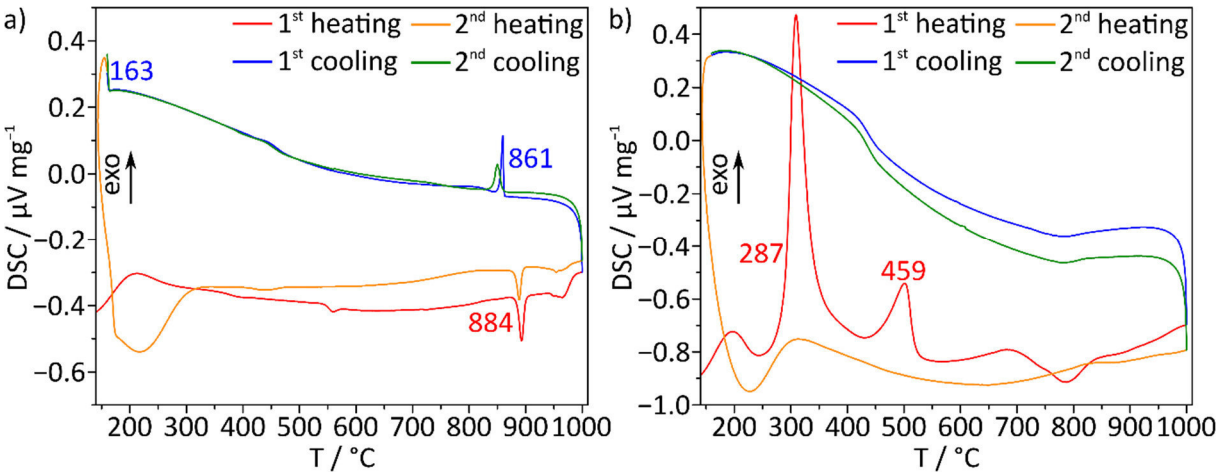

Figure S10. DSC curves of a) $Li_6B_{18}(Li_3N)_x$ and b) extracted $Li_{6-\delta}B_{18}(Tp)_x$ before treatment with H_2O; two measurement cycles were performed using heating/cooling rates of 10 °C min^{-1}. In a) the signal at 163 °C corresponds to solidification of elemental Li. The signals at 884/861 °C may be assigned to the reversible decomposition and formation of LiB.[3] Thermal analysis in combination with PXRD measurements of the products shows that the exothermic signal at 287 °C in b) corresponds to the decomposition of the tetragonal side phase, whereas 459 °C can be assigned to the decomposition of extracted $Li_{6-\delta}B_{18}(Tp)_x$.

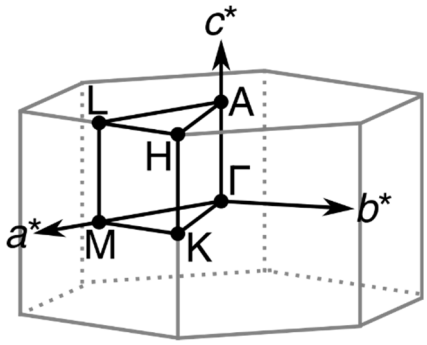

Figure S11. Brillouin zone for $Li_6B_{18}(Li_3N)$ in *P6/mmm* and related hexagonal space groups, showing symmetry points in the *k* space with respect to the reciprocal conventional vectors.

Table S4. Structure parameters for the electronic structure calculations of Li_6B_{18} in $P\bar{6}m2$ (a = 8.2709 Å, c = 4.1832 Å).

	x	*y*	*z*
B1_1	0.4478	0.1152	0
B1_2	−0.4478	−0.1152	0
B2	0.5	0	0.2981
Li1_1	1/3	2/3	-0.5
Li1_2	2/3	−2/3	0.5
Li2	0.1527	0.3055	−0.5
Li3	0	0	0

Table S5. Structure parameters for the electronic structure calculations of Li_6B_{18} in $P6_3/mmc$ (a = 8.2709 Å, c = 8.3664 Å).

	x	*y*	*z*
B1	0.4478	0.1152	0
B2	0.5	0	0.1491
Li1_1	1/3	2/3	0.75
Li1_2	1/3	2/3	0.25
Li2	0.1527	0.3055	0.75
Li3	0	0	0

Table S6. Structure parameters for the electronic structure calculations of Li_6B_{18} in $P\bar{6}2m$ (a = 8.2709 Å, c = 4.1832 Å).

	x	*y*	*z*
B1_1	0.4478	0.1152	0.5
B1_2	0.4478	0.3326	0.5
B2	0.5	0	0.7981
Li1	1/3	2/3	0
Li2	0.2420	0	0
Li3	0	0	0.5

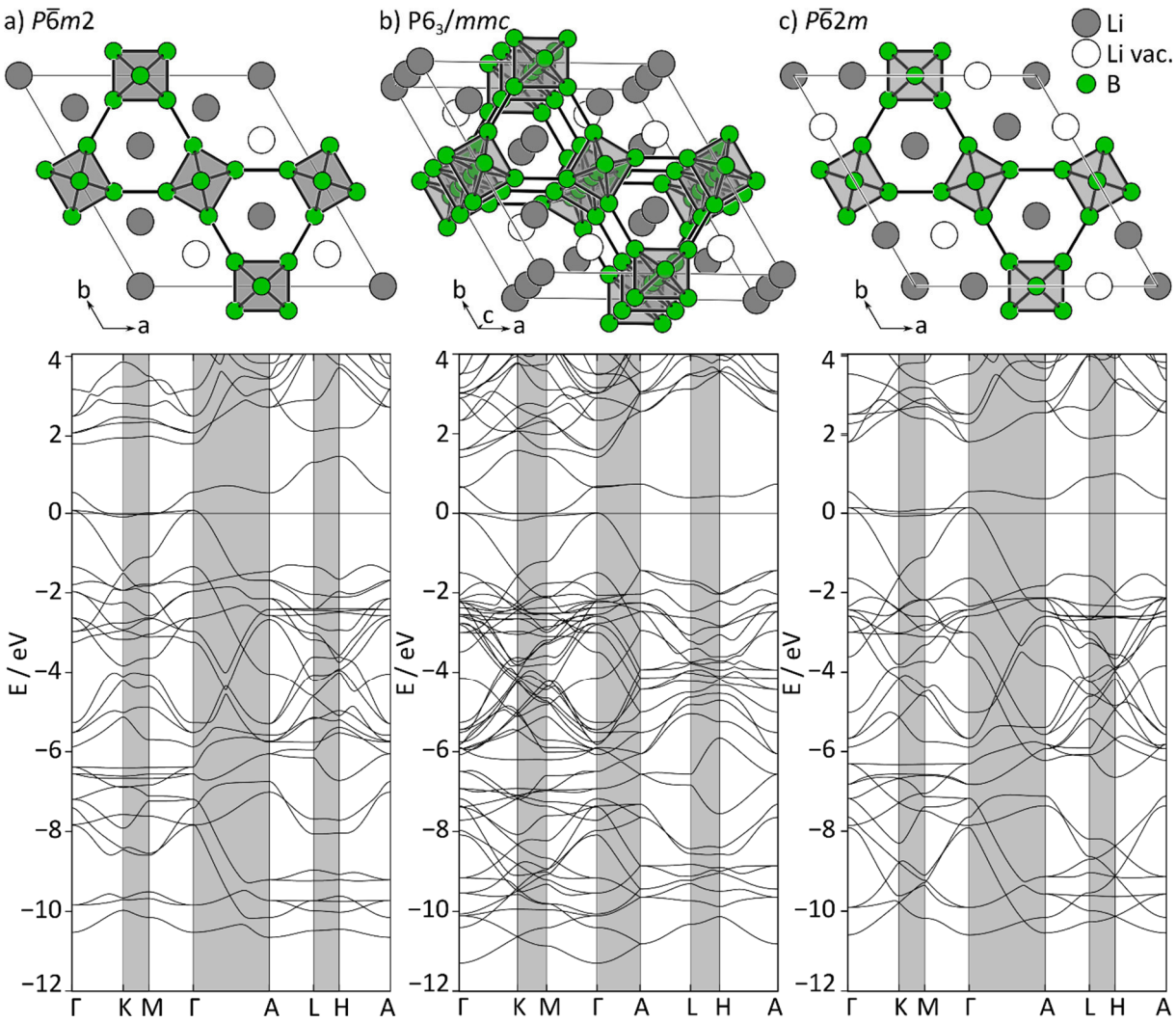

Figure S12. Structures of Li_6B_{18} in a) $P\bar{6}2m$, b) $P6_3/mmc$, and c) $P\bar{6}m2$ and the respective band structures. Void Li positions are marked by empty circles.

Table S7. Structure parameters for the electronic structure calculations of $B_{12}C_6$ in $P6/mmm$ (a = 8.2709 Å, c = 4.1832 Å).

	x	*y*	*z*
B1	0.4478	0.1152	0.5
C1	0.5	0	0.7981

Table S8. Structure parameters for the electronic structure calculations of $B_{12}C_6$ in $P6/m$ (a = 8.2709 Å, c = 4.1832 Å).

	x	*y*	*z*
B1	0.4478	0.1152	0.5
B2	0.5	0	0.7981
C1	0.4478	0.3326	0.5

Table S9. Structure parameters for the electronic structure calculations of $B_{12}C_6$ in $P\bar{6}2m$ (a = 8.2709 Å, c = 4.1832 Å).

	x	*y*	*z*
B1	0.4478	0.1152	0.5
B2	0.5	0	0.7981
C1	0.4478	0.3326	0.5

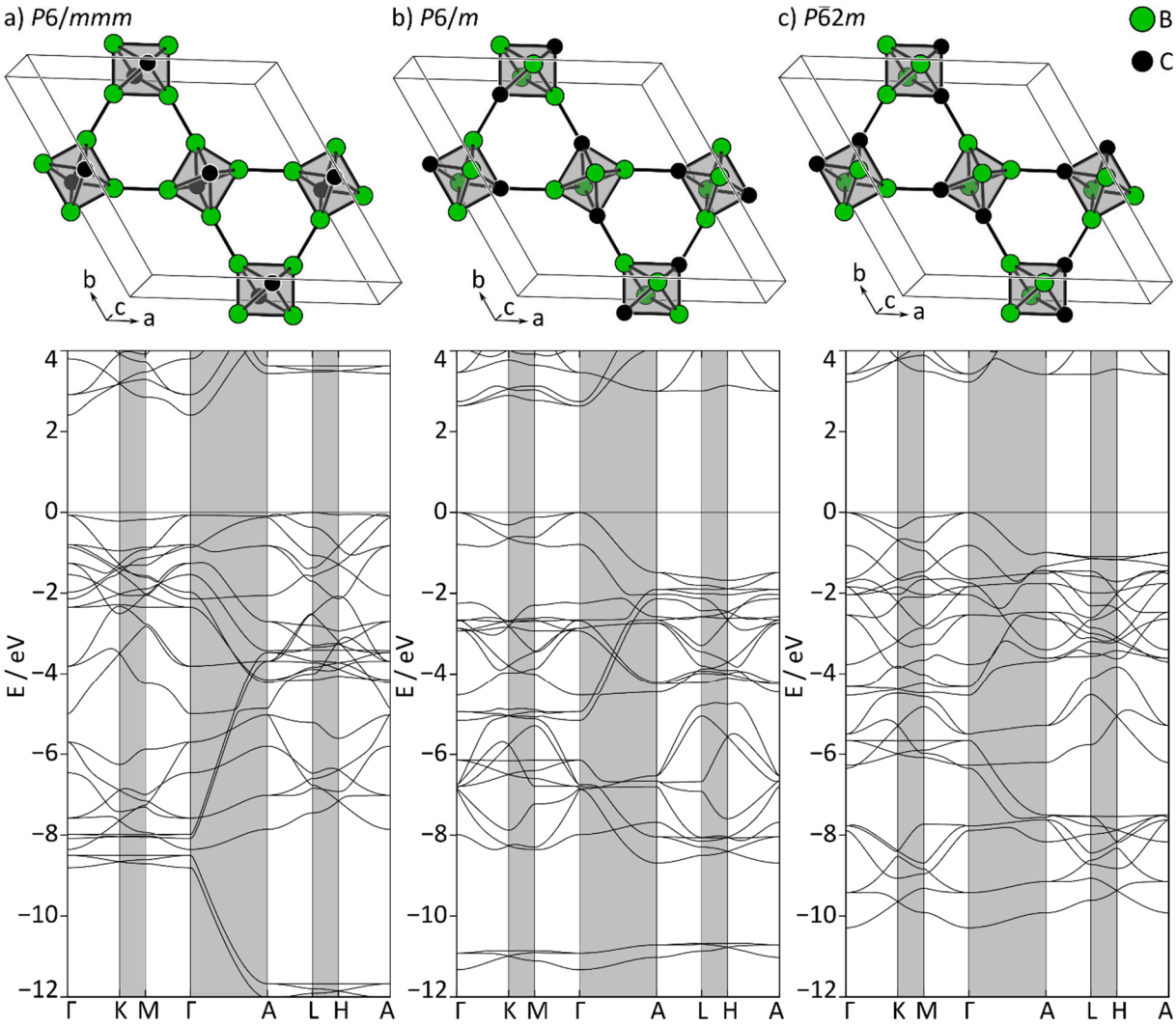

Figure S13. Structures of $B_{12}C_6$ in a) *P*6/*mmm*, b) *P*6/*m*, and c) $P\bar{6}2m$ and the respective band structures.

References

[1] N. Ogita, S. Nagai, N. Okamoto, F. Iga, S. Kunii, T. Akamtsu, J. Akimitsu, M. Udagawa, *J. Solid State Chem.* **2004**, *177*, 461–465.
[2] Z. Yahia, S. Turrell, G. Turrell, J. P. Mercurio, *J. Mol. Struct.* **1990**, *224*, 303–312.
[3] M. Wörle, R. Nesper, G. Mair, H. G. von Schnering, *Solid State Sci.* **2007**, *9*, 459–464.

5.6 A Novel Binary Li-C Phase Obtained from Lithium Flux Synthesis

Lavinia M. Scherf, Gabriele Raudaschl-Sieber, Ulrich Häussermann, Thomas F. Fässler*, *manuscript for publication.*

Abstract

Using the lithium flux technique, we have discovered a novel binary lithium carbide from fullerene C_{60} as a reactive carbon source. The new compound crystallizes in space group *P*2/*m* with cell parameters *a* = 8.298(2) Å, *b* = 6.327(3) Å, *c* = 10.424(3) Å, *β* = 109.33(1)°, and *V* = 516.4(3) Å^3. The diffusion-controlled reaction does not afford any single crystals suitable for structure determination by X-ray diffraction. Thus, the structure is yet to be solved from powder diffraction patterns. Elemental analysis suggests a composition of approximately LiC_2 or carbon-richer. From Raman and NMR spectroscopy, we deduce the presence of carbon polyanions containing conjugated double bonds or fused aromatic rings, which could represent fragments of the C_{60} structure. Decomposition of LiC_x with ethanol yields an amorphous, reddish brown solid, supporting our hypothesis of at least medium-sized carbon polyanions. If structural investigations can confirm this, LiC_x would open up a completely new class of binary metal carbides. At 710 °C, LiC_x decomposes quantitatively to the acetylide Li_2C_2, but slower decomposition at lower temperatures demonstrates that the compound is metastable.

Introduction

Binary metal carbides of the alkali and alkaline earth metals generally form salt-like structures consisting of the respective metal cations and carbon anions. To date, only very small or very large carbon anions were found to exist. The simplest carbon anion, the isolated methanide C^{4-} occurs in Be_2C,[1] Al_4C_3,[2] and Mg_2C, which was reported recently.[3] Alkali and alkaline earth metal acetylides A_2C_2[4-6] and EC_2[7-10] contain dimeric $[C{\equiv}C]^{2-}$ and represent the most frequent class of metal carbides. Triatomic allenide anions $[C{=}C{=}C]^{4-}$ were reported in Li_4C_3[11,12] and Mg_2C_3.[13,14] Most of the mentioned carbides can be synthesized in a reaction of the metal with graphite or with a gaseous hydrocarbon at elevated temperatures. Contrastingly, Li_4C_3 has only been obtained by reaction of propyne with *n*-butyllithium in solution.[11]

Due to their interesting properties, binary carbides containing large carbon polyanions such as graphite intercalation compounds and alkali metal fullerides have been investigated very thoroughly.[15] Alkali metal cations can reversibly intercalate in between the graphene sheets of graphite, forming stable compounds such as LiC_6, LiC_{12},[16] and superconducting AC_8 (*A* = K, Rb, Cs).[17] In 2005, the alkaline earth metal intercalation phase CaC_6 was found to be a superconductor up to a transition temperature of 11.5 K.[18,19] In addition, the reversibility of the intercalation process for lithium in graphite has made this carbon allotrope the most important anode material in commercial lithium ion batteries.[20]

The alkali metal fullerides A_3C_{60} are also superconductors with exceptionally high transition temperatures and are typically synthesized from fullerene and the respective alkali metal.[21] In these compounds the alkali metal cations occupy the tetrahedral voids of the cubic close-packed fullerene molecules. Addition of more alkali metal leads to structural changes such as polymerization in Li_4C_{60}.[22] For

lithium fullerides, alkali metal contents of up to $Li_{12}C_{60}$ have been reported, containing intercalated Li clusters.[23,24]

In comparison to the enormous variety of known hydrocarbon structures, the structural diversity of alkali metal carbides is very limited. Strobel et al. have predicted a number of possible lithium carbide structures at 0 and 40 GPa, including one-dimensional strands of fused aromatic rings next to known carbon anions. [25] Polymeric carbon anions have also been predicted as high-pressure forms of Li_2C_2 and CaC_2.[26] In addition, a large number of medium-sized carbon polyanions consisting of 4–59 carbon atoms is feasible. Herein, we present the synthesis and characterization of a novel binary lithium carbide phase LiC_x, which most likely contains polycyclic aromatic carbon anions and thus opens up a very new class of carbides with medium-sized polyanions.

Experimental Section

General Remarks. All steps of synthesis and sample preparation were performed inside an argon-filled glovebox (MBraun, $p(H_2O)$, $p(O_2)$ < 1.0 ppm). Li (> 99 %) was freed from oxide layers before use. Fullerene C_{60} powder (> 99 %, Hoechst) was used as purchased.

Synthesis. LiC_x was synthesized using a Li flux method (refer to Ref. [27] for more details on the flux synthesis technique). Thus, Li and C_{60} with Li:C ratios between 10:1 and 2:1 were filled into a stainless steel ampule equipped with a steel sieve. Prior to this, the C_{60} powder was pressed to a pellet to preclude any losses caused by powder falling through the sieve. The steel flux ampule was then welded shut and inserted into a steel capsule insulated with silica wool. The reaction mixture was heated inside a muffle furnace to the reaction temperature (350, 450, 575, or 700 °C) at a rate of 5 °C min^{-1} and allowed to react for 12 h. For the 575 and 700 °C reactions, the furnace was then slowly cooled down to 450 °C at a rate of 0.5 min^{-1}. After an additional dwell time of 3 h, excess lithium was removed by isothermal centrifugation at 3000 rpm for 3 min. The reaction products were still dense pellets, which shone silvery on the outside while the insides of the pellet appeared deeply black.

Annealing experiments. LiC_x samples were placed in stainless steel ampules, which were then welded, shut inside the glove box. The ampules were then heated inside a muffle furnace at a rate of 5 °C min^{-1}. The samples were held at the annealing temperature of 575 °C for 2 and 4 weeks, respectively, and then slowly cooled down to room temperature at 0.1 °C min^{-1}.

Reaction with ethanol. To investigate the reactivity of LiC_x, 3 mL ethanol was added to 27 mg LiC_x in a Schlenk tube. Gas formation was observed and a dark red suspension formed immediately. To ensure a complete reaction, the suspension was stirred at room temperature for 24 hours. Then, the dark red solution was removed by filtration and the reddish brown solid was washed with ethanol and dried under dynamic vacuum for at least 2 hours. Similarly, the ethanol was removed from the filtrate in dynamic vacuum.

Powder X-ray diffraction. Powder X-ray diffraction (PXRD) was carried out to determine the crystalline phases present in all synthesis products. Thus, the samples were finely ground in an agate mortar and then sealed inside 0.5 mm glass capillaries. The PXRD patterns were measured using a Stoe STADI P diffractometer equipped with a Ge(111) monochromator for Cu $K_{\alpha1}$ radiation (λ = 1.54056 Å) and a Dectris MYTHEN DCS 1K solid-state detector. A 5–89° 2ϑ range was irradiated for 30 s each in 0.07° steps of the position sensitive detector.

Raman spectroscopy. Raman spectra were measured using an inVia Raman microscope (Renishaw, RE04). The powdery samples were filled into a 0.5 mm glass capillary and irradiated with a 532 nm laser beam for 10 s at 1 % (LiC_x) and 0.5 % (LiC_x decomposition product) laser power using a microscope equipped with a 50-fold magnifying objective and a grating with 1800 lines mm^{-1}.

NMR spectroscopy. Solid-state NMR experiments were performed using a Bruker Avance 300-spectrometer equipped with a 4mm WVT MAS probe. The resonance frequencies of the measured nuclei at the operating field of 7 T are 116.6 MHz and 75.5 MHz for ^{7}Li and ^{13}C. Sample preparation was conducted under argon. ^{7}Li and ^{13}C single-pulse experiments under magic angle spinning (MAS) at 15 kHz were conducted at room temperature with 200 and 41400 scans, respectively, and a recycle delay of 4 and 2 s. The spectra were referenced to LiCl (aq) and adamantane (s) for ^{7}Li and ^{13}C.

Elemental analysis. Elemental analysis on LiC_x was performed by the microanalytical laboratory at TU München, yielding the following mass fractions: 71.62 % C, 0.08 % H, 2.45 % N, 20.1 % Li, 5–10 % Fe. Assuming a Fe fraction of 5.75 %, they correspond to molar fractions C : Li : N : H : Fe of 2.06 : 1 : 0.06 : 0.03 : 0.03.

Differential scanning calorimetry (DSC). Thermal analyses were performed in order to assess the thermal stability of LiC_x. The samples were sealed in Nb ampules and measured on a DSC machine (Netzsch, DSC 404 Pegasus) under a constant gas flow of 75 mL min^{-1}. The samples were heated to a maximum temperature (1000 °C and 600 °C, respectively) and cooled back down to 150 °C twice at a rate of 10 °C min^{-1}. The PROTEUS Thermal Analysis software was used to determine onset temperatures of the various DSC signals.[28]

Results and Discussion

Synthesis of LiC_x. In attempts to synthesize lithium-rich binary carbides such as Li_4C_3, we employed the lithium flux method using fullerene C_{60} as a reactive carbon precursor. C_{60} was pressed to a pellet and subsequently reacted with excess lithium at various temperatures. After dwelling, any unreacted Li was removed via isothermal centrifugation.[27] Since carbon is insoluble in liquid lithium below 1000 °C,[29] the reaction must proceed by Li diffusion into the C_{60} pellet. The pellet-shaped products are silvery on the outside and black inside. The silver coating is most likely caused by a thin film of Li metal. In addition, few light blue single crystals were observed on the pellet surfaces and were characterized as γ-$LiFeO_2$[30] by X-ray diffraction, indicating a slight reaction with the steel ampule material.

The reaction products were ground in an agate mortar and analyzed by powder X-ray diffraction (Figure 1a). For a reaction temperature of 350 °C, we observe a somewhat crystalline product which we cannot assign to any known phases. However, the main reflection of C_{60} is visible so that lithium fullerides could be present. The product of the reaction at 700 °C is clearly α-Li_2C_2. The 450 and 575 °C synthesis products both contain some α-Li_2C_2 as a side phase. The major component can be indexed with a monoclinic cell in space group $P2/m$ with a = 8.298(2) Å, b = 6.327(3) Å, c = 10.424(3) Å, β = 109.33(1)°, and V = 516.4(3) $Å^3$ (Figure 1b). It represents a novel binary lithium carbide, which we term LiC_x from now on. The PXRD pattern of the 575 °C indicates better crystallinity and a purer product so that this synthesis method was preferred for all further investigations.

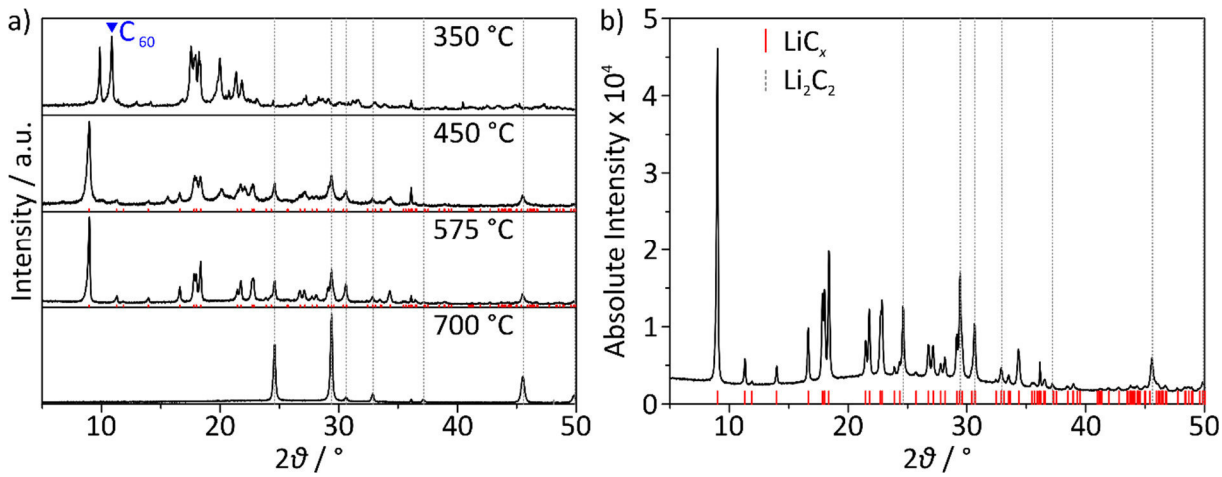

Figure 1. a) Experimental powder diffraction patterns of flux synthesis products prepared at different reaction temperatures. b) Experimental powder X-ray diffraction pattern of a LiC_x sample at 575 °C, indexed with a monoclinic *P*2/*m* cell. Characteristic reflections of α-Li_2C_2 are marked with dotted lines, whereas the reflection positions corresponding to the monoclinic cell of LiC_x are marked in red. The position of the (111) main reflection of C_{60} is marked in blue.

Due to the diffusion-controlled reaction, no single crystals of the novel binary Li-C phase could be obtained. Even prolonged annealing for several weeks did not afford any single crystals so that the structure of the new compound must be determined from powder diffraction data.

Characterization of LiC_x. To aid the structure solution from powder data, we performed a number of characterization methods on the novel Li-C compound. Elemental analysis yielded a Li:C ratio of 1:2. Considering the presence of lithium-richer Li_2C_2 as a side phase, this ratio can be viewed as the upper limit for the Li content in LiC_x. Additionally, traces of H, N, and Fe were observed. Due to their low molar fractions, we consider them to stem from impurities.

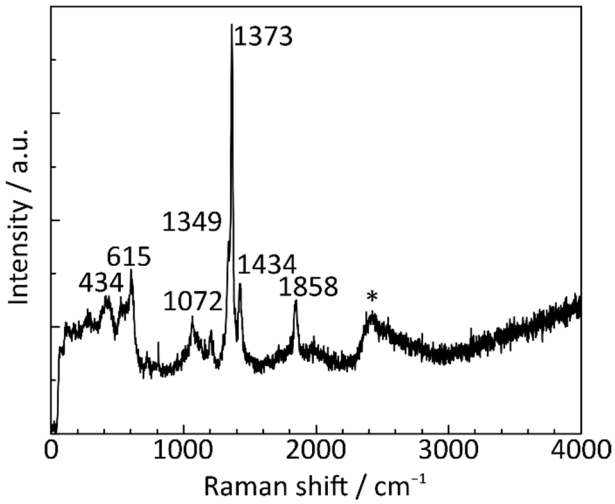

Figure 2. Raman spectrum of LiC_x. The asterisk marks an artefact signal.

A Raman spectrum of LiC_x exhibits several Raman bands (Figure 2), the most prominent being at 1373 cm^{-1}. It could represent a symmetric C–C stretching mode in LiC_x. This Raman shift is larger than that of allenides such as Mg_2C_3 (1213 cm^{-1})[13] and smaller than that of alkali metal fullerides (1433–1469 cm^{-1}).[31] Polycyclic aromatic hydrocarbons such as phenanthrene and its potassium and rubidium salts K_3phen and Rb_3phen also exhibit characteristic C–C stretching modes between 1300 and 1400 cm^{-1}, so that LiC_x could represent a carbon polyanion with conjugated double bonds. The acetylides

CaC_2 and Li_2C_2 have been reported to possess C–C stretching modes of 1864–1874 cm^{-1}.[32] Thus, the band we observe at 1858 cm^{-1} can reasonably be assigned to the Li_2C_2 impurity.

A ^{13}C MAS NMR spectrum of LiC_x (Figure 3a) supports the hypothesis of conjugated carbon polyanions. It contains two groups of signals at chemical shifts of 124–132 ppm and 170–178 ppm with an integral ratio of 3:1. The former lies in the range of aromatic carbon atoms, whereas the latter is comparable with NMR shifts of alkali metal fullerides[33,34] or of the central carbon atom in the allene anion of Mg_2C_3 (175 ppm).[13] The carbon atoms in Li_2C_2 are characterized by a very large spin-lattice relaxation time T_1 of 360 s,[35] so that we did not observe them with our experimental recycle delay of only 2 s. The ^7Li MAS NMR spectrum contains two signals: a large signal at −0.3 ppm corresponds to the lithium cations in LiC_x and Li_2C_2. This signal is in the typical range of diamagnetic Li compounds.[36] The much smaller signal at 264.8 ppm is caused by traces of metallic Li and exhibits a Knight shift.[37,38]

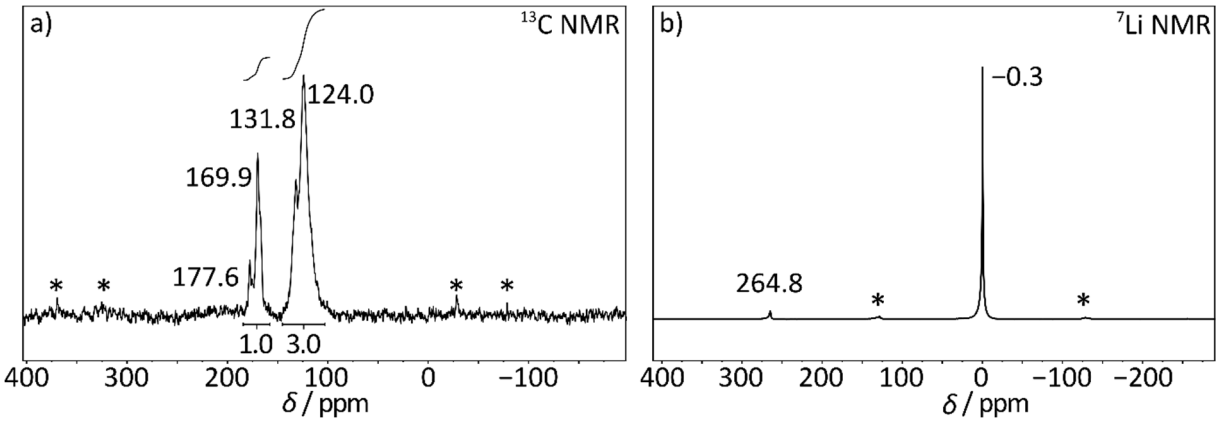

Figure 3. a) ^{13}C and b) ^7Li MAS NMR spectra of LiC_x. Rotational side bands are marked with an asterisk.

Reactivity of LiC_x with ethanol. In order to obtain more information about the identity of the carbon polyanions in LiC_x, we performed a controlled decomposition by treatment with ethanol. In this reaction, we expect a liberation of Li cations from the structure by protonation of the anionic carbon substructure. After adding the protic solvent, immediate gas formation is observed, most likely caused by the formation of acetylene from the Li_2C_2 impurity. In addition, the formerly black powder turns to a reddish brown color. The formation of a solid product, which is insoluble in ethanol, further indicates the presence of at least medium-sized polyanions in LiC_x. In contrast, the small carbon anions methanide, acetylide, and allenide are known to form the gases methane, acetylene, and propylene upon decomposition.

The dark red supernatant was removed from the insoluble product by Whatman filtration and characterized by PXRD and Raman spectroscopy. The fully amorphous material exhibits a Raman spectrum with a very strong fluorescence background (Figure 4). The discernible Raman bands are in the range of those expected for polycylic aromatic hydrocarbons,[39] but the low quality of the spectrum does not allow any more detailed interpretation. The red supernatant was characterized by removal of the solvent in dynamic vacuum and subsequent PXRD. The off-white powder contains mainly lithium ethanolate, proving the expected liberation of lithium. The red color of the ethanol solution is most likely caused by the iron impurities that had previously been found by elemental analysis.

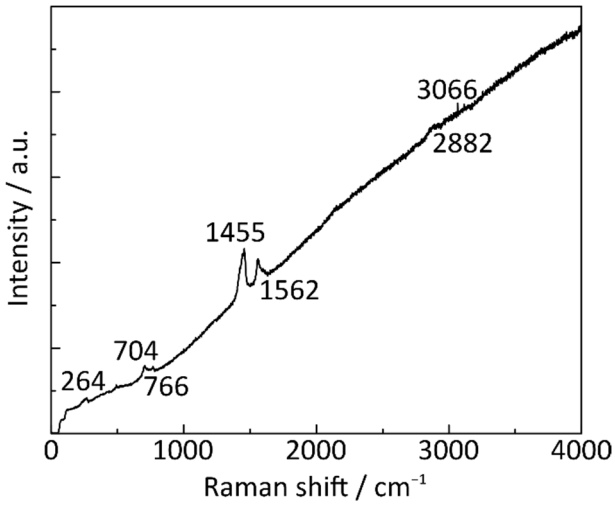

Figure 4. Raman spectrum of the reaction product of LiC_x with ethanol.

Thermal and magnetic properties of LiC_x. The thermal stability of the binary carbide was investigated by differential scanning calorimetry (DSC). The first heating curve exhibits an exothermic signal at 710 °C (Figure 5a). In addition, a reversible endothermic transition is observed at 458 °C (454 °C in the cooling curves). The latter corresponds to the well-known conversion of the side phase α-Li_2C_2 to its high temperature counterpart β-Li_2C_2.[6] PXRD patterns of the sample after DSC measurement feature α-Li_2C_2 as the only crystalline phase. Therefore, we assign the exothermic signal at 710 °C to the decomposition of LiC_x to Li_2C_2 and an amorphous phase not visible in the PXRD pattern. Annealing experiments at 575 °C show that the decomposition of LiC_x to Li_2C_2 also occurs very slowly at temperatures below 710 °C (Figure 5b), suggesting that LiC_x is a metastable compound.

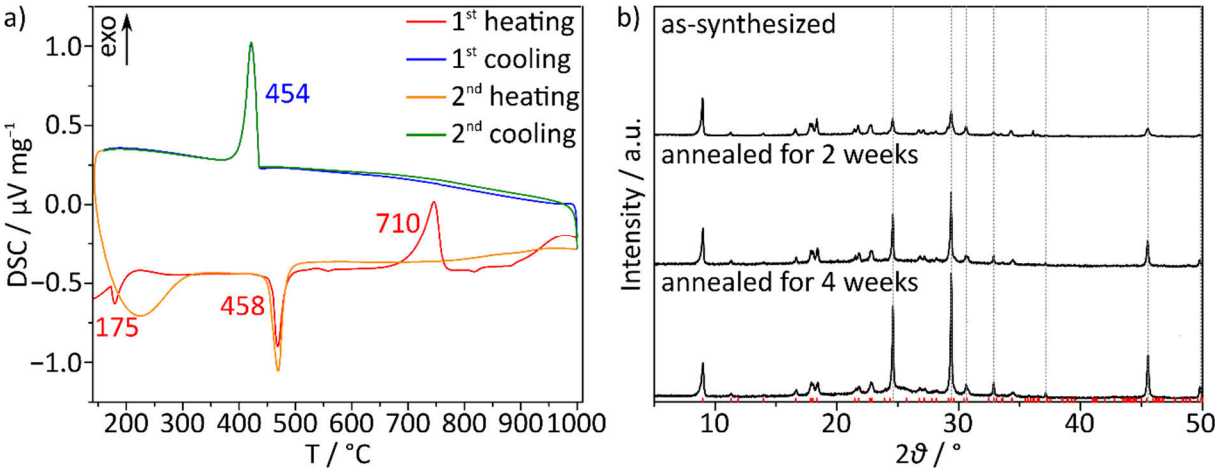

Figure 5. a) DSC curves of LiC_x; two measurement cycles were performed using heating/cooling rates of 10 °C min^{-1}. The endothermic signal at 175°C corresponds to the melting point of elemental Li. b) Powder diffraction patterns of the LiC_x as-synthesized and after annealing at 575 °C; to ensure comparability, the patterns are normalized to the intensity of the (001) reflection at 9.0° 2ϑ for the *P*2/*m* unit cell of LiC_x. The Li_2C_2 reflections are marked with dotted lines.

The magnetic properties of LiC_x were determined by SQUID measurements (Figure 6). The mass magnetization curve clearly shows Pauli paramagnetic behavior, suggesting that like alkali metal fullerides, LiC_x exhibits metallic properties. Alkali metal-doped polycyclic aromatic hydrocarbons such as phenanthrene, picene, and dibenzopentacene have recently been discovered to function as superconductors with high transition temperatures of up to 33 K.[40-43] However for LiC_x, which could

contain similar polycyclic carbon anions, we do not observe any indications for superconducting behavior down to 2 K.

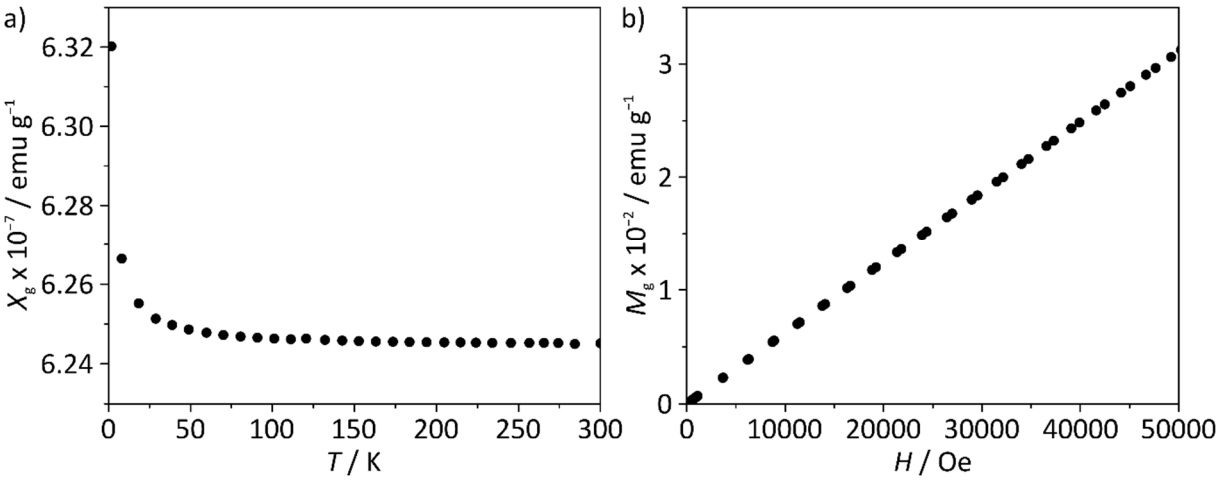

Figure 6. a) Mass susceptibility X_g of a LiC_x sample at a field intensity H of 5000 Oe over the temperature range of 2–300 K; b) mass magnetization M_g of a LiC_x sample at 300 K over the field intensity range of 0–50000 Oe. All data were corrected for sample holder diamagnetism.

Conclusions

In conclusion, we have prepared a novel binary lithium carbide by lithium flux synthesis with fullerene C_{60} as a reactive carbon precursor. The compound forms reproducibly with various Li:C ratios at 450–575 °C. Higher temperatures favor the formation of the acetylide Li_2C_2. The new compound LiC_x crystallizes in space group $P2/m$. Single crystals could not be obtained due to the diffusion-controlled reaction mechanism. Thus, the structure of LiC_x is yet to be determined from powder diffraction patterns. Elemental analysis suggests a stoichiometry of LiC_2 or lithium-poorer.

Using Raman and ^{13}C MAS NMR spectroscopy, we can narrow down the selection of possible carbide structures to polyanions with conjugated double bonds such as fused aromatic rings, possibly constituting fragments of the C_{60} structure. Upon reaction with ethanol, LiC_x forms an amorphous reddish brown product, whose Raman bands are similar to those of polycyclic aromatic hydrocarbons. This decomposition reaction further supports our hypothesis of medium-sized carbon polyanions. If confirmed by structural investigations, this find will open up a very new class of binary metal carbides with potentially interesting electronic and magnetic properties.

Thermal analysis shows that LiC_x decomposes exothermically to Li_2C_2 at 710 °C in DSC measurements. Annealing experiments demonstrate that the binary carbide is metastable and already decomposes slowly at lower temperatures. Investigations of the magnetic properties of LiC_x using a SQUID yielded Pauli paramagnetism, which is typical for metallic compounds. Down to 2K, superconductivity was not observed.

Author Information

Corresponding Author. * E-mail: Thomas.Faessler@lrz.tum.de

Notes. The authors declare no competing financial interest.

Acknowledgments

The authors are grateful to Sebastian Geier for measuring the Raman spectra and Marina Boyko for SQUID measurements. L.M.S. thanks Technische Universität for financial support through the Laura Bassi-Prize as well as Fonds der Chemischen Industrie and Studienstiftung des deutschen Volkes for her fellowships.

References

[1] E. Staritzky, *Anal. Chem.* **1956**, *28*, 915.
[2] M. von Stackelberg, E. Schnorrenberg, *Z. Phys. Chem., Abt. B* **1934**, *27*, 37–49.
[3] O. O. Kurakevych, T. A. Strobel, D. Y. Kim, G. D. Cody, *Angew. Chem. Int. Ed.* **2013**, *52*, 8930–8933.
[4] U. Ruschewitz, P. Müller, W. Kockelmann, *Z. Anorg. Allg. Chem.* **2001**, *627*, 513–522.
[5] S. Hemmersbach, B. Zibrowius, U. Ruschewitz, *Z. Anorg. Allg. Chem.* **1999**, *625*, 1440–1446.
[6] U. Ruschewitz, R. Pöttgen, *Z. Anorg. Allg. Chem.* **1999**, *625*, 1599–1603.
[7] P. Karen, A. Kjekshus, Q. Huang, V. L. Karen, *J. Alloy. Compd.* **1999**, *282*, 72–75.
[8] M. Knapp, U. Ruschewitz, *Chem. Eur. J.* **2001**, *7*, 874-880.
[9] V. Vohn, M. Knapp, U. Ruschewitz, *J. Solid State Chem.* **2000**, *151*, 111–116.
[10] V. Vohn, W. Kockelmann, U. Ruschewitz, *J. Alloy. Compd.* **1999**, *284*, 132–137.
[11] R. West, P. A. Carney, I. C. Mineo, *J. Am. Chem. Soc.* **1965**, *87*, 3788-3789.
[12] R. West, P. C. Jones, *J. Am. Chem. Soc.* **1969**, *91*, 6156-6161.
[13] T. A. Strobel, O. O. Kurakevych, D. Y. Kim, Y. Le Godec, W. Crichton, J. Guignard, N. Guignot, G. D. Cody, A. R. Oganov, *Inorg. Chem.* **2014**, *53*, 7020–7027.
[14] H. Fjellvaag, P. Karen, *Inorg. Chem.* **1992**, *31*, 3260–3263.
[15] M. S. Dresselhaus, G. Dresselhaus, *Adv. Phys.* **2002**, *51*, 1–186.
[16] O. Dolotko, A. Senyshyn, M. J. Mühlbauer, K. Nikolowski, H. Ehrenberg, *J. Power Sources* **2014**, *255*, 197–203.
[17] N. B. Hannay, T. H. Geballe, B. T. Matthias, K. Andres, P. Schmidt, D. MacNair, *Phys. Rev. Lett.* **1965**, *14*, 225–226.
[18] T. E. Weller, M. Ellerby, S. S. Saxena, R. P. Smith, N. T. Skipper, *Nat. Phys.* **2005**, *1*, 39–41.
[19] N. Emery, C. Hérold, M. d'Astuto, V. Garcia, C. Bellin, J. F. Marêché, P. Lagrange, G. Loupias, *Phys. Rev. Lett.* **2005**, *95*, 087003.
[20] M. T. McDowell, S. W. Lee, W. D. Nix, Y. Cui, *Adv. Mater.* **2013**, *25*, 4966–4985.
[21] K. Tanigaki, K. Prassides, *J. Mater. Chem.* **1995**, *5*, 1515–1527.
[22] S. Margadonna, D. Pontiroli, M. Belli, T. Shiroka, M. Riccò, M. Brunelli, *J. Am. Chem. Soc.* **2004**, *126*, 15032-15033.
[23] F. Giglio, D. Pontiroli, M. Gaboardi, M. Aramini, C. Cavallari, M. Brunelli, P. Galinetto, C. Milanese, M. Riccò, *Chem. Phys. Lett.* **2014**, *609*, 155–160.
[24] L. Cristofolini, M. Riccò, R. De Renzi, *Phys. Rev. B* **1999**, *59*, 8343–8346.
[25] Y. Lin, T. A. Strobel, R. E. Cohen, *Phys. Rev. B* **2015**, *92*, 214106.
[26] D. Benson, Y. Li, W. Luo, R. Ahuja, G. Svensson, U. Häussermann, *Inorg. Chem.* **2013**, *52*, 6402–6406.

[27] K. Puhakainen, M. Boström, T. L. Groy, U. Häussermann, *J. Solid State Chem.* **2010**, *183*, 2528–2533.
[28] *PROTEUS Thermal Analysis V4.8.2*, Netzsch-Gerätebau GmbH, Selb, **2006**.
[29] A. Kozlov, M. Seyring, M. Drüe, M. Rettenmayr, R. Schmid-Fetzer, *Int. J. Mater. Res.* **2013**, *104*, 1066–1078.
[30] M. Barré, M. Catti, *J. Solid State Chem.* **2009**, *182*, 2549–2554.
[31] M. S. Dresselhaus, G. Dresselhaus, P. C. Eklund, *J. Raman Spectrosc.* **1996**, *27*, 351–371.
[32] J. Nylén, S. Konar, P. Lazor, D. Benson, U. Häussermann, *J. Chem. Phys.* **2012**, *137*, 224507.
[33] M. Riccò, T. Shiroka, M. Belli, D. Pontiroli, M. Pagliari, G. Ruani, D. Palles, S. Margadonna, M. Tomaselli, *Phys. Rev. B* **2005**, *72*, 155437.
[34] C. H. Pennington, V. A. Stenger, *Rev. Mod. Phys.* **1996**, *68*, 855–910.
[35] T. M. Duncan, *Inorg. Chem.* **1989**, *28*, 2663–2668.
[36] H. Günther, *Lithium NMR,* in *eMagRes*, John Wiley & Sons, Ltd, **2007**.
[37] R. Bhattacharyya, B. Key, H. Chen, A. S. Best, A. F. Hollenkamp, C. P. Grey, *Nat. Mater.* **2010**, *9*, 504–510.
[38] C. P. Slichter, *Magnetic Interactions of Nuclei with Electrons,* in *Principles of Magnetic Resonance*, Springer Berlin Heidelberg, Berlin, Heidelberg, **1990**, pp. 87–144.
[39] J. Chen, Y.-W. Huang, Y. Zhao, *J. Raman Spectrosc.* **2015**, *46*, 64–69.
[40] X. F. Wang, R. H. Liu, Z. Gui, Y. L. Xie, Y. J. Yan, J. J. Ying, X. G. Luo, X. H. Chen, *Nat. Commun.* **2011**, *2*, 507.
[41] R. Mitsuhashi, Y. Suzuki, Y. Yamanari, H. Mitamura, T. Kambe, N. Ikeda, H. Okamoto, A. Fujiwara, M. Yamaji, N. Kawasaki, Y. Maniwa, Y. Kubozono, *Nature* **2010**, *464*, 76–79.
[42] M. Xue, T. Cao, D. Wang, Y. Wu, H. Yang, X. Dong, J. He, F. Li, G. F. Chen, *Sci. Rep.* **2012**, *2*, 389.
[43] Y. Kubozono, H. Goto, T. Jabuchi, T. Yokoya, T. Kambe, Y. Sakai, M. Izumi, L. Zheng, S. Hamao, H. L. T. Nguyen, M. Sakata, T. Kagayama, K. Shimizu, *Physica C: Superconductivity and its Applications* **2015**, *514*, 199–205.

5.7 Alkali Metals Extraction Reactions with the Silicides $Li_{15}Si_4$ and Li_3NaSi_6: Amorphous Si *versus allo*-Si

CHEMISTRY OF MATERIALS

Article

pubs.acs.org/cm

Alkali Metals Extraction Reactions with the Silicides $Li_{15}Si_4$ and Li_3NaSi_6: Amorphous Si *versus allo*-Si

Michael Zeilinger,[†] Laura-Alice Jantke,[†] Lavinia M. Scherf,[†] Florian J. Kiefer,[†] Gero Neubüser,[‡] Lorenz Kienle,[‡] Antti J. Karttunen,[§] Sumit Konar,[∥] Ulrich Häussermann,[∥] and Thomas F. Fässler*[,†]

[†]Department of Chemistry, Technische Universität München, Lichtenbergstraße 4, 85747 Garching b. München, Germany

[‡]Faculty of Engineering, Christian-Albrechts-University, Kiel, Kaiserstrasse 2, 24143 Kiel, Germany

[§]Department of Chemistry, Aalto University, FI-00076 Aalto, Finland

[∥]Department of Materials and Environmental Chemistry, Stockholm University, 10691 Stockholm, Sweden

Supporting Information

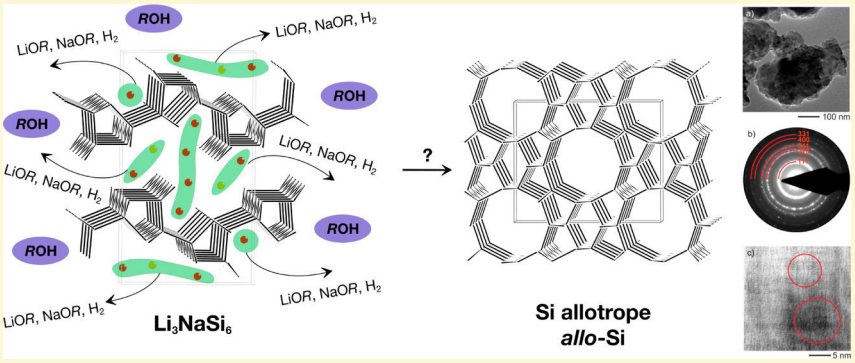

ABSTRACT: The silicides $Li_{15}Si_4$ and Li_3NaSi_6 were subjected to chemical extraction of the alkali metal component by liquid ammonia and ethanol, respectively, which after washing yielded black powders of amorphous silicon. The investigated reactions are interesting with respect to both the formation of novel Si modifications and the delithiation process in Si anode materials. The products termed *a*-Si (from $Li_{15}Si_4$) and *a-allo*-Si (from Li_3NaSi_6) were characterized by a combination of methodologies (X-ray diffraction, transmission electron microscopy, differential thermal analysis, Raman, atomic absorption, and energy-dispersive X-ray spectroscopy) which revealed (i) a porous microstructure for *a*-Si built from spherically shaped particles with sizes around 10 nm, (ii) partial surface oxidation of both materials and (iii) the presence of nanocrystalline Si in both materials. The result of the protic oxidation of Li_3NaSi_6 is at variance with earlier findings reporting the formation of a crystalline bulk allotrope of silicon (*allo*-Si) from the topotactic combination of silicon layers present as polyanions in Li_3NaSi_6. Additionally, quantum chemical calculations show that silicon layers in Li_3NaSi_6 cannot combine to energetically favorable allotropic forms of Si. This is different from Li_7Ge_{12}, where polyanionic germanium layers topotactically convert to the germanium allotrope *m-allo*-Ge upon oxidation.

1. INTRODUCTION

The search for new forms of semiconducting silicon and germanium attracts increasing attention because novel or superior electronic transport and optical properties—being real or envisioned—will allow improving performance and scalability of devices based on established semiconductor technologies.[1,2] Desired new crystalline forms range from nanomaterials (particles, wires, tubes),[1] nano- and mesostructures (e.g., nano- and mesoporous germanium)[3−7] to new allotropes.[8−13] Amorphous forms, which are widely used in thin film transistors and photovoltaic applications, are being tailored by impurity doping or by compositing with nanocrystalline particles.[14,15]

Nanosilicon is also in the midpoint of the search for electrochemically active anode materials since silicon possesses a ∼10 times higher capacity in Li ion batteries when compared to commercially used graphite.[16−18] Generally, $Li_{15}Si_4$ and amorphous Si phases are discussed during charging and discharging processes. Although there are numerous reports on the electrochemical lithiation of Si to form amorphous or crystalline Li−Si alloys and delithiation to form amorphous Si, a chemical delithiation of presynthesized $Li_{15}Si_4$ has not been reported.[19−22]

In general, Zintl phases comprising alkali or alkaline earth metals and silicon or germanium represent versatile precursors toward new forms of silicon and germanium. Metal extraction

Received: September 15, 2014
Revised: October 28, 2014
Published: October 30, 2014

   dx.doi.org/10.1021/cm503371e | *Chem. Mater.* 2014, 26, 6603−6612

from solid Zintl phases or the oxidation of Zintl anions in solution are established routes. Examples include the crystalline clathrate-II allotrope of silicon from simple thermal decomposition of NaSi into Na_xSi_{136} and subsequent Na extraction with I_2,[23] the crystalline germanium clathrate from the oxidation of Ge_9^{4-} Zintl ions in ionic liquids,[24] and the isolation of silicon sheets with a two-dimensional graphitic structure by the redox assisted exfoliation of $CaSi_2$.[25−27] Metal extraction allows also for bulk amorphous and nanocrystalline samples. This was shown by McMillan et al.[28] and Wang et al.,[14] respectively, by applying a solid state metathesis (SSM) reaction between NaSi or NaGe and NH_4X (X = Cl, Br), where NaX is subsequently removed by washing with alcohol or water. NaSi may also be directly oxidized by alcohols to yield nanosized amorphous Si.[29]

Zintl phases with layered polyanions are especially interesting for obtaining new allotropes because of their potential for topotactic reactions. Ideally, metal extraction will lead to a kinetically favored (low barrier) oxidative coupling of two-dimensional polyanions, retaining (or only slightly rearranging) their topology. Deintercalation reactions with Li_7Ge_{12} and Li_3NaSi_6, whose layered structures are shown in Figure 1, were

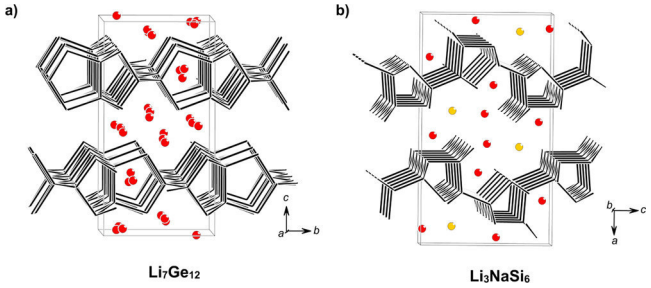

Figure 1. Zintl phases Li_7Ge_{12} and Li_3NaSi_6 containing polyanionic layers (a) $^2_\infty[Ge_{12}]^{7-}$ and (b) $^2_\infty[Si_6]^{4-}$ (black) being separated by Li (red) and Na (yellow) atoms.

already performed in the 1980s and yielded new allotropic forms of Ge and Si, named *allo*-Ge and *allo*-Si, respectively.[8−11] However, the structures of these *allo* forms eluded conclusive characterization. Only recently, a bulk synthesis strategy for microcrystalline *allo*-Ge (*m-allo*-Ge) was established and the structure of *allo*-Ge could be determined by a combination of experimental and quantum chemical methodologies.[13,30] Indeed, the five-ring topology of the initial $^2_\infty[Ge_{12}]^{7-}$ layers is strictly retained in *m-allo*-Ge. From *m-allo*-Ge, another allotrope of Ge—hexagonal 4*H*-Ge—can be obtained which is exclusively built from six-rings.[9,12] Subsequently, the thermochemistry and optical properties of these Ge allotropes were investigated in detail.[31] The situation for *allo*-Si remains unclear. In 2002, Conesa suggested structure models for *allo*-Si based on the $^2_\infty[Si_6]^{4-}$ layers in Li_3NaSi_6,[32] however, experimental validation is still missing.

Here, we describe metal extractions with Li_3NaSi_6 and $Li_{15}Si_4$. The former were aimed at renewed efforts into the synthesis and structural characterization of *allo*-Si, the latter to emulate by chemical means the delithiation process occurring electrochemically in silicon based lithium batteries (cycling Si against Li) where amorphous and crystalline $Li_{15}Si_4$ correspond to the fully lithiated (discharged) state.[19,20] We solve the quarter-century old puzzle of *allo*-Si and show that *allo*-Si is not accessible from Li_3NaSi_6. Instead, products essentially correspond to amorphous Si. Amorphous Si is also the product of the chemical delithiation of $Li_{15}Si_4$. However, there are subtle differences between both materials, which are introduced by the simultaneous formation of nanocrystalline Si.

2. EXPERIMENTAL SECTION

Solid-State Synthesis. Starting materials were lithium rods (99%, Rockwood-Lithium), sodium rods (99%, Chempur) and silicon powder (99.999%, Sigma-Aldrich). All steps of solid state synthesis and preparation of air- and moisture-sensitive samples were carried out in a glovebox (MBraun, Ar-atmosphere, H_2O and O_2 levels <0.1 ppm). Metal ampules (tantalum and niobium) for solid state synthesis were thoroughly cleaned, heated to 1000 °C under dynamic vacuum ($p < 1 \times 10^{-3}$ mbar) for at least 2 h and transferred to the glovebox. An all-glass Schlenk line supplied with Ar, which is dried over P_2O_5, molecular sieve and heated titanium sponge (T = 750 °C), was used for baking out ampules, encapsulating ampules in silica tubes, handling air- and moisture-sensitive materials, and reactions in inert atmosphere.

$Li_{15}Si_4$. Bulk samples of $Li_{15}Si_4$ were synthesized according to ref 33 by mechanical ball-milling of stoichiometric mixtures of elemental Li and Si in a RETSCH PM 100 planetary ball mill. The procedure yields large quantities (up to several grams) of X-ray pure $Li_{15}Si_4$.

Li_3NaSi_6. Li_3NaSi_6 was typically synthesized according to

$$Li_{12}Si_7 + 4NaSi + 13\ \alpha\text{-Si} \rightarrow 4Li_3NaSi_6$$

Stoichiometric mixtures of reactants with a total mass of 0.5 g were homogenized in an agate mortar, pressed to a pellet and sealed in a metal ampule which was then encapsulated in a silica jacket under vacuum. Ampules were heated in a muffle furnace to 550 °C at a rate of 5 K min^{-1} and annealed for 24 h. After slow cooling at 0.075 K min^{-1} the samples were recovered inside the glovebox. The procedure yields X-ray pure samples of Li_3NaSi_6 (see Figure S1a in the Supporting Information). Li_3NaSi_6 may also be obtained from annealing ball-milled mixtures of $Li_{15}Si_4$, Na, and α−Si (RETSCH PM 100 planetary ball mill, duration: 70 min, 250 rpm, 10 min interval, 5 min break, direction reversal, ball charge 3, ball size 15 mm diameter) with molar ratios 1:5:26 at 600 °C (total mass, 2.0 g; heating rate, 4 K min^{-1}; dwell time, 7 days; cooling rate, 0.075 K min^{-1} to room temperature) or from annealing ball-milled stoichiometric mixtures of the elements at 550 °C (total mass, 0.5−3.0 g; heating rate, 1−2 K min^{-1}; dwell time, 5−7 days; cooling rate, 0.1 K min^{-1} to room temperature). These samples always contained small amounts of impurities ($Li_{12}Si_7$ and/or α−Si, cf. Figure S1b in the Supporting Information). It was later recognized that when using Nb ampules, Li_3NaSi_6 samples also contained small amounts of $NbSi_2$ although this impurity could not be detected in powder X-ray diffraction patterns.

$Li_{12}Si_7$ and NaSi. The binary precursors for Li_3NaSi_6 were synthesized from stoichiometric mixtures of the elements with a total mass of 2.0 g each. The reactions were carried out in tantalum ampules which were encapsulated in silica jackets under vacuum. Sample annealing was done in a muffle furnace. For $Li_{12}Si_7$, the temperature was raised to 750 °C at 5 K min^{-1}, followed by 1 h dwelling, cooling to 400 °C at a rate of 0.5 K min^{-1}, dwelling for 6 h and subsequent quenching. For NaSi, the temperature was raised stepwise to 600 °C: 5 K min^{-1} to 500 °C, 1 h dwelling, 5 K min^{-1} to 600 °C. After a dwell time of 30 h a cooling rate of 5 K min^{-1} was applied. Samples were recovered inside the glovebox.

Extraction Reactions. One half gram of $Li_{15}Si_4$ was loaded into a custom-built extractor for liquid ammonia (Westfalen AG; dried over sodium). The apparatus, shown in Figure 2, is connected to a high-vacuum glass line that is supplied with purified argon (see above). The extraction process (taking place at −78 °C by using an isopropanol dry ice bath) was stopped after the color of the liquid ammonia solution had turned from deep to light blue after approximately 40 extraction cycles. After evaporating ammonia from the extractor, the solid black product consisting of amorphous silicon and $LiNH_2$ was recovered in the glovebox. To remove $LiNH_2$, 157 mg of the mixture were filled into a Schlenk flask. The powder was suspended in 20 mL of dry toluene (dried over Na). Subsequently, 50 mL of ethanol (dried over

dx.doi.org/10.1021/cm503371e | *Chem. Mater.* 2014, 26, 6603−6612

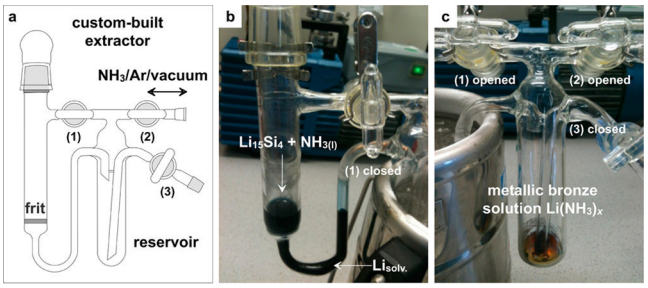

Figure 2. (a) Custom-built apparatus for extracting Li from $Li_{15}Si_4$ with liquid NH_3. $Li_{15}Si_4$ powder is loaded onto the frit inside the glovebox. When NH_3 is condensed onto $Li_{15}Si_4$ (sample space is cooled, −78 °C), a deep blue color is observed. (b) By closing valve 1, the extract is transported into the cooled reservoir. (c) By opening valve 1, and cooling the sample space, NH_3 can be recondensed onto the solid. (c) Thereafter, Li/$LiNH_2$ remains in the reservoir. The color is characteristic for a concentrated metallic bronze solution of Li in NH_3 denoted as $Li(NH_3)_x$.[34]

Na) was added slowly while stirring. After 5 min, the black suspension (pH ∼8) was transferred into an Erlenmeyer flask followed by adding 50 mL ethanol and 1 mL acetic acid to adjust the pH value (pH ∼5). After stirring shortly, the black solid was separated via centrifugation and washed three times with 20 mL ethanol. Finally, the powder was dried under vacuum while periodically heated to 150−200 °C with a heat gun. This procedure yielded 30−40 mg of a black product, thereafter termed *a*-Si.

Prior to subjecting Li_3NaSi_6 to extraction reactions, the material was ground in an agate mortar or ball-milled in a hermetically sealed stainless steel jar (RETSCH PM 100 planetary ball mill) for 8 h at 300 rpm (ball charge, 3; ball size, 15 mm diameter). A typical reaction with ball-milled starting material was carried out as follows: 135 mg of Li_3NaSi_6 were shortly (5−10 min) treated with 30 mL of ethanol under inert conditions. Subsequently, 4 mL of concentrated HCl solution were added. The solid product was separated by centrifugation, repeatedly washed (3−4 times) with 30 mL of a 1:1 ethanol−water mixture (V/V), dried under vacuum, and finally retained as a black fine powder (in the following termed *a-allo*-Si). The reactions were modified using *i*-PrOH, air, H_2O, HNO_3, HOAc, and Ph_2CO instead of EtOH. For details, see ref 35 and Table 1.

Powder X-ray Diffraction (PXRD). For examining the phase purity of precursor materials and phase analysis of products, laboratory PXRD patterns were recorded on a Stoe STADI P diffractometer (Ge(111) monochromator for Cu$K_{\alpha 1}$ radiation, λ = 1.54056 Å) equipped with a Dectris MYTHEN DCS 1K solid state detector. Samples were ground in agate mortar and sealed inside 0.3 mm glass capillaries. All measurements were performed in a 2θ range of 5−90° (PSD steps, 0.06−1.00°; time/step, 10−40 s). Rietveld refinements of crystalline samples were carried out with the TOPAS 4.0 software.[36] High-energy PXRD measurements for *a*-Si and *a-allo*-Si were carried out at the beamline P02.1, at PETRA III, DESY (Hamburg). This beamline operates at a fixed energy of approximately 60 keV. The wavelength has been determined to be 0.20727(6) Å by using a LaB_6 NIST standard. The beam size is approximately 0.8 mm in diameter. The materials were enclosed in 0.7 mm glass capillaries and placed in front of the detector. For both samples, 30 2D diffraction images, each obtained through the accumulation of 20 frames with an exposure time of one second per frame, were collected with a PerkinElmer amorphous silicon area detector (XRD1621) placed at 329 mm from the sample. The distance between the sample and the detector was determined with a LaB_6 NIST standard. The 2D diffraction images were then integrated into a linear scattering signal with the software Fit2D and averaged.[37] Pair distribution functions (PDFs) were extracted by using the PDFgetX3 software.[38] The different steps of the PDF extraction include the subtraction of the scattering signal from the container, the correction for Compton scattering, absorption effects, and multiple scattering, and normalization to obtain the function $S(Q)$. Finally, the pair distribution function, $G(r)$, is obtained by sine Fourier transformation of the normalized scattering intensity, $F(Q) = Q[S(Q)-1]$, to a maximum Q-value, Q_{max}, of 22.0 Å^{-1}. In PDFgetX3, the Fourier transformation is executed using exponential damping so as to suppress termination ripples, at the cost of reduced spatial resolution.

Differential Thermal Analysis (DTA). Differential thermal analysis was carried out with a NETZSCH DSC 404 Pegasus apparatus equipped with a DTA carrier system. Custom-built niobium crucibles were thoroughly cleaned, heated to 1000 °C under dynamic vacuum ($p < 1 \times 10^{-3}$ mbar) for 2 h and transferred to an Ar-filled glovebox. Crucibles were loaded with 20−30 mg of sample. The open

Table 1. Summary of Alkali Metal Extraction Reactions with Li_3NaSi_6 Targeting the Synthesis of *allo*-Si; Crystalline Products That Were Identified by Powder X-ray Diffraction Are Specified

no.	Li_3NaSi_6 (mg)	reagent	additional solvent (mL)	experimental details	crystalline phases identified by PXRD
1	135	(a) EtOH, 30 mL (dried over Na); (b) HCl, 4 mL		ball-milled Li_3NaSi_6 and EtOH were stirred in a Schlenk flask (5−10 min), 4 mL of HCl was added, washed with EtOH, dried under vacuum	*α*-Si, Na_8Si_{46}
2	600	EtOH (dried over Na), 15 mL/20 mL		stirred in a Schlenk flask for 14 days followed by decanting EtOH, stirred another day with 20 mL of EtOH, washed with EtOH, dried under vacuum[b]	Li_3NaSi_6, *α*-Si
3	100[a]	*i*-PrOH, 0.5 mL	Et_2O, 5	stirred in a Schlenk flask, 3 months, washed with Et_2O (4×), dried under vacuum[b]	Li_3NaSi_6, $NbSi_2$
4	400[a]	*i*-PrOH, 1 mL	Et_2O, 9	stirred in a Schlenk flask, 6 weeks, washed with Et_2O (3×), dried under vacuum[b]	*α*-Si
5	100[a]	*i*-PrOH, 0.75 mL	Et_2O, 14	stirred in a vial, 2 weeks, washed with Et_2O (3×)[c]	Li_3NaSi_6
6	300[a]	air		6 months[c]	Li_3NaSi_6
7	50[a]	H_2O, 5 mL		stirred in a vial, 2 weeks, washed with H_2O (2×)[c]	
8	100[a]	HNO_3 (68%), 6 mL		stirred in a Schlenk flask, 4 days, washed with H_2O (3×), dried under vacuum[b]	Li_3NaSi_6
9	50[a]	HOAc, 3 mL		stirred in a vial, 4 weeks, washed with H_2O (3×)[c]	*α*-Si
10	30[a]	buffer solution $NaHPO_4/KHPO_4$, 5 mL		stirred in a vial, 4 days, washed with H_2O[c]	Li_3NaSi_6
11a	1000[a]	Ph_2CO 5 M, 3 mL	THF, 10	stirred in a Schlenk flask, 3 months, washed with THF (4×), dried under vacuum[b]	Li_3NaSi_6, $NbSi_2$
11b	217 from 11a	H_2O, 5 mL		stirred in a vial,[c] 2 months, washed with H_2O (3×)	SiO_2, $NbSi_2$, Li_2SiO_3, Na_2SiO_3

[a]Li_3NaSi_6 was synthesized in a Nb ampule [b]Reacted, washed, and dried under inert conditions. [c]Sample handling carried out in air.

dx.doi.org/10.1021/cm503371e | *Chem. Mater.* 2014, 26, 6603−6612

end was closed by crimping and then sealed by arc-welding inside the glovebox under cooling. All measurements were performed under an Ar-flow rate of 60−70 mL min^{-1} and a heating/cooling rate of 10 K min^{-1}. An empty niobium crucible served as reference. Samples were recovered after the measurement by opening the niobium crucibles inside the glovebox. The Proteus Thermal Analysis program was used for data handling.[39]

Transmission Electron Microscopy (TEM). Transmission electron microscopy and selected-area electron diffraction (SAED) measurements were performed in a Tecnai F30 STwin microscope (300 kV, field emission gun (FEG) cathode, spherical aberration coefficient C_s = 1.2 mm). EDX nanoprobe analysis as part of the TEM examinations were carried out using a Si/Li detector (EDAX System). To prevent oxidation and contamination of the samples the entire procedure for TEM preparation was done in an Ar-filled glovebox. Ground samples of *a*-Si and *a-allo*-Si were placed onto a lacey-carbon grid and subsequently transferred to the TEM in an argon-filled bag. Heating experiments (cf. Figures S9 and S10 in the Supporting Information) were performed with a single-tilt heating stage to tentatively prove crystallization and morphology changes at elevated temperatures.

Attenuated Total Reflectance Fourier Transformed Infrared Spectroscopy. ATR-FT-IR spectra were recorded on a Varian 670 IR FT-IR spectrometer equipped with a Pike GladiATR ATR accessory and using a diamond ATR element. All measurements were performed at room temperature. The Varian Resolution Pro software was used for data handling.[40]

Raman Spectroscopy. Raman spectra for *a*-Si and *a-allo*-Si were measured using a LabRAM HR 800 spectrometer. The instrument is equipped with an 800 mm focal length spectrograph and an air-cooled (−70 °C), back thinned CCD detector. Samples were sealed in 0.7 mm glass capillaries. The capillaries were placed on a glass slide and samples were excited with an air-cooled double frequency Nd:YAG laser (532 nm). The laser was focused onto the sample using a 50X superlong working distance (WD = 20.5 mm) Mitutoyo objective. Measurements were performed in two steps. The samples were excited at 0.56 mW laser power (corresponding to a low power density of 5.5 × 10^{-6} mW μm^{-2}) and spectra were recorded at different spots of the sample. Next the samples were heated with the laser for 1 min by increasing the power to 14 mW and a spectrum was measured at this laser power and another one at the low laser power used in the initial examination (0.56 mW). The laser power was adjusted by a software controlled filter wheel with 6 ND filters. Spectra were collected with an exposure time of 60 s (10 accumulations) and using a grating of 600 lines mm^{-1}. All spectra were calibrated and normalized. The spatial resolution of the instrument is specified as 1 μm in diameter.

Elemental Analysis. A JEOL-JSM 7500F scanning electron microscope (SEM) equipped with an Oxford X-Max EDX (energy-dispersive X-ray spectroscopy) analyzer with Mn as internal standard was used to determine elements with atomic numbers larger than four. Samples were handled inside an Ar-filled glovebox or outside if not air-sensitive and fixed on a graphite platelet which was attached to an aluminum stub. The lithium content determination was carried out by atomic absorption spectroscopy using a Varian AA280FS device. C, H, N contents were determined by a Hekatech Euro EA CHNSO-Analyzer.

Computational Details. Quantum chemical calculations with the Perdew−Burke−Ernzerhof hybrid density functional method (DFT-PBE0)[41,42] were performed using the CRYSTAL09 software package.[43] Split-valence + polarization (SVP) quality basis sets were employed for Si, Na, and Li. The basis set for Si was taken from ref 44. For the alkali metals they were derived from the molecular def-SVP basis set (see the Supporting Information).

Both the lattice and the atomic parameters of Si trial structures (according to Conesa)[32] were allowed to relax within the constraints imposed by the space group symmetry for structural optimization. The shrinking factor (SHRINK) used for the generation of a Monkhorst−Pack-type grid of *k*-points in reciprocal space was 4 for lattice sizes larger 10 Å, 8 for lattices smaller or equal 10 Å, but larger than 5 Å and 16 for smaller lattice parameters. Tight tolerance factors of 8, 8, 8, 8, and 16 were used for the evaluation of the Coulomb and exchange integrals (TOLINTEG). Default optimization convergence thresholds and an extra-large integration grid (XLGRID) for the density-functional part were applied in all calculations. Another computational study concerned the full structural relaxation of the Si substructure of Li_3NaSi_6. Here the experimental structure of Li_3NaSi_6[11] was first fully optimized and the obtained lattice and Si atomic parameters used as a starting model for subsequent relaxation of an elemental Si structure. This step was performed without any symmetry constraints at DFT-PBE[41]/SVP level of theory. At this point the system was metallic and the Fermi surface was smeared with a width of 0.02 au. For the evaluation of the tolerance and exchange integrals (TOLINTEG), tight criteria of 7, 7, 7, 7, and 14 were used and for the density-functional part, a large integration grid (LGRID) was applied. The geometry optimization starting from the Si substructure in Li_3NaSi_6 naturally resulted in large changes in the geometry. Therefore, the optimization process had to be carried out carefully and was manually restarted several times to enable the reclassification of the two-electron integrals as the geometry became very different from the original geometry. Between the steps, the symmetry had to be lowered to space group *P*1 (1) and too big displacements from one point of the potential surface to the next had to be avoided by the keyword MAXTRADIUS. The resulting minimum structure was subsequently optimized at the DFT-PBE0/SVP level of theory and its space group determined with FINDSYM.[45] Stationary points were confirmed to be minima for all optimized structures by applying frequency calculations.[46,47]

3. RESULTS AND DISCUSSION

Chemical Extraction Experiments with $Li_{15}Si_4$ (Synthesis of *a*-Si). Because the structure of the highly air- and moisture-sensitive silicide $Li_{15}Si_4$ comprises isolated Si atoms that are embedded in a Li matrix,[33] nanoparticulate forms of Si could be obtained by a soft extraction of Li. Hence, chemical delithiation of $Li_{15}Si_4$ was realized using liquid ammonia. The extraction apparatus is shown and described in Figure 2. The blue color of liquid ammonia when condensed onto $Li_{15}Si_4$ powder clearly indicates the formation of solvated electrons (Figure 2b). The formation of a metallic bronze solution,[34] as shown in Figure 2c, typically indicates that Li is extracted. After several extraction cycles solely $LiNH_2$ was identified as crystalline phase in the PXRD pattern of the product (see Figure S2 in the Supporting Information; residual Li content: 21.9(1) wt % Li vs 48.1 wt % in $Li_{15}Si_4$). The IR spectrum essentially only shows NH stretching and HNH deformation modes at 3259 and 1560 cm^{-1}/1538 cm^{-1}, respectively (see Figure S3 in the Supporting Information).[48] Si−O vibrational bands that typically occur at around 800−1100 cm^{-1} and would indicate O impurities are not observed.[14] As the last step, $LiNH_2$ is removed by slowly reacting it with ethanol in a toluene suspension. Acetic acid was used to adjust to acidity as silicon dissolves under alkaline conditions. Alternatively, a buffered solution can be used to remove $LiNH_2$. The delithiation of $Li_{15}Si_4$ is formulated as follows

$$Li_{15}Si_4 \xrightarrow{NH_3} 15(1-x)Li_{NH_3} + 4Si + 15xLiNH_2 + 7.5xH_2$$

As can be seen from the PXRD pattern in Figure S2 in the Supporting Information, the dried black product is amorphous and will be termed *a*-Si in the following.

Chemical extraction experiments with Li_3NaSi_6 (synthesis of *a-allo*-Si). As described in the introduction section, the Zintl phase Li_3NaSi_6 consists of polyanionic layers $^2_\infty[Si_6]^{4-}$ which are separated by Li and Na ions.[11] Previous attempts to deintercalate Li_3NaSi_6 and combine the Si layers topotactically employed protic solvents according to

$$Li_3NaSi_6 + 4ROH \rightarrow 6\ allo\text{-}Si + 2H_2 + 3LiOR + NaOR$$

With water, an almost complete conversion (97%) to *allo*-Si was reported.[10,11] Crystallites of α-Si were found concomitantly.[10,11] Tentative unit-cell parameters for *allo*-Si were reported as orthorhombic, a = 13.29 Å, b = 3.79 Å, c = 12.63 Å.[10] However, the reflection positions calculated from those parameters differ substantially from the diffraction pattern of *allo*-Si compiled in the Powder Diffraction File (PDF 41−1111).

We diligently tried to reproduce the reaction of Li_3NaSi_6 with protic solvents to *allo*-Si. Generally, we found that the reactivity of Li_3NaSi_6 strongly depends on the degree of crystallization (consistent with ref 11). For instance, a thoroughly powdered crystalline sample of Li_3NaSi_6 (see Figure S4a in the Supporting Information) was allowed to react with ethanol for 15 days (Table 1, reaction 2). Thereafter, reflections from Li_3NaSi_6 are still recognizable in the PXRD pattern and the increased background with maxima at $2\theta \approx 28°$ and $\approx 53°$ indicates the presence of an amorphous phase (see Figure S4b in the Supporting Information). In contrast, when using ball-milled Li_3NaSi_6 as starting material (see Figure S5b in the Supporting Information) reactions were completed within several minutes (Table 1, reaction 1). The PXRD pattern of the product shows an amorphous background as well as Bragg reflections of α-Si and Na_8Si_{46} (see Figure S5c in the Supporting Information). This product is termed *a-allo*-Si in the following. The small clathrate impurity may have already been introduced in the synthesis of Li_3NaSi_6 although it is not recognizable in the PXRD pattern of the starting material (overlap of Bragg reflections). It may also be that ball-milling induces a partial decomposition of Li_3NaSi_6 leading to the formation of NaSi, which could be oxidized to form Na_8Si_{46} when treated with protic reagents.

Extraction reactions employing mixtures of 2-propanol and diethyl ether (Table 1, reactions **3**−**5**) yielded amorphous products beside α-Si and unreacted Li_3NaSi_6. In the case of reaction 3 the Li_3NaSi_6 starting material was synthesized in Nb ampules and contained a marginal $NbSi_2$ impurity (confirmed by EDX analysis). Crystalline $NbSi_2$ could not be observed in the PXRD pattern of the starting material but is clearly identified in the PXRD pattern of the oxidation product.

In contrast to alcohols, H_2O and acids rapidly oxidize Li_3NaSi_6 under formation of an amorphous phase. In some cases α-Si and unreacted Li_3NaSi_6 are identified as crystalline phases (Table 1, reactions **7**-**9**). Because all reactions employing protic solvents as oxidative reagents are accompanied by the formation of LiOH and NaOH, the pH value is critical regarding the dissolution of Si. In reaction 10 a $NaHPO_4/KHPO_4$ buffer solution was employed to compensate for the pH increase. We also tried to oxidize Li_3NaSi_6 using a solution of benzophenone in THF. After three months the PXRD pattern of the product showed an increased background and Bragg reflections of $NbSi_2$ and residual Li_3NaSi_6 (Table 1, reaction **11a**). Further oxidation of residual Li_3NaSi_6 with H_2O yielded Li_2SiO_3, Na_2SiO_3, and SiO_2 (**11b**).

In summary, deintercalation of Li_3NaSi_6 with protic solvents leads inevitably to the formation of amorphous products. In most cases, significant amounts of Li_3NaSi_6 remained unreacted. Complete reactions were only achieved with ball-milled starting material. Regardless of reaction conditions for the deintercalation of Li_3NaSi_6, we never observed the reflections reported for *allo*-Si (PDF 41−1111). Also, annealing partially oxidized samples of Li_3NaSi_6 at 300 °C for 2 weeks did not give rise to any new reflections. A closer inspection of the PXRD pattern of *allo*-Si reported in ref 11 and the database entry PDF 41−1111 reveals strong analogies to $NbSi_2$ (see Figure S6 in the Supporting Information). Li_3NaSi_6 employed in ref 11 was synthesized in Nb ampules at temperatures up to 800 °C, which readily explains the formation of $NbSi_2$. According to our experience, the presence of minor concentrations of $NbSi_2$ may not be recognizable in the diffraction pattern of crystalline Li_3NaSi_6 but will uncover in the PXRD pattern of the amorphous product after alkali metal extraction (i.e., reactions **3** and **11a**, Table 1).

Characterization of *a*-Si and *a-allo*-Si. *Elemental Analysis, FT-IR.* IR spectroscopic investigations clearly reveal Si−O vibrational modes for *a*-Si, in particular the Si−O stretching band at around 1069 cm^{-1} (Figure 3), indicating a slight partial surface oxidation.[14] This is additionally strengthened by SEM EDX examinations (see Figure S7 in the Supporting Information) and nanoprobe EDX analysis in the TEM (described below). The oxidation occurs during the removal of $LiNH_2$ with ethanol. According to SEM EDX, the average O content of *a*-Si samples is 12.8 ± 1.9 at. %. A slightly visible band at around 2100 cm^{-1} may indicate the presence of Si−H. However, this band is significantly weaker than observed for hydrogen-capped silicon nanoparticles.[49] Furthermore, traces of Na (<1 at. %) were detected by SEM EDX. The residual Li content in *a*-Si (∼1 wt %) was determined by atomic absorption spectroscopy. C, H, N impurities of *a*-Si samples are marginal (C, H, N < 1.2 wt %). In contrast to *a*-Si, the IR spectrum of *a-allo*-Si is essentially featureless. Si−O bands are barely visible. However, according to SEM EDX analysis *a-allo*-Si samples contain 7.4 ± 1.9 at. % O.

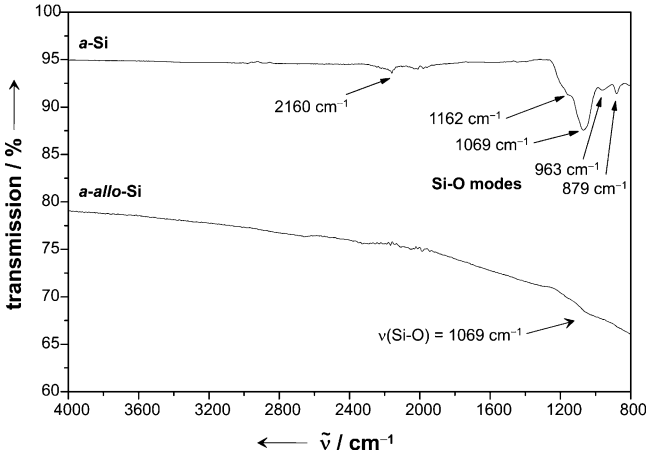

Figure 3. ATR-FT-IR spectra of *a*-Si and *a-allo*-Si.

TEM Analysis. Representative results of the TEM investigations are shown in Figures 4 and 5. The morphology of *a*-Si and *a-allo*-Si samples differs remarkably. Samples *a*-Si show a highly porous microstructure built of agglomerated particles with sizes around 10 nm (Figure 4a). The electron diffraction pattern (Figure 4b) corresponds to faint rings of diffuse intensity which indicates marginal sizes of coherently scattering domains and thus short-range ordering. The diameters of these rings correlate with the d-values of α-Si. HRTEM micrographs (Figure 4c) show the presence of α-Si nanocrystallites with sizes below 5 nm within the thin and electron transparent areas. The oxygen content as determined by nanoprobe EDX was

dx.doi.org/10.1021/cm503371e | *Chem. Mater.* 2014, 26, 6603−6612

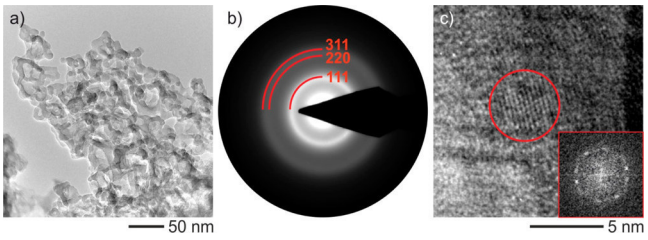

Figure 4. (a) Bright-field micrograph of *a*-Si particles, (b) electron diffraction pattern from *a*-Si sample containing diffuse concentric rings matching with nanocrystalline α-Si, (c) high-resolution micrograph showing crystalline nanoparticle (circled) in amorphous matrix and respective FFT-image showing sharp 111 reflections.

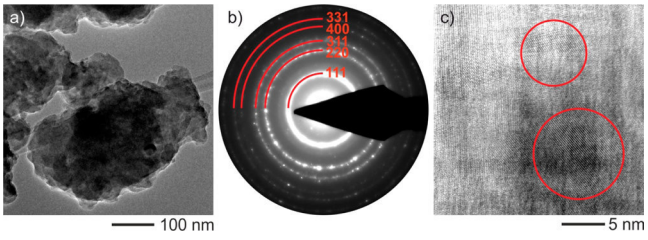

Figure 5. (a) Bright-field micrograph of *a-allo*-Si, (b) electron diffraction pattern from the circled area showing microcrystalline nature of the sample, (c) high-resolution micrograph showing crystalline nanoparticles (circled) in amorphous matrix.

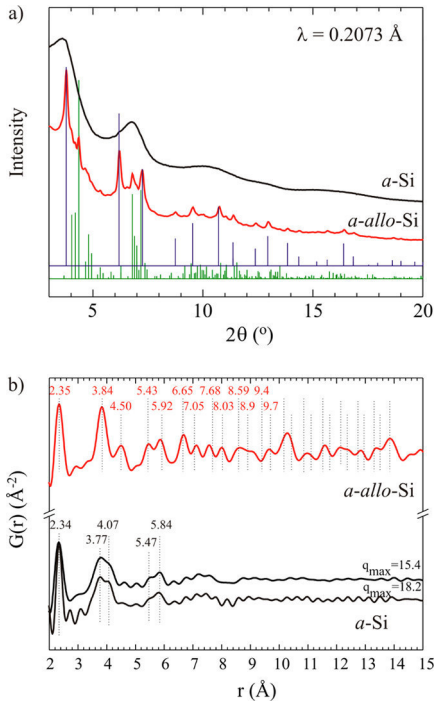

Figure 6. (a) High-energy X-ray diffraction patterns and (b) PDFs for the *a*-Si and *a-allo*-Si materials (λ = 0.20727(6) Å, Q_{max} = 21.0 Å^{-1}).

about 8 at. % on average and up to 40 at. % in thin areas close to the boundary of particles. This agrees roughly with the result of the SEM EDX analysis. The oxygen containing areas do not show any structural ordering, thus, they are not indicated by any prominent intensity within the electron diffraction patterns.

Samples *a-allo*-Si consist of larger particles with minimum sizes of 50 nm (see Figure 5a). These particles contain crystallites of α-Si with sizes large enough to yield coherent scattering (cf. the fully indexed diffraction pattern in Figure 5b). Consequently, the width of the diffraction circles is considerably lower compared to *a*-Si (cf. Figure 4b). Moreover, the diffuse intensities clearly segregate into Bragg intensities as expected for rotationally disordered microcrystals of α-Si. Indeed, HRTEM confirms the presence of α-Si crystallites with sizes up to 10 nm in *a-allo*-Si (Figure 5c). For *a-allo*-Si the average oxygen content as established by nanoprobe EDX was comparable to *a*-Si (ca. 10 at. %), but the maximum value determined on the edges was only 15 at. %.

PXRD Investigations. The high energy diffraction patterns and PDFs for *a*-Si and *a-allo*-Si are compiled in Figure 6. In agreement with the TEM investigations the diffraction pattern of *a*-Si is void of sharp Bragg peaks. Broad maxima are located around 2θ = 4, 7, and 10.5° corresponding to d = 3.28, 1.75, and 1.19 Å, respectively.

The amorphous contribution to the pattern of *a-allo*-Si is modulated by the Bragg peaks of crystalline Si, which again reflects the finding from the TEM analysis. The minimum crystallite size yielding sharp Bragg peaks in X-ray diffraction is 4−5 nm.[50] The diffraction pattern of *a-allo*-Si contains also Bragg peaks from the Na_8Si_{46} impurity. The positions of the peaks in the PDF for *a-allo*-Si closely correspond to the separation of atom pairs in crystalline Si. The PDF for *a*-Si resembles amorphous Si with a sharp first neighbor peak at 2.35 Å and a broad second neighbor peak at 3.8 Å.[51,52] In contrast with amorphous Si this peak is clearly asymmetric. This asymmetry is robust with respect to variations of Q*max* and indicates that the second peak is actually split. An analogous phenomenon has been recently observed and analyzed for amorphous Ge and attributed to a fraction of third neighbors being closer than some second ones, indicating structural relaxation (i.e., deviation from a continuous random network).[53] This interpretation is not applicable for our *a*-Si material which—according to the TEM analysis—represents a mixture of nanocrystalline Si embedded in an amorphous environment. Rather, the PDF for *a*-Si appears as a convolution of amorphous Si and sub-Bragg sized crystallites (2−4 nm). The contribution from the latter dominates the medium range of r (4−8 Å). Indeed the third peak centered at 5.7 Å for amorphous Si[51,52] is clearly split according to crystalline Si (5.47 and 5.86 Å), whereas the faint fourth peak (centered at around 7 Å for amorphous Si)[51,52] may indicate fine structure, mirroring distances from the center of crystallites to their (relaxed) interface with amorphous environment. It is tempting to interpret *a*-Si as paracrystalline Si where the crystallite size is large enough to express with distinct pairs in the PDF.[54] However, because of the partial oxidation of *a*-Si such conclusions remain highly ambiguous. The peaks in the PDF for *a-allo*-Si essentially correspond to crystalline Si, which is expected from the presence of crystallites larger than 5 nm.

Raman Spectroscopy. Figure 7 shows Raman spectra for *a*-Si and *a-allo* Si, respectively. Focusing first on *a*-Si (Figure 7a), the majority of observed spectra correspond to amorphous Si characterized by a broad maximum at 460−470 cm^{-1} (the TO_1 band), weaker bands at 380 and 300 cm^{-1} assigned to LO and LA, respectively, and a pronounced TA like band at low wavenumbers. Occasionally spectra characteristic of nanocrystalline (*nc*) Si (2−4 nm crystallite size) could also be obtained. Those display a sharp and asymmetric TO_2 peak at 500 cm^{-1}.[55] It is important to note that spectra of amorphous and *nc*-Si can only be observed when applying the lowest

dx.doi.org/10.1021/cm503371e | *Chem. Mater.* 2014, 26, 6603−6612

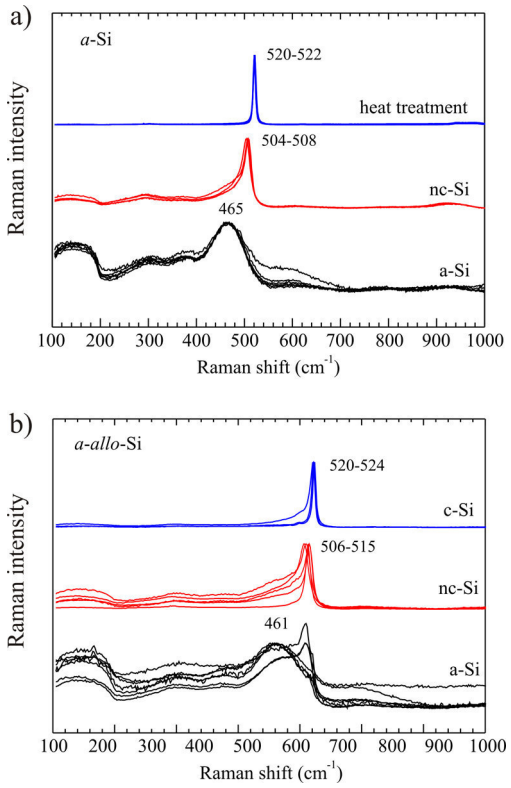

Figure 7. Raman spectra for (a) *a*-Si and (b) *a-allo*-Si. The spectra in the upper panel in a) were obtained from different parts of the a-Si sample after increasing the laser power.

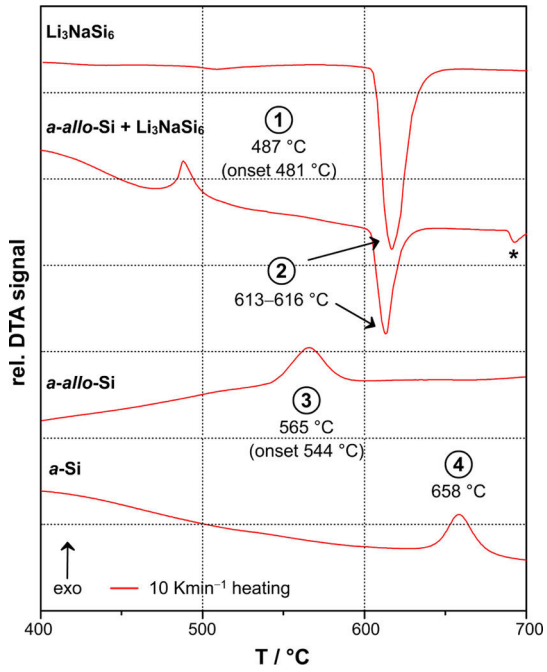

Figure 8. First DTA heating traces of thermograms recorded for Li_3NaSi_6, partially oxidized Li_3NaSi_6 (Li_3NaSi_6/*a-allo*-Si mixture), *a-allo*-Si, and *a*-Si (T_{max} = 750 °C, ±10 K min^{-1} heating/cooling rate, heat effects marked with * could not be assigned).

possible power density (0.56 W/5.5 × 10^{-6} mW μm^{-2}). Amorphous spectra did not change with time whereas *nc*-Si spectra showed well-known variations attributed to temperature increase.[56,57] When increasing laser power, amorphous and *nc*-Si spectra convert into a spectrum characteristic for (bulk) crystalline Si. The sharp and symmetric peak of the TO_2 band shifts to 519−521 cm^{-1} and only varies slightly with temperature. The two phonon contributions at lower wavenumbers are absent.

Raman spectra for the *a-allo*-Si sample (Figure 7b) mirror the three constituents of this sample. First there are spectra reflecting a solely amorphous state. However, these spectra were frequently convoluted with contribution from *nc*-Si. Note that the shape of such spectra has been considered to be typical of paracrystalline Si.[50] Vice versa, spectra of *nc*-Si with a pronounced asymmetry stemming from an amorphous silicon contribution were recorded. Finally, we also obtained spectra corresponding to bulk crystalline Si. Those spectra are attributed to Si crystallites with a size larger than 5 nm. Accordingly, *a-allo*-Si contains α-Si crystallites with a large size variation (2 to ∼10 nm), whereas α-Si crystallites in *a*-Si have sub-Bragg size (2−4 nm).

DTA Investigations. The amorphous-to-crystalline phase transition of *a*-Si and *a-allo*-Si was investigated by differential thermal analysis. Figure 8 shows the first heating traces for (i) Li_3NaSi_6, (ii) partially deintercalated Li_3NaSi_6 (i.e., a mixture of Li_3NaSi_6 and *a-allo*-Si), (iii) *a-allo*-Si, and (iv) *a*-Si. Li_3NaSi_6 decomposes at around 600 °C (effect 2) into $Li_{12}Si_7$, NaSi, and α-Si (see Figure S8 in the Supporting Information). For the Li_3NaSi_6/*a-allo*-Si mixture, an additional exothermic effect is observed at 487 °C (effect 1). Comparing the PXRD patterns of the pure Li_3NaSi_6 sample and the Li_3NaSi_6/*a-allo*-Si mixture after DTA investigations (see Figures S4c and S8 in the Supporting Information), the latter clearly reveals larger portions of α-Si. The heating trace of the *a-allo*-Si sample only contains an irreversible exothermic effect that is markedly shifted to higher temperatures (effect 3 at 565 °C). The subsequently recorded PXRD pattern corresponds to α-Si (see Figure S5d in the Supporting Information). Thus, effect 1 and 3 are attributed to the amorphous-to-crystalline transition of *a-allo*-Si. The temperatures for the Li_3NaSi_6/*a-allo*-Si mixture and the *a-allo*-Si sample embrace the reported phase transition of *allo*-Si at ∼527 °C.[11]

The variation in temperature is ascribed to different concentrations of sub-Bragg sized nanocrystals (2−4 nm), that is the presence of different concentrations of crystallization nuclei in both samples. We assume that in *a*-Si the concentration of sub-Bragg sized crystallites is considerably smaller than in *a-allo*-Si. The phase transition of *a*-Si occurs at 658 °C (effect 4) which is similar to amorphous silicon obtained from ball milling at a heating rate of 40 K min^{-1}, but lower than the crystallization temperature for ion-implanted amorphous silicon (around 690 °C).[58,59] Thus, for *a*-Si, nucleation (i.e., the formation of a critical concentration of critically sized nuclei) has to be induced prior to the transition, which explains the shift to higher temperatures. It is interesting to note that when heating individual particles of both *a*-Si and *a-allo*-Si in the TEM, crystallization is not observed below 700 °C (cf. Supporting Information, Figures S9 and S10).

Allotropism of Si (Or How Feasible is *allo*-Si?). As described above, the existence of a crystalline allotropic form of silicon obtained from Li_3NaSi_6 through oxidation is highly questionable. This is in contrast to *m-allo*-Ge, which is readily prepared from delithiating Li_7Ge_{12}. Both Li_7Ge_{12} and Li_3NaSi_6 possess two-dimensional polyanions with five-membered rings, yet their topotactic combination leads to different branches of three-dimensional structures. According to Conesa, the

dx.doi.org/10.1021/cm503371e | *Chem. Mater.* 2014, 26, 6603−6612

combination of layers in Li_7Ge_{12} results in "**G**" structures, whereas "**S**" structures are derived from Li_3NaSi_6.[32]

The two-dimensional slabs $^2_\infty[Si_6]^{4-}$ in Li_3NaSi_6 are built of four (4b), three (3b), and two (2b) bonded Si atoms, respectively (cf. Figure 9). Based on this structure, Conesa's

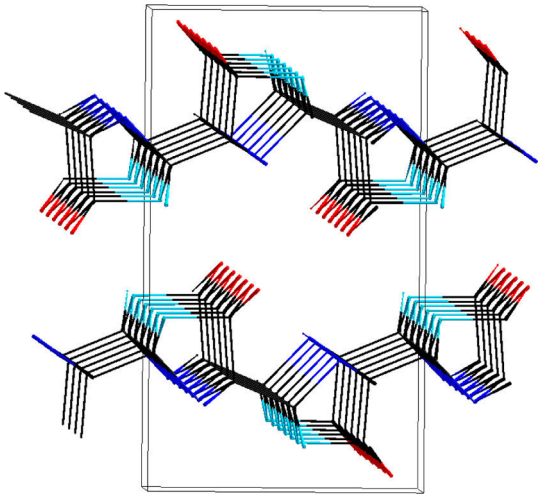

Figure 9. Si substructure in the phase Li_3NaSi_6. The four (Si^0), three (Si^-), and two (Si^{2-}) connected Si atoms are shown in black, light/dark blue, and red, respectively. For the four different groups of *allo*-Si networks derived from this layered structure, the charged atoms are connected differently.

S group follows, which can be divided into four smaller structure groups. The **SA** group is built by connecting 2b-Si atoms (red) of neighboring layers and bonding them to 3b-Si atoms of their own layers (dark blue). The light blue 3b-Si atoms are bonded to the light blue ones of the neighboring layer. **SB** is a connection of red Si^{2-} atoms (2b) with light blue Si^- atoms (3b) of the neighboring layer and dark blue Si^- atoms (3b) of their own layer. For structures **SC**, the 2b-Si^{2-} atoms are connected to dark blue 3b-Si^- atoms and to the red Si^{2-} of the neighboring layer. The 3b-Si^- atoms (light blue) are connected to the same kind of the next layer. For each of these types four structure variations exist. The fourth group **SD** is built by connecting red Si^{2-} atoms (2b) to both Si^- atoms (3b) of the next layer. For such a network, only one structure type is possible, the **TON** zeolite-type network (ZSM-22).

A comparison of total energies of the computationally relaxed Conesa **S**-type Si structures (Figure 10) shows that **SD** is the favored structure with an energy difference to α-Si of 13.7 kJ (mol Si)$^{-1}$ (Si–Si distances, 2.34–2.40 Å; angles, 90.7–142.9°; crystallographic density, 2.011 g cm^{-3}, Figure 11a). Its

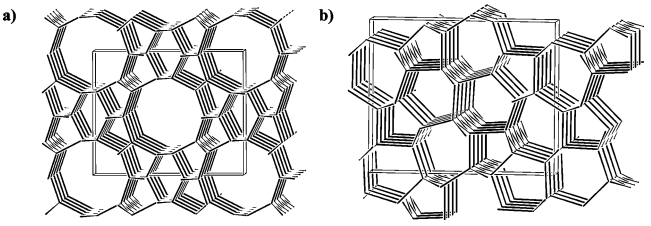

Figure 11. (a) Most stable network (**SD**) derived from the Si substructure of Li_3NaSi_6 with view along the *c*-direction emphasizing the one-dimensional channel structure built from 10-, 6-, and 5-membered rings; (b) network of the structure **SC1** with view along the *a*-direction. It is built of 6- and 5-membered rings.

structure has the lowest density of all **G** and **S** group networks and is equivalent to the zeolite network **TON**. As shown in Figure 11a it contains 10-, 6-, and 5-membered rings which form parallel channels proceeding along the *c*-axis. The diameter of the largest channel ranges from 6.6 to 7.4 Å. In energy, this framework is followed by **SC1** (Figure 11b) with a relative energy of 14.0 kJ (mol Si)$^{-1}$. Si–Si distances vary from 2.31 to 2.43 Å and angles range from 92.0 to 128.4°. The crystallographic density of this structure is 2.292 g cm^{-3} which is close to that of α-Si (2.290 g cm^{-3}). **SC1** also displays one-dimensional channels, which run along the *a* direction and are based on 6- and 5-membered rings (Figure 11b).

To simulate computationally the topotactic recombination of Si layers in Li_3NaSi_6 (cf. Figure 9) to *allo*-Si, we carried out a full relaxation of the Si substructure in Li_3NaSi_6 without any symmetry restrictions. This resulted in a true local minimum with *Cmcm* space group symmetry being the **TON** (**SD**)

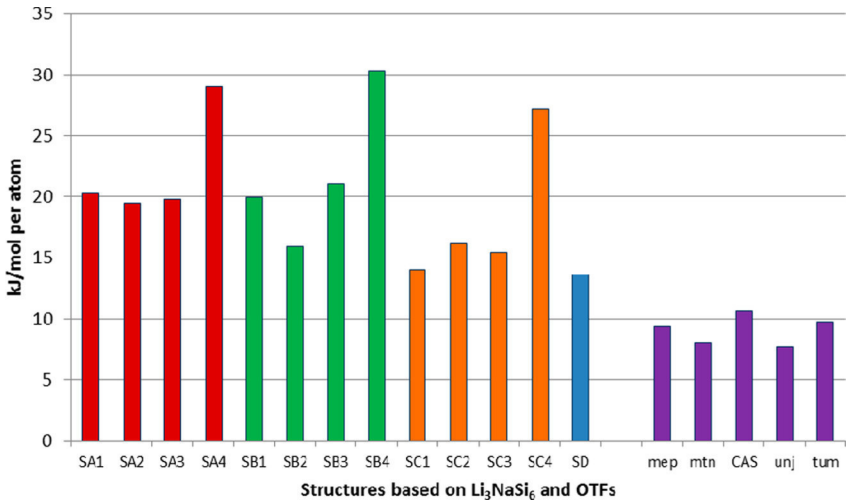

Figure 10. Energies relative to α-Si for Conesa's **S**-type structures (derived from the Si substructure of Li_3NaSi_6). The four different network classes are colored differently; **SA** in red, **SB** in green, **SC** in orange, and **SD** in blue. The energy difference to well-known open tetrahedral frameworks[60] is depicted as well (violet). All relative energies are also listed in Table S1 in the Supporting Information.

dx.doi.org/10.1021/cm503371e | *Chem. Mater.* 2014, 26, 6603–6612

structure, which was also the favored of all "handmade" structures of Conesa, highlighting the key role of this network. Furthermore, the structure with the smallest density is favored in the present structural relaxation without any initial specification of Si−Si bonds.

Importantly, the most favorable structures that follow from the combination of two-dimensional slabs $^{2}_{\infty}[Si_6]^{4-}$ are rather high in energy, around 14 kJ (mol Si)$^{-1}$ with respect to the ground state structure of Si (α-Si). Several clathratic and zeolitic open tetrahedral frameworks have a considerably lower energy and are only by about 7 kJ (mol Si)$^{-1}$ less stable than α-Si. Such frameworks are also included in Figure 10. As already shown earlier the clathrate-II framework **mtn** and the chiral **unj** framework appear most favorable as Si allotropes.[61,62] The crystallographic densities of those frameworks are lower compared to the "**S**" structures and range from 1.979 g cm^{-3} (**mtn**) to 2.180 g cm^{-3} (**tum**) (see Table S1 in the Supporting Information). In contrast the total energies of Conesa "**G**" structures (derived from Li_7Ge_{12} layers) compare closely with the clathratic and zeolitic frameworks (cf. Figure S11, Table S1 in the Supporting Information) and are favored over the "**S**" structures derived from Li_3NaSi_6. This strongly supports the experimental observation that Li_3NaSi_6 is not a suitable precursor for topotactic formation of *allo*-Si, whereas *allo*-Ge is readily obtained from Li_7Ge_{12}.

CONCLUSION

Alkali metal extraction reactions with the silicides $Li_{15}Si_4$ and Li_3NaSi_6 lead to amorphous products termed *a*-Si and *a-allo*-Si, respectively. *a*-Si possesses a porous microstructure which is built from spherically shaped particles with a diameter of around 10 nm. The amorphous particles contain sub-Bragg sized (below 5 nm) Si crystallites which are revealed in TEM investigations and Raman spectroscopy. They have a partially oxidized surface, which is introduced in the purification process of *a*-Si. Extraction reactions with $Li_{15}Si_4$ chemically emulate the delithiation process occurring in silicon-based lithium batteries. The porous microstructure of *a*-Si might bear close resemblance with electrochemically obtained amorphous Si.

a-allo-Si does not display a distinguished microstructure but consists of irregularly shaped particles with sizes larger than 50 nm. These particles contain sub-Bragg-sized and Bragg-sized crystallites with sizes up to 10 nm. The considerably lower crystallization temperature of *a-allo*-Si (around 570 °C) compared to *a*-Si (around 660 °C) suggests that the concentration of sub-Bragg-sized particles (acting as crystallization nuclei) is significantly larger in the former material. The formation of *a-allo-Si* from Li_3NaSi_6 contradicts earlier findings, reporting the formation of a crystalline bulk allotrope of silicon (*allo*-Si) from the topotactic combination of silicon layers present as polyanions in Li_3NaSi_6. Quantum chemical calculations show that the combination of Li_3NaSi_6 silicon layers does not lead to energetically favorable allotropic forms of Si. This is different to Li_7Ge_{12}, where polyanionic germanium layers topotactically convert to the germanium allotrope *m-allo*-Ge upon oxidation.

The alkali metal extraction reactions reported herein expand the methods for the fabrication of small nanoparticles. Further examples include the first commonly recognized successful production of Si nanoclusters capped with alkyl groups[63] via $SiCl_4 + RSiCl_3 + Na \rightarrow Si + NaCl$ and the magnesiothermic reduction of silica[64] to form porous nanostructured Si, which was investigated as potential anode material.[65] In addition, small uncapped Si nanoparticles of 5−20 nm can be obtained without aggregation using a reverse micelles technique also showing a SiO_2 coverage. The decreased particle size of Si enhances the cycling stability of Si anodes. Using conductive additives, reversible capacities above 2000 mAh g^{-1} were achieved with particles in the range of 5 to 20 nm. Smaller particles, however, increase the irreversible capacity losses.[66]

ASSOCIATED CONTENT

Supporting Information

PXRD patterns of Li_3NaSi_6 samples from different reactions (Figure S1), PXRD patterns of (a) $Li_{15}Si_4$ bulk material, the sequential products after (b) Li-extraction with liquid ammonia, (c) subsequent treatment with ethanol, and (d) differential thermal analysis (Figure S2), ATR-FT-IR spectra of the *a*-Si/$LiNH_2$ mixture obtained after Li extraction from $Li_{15}Si_4$ (Figure S3), PXRD patterns of Li_3NaSi_6, the product after partial oxidation with ethanol and subsequent DTA-investigation (Figure S4), PXRD patterns of Li_3NaSi_6 before and after ball-milling, the product after treatment with ethanol/HCl and subsequent DTA investigation (Figure S5), PXRD pattern of a $NbSi_2$ sample referenced with the database entry for *allo*-Si and $NbSi_2$ (Figure S6), results from EDX investigations of *a*-Si (Figure S7), Rietveld fit to the PXRD pattern of Li_3NaSi_6 after DTA (Figure S8), results from TEM heating experiments of *a*-Si and *a-allo*-Si (Figures S9 and S10), comparison of the total energies of networks optimized on the basis of Conesa's **G**-type structures (Figure S11), DFT-PBE0 results in tabular format (Table S1), and basis sets for Na and Li employed in the theoretical calculations. This material is available free of charge via the Internet at http://pubs.acs.org.

AUTHOR INFORMATION

Corresponding Author

*E-mail: Thomas.Faessler@lrz.tum.de.

Notes

The authors declare no competing financial interest.

ACKNOWLEDGMENTS

This work has been funded by the Deutsche Forschungsgemeinschaft project number FA 198/11−1, Academy of Finland (Grant 138560/2010), as well as the National Science Foundation through Grant DMR-1007557. M.Z. and L.M.S. thank the Fonds der Chemischen Industrie for their fellowships. L.A.J. is grateful for her Christiane Nüsslein-Volhard Stiftung fellowship. M.Z. thanks F. Kraus for providing the custom-built extractor. This work was also supported by the Swedish Research Council through grants 2010-4827 and 2011-6512. The authors acknowledge PETRA III, DESY (Hamburg), for provision of synchrotron radiation beamtime and thank Drs Hanns-Peter Liermann and Jozef Bednarcik for assistance in using beamline P02.1.

REFERENCES

(1) Okamoto, H.; Sugiyama, Y.; Nakano, H. *Chem.—Eur. J.* **2011**, *17*, 9864.
(2) Miles, R. W.; Zoppi, G.; Forbes, I. *Mater. Today* **2007**, *10*, 20.
(3) Sun, D.; Riley, A. E.; Cadby, A. J.; Richman, E. K.; Korlann, S. D.; Tolbert, S. H. *Nature* **2006**, *441*, 1126.
(4) Armatas, G. S.; Kanatzidis, M. G. *Science* **2006**, *313*, 817.
(5) Armatas, G. S.; Kanatzidis, M. G. *Nature* **2006**, *441*, 1122.
(6) Armatas, G. S.; Kanatzidis, M. G. *Adv. Mater.* **2008**, *20*, 546.

(7) Armatas, G. S.; Kanatzidis, M. G. *J. Am. Chem. Soc.* **2008**, *130*, 11430.
(8) Grüttner, A. *Dissertation*, Universität Stuttgart, Stuttgart, Germany, 1982.
(9) Grüttner, A.; Nesper, R.; von Schnering, H. G. *Angew. Chem., Int. Ed.* **1982**, *21*, 912.
(10) Schwarz, M. *Dissertation*, Universität Stuttgart, Stuttgart, Germany, 1988.
(11) von Schnering, H. G.; Schwarz, M.; Nesper, R. *J. Less-Common Met.* **1988**, *137*, 297.
(12) Kiefer, F.; Hlukhyy, V.; Karttunen, A. J.; Fässler, T. F.; Gold, C.; Scheidt, E. W.; Scherer, W.; Nylen, J.; Häussermann, U. *J. Mater. Chem.* **2010**, *20*, 1780.
(13) Kiefer, F.; Karttunen, A. J.; Döblinger, M.; Fässler, T. F. *Chem. Mater.* **2011**, *23*, 4578.
(14) Wang, J.; Ganguly, S.; Sen, S.; Browning, N. D.; Kauzlarich, S. M. *Polyhedron* **2013**, *58*, 156.
(15) Meillaud, F.; Shah, A.; Droz, C.; Vallat-Sauvain, E.; Miazza, C. *Sol. Energy Mater. Sol. Cells* **2006**, *90*, 2952.
(16) Iwamura, S.; Nishihara, H.; Kyotani, T. *J. Power Sources* **2013**, *222*, 400.
(17) Szczech, J. R.; Jin, S. *Energy Environ. Sci.* **2011**, *4*, 56.
(18) Kim, H.; Seo, M.; Park, M.-H.; Cho, J. *Angew. Chem., Int. Ed.* **2010**, *49*, 2146.
(19) Obrovac, M. N.; Christensen, L. *Electrochem. Solid-State Lett.* **2004**, *7*, A93.
(20) Hatchard, T. D.; Dahn, J. R. *J. Electrochem. Soc.* **2004**, *151*, A838.
(21) Key, B.; Bhattacharyya, R.; Morcrette, M.; Seznec, V.; Tarascon, J. M.; Grey, C. P. *J. Am. Chem. Soc.* **2009**, *131*, 9239.
(22) Key, B.; Morcrette, M.; Tarascon, J. M.; Grey, C. P. *J. Am. Chem. Soc.* **2011**, *133*, 503.
(23) Ammar, A.; Cros, C.; Pouchard, M.; Jaussaud, N.; Bassat, J. M.; Villeneuve, G.; Duttine, M.; Menetrier, M.; Reny, E. *Solid State Sci.* **2004**, *6*, 393.
(24) Guloy, A. M.; Ramlau, R.; Tang, Z.; Schnelle, W.; Baitinger, M.; Grin, Y. *Nature* **2006**, *443*, 320.
(25) Kautsky, H.; Haase, L. *Z. Naturforsch.* **1953**, *B8*, 45.
(26) Kautsky, H.; Haase, L. *Chem. Ber.* **1953**, *86*, 1226.
(27) Tchalala, M. R.; Ali, M. A.; Enriquez, H.; Kara, A.; Lachgar, A.; Yagoubi, S.; Foy, E.; Vega, E.; Bendounan, A.; Silly, M. G.; Sirotti, F.; Nitshe, S.; Chaudanson, D.; Jamgotchian, H.; Aufray, B.; Mayne, A. J.; Dujardin, G.; Oughaddou, H. *J. Phys.: Condens. Matter* **2013**, *25*, No. 442001.
(28) McMillan, P. F.; Gryko, J.; Bull, C.; Arledge, R.; Kenyon, A. J.; Cressey, B. A. *J. Solid State Chem.* **2005**, *178*, 937.
(29) Annou, K.; Pelosi, M.; Gershinsky, G.; Favier, F.; Cuminal, Y.; Tillard, M.; Zitoun, D. *Mater. Renew. Sustain. Energy* **2014**, *3*, 32.
(30) Kiefer, F.; Fässler, T. F. *Solid State Sci.* **2011**, *13*, 636.
(31) Zaikina, J. V.; Muthuswamy, E.; Lilova, K. I.; Gibbs, Z. M.; Zeilinger, M.; Snyder, G. J.; Fässler, T. F.; Navrotsky, A.; Kauzlarich, S. M. *Chem. Mater.* **2014**, *26*, 3263.
(32) Conesa, J. C. *J. Phys. Chem. B* **2002**, *106*, 3402.
(33) Zeilinger, M.; Baran, V.; van Wüllen, L.; Häussermann, U.; Fässler, T. F. *Chem. Mater.* **2013**, *25*, 4113.
(34) Zurek, E.; Edwards, P. P.; Hoffmann, R. *Angew. Chem., Int. Ed.* **2009**, *48*, 8198.
(35) Kiefer, F. *Dissertation*, Technische Universität München, Munich, Germany, 2010.
(36) *TOPAS—Rietveld Software*, version 4.0; Bruker AXS: Madison, WI, 2009.
(37) Hammersley, A. P.; Svensson, S. O.; Hanfland, M.; Fitch, A. N.; Häusermann, D. *J. High Pressure Res.* **1996**, *14*, 235.
(38) Juhás, P.; Davis, T.; Farrow, C. L.; Billinge, S. J. L. *J. Appl. Crystallogr.* **2013**, *46*, 560.
(39) *Netzsch Proteus Thermal Analysis*, version 4.8.2; Netzsch-Gerätebau: Selb, Germany, 2006.
(40) *Resolution Pro*, version 5.1.0.822; Varian: Santa Clara, CA, 2009.
(41) Perdew, J. P.; Burke, K.; Ernzerhof, M. *Phys. Rev. Lett.* **1996**, *77*, 3865.
(42) Adamo, C.; Barone, V. *J. Chem. Phys.* **1999**, *110*, 6158.
(43) Dovesi, R.; Orlando, R.; Civalleri, B.; Roetti, C.; Saunders, V. R.; Zicovich-Wilson, C. M. *Z. Kristallogr.* **2005**, *220*, 571.
(44) Karttunen, A. J.; Fässler, T. F.; Linnolahti, M.; Pakkanen, T. A. *Inorg. Chem.* **2011**, *50*, 1733.
(45) Stokes, H. T.; Hatch, D. M. *J. Appl. Crystallogr.* **2005**, *38*, 237.
(46) Zicovich-Wilson, C. M.; Pascale, F.; Roetti, C.; Saunders, V. R.; Orlando, R.; Dovesi, R. *J. Comput. Chem.* **2004**, *25*, 1873.
(47) Pascale, F.; Zicovich-Wilson, C. M.; Gejo, F. L.; Civalleri, B.; Orlando, R.; Dovesi, R. *J. Comput. Chem.* **2004**, *25*, 888.
(48) Bohger, J. P. O.; Essmann, R. R.; Jacobs, H. *J. Mol. Struct.* **1995**, *348*, 325.
(49) Neiner, D.; Kauzlarich, S. M. *Chem. Mater.* **2010**, *22*, 487.
(50) Voyles, P. M.; Zotov, N.; Nakhmanson, S. M.; Drabold, D. A.; Gibson, J. M.; Treacy, M. M. J.; Keblinski, P. *J. Appl. Phys.* **2001**, *90*, 4437.
(51) Laaziri, K.; Kycia, S.; Roorda, S.; Chicoine, M.; Robertson, J. L.; Wang, J.; Moss, S. C. *Phys. Rev. B* **1999**, *60*, 13520.
(52) Laaziri, K.; Kycia, S.; Roorda, S.; Chicoine, H.; Robertson, J. L.; Wang, J.; Moss, S. C. *Phys. Rev. Lett.* **1999**, *82*, 3460.
(53) Roorda, S.; Martin, C.; Droui, M.; Chicoine, M.; Kazimirov, A.; Kycia, S. *Phys. Rev. Lett.* **2012**, *108*, 255501.
(54) The paracrystalline model is a revision of the continuous random network model and is defined as highly strained, microcrystalline grains surrounded by fully amorphous material. In contrast to a microcrystalline phase, the paracrystalline model lacks defined grain boundaries. See ref 50.
(55) Duan, Y.; Kong, J. F.; Shen, W. Z. *J. Raman Spectrosc.* **2012**, *43*, 756.
(56) Mishra, P.; Jain, K. P. *Phys. Rev. B* **2000**, *62*, 14790.
(57) Nikolenko, A. S. *Semicond. Phys. Quantum Electron. Optoelectron.* **2013**, *16*, 86.
(58) Shen, T. D.; Koch, C. C.; McCormick, T. L.; Nemanich, R. J.; Huang, J. Y.; Huang, J. G. *J. Mater. Res.* **1995**, *10*, 139.
(59) Poate, J. M. *Nucl. Instrum. Methods* **1983**, *209/210*, 211.
(60) Zeilinger, M.; van Wüllen, L.; Benson, D.; Kranak, V. F.; Konar, S.; Fässler, T. F.; Häussermann, U. *Angew. Chem., Int. Ed.* **2013**, *52*, 5978.
(61) Pickard, C. J.; Needs, R. J. *Phys. Rev. B* 2010, *81*.
(62) Zwijnenburg, M. A.; Jelfs, K. E.; Bromley, S. T. *Phys. Chem. Chem. Phys.* **2010**, *12*, 8505.
(63) Heath, J. R. *Science* **1992**, *258*, 1131.
(64) Bao, Z.; Weatherspoon, M. R.; Shian, S.; Cai, Y.; Graham, P. D.; Allan, S. M.; Ahmad, G.; Dickerson, M. B.; Church, B. C.; Kang, Z.; Abernathy, H. W., III; Summers, C. J.; Liu, M.; Sandhage, K. H. *Nature* **2007**, *446*, 172.
(65) Yu, Y.; Gu, L.; Zhu, C.; Tsukimoto, S.; van Aken, P. A.; Maier, J. *Adv. Mater.* **2010**, *22*, 2247.
(66) Kim, H.; Seo, M.; Park, M.-H.; Cho, J. *Angew. Chem., Int. Ed.* **2010**, *49*, 2146.

SUPPORTING INFORMATION

Alkaline metal extraction reactions with the silicides $Li_{15}Si_4$ and Li_3NaSi_6: amorphous Si *vs. allo*-Si

Michael Zeilinger[a], Laura-Alice Jantke[a], Lavinia M. Scherf[a], Florian J. Kiefer[a], Gero Neubüser[b], Lorenz Kienle[b], Antti J. Karttunen[c], Sumit Konar[d], Ulrich Häussermann[d], Thomas F. Fässler[a,*]

[a]Department of Chemistry, Technische Universität München, Lichtenbergstraße 4, 85747 Garching b. München, Germany

[b]Technical Faculty, Christian-Albrechts-University, Kiel, Kaiserstrasse 2, 24143 Kiel, Germany

[c]Department of Chemistry, Aalto University, FI-00076 Aalto, Finland

[d]Department of Materials and Environmental Chemistry, Stockholm University, 10691 Stockholm, Sweden

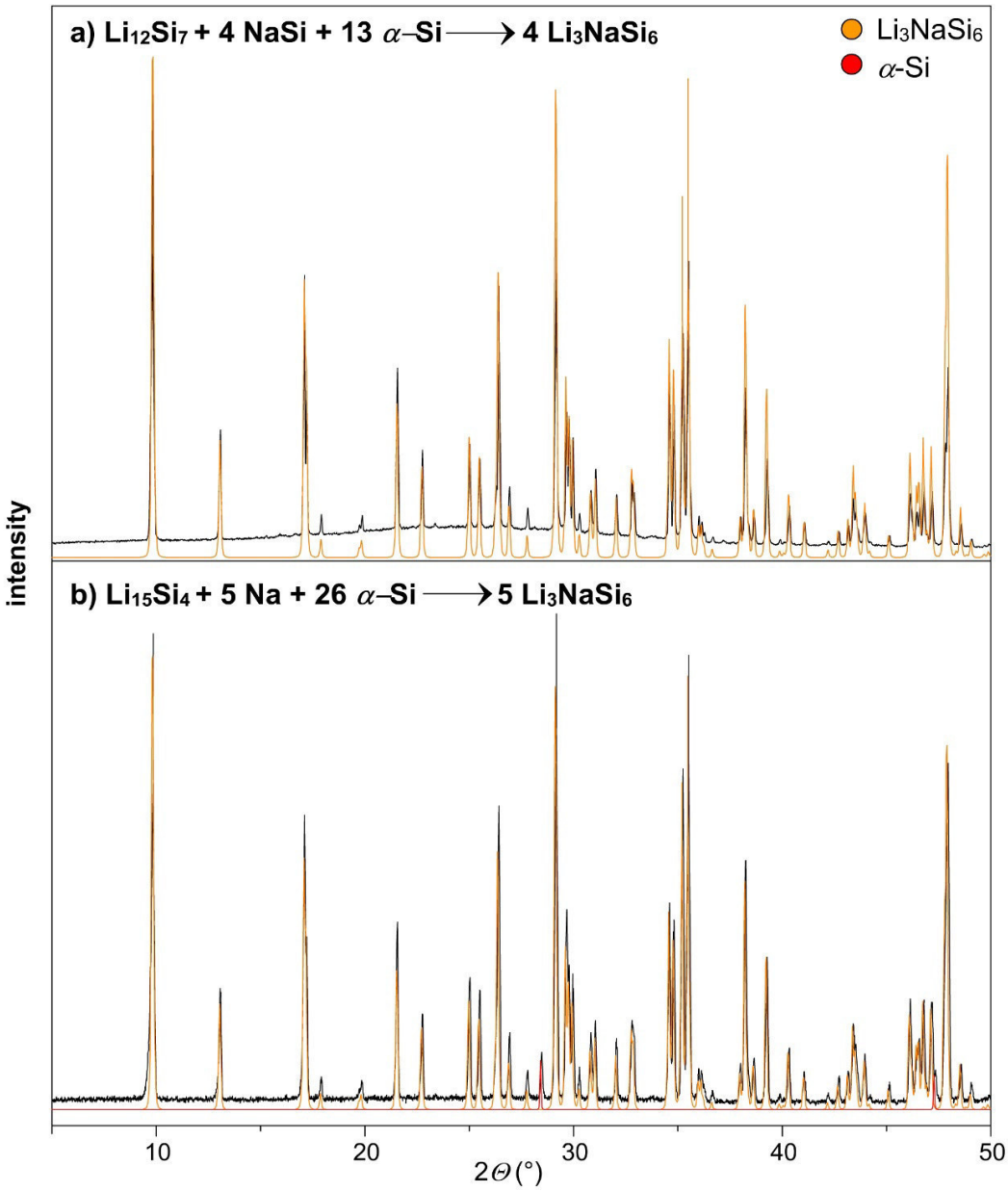

Figure S1. PXRD patterns of Li_3NaSi_6 synthesized from a) a mixture of $Li_{12}Si_7$, NaSi and α-Si and b) a ball-milled mixture of $Li_{15}Si_4$, Na and α-Si (Li_3NaSi_6 (calc.) = orange, α-Si (calc.) = red).

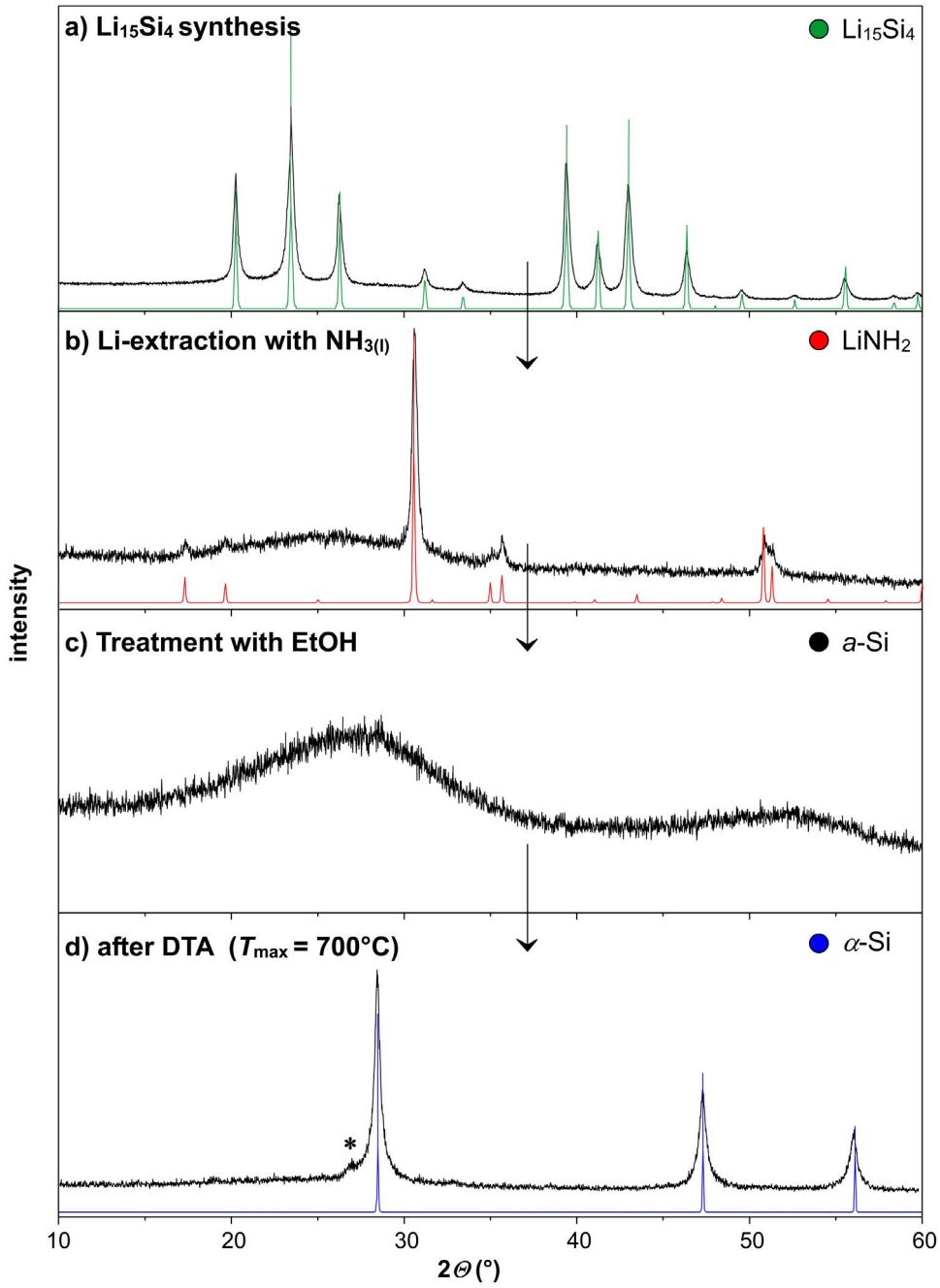

Figure 2. PXRD patterns of a) $Li_{15}Si_4$ bulk material, the sequential products after b) Li-extraction with liquid ammonia, c) subsequent treatment with ethanol, and d) differential thermal analysis (calculated patterns for $Li_{15}Si_4$, $LiNH_2$, and α–Si are shown in green, red and blue, respectively; * corresponds to the (111)-reflection of Li_2SiO_3).

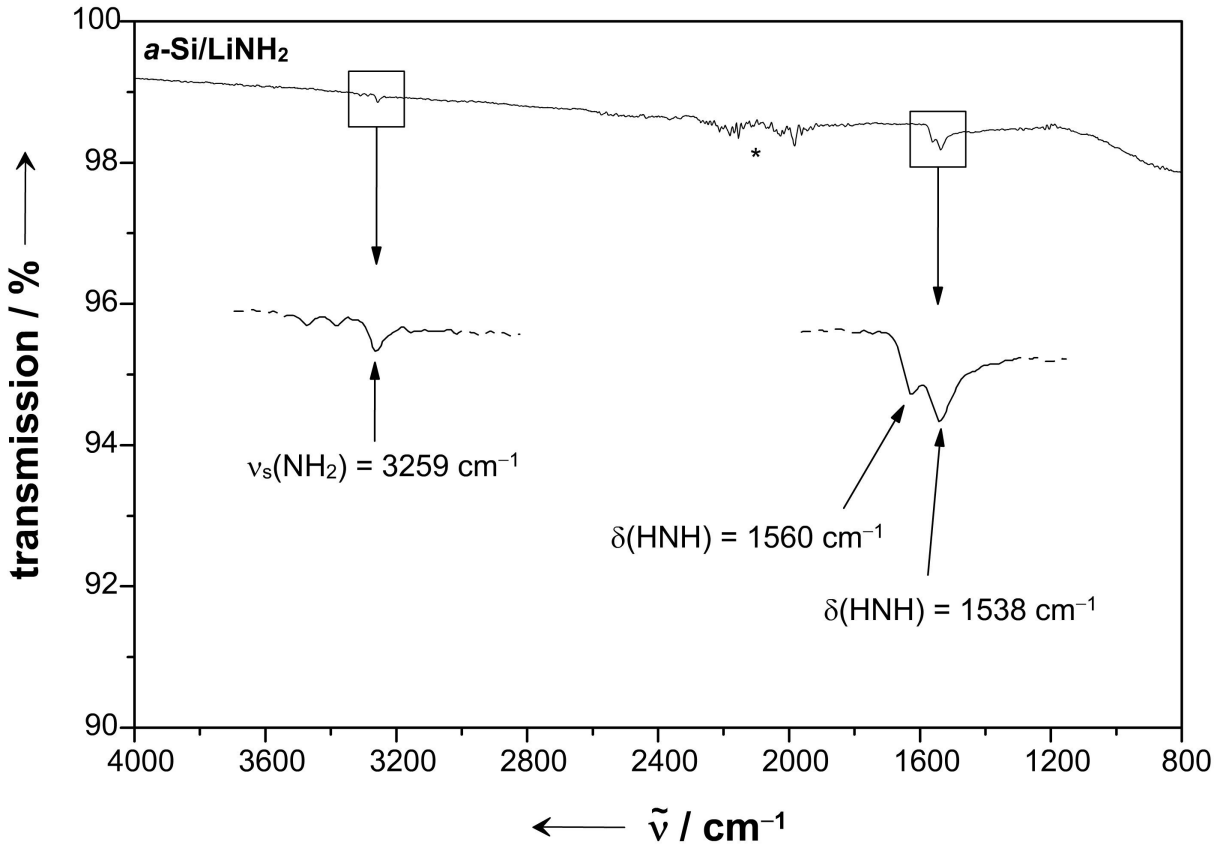

Figure S3. ATR-FT-IR spectrum recorded for the *a*-Si/$LiNH_2$ intermediate after Li extraction from $Li_{15}Si_4$ (*self-absorption of diamond).

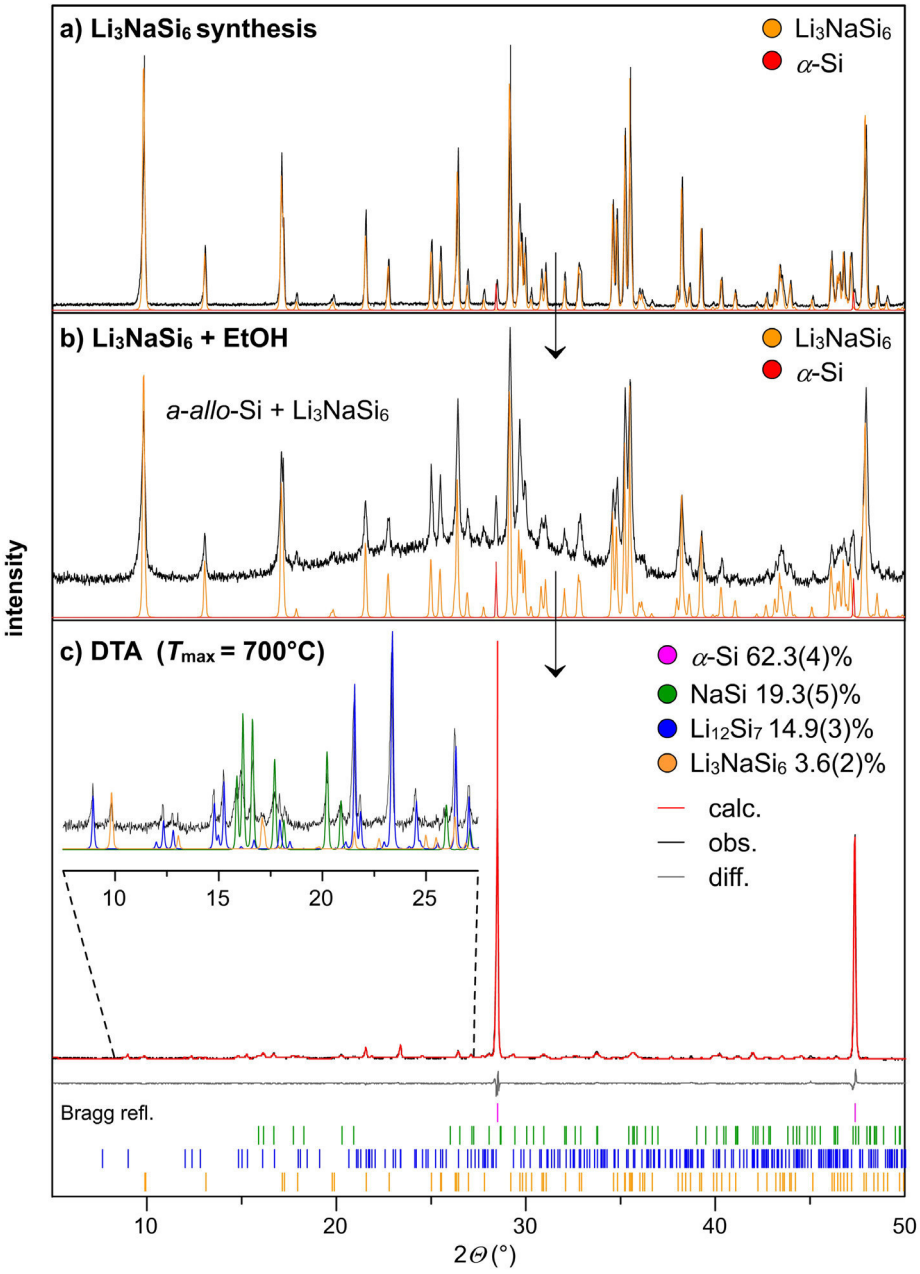

Figure S4. PXRD patterns of a) Li_3NaSi_6 (synthesized from $Li_{15}Si_4$, Na and α-Si), b) the product after partial oxidation with ethanol (reaction time: 15 days) and c) subsequent DTA-investigation ($T_{max.}$ = 700 °C, ±10 K·min^{-1} heating/cooling rate; calculated patterns for Li_3NaSi_6, α-Si, NaSi, and $Li_{12}Si_7$ are shown in orange, red/pink, green and blue). For the PXRD pattern shown in (c), a Rietveld fit was applied giving the weight fractions of all components (R_p = 5.82, R_{wp} = 8.12, *GOF* = 1.56).

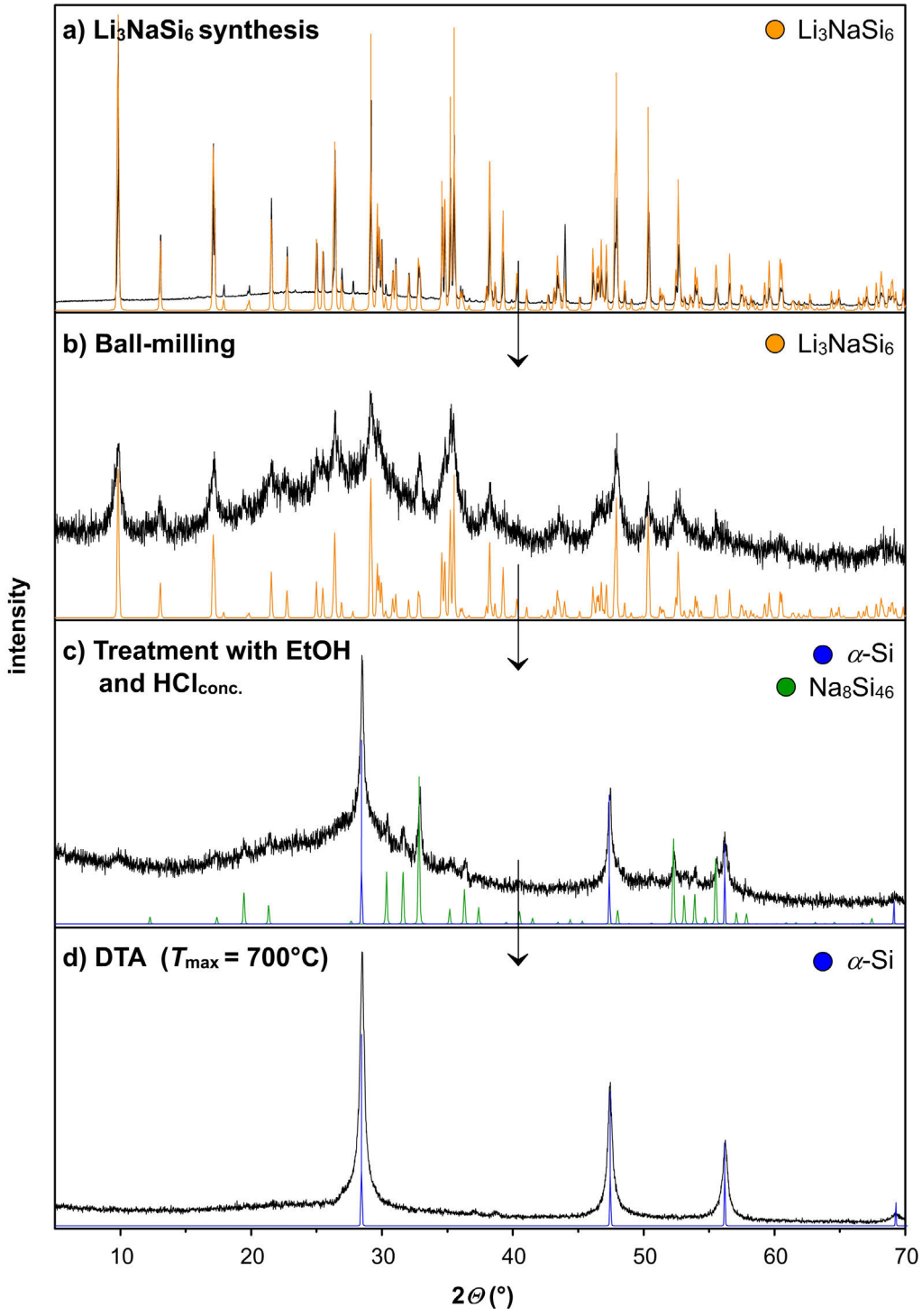

Figure S5. PXRD patterns of Li_3NaSi_6 before (a) and after ball-milling (b), the product after treatment with ethanol and $HCl_{conc.}$ (reaction time: 5–10 min) (c) and subsequent DTA investigation applying $T_{max.}$ = 700 °C, ±10 $Kmin^{-1}$ heating/cooling rate (d). Calculated patterns for Li_3NaSi_6, α-Si, and Na_8Si_{46} are shown in orange, blue, and green, respectively.

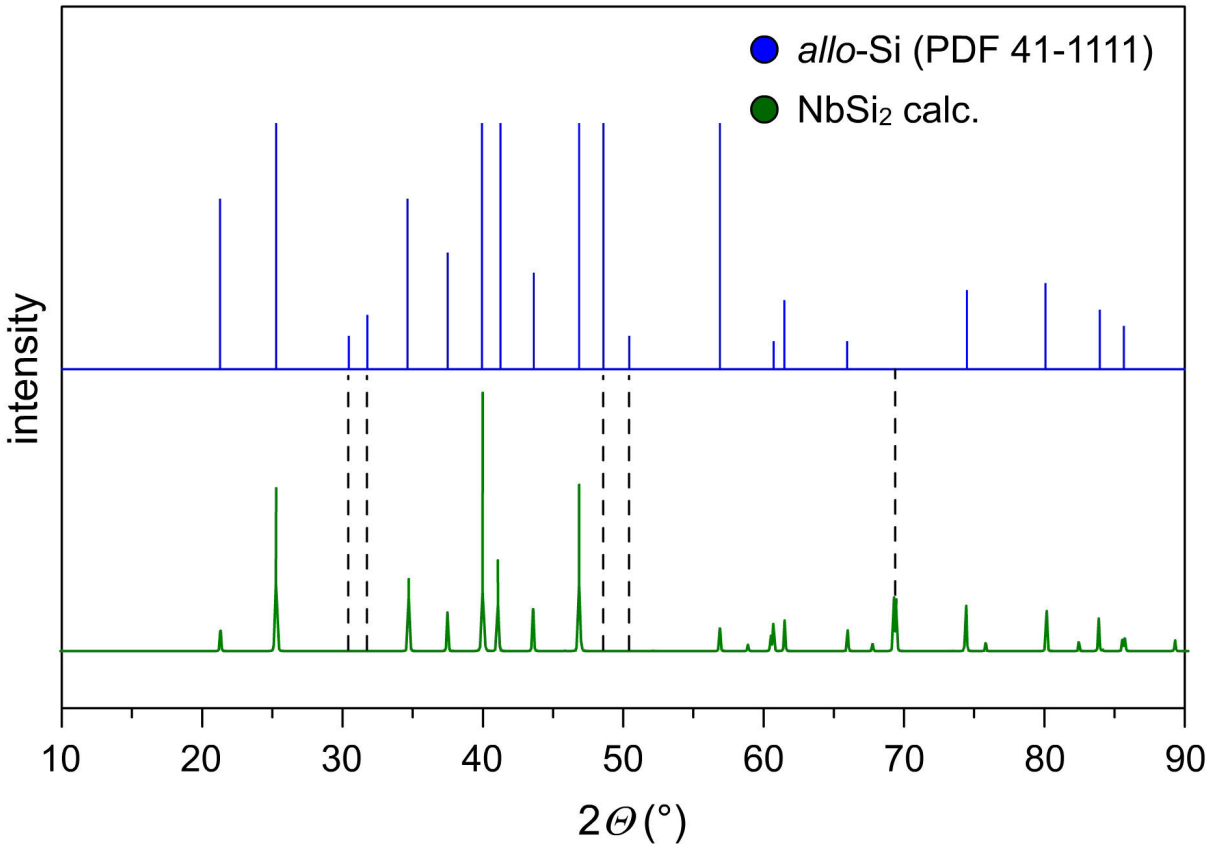

Figure S6. Bragg reflection positions and relative intensities for *allo*-Si (PDF 41-1111, blue) compared with the calculated powder X-ray diffraction pattern of $NbSi_2$ (green). The Bragg reflection at ~68°, which should be observed for $NbSi_2$, is not matched by the *allo*-Si pattern.

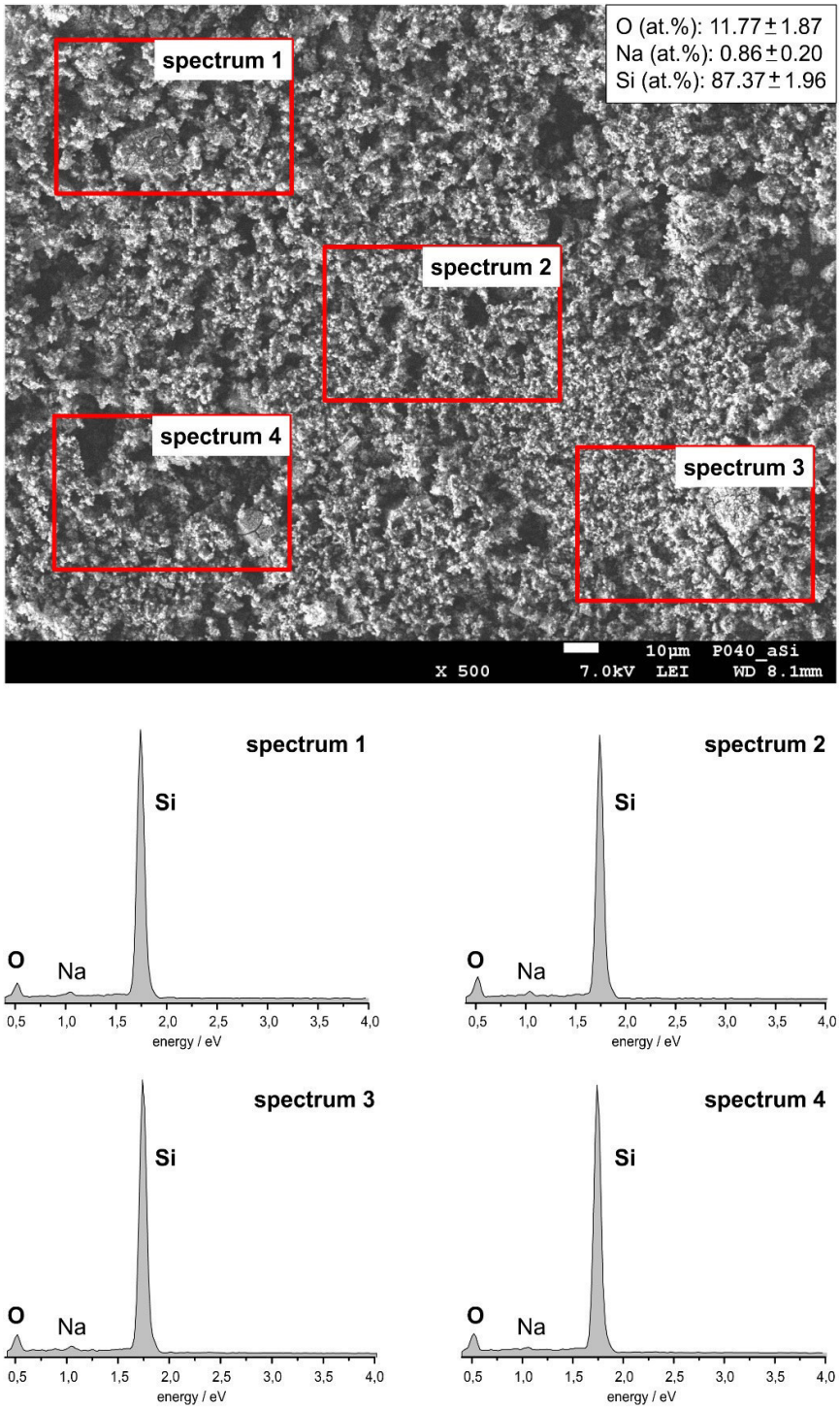

Figure S7. SEM EDX results for *a*-Si (data acquisition: 60 s exposure time at 7.00 kV for each spectrum).

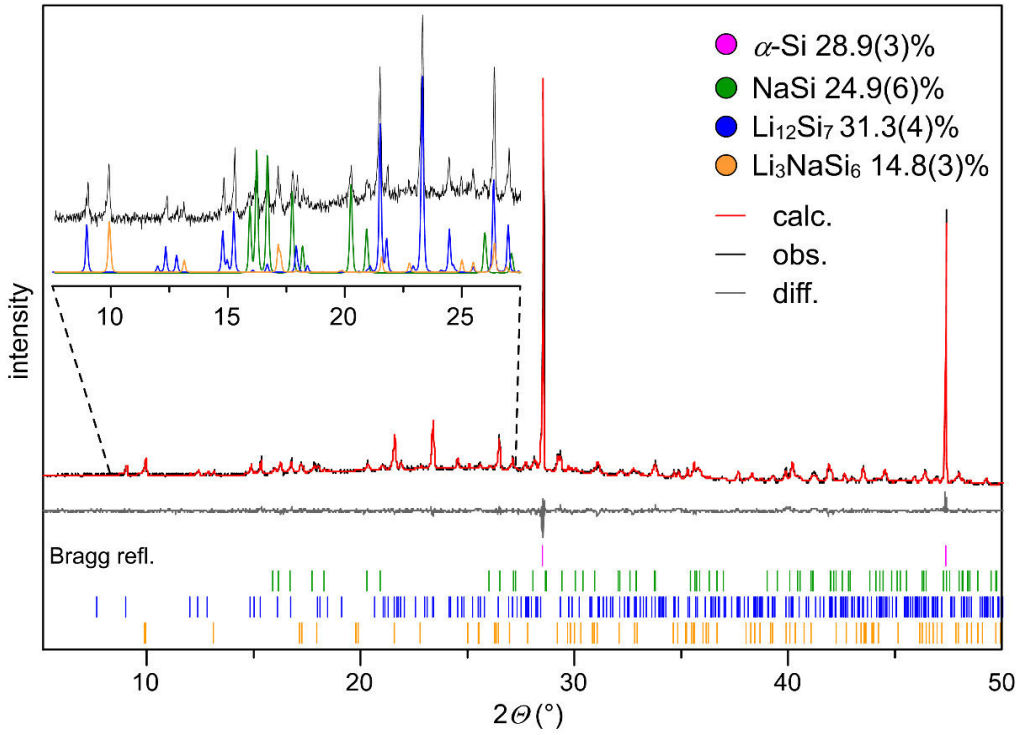

Figure S8. Rietveld fit to the PXRD pattern of Li_3NaSi_6 after DTA investigations ($T_{max.}$ = 700 °C, ±10 K·min^{-1} heating/cooling rate; α-Si (pink), NaSi (green), $Li_{12}Si_7$ (blue), Li_3NaSi_6 (orange), corresponding weight fractions are given; R_p = 4.38, R_{wp} = 5.90, *GOF* = 1.08).

TEM Heating experiments

To investigate the evolution of structural properties at elevated temperatures for both *a*-Si and *a-allo*-Si in-situ heating experiments were performed. The microstructure of the samples was not modified by electron beam irradiation at room temperature; thus, the structural changes observed at elevated temperatures represent intrinsic effects induced by heating. While heating up to 700 °C in steps of 50 °C the respective sample was analyzed at two defined positions which were manually kept in focus.

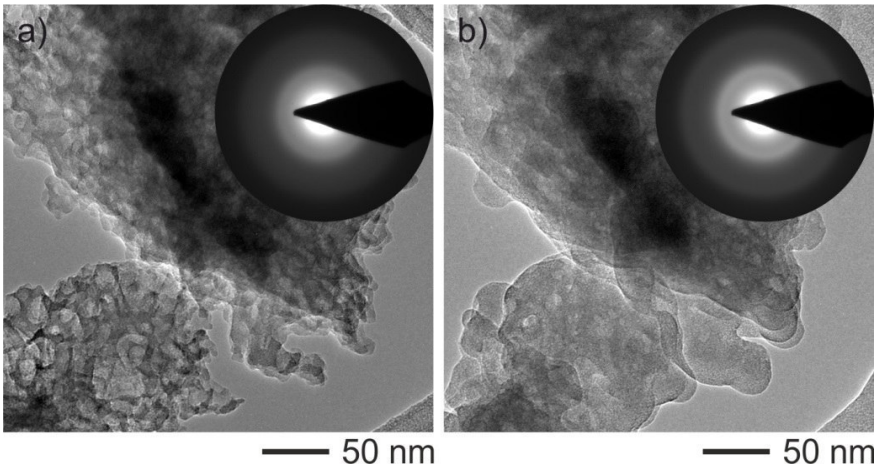

Figure S9. Bright field images recorded in the course of in-situ heating on *a*-Si sample with inserted electron diffraction patterns. a) T = RT and b) T = 100 °C.

As depicted in Figure S9a *a*-Si is highly porous at room temperature (heating stage off). Heating causes particle agglomeration starting already at 50 °C. At T = 100 °C (Figure S9b) the initially observed porosity is lost and a dense material is produced by grain coarsening. The diffraction patterns exclude heat induced crystallization even up to the final temperature of 700 °C.

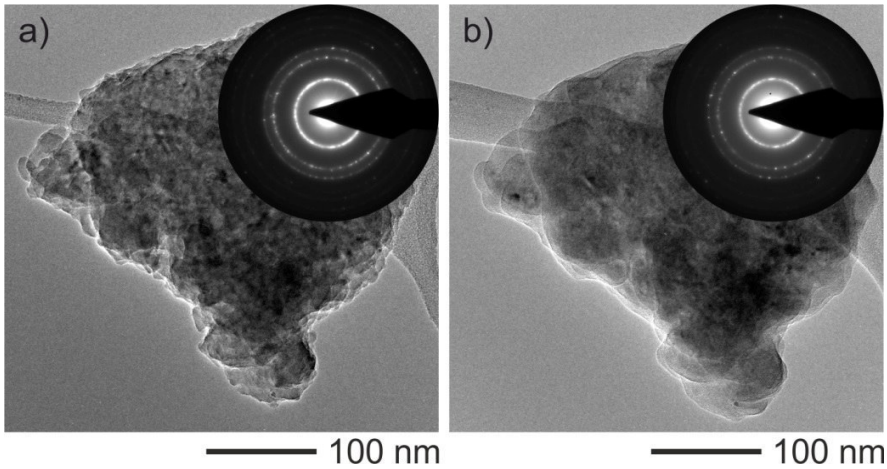

Figure S10. Bright field images recorded in the course of in-situ heating on *a-allo*-Si sample with inserted electron diffraction patterns. a) T = RT and b) T = 100 °C.

Particles of *a-allo*-Si show related microstructural changes (Figure S10). Sintering of the particles occurs at relatively low temperature (T = 100 °C) and compared to the initial polycrystalline nature no further crystallization was observed up to 700 °C.

Basis set details for Na and Li

Na: The molecular def-SVP basis set was modified as follows: The exponents of two diffuse outermost s-type functions (0.052 and 0.028) were increased to 0.25 and 0.10 by dividing the third outermost s-exponent of 0.648 by a factor of 2.5. The exponent of a diffuse outermost p-type function (0.052) was increased to 0.10 and the outermost s and p functions were combined into a single sp-type function to increase the efficiency of the CRYSTAL code. A d-type polarization function with an exponent of .265 was added by taking the average of two d-type polarization functions in set def2-TZVP basis set (exponents 0.43 and 0.10; Weigend, F.; Ahlrichs, R. *Phys. Chem. Chem. Phys.* **2005,** *7*, 3297–3305).

Li: The molecular def-SVP basis set was modified as follows: The exponents of two diffuse outermost s-type functions (0.0528 and 0.021) were increased to 0.36 and 0.18 by dividing the third outermost s-exponent of 0.722 by a factor of 2.0. The contracted p-type polarization function with exponents of 0.45 and 0.10 was replaced by a primitive function with an exponent of 0.18 and the outermost s and p functions were combined into a single sp-type function to increase the efficiency of the CRYSTAL code.

Basis sets listed in CRYSTAL09 input format

```
11 6
0 0 5 2.0 1.0
  4098.2003908     -.58535911879E-02
  616.49374031     -.43647161872E-01
  139.96644001     -.19431465884
  39.073441051     -.48685065731
  11.929847205     -.41881705137
0 0 3 2.0 1.0
  20.659966030      .85949689854E-01
  1.9838860978     -.56359144041
  .64836323942     -.51954009048
0 0 1 1.0 1.0
  0.25              1.0000000000
0 1 1 0.0 1.0
  0.10              1.0 1.0
0 2 5 6.0 1.0
  75.401862017     .154353625324E-01
  17.274818978     .997382931840E-01
  5.1842347425     .312095939659
  1.6601211973     .492956748074
  .51232528958     .324203983180
0 3 1 0.0 1.0
  0.265             1.0
```

```
3 3
0 0 5 2.0 1.0
  266.27785516      .64920150325E-02
  40.069783447      .47747863215E-01
  9.0559944389      .20268796111
  2.4503009051      .48606574817
  .72209571855      .43626977955
0 0 1 1.0 1.0
  0.36  1.0000000000
0 1 1 0.0 1.0
  0.18  1.0 1.0
```

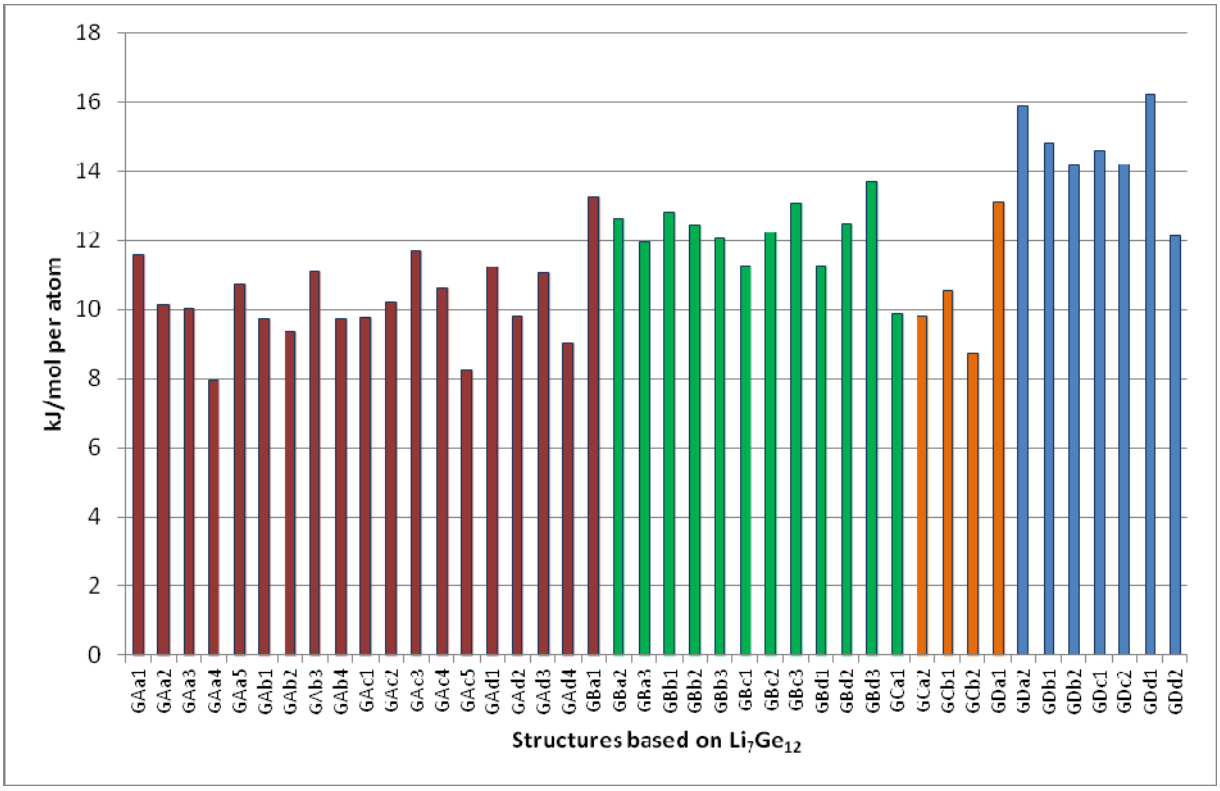

Figure S11. Comparison of the total energies (in kJ·(mol·Si)$^{-1}$**)** of networks optimized for Si, but on the basis of Conesa's **G**-type structures (derived from the Ge substructure of Li_7Ge_{12}). The single groups **GA** (red), **GB** (green), **GC** (orange), and **GD** (blue) refer to different ways of layer connections.

Table S1. Comparison of all calculated Si networks

Name	ρ/g·cm^{-3}	ΔE/kJ·mol^{-1}	band gap/eV
GAa1	2.124	11.60	2.30
GAa2	2.167	10.13	2.47
GAa3	2.190	10.01	2.00
GAa4	2.220	7.96	2.23
GAa5	2.132	10.74	2.58
GAb1	2.171	9.74	2.48
GAb2	2.199	9.38	2.08
GAb3	2.129	11.09	2.00
GAb4	2.171	9.74	2.48
GAc1	2.120	9.77	2.45
GAc2	2.160	10.19	2.31
GAc3	2.129	11.70	2.38
GAc4	2.194	10.61	1.92
GAc5	2.200	8.22	1.78
GAd1	2.162	11.25	2.22
GAd2	2.196	9.79	2.04
GAd3	2.123	11.07	2.43
GAd4	2.161	9.02	2.22
GBa1	2.139	13.29	2.22
GBa2	2.144	12.64	2.56
GBa3	2.150	11.96	2.80
GBb1	2.139	12.80	2.33
GBb2	2.145	12.45	2.62
GBb3	2.152	12.07	2.69
GBc1	2.140	11.27	2.50
GBc2	2.141	12.24	2.61
GBc3	2.143	13.07	2.60
GBd1	2.140	11.26	2.73
GBd2	2.140	12.50	2.62

GBd3	2.140	13.69	2.34
GCa1	2.158	9.87	2.59
GCa2	2.165	9.81	2.60
GCb1	2.162	10.55	2.45
GCb2	2.154	8.74	2.61
GDa1	2.183	13.09	2.03
GDa2	2.095	15.89	1.86
GDb1	2.104	14.80	2.24
GDb2	2.166	14.16	1.55
GDc1	2.169	14.59	1.64
GDc2	2.093	14.21	2.03
GDd1	2.098	16.23	2.13
GDd2	2.177	12.13	1.61
SA1	2.239	20.30	0.85
SA2	2.238	19.49	1.62
SA3	2.227	19.77	0.97
SA4	2.233	29.07	0.77
SB1	2.148	19.95	1.07
SB2	2.146	15.94	1.74
SB3	2.153	21.02	1.12
SB4	2.167	30.32	0.73
SC1	2.292	14.00	1.50
SC2	2.303	16.13	1.50
SC3	2.294	15.42	1.78
SC4	2.286	27.23	-
SD	2.011	13.66	1.74
mep	2.004	9.40	2.78
mtn	1.979	8.06	2.83
CAS	2.127	10.66	1.84
unj/NGS	2.105	7.70	3.01
tum	2.180	9.76	2.54

STRUCTURAL PARAMETERS

Structural parameters of computationally optimized silicon structure (given in CRYSTAL09 input format)

```
Space group number
Minimal set of lattice parameters a, b, c, α, β, γ
Number of non-equivalent atoms in the assymetric unit
<atomic number> <fractional x> < fractional y> < fractional z>
```

α-Si

```
227
5.45503610 5.45503610 5.45503610 90.000000 90.000000 90.000000
1
14     1.250000000000E-01  1.250000000000E-01  1.250000000000E-01
```

GAa1

```
51
11.51968402 7.60210801 7.99343475 90.000000
7
14     2.500000000000E-01  0.000000000000E+00  3.336306420909E-01
14     2.500000000000E-01  5.000000000000E-01  3.358211129809E-01
14     2.500000000000E-01  2.554225539019E-01  1.602651561979E-01
14    -9.716186319573E-02  0.000000000000E+00  4.544689545843E-01
14    -9.839815176519E-02  5.000000000000E-01  4.662949034080E-01
14    -1.477049689831E-01 -2.559722310182E-01  3.045386908748E-01
14    -1.003273320247E-01 -3.390758160078E-01  2.995589950820E-02
```

GAa2

```
6
7.95492313 7.53697027 11.44136475 90.030957
22
14    -3.308570690944E-01  1.185735531344E-21  2.512564781479E-01
14    -3.307143575920E-01  5.000000000000E-01  2.115755298555E-01
14    -4.567366428087E-01  1.185735542298E-21 -4.129105831114E-01
14    -4.625037369079E-01  5.000000000000E-01 -4.249541371376E-01
14    -1.545829148461E-01 -2.479291033927E-01  2.290482249716E-01
14     3.074829605624E-01 -2.565855541145E-01  3.338479321754E-01
14     3.266059259271E-02 -3.399192051343E-01  3.806010482918E-01
14    -4.410515326580E-01  1.185735547712E-21 -1.096843392947E-01
14    -4.703027360977E-01 -5.000000000000E-01 -1.189239300664E-01
14     3.037558758881E-01 -2.373519759800E-01  1.291255811344E-01
14     2.774089339692E-02 -1.646773157259E-01  6.966900818622E-02
14     3.350195629936E-01  1.185735522207E-21 -2.575190594118E-01
14     3.377085729811E-01  5.000000000000E-01 -2.734869698881E-01
14     4.486247504013E-01  1.185735550446E-21  3.938362953050E-01
14     4.799100701424E-01  5.000000000000E-01  3.744542745197E-01
14     1.597315330547E-01 -2.568125929163E-01 -2.631744294154E-01
14    -3.022823035631E-01 -2.566097714812E-01 -3.685895714783E-01
14    -2.747480612895E-02 -3.368014325965E-01 -4.169901208292E-01
14     4.832009635135E-01  1.185735553911E-21  8.788461276686E-02
14     4.400596392568E-01  5.000000000000E-01  7.383454354127E-02
14    -2.975098087572E-01 -2.607247673881E-01 -1.630832310750E-01
14    -2.184076426449E-02 -3.338415735472E-01 -1.027557995745E-01
```

GAa3

```
59
11.43732402 7.46648355 7.94834712 90.000000
7
14    -5.000000000000E-01  0.000000000000E+00  3.308634430102E-01
14    -5.000000000000E-01 -5.000000000000E-01  3.336502288773E-01
14    -5.000000000000E-01  2.577688215275E-01  1.527536060586E-01
14     1.537619332775E-01  0.000000000000E+00  4.723801417456E-01
14     1.503059970699E-01 -5.000000000000E-01  4.493102626383E-01
14     1.026528996772E-01  2.387486104244E-01  3.010401792182E-01
14     1.628198749591E-01  1.679123108520E-01  2.572478686383E-02
```

GAa4

```
57
7.88777246 11.34980856 7.48053954 90.000000 90.000000 90.000000
6
14     3.308401228268E-01  2.776393443943E-01 -2.500000000000E-01
14    -1.533866339042E-01 -2.500000000000E-01  0.000000000000E+00
14     4.364442887590E-01 -4.150174140047E-01  2.500000000000E-01
14     4.850386860133E-01 -3.876989632456E-01 -2.500000000000E-01
14     3.014252175481E-01 -3.528420841575E-01 -1.157353482175E-02
14     2.500083519762E-02 -4.131219487405E-01 -8.545510489538E-02
```

GAa5

```
53
7.62005107 7.96949177 11.48081914 90.000000
6
14     0.000000000000E+00 -3.356932538554E-01 -2.623061297915E-01
14    -2.500000000000E-01 -1.614369712208E-01 -2.500000000000E-01
14    -5.000000000000E-01 -4.725965273923E-01  3.991156159656E-01
14     0.000000000000E+00 -4.464592422698E-01  4.055164554202E-01
14    -2.577013312525E-01 -3.043600559211E-01  3.523764677403E-01
14    -3.406789048650E-01 -2.913883652888E-02  3.990176361547E-01
```

GAb1

```
12
22.86874316 7.54679951 7.93493979 90.102551
11
14    -1.340795586098E-01  2.261847200735E-18 -3.350824571481E-01
14    -1.173181927276E-01 -5.000000000000E-01 -3.325580185760E-01
14     2.044925145484E-01 -1.980271610523E-17 -4.373571242234E-01
14     1.979090873799E-01 -5.000000000000E-01 -4.797390345728E-01
14     1.269270793314E-01 -2.514402651751E-01  1.574937861765E-01
14     1.769659845633E-01 -2.620401156207E-01 -3.008356719040E-01
14     2.068503260275E-01 -3.348165171401E-01 -2.434801346658E-02
14     5.130723416901E-02  2.788277178583E-18 -4.753109129268E-01
14     4.711221246905E-02 -5.000000000000E-01 -4.475264412154E-01
14     7.447568108203E-02 -2.425776359688E-01 -3.045438390833E-01
14     5.073871633496E-02 -1.602681902517E-01 -2.932800132083E-02
```

GAb2

```
35
7.47283467 22.82357067 7.92704399 90.000000
13
14     0.000000000000E+00 -5.000000000000E-01  3.257616970615E-01
14     0.000000000000E+00  0.000000000000E+00  3.262657629855E-01
14     2.568936234327E-01  2.059291174921E-17  1.464239341829E-01
14     5.000000000000E-01  1.715509271810E-01  4.343298008063E-01
14     0.000000000000E+00  1.770596331105E-01  4.750966580626E-01
14     2.599894759386E-01  5.145631255370E-02 -3.064804135725E-01
14     3.319811801301E-01  8.193263213140E-02 -3.119199284081E-02
14     0.000000000000E+00  2.592039941030E-01 -3.382203813783E-01
14    -2.500000000000E-01  2.500000000000E-01 -1.596459874479E-01
14     5.000000000000E-01  7.538572616620E-02 -4.781707470387E-01
14     0.000000000000E+00  7.695148912717E-02 -4.544789074685E-01
14    -2.384544153694E-01  1.988119487109E-01  2.953287972102E-01
14    -1.656098527197E-01  1.691267788097E-01  1.931205933211E-02
```

GAb3

```
35
7.61259950 22.99784657 7.97834643 90.000000
13
14    -1.516028706329E-20 -2.425218964616E-01  3.305725291427E-01
14    -2.500000000000E-01  2.500000000000E-01  1.563608910109E-01
14    -1.008594493835E-20  7.557317132660E-02  4.510427608286E-01
14    -5.000000000000E-01  7.682342536707E-02  4.607230444884E-01
14    -2.576816667795E-01  1.989214515800E-01 -3.093137666044E-01
14    -3.407459619346E-01  1.757207847793E-01 -3.429073263372E-02
14    -1.359096035029E-21  1.932253964954E-39 -3.369838293810E-01
14    -1.359096035029E-21 -5.000000000000E-01 -3.415668850266E-01
14    -2.560166859699E-01  0.000000000000E+00 -1.651319748471E-01
14     2.305364761610E-21  1.712516465771E-01 -4.502808117513E-01
14    -5.000000000000E-01  1.767499238514E-01 -4.786851965393E-01
14     2.561861384154E-01  5.124958395992E-02  3.000329287637E-01
14     3.393132608228E-01  7.507441292378E-02  2.512612790983E-02
```

GAb4

```
12
22.86831111 7.54631619 7.93466666 89.898170
11
14    -1.173162858903E-01 -5.000000000000E-01  3.325862857015E-01
14    -1.340682369037E-01 -4.445273715588E-17  3.350196293937E-01
14     5.131247315794E-02  6.679809623087E-18  4.753211287382E-01
14     4.711229292678E-02  5.000000000000E-01  4.475108632253E-01
14     1.269372204135E-01  2.514813166892E-01 -1.574690417449E-01
14     7.447846296758E-02  2.425718035937E-01  3.045255063905E-01
14     5.073881123783E-02  1.602720064215E-01  2.931140850500E-02
14     2.044776993101E-01 -4.229657275404E-18  4.374281674220E-01
14     1.979154293482E-01  5.000000000000E-01  4.797493713033E-01
14     1.769645890401E-01  2.620275014843E-01  3.008707488997E-01
14     2.068533289797E-01  3.348195006807E-01  2.439487768602E-02
```

GAc1

```
63
7.67033413 15.86240204 11.52902569 90.000000
7
14     5.000000000000E-01 -1.563434594731E-01 -2.500000000000E-01
14     0.000000000000E+00 -1.771758565861E-01 -2.500000000000E-01
14     2.359779368353E-01  8.057260000981E-02  2.500000000000E-01
14     0.000000000000E+00  2.399270933515E-01 -4.005535232688E-01
14     0.000000000000E+00 -2.798383265381E-01 -4.036143125005E-01
14     2.384183851412E-01  1.530644509859E-01 -3.522113430500E-01
14     1.571626211551E-01  1.512684972447E-02 -3.998934582414E-01
```

GAc2

```
8
15.90655125 7.54915599 11.46071405 90.026562
22
14    -1.659747257477E-01  5.000000000000E-01  2.513693253843E-01
14    -1.440924600222E-01 -2.215848872839E-17  2.526062384774E-01
14     2.780364647864E-01  2.938403236946E-17 -4.005944076960E-01
14    -2.169378025776E-01  1.350635576160E-17 -3.964237347542E-01
14    -6.743806173531E-02 -2.662404567391E-01  2.496475513448E-01
14     1.637162728157E-01  2.608298738608E-01  3.547809724436E-01
14     2.643580300174E-02  3.406233847177E-01  4.035929050738E-01
14     2.829344968645E-01  1.351430628542E-17 -9.411202188344E-02
14    -2.198040438826E-01 -1.879973527147E-18 -9.278811523899E-02
14     1.618371771266E-01  2.622754334891E-01  1.496668225228E-01
14     2.419245194127E-02  3.358351965944E-01  8.883102451039E-02
14     1.769428910899E-01  5.000000000000E-01 -2.375644014387E-01
14     1.787753912587E-01  4.434381159996E-18 -2.515440110697E-01
14     2.332153153769E-01 -1.451977931512E-17  4.058267228394E-01
14    -2.490409025385E-01 -5.971255987272E-20  4.036617605200E-01
14     8.975577653030E-02  2.473409679996E-01 -2.426493970969E-01
14    -1.410403662426E-01 -2.548483767646E-01 -3.478276711894E-01
14    -3.661878110983E-03 -3.376996062203E-01 -3.944936761957E-01
14     2.318285953005E-01  1.131335588558E-18  9.765475232969E-02
14    -2.500010567451E-01 -3.112949208385E-17  1.050663445082E-01
14    -1.394054317599E-01 -2.453197188619E-01 -1.428894906207E-01
14    -1.832825148330E-03 -1.679738162261E-01 -8.325326678168E-02
```

GAc3

```
64
7.59110323 16.01372881 11.49003408 90.000000
6
14    -5.000000000000E-01  1.677657393491E-01  2.578999759794E-01
14     2.500000000000E-01  8.065073927843E-02  2.500000000000E-01
14     0.000000000000E+00 -2.721773036127E-01 -3.993640725212E-01
14     0.000000000000E+00  2.314958964385E-01 -4.051875598673E-01
14    -2.456293564192E-01  1.517380201210E-01 -3.524503268273E-01
14    -1.613365185025E-01  1.468844377344E-02 -3.991011230994E-01
```

GAc4

```
64
7.44740202 15.92651865 11.42654329 90.000000
6
14    -5.000000000000E-01 -8.441695590100E-02  2.557604547938E-01
14     2.500000000000E-01 -1.738812231366E-01  2.500000000000E-01
14     5.000000000000E-01 -1.721191595594E-02 -4.018750616111E-01
14     0.000000000000E+00 -2.138430954586E-02 -4.018575237245E-01
14     2.552877887534E-01 -9.955603273772E-02 -3.525282886114E-01
14    -1.692747071907E-01  2.632524699805E-01 -4.121409513935E-01
```

GAc5

```
63
7.51336682 15.76884262 11.40574050 90.000000
7
14     5.000000000000E-01  9.708832510940E-02 -2.500000000000E-01
14     0.000000000000E+00  7.256071752163E-02 -2.500000000000E-01
14     2.307579956379E-01 -1.733670236419E-01  2.500000000000E-01
14     0.000000000000E+00 -2.808080668871E-02 -4.053803751846E-01
14     5.000000000000E-01 -1.057152891076E-02 -3.989557190020E-01
14    -2.616447265754E-01 -9.895900672270E-02 -3.528341428131E-01
14     1.639327882210E-01  2.632184695324E-01 -4.145208531868E-01
```

GAd1

```
12
15.97468510 7.51335364 13.97321350 124.903903
11
14    -4.552396378288E-02 -2.125092300497E-18  2.448146802978E-01
14    -3.648184340956E-02  5.000000000000E-01  2.581030947573E-01
14     7.147830599262E-02 -2.458188264567E-17 -4.025116318239E-01
14    -4.331916184505E-01 -8.366756564251E-18 -4.024229292956E-01
14    -4.822765631250E-02  2.472179353111E-01 -2.532556027169E-01
14    -3.268988144364E-01  2.446115347914E-01 -3.533352657203E-01
14    -2.194706671648E-01  1.684011018444E-01 -4.128590207199E-01
14     2.197924519322E-01 -2.749629249132E-17 -9.573838383623E-02
14    -2.795318362484E-01  3.689755503755E-18 -1.008457734123E-01
14    -2.260714755083E-01 -2.542933587715E-01 -1.483923295199E-01
14    -6.539516701884E-02  3.369232552332E-01 -1.011621571080E-01
```

GAd2

```
42
22.85553701 7.49812251 15.80198454 90.000000
13
14     0.000000000000E+00 -3.139961861997E-17 -1.656096975158E-01
14     0.000000000000E+00  5.000000000000E-01 -1.404125105905E-01
14     0.000000000000E+00 -2.307388899743E-01 -6.460659735280E-02
14    -1.727993131672E-01  6.280917598545E-17  2.795995431036E-01
14    -1.750206326666E-01 -1.570488440399E-17 -2.184555033887E-01
14     5.130618903346E-02  2.381895668954E-01  1.628579597942E-01
14     8.211143254135E-02 -1.639880161808E-01  2.517074188874E-02
14     2.453278174297E-01  2.747577606313E-17  1.765030899008E-01
14    -2.500000000000E-01 -2.500000000000E-01  8.762164822057E-02
14    -7.799477862238E-02 -3.139908759761E-17 -2.669736538520E-01
14    -7.337386297788E-02  3.142209542669E-17  2.522252845071E-01
14     1.987801858812E-01 -2.550038998487E-01 -1.396093839386E-01
14     1.687968074605E-01  3.315155714438E-01 -1.720671287193E-03
```

GAd3

```
42
23.04554151 7.64227689 15.90204450 90.000000
13
14    -2.524490477796E-01 -4.192196157339E-21 -1.638594986435E-01
14    -2.500000000000E-01 -2.500000000000E-01 -7.710665601062E-02
14     7.676093679912E-02 -2.053824811723E-20  2.827384005768E-01
14     7.503590552973E-02 -2.704777918438E-20 -2.348104008724E-01
14    -1.988874547527E-01  2.454596926519E-01  1.561858433279E-01
14    -1.758464716042E-01 -1.607951061293E-01  1.855376846119E-02
14     0.000000000000E+00 -8.736885265302E-21  1.810151920605E-01
14     0.000000000000E+00  5.000000000000E-01  1.607968759359E-01
14     0.000000000000E+00  2.359980648966E-01  8.463109658581E-02
14     1.740093573094E-01 -2.723787462468E-20 -2.697748666672E-01
14     1.732159211573E-01 -1.857177967917E-20  2.365883361796E-01
14    -5.114230336473E-02 -2.392999289423E-01 -1.486515050672E-01
14    -7.530878851271E-02  1.576218887930E-01 -1.086182929526E-02
```

GAd4

```
12
15.83112051 7.58543777 13.92366345 124.611090
11
14    -2.717676555532E-02 -5.000000000000E-01 -2.453736257825E-01
14    -5.288787944307E-02 -1.191159455779E-18 -2.507569950352E-01
14     2.321001711716E-01  1.770852553607E-17  4.054474907005E-01
14     2.072854819979E-01 -5.000000000000E-01  3.972050402193E-01
14    -4.852044945427E-02  2.331662621515E-01  2.454925014840E-01
14     2.725221988499E-01 -2.606831013570E-01  3.511081845864E-01
14    -6.580750244005E-02  1.586675127916E-01  3.992454030486E-01
14     7.580868458738E-02  6.095918184642E-18  9.475002957414E-02
14     6.191916789540E-02 -5.000000000000E-01  9.967252532011E-02
14     1.720500537468E-01  2.617945136152E-01  1.460189645837E-01
14    -2.206146781438E-01  1.632778918450E-01  8.473735556635E-02
```

GBa1

```
11
7.50768768 11.67031708 7.93400123 90.405423
10
14     1.226052793064E-01 -2.500000000000E-01  4.174032163198E-01
14    -3.727285076445E-01 -2.500000000000E-01  4.170450262641E-01
14    -1.198992235383E-01 -2.500000000000E-01 -4.070511528300E-01
14     3.717879786897E-01 -2.500000000000E-01 -4.075777388064E-01
14     1.207958781465E-01 -9.865440495299E-02  2.246270017454E-01
14    -3.698252989899E-01 -9.999163152596E-02  2.044210418223E-01
14     1.150234054224E-01  1.505544089351E-01 -4.668196506009E-02
14    -3.644115321988E-01  1.473911305826E-01 -5.769283656006E-02
14     3.708022829628E-02  9.490077683004E-02  2.303290224265E-01
14    -2.904640717571E-01  9.564678547020E-02  2.249289927922E-01
```

GBa2

```
3
7.52041460 7.91436660 11.64968695 90.068657
18
14    -1.375502660084E-36 -4.049346519515E-01  0.000000000000E+00
14    -5.000000000000E-01 -4.046822938487E-01  0.000000000000E+00
14    -2.458130347341E-01  4.199737672524E-01 -9.744016624059E-04
14     2.468164585656E-01  2.116775971957E-01  3.463068637762E-01
14    -2.436519471677E-01  2.435198828764E-01  3.531968689049E-01
14     2.387957018350E-01 -4.327476337487E-02  1.082684770004E-01
14    -2.407503410234E-01 -3.676539380398E-02  9.374848236063E-02
14     1.616492655958E-01  2.389148118166E-01  1.543829044454E-01
14    -1.653107384141E-01  2.417595612513E-01  1.553747282788E-01
14    -2.475366755268E-01  4.306100898873E-01 -4.860389664234E-01
14    -1.084202172486E-19 -3.938232100860E-01 -5.000000000000E-01
14    -5.000000000000E-01 -3.951911230093E-01 -5.000000000000E-01
14    -6.440677660826E-03 -2.119190991167E-01  1.516294788356E-01
14    -4.953206388950E-01 -1.917944450558E-01  1.503900746391E-01
14    -9.118783363616E-03  6.010035726075E-02  4.007054889541E-01
14    -4.884728454206E-01  7.091694247485E-02  3.976743197906E-01
14    -9.064680200223E-02 -2.171151511272E-01  3.455730458414E-01
14    -4.136208489557E-01 -2.117735180888E-01  3.462277261175E-01
```

GBa3

```
14
7.89277567 11.62356723 7.53554381 90.390618
8
14     4.181580594609E-01  2.355793770366E-01 -3.767326467415E-01
14    -4.073406444375E-01  2.512544003909E-01 -1.256684624017E-01
14    -1.985806417380E-01 -9.568279485757E-02  3.709550818782E-01
14    -2.312387312652E-01 -1.030312487842E-01 -1.177059286281E-01
14     5.705914946373E-02  1.418408744049E-01  3.620268857579E-01
14     4.961926559686E-02  1.564461870561E-01 -1.170554403365E-01
14    -2.256907886647E-01  9.634386350654E-02  2.828862373657E-01
14    -2.289039891908E-01  9.530539274734E-02 -3.921506324302E-02
```

GBb1

```
13
23.29685296 7.93232395 12.27226127 17.843820
9
14    -5.000000000000E-01 -4.166300973316E-01 -2.500000000000E-01
14    -2.775557561563E-17 -4.201418897328E-01 -2.500000000000E-01
14     2.536764634918E-01  4.067597355660E-01  2.395731501838E-01
14     4.285495638368E-01  2.240156325251E-01  2.398436670755E-01
14    -8.121986844578E-02  2.065596146343E-01  2.642923961663E-01
14     3.066317530315E-01 -5.080406885744E-02  2.281771398459E-01
14    -2.042669784508E-01 -5.627134483975E-02  2.691135561743E-01
14     4.132207164350E-01  2.266293894226E-01  7.533011254131E-02
14    -2.588727919742E-01  2.258888308557E-01  4.247386417974E-01
```

GBb2

```
8
7.52518207 23.28413238 7.90955733 90.456101
18
14     2.522523948323E-01 -1.540743955510E-33 -3.966817952767E-01
14    -2.411002435750E-01 -2.018558256493E-17 -3.939324003501E-01
14    -5.651595889631E-04 -1.971248297356E-19  4.282297182280E-01
14    -4.905049627374E-01  1.540743955510E-33  4.309565749289E-01
14    -3.463844570479E-03 -1.776277673991E-01  2.545279631771E-01
14    -4.907008008834E-01 -1.722680088860E-01  2.186905600036E-01
14    -5.345119360126E-03 -5.002544160141E-02 -2.318660291786E-02
14    -4.848032019303E-01 -5.117763877431E-02 -3.819647503789E-02
14    -8.293483994214E-02 -7.895103555189E-02  2.541070973004E-01
14    -4.077944278726E-01 -7.582100804695E-02  2.449219785851E-01
14     4.685366134633E-03  2.583493687914E-01  4.398690971722E-01
14     2.557869361963E-01 -2.483510148299E-01 -3.857297397794E-01
14     2.484100389903E-01 -7.457998719302E-02 -1.838701488867E-01
14    -2.405890332468E-01 -7.667217507796E-02 -2.016488029204E-01
14     2.412582820949E-01 -1.948728751710E-01  7.866093960621E-02
14    -2.373566988638E-01 -2.043980974883E-01  7.155351586878E-02
14     1.651840158407E-01 -1.717525589894E-01 -2.048583560921E-01
14    -1.580326870526E-01 -1.744135513952E-01 -2.057470748440E-01
```

GBb3

```
13
23.26527697 7.88633680 12.24148553 162.089846
9
14     5.551115123126E-17  4.099262984061E-01  2.500000000000E-01
14     5.000000000000E-01  4.063162094375E-01  2.500000000000E-01
14     2.448492124631E-01 -4.173906536576E-01 -2.431624780413E-01
14    -3.323751319196E-01  2.323476049395E-01  2.300050715683E-01
14     1.731622850653E-01  1.965071481868E-01  2.529741337068E-01
14    -4.571184570254E-01 -4.472675549684E-02  2.358876449565E-01
14     6.504091622742E-02 -6.041255179964E-02  2.782051109943E-01
14     4.900739083163E-01  2.328228542854E-01  7.265644929330E-02
14     1.641433761235E-01  2.234837519548E-01  4.272718225120E-01
```

GBc1

```
11
8.66677409 11.67118177 7.56979337 65.133505
10
14    -1.037761682431E-01  2.500000000000E-01  4.370097383711E-01
14    -5.898026630138E-02  2.500000000000E-01 -9.943158876504E-02
14     8.214886777477E-02  2.500000000000E-01  1.040029666026E-01
14     1.005598330066E-01  2.500000000000E-01 -4.352343411944E-01
14     2.651672478786E-01 -1.009002174400E-01  1.600669824242E-03
14     3.063557744891E-01 -9.869890436694E-02  4.658623544045E-01
14    -4.579035478662E-01  1.503816417396E-01 -1.354291110749E-01
14    -4.359296357174E-01  1.476233518170E-01  3.257997792526E-01
14     2.646445742743E-01  9.385841892323E-02  8.379772978969E-02
14     2.799900387630E-01  9.502296200378E-02  3.954541355577E-01
```

GBc2

```
5
7.53763698 15.81223377 11.65174918 89.650278
18
14     3.117713003799E-17 -3.011839721123E-01  0.000000000000E+00
14    -1.558856501899E-17  2.201417296287E-01  0.000000000000E+00
14    -2.353744904740E-01 -2.038439945826E-01  2.180138713933E-03
14     2.442709457102E-01 -1.052072287719E-01 -3.539096781139E-01
14    -2.425959397989E-01 -1.089093024260E-01 -3.450620532195E-01
14    -2.354658256189E-01  2.632292176078E-02 -8.969221652541E-02
14     2.371044364583E-01  2.772630470721E-02 -1.122558840512E-01
14     1.613248363817E-01 -1.140107007209E-01 -1.589730976965E-01
14    -1.593324165873E-01 -1.120162105481E-01 -1.511461092341E-01
14    -2.446930352738E-01 -2.091411098347E-01 -4.905479615936E-01
14     6.158268339718E-17 -2.993003862537E-01 -5.000000000000E-01
14    -3.209238430557E-17  2.068229071157E-01 -5.000000000000E-01
14    -4.936208527949E-01  9.759324469761E-02 -1.512791206408E-01
14    -4.654126419475E-03  1.173381149357E-01 -1.496034017994E-01
14    -4.923695332292E-01 -3.028669973814E-02 -3.977416617996E-01
14    -5.197397081012E-03 -2.181742479372E-02 -4.004447650968E-01
14    -4.124984738800E-01  1.105474769731E-01 -3.463268962269E-01
14    -8.734105521930E-02  1.169744691525E-01 -3.448428612807E-01
```

GBc3

```
14
8.77580703 11.62939017 7.51063379 64.804899
8
14     4.184560977152E-01  2.404677882972E-01 -8.226828174646E-02
14    -4.070112863368E-01  2.523194869420E-01  8.063233118433E-02
14    -2.110633201787E-01 -1.035358610872E-01  4.721249627912E-01
14    -2.184170824256E-01 -9.453762790406E-02 -1.353051839225E-02
14     5.430825246051E-02  1.378373710884E-01  3.445419853685E-01
14     5.197246373771E-02  1.601447468772E-01 -1.415848594938E-01
14    -2.278248381097E-01  9.262408335898E-02  4.025762489968E-01
14    -2.240362443623E-01  1.001375909167E-01  7.480160623443E-02
```

GBd1

```
15
23.31004099 15.74882190 12.23354769 161.979260
9
14     0.000000000000E+00 -3.013150886029E-02  2.500000000000E-01
14     5.000000000000E-01 -5.063746250088E-02  2.500000000000E-01
14    -2.650495893375E-01  4.613645737666E-02 -2.786519301401E-01
14    -8.001912986068E-02  1.335898442016E-01 -2.598459105700E-01
14     4.297979936088E-01  1.516205624480E-01 -2.401145287221E-01
14     2.835050500837E-01 -2.244590895330E-01 -2.759092188907E-01
14    -1.821254751307E-01 -2.219766369090E-01 -2.232146328894E-01
14     4.193236477330E-01  1.368206653298E-01 -6.829890445032E-02
14    -2.628949810755E-01  1.362120865220E-01 -4.302386078743E-01
```

GBd2

```
8
7.53251971 23.31904907 8.78935269 64.150537
18
14    -5.033601794929E-02  1.540743955510E-33 -4.046984464523E-01
14     4.403077028279E-01  0.000000000000E+00 -3.647825481466E-01
14     2.933485746542E-01  0.000000000000E+00  4.480451145360E-01
14    -2.282576577972E-01  2.015535775916E-17  4.352037449339E-01
14    -1.257864066929E-01 -1.755959747778E-01  2.417817766605E-01
14     3.777804179741E-01 -1.737732244832E-01  2.541444040719E-01
14     6.318377769970E-04 -5.142275882289E-02 -2.639799568013E-02
14    -4.802400314429E-01 -4.967023899119E-02 -1.251472344700E-02
14     4.594163538815E-01 -7.723772231652E-02  2.644903425468E-01
14    -2.160336378247E-01 -7.797057415409E-02  2.561506671697E-01
14    -2.260753980266E-01  2.529335426284E-01  4.518516864841E-01
14     4.353670661507E-01  2.490653449042E-01 -3.736120733983E-01
14    -1.552833053431E-01 -7.520309279061E-02 -1.986706465436E-01
14     3.388360258104E-01 -7.531918231976E-02 -1.634591217577E-01
14    -2.976852572897E-01 -2.035873142310E-01  8.354009386840E-02
14     2.134485322277E-01 -1.956056008244E-01  8.872767875556E-02
14     4.342952858101E-01 -1.720986534006E-01 -1.932465200971E-01
14    -2.375227838793E-01 -1.734154528433E-01 -1.943045010686E-01
```

GBd3

```
15
7.49563277 15.88947064 12.24114924 107.669141
9
14     5.551115123126E-17 -2.011985516124E-01 -2.500000000000E-01
14     5.000000000000E-01 -2.063539472313E-01 -2.500000000000E-01
14    -2.575543551420E-01  2.086577033066E-01 -2.557410111790E-01
14     3.327086972727E-01 -1.100301426678E-01  4.025036973140E-01
14    -1.800194064824E-01 -1.040987995372E-01  3.992128521818E-01
14     4.563110202346E-01  2.291609287399E-02 -3.491856508882E-01
14    -5.889764383178E-02  2.900397488350E-02 -3.525960836208E-01
14    -1.620000901152E-01 -1.117557629972E-01 -4.048176451530E-01
14    -4.900715284773E-01 -1.154250115981E-01 -4.033479594156E-01
```

GCa1

```
5
12.11953109 7.97220424 7.53190587 108.780110
9
14     3.351173003643E-22 -3.420864099329E-01 -8.495002510058E-23
14     1.387778780781E-17 -3.388084300156E-01 -5.000000000000E-01
14     1.651133490462E-03 -1.635109540398E-01  2.437808361144E-01
14    -1.546691245689E-01  4.641871118796E-01 -7.166713440931E-02
14     3.497601015777E-01 -5.636497786533E-02  4.143337570341E-01
14     8.831247972003E-02  2.944633804878E-01 -1.942064035719E-01
14     1.164536415398E-01  2.988411242899E-01  3.007484461508E-01
14     1.523638152470E-01  2.431403243509E-02 -8.507486130570E-02
14     1.581335699761E-01  1.968770278711E-02  2.428421456268E-01
```

GCa2

```
5
12.10087582 7.94450060 7.52897198 108.431755
9
14     1.677897628787E-02 -3.450186979728E-01 -2.446906641658E-01
14    -1.670477943808E-52 -1.708605248248E-01 -3.370431415997E-36
14     5.551115123126E-17 -1.657794115091E-01 -5.000000000000E-01
14     3.408406006485E-01 -6.607057332144E-02  1.745187088107E-01
14    -1.461490964442E-01  4.653990827291E-01 -3.308645425737E-01
14     1.043665726588E-01  2.966802219096E-01  6.184291781082E-02
14     9.982838959599E-02  2.870901042167E-01 -4.574772804000E-01
14     1.525156007571E-01  1.667266386960E-02  1.633433492839E-01
14     1.574404322246E-01  1.710216673621E-02  4.901335672851E-01
```

GCb1

```
9
8.82983478 11.45727996 7.51075752 115.183551
8
14    -3.437756783375E-01 -7.681978042536E-03 -4.210688174929E-01
14    -1.671363416680E-01  7.862004057199E-04 -8.287903789743E-02
14     4.486977410626E-01  1.519473356473E-01  4.675460605776E-01
14    -4.808859897596E-02 -3.465884365455E-01 -1.571536125013E-02
14     2.950004578101E-01 -1.142026605491E-01  1.516239995888E-01
14     2.898132005683E-01 -9.051373531018E-02 -3.580392166728E-01
14     1.775695215641E-02 -1.548309523265E-01  9.634636555307E-02
14     2.009226738420E-02 -1.539776431918E-01  4.249860075939E-01
```

GCb2

```
8
8.84543352 11.50786176 7.57899918 116.548640
10
14    -3.464373806147E-01 -5.722986677374E-21 -4.181877523083E-01
14    -3.007644145348E-01 -8.086554703648E-22  8.975248392929E-02
14    -1.390221277931E-01  1.444405574873E-21 -8.679177377935E-02
14    -1.584987445156E-01 -2.610939613677E-21  4.368483996958E-01
14    -1.099655222971E-02 -3.498770490935E-01 -2.101067628104E-02
14     4.494803759442E-01  1.540517487608E-01  4.776381002802E-01
14     3.005937304937E-01 -1.003749271848E-01 -3.463395746437E-01
14     3.247645814207E-01 -1.038654566828E-01  1.419982623181E-01
14     2.943543847441E-02 -1.564258018990E-01 -4.002454849150E-01
14     4.558375962588E-02 -1.561656932603E-01 -7.224130552724E-02
```

GDa1

```
28
7.43782109 5.83111545 7.84977267 90.000000
6
14     2.500000000000E-01  3.400292707726E-02 -3.330294922002E-01
14     1.618016316139E-36  0.000000000000E+00 -1.556087681541E-01
14    -2.500000000000E-01 -3.130777913942E-01  4.466119562843E-01
14     2.500000000000E-01 -2.841970016451E-01  4.773247388183E-01
14    -1.012987358375E-02  1.996923286910E-01  2.972511220710E-01
14    -8.301039798873E-02  3.233874261032E-01  1.755966055483E-02
```

GDa2

```
25
7.57049563 5.90188979 7.93923492 90.000000 90.000000 90.000000
7
14     3.179993157838E-36  0.000000000000E+00 -3.317755115224E-01
14    -5.000000000000E-01  0.000000000000E+00 -3.314607784709E-01
14    -2.540328419967E-01  0.000000000000E+00 -1.579479917192E-01
14     3.179993157838E-36 -2.979853028507E-01  4.554141035298E-01
14    -5.000000000000E-01 -2.999627393408E-01  4.754017175112E-01
14     2.590927888692E-01  1.986179653488E-01  3.060703246884E-01
14     3.385911708657E-01  2.980604297874E-01  2.746233314896E-02
```

GDb1

```
35
7.59541431 11.78051366 7.89549016 90.000000
6
14     0.000000000000E+00  2.642005531346E-01  3.302794401611E-01
14    -2.500000000000E-01  2.500000000000E-01  1.571668848929E-01
14     0.000000000000E+00 -1.026992514975E-01 -4.850260810050E-01
14     5.000000000000E-01 -9.901998071532E-02 -4.480312177424E-01
14    -2.399029541396E-01  1.508919669789E-01 -3.077034648807E-01
14    -1.593408583616E-01  1.013855755626E-01 -2.834104827259E-02
```

GDb2

```
35
7.43144955 11.69900794 7.89262403 90.000000
7
14    -2.143692597877E-22 -2.919150072659E-23  3.308389861378E-01
14    -2.143692597877E-22 -5.000000000000E-01  3.253973587588E-01
14    -2.425957962051E-01 -5.978546026366E-22  1.498959020619E-01
14     7.387083006208E-22  1.510403570648E-01 -4.752164457752E-01
14     5.000000000000E-01  1.477707544546E-01 -4.594846137887E-01
14     2.402298817750E-01 -9.985686855409E-02 -3.028550744134E-01
14     1.688159009659E-01 -1.615324449463E-01 -2.401643305973E-02
```

GDc1

```
39
5.84848658 7.41715198 15.79905490 90.000000
6
14    -1.638960994073E-02  2.500000000000E-01  1.659092170796E-01
14     8.236518084953E-36  6.530358532011E-21  7.701019242520E-02
14    -3.065101594993E-01 -2.500000000000E-01 -2.341674137868E-01
14    -2.908437149519E-01  2.500000000000E-01 -2.286131248455E-01
14    -1.993882547451E-01 -4.926285748986E-01 -1.492044483476E-01
14    -3.219448837099E-01 -4.197745848825E-01 -9.929987088677E-03
```

GDc2

```
38
5.90505566 7.63274399 15.76074160 90.000000
7
14     0.000000000000E+00 -5.000000000000E-01  1.633551210513E-01
14     0.000000000000E+00  0.000000000000E+00  1.837944206252E-01
14     0.000000000000E+00  2.366205252542E-01  8.788958846703E-02
14    -2.990400303232E-01  0.000000000000E+00  2.859247368472E-01
14    -2.982252297083E-01  0.000000000000E+00 -2.345099525256E-01
14    -1.984835899147E-01 -2.368544151286E-01 -1.452892739785E-01
14    -2.985062921606E-01 -1.578563086331E-01 -5.445297834880E-03
```

GDd1

```
42
7.55498438 11.79093278 15.91157524 90.000000
6
14     0.000000000000E+00 -2.443818206969E-01 -1.644112182880E-01
14     2.500000000000E-01 -2.500000000000E-01 -7.760586014860E-02
14     0.000000000000E+00 -1.012890196698E-01  2.315704157406E-01
14     0.000000000000E+00 -9.985055217040E-02 -2.639652661515E-01
14     2.548567174531E-01  1.508153076484E-01  1.540219825233E-01
14    -3.378965268707E-01  1.013157871508E-01  1.538898190048E-02
```

GDd2

```
42
7.48047459 11.67321414 15.64376015 90.000000
7
14    -5.000000000000E-01 -3.048897875608E-21 -1.614652827886E-01
14     5.410694421563E-22 -5.270635310155E-21 -1.863372786197E-01
14    -2.310807450650E-01  1.005559707372E-17 -8.598569531774E-02
14    -7.183121700806E-21  1.470044077851E-01  2.322037977478E-01
14    -1.996396385265E-21  1.521803269252E-01 -2.858765281339E-01
14    -2.373100507738E-01 -1.001332952628E-01  1.411610666961E-01
14     1.643876186964E-01 -1.632072200375E-01  1.246286507922E-03
```

SA1

```
14
3.79879281 9.41123660 15.15656702 113.199478
6
14    -1.603403382562E-01  5.528069091711E-02  4.241669445307E-01
14    -4.736236411331E-01  3.865406673053E-01  1.974468854905E-01
14    -4.243474896960E-01 -4.475032883607E-01 -4.249135015291E-01
14    -1.937908961109E-01 -4.776811351979E-01  3.384545419622E-01
14    -3.044180218588E-01 -1.997939978661E-01 -3.922820236252E-01
14    -8.382466762014E-02 -2.579346748415E-01  2.778453059092E-01
```

SA2

```
14
3.79869550 14.10610184 11.13781830 123.426255
6
14     3.683449455740E-01 -4.253832417074E-01  4.418030349303E-01
14    -3.178694411755E-01 -1.991886760511E-01  1.112948730396E-01
14     1.628932350954E-01 -4.257430584313E-01  4.859707997928E-02
14    -4.438067354189E-01 -3.397499480721E-01 -2.350288260082E-02
14    -3.828638700633E-01 -3.896355015967E-01  2.988436513015E-01
14     4.150060650640E-01 -2.226741738843E-01  2.564720948725E-01
```

SA3

```
18
9.39598538 14.01473043 3.80171951
6
14     4.453422003931E-01 -4.235405429278E-01 -4.515913973191E-01
14    -1.132457671427E-01  1.991621066607E-01 -3.907613275706E-01
14     5.233821669146E-02 -4.245762023756E-01  1.615104031575E-01
14     2.300920498117E-02  3.391588444943E-01 -3.230827691275E-01
14     3.003727264150E-01 -3.917297080764E-01  6.900940524734E-02
14     2.426061537846E-01  2.770633709954E-01 -1.245392590196E-01
```

SA4

```
34
9.59482095 13.83278547 3.76180196
6
14     5.482681157093E-02 -4.226024838344E-01  3.220324694481E-01
14    -3.876911643296E-01  1.929027382053E-01 -4.706171583443E-01
14     5.243645698824E-02  7.584062907597E-02  4.274258592031E-01
14     4.826576693596E-01  3.363302474130E-01  4.379605688431E-01
14     2.044264521411E-01 -3.909117741787E-01 -1.371627835988E-01
14     2.564035480674E-01  2.787844308194E-01 -4.957889555512E-01
```

SB1

```
14
3.79989848 9.64283210 14.32576473 98.535761
6
14     1.363089844485E-01  1.755289331525E-01 -8.954560585153E-02
14     9.563659279328E-02 -3.524838414482E-01  1.993585768733E-01
14     2.389743664257E-01  3.063741801752E-01 -4.246732848300E-01
14     2.314736557236E-01 -2.785753155109E-01 -1.559763954978E-01
14     3.649211850020E-01 -3.909874256413E-02  1.253878326440E-01
14     3.806449339260E-01  4.974918969217E-01 -2.118023021040E-01
```

SB2

```
14
3.81270689 14.20064425 9.77893864 101.079965
6
14     1.975074421173E-01 -8.868899509884E-02 -1.723172920195E-01
14    -2.224358671803E-01  1.981412707425E-01  3.537067490716E-01
14    -1.400350365655E-01 -4.244768548383E-01 -3.061776131758E-01
14     3.993656546724E-01 -1.563669289772E-01  2.739332854793E-01
14     2.497672102629E-01  1.277939097620E-01  3.969545377438E-02
14    -3.504554523411E-01 -2.102462068422E-01 -4.979459241721E-01
```

SB3

```
19
14.15329843 3.79872004 9.63300000
6
14     4.110585307345E-01  6.265447812573E-02 -4.259581893984E-01
14     3.017203441350E-01 -1.198521092120E-01  3.972371989129E-01
14    -4.246261052909E-01  1.371703923170E-01 -4.433164968064E-01
14    -1.567885586052E-01  3.424877111639E-01 -2.793794598029E-02
14     1.256814287275E-01  4.231941616351E-01  2.097826819046E-01
14    -2.111356173939E-01  1.419332122004E-01 -2.511695484783E-01
```

SB4

```
33
14.03013049 9.76773911 3.75479302
6
14     4.093518045758E-01  3.236125958836E-01  4.919883079051E-01
14    -3.050015990135E-01 -1.513056278887E-01 -3.199325850540E-01
14     7.471806210964E-02  1.974903254819E-01 -4.300932441695E-01
14     3.416455050974E-01 -2.225622167174E-01 -4.154491128509E-01
14    -3.755166387735E-01 -4.665199285237E-01 -4.749005335711E-01
14     2.885243322777E-01  4.959727502980E-03 -3.434328322596E-01
```

SC1

```
14
3.79536940 10.22995946 12.58083537 95.078688
6
14    -7.473113983735E-02  1.143926747060E-01  6.426269046737E-03
14    -1.779641440326E-01  1.766526967948E-01  1.851927143976E-01
14     4.110011185519E-01  4.392990383896E-01 -7.666270313764E-02
14     1.363890977741E-01 -1.296507582974E-02 -3.183659047397E-01
14     3.991916541821E-01  2.086289046087E-01 -7.482807905567E-02
14     3.179556636571E-01  1.985229197387E-01 -2.636924476369E-01
```

SC2

```
14
3.65875 12.1079 10.43006 108.04197
6
14   -0.00569    0.49341   -0.38837
14    0.13920    0.68374   -0.67654
14    0.88608    0.57690   -0.06232
14    0.41225    0.81688   -0.51684
14    0.58121    0.57399   -0.29048
14    0.53426    0.76413   -0.29998
```

SC3

```
18
10.25118222 12.51361424 3.78814918
6
14     3.843057392786E-01  4.904036133204E-01 -6.448589038786E-02
14     3.192240026298E-01  3.131803413243E-01  1.138044813728E-01
14     6.293182797120E-02 -4.227496518740E-01  3.231941482269E-01
14    -4.851210002322E-01 -1.822605756148E-01  1.873069782155E-01
14     2.914250385330E-01 -4.270923930651E-01  4.189154776264E-01
14     3.052910441773E-01 -2.382031637309E-01  3.735148735192E-01
```

SC4

```
34
10.32789655 12.60145959 3.74789243
6
14    -3.860299534978E-01 -4.869681535342E-01  3.931844219766E-01
14     3.232716076693E-01  3.159150034130E-01  1.036010732916E-01
14    -6.390159720445E-02  4.235233939973E-01  2.432256938691E-02
14     4.829513370260E-01  1.814991524737E-01  3.269178147935E-02
14    -2.913688680667E-01  4.250805873289E-01 -6.975745673560E-02
14    -3.025462324739E-01  2.384715450045E-01  7.638761060111E-02
```

SD

```
63
10.32789655 12.60145959 3.74789243
6
14    -3.860299534978E-01 -4.869681535342E-01  3.931844219766E-01
14     3.232716076693E-01  3.159150034130E-01  1.036010732916E-01
14    -6.390159720445E-02  4.235233939973E-01  2.432256938691E-02
14     4.829513370260E-01  1.814991524737E-01  3.269178147935E-02
14    -2.913688680667E-01  4.250805873289E-01 -6.975745673560E-02
14    -3.025462324739E-01  2.384715450045E-01  7.638761060111E-02
```

mep

```
223
10.21628464
3
14     0.000000000000E+00  3.080457631353E-01  1.170622392585E-01
14     1.836328729915E-01  1.836328729915E-01  1.836328729915E-01
14     2.500000000000E-01  0.000000000000E+00 -5.000000000000E-01
```

mtn

```
227
14.72399514
3
14    -1.250000000000E-01 -1.250000000000E-01 -1.250000000000E-01
14    -2.169943502463E-01 -2.169943502463E-01 -2.169943502463E-01
14     3.174641942200E-01 -1.825358057800E-01  1.295011757420E-01
```

CAS

```
63
3.83423475 10.74044913 12.72663951
3
14    -3.049695997126E-17  2.570866137000E-01 -5.511620526110E-02
14    -7.624239992815E-18  7.133361706975E-02 -1.573697463423E-01
14    -5.000000000000E-01 -2.898655627853E-02 -9.052835284157E-02
```

NGS

```
178
5.47157777 5.10710666
1
14    -2.322685208250E-01  2.322685208250E-01  4.166666666667E-01
```

tum

```
137
7.45563568 9.20081520
3
14    -1.946318569050E-02  1.946318569050E-02  2.500000000000E-01
14     2.500000000000E-01 -8.703908518123E-02 -4.156697554256E-01
14     2.500000000000E-01  4.142344254555E-01  3.688471736737E-01
```

5.8 Synthesis and Characterization of *a-allo*-$Si_{1-x}Ge_x$

Lavinia M. Scherf, Gero Neubüser, Lorenz Kienle, Thomas F. Fässler*, *manuscript for publication.*

Abstract

$Si_{1-x}Ge_x$ alloys play an important role in solar cell and electronics technologies and are also being investigated as potential lithium ion battery anode materials. We have now synthesized amorphous $Si_{1-x}Ge_x$ with a low Ge content of approximately 16 %. The alloy is prepared by alkali metal extraction of the mixed tetrel Zintl phase $Li_3NaSi_{6-v}Ge_v$ with ethanol. Due to the analogous synthesis route to *a-allo*-Si, we term the new mixed tetrel phase *a-allo*-$Si_{1-x}Ge_x$. The amorphous material crystallizes at 579 °C and contains some microcrystalline *α*-Si, which originates from impurities in the precursor phase. Transmission electron microscopy shows that *a-allo*-$Si_{1-x}Ge_x$ consists of amorphous particles on the nanoscale. Raman spectra exhibit three bands, which correspond to Si–Si, Si–Ge, and Ge–Ge stretching modes, proving that the tetrel elements in *a-allo*-$Si_{1-x}Ge_x$ are mixed on an atomic level.

Introduction

The tetrel elements Si and Ge are fully miscible across the complete compositional range. Their cubic mixed crystals adhere to Vegard's rule with cell parameters increasing almost linearly with increasing Ge content.[1] $Si_{1-x}Ge_x$ thus represents an adjustable material, whose properties can be tuned by stoichiometrical changes to fit specific applications. Both Si and Ge are being commercially used or investigated as solar cell, transistor, and lithium ion battery (LIB) anode materials. While silicon is much more abundant, much cheaper, and easier to handle due to surface passivation, (partial) substitution with germanium offers improved properties in all three applications.

In solar cells, Ge offers much stronger optical absorption of sun light so that higher energy conversion efficiencies can be achieved. For example, polycrystalline $Si_{1-x}Ge_x$ thin films have been shown to be most promising as solar cell materials with a Ge content of $x = 0.8$.[2] In transistor technology, $Si_{1-x}Ge_x$ materials enable applications in high frequency electronics.[3] As a LIB anode material, Ge offers a 400-fold increased Li ion diffusivity than Si[4,5] and its electronic conductivity is four orders of magnitude larger than that of Si.[6] Therefore, a number of mixed $Si_{1-x}Ge_x$ nanostructures have been investigated in LIB anodes, showing good cycling stability and charge/discharge capacities.[7-10]

However, the selection of available $Si_{1-x}Ge_x$ materials is very limited in comparison to Si allotropes and morphologies.[11] Zintl phases have been shown to be ideal precursors for the synthesis of novel tetrel element allotropes and morphologies. Crystalline allotropes were obtained by alkali metal extraction from Li_7Ge_{12} (*allo*-Ge),[12,13] and Li_3NaSi_6 (*allo*-Si).[14] However, *allo*-Si was never structurally characterized and we have obtained an amorphous product under similar reaction conditions.[15] Thermal decomposition of NaSi and oxidation of Na_4Ge_9 with the ionic liquid dodecyltrimethylammonium chloride yielded the guest-free clathrates $\square_{24}Si_{136}$ and $\square_{24}Ge_{136}$.[16,17] Thermal degassing of $NaSi_6$ affords another crystalline open framework allotrope, Si_{24}.[18] Oxidation of Mg_2Ge or K_4Ge_9 solutions containing structure directing agents produces different mesoporous Ge morphologies.[19-22] In additon, a variety of lithium-rich silicides was employed as precursors for the formation of amorphous

Si, which comprises a layered microstructure. This material exhibited a very promising cycling stability in Li-ion half cells by mitigating the stress exerted by volume expansion.[23]

Recently, we have investigated the miscibility of Si and Ge in mixed tetrel Zintl phases.[24] Now having a selection of suitable precursors, we can use them to prepare new $Si_{1-x}Ge_x$ allotropes and morphologies. Herein, we report the synthesis of amorphous $Si_{1-x}Ge_x$, termed *a-allo*-$Si_{1-x}Ge_x$, using the Zintl phase $Li_3NaSi_{6-v}Ge_v$. Similar to the recently reported synthesis of *a-allo*-Si from Li_3NaSi_6, the mixed tetrel phase was employed as a precursor for alkali metal extraction with ethanol. *a-allo*-$Si_{1-x}Ge_x$ represents a potential anode material by combining the beneficial properties of Si and Ge. The material is characterized by powder X-ray diffraction, differential scanning calorimetry, transmission electron microscopy, and Raman spectroscopy.

Experimental Section

General Remarks. The synthesis and sample preparation of $Li_3NaSi_{6-v}Ge_v$ was performed inside an argon-filled glovebox (MBraun, $p(H_2O)$, $p(O_2)$ < 1.0 ppm). $Li_3NaSi_{6-v}Ge_v$ (v = 0.5) was synthesized from $Li_{12}Si_7$, $Na_4Si_2Ge_2$, and Si as published previously.[24] Ethanol was dried over Na and benzophenone. Concentrated HCl was used as purchased.

Synthesis of *a-allo*-$Si_{1-x}Ge_x$. For increased reactivity, $Li_3NaSi_{6-v}Ge_v$ was finely ground using a ball mill. 1.9 g of the starting material were placed inside a 50 mL stainless steel grinding jar, to which 3 stainless steel grinding balls with 15 mm diameter were added. The grinding jar was closed airtightly and placed in a planetary ball mill (Retsch, PM 100). The reactant was ground at 300 rpm for 8 h in 10 min intervals followed by a 5 min break and a change of rotational direction. The resulting black powder was characterized by powder X-ray diffraction.

Subsequently, 40 mL ethanol were slowly added to 1.75 g $Li_3NaSi_{6-v}Ge_v$ inside a Schlenk flask cooled with an ice bath. Vigorous gas formation was observed upon stirring the black suspension for 5 min. 5 mL of concentrated HCl were then added to the reaction mixture, which was stirred for additional 5 min. The suspension was then filtered using a POR 4 glass frit and washed with copious amounts of a 1:1 mixture of deionized water and ethanol. The black product was dried overnight at 120 °C.

Powder X-ray diffraction. Powder X-ray diffraction (PXRD) was carried out to determine the crystalline phases present in all synthesis products. Thus, the samples were finely ground in an agate mortar and then sealed inside 0.3 mm glass capillaries. The PXRD patterns were measured using a Stoe STADI P diffractometer equipped with a Ge(111) monochromator for Cu $K_{\alpha1}$ radiation (λ = 1.54056 Å) and a Dectris MYTHEN DCS 1K solid-state detector. A 5–87.5° 2ϑ range was irradiated for 15 s each in 1.5° steps of the position sensitive detector.

Differential scanning calorimetry (DSC). Thermal analyses were performed in order to assess the thermal stability of *a-allo*-$Si_{1-x}Ge_x$. The sample was sealed in Nb ampules and measured on a DSC machine (Netzsch, DSC 404 Pegasus) under a constant gas flow of 75 mL min^{-1}. The sample was heated to 700 C° and cooled back down to 150 °C twice at a rate of 10 °C min^{-1}. The PROTEUS Thermal Analysis software was used to determine the onset temperature of the DSC signal.[25]

Transmission electron microscopy (TEM). TEM and selected-area electron diffraction (SAED) experiments were performed using a Tecnai F30 STwin microscope (field emission gun cathode,

spherical aberration coefficient C_S = 1.2 nm) equipped with a Si/Li detector (EDAX) for EDX nanoprobe analysis.

Raman spectroscopy. Raman spectra were measured using a SENTERRA Raman spectrometer (Bruker). The powdery samples were filled into a 0.3 mm glass capillary and irradiated with a 785 nm laser beam with an exposure time of 5x30s at 5 mW and 1 mW (after irradiation for 60 s at 10 mW) laser power using a microscope equipped with a 50-fold magnifying objective and a 1200a grid.

Results and Discussion

Synthesis of *α-allo*-$Si_{1-x}Ge_x$. In analogy to the synthesis of *α-allo*-Si from Li_3NaSi_6 by alkali metal extraction with ethanol,[15] *α-allo*-$Si_{1-x}Ge_x$ was prepared from the mixed tetrel precursor $Li_3NaSi_{6-v}Ge_v$ (v = 0.5), which we have previously shown to exist in the range of $0 \leq v \leq 0.5$.[24] To ensure complete reaction, the starting material was rendered more reactive by grinding in a planetary ball mill. PXRD patterns of as-synthesized $Li_3NaSi_{6-v}Ge_v$ and $Li_3NaSi_{6-v}Ge_v$ after ball-milling show significantly broadened reflections (Figure 1a and b), indicating a significant particle size reduction. The starting material was then treated with excess amounts of ethanol, following the equation stated below.

$Li_3NaSi_{6-v}Ge_v + 4\ EtOH \rightarrow 6\ \alpha\text{-}allo\text{-}Si_{1-x}Ge_x + 3\ LiOEt + NaOEt + H_2$

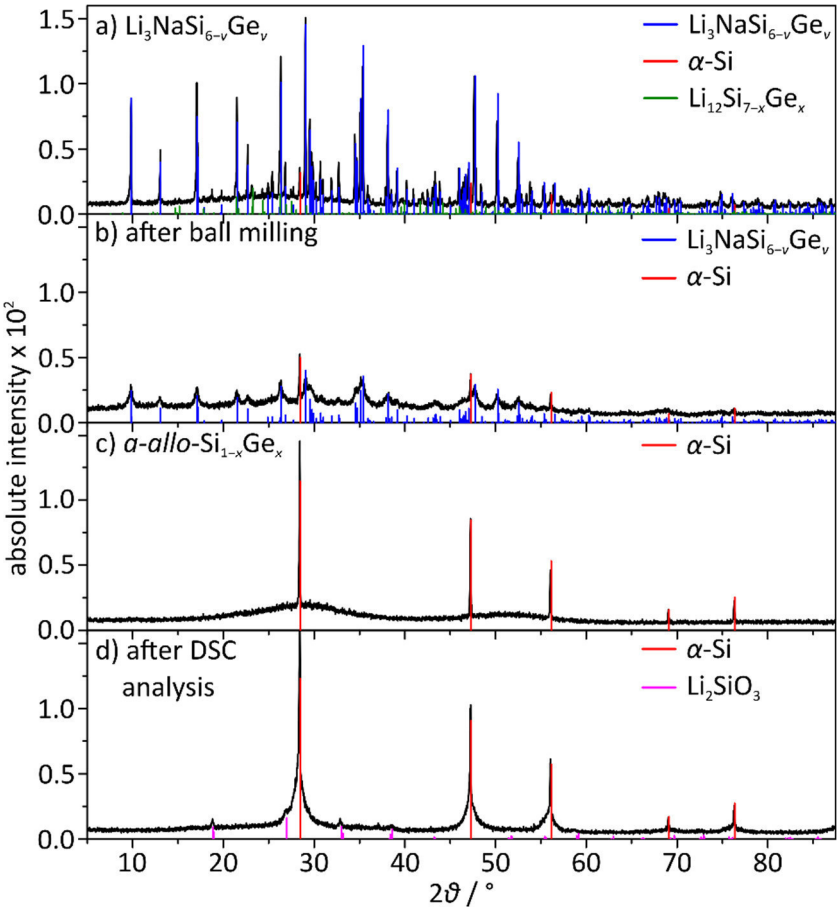

Figure 1. Experimental powder X-ray diffraction patterns of a) as-synthesized $Li_3NaSi_{6-v}Ge_v$, b) $Li_3NaSi_{6-v}Ge_v$ after ball milling, c) as-synthesized *α-allo*-$Si_{1-x}Ge_x$, and d) *α-allo*-$Si_{1-x}Ge_x$ after DSC analysis.

This reaction proceeds vigorously and is accompanied by significant H_2 gas formation and heating of the solution. Workup with concentrated hydrochloric acid for neutralization of the solution, washing with a mixture of ethanol and deionized water, followed by drying at 120 °C affords a mainly amorphous material (Figure 1c). This product contain some crystalline *α*-Si, which originates from the *α*-Si-containing precursor.

Characterization of *a-allo*-$Si_{1-x}Ge_x$. In order to prove the identity of the amorphous material, we performed thermal analysis up to 700 °C using differential scanning calorimetry (DSC). Heating of amorphous samples often leads to their crystallization, allowing characterization by X-ray diffraction methods. The first DSC heating trace of an *a-allo*-$Si_{1-x}Ge_x$ sample contains one main, exothermic signal with an onset temperature of 579 °C (Figure 2). This signal in the range of crystallization temperatures observed for *a-allo*-Si (prepared from Li_3NaSi_6) and *a*-Si (prepared from $Li_{15}Si_4$).[15] A PXRD pattern of the post-DSC sample exhibits a larger content of *α*-Si next to traces of Li_2SiO_3 (Figure 1d), which suggest slight surface oxidation of the amorphous material. In addition, the amorphous background present in the PXRD pattern of as-synthesized *a-allo*-$Si_{1-x}Ge_x$ is not visible in the post-DSC pattern, demonstrating that the exothermic DSC signal indeed corresponds to the crystallization of an amorphous material. The *α*-Si reflections are not significantly shifted, so that we cannot prove the incorporation of Ge into *a-allo*-$Si_{1-x}Ge_x$ at this point. However, we only expect a Ge content of approximately 8.3 %, which cannot cause a large increase in cell parameters.

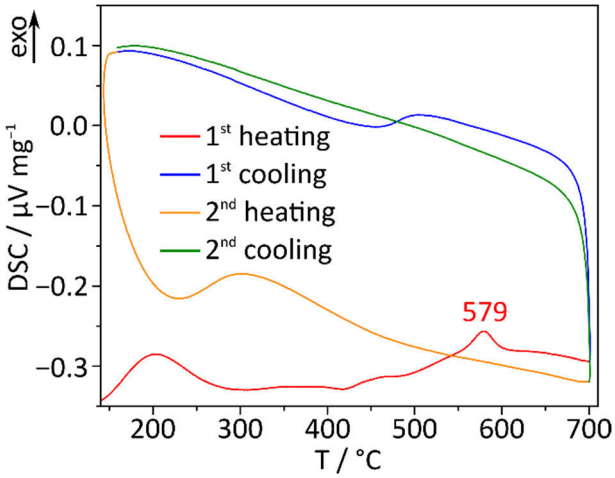

Figure 2. DSC curves of *a-allo*-$Si_{1-x}Ge_x$; two measurement cycles were performed using heating/cooling rates of 10 °C min^{-1}.

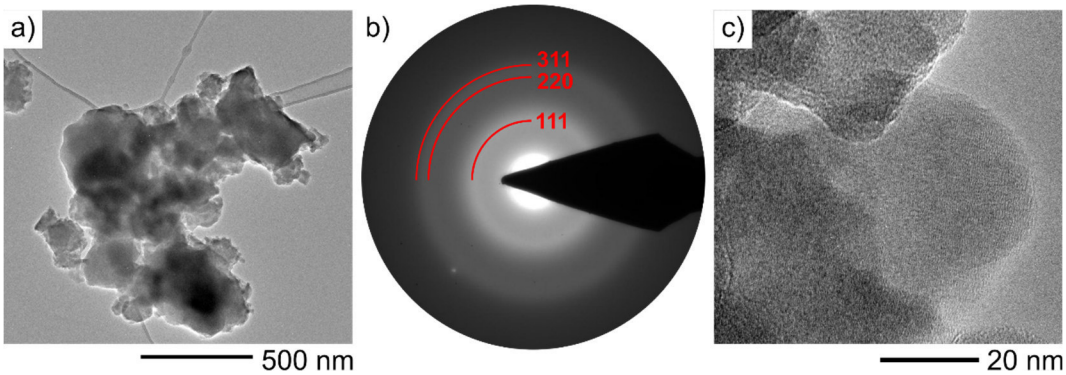

Figure 3. a) TEM bright-field micrograph, b) SAED pattern, and c) high resolution micrograph of *a-allo*-$Si_{1-x}Ge_x$.

Transmission electron microscopy (TEM) images of *a-allo*-$Si_{1-x}Ge_x$ show amorphous particles in the nanoscale (Figure 3). Selected-area electron diffraction patterns of such amorphous particles exhibit

diffuse rings with *d* values that are slightly enlarged with respect to *α*-Si (Figure 3b). Thus, we can now assume that Si and Ge are indeed mixed in *a-allo*-$Si_{1-x}Ge_x$. This is also confirmed by energy-dispersive X-ray spectroscopy (EDX). Several EDX measurements on different sample locations yield a Si:Ge ratio of 84:16 for the amorphous substance. The Ge content is thus even larger than expected. However, the presence of unreacted α-Si originating from the precursor phase $Li_3NaSi_{6-v}Ge_v$ results in a lower Si content in all other present phases. In addition to Si and Ge, EDX also indicates traces of Na as well as O, most likely from surface oxidation, in the samples.

In order to examine whether Si and Ge in *a-allo*-$Si_{1-x}Ge_x$ are mixed on an atomic level, we performed Raman spectroscopy. The corresponding Raman spectrum exhibits three different Raman bands at 283 cm^{-1}, 387 cm^{-1}, and 498 cm^{-1} (Figure 4), which we can assign to Ge–Ge, Si–Ge, and Si–Si stretching vibrations, respectively.[26] As expected for *a-allo*-$Si_{1-x}Ge_x$ with only a small Ge content, the Si–Si band shows by far the largest intensity. Prolonged irradiation of the sample with the laser beam resulted in crystallization of the sample. The Raman spectrum of crystallized $Si_{1-x}Ge_x$ again contains three signals at 298 cm^{-1}, 402 cm^{-1}, and 514 cm^{-1}, corresponding to the three different stretching modes.[27] The blue-shift of the signal is typical for a crystalline product.

Therefore, the Raman spectra prove that Si and Ge are mixed on an atomic level in *a-allo*-$Si_{1-x}Ge_x$. Crystallization of the amorphous material yields atomically mixed and crystalline $Si_{1-x}Ge_x$.

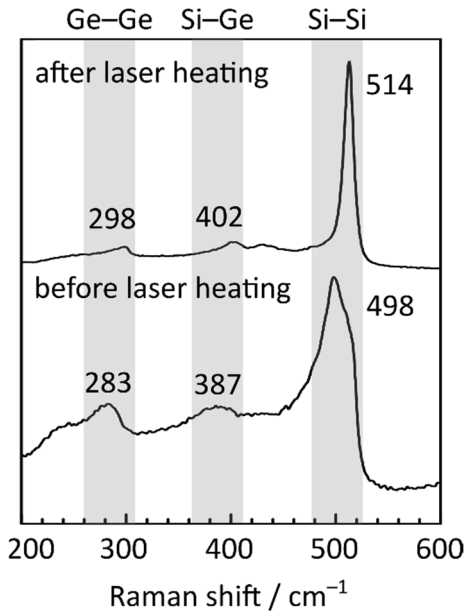

Figure 4. Raman spectra of *a-allo*-$Si_{1-x}Ge_x$ synthesized by ethanol extraction of $Li_3NaSi_{6-v}Ge_v$.The top spectrum was measured after increasing the laser power, which resulted in crystallization of the samples. Grey shaded areas denote the typical Raman shifts of Si–Si, Si–Ge, and Ge–Ge bonds in (nano-)crystalline samples.

Conclusions

In conclusion, we have synthesized *a-allo*-$Si_{1-x}Ge_x$ by alkali metal extraction with ethanol using the mixed tetrel Zintl phase $Li_3NaSi_{6-v}Ge_v$ (v = 0.5) as a precursor. As in *a-allo*-Si, an amorphous product was obtained, which contains some microcrystalline *α*-Si. The amorphous material crystallizes at 579 °C as shown by DSC measurements. Transmission electron microscopy demonstrates that *a-allo*-$Si_{1-x}Ge_x$ consists of nanoscale particles, whose cell parameters are slightly enlarged with respect to

those of Si due to the presence of Ge. EDX indicates a Ge content of 16 % in the amorphous particles. Raman spectra of *a-allo*-$Si_{1-x}Ge_x$ exhibit Ge–Ge, Si–Ge, and Si–Si stretching modes and thus prove that the tetrel elements in the novel material are mixed on an atomic level.

Considering that layered amorphous Si prepared from lithium-rich binary silicides has recently been shown to behave as a high-performance anode material in lithium ion batteries,[23] *a-allo*-$Si_{1-x}Ge_x$ could exhibit even better cycling properties due to the advantages of incorporated Ge. Thus, the material is currently being tested in Li half-cells. In addition, other mixed-silicides such as $Li_{12}Si_{7-x}Ge_x$ should be investigated as precursors for functional $Si_{1-x}Ge_x$ materials. Unlike $Li_3NaSi_{6-v}Ge_v$, some of them exhibit full miscibility of Si and Ge in their anionic substructure and thus promise highly tunable materials.

Author Information

Corresponding Author. * E-mail: Thomas.Faessler@lrz.tum.de

Notes. The authors declare no competing financial interest.

Acknowledgments

The authors are grateful to Sebastian Geier for measuring the Raman spectra. L.M.S. thanks Technische Universität for financial support through the Laura Bassi-Prize as well as Fonds der Chemischen Industrie and Studienstiftung des deutschen Volkes for her fellowships.

References

[1] J. P. Dismukes, L. Ekstrom, R. J. Paff, *J. Phys. Chem.* **1964**, *68*, 3021–3027.
[2] R. Lechner, M. Buschbeck, M. Gjukic, M. Stutzmann, *Phys. Status Solidi C* **2004**, *1*, 1131–1143.
[3] L. Hao, H. M. Rein, T. Suttorp, J. Bock, *IEEE J. Solid-State Circuits* **2004**, *39*, 1650–1658.
[4] H. Jia, R. Kloepsch, X. He, J. P. Badillo, P. Gao, O. Fromm, T. Placke, M. Winter, *Chem. Mater.* **2014**, *26*, 5683–5688.
[5] C. S. Fuller, J. C. Severiens, *Phys. Rev.* **1954**, *96*, 21–24.
[6] J. Grätz, C. C. Ahn, R. Yazami, B. Fultz, *J. Electrochem. Soc.* **2004**, *151*, A698–A702.
[7] T. Song, H. Cheng, H. Choi, J.-H. Lee, H. Han, D. H. Lee, D. S. Yoo, M.-S. Kwon, J.-M. Choi, S. G. Doo, H. Chang, J. Xiao, Y. Huang, W. I. Park, Y.-C. Chung, H. Kim, J. A. Rogers, U. Paik, *ACS Nano* **2012**, *6*, 303–309.
[8] J. Yu, N. Du, J. Wang, H. Zhang, D. Yang, *J. Alloy. Compd.* **2013**, *577*, 564–568.
[9] T. Song, H. Cheng, K. Town, H. Park, R. W. Black, S. Lee, W. I. Park, Y. Huang, J. A. Rogers, L. F. Nazar, U. Paik, *Adv. Funct. Mater.* **2014**, *24*, 1458–1464.
[10] H. Kim, Y. Son, C. Park, M.-J. Lee, M. Hong, J. Kim, M. Lee, J. Cho, H. C. Choi, *Nano Lett.* **2015**, *15*, 4135–4142.
[11] B. Haberl, T. A. Strobel, J. E. Bradby, *Appl. Phys. Rev.* **2016**, *3*, 040808.
[12] A. Grüttner, R. Nesper, H. G. von Schnering, *Angew. Chem. Int. Ed. Engl.* **1982**, *21*, 912–913.
[13] F. Kiefer, A. J. Karttunen, M. Döblinger, T. F. Fässler, *Chem. Mater.* **2011**, *23*, 4578–4586.
[14] H. G. von Schnering, M. Schwarz, R. Nesper, *J. Less-Common Met.* **1988**, *137*, 297–310.

[15] M. Zeilinger, L.-A. Jantke, L. M. Scherf, F. J. Kiefer, G. Neubüser, L. Kienle, A. J. Karttunen, S. Konar, U. Häussermann, T. F. Fässler, *Chem. Mater.* **2014**, *26*, 6603–6612.
[16] A. Ammar, C. Cros, M. Pouchard, N. Jaussaud, J.-M. Bassat, G. Villeneuve, M. Duttine, M. Ménétrier, E. Reny, *Solid State Sci.* **2004**, *6*, 393–400.
[17] A. M. Guloy, R. Ramlau, Z. Tang, W. Schnelle, M. Baitinger, Y. Grin, *Nature* **2006**, *443*, 320–323.
[18] D. Y. Kim, S. Stefanoski, O. O. Kurakevych, T. A. Strobel, *Nat. Mater.* **2015**, *14*, 169–173.
[19] G. S. Armatas, M. G. Kanatzidis, *Science* **2006**, *313*, 817–820.
[20] G. S. Armatas, M. G. Kanatzidis, *Adv. Mater.* **2008**, *20*, 546–550.
[21] G. S. Armatas, M. G. Kanatzidis, *Nature* **2006**, *441*, 1122–1125.
[22] M. M. Bentlohner, M. Waibel, P. Zeller, K. Sarkar, P. Müller-Buschbaum, D. Fattakhova-Rohlfing, T. F. Fässler, *Angew. Chem. Int. Ed.* **2016**, *55*, 2441–2445.
[23] L. Zhao, D. J. Dvorak, M. N. Obrovac, *J. Power Sources* **2016**, *332*, 290–298.
[24] L. M. Scherf, N. Riphaus, T. F. Fässler, *Z. Anorg. Allg. Chem.* **2016**, *642*, 1143–1151.
[25] *PROTEUS Thermal Analysis V4.8.2*, Netzsch-Gerätebau GmbH, Selb, **2006**.
[26] N. J. Shevchik, J. S. Lannin, J. Tejeda, *Phys. Rev. B* **1973**, *7*, 3987–3991.
[27] M. Alonso, K. Winer, *Phys. Rev. B* **1989**, *39*, 10056–10062.

5.9 Searching for Open Tetrahedral Frameworks (OTFs) and Electron-Poor Framework Semiconductors (EPFSs) in the (Li-)B-Si System

Lavinia M. Scherf, Nathalie Riphaus, Gero Neubüser, Lorenz Kienle, Thomas F. Fässler*, *manuscript for publication*.

Abstract

The synthesis of novel open tetrahedral frameworks (OTFs) and electron-poor framework semiconductors (EPFSs) in the (Li-)B-Si system was attempted. Reactive precursors were employed to enable the formation of kinetically preferred and potentially metastable products under relatively mild conditions. Nano-B, LiB, and α-SiB_3 proved to be suitable starting materials in this context. However, the solid-state reactions aimed at the synthesis of Li-B-Si OTFs only yielded previously known binary and ternary lithium silicides and borides. Heterogeneous reactions of alkali metal silicides and germanides with boron halides employed the exothermic formation of alkali metal halides as a driving force. These reactions yielded different amorphous products, including lithium silicides, silicon, and germanium. The boron halides seem to function only as an oxidizing agent, as no incorporation of boron into the oxidized silicon structures was observed.

Introduction

Recently, Zintl phases[1] comprising open tetrahedral frameworks (OTFs) have attracted large research interest.[2] Open tetrahedral frameworks are constructed from tetrahedrally four-coordinated framework atoms and are characterized by the presence of large empty cages or channels. Group III and IV (semi-)metals typically represent the four-coordinated atoms whereas alkali metal cations occupy the voids in these host-guest structures and donate their valence electrons to any electron-deficient framework atoms.

Prominent examples of Zintl phase OTFs are the clathrate-I and clathrate-II structures observed in, e.g., $K_8Zn_4Sn_{42}$,[3] $K_7B_7Si_{39}$,[4] $Sr_8Ga_{16}Ge_{30}$,[5] and $Ba_{16}Ga_{32}Sn_{104}$.[6] They are all semiconductors and promising materials for thermoelectric applications. Related clathrate structures such as Na_8Si_{46}[7] and $A_8Na_{16}Si_{136}$ (A = Rb, Cs)[8] do not strictly obey the Zintl Klemm concept[9] and have metallic properties. $Na_xBa_ySi_{46}$[10] and Ba_8Si_{46}[11] are even superconductors. In contrast to the clathrate structures which are characterized by large cages in the tetrahedral framework, Zintl phases like Na_2ZnSn_5,[12] $Eu_4Ga_8Ge_{16}$,[13] and $LiBSi_2$[14] comprise open channels which are filled by the cationic species.

With the exceptions of $K_7B_7Si_{39}$ and $LiBSi_2$, none of the published OTFs contains second-row elements, which constitute the tetrahedral framework. In $K_7B_7Si_{39}$, boron and silicon share a framework position whereas in $LiBSi_2$, the B and Si sites are strictly separated. The latter has so far been obtained under the extreme conditions of 90 h at 1000 °C and 10 GPa. Thus, we have attempted to synthesize $LiBSi_2$ under milder conditions under which also other OTFs in the Li-Si-B system could be kinetically preferred products.

Electron-poor framework semiconductors such as Zn_4Sb_3 and SiB_3 are defined by a valence electron concentration VEC of $3 < VEC < 4$.[15] Unlike in Zintl phase OTFs, all atoms participate in the framework, forming only weakly polar bonds. The electron-poor compounds cannot form simple tetrahedral

framework structures. Instead, localized multi-center bonds evoke very complex structures, comparable to the modifications of elemental boron.

Indeed, both Zn_4Sb_3[15] and SiB_3[16] occur in different ordered and disordered modifications. α-Zn_4Sb_3 and β-SiB_3 are fully ordered, whereas β-Zn_4Sb_3 and α-SiB_3 are heavily disordered and their actual compositions have been disputed frequently. In addition, Zn_4Sb_3 and α -SiB_3 are narrow-band gap semiconductors, rendering them ideal candidates for thermoelectric materials. β-Zn_4Sb_3 in particular has been shown to be one of the most efficient thermoelectric materials known to date.[17,18]

Again, the synthesis of binary silicon-boron compounds so far requires relatively harsh conditions. However, it is well known that suspensions of Si-containing Zintl phases can be oxidized to Si nanoparticles using $SiCl_4$ and other oxidants under much milder conditions.[19-22] In addition, B nanoparticles have been prepared by reducing BBr_3 solutions using sodium naphthalenide.[23] Here, we attempt to combine the two reactions in order to prepare binary Si-B EPFSs in reactions of alkali metal silicides (and germanides) with different boron halides.

Experimental Section

Solid-State Syntheses. All steps of synthesis and preparation were performed in an Ar-filled glovebox (MBraun, $p(H_2O)$, $p(O_2)$ < 1.0 ppm). If not stated otherwise, all starting materials were purchased or synthesized by literature procedures[14,24-26] and then used without further purification. Lithium was freed from surrounding oxide layers before use. All solid-state syntheses including boron or boron-containing starting materials were carried out in custom-built boron nitride crucibles to avoid side reactions of any components with the reaction container. The BN crucibles were sealed in niobium ampules.

LiSi was prepared by mechanical alloying of the elements. Stoichiometric amounts with a total mass of 2 g were placed in a WC milling jar containing three WC grinding with a diameter of 15 mm. The milling jar was closed tightly and rotated inside a planetary ball mill (Retsch, PM 100) for 12 h at 300 rpm. α-SiB_3 was prepared by heating a 1:4 mixture of Si and B to 1200 °C for 3 h. The reaction was performed in BN crucibles enclosed inside a Nb ampule.The various solid-state reactions performed in the Li-B-Si system are summarized in Table 1.

Table 1. Experimental details on the solid-state reactions in the Li-S-B system. T_{max} and t_{anneal} denote reaction temperature and annealing time.

B reagent	Si reagent	ratio	T_{max}	t_{anneal}	Cooling rate	Crystalline reaction products
nano-B	Si	1:1:1 (Li)	900 °C	12 h	0.2 °C min^{-1}	Li_2B_6, $Li_{12}Si_7$, Si
nano-B	Si	1:1:2 (Li)	900 °C	12 h	0.2 °C min^{-1}	Li_2B_6, $Li_{12}Si_7$, Si
nano-B	Si	1:2:1 (Li)	900 °C	12 h	0.2 °C min^{-1}	$Li_2B_{12}Si_2$, $Li_{12}Si_7$, Si
nano-B	LiSi	1:1	[a]	[a]	[a]	LiSi, Si
nano-B	LiSi	[b]	[b]	[b]	[b]	$Li_{12}Si_7$, Si
nano-B	LiSi	1:1	1600 °C	5 min	[c]	Li_3B_{14}, $Li_{12}Si_7$, Si
nano-B	$Li_{17}Si_4$	4:1	750 °C	12 h	0.5 °C min^{-1} [d]	Li_2B_6, $Li_{17}Si_4$, $Li_{13}Si_4$
nano-B	$Li_{17}Si_4$	2:1	600 °C	48 h	0.5 °C min^{-1}	LiB, $Li_{13}Si_4$
nano-B	$Li_{17}Si_4$	4:1	600 °C	48 h	0.5 °C min^{-1}	$Li_6B_{18}(Li_2O)_x$, $Li_{13}Si_4$

nano-B	$Li_{17}Si_4$	8:1	600 °C	48 h	0.5 °C min^{-1}	$Li_6B_{18}(Li_2O)_x$, LiB, $Li_{13}Si_4$
LiB	Si	1:2	[a]	[a]	[a]	Si
LiB	LiSi	1:1	[a]	[a]	[a]	LiSi, Si
LiB	LiSi	1:1	750 °C	1h	0.5 °C min^{-1}	Li_3B_{14}, $Li_{12}Si_7$, Si
LiB	LiSi	1:3	750 °C	1h	0.5 °C min^{-1}	$Li_{12}Si_7$
LiB	LiSi	3:1	750°C	1h	0.5 °C min^{-1}	Li_2B_6, LiB, Li_7Si_3
LiB	LiSi	1:1	1450 °C	5 min	[c]	Li_2B_6, $Li_{12}Si_7$, Si
LiB	$Li_{15}Si_4$	4:1	750 °C	1h	0.5 °C min^{-1}	Li_2B_6, $Li_{13}Si_4$
LiB	$Li_{15}Si_4$	4:3	750 °C	1h	0.5 °C min^{-1}	Li_2B_6, $Li_{13}Si_4$
LiB	$Li_{15}Si_4$	12:1	750 °C	1h	0.5 °C min^{-1}	Li_2B_6, $Li_{13}Si_4$
LiB	α-SiB_3	1:1	900 °C	3 d	0.5 °C min^{-1}	$Li_2B_{12}Si_2$, Li_2B_6, Si
LiB	α-SiB_3	4:1	800 °C	3 d	0.5 °C min^{-1}	Li_2B_6, Si
LiB	α-SiB_3	4:1	500 °C	9 d	0.5 °C min^{-1}	Li_2B_6, Li_7Si_3, α-SiB_3
LiB	α-SiB_3	1:1:4 (Li)	800 °C	3 d	0.5 °C min^{-1}	Li_2B_6, Li_7Si_3
LiB	α-SiB_3	1:1:4 (Li)	500 °C	9 d	0.5 °C min^{-1}	Li_3B_{14}, LiB, $Li_{13}Si_4$
α-SiB_3	LiSi	1:1	900 °C	3 d	0.5 °C min^{-1}	$Li_2B_{12}Si_2$, Si
α-SiB_3	LiSi	1:4	800 °C	3 d	0.5 °C min^{-1}	$Li_2B_{12}Si_2$, Li_2B_6, $Li_{12}Si_7$, α-SiB_3, Si
α-SiB_3	LiSi	1:4	500 °C	9 d	0.5 °C min^{-1}	$Li_{12}Si_7$, Si
$LiBH_4$	Si	1:2	450 °C	72 h	0.5 °C min^{-1}	$Li_{12}Si_7$, Si
$LiBH_4$	Si	1:2	[a]	[a]	[a]	$LiBH_4$, Si
$LiBH_4$[e]	Si[e]	1:2	400 °C	36 h	5 °C min^{-1}	Si
$LiBH_4$[e]	Si[e]	1:2	750 °C	36 h	5 °C min^{-1}	$Li_{12}Si_7$, Si
$LiBH_4$	LiSi	1:1	450 °C	72 h	0.5 °C min^{-1}	$Li_{12}Si_7$, Si
$LiBH_4$	LiSi	1:1	[a]	[a]	[a]	$LiBH_4$, LiSi, Si
$LiBH_4$[e]	LiSi[e]	1:1	400 °C	48 h	5 °C min^{-1}	Si
$LiBH_4$[e]	LiSi[e]	1:1	750 °C	36 h	5 °C min^{-1}	$Li_{12}Si_7$, Si
B_2O_3	$Li_{12}Si_7$	3:2	[a]	[a]	[a]	$Li_{12}Si_7$
B_2O_3	$Li_{12}Si_7$	3:2	750 °C	36 h	5 °C min^{-1}	$Li_{12}Si_7$, Si, Li_4SiO_4
B_2O_3	$Li_{17}Si_4$	1:1	750 °C	12 h	0.5 °C min^{-1} [d]	$Li_{13}Si_4$, $Li_8O_2(SiO_4)$, Li_2O
B_2O_3	Si	1:4:24 (Li)	750 °C	12 h	0.5 °C min^{-1} [d]	$Li_{13}Si_4$, Li_2O

[a] Mechanical alloying using a planetary ball mill: WC grinding jar, three 15 mm grinding balls, 12 h, 300 rpm.

[b] This reaction yielded the same product mixture in all combinations of starting material ratios 1:2, 1:1, and 2:1 and reaction temperatures 450 °C, 575 °C, and 900 °C.

[c] The reactions were performed in an induction furnace with total cool-down times of about 15 min.

[d] An annealing step was added at 400 °C (24 h).

[e] Before the synthesis, the starting materials were thoroughly mixed by grinding in a ball mill.

Heterogeneous Syntheses. All steps of heterogeneous synthesis and preparation were performed under inert conditions. Solid precursors were handled inside an Ar-filled glovebox and reactions and work-up were carried out under standard Schlenk conditions. Dry DMSO was employed without further purification, ethanol was dried over Na, and all other solvents were obtained from a solvent purification system (MBraun, MB-SPS). All solvents were stored over molecular sieve (3 Å). The various alkali metal silicides and germanides were prepared by literature procedures as described in the

previous section.[24-30] For increased reactivity, Li_3NaSi_6 was finely ground in a planetary ball mill before use (50 mL stainless steel milling jar, three steel grinding balls with 15 mm diameter, 8h grinding at 300 rpm). The *N*-heterocyclic borane *N,N'*-bis(2,6-diisopropylphenyl)-2-bromo-2,3-dihydro-1*H*-1,3,2-diazaborole (NHB-Br) was prepared as published previously.[31]

Different boron halides were added to suspensions of various alkali metal silicides and germanides (s. Table 2 for experimental details). The resulting reaction mixture was stirred under the conditions given in Table 2. Reactions in hexane at 100 °C were carried out inside pressure-proof reaction vessels. Subsequently, the solid product was allowed to settle and the supernatant was removed by filtration. The residue was then dried *in vacuo* and characterized by powder X-ray diffraction. At this point it was decided whether a full reaction had occurred fully (at most traces of starting material), incompletely (significant amounts of starting material remaining), or not at all (at most traces of alkali metal bromides observed).

For successful reactions, the alkali metal bromides were removed by washing with THF (for LiBr) and DMSO (for NaBr) if necessary. After that, the solid product was again dried *in vacuo* and subjected to further characterization.

Table 2. Experimental details on the heterogeneous reactions. *T*, *t*, and RT stand for reaction temperature, reaction time, and room temperature. Dicyclohexyliodoborane is abbreviated as BCy_2I, *N,N'*-bis(2,6-diisopropylphenyl)-2-bromo-2,3-dihydro-1*H*-1,3,2-diazaborole is abbreviated as NHB-Br, and tetrahydrofurane is abbreviated as THF.

Si/Ge reagent	B reagent	ratio	solvent	*T*	*t*	Result before work-up
Li_7Ge_{12}	BBr_3	1:6	toluene	100 °C	1 w	No reaction
$Li_{12}Si_7$	BBr_3	1:3	hexane	RT	3 d	No reaction
$Li_{12}Si_7$	BBr_3	1:10	toluene	100 °C	1 w	Reaction incomplete
$Li_{18}Na_2Ge_{17}$	BBr_3	1:17	toluene	100 °C	2 w	Reaction incomplete
$Li_{17}Si_4$	BBr_3	1:6	hexane	RT	3 d	Reaction incomplete
$Li_{17}Si_4$	BBr_3	1:6	hexane	RT	4 w	Reaction incomplete
$Li_{17}Si_4$	BBr_3	1:12	hexane	RT	4 w	Reaction incomplete
$Li_{17}Si_4$	BBr_3	1:12	hexane	RT[a]	2 w	Reaction incomplete
$Li_{17}Si_4$	BBr_3	1:12	CH_2Cl_2	RT[a]	2 w	Reaction incomplete
$Li_{17}Si_4$	BBr_3	1:12	-	RT[a]	2 w	Reaction incomplete
Na_4Si_4	BBr_3	1:3	hexane	RT	1 w	Reaction incomplete
Na_4Si_4	BBr_3	1:3	toluene	100 °C	4 d	Reaction incomplete
Na_4Si_4	BBr_3	1:3	hexane	100 °C	6 d	Full reaction
K_4Si_4	BBr_3	1:3	hexane	RT	8 d	Full reaction
$Li_{15}Si_4$[b]	BBr_3	1:11	hexane	RT[a]	2 w	Reaction incomplete
$Li_{15}Si_4$[b]	BBr_3	1:12	hexane	100 °C	2 d	Reaction incomplete
$Li_{15}Si_4$[b,c]	BBr_3	1:12	hexane	100 °C	5 d	Full reaction
$Li_{15}Si_4$[b]	BBr_3	1:12	toluene	100 °C	4 d	Full reaction
$Li_{15}Ge_4$[b]	BBr_3	1:12	hexane	RT	1 w	Reaction incomplete
$Li_{15}Ge_4$[b]	BBr_3	1:12	toluene	100 °C	4 d	Full reaction, some Li_7Ge_3, LiGe
Li_3NaSi_6[b]	BBr_3	1:5.5	toluene	100 °C	5 d	Full reaction
Li_3NaSi_6[b]	BBr_3	1:5.5	toluene	RT	1 w	Full reaction
Li_3NaSi_6[b]	BBr_3	1:5.5	toluene	100 °C	2 d	Full reaction
Li_3NaSi_6[b]	BBr_3	3:4	toluene	100 °C	1 d	Full reaction
Li_3NaSi_6[b]	BI_3	3:4	toluene	RT	1 d	Full reaction

Li_3NaSi_6[b]	BCy_2I	1:10	toluene	100 °C	1 d	Full reaction
Li_3NaSi_6[b]	BCy_2I	1:4	toluene	100 °C	1 d	Full reaction
Li_3NaSi_6[b]	BCy_2I	1:4	THF	66 °C	1 d	Full reaction
Li_3NaSi_6[b]	NHB-Br	1:4	toluene	100 °C	1 d	No reaction

[a] Stirred in ultrasonic bath.

[b] Ball-milled starting material.

[c] Si reagent was activated by heating overnight before the B reagent was added.

Powder X-ray diffraction. Powder X-ray diffraction (PXRD) was carried out to determine the crystalline phases present in all synthesis products. Thus, the samples were finely ground in an agate mortar and then sealed inside 0.3 mm or 0.5 mm glass capillaries. The PXRD patterns were measured using a Stoe STADI P diffractometer equipped with a Ge(111) monochromator for Cu $K_{\alpha 1}$ radiation (λ = 1.54056 Å) and a Dectris MYTHEN DCS 1K solid-state detector. A 5 – 87.5° 2ϑ range was irradiated for 15 s each in 1.5° steps of the position sensitive detector.

Differential scanning calorimetry (DSC). Thermal analyses were performed in order to crystallize the amorphous materials obtained in heterogeneous reactions. The samples were sealed in Nb ampules and measured on a DSC machine (Netzsch, DSC 404 Pegasus) under a constant gas flow of 75 mL min^{-1}. The samples were heated to 1000 °C and cooled back down to 150 °C twice at a rate of 10 °C min^{-1}. The PROTEUS Thermal Analysis software was used to determine onset temperatures of the various DSC signals.[32]

Raman spectroscopy. The Raman spectrum of the reaction product of Li_3NaSi_6 and BBr_3 in toluene was measured using an inVia Raman microscope (Renishaw, RE04). The powdery sample was filled into a 0.5 mm glass capillary and irradiated with a 532 nm laser beam for 1 s at 10 % laser power using a microscope equipped with a 50-fold magnifying objective and a grating with 1800 lines mm^{-1}. 150 such measurements were averaged to yield the final Raman spectrum.

Transmission electron microscopy. Transmission electron microscopy (TEM) and selected-area electron diffraction (SAED) was performed using a Tecnai F30 STwin microscope (field emission gun cathode, spherical aberration coefficient C_S = 1.2 nm) equipped with a Si/Li detector (EDAX) for EDX nanoprobe analysis. Electron energy loss spectroscopy (EELS) was performed using a JEM-2100 microscope (JEOL, 200 kV, LaB_6, spherical aberration coefficient C_S = 1.0 nm) equipped with an EDX detector (SDD, Oxford). TEM samples were prepared in a glovebox by placing the materials onto lacey-carbon grids, which were subsequently transferred to the TEM in argon-filled bags.

Results and Discussion

OTF synthesis attempts. For boride syntheses starting from elemental boron, very high reaction temperatures are typically needed in order to break apart the very stable boron polyhedra. Thus, the most thermodynamically stable products are always obtained. For the synthesis of potentially metastable Li-Si-B OTFs, we therefore employed a number of activated B reagents. This strategy could allow lower reaction temperatures and thus the formation of kinetically favored products. The results of all OTF synthesis attempts are listed in Table 1.

Nanoparticles of amorphous boron (nano-B, Pavezyum) have demonstrated a significantly increased reactivity in the synthesis of superconducting MgB_2.[33] In the present experiments, nano-B readiliy reacts with elemental Li and Si as well as $Li_{17}Si_4$. However, only previously known binary and ternary borides and silicides such as Li_2B_6,[34] $Li_{12}Si_7$,[35] $Li_{13}Si_4$,[36,37] $Li_6B_{18}(Li_2O)_x$,[38] and $Li_2B_{12}Si_2$[39] were obtained (Table 1). Reactions of nano-B with LiSi only yield crystalline boride (Li_3B_{14})[40] when performed in an induction oven at 1600 °C. At lower temperatures, only the decomposition products of LiSi, $Li_{12}Si_7$ and Si, are observed by powder X-ray diffraction (PXRD).

Lithium boride LiB comprises linear borynide chains which are isoelectronic to polycumulene.[41] This anionic substructure should be easier to break apart than boron polyhedra so that LiB is a promising starting material for Li-B-Si syntheses. In addition, it has been used successfully as a precursor for $LiBSi_2$.[14] Thus, LiB was reacted with Si, LiSi, and $Li_{15}Si_4$ by mechanical alloying and under various high temperature conditions (Table 1). LiSi and $Li_{15}Si_4$ were selected because they are known to decompose peritectically, forming reactive species at elevated temperatures.[42,43] Mechanical alloying did not induce any reaction of LiB with any the Si reagents. At relatively mild temperatures of 500–800 °C LiB reacted readily but again only mixtures of previously known binary and ternary lithium borides and silicides were obtained.

The EPFS α-SiB_3 comprises boron icosahedra with Si atoms partially substituting icosahedral sites.[44,45] α-SiB_3 was demonstrated to be metastable, rendering it an additional promising precursor for lower temperature Li-Si-B phase syntheses. Indeed, α-SiB_3 reacts with LiSi and LiB at mild temperatures (Table 1), but the reactions only yield previously known binary and ternary lithium borides and silicides.

In addition, we tested $LiBH_4$ and B_2O_3 as B reagents for the synthesis of Li-B-Si OTFs. As Table 1 shows, the formation of any crystalline borides was never observed, although the reactions were performed with different Si reagents at up to 750 °C. Instead, only Si and lithium silicides were detected by PXRD. Apparently, $LiBH_4$ decomposes to an amorphous phase under these conditions. B_2O_3 is an amorphous starting material that does not seem to undergo any reaction with lithium silicides.

EPFS synthesis attempts. The synthesis of kinetically favored EPFSs in the Si-B system was attempted in various heterogeneous reactions, which are listed in Table 2. In all cases, alkali metal silicides (and germanides) A_xSi_y were reacted with boron halides BX_3 according to Equation (1).

$$3/x\ A_xSi_y + BX_3 \rightarrow \text{“}BSi_{3y/x}\text{”} + 3\ AX \qquad (1)$$

The boron halide was always added to a suspension of the alkali metal tetrelide in an organic solvent. After stirring for an extended time at room or elevated temperature, the remaining solid was isolated and characterized via PXRD.

The exothermic formation of alkali metal halides drives these reactions. However, they do not proceed as vigorously as expected. For example, even when Li_7Ge_{12} is stirred with an excess of BBr_3 in toluene at 100 °C for one week, no reaction is observed and the starting material remains unchanged. Similarly, after the reaction of $Li_{12}Si_7$, $Li_{17}Si_4$, or $Li_{18}Na_2Ge_{17}$ with BBr_3 under similar conditions, significant amounts of starting material remain next to LiBr (and NaBr). Only for Na_4Si_4, K_4Si_4, $Li_{15}Si_4$, $Li_{15}Ge_4$, and Li_3NaSi_6 a full reaction with BBr_3 was observed, characterized by the formation of alkali metal bromide and the absence (or only trace amounts) of the starting material. Thus, the reaction conditions were optimized and some of the resulting reaction products were thoroughly characterized, as described below.

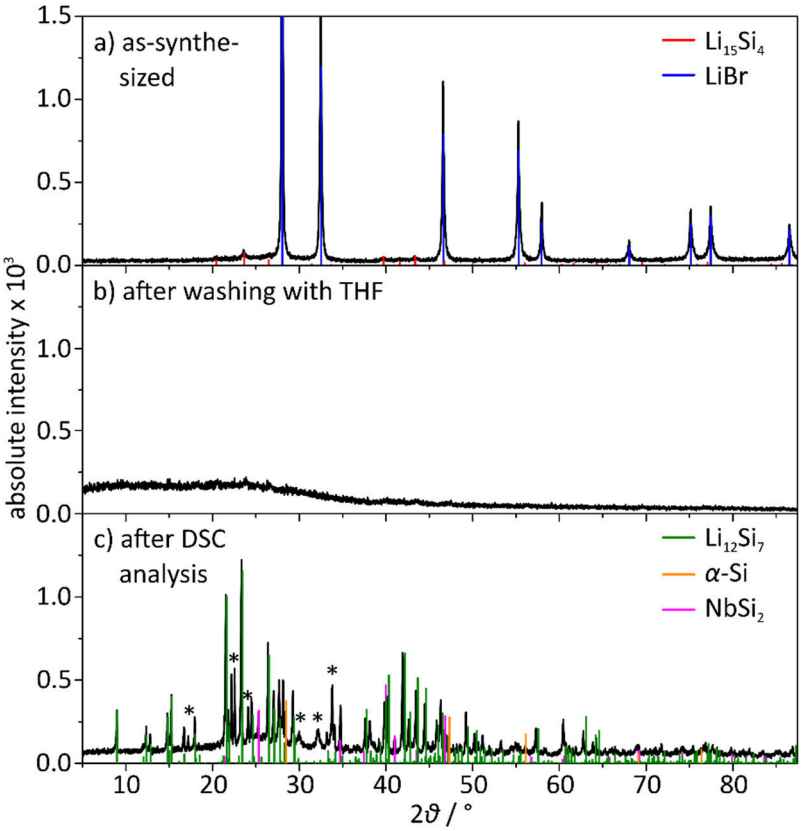

Figure 1. PXRD patterns of the product of the reaction of $Li_{15}Si_4$ with BBr_3 in toluene at 100 °C a) as-synthesized, b) after washing with THF, and c) after DSC analysis. Reflections marked with * could not be assigned.

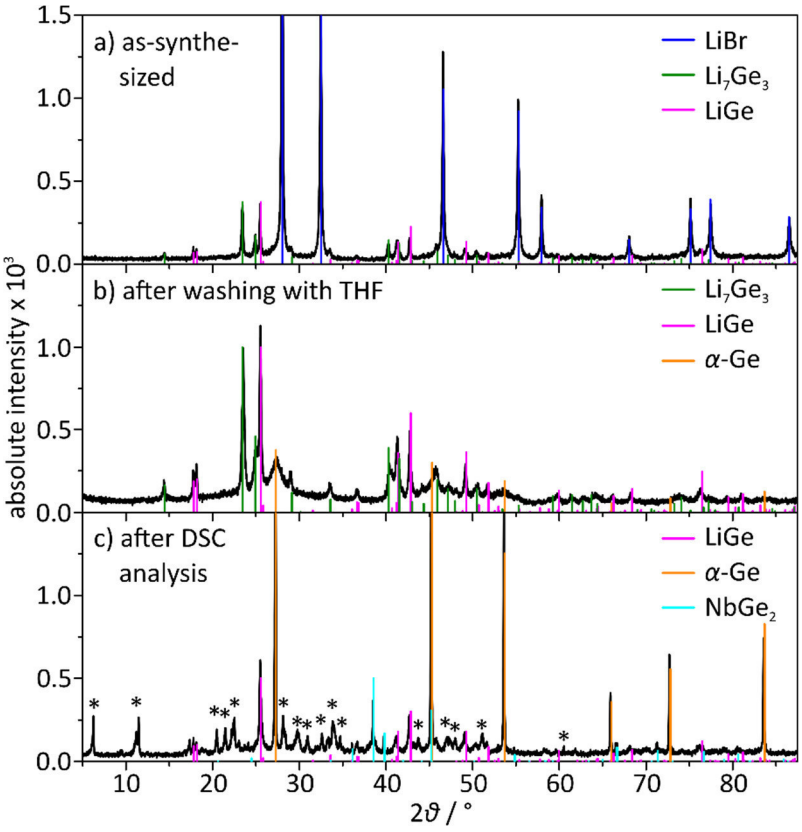

Figure 2. PXRD patterns of the product of the reaction of $Li_{15}Ge_4$ with BBr_3 in toluene at 100 °C a) as-synthesized, b) after washing with THF, and c) after DSC analysis. Reflections marked with * could not be assigned.

The reaction of $Li_{15}Si_4$ with BBr_3 was initially performed in hexane at room temperature. Further experiments showed that the reaction proceeds more completely when the reaction is carried out in 100 °C in a pressure tube. Activation of $Li_{15}Si_4$ was achieved by stirring it overnight in hexane at 100 °C before adding BBr_3 and resulted in full conversion of the starting material. For easier handling, high-boiling toluene was later chosen as the preferred solvent. After the reaction, a fine black powder was obtained which comprises only LiBr and traces of $Li_{15}Si_4$ as crystalline phases (Figure 1a).

LiBr was then removed by repeated washing of the black solid with THF, and the resulting product is essentially amorphous according to PXRD (Figure 1b). Thermal analysis of the product via differential scanning calorimetry (DSC) detects a broad exothermic signal at 429 °C, which could originate from a crystallization process of the amorphous material (Figure S1). Reversible signals at 596 °C and 636 °C most likely correspond to melting processes of a mixture of $Li_{12}Si_7$ and α-Si, which are found to be present in the post-DSC sample (Figure 1c). In addition, $NbSi_2$ stemming from the reaction of Si with the Nb ampule material and some unassigned reflections are observed. Therefore, the amorphous reaction product most likely comprises amorphous lithium silicides and/or silicon. Electron energy loss spectroscopy (EELS) of the sample shows that it does not contain any boron, suggesting that the reduced boron species are soluble and removed by the washing process.

The reaction of $Li_{15}Ge_4$ with BBr_3 proceeds similarly. However, the synthesis product contains crystalline Li_7Ge_3 and LiGe next to LiBr (Figure 2a). These binary germanides were not observed in PXRD patterns of the starting material $Li_{15}Ge_4$. Removal of LiBr using THF affords the same two lithium germanides with elemental germanium, which is characterized by very broad reflections in the PXRD pattern (Figure 2b). Thermal analysis reveals several signals, which cannot be fully assigned (Figure S2). The resulting product contains crystalline LiGe, α-Ge, $NbGe_2$, and small amounts of at least one additional phase, which could not be identified (Figure 2c).

Finely ground Li_3NaSi_6 also readily reacts with BBr_3 in toluene and full reaction is observed even at room temperature and without excess amounts of BBr_3 (Figure 3a). For the removal of NaBr, which is insoluble in THF, an additional washing step with DMSO was introduced. The PXRD pattern of the washed product exhibits traces of Li_3NaSi_6 next to α-Si, which was already present in the starting material (Figure 3b). Thermal analysis of the product shows an exothermic signal at 378 °C corresponding to crystallization (Figure S3). Few small DSC signals cannot be assigned conclusively. The post-DSC product mainly consists of α-Si (Figure 3c), suggesting that amorphous Si was present before. Again, EELS does not detect any boron in the sample.

A Raman spectrum of the amorphous reaction product supports the hypothesis of amorphous Si as the main product of the reaction of Li_3NaSi_6 and BBr_3 (Figure S4). Transmission electron microscopy (TEM) further proves the presence of amorphous Si. TEM micrographs show porous Si particles of 100–500 nm (Figure 4a) which can be assigned to amorphous and nanocrystalline Si by selected area electron diffraction (SAED, Figure 4b). Space-resolved EDX data show that the particles comprise mainly Si. Traces of O, Na, and F[46] are found only on the surface of the particles (Figure 4, d). B could not be detected with this method.

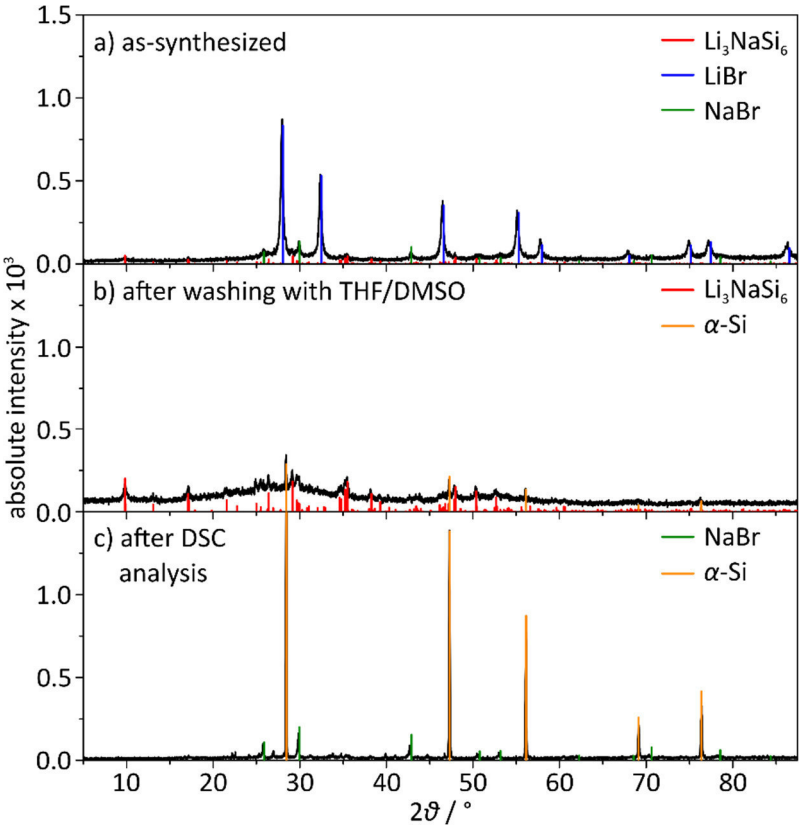

Figure 3. PXRD patterns of the product of the reaction of Li_3NaSi_6 with BBr_3 in toluene a) as-synthesized, b) after washing with THF and DMSO, and c) after DSC analysis.

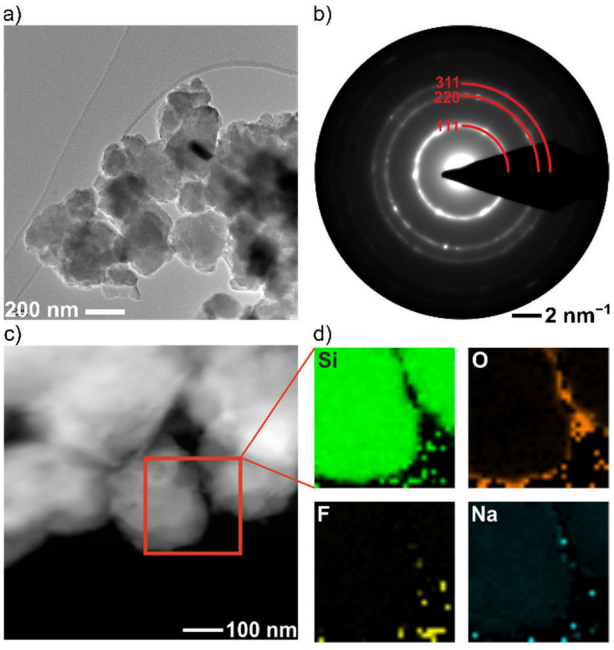

Figure 4. a) TEM micrograph of the product of the reaction of Li_3NaSi_6 with BBr_3 in toluene, showing porous particles of 100–500 nm; b) SAED pattern displaying diffuse rings and some discrete reflections which can be assigned to α-Si, c) TEM micrograph showing the area on which EDX measurements were performed and d) space-resolved EDX data exhibiting the distribution of Si, O, F, and Na.

Due to the high viscosity of DMSO, the removal of NaBr from the reaction product is very tedious. Since NaI is soluble THF, BI_3 was employed as an alternative to BBr_3. The reaction with Li_3NaSi_6 proceeds analogously (Table 2) and the alkali metal iodides can be easily removed by washing with THF.

Li_3NaSi_6 comprises two-dimensional polysilicide sheets which are separated by the alkali metal cations.[47] Like in $CaSi_2$, an efficient precursor for functionalized polysilane sheets,[48-53] two-dimensional polysilicon sheets could be exfoliated and stabilized by functionalization of Li_3NaSi_6. Thus, boron monohalides BR_2X were tested as functionalization reagents (Table 2). However, the *N*-heterocyclic bromoborane *N,N*'-bis(2,6-diisopropylphenyl)-2-bromo-2,3-dihydro-1*H*-1,3,2-diazaborole (NHB-Br) does not react with BBr_3. The reaction of dicyclohexyliodoborane BCy_2I with Li_3NaSi_6 afforded products, which are very similar to those of the reaction of Li_3NaSi_6 with BBr_3. Raman spectra of the product do not display any C–C or C–H bands.

Therefore, like the other boron halides BCy_2I solely acts as an oxidizing agent for the alkali metal silicide and is not incorporated into the silicon structure.

Conclusions

Overall, we have attempted to prepare new open tetrahedral frameworks in the Li-Si-B system by employing different reactive B precursors. Nano-B, LiB, and α-SiB_3 have proven to be suitable reagents and allowed reactions with Si or several lithium silicides at comparatively low temperatures. However, only previously known lithium silicides and borides, excluding $LiBSi_2$, were obtained. In contrast, reactions with $LiBH_4$ and B_2O_3 did not yield any crystalline borides under similarly mild conditions.

The synthesis of novel electron-poor framework semiconductors was attempted by reactions of alkali metal silicides and germanides with boron halides, using the exothermic formation of alkali metal halides as the driving force. The heterogeneous reactions, which were typically carried out in organic solvents, proceeded sluggishly and only for few alkali metal silicides and germanies full decomposition of the starting material was observed. In these reactions, the boron halides seem to function solely as oxidizing agents and an incorporation of boron into the resulting silicon structures was not observed. Oxidation of $Li_{15}Si_4$ afforded amorphous lithium silicides and/or silicon, whereas upon oxidation of $Li_{15}Ge_4$ crystalline Li_7Ge_3 and LiGe were observed next to essentially amorphous Ge. Reactions of Li_3NaSi_6 with various boron halides led to the formation of amorphous Si as proven by Raman spectroscopy and TEM.

Associated Content

Supporting Information. DSC curves of reaction products of $Li_{15}Si_4$, $Li_{15}Ge_4$, and Li_3NaSi_6 with BBr_3, respectively (Figures S1–S3); Raman spectrum of the reaction product of Li_3NaSi_6 with BBr_3 (Figure S4).

Author Information

Corresponding Author. * E-mail: Thomas.Faessler@lrz.tum.de

Notes. The authors declare no competing financial interest.

Acknowledgments

L.M.S. thanks Fonds der Chemischen Industrie and Studienstiftung des deutschen Volkes for her fellowships.

References

[1] Zintl phases are intermetallic phases consisting of electropositive alkali or alkaline earth metals and more electronegative group III-VI metals, semimetals, and small band-gap semiconductors. They are characterized by a strongly heteropolar bonding situation and can be described by a formal electron transfer form the electropositive to the more electronegative component.
[2] M. Beekman, G. S. Nolas, *J. Mater. Chem.* **2008**, *18*, 842–851.
[3] V. Baran, A. Fischer, W. Scherer, T. F. Fässler, *Z. Anorg. Allg. Chem.* **2013**, *639*, 2125–2128.
[4] W. Jung, J. Lörincz, R. Ramlau, H. Borrmann, Y. Prots, F. Haarmann, W. Schnelle, U. Burkhardt, M. Baitinger, Y. Grin, *Angew. Chem. Int. Ed.* **2007**, *46*, 6725–6728.
[5] G. S. Nolas, J. L. Cohn, G. A. Slack, S. B. Schujman, *Appl. Phys. Lett.* **1998**, *73*, 178–180.
[6] R. Kröner, K. Peters, H. G. v. Schnering, R. Nesper, *Z. Kristallogr. - New Cryst. Struct.* **1998**, *213*, 704.
[7] C. Cros, M. Pouchard, P. Hagenmuller, *C. R. Hebd. Seances Acad. Sci.* **1965**, *260*, 4764–4767.
[8] S. Bobev, S. C. Sevov, *J. Solid State Chem.* **2000**, *153*, 92–105.
[9] E. Zintl, *Angew. Chem.* **1939**, *52*, 1–6.
[10] H. Kawaji, H. Horie, S. Yamanaka, M. Ishikawa, *Phys. Rev. Lett.* **1995**, *74*, 1427–1429.
[11] S. Yamanaka, E. Enishi, H. Fukuoka, M. Yasukawa, *Inorg. Chem.* **2000**, *39*, 56–58.
[12] S. Stegmaier, S.-J. Kim, A. Henze, T. F. Fässler, *J. Am. Chem. Soc.* **2013**, 10654–10663.
[13] J. D. Bryan, G. D. Stucky, *Chem. Mater.* **2001**, *13*, 253–257.
[14] M. Zeilinger, L. van Wüllen, D. Benson, V. F. Kranak, S. Konar, T. F. Fässler, U. Häussermann, *Angew. Chem. Int. Ed.* **2013**, *52*, 5978–5982.
[15] U. Häussermann, A. S. Mikhaylushkin, *Dalton Trans.* **2010**, *39*, 1036–1045.
[16] J. R. Salvador, D. Bilc, S. D. Mahanti, M. G. Kanatzidis, *Angew. Chem. Int. Ed.* **2003**, *42*, 1929–1932.
[17] T. Caillat, J. P. Fleurial, A. Borshchevsky, *J. Phys. Chem. Solids* **1997**, *58*, 1119–1125.
[18] G. J. Snyder, M. Christensen, E. Nishibori, T. Caillat, B. B. Iversen, *Nat. Mater.* **2004**, *3*, 458–463.
[19] R. A. Bley, S. M. Kauzlarich, *J. Am. Chem. Soc.* **1996**, *118*, 12461–12462.
[20] D. Mayeri, B. L. Phillips, M. P. Augustine, S. M. Kauzlarich, *Chem. Mater.* **2001**, *13*, 765–770.
[21] D. Neiner, H. W. Chiu, S. M. Kauzlarich, *J. Am. Chem. Soc.* **2006**, *128*, 11016–11017.
[22] B. M. Nolan, T. Henneberger, M. Waibel, T. F. Fässler, S. M. Kauzlarich, *Inorg. Chem.* **2015**, *54*, 396–401.
[23] A. L. Pickering, C. Mitterbauer, N. D. Browning, S. M. Kauzlarich, P. P. Power, *Chem. Commun.* **2007**, 580–582.
[24] M. Zeilinger, D. Benson, U. Häussermann, T. F. Fässler, *Chem. Mater.* **2013**, *25*, 1960–1967.
[25] M. Zeilinger, L.-A. Jantke, L. M. Scherf, F. J. Kiefer, G. Neubüser, L. Kienle, A. J. Karttunen, S. Konar, U. Häussermann, T. F. Fässler, *Chem. Mater.* **2014**, *26*, 6603–6612.
[26] L. M. Scherf, N. Riphaus, T. F. Fässler, *Z. Anorg. Allg. Chem.* **2016**, *642*, 1143–1151.
[27] L. M. Scherf, J. Hattendorff, I. Buchberger, S. Geier, H. Gasteiger, T. F. Fässler, *submitted*.
[28] L. M. Scherf, M. Zeilinger, T. F. Fässler, *Inorg. Chem.* **2014**, *53*, 2096–2101.
[29] L. M. Scherf, O. Pecher, K. J. Griffith, F. Haarmann, C. P. Grey, T. F. Fässler, *Eur. J. Inorg. Chem.* **2016**, *2016*, 4674–4682.
[30] M. Zeilinger, T. F. Fässler, *Dalton Trans.* **2014**, *43*, 14959–14970.
[31] Y. Segawa, Y. Suzuki, M. Yamashita, K. Nozaki, *J. Am. Chem. Soc.* **2008**, *130*, 16069–16079.
[32] *PROTEUS Thermal Analysis V4.8.2*, Netzsch-Gerätebau GmbH, Selb, **2006**.
[33] A. Bateni, S. Repp, R. Thomann, S. Acar, E. Erdem, M. Somer, *Appl. Phys. Lett.* **2014**, *105*, 202605.
[34] G. Mair, H. G. von Schnering, M. Wörle, R. Nesper, *Z. Anorg. Allg. Chem.* **1999**, *625*, 1207–1211.

[35] H. G. von Schnering, R. Nesper, J. Curda, K.-F. Tebbe, *Angew. Chem. Int. Ed. Engl.* **1980**, *19*, 1033–1034.
[36] U. Frank, W. Müller, H. Schäfer, *Z. Naturforsch. B* **1975**, *30*, 10–13.
[37] M. Zeilinger, T. F. Fässler, *Acta Crystallogr. Sect. E* **2013**, *69*, i81–i82.
[38] M. Wörle, R. Nesper, G. Mair, H. G. von Schnering, *Solid State Sci.* **2007**, *9*, 459–464.
[39] N. Vojteer, M. Schroeder, C. Röhr, H. Hillebrecht, *Chem. Eur. J.* **2008**, *14*, 7331–7342.
[40] G. Mair, R. Nesper, H. G. von Schnering, *J. Solid State Chem.* **1988**, *75*, 30–40.
[41] M. Wörle, R. Nesper, T. K. Chatterji, *Z. Anorg. Allg. Chem.* **2006**, *632*, 1737–1742.
[42] J. Evers, G. Oehlinger, G. Sextl, *Angew. Chem. Int. Ed.* **1993**, *32*, 1442–1444.
[43] M. Zeilinger, V. Baran, L. van Wüllen, U. Häussermann, T. F. Fässler, *Chem. Mater.* **2013**, *25*, 4113–4121.
[44] T. L. Aselage, *J. Mater. Res.* **1998**, *13*, 1786–1794.
[45] T. L. Aselage, D. R. Tallant, *Phys. Rev. B* **1998**, *57*, 2675–2678.
[46] The F impurities could originate from BF_3 which is a potential starting material in the commercial synthesis of BBr_3.
[47] H. G. von Schnering, M. Schwarz, R. Nesper, *J. Less-Common Met.* **1988**, *137*, 297–310.
[48] S. Yamanaka, H. Matsu, M. Ishikawa, *Mater. Res. Bull.* **1996**, *31*, 307–316.
[49] H. Nakano, M. Nakano, K. Nakanishi, D. Tanaka, Y. Sugiyama, T. Ikuno, H. Okamoto, T. Ohta, *J. Am. Chem. Soc.* **2012**, *134*, 5452–5455.
[50] H. Okamoto, Y. Kumai, Y. Sugiyama, T. Mitsuoka, K. Nakanishi, T. Ohta, H. Nozaki, S. Yamaguchi, S. Shirai, H. Nakano, *J. Am. Chem. Soc.* **2010**, *132*, 2710–2718.
[51] H. Okamoto, Y. Sugiyama, K. Nakanishi, T. Ohta, T. Mitsuoka, H. Nakano, *Chem. Mater.* **2015**, *27*, 1292–1298.
[52] T. Helbich, A. Lyuleeva, I. M. D. Höhlein, P. Marx, L. M. Scherf, J. Kehrle, T. F. Fässler, P. Lugli, B. Rieger, *Chem. Eur. J.* **2016**, *22*, 6194–6198.
[53] T. Helbich, A. Lyuleeva, T. Ludwig, L. M. Scherf, T. F. Fässler, P. Lugli, B. Rieger, *Adv. Funct. Mater.* **2016**, *26*, 6711–6718.

SUPPORTING INFORMATION

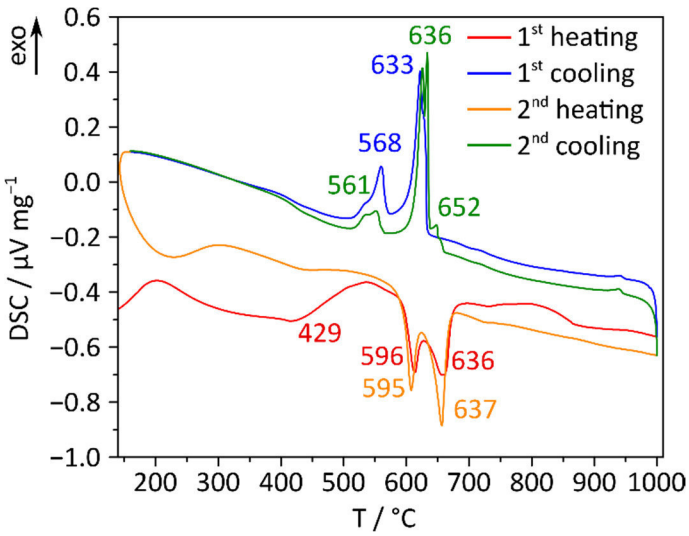

Figure S1. DSC curve of the product of the reaction of $Li_{15}Si_4$ and BBr_3 in toluene at 100 °C.

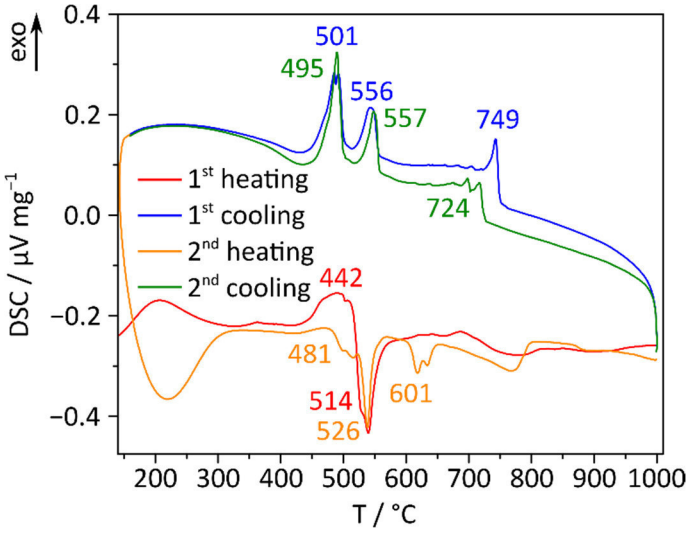

Figure S2. DSC curve of the product of the reaction of $Li_{15}Ge_4$ and BBr_3 in toluene at 100 °C.

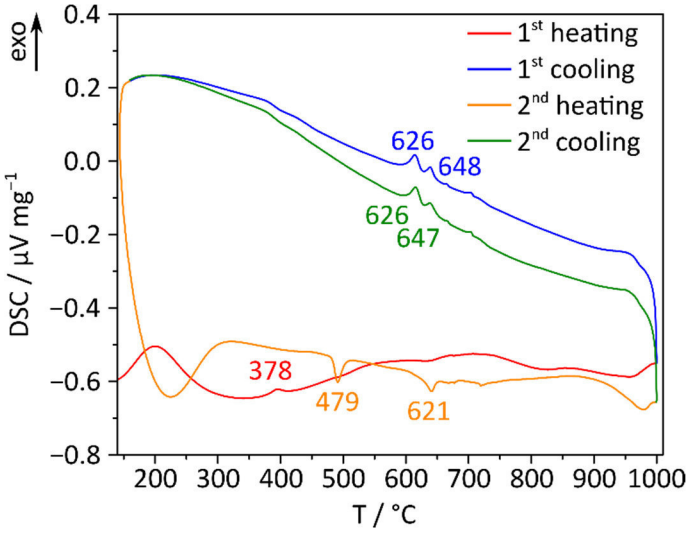

Figure S3. DSC curve of the product of the reaction of Li_3NaSi_6 and BBr_3 in toluene.

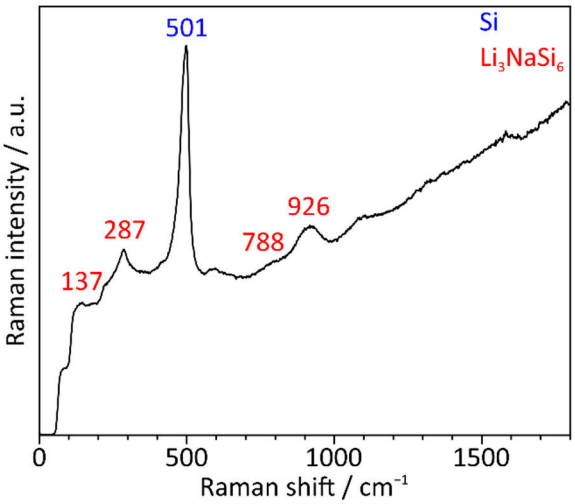

Figure S4. Raman spectrum of the product of the reaction of Li_3NaSi_6 with BBr_3 in toluene after washing with THF and DMSO.

5.10 Electrochemical Synthesis of the Allotrope *allo*-Ge and Investigations on the Use as an Anode Material

Lavinia M. Scherf,† Johannes Hattendorff,† Irmgard Buchberger, Sebastian Geier, Hubert A. Gasteiger, Thomas F. Fässler*, *submitted for publication*.

† These authors contributed equally to this work.

Journal Name

ARTICLE

Electrochemical Synthesis of the Allotrope *allo*-Ge and Investigations on the Use as an Anode Material

L. M. Scherf,[a]† J. Hattendorff,[b]† I. Buchberger,[b] S. Geier,[a] H. A. Gasteiger,[b] T. F. Fässler[a]

Received 00th January 20xx,
Accepted 00th January 20xx

DOI: 10.1039/x0xx00000x

www.rsc.org/

Due to the high lithium-ion mobility and high theoretical capacity, elemental germanium is an interesting candidate for anode materials. The layered Ge modification *allo*-Ge just recently obtained as a microcrystalline powder by topochemical oxidation of Li_7Ge_{12} with ethanol has now for the first time been observed by electrochemical delithiation of Li_7Ge_{12}. The investigation of the Li-ion battery performance of *allo*-Ge is reported with operando PXRD phase monitoring compared to α-Ge. In addition, an alternative synthesis of Li_7Ge_{12} by reaction of LiGe and α-Ge is presented. Cycling experiments of coin half-cells containing *allo*-Ge and α-Ge electrodes, respectively, show that the cycling stability of *allo*-Ge is inferior to common α-Ge. After an initial amorphization step, all Ge half-cells shuttle between the following phases: crystalline $Li_{15}Ge_4$ ↔ amorphous phase (most likely $Li_{13}Ge_4$) ↔ crystalline Li_7Ge_3 ↔ amorphous Ge. According to operando PXRD, *allo*-Ge capacity losses during cycling seem to be characterized by electronically disconnected Li_7Ge_3. The inferior cycling stability of *allo*-Ge, which consists of stacked Ge sheets, is therefore attributed to a morphological predisposition towards ageing and contact loss in LIBs.

Introduction

Lithium-ion battery technology has made big advances in the last decades. However, especially for mobile power supply applications new materials having better energy density with respect to weight and volume are needed. On the anode side, group IV conversion materials like Si, Ge, and Sn promise higher specific capacities than the currently used graphite anodes with 372 mAh/g.[1, 2] For Ge, a capacity of 1568 mAh/g can be achieved for the Li-richest phase $Li_{17}Ge_4$.[3] However, recent literature[4, 5] suggests that $Li_{15}Ge_4$ is the final phase on lithiation in a typical battery system, representing a capacity of up to 1385 mAh/g. This is less than for Si, but the lithium ion diffusivity in Ge is 400x larger than in Si and reaches $6.5 \cdot 10^{-12}$ cm²/s[6, 7] at room temperature. The electronic conductivity of Ge is also four orders of magnitude higher than for Si due to its lower band gap.[8] The main drawback of Si and Ge is significant aging due to large volume expansion and thus high stresses during lithiation. For Ge, a volume expansion of 246% was reported.[9]

In the last decade, many different approaches are currently investigated to solve the issue of volume expansion in elemental Ge anodes. The most common methods are dilution with C, by mixing Ge and C either macroscopically during electrode manufacturing or microscopically, e.g. in Ge-C nano-composites[10, 11] and Ge nanoparticle-carbon nanotube (Ge@CNT) hybrids.[12, 13] In addition, stable porous structures are synthesized that are less affected by volume changes, e.g. macroporous Ge.[6] These methods have in common that they are all based on cubic α-Ge which crystallizes in the diamond structure type (Fig. 1b). In-situ investigations of α-Ge-based anode materials agree on a conversion mechanism in lithium ion batteries. Grey *et al.* were able to show by ex-situ powder X-ray diffraction (PXRD) and operando NMR spectroscopy that upon lithiation (C/50), micron-sized α-Ge converts below 300 mV to crystalline Li_7Ge_3 and further to an amorphous material before finally crystalline $Li_{15}Ge_4$ is formed below 150 mV.[4] Complete discharge yields an overlithiated $Li_{15+\delta}Ge_4$ phase. Other in-situ and ex-situ experiments on crystalline Ge,[14] thin Ge films,[15] carbon-coated Ge[11] and Ge@CNT[13] have yielded similar results.

Other Ge allotropes or nanostructures could undergo a different (de-)lithiation mechanism and thus allow for a better anode material performance. Zintl phases[16] have been established to be suitable precursors for novel Ge nanostructures and allotropes. For example, Kanatzidis et al. have shown that oxidation of K_4Ge_9 and Mg_2Ge with different oxidants in presence of surfactants yields different mesoporous Ge materials.[17-21] Depending on the reaction conditions, hexagonal or cubic structures are obtained. Tolbert et al. were able to synthesize nanoporous hexagonal Ge from polymeric $^1{}_\infty[Ge_9]^{2-}$ solutions using ferrocenium hexafluorophosphate as the oxidant.[22] Ge nanoparticles can be prepared by oxidation of $Na_{12}Ge_{17}$ with alcohols[23] and the guest-free Ge clathrate

[a] *Lehrstuhl für Anorganische Chemie mit Schwerpunkt Neue Materialien, Department of Chemistry, Technische Universität München, Lichtenbergstr. 4, 85749 Garching b. München, Germany.*
[b] *Lehrstuhl für Technische Elektrochemie, Department of Chemistry, Technische Universität München, Lichtenbergstr. 4, 85749 Garching b. München, Germany*
† These authors contributed equally to this work.

Electronic Supplementary Information (ESI) available: Powder X-ray diffraction patterns of LiGe, Li_7Ge_{12}, extracted Li_7Ge_{12} electrode materials, *allo*-Ge, and α-Ge; particle size analysis data; coin cell dQ/dV curves; ex-situ PXRD patterns of post-cycling coin cell anode materials; selected in-situ PXRD patterns; dQ/DV plot for α-Ge pouch cells. See DOI: 10.1039/x0xx00000x

Journal Name

ARTICLE

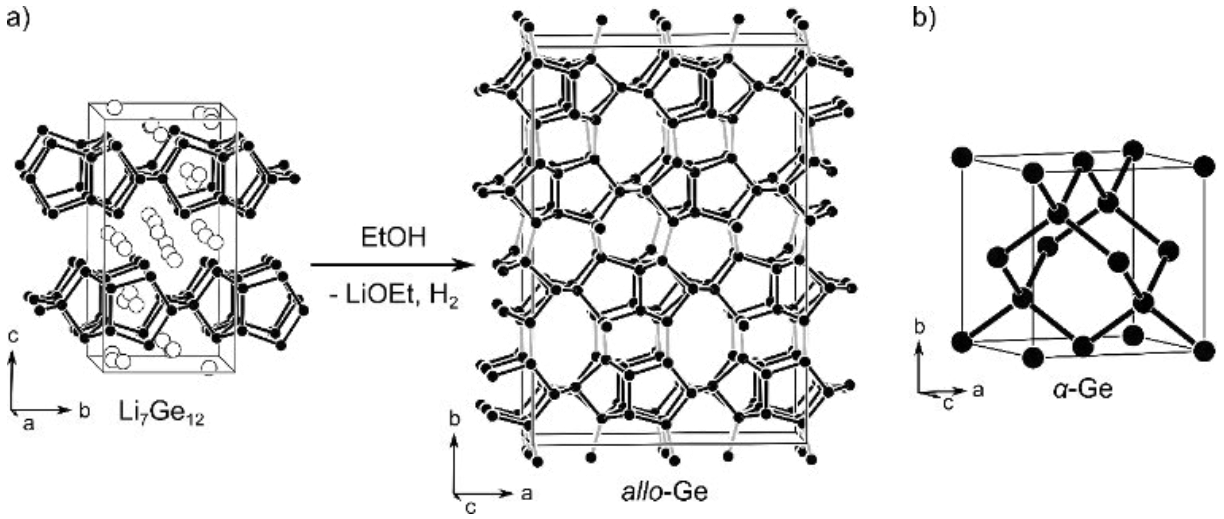

Fig. 1. a) The Zintl phase Li_7Ge_{12} reacts topochemically with protic solvents such as ethanol to *allo*-Ge. Ge atoms are shown in black, Li atoms in white; bonds formed in the reaction are marked in grey.[24] b) α-Ge crystallizes in the diamond structure type.[25]

$\square_{24}Ge_{136}$ is available by soft oxidation of Na_4Ge_9 in ionic liquids.[26] Using a templating method, dissolved $[Ge_9]^{4-}$ clusters can be oxidized to undoped and P-doped inverse opal-structured Ge films.[27] In addition, the Zintl phase Li_7Ge_{12} which comprises polyanionic $^2_\infty[Ge_{12}]^{7-}$ sheets that are separated by Li^+ cations,[28] acts as precursor for an alternative Ge allotrope. The formation of *allo*-Ge in a topochemical reaction of Li_7Ge_{12} with protic solvents was recently advanced towards a bulk synthesis and structurally characterized (Fig. 1a).[24] At elevated temperatures, *allo*-Ge transforms into the Ge allotrope, 4*H*-Ge, and then to well-known cubic α-Ge .[29, 30]

So far, Li_7Ge_{12} has only been oxidized to *allo*-Ge by chemical means. However, a similar reaction could reasonably occur upon electrochemical oxidation. In contrast to the conversion mechanism occurring in α-Ge anodes, an intercalation mechanism is conceivable for *allo*-Ge lithiation and delithiation since it forms topochemically (Fig. 1a). In analogy to the intercalation of Li into graphite anodes, the volume differences between the charged and discharged states could then be significantly smaller than in the conversion of fully isotropic α-Ge.

Herein, we first show the electrochemical production of *allo*-Ge from Li_7Ge_{12} in standard coin cells via ex-situ XRD analysis. In addition, we investigate the electrochemical cycling properties of *allo*-Ge in comparison to the standard α-Ge. For this purpose, non-optimized micrometer-sized particles are tested versus metallic Li in standard coin cells and in pouch cells with operando XRD analysis.

Results

Electrochemical delithiation of Li_7Ge_{12}

Previously, the amount of Li_7Ge_{12} per synthesis was limited to 1 g per sample due to the arc-melting procedure.[28] Since we desired substantial amounts of phase-pure material for this study, we initially developed an alternative synthesis route. Preparation of Li_7Ge_{12} via annealing of a stoichiometric mixture of binary LiGe and α-Ge proved to fulfill these requirements. Li_7Ge_{12} synthesized like this is nearly phase-pure, containing less than 3 mass % α-Ge according to Rietveld refinement (PXRD patterns are shown in the ESI, Fig. S1 and S2).

For the electrochemical delithiation of Li_7Ge_{12} we mixed 80 wt % Li_7Ge_{12}, 10 % carbon black (C65, TIMCAL) and 10 % polyethyleneoxide as a binder.[31] The electrode preparation was performed inside the glovebox to prevent oxidation of Li_7Ge_{12}. According to the PXRD analysis, the resulting coating still contains Li_7Ge_{12} next to α-Ge from the Li_7Ge_{12} synthesis (Fig. 2a) and was then then coated onto Cu foil (loading around 2.8 mg cm^{-2}). In the assembly of CR2032 coin cells, the electrode and the Li counter electrode were separated by glass fiber separators to which an electrolyte (EC:EMC, 3:7 wt % with 1M $LiPF_6$) was added.

A coin cell was then delithiated to 2 V at C/80, disassembled inside a glovebox, and the anode material was characterized by ex-situ PXRD. The diffraction pattern (Fig. 2b) shows that, indeed, Li_7Ge_{12} can be electrochemically delithiated to form *allo*-Ge. However, traces of Li_7Ge_{12} remain in addition to some α-Ge, which was already present in the starting material.

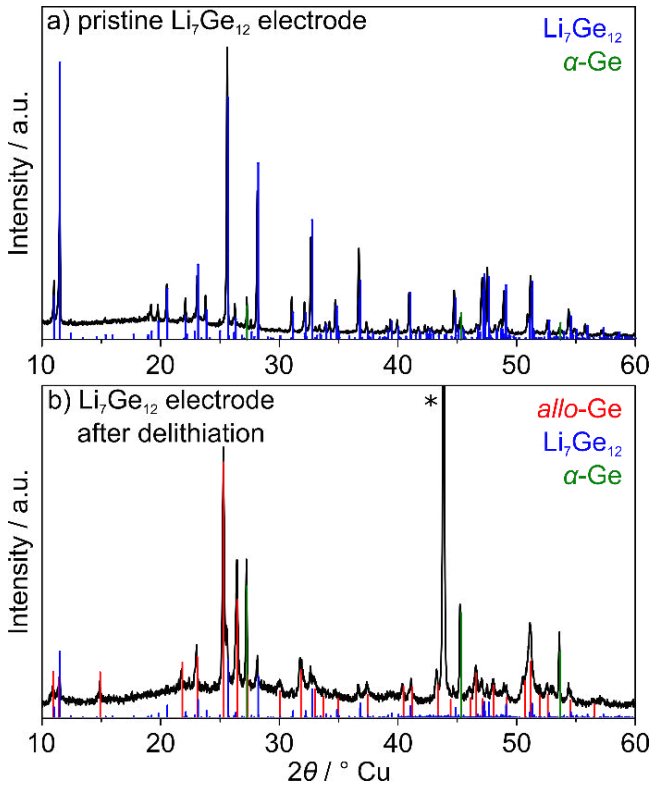

Fig. 2. Powder diffraction pattern of a) the pristine Li_7Ge_{12} coating and b) the electrode material extracted from a Li_7Ge_{12} coin half-cell after one delithiation step; theoretical powder patterns of *allo*-Ge,[24] α-Ge,[25] and Li_7Ge_{12}[28] are given in red, blue, and green, respectively; the reflex marked by an asterisk corresponds to diamond powder which was added to the extracted electrode material for easier handling.

In order to find out whether the delithiation of Li_7Ge_{12} is reversible, we also ran a coin cell for a delithiation/lithiation cycle, and another one for 1.5 cycles (Fig. S4). Fig. S3 in the ESI demonstrates that delithiation is not reversible: most *allo*-Ge formed in the first half-cycle disappears during the first lithiation process and a broad signal corresponding to amorphous material appears. Trace amounts of Li_7Ge_{12}, *allo*-Ge, and α-Ge remain present and do not differ between the 1 and 1.5 cycle samples.

Electrochemical analysis of *allo*-Ge as an anode material

Although the electrochemical delithiation of crystalline Li_7Ge_{12} to crystalline *allo*-Ge is not reversible, we still were interested if *allo*-Ge can be used as an anode material. For better comparability with α-Ge, *allo*-Ge was synthesized chemically in this experiment. Thus, the Ge allotrope was prepared by oxidation of Li_7Ge_{12} in ethanol as previously described (the corresponding PXRD pattern is shown in the ESI, Fig. S5).[24] The particle size of *allo*-Ge was varied by ball-milling Li_7Ge_{12} before the oxidation reaction. As a reference, we also prepared α-Ge for the electrochemical study (Fig. S6). To rule out particle size effects, careful attention was paid to obtaining similar particle sizes for both materials. The particle size distribution of the micron-sized crystalline Ge powders was characterized by laser scattering, yielding median volume-based particle sizes of 13.6 µm and 8.8 µm for two batches of *allo*-Ge and 9.0 µm for α-Ge (Fig. S7).

SEM images of both materials clearly show very different morphologies for the two Ge modifications (Fig. 3). *allo*-Ge mainly consists of fanned out sheets and some small broken bits whereas α-Ge is characterized by sharp edges and some small tetrahedral particles. The layered structure and morphology of *allo*-Ge synthesized by chemical deintercalation of Li suggests again that electrochemical lithiation of the material could proceed by a reversible intercalation mechanism like in graphite anodes.

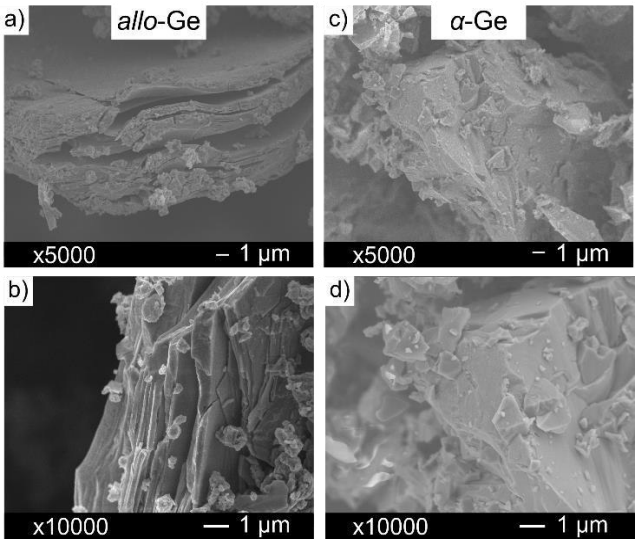

Fig. 3. SEM images of a) *allo*-Ge at 5000-fold magnification, b) *allo*-Ge at 10000-fold magnification, c) α-Ge at 5000-fold magnification, d) α-Ge at 10000-fold magnification.

To investigate the electrochemical performance of *allo*-Ge, we prepared electrodes of 80 wt % Ge, 10 % carbon black (C65, TIMCAL) and 10 % polyvinylidene fluoride as a binder on Cu foil. The electrode and the Li counter electrode were separated by a glass fiber separator to which an electrolyte (EC:EMC, 3:7 wt% with 1M $LiPF_6$) was added. CR2032 coin cells and custom-designed pouch cells were built for electrochemical cycling and operando PXRD experiments, respectively. Reference α-Ge cells were built analogously. All cells were cycled at C/20 between 0.01 V and 1.5 V. Coin cell experiments were repeated with three cells each. All electrochemical experiments are listed in the experimental section.

The potential curves in Fig. 4a for *allo*-Ge coin cells (median volume-based particle size 9.0 µm) show a relatively fast potential drop during the first lithiation, reaching a plateau at 0.42 V, which according to the Gibbs phase rule represents the concurrent existence of two phases. Upon further lithiation, the potential curve passes two additional plateaus near 0.17 V and 0.12 V. Each plateau corresponds to a peak in the corresponding dQ/dV plot (Fig. S8). Finally, a lithiation capacity of 1470 mAh/g is reached at 0.01 V. At the beginning of delithiation, an initially high overpotential results in a fast potential rise to nearly 0.5 V. Subsequent delithiation is accompanied with potential stabilization at 0.42 V and again at 0.6 V which is followed by a

fast potential rise at the end of delithiation, yielding a total delithiation capacity of 1350 mAh/g. This corresponds to an irreversible capacity loss of 8% in the first charge/discharge cycle. For the second and subsequent cycles, the first plateau in lithiation is smeared out, indicating a different lithiation path than in the first cycle. During further cycling, the capacities decline fast and the whole voltage curve is compressed, which hints at a loss of active material, e.g. through contact loss.

Fig. 4. a) First and second cycle of *allo*-Ge and α-Ge coin half-cells beginning with the first lithiation cycle to 0.01 V. An overpotential (probably caused by the Li counter electrode) leads to a transient plateau at the beginning of delithiation and

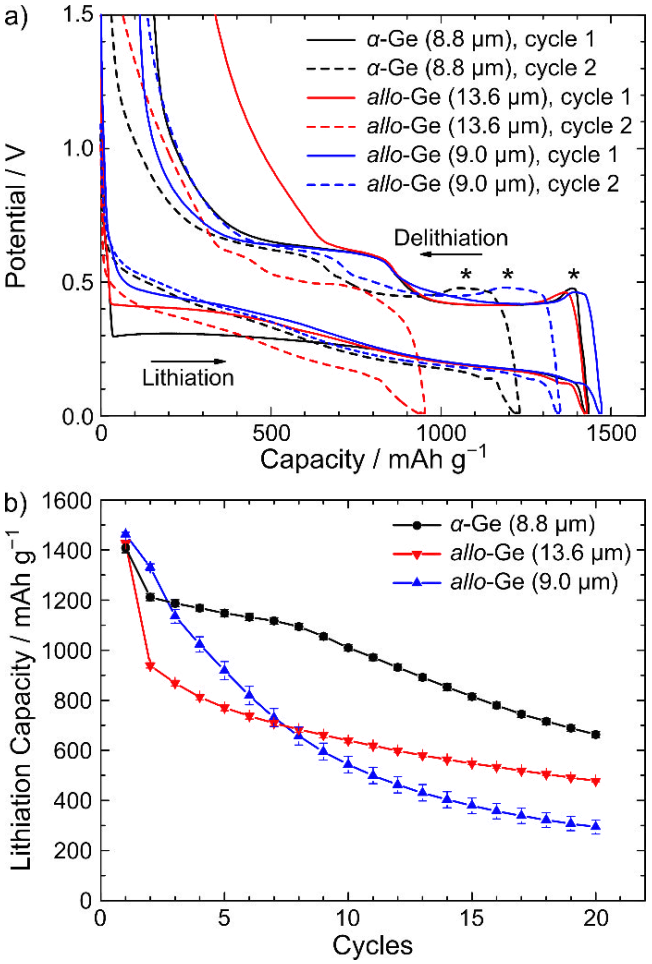

is marked by (*). b) Discharge (lithiation of Ge) capacities of all coin cell types. The mean capacity with error bars is plotted.

The potential curves in Fig. 4a for α-Ge (median volume-based particle size 8.8 µm) show their well-known behavior:[4] As published previously the potential drops relatively fast during the first lithiation and passes three plateaus at 0.31 V, 0.18 V, and 0.13 V (Fig. S9). Upon full lithiation at 0.01 V, a capacity of 1420 mAh/g is reached. This is slightly more than expected for the final phase $Li_{15}Ge_4$, but additional capacity could be explained by electrolyte reduction and formation of an SEI or a certain overlithiation, as mentioned above. During delithiation the potential stabilizes at 0.42 V at an overpotential of ca. 0.3 V above the lithiation curve, followed by another plateau at 0.63 V. Only 1300 mAh/g are recovered during delithiation up to 1.5 V, representing an irreversible loss of 10%. The second lithiation looks very similar to the potential vs. capacity relationship of *allo*-Ge.

Overall, we find similar potential characteristics for *allo*- and α-Ge. During subsequent cycling a significant loss of capacity is observed for both materials (Fig. 4b), probably due to the known problem for large Si or Ge particles that suffer from mechanical stress caused by volume changes during cycling. However, *allo*-Ge is significantly less stable than α-Ge with respect to cycling stability. This observation is independent of particle size, since coin cells with median *allo*-Ge particles of 13.6 µm and 9.0 µm both dramatically lose capacity during cycling. Repetition of the coin cell experiments showed very similar potential curves and also capacities varied only by a few percent as indicated by the error bars derived from three independent repeat experiments.

Operando XRD analysis

In order to understand the electrochemical behavior of the *allo*-Ge cells and their lithiation path in comparison to α-Ge, we performed operando PXRD measurements, monitoring all crystalline phase transformations. The obtained diffraction patterns contain reflections from the Li foil counter electrode, the Al composite foil, and the Cu current collector foils. The potential curve for both *allo*-Ge and α-Ge in the pouch cell system is very similar to the coin cell reference, though over-potential is a little higher and plateaus are less prominent. Initial lithiation capacity reached 1300 and 1200 mAh/g, respectively, from which around 1000 mAh/g were recovered during delithiation.

Upon lithiation of the *allo*-Ge electrode at C/20, *allo*-Ge disappears quickly and crystalline $Li_{15}Ge_4$ forms suddenly just before full lithiation (Fig. 5). Upon delithiation, $Li_{15}Ge_4$ disappears and crystalline Li_7Ge_3 is formed concurrently. During further delithiation the characteristic reflections for Li_7Ge_3 decrease in intensity but remain present. During two additional charge/discharge cycles the *allo*-Ge cell also seems to shuttle between crystalline $Li_{15}Ge_4$ and amorphous Ge with Li_7Ge_3 present at all stages. The presence of Li_7Ge_3 in the delithiated state was also proven by ex-situ XRD analysis of *allo*-Ge coin cell material after one and three charge/discharge cycles, respectively (Fig. S10).

In summary, we observe the same crystalline phases as Grey et al. found in their detailed phase analysis of α-Ge nanoparticles,[4] suggesting a similar conversion mechanism. They, however, observed Li_7Ge_3 already during the first lithiation of α-Ge at C/50 via operando NMR and ex-situ PXRD, while we do not detect crystalline Li_7Ge_3 until the first delithiation step. In contrast, Notten *et al.* did not observe any crystalline Li_7Ge_3 formation in their operando PXRD analysis of Ge thin-film electrodes at 1C.[15]

Journal Name

ARTICLE

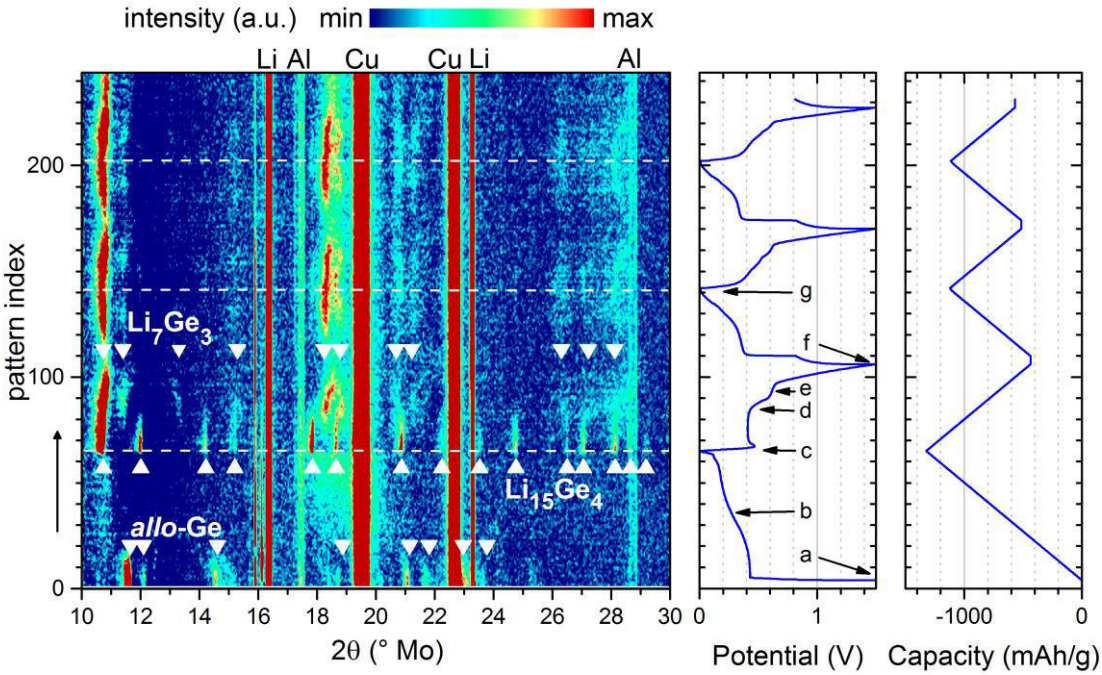

Fig. 5. *allo*-Ge (median volume-based particle size 13.6 μm) operando cell diffraction patterns as well as potential and capacity for the first three lithiation and delithiation cycles. The main reflections of all observed crystalline phases are marked. Letters a–g indicate selected patterns in Fig. S11.

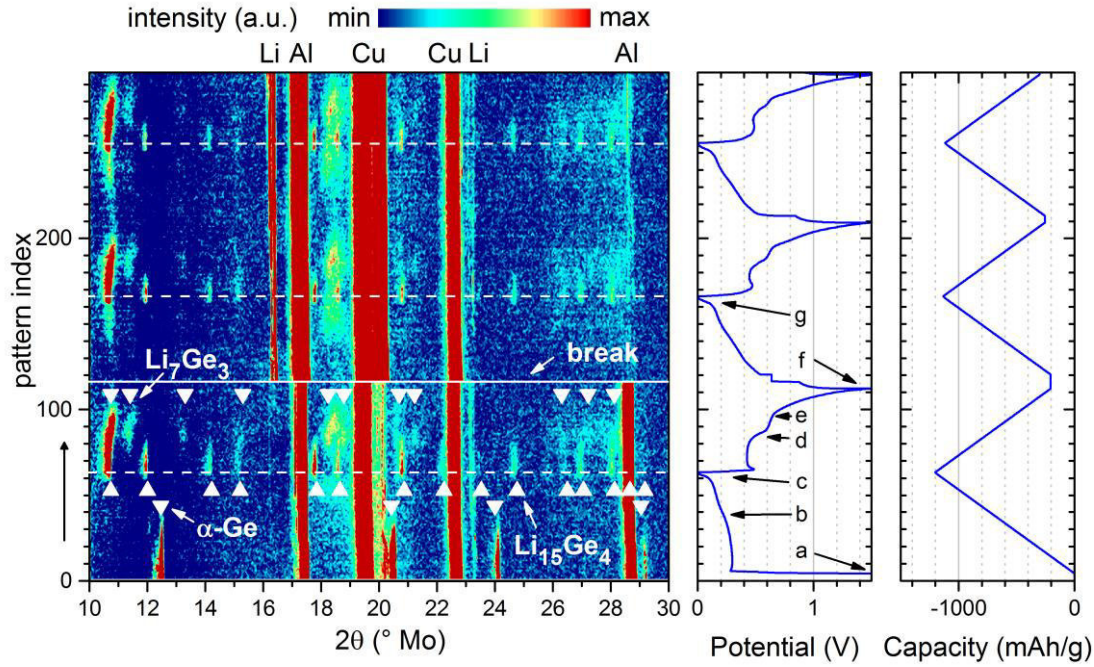

Fig. 6. α-Ge (median volume-based particle size 9.0 μm) operando cell diffraction patterns as well as potential and capacity for the first three lithiation and delithiation cycles. The main reflections of all observed crystalline phases are marked. Letters a–g indicate selected patterns in Fig. S12.

Journal Name

ARTICLE

In our α-Ge reference analysis we observe similar phase transitions as in the *allo*-Ge pouch cells (Fig. 6). During the first lithiation at C/20, α-Ge disappears more slowly than *allo*-Ge previously. Before full lithiation we again observe a sudden formation of crystalline $Li_{15}Ge_4$. During delithiation, crystalline Li_7Ge_3 appears concurrently with a $Li_{15}Ge_4$ fade-out. In contrast to the allo-Ge cells, Li_7Ge_3 is converted into amorphous phases, leaving only amorphous Ge at the first full delithiation. An ex-situ PXRD analysis of α-Ge coin cell electrode material after one full discharge/charge cycle supports this observation (Fig. S9). The cycling behavior of phase transformations inside the α-Ge cell was also observed for three full cycles, indicating the expected continuous cycling between crystalline $Li_{15}Ge_4$ and amorphous Ge. As in the *allo*-Ge pouch cells, we cannot detect crystalline Li_7Ge_3 during the first lithiation step. Most strikingly, we have found that upon repeated cycling, more and more Li_7Ge_3 remains unaffected by the applied voltage. It thus seems as if the Li_7Ge_3 were no longer electrically connected. This effect is worse for *allo*-Ge, suggesting that its heavy capacity loss may be caused by the partially irreversible formation of crystalline Li_7Ge_3.

Now we can correlate the phase transitions for the *allo*-Ge cells observed by operando PXRD to the potential curve in more detail. Every potential plateau represents a transition from one phase to another and is best seen as a peak in the dQ/dV plot. In both the coin and pouch cell data three peaks can be identified on lithiation and delithiation (Fig. 7a). This suggests that at least four phases exist between (and including) Ge and $Li_{15}Ge_4$.

The first transition for lithiation at 0.42 V (1a) in the dQ/dV plot corresponds well to the presence of crystalline *allo*-Ge until 0.40 V (Fig. 5 and 7a). A second transition at 0.18 V (2a) cannot be clearly attributed to any crystalline phase in the diffraction pattern. The third transition at 0.12 V (3) is again identified by the emergence of $Li_{15}Ge_4$ starting from 0.12 V. For delithiation, the first transition at 0.42 V (1') is associated with $Li_{15}Ge_4$ disappearing until 0.42 V. The second transition (again very weak) is located at 0.52 V (2') and overlaps with the presence of Li_7Ge_3 starting at 0.41 V. The third transition at 0.62 V (3') probably represents a decomposition of Li_7Ge_3, since the main reflections of Li_7Ge_3 decrease in intensity until ca. 0.8 V. As previously mentioned, Li_7Ge_3 does not vanish completely.

During the second lithiation, the first transition moves to 0.35V (1b) which can be explained by formation of Li_7Ge_3 as the intensity of Li_7Ge_3 reflections increases significantly from 0.38 V (Fig. 5 and 7a). Further cycling follows the described route but less and less $Li_{15}Ge_4$ is observed at full lithiation. The resulting (de-)lithiation mechanism is summarized in Fig. 7b. For the lithiation and delithiation of the α-Ge cells, potential curves and operando PXRD data can be correlated analogously (Fig. 6 and S13).

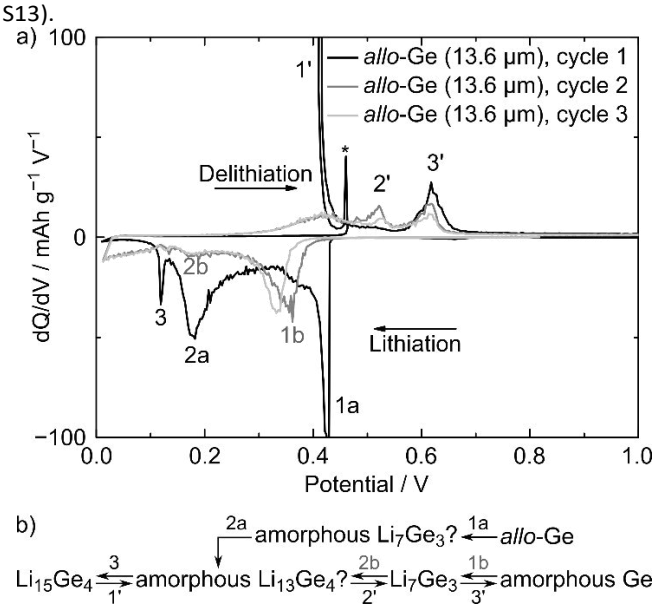

Fig. 7. a) dQ/dV plot of *allo*-Ge in operando PCRD pouch half-cell. An overpotential leads to an artifact peak and is marked by (*), b) proposed (de-)lithiation mechanism for *allo*-Ge.

Discussion

According to our data, *allo*-Ge behaves very similarly to α-Ge as an anode material. Although *allo*-Ge is essentially formed in a deintercalation reaction, both crystalline allotropes undergo the following conversion mechanism when used as LIB anode materials. Initially both materials are amorphized during the first lithiation step. In contrast, Grey *et al.* found a direct conversion of α-Ge to crystalline Li_7Ge_3 upon lithiation of 1–3 µm α-Ge particles at C/50.[4] Maybe this crystalline-to-crystalline conversion is unfavorable at a faster cycling rate of C/20 so that amorphous Li_7Ge_3 could be formed under our conditions. This assumption seems likely since we do observe the formation of crystalline Li_7Ge_3 at similar potentials when lithiation starts from amorphous Ge during all subsequent lithiation steps. However, we obviously cannot prove this with our operando PXRD methods. For comparison, Notten et al. did not observe any crystalline Li_7Ge_3 when cycling their Ge thin-film electrodes at an even faster cycling rate of 1C.[15,32]

The second phase transition during lithiation of both *allo*- and α-Ge cannot be attributed to the formation of any crystalline phase, supporting the formation of amorphous material resembling $Li_{13}Ge_4$[33] which was also reported by Grey et al.[4] As expected, the third and final phase transition during lithiation of the Ge anode materials corresponds to the formation of

$Li_{15}Ge_4$ as the endpoint of discharge. During delithiation this phase sequence is most likely reversed with amorphous Ge representing the fully charged state of the half-cells.
Since *allo*- and α-Ge follow the same lithiation/delithiation mechanisms, their different long-term cycling behavior (cf. Fig. 4b) is arguably not caused simply by the different connectivities of Ge atoms in the respective structures. Although some differences in the pouch cell experiments might be caused by different particle sizes (13.6 μm for *allo*-Ge and 8.8 μm for α-Ge), our coin cell test with comparable particle sizes shows that even then *allo*-Ge performs worse in the long run (cf. Fig. 4b). Yet, there is a difference in morphology which could be a reason for the different cycling behavior. The stacked sheets in *allo*-Ge could be more labile with respect to contact loss upon (dis-)charging. Crystalline Li_7Ge_3 is often observed during (de-)lithiation. In case of *allo*-Ge our operando PXRD measurements show that already during the first delithiation step some Li_7Ge_3 is not converted back to amorphous Ge. Together with the large capacity fade observed in cycling experiments this points to a possible contact loss in the state of Li_7Ge_3, suggesting that some particles of this intermediate phase no longer participate in the (dis-)charging process. It is, however, difficult to point to one conclusive explanation for the different cycling behavior because both systems are not optimized for cycling stability in terms of particle sizes and electrode compositions.

Experimental Section

Materials and Reagents

The synthesis, characterization and manipulation of Zintl phases was carried out under inert gas conditions, using standard Schlenk techniques or by working in a glove box (MBraun, Ar atmosphere, $H_2O < 0.1$ ppm, $O_2 < 0.1$ ppm).

Synthesis of LiGe

LiGe was prepared from the pure elements (Li rods 99 %, Rockwood-Li; 99.999 % Ge pieces, Evochem) in a tantalum ampule. The sealed ampule containing the stoichiometric reaction mixture with a total mass of 1.5 g was encapsulated inside a silica jacket under vacuum and then heated to 650 °C for 1 h. The resulting melt was cooled at a rate of 0.5 °C min^{-1} to 400 °C at which temperature annealing of the reaction product was allowed for 6 h. PXRD analysis confirms that the reaction product is phase-pure.

Synthesis of Li_7Ge_{12}

Li_7Ge_{12} was first prepared according to the literature procedure.[28] Then the synthesis route was abridged according to the following reaction.
7 LiGe + 5 Ge → Li_7Ge_{12}
A stoichiometric mixture of the starting materials LiGe and Ge with a total weight of 2.5 g was prepared by thorough grinding using an agate mortar. The fine powder was then transferred into a tantalum ampule, encapsulated inside a silica jacket under vacuum and annealed at 480 °C for 72 h. PXRD analysis confirms that the reaction product is phase-pure.

Synthesis of *allo*-Ge for electrochemical analysis

7.5 mL ethanol were added to 2.367 g Li_7Ge_{12} and the resulting suspension was stirred for 24 h. Gas evolution indicates the immediate start of the oxidation reaction upon ethanol addition. After the reaction was finished, the suspension was filtered using a filtering crucible and the powdery black product was washed repeatedly using ethanol and deionized water. The obtained *allo*-Ge was then dried for 24 h at 120 °C.

Scanning Electron Microscopy

Scanning electron micrographs were recorded with a JEOL JSM-6500F scanning electron microscope equipped with a field emission gun operated at 5–30 kV.

Particle Size Analysis

Particle sizes of the microcrystalline Ge powders were measured by laser scattering. The powders were suspended in deionized water and consequently characterized using a Horiba LA-950 instrument.

Li_7Ge_{12} cell preparation

All preparation steps for Li_7Ge_{12} cells were performed inside a glovebox. A mixture of 80 wt% Li_7Ge_{12}, 10 % carbon black (C65, TIMCAL) and 10 % binder polyethylene oxide (PEO) was dissolved in toluene and stirred on a hot plate for 20 min at 60 °C. The slurry was coated onto a copper foil (10 μm thickness) using a Mayer rod (250 μm) and dried overnight at room temperature under Ar atmosphere.
Single-side coated electrodes of 14 mm diameter were punched out. Loadings of Li_7Ge_{12} cells are around 2.8 mg cm^{-2}. Electrodes were not calandered and dried overnight under vacuum. As a separator, two layers of 250 μm thick glass fiber were used and some hundred μL of electrolyte (ethylene carbonate (EC) : ethyl methyl carbonate (EMC), 3:7 wt% with 1M $LiPF_6$) were added. Thin Li foil (Rockwood Lithium) acted as an oversized counter electrode.

Allo-Ge and α-Ge cell preparation

For *allo*-Ge and α-Ge electrodes a mixture of 80wt% Ge, 10% carbon black (C65, TIMCAL) and 10% binder polyvinylidene fluoride (PVDF, Kynar, HSV900) was dissolved in N-methyl-pyrrolidone (NMP) in a planetary vacuum mixer (Thinky, ARV-310). This recipe closely follows earlier literature,[4] but is not optimized regarding stability and cycle life. This slurry was coated with a doctor blade on a copper foil (MTI) and dried at 60°C on a hot plate.
For CR2032 coin cells, single-side coated electrodes of 14 mm diameter were punched out. For pouch cells, single-side coated electrodes with a coated part of 1.5 to 2 cm^2 and a cleaned Cu current collector tab were cut out (**Fig. 8b**). Loadings are in the range of 6.0 to 6.8 mAh/cm^2. For comparison with earlier work, the expected theoretical capacity was set to 1600 mAh/g_{Ge}.

Journal Name

ARTICLE

Table 1. Experimental overview of allo-Ge and α-Ge cells. The median particle size is given for each material.

test and material	no. of cells	loading in mg/cm²	loading in mAh/cm²	procedure
Coin cells				
T1 α-Ge 8.8 µm	3	4.2±0.3	6.7±0.4	C/20 cycling
T1 *allo*-Ge 13.6 µm	3	3.9±0.1	6.3±0.2	C/20 cycling
T1 *allo*-Ge 9.0 µm	3	4.0±0.1	6.4±0.1	C/20 cycling
T2 α-Ge 8.8 µm	1	4.2	6.7	1x C/20 cycle + post mortem XRD
T2 *allo*-Ge 13.6 µm	1+1	3.7	6.0	1x+3x C/20 cycle + post mortem XRD
Pouch cells				
T3 α-Ge 8.8 µm	1	4.3	6.8	C/20 cycling XRD
T3 *allo*-Ge 13.6 µm	1	3.8	6.0	C/20 cycling XRD

Electrodes were not calandered and porosity is not a limiting factor and relatively high, ranging from 50 to 80 %. All electrodes were dried overnight at 120 °C under vacuum. Final assembly of coin and pouch cells was done in a glove box (Ar atmosphere, typically <1 ppm H_2O and O_2). As a separator two to three layers of 250 µm thick glass fiber were used and some hundred µL of electrolyte (ethylene carbonate (EC) : ethyl methyl carbonate (EMC), 3:7 wt% with 1M $LiPF_6$) were added. Thin Li foil (Rockwood Lithium) acted as an oversized counter electrode. The different *allo*-Ge and α-Ge cells prepared in this work are summarized in Table 1.

Electrochemical analysis of Li_7Ge_{12} cells

The Li_7Ge_{12} coin cells were run on a battery cycler (Maccor or Biologic VMP3) in a C/80 cycling procedure. A charge – i.e. delithiation of Li_7Ge_{12} – at constant current (CC) down to 0.02 V was followed by a discharge (CC) – i.e. lithiation – to 2.0 V. Cells were tested for 0.5, 1, and 1.5 cycles.

Electrochemical analysis of *allo*-Ge and α-Ge cells

Allo-Ge and α-Ge coin cells were run on a battery cycler (Maccor or Biologic VMP3) in a C/80 (Li_7Ge_{12}) and C/20 cycling (*allo*-Ge and α-Ge) procedure, respectively. A discharge - i.e. lithiation of Ge - at constant current (CC) down to 0.01 V was followed by a charge (CC) – i.e. delithiation - with a constant voltage (CV) phase at 1.5 V and a cut-off of C/40. Cells of the test T1 saw 20 cycles. Cells of the test T2 saw only one or three cycles.
Pouch cells were cycled at C/20 in the same way as above, but CC for both discharge and charge. After charging a short rest period under open circuit conditions was applied. Each cell underwent formation and two more cycles. Meanwhile the cell was monitored by operando PXRD. The α-Ge cell was cycled once and then stored for one week before being analyzed for another two cycles. The cell containing *allo*-Ge was measured in one run.

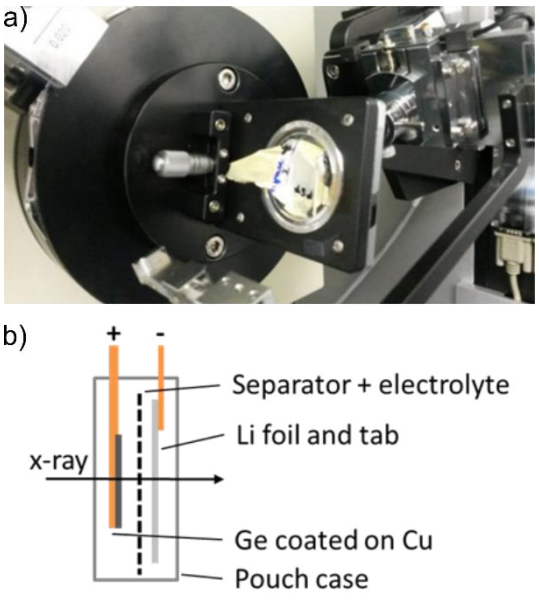

Fig. 8. a) Pouch cell mounted on X-ray diffractometer. b) Scheme of pouch cell with Ge-coated working electrode and Li counter electrode. For operando measurements, the beam passes the middle of the cell.

Operando Powder X-ray Diffraction (PXRD)

Operando powder patterns of pouch cells were recorded using a Stoe STADI P diffractometer equipped with a Ge(111) monochromator for Mo Kα radiation (λ = 0.70930 Å) and a Dectris MYTHEN DCS 1K solid state detector. The samples were measured continuously in 1° steps within a 2θ range of 10–50° (15 seconds/step). The measurement setup is depicted in Fig. 8.

Ex-situ PXRD

All starting materials as well as anode materials before and after cycling in coin cells were characterized using powder X-ray diffraction. For post mortem PXRD, the electrodes were extracted under Ar atmosphere. The samples were filled inside glass capillaries, which were sealed inside the glove-box. Powder patterns were recorded using a Stoe STADI P diffractometer equipped with a Ge(111) monochromator for Cu Kα radiation (λ = 1.54056 Å) and a Dectris MYTHEN DCS 1K solid state detector. The samples were measured within a 2θ range of 5–87.5°.

Conclusions

In summary, we have shown that the Zintl phase Li_7Ge_{12} can be electrochemically deintercalated to form *allo*-Ge in analogy to the chemical oxidation using protic solvents. Attempts to electrochemically cycle Li_7Ge_{12} coin cells between the *allo*-Ge and Li_7Ge_{12} failed however. Thus, this topochemical reaction seems to be irreversible.

We further tested the electrochemical performance of chemically synthesized *allo*-Ge and also α-Ge as a reference in half-cells versus Li and furthermore utilized operando PXRD analysis to observe the phase transformations occurring inside the cells. In contrast to the initial idea of a possible (de-)intercalation mechanism for *allo*-Ge, both Ge modifications basically follow the same three-step conversion mechanism. The latter is in good agreement with previous works on the phase transitions in α-Ge electrode materials: after the first cycle both cell types shuttle between the following phases: amorphous Ge ↔ crystalline Li_7Ge_3 ↔ amorphous phase (most likely $Li_{13}Ge_4$) ↔ crystalline $Li_{15}Ge_4$. Long-term cycling experiments show, however, that *allo*-Ge cells lose capacity faster than their α-Ge counterparts. We interpret this as a morphological predisposition of *allo*-Ge to rapid aging and loss of electrical contact due to its stacked sheet morphology. Concurrently, electronically disconnected Li_7Ge_3 seems to accumulate especially in the *allo*-Ge cells as it is retained more and more in fully delithiated cells.

Improving electrode recipes and using smaller particle sizes promises better cycling stability in the future. Thus, it seems worthwhile to compare optimized versions of both materials again and analyze the performance differences in order to learn more about the effect of morphology on cycling stability in the Ge anode system.

Acknowledgements

L.M.S. is grateful to Technische Universität München for financial support through the Laura-Bassi Prize and to Fonds der chemischen Industrie and the Studienstiftung des Deutschen Volkes for her fellowships. LMU – REM Messungen Funding for J. H. and I. B. was provided by the BMBF (Federal ministry of Education and research, Germany), ExZellTUM project, grant number 03X4633A.

Notes and references

1 E. J. Berg, C. Villevieille, D. Streich, S. Trabesinger and P. Novák, *J. Electrochem. Soc.*, 2015, **162**, A2468-A2475.
2 M. T. McDowell, S. W. Lee, W. D. Nix and Y. Cui, *Adv. Mater.*, 2013, **25**, 4966–4985.
3 M. Zeilinger and T. F. Fässler, *Dalton Trans.*, 2014, **43**, 14959–14970.
4 H. Jung, P. K. Allan, Y.-Y. Hu, O. J. Borkiewicz, X.-L. Wang, W.-Q. Han, L.-S. Du, C. J. Pickard, P. J. Chupas, K. W. Chapman, A. J. Morris and C. P. Grey, *Chem. Mater.*, 2015, **27**, 1031–1041.
5 K. C. Klavetter, S. M. Wood, Y.-M. Lin, J. L. Snider, N. C. Davy, A. M. Chockla, D. K. Romanovicz, B. A. Korgel, J.-W. Lee, A. Heller and C. B. Mullins, *J. Power Sources*, 2013, **238**, 123-136.
6 H. Jia, R. Kloepsch, X. He, J. P. Badillo, P. Gao, O. Fromm, T. Placke and M. Winter, *Chem. Mater.*, 2014, **26**, 5683–5688.
7 C. S. Fuller and J. C. Severiens, *Phys. Rev.*, 1954, **96**, 21-24.
8 J. Grätz, C. C. Ahn, R. Yazami and B. Fultz, *J. Electrochem. Soc.*, 2004, **151**, A698–A702.
9 X. H. Liu, Y. Liu, A. Kushima, S. Zhang, T. Zhu, J. Li and J. Y. Huang, *Adv. Energy Mater.*, 2012, **2**, 722-741.
10 G. Cui, L. Gu, L. Zhi, N. Kaskhedikar, P. A. van Aken, K. Müllen and J. Maier, *Adv. Mater.*, 2008, **20**, 3079-3083.
11 S. Yoon, C.-M. Park and H.-J. Sohn, *Electrochem. Solid-State Lett.*, 2008, **11**, A42-A45.
12 R. A. DiLeo, S. Frisco, M. J. Ganter, R. E. Rogers, R. P. Raffaelle and B. J. Landi, *J. Phys. Chem. C*, 2011, **115**, 22609-22614.
13 W. Tang, Y. Liu, C. Peng, M. Y. Hu, X. Deng, M. Lin, J. Z. Hu and K. P. Loh, *J. Am. Chem. Soc.*, 2015, **137**, 2600–2607.
14 L. Y. Lim, N. Liu, Y. Cui and M. F. Toney, *Chem. Mater.*, 2014, **26**, 3739–3746.
15 L. Baggetto and P. H. L. Notten, *J. Electrochem. Soc.*, 2009, **156**, A169–A175.
16 Zintl phases are polar intermetallic compounds that can be described by a salt-like complete valence-electron transfer from electropositive group 1 or 2 metals to more electronegative group 13 to 16 p block metals.
17 G. S. Armatas and M. G. Kanatzidis, *Science*, 2006, **313**, 817–820.
18 G. S. Armatas and M. G. Kanatzidis, *Adv. Mater.*, 2008, **20**, 546–550.
19 G. S. Armatas and M. G. Kanatzidis, *Nature*, 2006, **441**, 1122–1125.
20 G. S. Armatas and M. G. Kanatzidis, *Struct. Bond.*, 2011, **140**, 133-154.
21 T. F. Fässler, *Angew. Chem. Int. Ed.*, 2007, **46**, 2572–2575.
22 D. Sun, A. E. Riley, A. J. Cadby, E. K. Richman, S. D. Korlann and S. H. Tolbert, *Nature*, 2006, **441**, 1126–1130.
23 M. Pelosi, M. Tillard and D. Zitoun, *J. Nanopart. Res.*, 2013, **15**, 1-12.
24 F. Kiefer, A. J. Karttunen, M. Döblinger and T. F. Fässler, *Chem. Mater.*, 2011, **23**, 4578–4586.

25 M. E. Straumanis and E. Z. Aka, *J. Appl. Phys.*, 1952, **23**, 330–334.
26 A. M. Guloy, R. Ramlau, Z. Tang, W. Schnelle, M. Baitinger and Y. Grin, *Nature*, 2006, **443**, 320–323.
27 M. M. Bentlohner, M. Waibel, P. Zeller, K. Sarkar, P. Müller-Buschbaum, D. Fattakhova-Rohlfing and T. F. Fässler, *Angew. Chem. Int. Ed.*, 2016, **55**, 2441–2445.
28 F. Kiefer and T. F. Fässler, *Solid State Sci.*, 2011, **13**, 636–640.
29 F. Kiefer, V. Hlukhyy, A. J. Karttunen, T. F. Fässler, C. Gold, E.-W. Scheidt, W. Scherer, J. Nylén and U. Häussermann, *J. Mater. Chem.*, 2010, **20**, 1780–1786.
30 J. V. Zaikina, E. Muthuswamy, K. I. Lilova, Z. M. Gibbs, M. Zeilinger, G. J. Snyder, T. F. Fässler, A. Navrotsky and S. M. Kauzlarich, *Chem. Mater.*, 2014, **26**, 3263–3271.
31 Polyvinylidene fluoride cannot be employed as a binder because we observe an immediate reaction with Li_7Ge_{12}.
32 In our PXRD patterns Li_7Ge_3 is barely crystalline so that in the lower quality diffraction patterns by Notten et al. Li_7Ge_3 reflections might just not be discernible from the background.
33 In Ref. [4] Grey et al. describe the amorphous stage as phase that locally resembles Li_7Ge_2. However, the compound intially reported as Li_7Ge_2 was later corrected to $Li_{13}Ge_4$: R. Nesper, Habilitation, Universität Stuttgart (Stuttgart), 1988.

Electrochemical Synthesis of the Allotrope *allo*-Ge and Investigations on the Use as an Anode Material

L. M. Scherf,[a]† J. Hattendorff,[b]† I. Buchberger,[b] S. Geier,[a] H. A. Gasteiger,[b] T. F. Fässler[a]

[a] Lehrstuhl für Anorganische Chemie mit Schwerpunkt Neue Materialien, Department of Chemistry, Technische Universität München, Lichtenbergstr. 4, 85749 Garching b. München, Germany.

[b] Lehrstuhl für Technische Elektrochemie, Department of Chemistry, Technische Universität München, Lichtenbergstr. 4, 85749 Garching b. München, Germany.

† These authors contributed equally to this work.

Contents

PXRD pattern of LiGe 2

PXRD pattern of Li_7Ge_{12} 2

PXRD patterns of extracted Li_7Ge_{12} electrode materials 3

Potential plot of Li_7Ge_{12} half-cells 3

PXRD pattern of *m-allo*-Ge 4

PXRD pattern of α-Ge 4

Particle Size Analysis 5

Coin Cell dQ/dV Curves 5

Ex-situ PXRD patterns of coin cell anode materials after cycling 6

Selected in-situ PXRD patterns 7

dQ/dV Plot for α-Ge pouch cells 8

References 8

PXRD pattern of LiGe

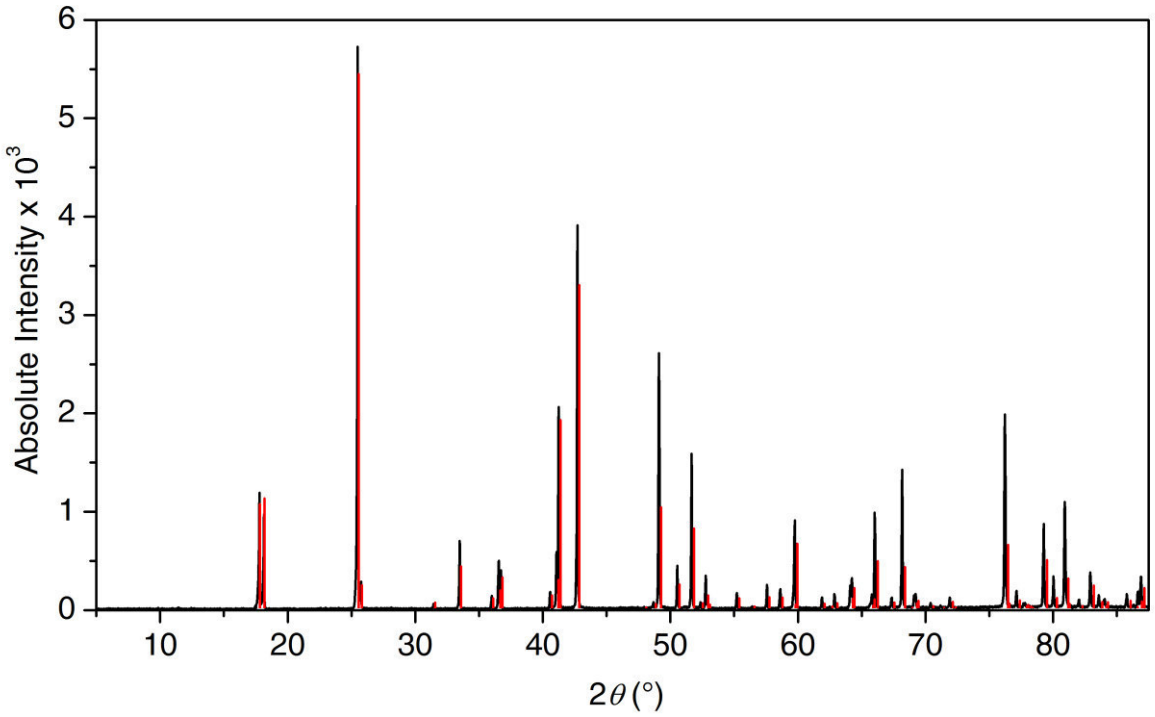

Fig. S1: Experimental (black) and calculated (red) PXRD patterns of LiGe. PSD steps 1.5 °, time/step 15 s.

PXRD pattern of Li_7Ge_{12}

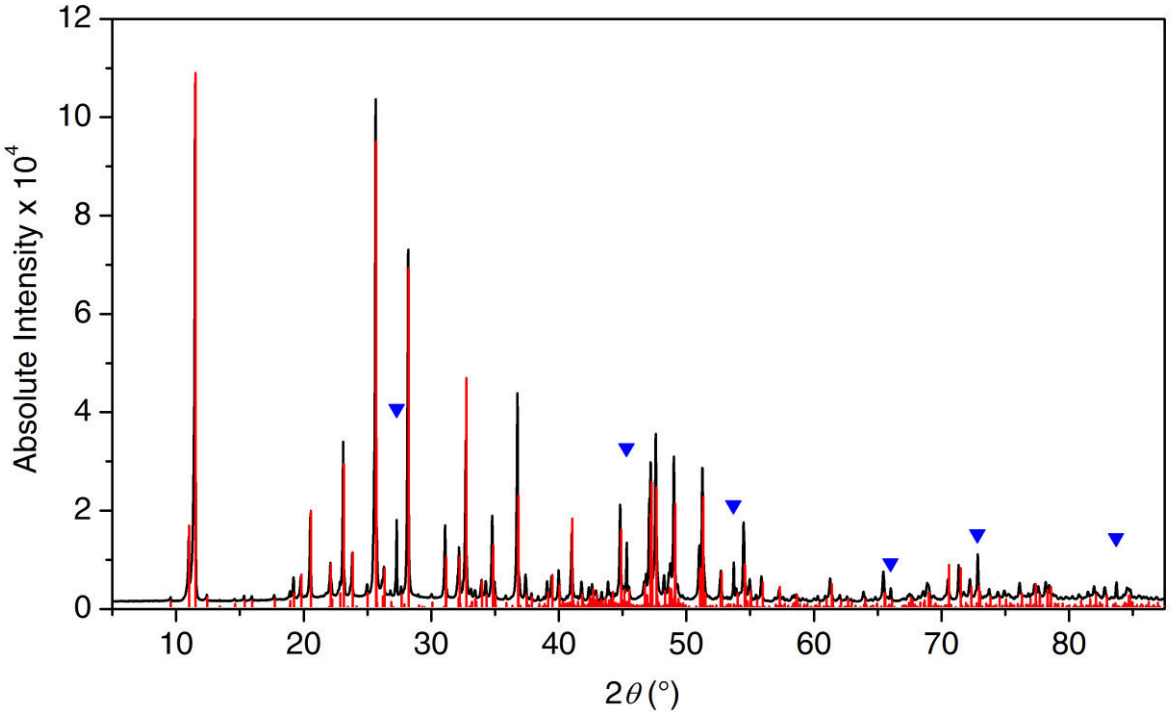

Fig. S2: Experimental (black) and calculated (red) PXRD patterns of Li_7Ge_{12}. Blue triangles denote traces of α-Ge. PSD steps 0.07 °, time/step 45 s.

PXRD patterns of extracted Li_7Ge_{12} electrode materials

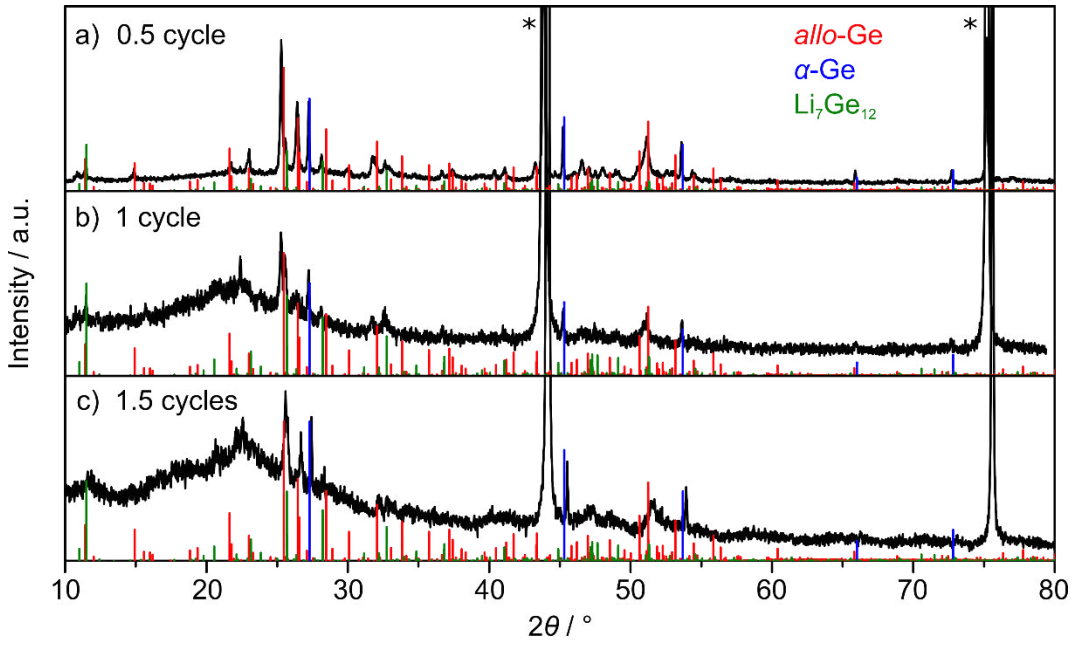

Fig. S3. Powder diffraction patterns of electrode material extracted from coin cells; a) after one delithiation step *allo*-Ge has clearly been formed, b) after one full delithiation/lithiation cycle less allo-Ge is present and a broad signal appears around 22°, c) after 1.5 cycles the ratio of crystalline phases does not change anymore but the broad signal grows; theoretical powder patterns of *allo*-Ge,[1] α-Ge,[2] and Li_7Ge_{12}[3] are given in red, blue, and green, respectively; diamond powder was added to all electrode materials post-cycling for easier handling of the material, corresponding reflexes are marked by an asterisk.

Potential plot of Li_7Ge_{12} half-cells

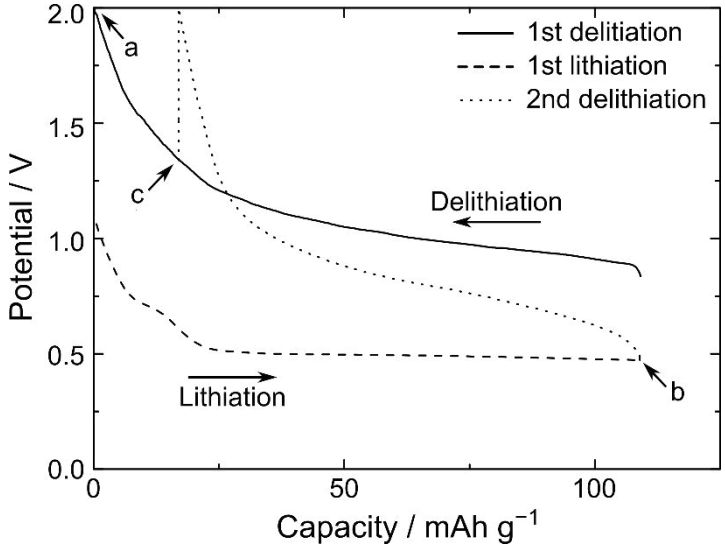

Fig. S4. Potential curves of the first 1.5 cycles of Li_7Ge_{12} half-cells beginning with the first delithiation cycle to 2 V. The powder diffraction state of powder diffraction patterns a–c in Fig. S3 are marked with the respective letters.

PXRD pattern of *m-allo*-Ge

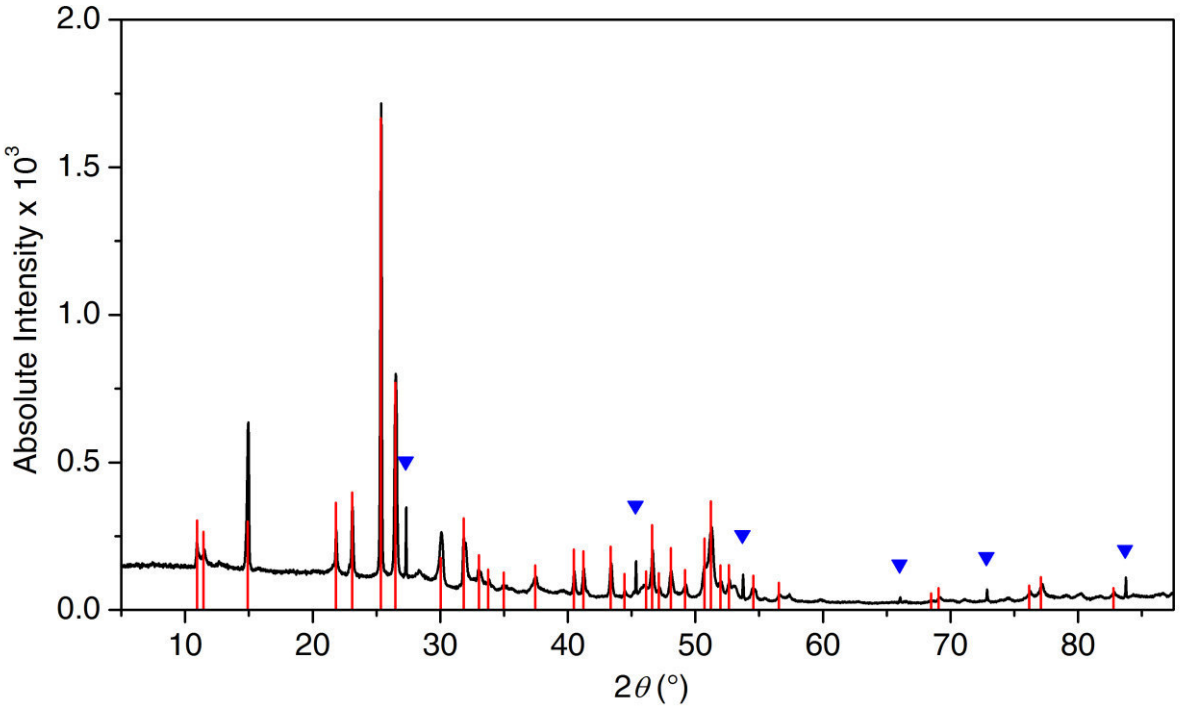

Fig. S5: Experimental (black) and calculated (red) PXRD patterns of *m-allo*-Ge. Blue triangles denote traces of α-Ge. PSD steps 0.07 °, time/step 30 s.

PXRD pattern of α-Ge

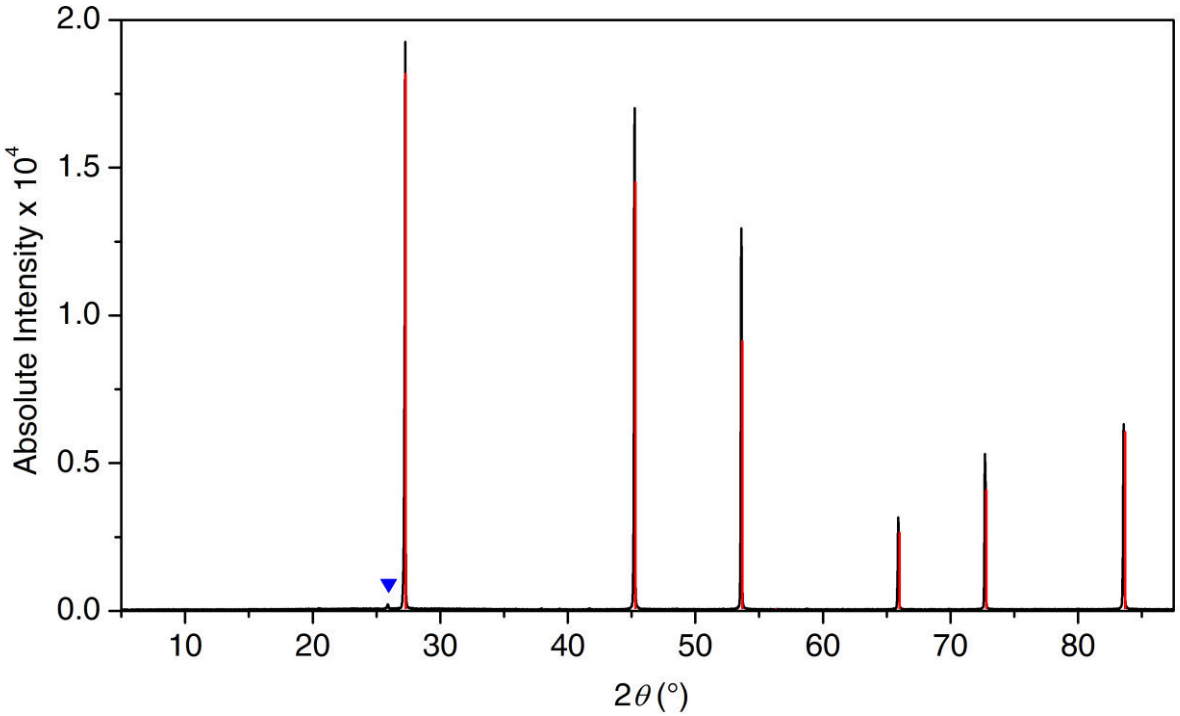

Fig. S6: Experimental (black) and calculated (red) PXRD patterns of α-Ge. The blue triangle marks traces of GeO_2. PSD steps 1.5 °, time/step 15 s.

Particle Size Analysis

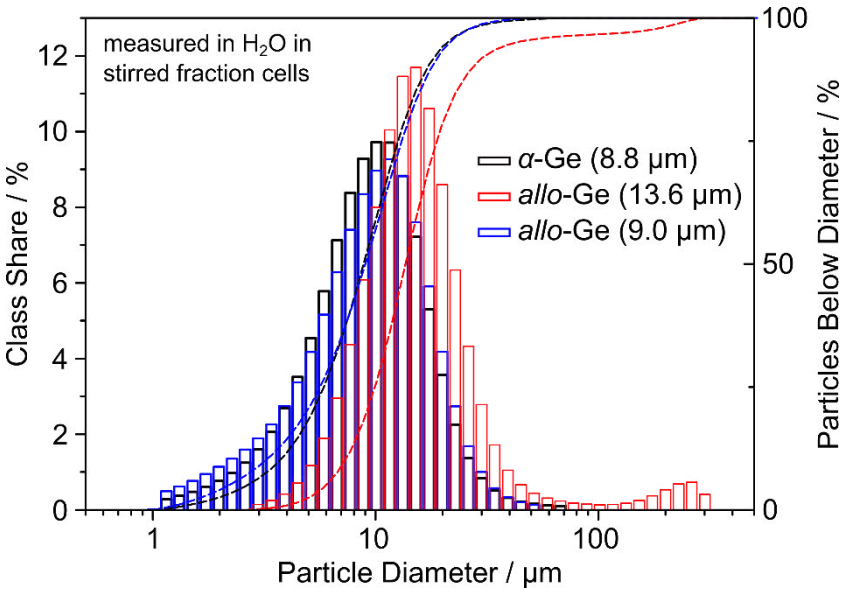

Fig. S7. Particle size analysis of Ge anode materials in H_2O in stirred fraction cell by laser scattering, volume-based distribution. The median of the respective samples is given.

Coin Cell dQ/dV Curves

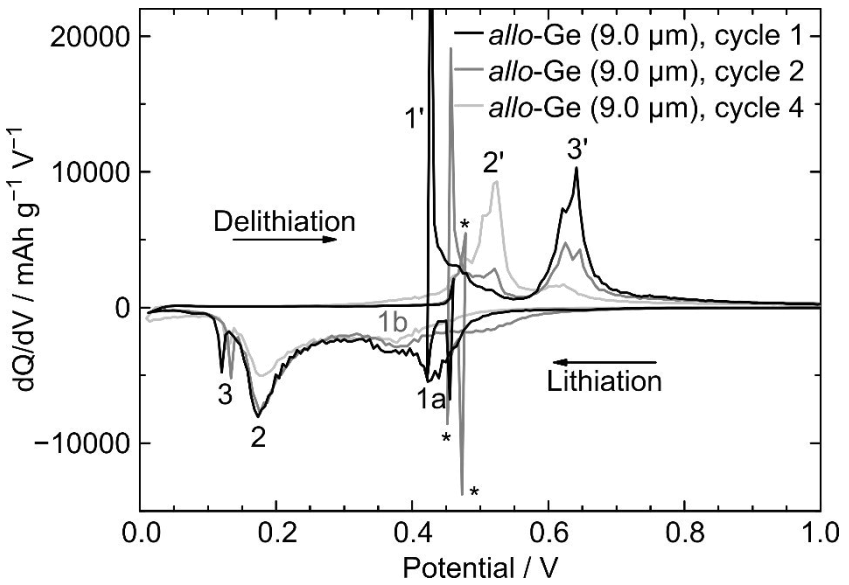

Fig. S8. dQ/dV curves from *allo*-Ge coin cells. Features marked with (*) are artifacts due to over-potentials. First, second and fourth cycles shown.

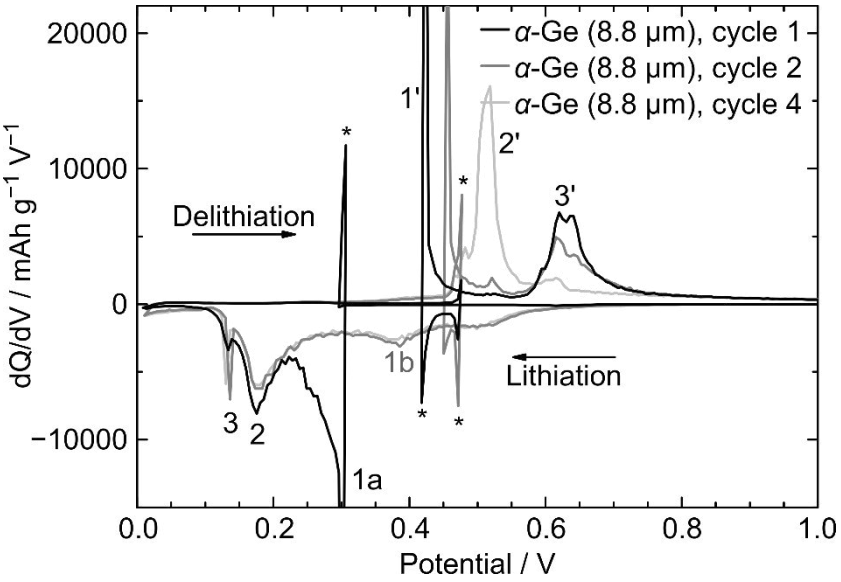

Fig. S9. dQ/dV curves for α-Ge coin cells. Features marked with (*) are artifacts due to overpotentials. First, second and fourth cycles shown.

Ex-situ PXRD patterns of coin cell anode materials after cycling

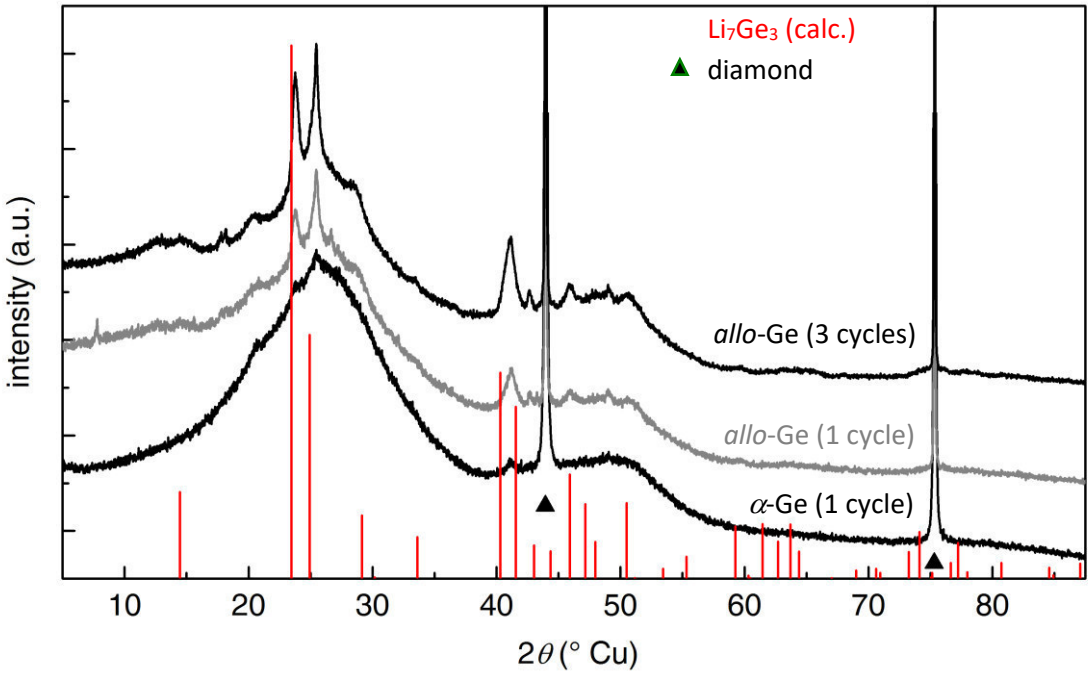

Fig. S10. *Ex-situ*-PXRD patterns of anode materials α–Ge after 1 discharge/charge cycle, *allo*-Ge after 1 discharge/charge cycle, and *allo*-Ge after 3 discharge/charge cycles. All materials contain varying amounts of a crystalline phase resembling Li_7Ge_3 (calculated diffraction pattern in red). Black triangles denote reflections of diamond which was mixed with the anode materials for easier handling.

Selected in-situ PXRD patterns

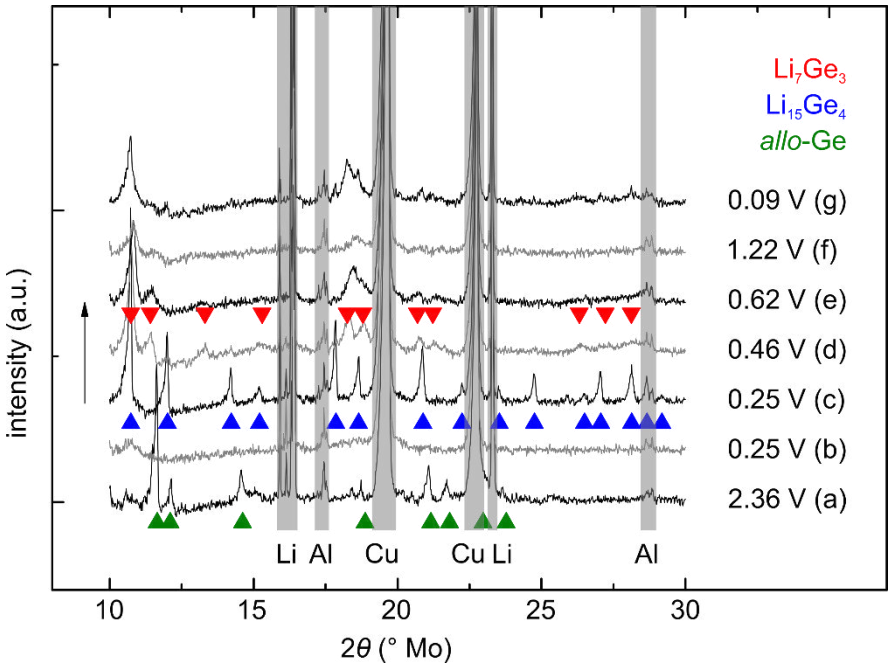

Fig. S11. Selected diffraction patterns from *allo*-Ge pouch cell. Data shown is averaged over 4 raw data files, i.e. one hour of measurement. The main reflections of all observed crystalline phases are marked. The average voltage and the position in Fig. 5 is indicated.

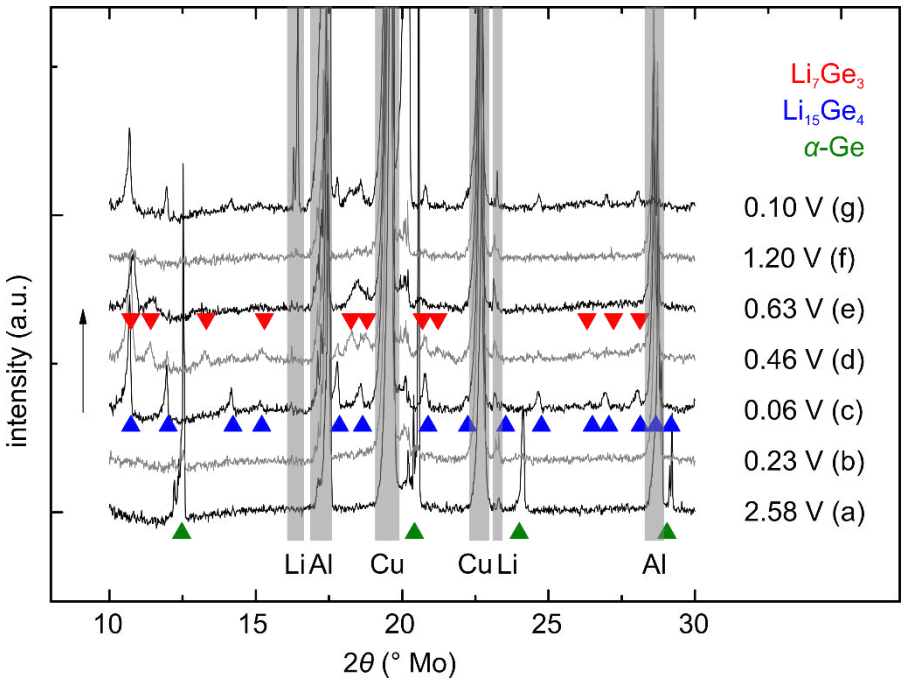

Fig. S12. Selected diffraction patterns from α-Ge pouch cell. Data shown is averaged over 4 raw data files, i.e. one hour of measurement. The main reflections of all observed crystalline phases are marked. The average voltage and the position in Fig. 6 is indicated.

dQ/dV Plot for α-Ge pouch cells

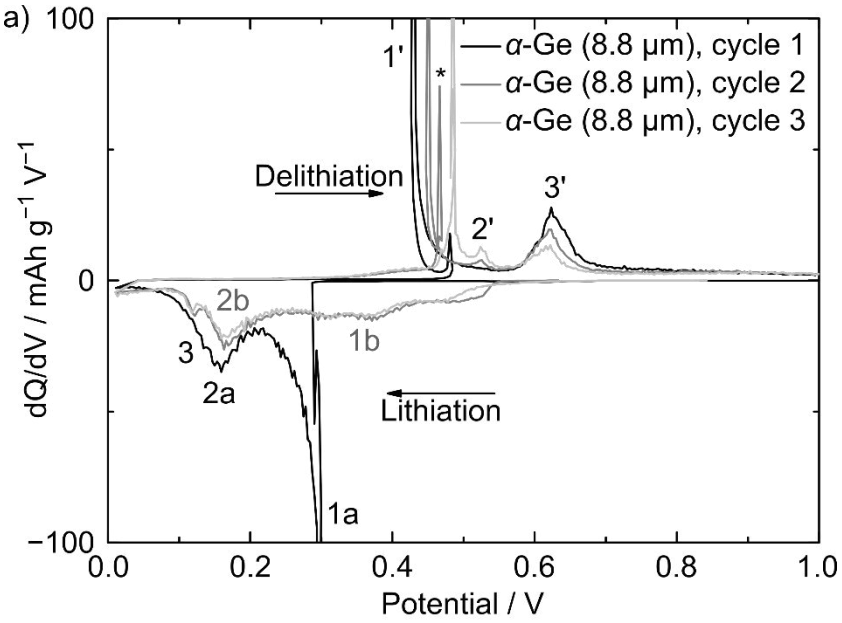

b) **Proposed (de-)lithiation mechanism for *α*-Ge:**

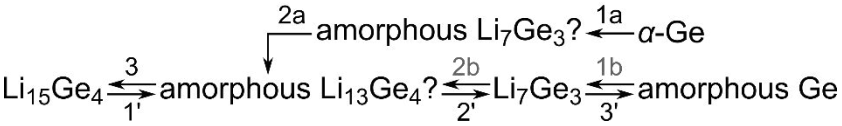

Fig. S13. a) dQ/dV plot of α-Ge in in-situ PCRD pouch cell. An overpotential leads to an artifact peak and is marked by (*), b) proposed (de-)lithiation mechanism for α-Ge, in agreement with Grey *et al.*[4]

References

1 F. Kiefer, A. J. Karttunen, M. Döblinger and T. F. Fässler, *Chem. Mater.*, 2011, **23**, 4578–4586.

2 M. E. Straumanis and E. Z. Aka, *J. Appl. Phys.*, 1952, **23**, 330–334.

3 F. Kiefer and T. F. Fässler, *Solid State Sci.*, 2011, **13**, 636–640.

4 H. Jung, P. K. Allan, Y.-Y. Hu, O. J. Borkiewicz, X.-L. Wang, W.-Q. Han, L.-S. Du, C. J. Pickard, P. J. Chupas, K. W. Chapman, A. J. Morris and C. P. Grey, *Chem. Mater.*, 2015, **27**, 1031–1041.

5.11 Radical-Induced Hydrosilylation Reactions for the Functionalization of Two-Dimensional Hydride Terminated Silicon Nanosheets

ChemPubSoc Europe

DOI: 10.1002/chem.201505134

CHEMISTRY
A European Journal
Communication

Surface Chemistry

Radical-Induced Hydrosilylation Reactions for the Functionalization of Two-Dimensional Hydride Terminated Silicon Nanosheets

Tobias Helbich,[a] Alina Lyuleeva,[b] Ignaz M. D. Höhlein,[a] Philipp Marx,[a] Lavinia M. Scherf,[c] Julian Kehrle,[a] Thomas F. Fässler,[c] Paolo Lugli,[b] and Bernhard Rieger*[a]

Abstract: Herein we present the functionalization of freestanding silicon nanosheets (SiNSs) by radical-induced hydrosilylation reactions. An efficient hydrosilylation of Si–H terminated SiNSs can be achieved by thermal initiation or the addition of diazonium salts with a variety of alkene or alkyne derivatives. The radical-induced hydrosilylation is applicable for a wide variety of substrates with different functionalities, improving the stability and dispersibility of the functional SiNSs in organic solvents and potentially opening up new fields of application for these hybrid materials.

Silicon nanosheets (SiNSs) are two-dimensional semiconducting materials with a layer thickness in the nano-regime and sheet sizes up to the micro-scale.[1] Like graphene they combine outstanding structural and electronic characteristics. As the electronic properties of these two materials differ from each other, SiNSs should hence expand the field of applications for 2D nanomaterials.

According to theoretical and experimental studies the band gap of SiNSs is tunable by physical strain,[2] the degree of hydrogenation, termination with heteroatoms,[3,4] and surface functionalization with different substrates.[5,6] Additionally, SiNSs exhibit unique optical properties such as a layer-thickness-dependent absorption edge[7] and photoluminescence (PL) emission arising from an enhanced direct band gap transition.[8,9] Hence SiNSs are promising candidates for microelectronics such as novel field effect transistors (FET)[5,10] and photovoltaic solar cells[9] and have already been proven to exhibit potential for lithium ion battery application.[11–13]

Several routes have been reported for the production of SiNSs. They can be synthesized by magnesiothermic reduction of SiO_2[14,15] or grown on supports such as Ag and Si by chemical vapor deposition.[8,16,17] Another straightforward and easily scalable route is chemical exfoliation from $CaSi_2$.[18,19] The Zintl salt $CaSi_2$ consists of interconnected Si_6 rings which form puckered two dimensional, anionic silicon sheets and planar monolayers of Ca^{2+} ions. Through treatment with hydrochloric acid the Ca^{2+} ions can be deintercalated giving exfoliated hydride terminated SiNSs (Figure 1).

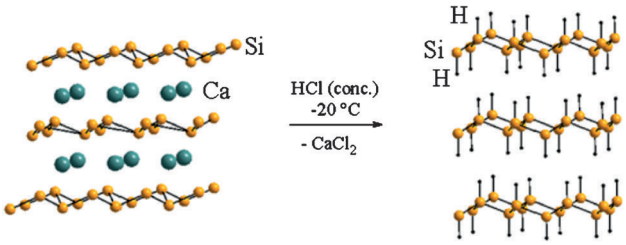

Figure 1. Synthesis of layered polysilanes by chemical exfoliation from $CaSi_2$.

Due to their structural properties (i.e., sp^3 character), hydride terminated SiNSs are also referred to as layered polysilanes.[20] They are prone to oxidation under ambient conditions and must therefore be functionalized to be of further use. Additionally functionalization breaks up the stacked structure of non-functionalized SiNSs, rendering freestanding monolayers. Functionalized SiNSs are dispersible in organic solvents which facilitates their handling and characterization.

So far only three different methods have been published in which the functionalization of hydride terminated SiNSs with organic compounds is described. The reaction with *n*-alkylamines leads to stable Si–N–Si derivatives which exhibit blue PL,[21,22] while the conversion of SiNSs with the Grignard compound PhMgBr renders $(Si_6H_4Ph_2)_n$ layers.[1] Additionally Pt-catalyzed hydrosilylation with 1-hexene enables the functionalization of SiNSs and yields stable colloidal dispersions in chloroform.[23]

Hydrosilylation reactions can be used to react molecular and surface Si–H groups with various unsaturated substrates. The reaction does not take place spontaneously, but needs initia-

[a] T. Helbich, Dr. I. M. D. Höhlein, P. Marx, J. Kehrle, Prof. Dr. B. Rieger
Wacker-Lehrstuhl für Makromolekulare Chemie
Technische Universität München, Lichtenbergstrasse 4
85747 Garching (Germany)
E-mail: rieger@tum.de

[b] A. Lyuleeva, Prof. Dr. P. Lugli
Institute for Nanoelectronics, Technische Universität München
Arcisstrasse 21, 80333 Munich (Germany)

[c] L. M. Scherf, Prof. Dr. T. F. Fässler
Lehrstuhl für Anorganische Chemie mit Schwerpunkt Neue Materialien
Technische Universität München, Lichtenbergstrasse 4
85747 Garching (Germany)

Supporting information for this article is available on the WWW under http://dx.doi.org/10.1002/chem.201505134.

tion. On the molecular level it can be mediated by a catalyst, while on surfaces, thermally or initiator-induced radical reactions are also possible.[24–26] The latter are easily feasible, cost-efficient and tolerant towards a broad variety of functional groups. Another advantage is that radical-induced hydrosilylation is conducted without the introduction of transition metal impurities which are known to alter the PL properties of silicon nanomaterials[27,28] and lead to increased surface oxidation.[29] Despite their advantages, radical-induced hydrosilylation reactions have not yet been examined for the surface functionalization of SiNSs.

In this work the reactivity of SiNSs towards unsaturated compounds with different functionalities was examined (Scheme 1). The reactions were conducted in the absence of a catalyst under thermal initiation (130 °C) or by the addition of a diazonium salt as radical initiators with a variety of functional substrates. The resulting hybrid materials were fully characterized by FTIR, NMR spectroscopy, AFM, TGA, XRD and PL measurements.

The hydride-terminated SiNSs used in this work were synthesized following a literature known procedure.[19] $CaSi_2$ was chemically exfoliated with HCl (conc.) at −20 °C for 7 days. To remove residual oxide the obtained SiNSs were then etched with hydrofluoric acid and extracted with dichloromethane. As can be seen from the Si–H stretching- (≈2100 cm^{-1}), scissoring- (≈900 cm^{-1}) and wagging bands (≈860 cm^{-1}) in FTIR spectra of the freshly etched SiNSs, the resulting silicon sheets are hydride-terminated with only slight traces of Si–O (≈1100 cm^{-1}) and no Si–OH (Figure 2a).

To understand the reactivity of the SiNSs towards unsaturated carbon compounds, control experiments were conducted without a radical initiator at room temperature in the dark. Therefore the HF treated SiNSs (15 mg) were dispersed in a mixture of dry toluene (2 mL) and 1-dodecene (3 mmol), degassed by three freeze-thaw-pump cycles and subsequently stirred overnight under argon in the dark.

Neither molecular silanes[30,31] (see the Supporting Information) nor hydride terminated silicon surfaces of bulk silicon[32] or nanostructured silicon[33] show functionalization under these conditions. Therefore we were surprised to observe a significant amount of dodecyl groups on the SiNSs in FTIR measurements (Figure 2c) and TGA (Figure S7 in the Supporting Information). However this functionalization method is not sufficient to fully

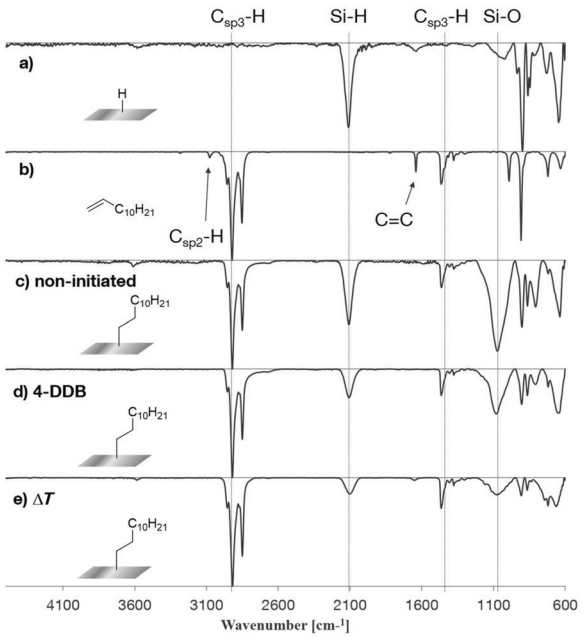

Figure 2. FTIR spectra of: a) freshly etched SiNSs, b) 1-dodecene and 1-dodecene-functionalized SiNSs, c) without the addition of an initiator, d) with 4-DDB, and e) Δ*T*-induced hydrosilylation.

prevent stacking of the SiNSs (Figure S8 in the Supporting Information). Additionally, after the workup strong Si–O and residual Si–H bands, visible in IR spectra indicate, that the functionalization only takes place to a minor extent.

The cause for this unprecedented reactivity is not fully understood and remains part of the ongoing research in our group. Potential explanations are the very high surface area and energy which results in a higher reactivity of the nanomaterial[34] or the surface activation by traces of oxygen which were shown to initiate hydrosilylations on SiNCs.[35]

To achieve a higher degree of surface functionalization, the SiNSs were subsequently treated with 1-dodecene under radical initiation conditions (Scheme 1).

Diazonium salts are known to be mild radical initiators for hydrosilylation reactions on nanostructured silicon.[36] Especially 4-decylbenzene diazonium tetrafluoroborate (4-DDB) is suitable due to its solubility in nonpolar solvents.[26] Additionally elevated temperatures can initiate hydrosilylation.[35]

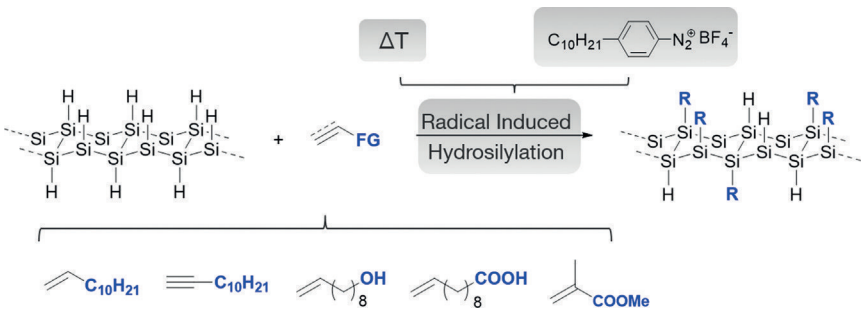

Scheme 1. Schematic overview of the executed functionalization methods: Thermal and diazonium salt induced hydrosilylations are applicable on a broad variety of substrates.

Exfoliated SiNSs (15 mg) were etched with HF (48%), extracted and dispersed in a mixture of dry toluene (2 mL) with 1-dodecene (3 mmol). After degassing, 4-DDB (15 μmol) was added and the reaction mixture was stirred at room temperature, overnight. For thermal functionalization Si–H-terminated SiNSs were dispersed in 1-dodecene (1 mL), degassed and subsequently stirred at 130 °C, overnight.

The mechanism for both initiation conditions is proposed to proceed by the formation of silyl-radicals.[37] The 4-DDB-induced functionalization occurs through reduction of the diazonium compound, release of nitrogen and hence the formation of an aryl radical. After deprotonation a silyl surface radical is formed which then reacts with the unsaturated compound, leading to the Si–C bond and a carbon centered radical. Abstraction of a neighboring hydrogen radical again forms a silicon surface radical and the hydrosilylation proceeds as a radical chain reaction (Scheme 2a).[26,38]

Thermally induced hydrosilylation is stated to be dependent on the reaction temperature. While temperatures $\geq$150 °C provide enough energy to homolytically cleave Si–H bonds and thus induce the radical chain propagation (Scheme 2b), for temperatures between 80–150 °C traces of oxygen are proposed to accelerate hydrogen abstraction (Scheme 2c).[35]

After the reaction, the FTIR spectra of the functionalized SiNSs (Figure 2d and e) show strong C_{sp3}–H bands ($\approx$2920 cm^{-1}, $\approx$1460 cm^{-1}) while only weak bands of residual Si–H ($\approx$2100 cm^{-1}) and Si–O ($\approx$1100 cm^{-1}) are present. This indicates a higher coverage of the SiNSs with dodecyl groups in contrast to functionalization without radical initiation, which is also supported by differences in the weight loss of the differently functionalized material in TGA measurements (Figure S7 in the Supporting Information).

Additionally we confirmed the 4-DDB and thermally induced functionalization with ^{1}H NMR experiments in solution (Figure 3). Due to the restricted freedom of movement of the organic substrates attached to the Si surface the spectra can only qualitatively be used to show the successful functionalization and purification. The peaks of the double bond (A: δ = 5.82 ppm; B + C: δ = 4.96 ppm) and the methylene group next to it (D: δ = 2.04 ppm) have vanished and the spectra still show the peaks of the terminal CH_3 group (F: δ = 0.85 ppm) and of the $-CH_2$ groups (E: δ = 1.25 ppm) of the alkyl chain.

Atomic force microscope (AFM) images of the 1-dodecene-functionalized SiNSs show freestanding monolayers with a thickness of about 2.0 nm (Figure 4) which is similar to the

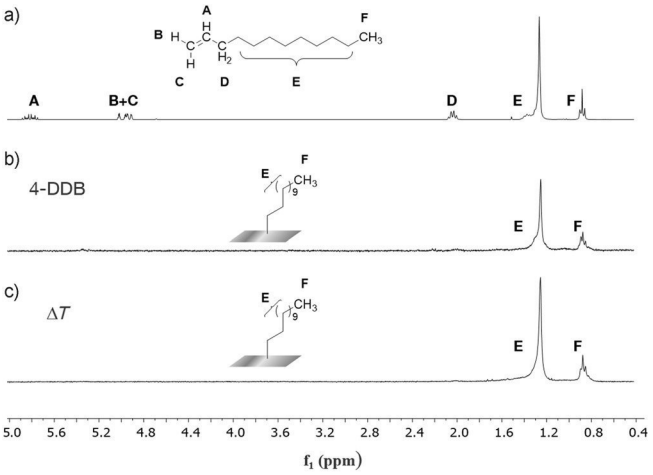

Figure 3. NMR spectra of: a) 1-dodecene, 1-dodecene-functionalized SiNSs with b) 4-DDB, and c) ΔT-induced hydrosilylation.

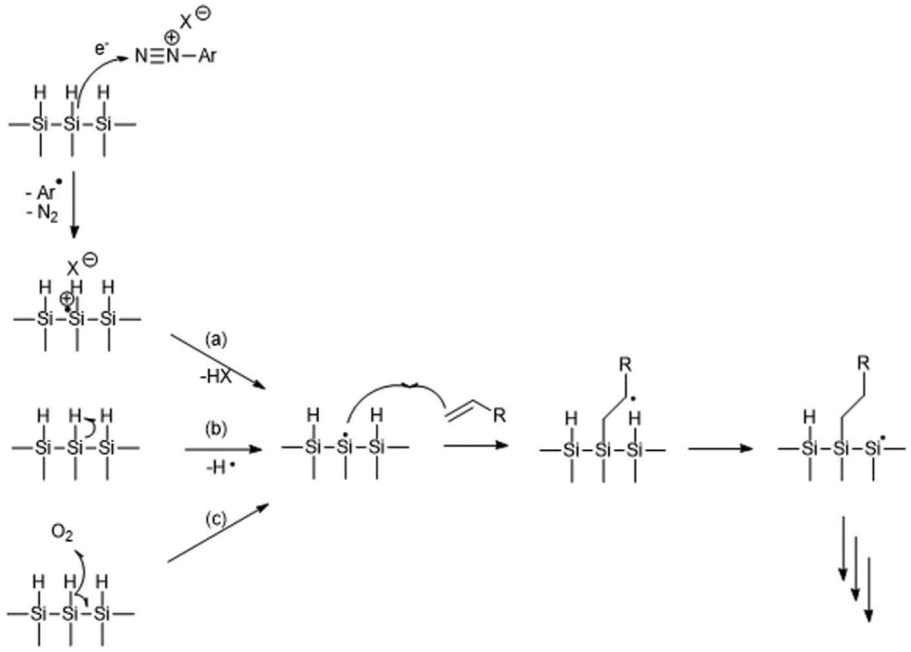

Scheme 2. Proposed mechanism for the: a) diazonium-compound induced mechanism and thermally induced hydrosilylation at temperatures between b) 80–150 °C, and c) $\geq$150 °C.[25,35,39]

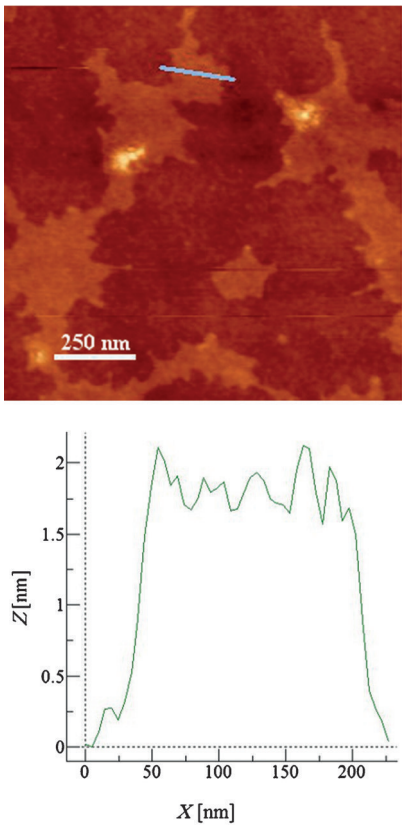

Figure 4. Non-contact mode AFM image of 4-DDB-induced 1-dodecene-functionalized SiNSs (top) and their line profile (bottom) taken along the line in the left image.

thickness of the 1-hexene-functionalized SiNSs reported by Nakano et al.[23]

XRD patterns recorded from the non-functionalized and 1-dodecene-functionalized SiNSs show that the characteristic reflections of the stacked, non-functionalized sheets decrease significantly in intensity when the SiNSs are functionalized without the initiator and even further with radical initiation (Figure S8 in the Supporting Information). The long dodecyl chains on the surface seem to stabilize the monolayers and hinder the SiNSs from stacking, resulting in a less ordered material.

Besides the model substrate 1-dodecene, functional substrates are promising candidates for further applications of the hybrid nanomaterials. Hence, to demonstrate the broad applicability of thermally and diazonium salt-induced hydrosilylations with hydride terminated SiNSs, a number of functional alkenes and alkynes were used. In this context we explored the functionalization with 10-undecenoic acid, 1-dodecyne, 9-decen-1-ol and *tert*-butyl methacrylate (*t*BuMA). In the case of *t*BuMA thermal hydrosilylation leads to a vast excess of polymerized alkene. No such side reaction could be observed in the 4-DDB-induced functionalization of the SiNSs, demonstrating the advantage of this mild method.

FTIR spectra of the functionalized SiNSs (4-DDB: Figure 5; ΔT: Figure S9 in the Supporting Information) with the different substrates confirm the successful reaction exhibiting the expected bands such as C_{sp3}–H ($\approx$2920 cm^{-1}), C=C ($\approx$1640 cm^{-1}), C=O ($\approx$1700 cm^{-1}), OH ($\approx$2920 cm^{-1}), C–O ($\approx$1150 cm^{-1}) while only traces of Si–H ($\approx$2100 cm^{-1}), and Si–O ($\approx$1100 cm^{-1}) can be detected. SiNS–$C_{10}H_{20}$OH and SiNS–$C_{10}H_{20}$COOH are dispersible in protic solvents such as ethanol and methanol while for SiNS–$C_{12}H_{25}$ and SiNS–CHCH–$C_{10}H_{21}$ nonpolar hydrocarbons such as toluene and benzene are the solvents of choice. Further reactions are possible with the thus introduced functionalities on the SiNSs surface. This approach is currently under investigation and should open up new fields of applications.

The hybrid materials exhibit similar photoluminescence properties to the non-functionalized materials, namely an emis-

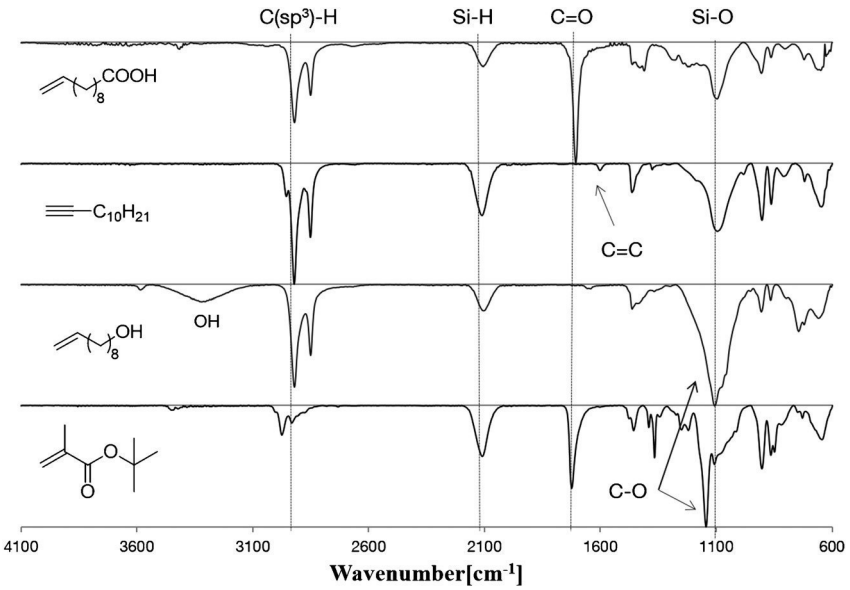

Figure 5. FTIR spectra of functionalized SiNSs by 4-DDB-induced hydrosilylation.

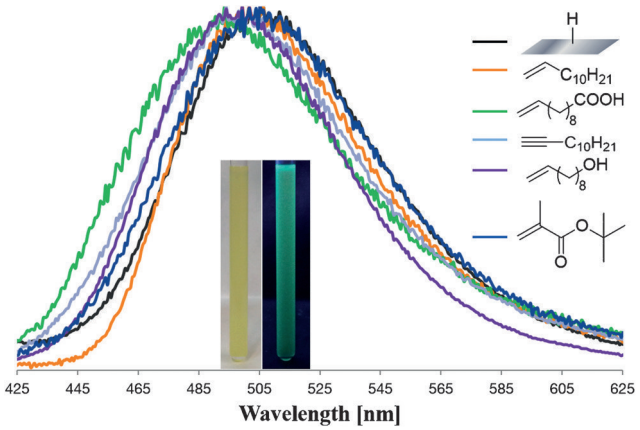

Figure 6. PL spectra of freshly etched and functionalized SiNSs by 4-DDB-induced hydrosilylation.

sion at $\lambda_{max} \approx 500$ nm (Figure 6, Figure S10 in the Supporting Information). This is in accord with the functionalized SiNCs which show similar PL for Si–H– and Si–C-capped SiNCs.[26]

In summary we present the first radical-induced hydrosilylation approach for the efficient functionalization of hydride terminated SiNSs. High temperatures (130 °C) or the addition of diazonium compounds successfully initiate the reaction. With this method SiNSs are functionalized with (non-)functional alkenes and alkynes, introducing alkyl, hydroxyl-, carboxy- and ester groups which improve the dispersibility properties. The free-standing SiNSs were found to have a thickness of about 2 nm and exhibit PL (≈500 nm). Additionally, we demonstrate that NMR experiments in solution can be used to show the successful functionalization of the SiNSs. The obtained functional hybrid materials should be valuable for subsequent reactions and open up possibilities for new applications, for example, in electronics or optoelectronic devices.

Acknowledgements

M. Knaus, R. Csiki, M. Kloberg and K. Melzer are thanked for their support as well as TUM Graduate School and IGSSE. The authors thank the DFG for financial support of Alberta/Technische Universität München Graduate School for Functional Hybrid Materials ATUMS (IRTG2022). T.H. and L.M.S. are thankful for their fellowship from Studienstiftung des deutschen Volkes. I.M.D.H. and L.M.S. gratefully acknowledge the funding from Fonds der Chemischen Industrie.

Keywords: hydrosilylation · layered polysilane · nanotechnology · silicon nanosheets · surface chemistry

[1] Y. Sugiyama, H. Okamoto, T. Mitsuoka, T. Morikawa, K. Nakanishi, T. Ohta, H. Nakano, *J. Am. Chem. Soc.* **2010**, *132*, 5946 – 5947.
[2] F. Li, R. Lu, Q. Yao, E. Kan, Y. Liu, H. Wu, Y. Yuan, C. Xiao, K. Deng, *J. Phys. Chem. C* **2013**, *117*, 13283 – 13288.
[3] T. H. Osborn, A. a. Farajian, O. V. Pupysheva, R. S. Aga, L. C. Lew Yan Voon, *Chem. Phys. Lett.* **2011**, *511*, 101 – 105.
[4] F. Zheng, C. Zhang, *Nanoscale Res. Lett.* **2012**, *7*, 422.
[5] N. Gao, W. T. Zheng, Q. Jiang, *Phys. Chem. Chem. Phys.* **2012**, *14*, 257.
[6] Y. Ding, Y. Wang, *Appl. Phys. Lett.* **2012**, *100*, 083102.
[7] Y. Liu, H. Shu, P. Liang, D. Cao, X. Chen, W. Lu, *J. Appl. Phys.* **2013**, *114*, 094308.
[8] U. Kim, I. Kim, Y. Park, K.-Y. Y. Lee, S.-Y. Y. Yim, J.-G. G. Park, H.-G. G. Ahn, S.-H. H. Park, H.-J. J. Choi, *ACS Nano* **2011**, *5*, 2176 – 2181.
[9] H. Okamoto, Y. Sugiyama, H. Nakano, *Chem. Eur. J.* **2011**, *17*, 9864 – 9887.
[10] O. D. Restrepo, R. Mishra, J. E. Goldberger, W. Windl, *J. Appl. Phys.* **2014**, *115*, 033711.
[11] Y. Kumai, S. Shirai, E. Sudo, J. Seki, H. Okamoto, Y. Sugiyama, H. Nakano, *J. Power Sources* **2011**, *196*, 1503 – 1507.
[12] Y. Kumai, H. Kadoura, E. Sudo, M. Iwaki, H. Okamoto, Y. Sugiyama, H. Nakano, *J. Mater. Chem.* **2011**, *21*, 11941.
[13] Y. Kumai, H. Nakano, *Jpn. J. Appl. Phys.* **2015**, *54*, 035201.
[14] W.-S. Kim, Y. Hwa, J.-H. Shin, M. Yang, H.-J. Sohn, S.-H. Hong, *Nanoscale* **2014**, *6*, 4297 – 4302.
[15] Z. Lu, J. Zhu, D. Sim, W. Zhou, W. Shi, H. H. Hng, Q. Yan, *Chem. Mater.* **2011**, *23*, 5293 – 5295.
[16] B. Lalmi, H. Oughaddou, H. Enriquez, A. Kara, S. Vizzini, B. Ealet, B. Aufray, *Appl. Phys. Lett.* **2010**, *97*, 223109.
[17] P. Vogt, P. De Padova, C. Quaresima, J. Avila, E. Frantzeskakis, M. C. Asensio, A. Resta, B. Ealet, G. Le Lay, *Phys. Rev. Lett.* **2012**, *108*, 155501.
[18] O. Böhm, J. Hassel, *Z. Anorg. Allg. Chem.* **1927**, *160*, 152; Hassel, *Z. Anorg. Allg. Chem.* **1927**, *160*, 152.
[19] S. Yamanaka, H. Matsu-ura, M. Ishikawa, *Mater. Res. Bull.* **1996**, *31*, 307 – 316.
[20] H. Nakano, T. Mitsuoka, M. Harada, K. Horibuchi, H. Nozaki, N. Takahashi, T. Nonaka, Y. Seno, H. Nakamura, *Angew. Chem. Int. Ed.* **2006**, *118*, 6451 – 6454; *Angew. Chem.* **2006**, *118*, 6451 – 6454.
[21] H. Okamoto, Y. Kumai, Y. Sugiyama, T. Mitsuoka, K. Nakanishi, T. Ohta, H. Nozaki, S. Yamaguchi, S. Shirai, H. Nakano, *J. Am. Chem. Soc.* **2010**, *132*, 2710 – 2718.
[22] H. Okamoto, Y. Sugiyama, K. Nakanishi, T. Ohta, T. Mitsuoka, H. Nakano, *Chem. Mater.* **2015**, *27*, 1292 – 1298.
[23] H. Nakano, M. Nakano, K. Nakanishi, D. Tanaka, Y. Sugiyama, T. Ikuno, H. Okamoto, T. Ohta, *J. Am. Chem. Soc.* **2012**, *134*, 5452 – 5455.
[24] J. G. C. Veinot, *Chem. Commun.* **2006**, 4160 – 4168.
[25] J. M. Buriak, *Chem. Commun.* **1999**, 1051 – 1060.
[26] I. M. D. Höhlein, J. Kehrle, T. Helbich, Z. Yang, J. G. C. Veinot, B. Rieger, *Chem. Eur. J.* **2014**, *20*, 4212 – 4216.
[27] D. Andsager, J. Hilliard, J. M. Hetrick, L. H. AbuHassan, M. Plisch, M. H. Nayfeh, *J. Appl. Phys.* **1993**, *74*, 4783.
[28] S. Li, I. N. Germanenko, M. S. El-Shall, *J. Phys. Chem. B* **1998**, *102*, 7319 – 7322.
[29] J. M. Holland, M. P. Stewart, M. J. Allen, J. M. Buriak, *J. Solid State Chem.* **1999**, *147*, 251 – 258.
[30] I. Ojima, N. Clos, R. Donovan, P. Ingallina, *Organometallics* **1990**, *9*, 3127 – 3133.
[31] B. Marciniec, in Comprehensive Handbook on Hydrosilylation (Ed.: B. Marciniec), Pergamon, Amsterdam, **1992**.
[32] R. L. Cicero, M. R. Linford, C. E. D. Chidsey, *Langmuir* **2000**, *16*, 5688 – 5695.
[33] Y. Yu, C. M. Hessel, T. D. Bogart, M. G. Panthani, M. R. Rasch, B. A. Korgel, *Langmuir* **2013**, *29*, 1533 – 1540.
[34] E. Roduner, *Chem. Soc. Rev.* **2006**, *35*, 583 – 592.
[35] Z. Yang, M. Iqbal, A. R. Dobbie, J. G. C. Veinot, *J. Am. Chem. Soc.* **2013**, *135*, 17595 – 17601.
[36] D. Wang, J. M. Buriak, *Langmuir* **2006**, *22*, 6214 – 6221.
[37] M. Woods, S. Carlsson, Q. Hong, S. N. Patole, L. H. Lie, A. Houlton, B. R. Horrocks, *J. Phys. Chem. B* **2005**, *109*, 24035 – 24045.
[38] J. M. Buriak, *Chem. Rev.* **2002**, *102*, 1271 – 1308.
[39] I. M. D. Höhlein, J. Kehrle, T. K. Purkait, J. G. C. Veinot, B. Rieger, *Nanoscale* **2015**, *7*, 914 – 918.

Received: December 22, 2015
Published online on March 15, 2016

CHEMISTRY
A European Journal

Supporting Information

Radical-Induced Hydrosilylation Reactions for the Functionalization of Two-Dimensional Hydride Terminated Silicon Nanosheets

Tobias Helbich,[a] Alina Lyuleeva,[b] Ignaz M. D. Höhlein,[a] Philipp Marx,[a] Lavinia M. Scherf,[c] Julian Kehrle,[a] Thomas F. Fässler,[c] Paolo Lugli,[b] and Bernhard Rieger*[a]

chem_201505134_sm_miscellaneous_information.pdf

Contents

General Information 2
Syntheses and Procedures 2
Synthesis of $CaSi_2$ 2
Synthesis of Layered Polysilanes *via* Chemical Exfoliation 3
Etching of Silicon Nanosheets 3
Functionalization of Silicon Nanosheets Without Initiators 3
4-Decylbenzene Diazonium Tetrafluoroborate-Induced Functionalization 4
Thermal Induced Functionalization 4
Hydrosilylation Reactivity of Molecular Silanes 5
Figures 9
TGA Comparison of the Different Initiation Methods 9
XRD Patterns 9
FTIR Spectra of Functionalized Silicon Nanosheets 10
PL Spectra 10
TGA Measurements 11

General Information

All reactants and reagents were purchased from *Sigma-Aldrich* and used without further purification if not stated otherwise. *Tert*-butylmethacrylate was distilled under reduced pressure and stored over molecular sieve. Toluene was dried prior to use with a *MBraun* solvent purification system *MB SPS-800* whereby argon 5.0 (99.9990 %, *Westfalen AG*) was used as inert gas. Acetone was dried over molecular sieve, degassed via 3 freeze-pump-thaw cycles and stored under argon. For storage of the exfoliated SiNSs a *LABmaster 130 (MBraun)* glove box was used with argon 4.8 (99.998 %, *Westfalen AG*). Air or water sensitive reactions were executed under standard Schlenk techniques.

For **NMR** measurements the functionalized SiNSs were freeze dried from benzene. The spectra were measured on an *ARX-300* from *Bruker* at 300 K. The chemical shifts (δ) are given in ppm and are calibrated to the rest proton signal of the deuterated solvent. **FTIR** spectra were measured with a *Bruker Vertex 70 FTIR* using a *Platinum ATR* from *Bruker*. **PL** spectra were taken with an *AVA-Spec 2048* from *Avantes* using a *Prizmatrix (LED Current controller)* as light source in toluene or ethanol. **TGA** measurements were executed with a *Netzsch TG 209 F 1 Libra* with heating rates of 10 K/min and argon flow rates of 20 mL/min under argon 4.8 (99.998 %, *Westfalen AG*). For **AFM** measurements (contact mode, Asylum Research MFP-3D AFM with an ARC Controller) thin films of SiNS-$C_{12}H_{25}$ (15 mg of exfoliated sheets in 2 mL of toluene) were spin coated (90 seconds, 1000 RPM) on Si/SiO_2 substrates. For **Powder X-ray Diffraction Analysis** powder diffraction patterns were recorded using a Stoe STADI P diffractometer equipped with a Ge(111) monochromator for Cu Kα radiation (λ = 1.54056 Å) and a Dectris MYTHEN DCS 1K solid-state detector. Samples were ground in an agate mortar and filled into 0.5 mm glass capillaries which were then sealed. The samples were measured within a 2ϑ-range of 5–89° (PSD steps, 0.075°; time/step, 41 s).

Syntheses and Procedures

Synthesis of $CaSi_2$

A stoichiometric mixture of calcium (Alfa Aesar, 99.5 %) and silicon (Wacker, 99.99 %) was pressed to a pellet and subsequently melted together in an arc furnace installed in an argon-filled glovebox. To ensure homogenization, the resulting silver colored, metallic regulus was melted from both sides, ground thoroughly in an agate mortar, pressed to a pellet, melted from both sides in the arc furnace and ground to a powder again. A powder diffraction pattern of the resulting product shows that phase-pure $CaSi_2$ could be obtained.

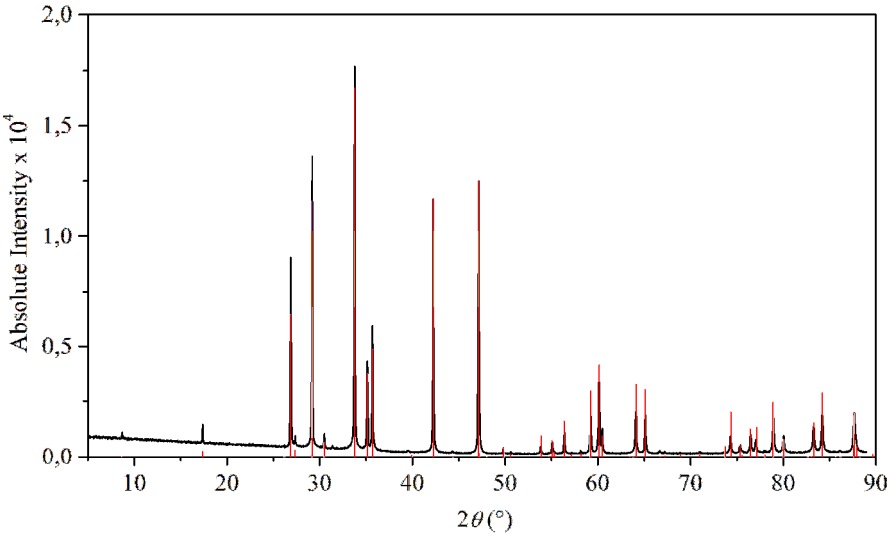

Figure S1. Experimental (black) and theoretical (red) powder diffraction patterns of $CaSi_2$.

Synthesis of Layered Polysilanes *via* Chemical Exfoliation

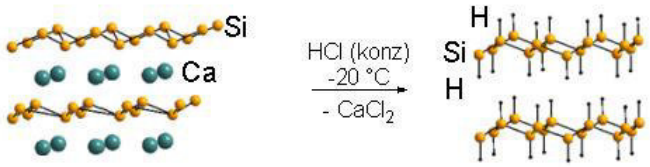

100 mL of HCl (conc.) in a schlenk flask were cooled to -30 °C and 1.00 g of $CaSi_2$ was added under argon and stirred at -20 °C for 7 d. Then the reaction mixture was transferred into another schlenk flask *via* cannula and subsequently filtered off with a glass frit. The yellow filter cake was then washed with dry, degassed acetone and dried under vacuum. The thus obtained exfoliated $(Si_6H_6)_n$ was stored under argon in a glove box.

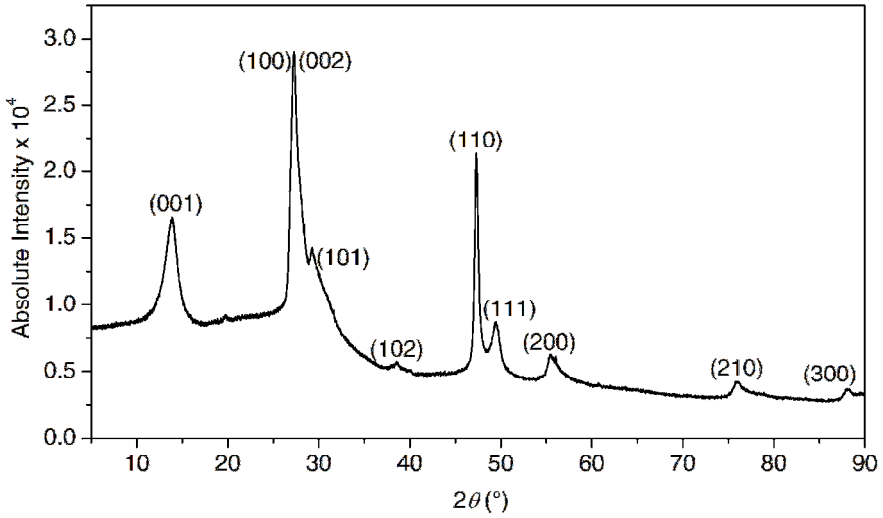

Figure S2. Powder diffraction patterns of as-synthesized SiNSs. The reflections of the regularly stacked sheets can be indexed by a hexagonal unit cell with *a* = 3.8331 Å and c = 6.3751 Å.

Etching of Silicon Nanosheets

60.0 mg of the yellow $(Si_6H_6)_n$ sheets were dispersed in EtOH/H_2O/HF (conc.) (1 mL/1 mL/1 mL) (*Caution: HF is highly dangerous and must be handled with extreme care)* and immediately extracted with 3 × 5 mL dichloromethane into PTFE centrifugation tubes. To the dispersion were then added 40 mL of toluene and the SiNSs isolated by centrifugation (9000 rpm/5 min). The supernatant was discarded and the SiNSs redispersed in 2 mL of dry toluene to remove residual traces of water. After centrifugation the SiNSs corresponding to 15 mg were dispersed in 2 mL of dry toluene (for DDB-induced functionalization) or in 1 mL of the substrate (for thermal-induced functionalization).

Functionalization of Silicon Nanosheets Without Initiator

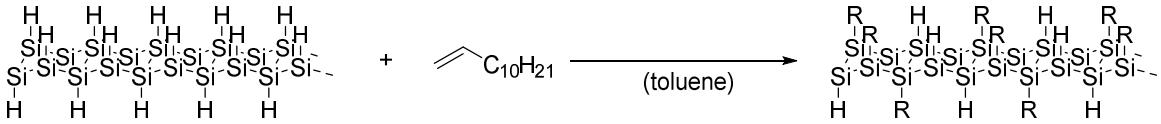

$R = C_{12}H_{25}$

2 mL of the dispersion of hydride-terminated SiNSs in dry, degassed toluene (corresponds to 15 mg exfoliated $(Si_6H_6)_n$) are transferred into a baked out schlenk tube covered with aluminum foil and 3 mmol of 1-dodecene are added. Then the reaction mixture is degassed *via* three freeze-thaw-pump cycles in the dark. After stirring over night at room temperature in the dark, the mixture is transferred into a centrifuge tube, mixed with 3 mL of ethanol and centrifuged (9000 rpm/4 min). Afterwards

the residue is twice redispersed in a minimal amount of toluene and centrifuged with 1 mL of methanol. The SiNSs were then freeze dried from benzene for further analytics.

4-Decylbenzene Diazonium Tetrafluoroborate-Induced Functionalization

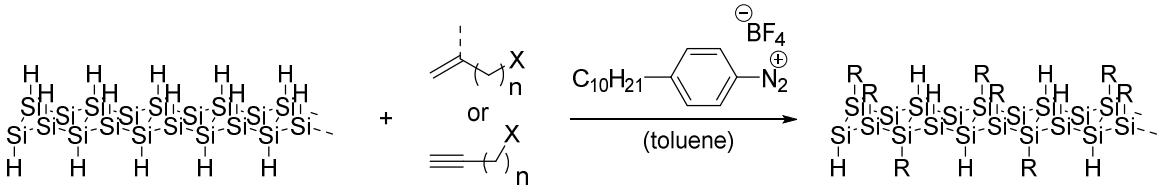

2 mL of the dispersion of hydride-terminated SiNSs in dry, degassed toluene (corresponds to 15 mg exfoliated $(Si_6H_6)_n$) were transferred into a baked out schlenk tube and 3.00 mmol of the substrate were added. Then the reaction mixture was degassed *via* three freeze-thaw-pump cycles and 5.00 mg of 4-DDB was added under argon. After stirring overnight at rt the mixture was transferred into a centrifuge tube, mixed with 3 mL of methanol (for dodecene, dodecyne, ^{t}BuMA) or pentane (for undeceneoic acid, decenol) respectively and centrifuged (9000 rpm/4 min). Afterwards the residue was twice redispersed in a minimal amount of toluene (or ethanol respectively) and centrifuged with 2 mL of the corresponding anti-solvent. The SiNSs were then redispersed in toluene (or ethanol) for further use.

Thermal Induced Functionalization

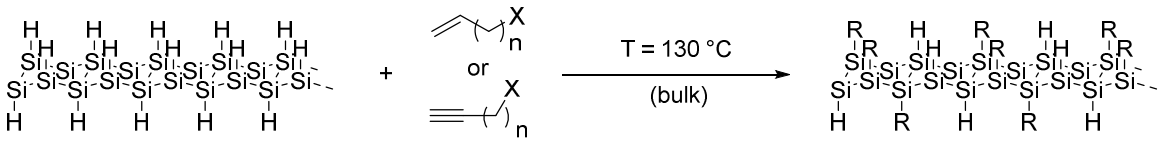

After dispersion of 15.0 mg of the hydride-terminated SiNSs in 1 mL of the substrate the reaction mixture was transferred into a baked out schlenk tube and degassed *via* three freeze-thaw-pump cycles, filled with argon and stirred at 130 °C over night. Afterwards the mixture was transferred into a PTFE centrifuge tube, mixed with 3 mL of ethanol (for dodecene, dodecyne) or pentane respectively (for undeceneoic acid, decenol) and centrifuged (9000 rpm/5 min). Then the residue was twice redispersed in a minimal amount of toluene (or ethanol respectively) and centrifuged with 2 mL of the respective anti solvent. The SiNSs were then redispersed in toluene (or ethanol) for further use.

Hydrosilylation Reactivity of Molecular Silanes

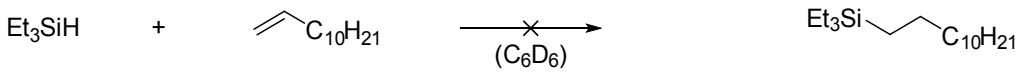

100 µL (546 µmol, 1 eq) of Et_3SiH and 655 µmol (1.2 eq) of the 1-dodecene are stirred in 1.5 mL of deuterated benzene in the glove box. After the given time an aliquot is taken for immediate ^{1}H-NMR analysis.

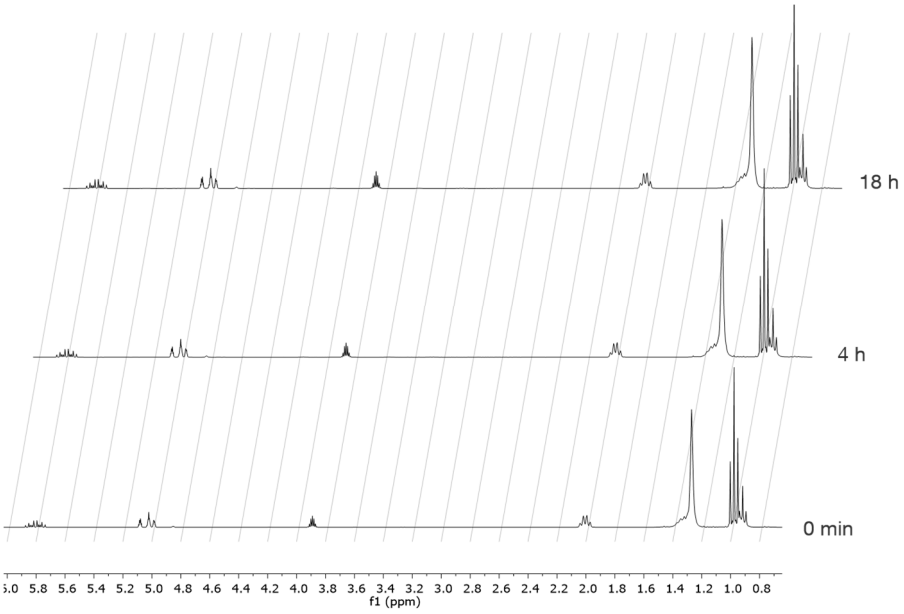

Figure S3. NMR spectra of the reaction mixture of triethylsilane with 1-dodecene after 0 min, 4 h and 18 h.

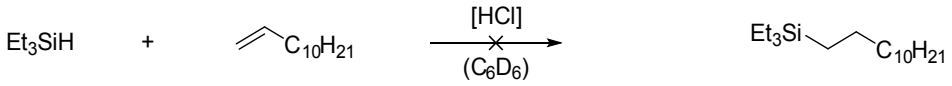

100 µL (546 µmol, 1 eq) of Et_3SiH and 655 µmol (1.2 eq) of the 1-dodecene are stirred in 1.5 mL of deuterated benzene in the glove box and 20.0 µL HCl (2.0 M in diethylether) were added. After the given time an aliquot is taken for immediate ^{1}H-NMR analysis.

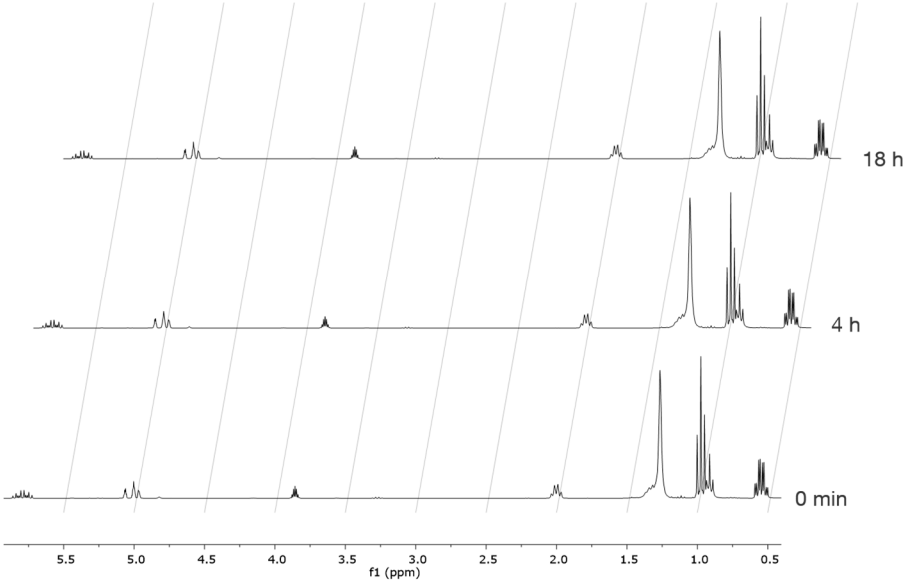

Figure S4. NMR spectra of the reaction mixture of triethylsilane with 1-dodecene and catalytic amounts of HCl after 0 min, 4 h and 18 h.

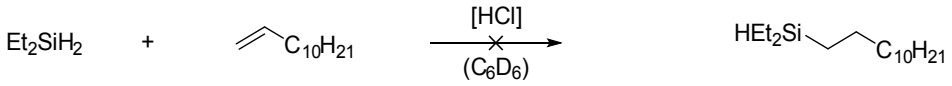

58 µL (450 µmol, 1eq) Et_2SiH_2 and 100 µL (1 eq) of the 1-dodecene are stirred in 1.5 mL of deuterated benzene in the glove box. After the given time an aliquot is taken for immediate ^{1}H-NMR analysis.

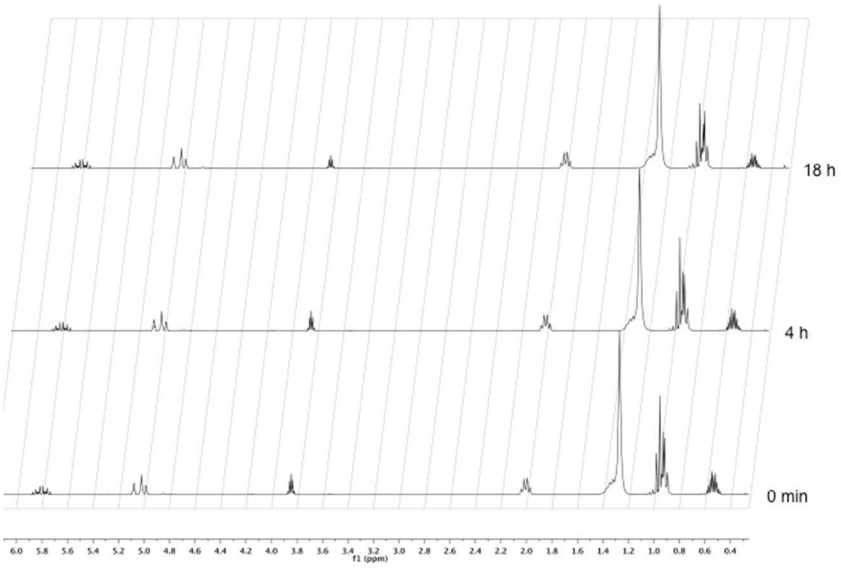

Figure S5. NMR spectra of the reaction mixture of diethylsilane with 1-dodecene after 0 min, 4 h and 18 h.

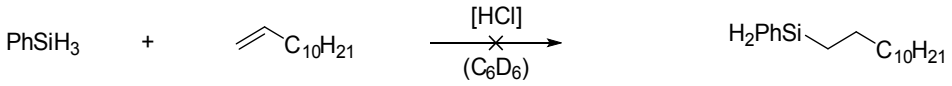

55 µL (450 µmol, 1eq) $PhSiH_3$ and 100 µL (1 eq) of the 1-dodecene are stirred in 1.5 mL of deuterated benzene in the glove box. After the given time an aliquot is taken for immediate ^{1}H-NMR analysis.

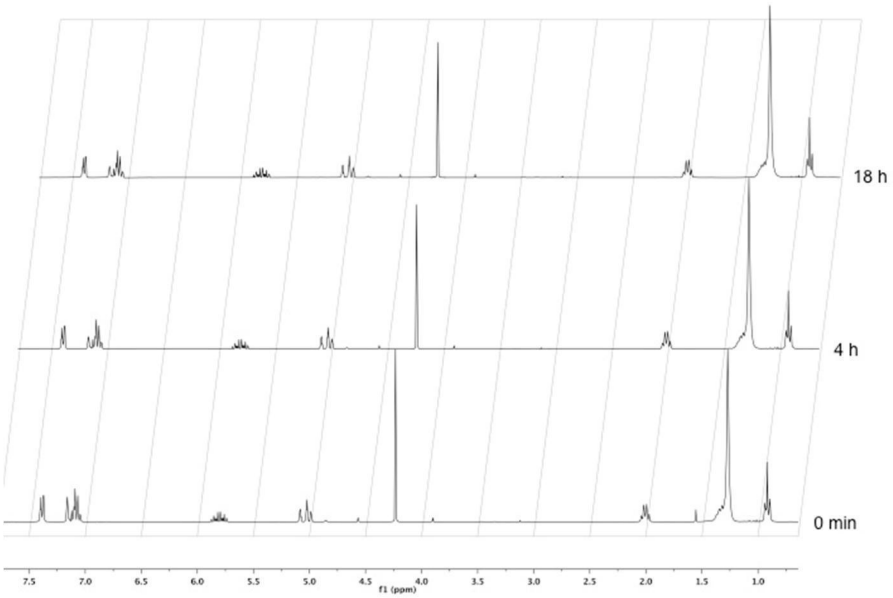

Figure S6. NMR spectra of the reaction mixture of phenylsilane with 1-dodecene after 0 min, 4 h and 18 h.

Molecular silanes cannot be reacted with 1-dodecene in the dark at room temperature (in the presence or absence of HCl) without any activation.

Figures

TGA Comparison of the Different Initiation Methods

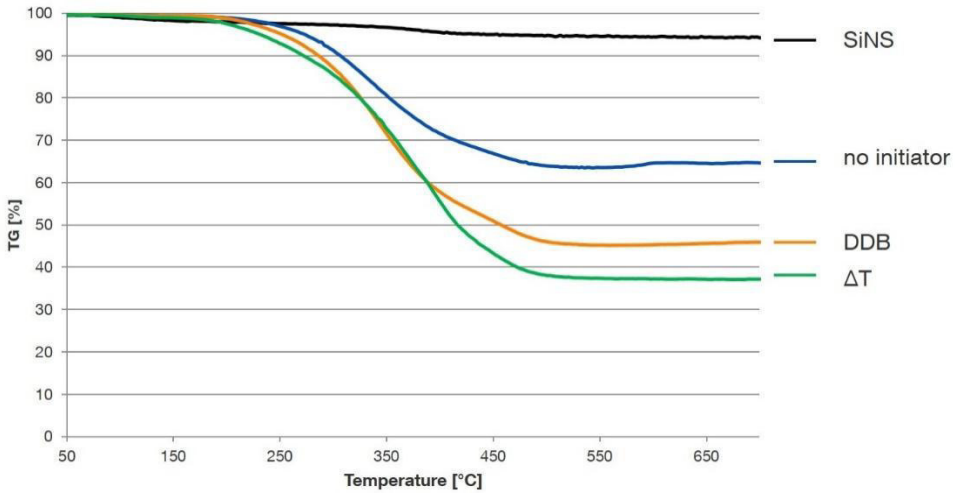

Figure S7. TGA measurements of unfunctionalized and 1-dodecene functionalized SiNSs.

XRD Patterns

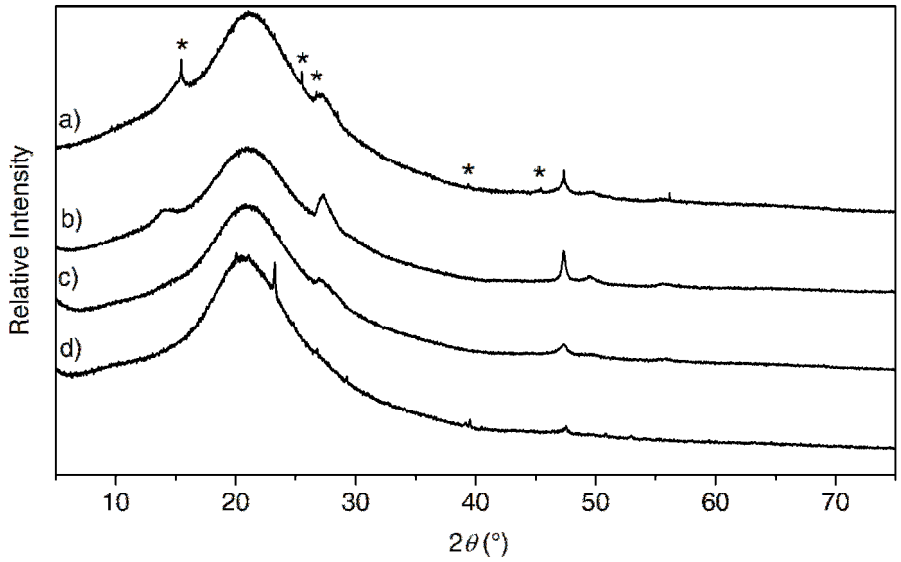

Figure S8. Powder diffraction patterns of (a) HF-etched SiNS-H, 1-dodecene functionalized SiNSs (b) without the addition of initiator (c) *via* DDB and (d) thermal initiation. Reflections marked with * correspond to traces of CaSiF6 * 2 H2O (PDF 44-0751). The increased background signal centered around 21° 2θ is caused by the silica capillaries employed.

XRD patterns recorded from the non-functionalized and 1-dodecene functionalized SiNSs show that the characteristic reflections of stacked sheets decrease significantly in intensity with the increasing content of organic material. The surface functionalization hinders the SiNSs from stacking, resulting in a less ordered material.

FTIR Spectra of Functionalized Silicon Nanosheets

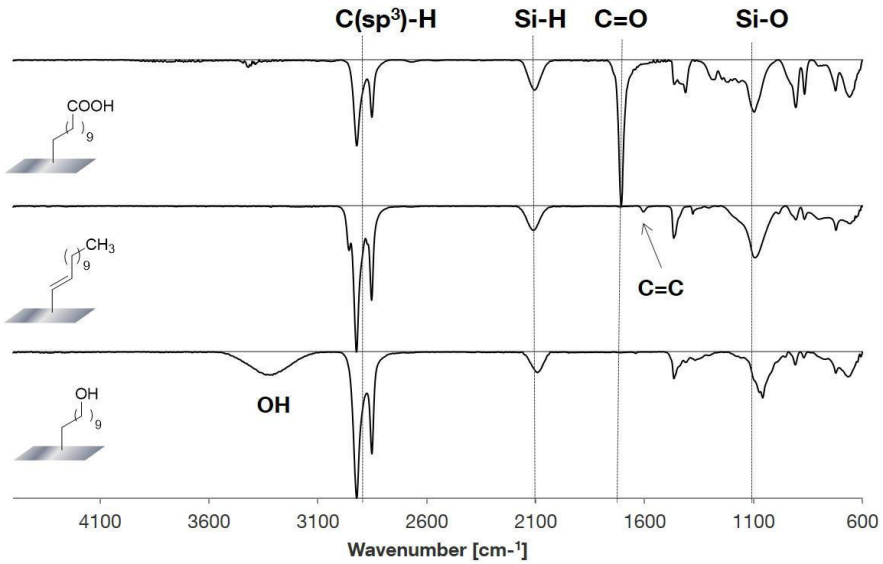

Figure S9. FTIR spectra of functionalized SiNSs *via* thermal-induced hydrosilylation.

PL Spectra

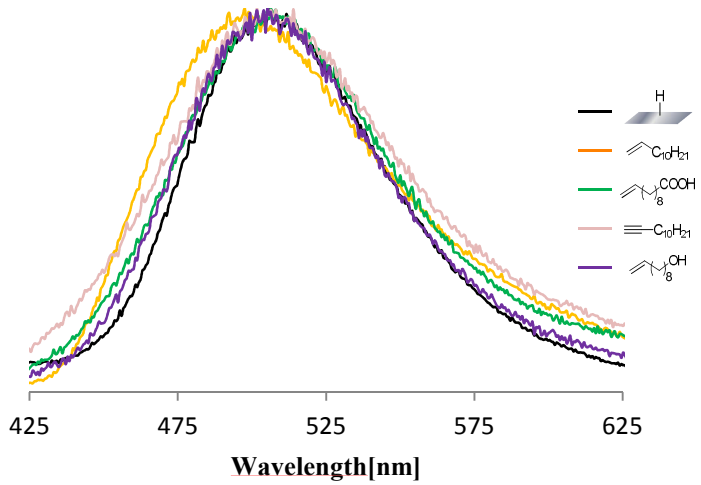

Figure S10. PL spectra of freshly etched and functionalized SiNSs via thermal-induced hydrosilylation. Excitation wavelength 365 nm.

TGA Measurements

TGA measurements were executed with the unfunctionalized SiNSs. Unfunctionalized SiNSs lose 5% of their mass as can be seen in Fig. S6. This indicates the pyrolysis of the silicon monolayers at elevated temperatures and is different from TGA measurements with silicon nanocrystals for example, which do not show any loss.[5] Additionally it can be seen that the functionalization of the sheets with organic compounds is successful and that the stability of the functionalized SiNSs is dependent on the substrates (see also Fig. S8).

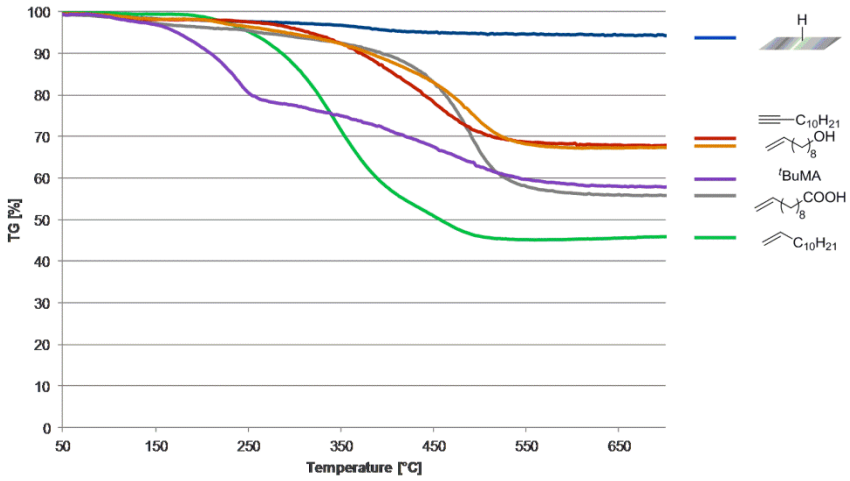

Figure S11. TGA measurements of unfunctionalized and functionalized SiNSs (4-DDB induced).

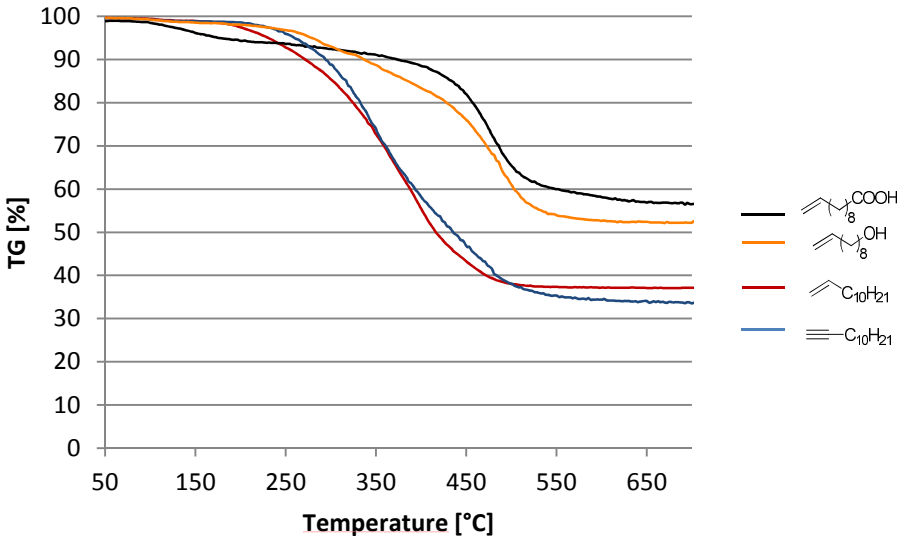

Figure S12 TGA measurements of thermally-induced functionalized SiNSs.

Table S1 TG data from functionalized SiNSs.

reagent	initiation method	weigh tloss [%]	molecular weight [g/mol]	weight loss/molecular weight
dodecene	4-DDB	54,06	169,33	0,32
	ΔT	62,88	169,33	0,37
undecenoic acid	4-DDB	44,30	185,28	0,24
	ΔT	43,48	185,28	0,23
dodecyne	4-DDB	32,08	167,31	0,19
	ΔT	47,38	167,31	0,28
decenol	4-DDB	32,71	157,27	0,21
	ΔT	47,80	157,27	0,30
tBuMA	4-DDB	42,17	143,2	0,29

Table S1 shows the ratio of weight loss/molecular weight of the attached organic substrates in order to get comparable values of how many molecules are on the surface. For the thermal initiation, higher weight loss is observed compared to 4-DDB. On silicon nanocrystals thermal initiation is known to lead to oligomerization of the substrates on the silicon surface.[6] This can be the case as well for SiNSs and as such explain the different weight loss ratios.

(1) Yu, Y.; Hessel, C. M.; Bogart, T. D.; Panthani, M. G.; Rasch, M. R.; Korgel, B. A. *Langmuir* **2013**, *29*, 1533.

(2) Cicero, R. L.; Linford, M. R.; Chidsey, C. E. D. *Langmuir* **2000**, *16*, 5688.

(3) Roduner, E. *Chem. Soc. Rev.* **2006**, *35*, 583.

(4) Pavesi, L.; Turan, R. *Silicon Nanocrystals*; Pavesi, L., Turan, R., Eds.; Wiley-VCH Verlag GmbH & Co. KGaA: Weinheim, Germany, 2010.

(5) Kehrle, J.; Höhlein, I. M. D.; Yang, Z.; Jochem, A.; Helbich, T.; Kraus, T.; Veinot, J. G. C.; Rieger, B. *Angew. Chemie Int. Ed.* **2014**, *53*, 12494.

(6) Yang, Z.; Iqbal, M.; Dobbie, A. R.; Veinot, J. G. C. *J. Am. Chem. Soc.* **2013**, *135*, 17595.

6 COMPLETE LIST OF PUBLICATIONS

Publications

[11] *Electrochemical Synthesis of the Allotrope allo-Ge and Investigations on the Use as an Anode Material*
L. M. Scherf, J. Hattendorff, I. Buchberger, S. Geier, H. Gasteiger, T. F. Fässler
Submitted.

[10] *Lewis Acid Induced Functionalization of Photoluminescent Two-Dimensional Silicon Nanosheets for the Fabrication of Functional Hybrid Films*
T. Helbich, A. Lyuleeva, P. Marx, **L. M. Scherf**, T. Purkait, T. F. Fässler, J. G. C. Veinot, P. Lugli, B. Rieger
Adv. Funct. Mat. **2017**, *accepted*.

[9] *Site-Specific Substitution Preferences in the Solid Solutions $Li_{12}Si_{7-x}Ge_x$, $Li_{12-y}Na_ySi_7$, $Na_7LiSi_{8-z}Ge_z$, and $Li_3NaSi_{6-v}Ge_v$*
L. M. Scherf, N. Riphaus, T. F. Fässler
Z. Anorg. Allg. Chem. **2016**, *642*, 1143–1151.

[8] *The Ternary Zintl Phases $K_{4-x}Na_xSi_4$ ($1 \leq x \leq 2.2$) and K_7NaSi_8 – Synthesis, Crystal Structure, and Solid State NMR Spectroscopic Investigations*
L. M. Scherf, O. Pecher, K. J. Griffith, F. Haarmann, C. P. Grey, T. F. Fässler
Eur. J. Inorg. Chem. **2016**, *2016*, 4674–4682.

[7] *One-Step Synthesis of Photoluminescent Covalent Polymeric Nanocomposites from 2D Silicon Nanosheets*
T. Helbich, A. Lyuleeva, T. Ludwig, **L. M. Scherf**, T. F. Fässler, P. Lugli, B. Rieger
Adv. Funct. Mat. **2016**, *26*, 6711–6718.

[6] *Radical-Induced Hydrosilylation Reactions for the Functionalization of Two-Dimensional Hydride Terminated Silicon Nanosheets*
T. Helbich, A. Lyuleeva, I. M. D. Höhlein, P. Marx, **L. M. Scherf**, J. Kehrle, T. F. Fässler, P. Lugli, B. Rieger
Chem. Eur. J. **2016**, *22*, 6194–6198.

[5] *Very Short $[Ge_2]^{4-}$ Dumbbell in the Zintl Phase Li_3NaGe_2 – A Solid State Equivalent to Molecular O_2*
L. M. Scherf, A. J. Karttunen, O. Pecher, P. C. M. M. Magusin, C. P. Grey, T. F. Fässler
Angew. Chem. **2016**, *128*, 1087–1091; *Angew. Chem. Int. Ed.* **2016**, *55*, 1075–1079.

Highlighted in U. Ruschewitz *Angew. Chem.* **2016**, *128*, 3320–3322; *Angew. Chem. Int. Ed.* **2016**, *55*, 3264–3266.

[4] *Alkali metal extraction reactions with the silicides $Li_{15}Ge_4$ and Li_3NaSi_6: amorphous Si vs. allo-Si*
M. Zeilinger, L. A. Jantke, **L. M. Scherf**, F. J. Kiefer, G. Neubüser, L. Kienle, A. J. Karttunen, S. Konar, U. Häussermann, T. F. Fässler
Chem. Mater. **2014,** *26*, 6603–6612.

[3] *$Li_{18}Na_2Ge_{17}$ – a Compound Demonstrating Cation Effects on Cluster Shapes and Crystal Packing in Ternary Zintl Phases*
L. M. Scherf, M. Zeilinger, T. F. Fässler
Inorg. Chem. **2014,** *53,* 2096–2101.

[2] *Implications of the Crystal Structure of the Ammonia Solvate $[Au(NH_3)_2]Cl \cdot 4NH_3$*
L. M. Scherf, S. A. Baer, F. Kraus, S. M. Bawaked, H. Schmidbaur
Inorg. Chem. **2013,** *52,* 2157–2161.

[1] *µ-Oxido-bis(pentammineisen(III))-tetrachlorid-Ammoniak(1/8), $[Fe_2(\mu\text{-}O)(NH_3)_{10}]Cl_4 \cdot 8NH_3$*
M. B. Fichtl, **L. M. Scherf**, S. A. Baer, F. Kraus
Z. Naturforsch. **2011,** *66b,* 784–792.

Conference Contributions

[4] *Alkali Metal Tetrelide Phases as Precursors for Innovative Silicon-Based Materials*
L. M. Scherf,* T. F. Fässler
Poster, 132nd BASF International Summer Course, 2016, Ludwigshafen.

[3] *Intermetallic Phases A-Si-E (A = Li, Na; E = B, Ge) as Precursors for Silicon-based Semiconductor Materials*
L. M. Scherf*
Oral presentation, mini-symposium of Fonds der chemischen Industrie scholars, 2015, München.

[2] *The First Unsubstituted Ge_2^{4-} Dimer with a True Ge=Ge Double Bond in Li_3NaGe_2 – a Solid State Analog to Molecular Oxygen*
L. M. Scherf,* A. J. Karttunen, O. Pecher, P. Magusin, M. Zeilinger, C. Grey, T. F. Fässler
Poster, GDCh Scientific Forum Chemistry 2015, Dresden.

[1] *Alkali metal extraction reactions with the silicides $Li_{15}Ge_4$ and Li_3NaSi_6: amorphous Si vs. allo-Si*
M. Zeilinger, L. A. Jantke, **L. M. Scherf**,* F. J. Kiefer, G. Neubüser, L. Kienle, A. J. Karttunen, S. Konar, U. Häussermann, T. F. Fässler
Oral presentation, 2015 MRS Spring Meeting & Exhibit, San Francisco, USA.

* presenter